

①

AGARD-LS-162

AGARD-LS-162

AD-A202 423



AGARD LECTURE SERIES No.162

**Media Effects on Electronic Systems
in the High Latitude Region**

DTIC
ELECTE
OCT 25 1988
S H D



**DISTRIBUTION AND AVAILABILITY
ON BACK COVER**

DISTRIBUTION STATEMENT A
Approved for public release
Distribution Unlimited

88 1024 172

AGARD-LS-162

NORTH ATLANTIC TREATY ORGANIZATION
ADVISORY GROUP FOR AEROSPACE RESEARCH AND DEVELOPMENT
(ORGANISATION DU TRAITE DE L'ATLANTIQUE NORD)

AGARD Lecture Series No.162
MEDIA EFFECTS ON ELECTRONIC SYSTEMS IN THE HIGH LATITUDE REGION

This material in this publication was assembled to support a Lecture Series under the sponsorship of the Electromagnetic Wave Propagation Panel of AGARD and the Consultant and Exchange Programme of AGARD presented on 29—30 September 1988 in Ottawa, Canada, on 24—25 October 1988 in Geilo, Norway and on 27—28 October 1988 in London, United Kingdom.

THE MISSION OF AGARD

According to its Charter, the mission of AGARD is to bring together the leading personalities of the NATO nations in the fields of science and technology relating to aerospace for the following purposes:

- Recommending effective ways for the member nations to use their research and development capabilities for the common benefit of the NATO community;
- Providing scientific and technical advice and assistance to the Military Committee in the field of aerospace research and development (with particular regard to its military application);
- Continuously stimulating advances in the aerospace sciences relevant to strengthening the common defence posture;
- Improving the co-operation among member nations in aerospace research and development;
- Exchange of scientific and technical information;
- Providing assistance to member nations for the purpose of increasing their scientific and technical potential;
- Rendering scientific and technical assistance, as requested, to other NATO bodies and to member nations in connection with research and development problems in the aerospace field.

The highest authority within AGARD is the National Delegates Board consisting of officially appointed senior representatives from each member nation. The mission of AGARD is carried out through the Panels which are composed of experts appointed by the National Delegates, the Consultant and Exchange Programme and the Aerospace Applications Studies Programme. The results of AGARD work are reported to the member nations and the NATO Authorities through the AGARD series of publications of which this is one.

Participation in AGARD activities is by invitation only and is normally limited to citizens of the NATO nations.

The content of this publication has been reproduced
directly from material supplied by AGARD or the authors.

Published September 1988

Copyright © AGARD 1988
All Rights Reserved

ISBN 92-835-0478-X



*Printed by Specialised Printing Services Limited
40 Chigwell Lane, Loughton, Essex IG10 3TZ*

ABSTRACT

With the advent of new systems operating at high latitudes in the field of detection, navigation and communications, and with the new experiments at high latitudes ranging from incoherent scatter studies to satellites for studying high latitude irregularity structure, it is of considerable importance to relate the advances in high latitude studies to military systems. The concept of this Lecture Series is to bring together these two areas.

The behaviour of the propagation environment at high latitudes differs from that at lower latitudes, affecting radiowave propagation across the RF spectrum. The differences are ascribed to rugged terrain, severe climatic conditions, and influences of the interplanetary and magnetospheric geophysical events which are guided earthward by the geomagnetic field.

The high-latitude ground region is characterised by a rugged terrain and by a tremendous variation in ground electrical characteristics.

The severe climatic conditions include a large daily and seasonal temperature variation, extremes of temperatures, high winds, ice accumulation, precipitation (rain, snow, ice crystals, sleet, hail), surface and elevated temperature inversions which produce large refractive gradients and ducts.

The high latitude ionosphere is affected by two major phenomena: energetic particles from the sun and from the outer magnetosphere penetrate the atmosphere and create ionisation at various altitudes; and the solar wind induces an electric field perpendicular to the magnetic field which causes ionisation drifts and thus contributes to the formation of ionisation irregularities. Some of the ionospheric propagation anomalies created include: auroral oval absorption and polar cap absorption; sporadic E, small scale irregularities (spread F) giving rise to scattering and fading phenomena and causing transionospheric amplitude and phase scintillations; effects of magnetic substorm activity, density troughs and large sheets of field-aligned ionisation.

The Lecture Series directs its attention to propagation problems and solutions for many systems. These topics include satellite communications over polar and auroral latitudes, over-the-horizon radar, low frequency propagation under high latitude conditions, remote sensing of targets and high latitude regions by active and passive EM systems and HF communications at auroral and polar latitudes. Unique lower atmospheric effects and multipath problems of importance at high latitudes are discussed.

With the NATO northern flank nations (in both the European and North American sectors) situated in the high-latitude region, with NATO air routes across the Atlantic traversing that region, and with surveillance and early-warning systems looking in the direction of the region, the propagation characteristics of the high-latitude region are of critical importance to the mission of the alliance in the areas of communications, navigation and surveillance.

This Lecture Series, sponsored by the Electromagnetic Wave Propagation Panel of AGARD, has been implemented by the Consultant and Exchange Programme of AGARD.

Compte tenu de l'arrivée de nouveaux systèmes de détection, de navigation et de transmission, fonctionnant aux hautes latitudes, et des études expérimentales réalisées dans différents domaines, allant de la dispersion incohérente aux satellites destinés à l'étude de la structure des irrégularités des milieux de propagation, l'établissement de rapports entre les progrès réalisés dans ce domaine et les systèmes militaires est d'une importance considérable. L'objet de ce Cycle de Conférences est de réunir ces deux domaines.

Le comportement de l'environnement de propagation aux hautes latitudes est différent de celui aux autres latitudes. Il affecte la propagation radioélectrique sur tout le spectre HF. Ces différences peuvent être attribuées à des accidents de terrain, à des conditions climatiques sévères et à l'influence des phénomènes géophysiques de la magnétosphère et aux phénomènes interplanétaires, qui sont attirés vers la terre par le champ géomagnétique.

La zone terrestre des régions arctiques est caractérisée par un terrain accidenté et par des variations énormes dans les caractéristiques électriques du sol.

Les conditions climatiques sévères comprennent les écarts importants de température journaliers et saisonniers, des limites de température extrêmes, des vents forts, de l'accumulation de glace, neige fondue, grêle) et des inversions de température en surface et en altitude, qui créent des gradients de réfraction accentués et des ducts.

L'ionosphère aux hautes latitudes est perturbée par ces deux phénomènes: les particules énergétiques en provenance du soleil et de la magnétosphère supérieure pénètrent l'atmosphère et ionisent les couches aux différentes altitudes; le vent solaire induit un champ électrique perpendiculaire au champ magnétique qui provoque des dérives d'ionisation, contribuant ainsi à la formation d'irrégularités d'ionisation. Parmi les anomalies de propagation ionosphériques créées on constate: l'absorption aurorale ovale, l'absorption par la calotte polaire, une couche E sporadique; des petites irrégularités (F diffus) qui engendrent des phénomènes de dispersion et d'affaiblissement et provoquent des scintillations de phase et d'amplitude.

transionosphériques, les perturbations causées par les sous-orages magnétiques, les creux d'ionisation et les grands noyaux d'ionisation, alignés sur le champ magnétique.

Ce cycle de conférences porte sur les problèmes de propagation et leurs solutions pour un grand nombre de systèmes. Les sujets discutés comprennent les communications par satellite aux latitudes polaires et aurorales, les systèmes radar transhorizon, la propagation à basse fréquence dans la zone arctique, la télédétection de cibles et de régions aux hautes latitudes au moyen de systèmes EM et les transmissions RF aux latitudes polaires et aurorales. Les phénomènes spécifiques à la basse atmosphère et certains problèmes créés par les trajets multiples, qui revêtent une importance particulière aux hautes latitudes, sont également discutés.

Les caractéristiques de propagation des régions aux hautes latitudes sont d'une importance primordiale pour la mission de l'Alliance dans les domaines des communications, de la navigation et de la surveillance, compte tenu du fait que les nations membres de l'OTAN du flanc nord tant en Europe qu'en Amérique du Nord se trouvent dans des régions aux hautes latitudes, que les routes aériennes de l'OTAN transatlantiques survolent ces régions et que les systèmes de surveillance et d'alerte lointaine sont orientés dans cette direction.

Ce Cycle de conférences est présenté dans le cadre du Programme des Consultants et des Echanges, sous l'égide du Panel AGARD sur la propagation des ondes électromagnétiques.

LIST OF AUTHORS/SPEAKERS

Lecture Series Director: Dr H. Soicher
 Center for Command Control & Comm. Systems
 US Army Communications-Electronics Command
 ATTN: AMSEL-RD-C3-TA-1
 Fort Monmouth, N.J. 07703-5202
 United States

AUTHORS/SPEAKERS

Dr Pierre Bauer
 CNRS
 Directeur du Service d'Aeronomie
 B.P.N. 3
 91371 Verrières le Buisson
 France

Dr J. Belrose
 Communications Research Center
 Department of Communications
 P.O. Box 11490, Station H
 Ottawa, K2H 8S2
 Canada

Dr Edward Fremouw
 NW Research Assoc., Inc.
 P.O. Box 3027
 Bellevue, WA 98009
 USA

Dr Dag T. Gjessing
 NTNF/PPM
 P.O. Box 25
 N-2007 Kjeller
 Norway

Dr John K. Hargreaves
 Lune Cottage
 Hornby, Lancaster LA2 8LL
 United Kingdom

Prof. Helmut Jeske
 University of Hamburg
 Meteorologisches Institut der Universität
 Bundesstrasse 55
 D-2000 Hamburg 13
 Germany



Accession For	
NTIS GRA&I	<input checked="" type="checkbox"/>
DTIC TAB	<input type="checkbox"/>
Unannounced	<input type="checkbox"/>
Justification	
By _____	
Distribution/	
Availability Codes	
Dist	Avail and/or Special
A-1	

CONTENTS

	Page
ABSTRACT	iii
LIST OF SPEAKERS	iv
	Reference
MEDIA EFFECTS ON ELECTRONIC SYSTEMS IN THE HIGH LATITUDE REGION by H.Soicher	1
THE HIGH-LATITUDE IONOSPHERE: GEOPHYSICAL BASIS by J.K.Hargreaves	2
TRANSIONOSPHERIC PROBING AND PROPAGATION by E.Fremouw	3
GROUND/LOWER ATMOSPHERIC CONSIDERATION by H.Jeske	4
HF COMMUNICATIONS AND REMOTE SENSING IN THE HIGH LATITUDE REGION by J.S.Belrose	5
HF RADAR PROBING (INCLUDING MODIFICATION) by P.Bauer	6
THE HIGH-LATITUDE IONOSPHERE: DYNAMICAL ASPECTS, AND MODELS by J.K.Hargreaves	7
SATELLITE IN-SITU PROBING by E.Fremouw	8
INCOHERENT/COHERENT SCATTER by P.Bauer	9
PROPAGATION MEDIUM ADAPTIVE TECHNIQUES FOR ADVERSE COMMUNICATIONS AND FOR REMOTE SENSING by D.T.Gjessing	10
BIBLIOGRAPHY	B

MEDIA EFFECTS ON ELECTRONIC SYSTEMS IN THE HIGH LATITUDE REGION

Haim Soicher

Center for C3 Systems
US Army Communications-Electronics Command
Fort Monmouth, NJ 07703-5202

ABSTRACT

The behavior of the propagation environment at high latitudes differs from that at lower latitudes, affecting radiowave propagation across the RF spectrum. The differences are ascribed to rugged terrain, severe climatic conditions, and influences of the interplanetary and magnetospheric geophysical events which are guided earthward by the magnetic field. [AGARD, 1985]

The high-latitude ground region is characterized by a rugged terrain and by a tremendous variation in ground electrical characteristics.

The severe climatic conditions include a large daily and seasonal temperature variation, extremes of temperatures, high winds, ice accumulation, precipitation (rain, snow, ice crystals, sleet, hail), surface and elevated temperature inversions which produce large refractive gradients and ducts.

The high latitude ionosphere is affected by two major phenomena: energetic particles from the sun and from the outer magnetosphere penetrate the atmosphere and create ionization at various altitudes, and the solar wind induces an electric field perpendicular to the magnetic field which causes ionization drifts and thus contributes to the formation of ionization irregularities. Some of the ionospheric propagation anomalies created include: auroral oval absorption and polar cap absorption; sporadic E, small scale irregularities (spread F) giving rise to scattering and fading phenomena and causing transionospheric amplitude and phase scintillations; effects of magnetic substorm activity, density troughs and large sheets of field-aligned ionization.

The Lecture Series will direct its attention to propagation problems and solutions for many systems. These topics include satellite communications over polar and auroral latitudes, over-the-horizon radar, low frequency propagation under high latitude conditions, remote sensing of targets and high latitude regions by active and passive EM systems and HF communications at auroral and polar latitudes. Unique lower atmospheric effects and multipath problems of importance at high latitudes will be discussed.

Introduction

The optimum path of electromagnetic waves is through a vacuum. Since nature has not provided for such a luxury, the propagation medium which separates transmitter and receiver in a communications system, or a remote sensing system from its target influences electromagnetic waves in a number of ways. As a matter of fact, the propagation medium, be it the earth's surface, the lower atmosphere, the ionosphere or the space environment controls the operational characteristics and capabilities of communications, navigation and surveillance systems. The medium may be a vehicle to achieve desired goals, e.g. long range HF communication/remote sensing by ionospheric reflection, or it may pose fundamental limitation on ultimate system performance, e.g. signal attenuation by gaseous absorption in the atmosphere. Since the propagation medium is variable in both space and time, the system design challenge is to adapt to changing conditions in an optimal way. This is especially significant since systems are becoming more complex and are expected to operate under a wide variety of natural and man-made stressful conditions.

The high latitude region is certainly a "stressful" environment for electromagnetic wave propagation. Many of the main media effects on propagation, i.e., attenuation, reflection/refraction, polarization/frequency changes, diffraction, multipath, ducting and time delay, are especially significant in the high latitude region. As such, adaptability of system design to changing medium is particularly difficult.

Ground Wave Propagation

The earth's surface will absorb, reflect, diffract and scatter radio waves. An important parameter relevant to the transmission of ground waves is ground conductivity. The effective conductivity will depend upon vegetation, moisture content of the soil, terrain, geological structure, permafrost, snow and ice cover, etc.

In the high latitude region, the conductivity can vary by orders of magnitude while relative permittivity can vary by two orders of magnitude. For example, soft new snow may have as low conductivity as 10^{-11} to 3×10^{-11} Siemens/meter (at -10°C to -40°C , respectively), and is thus a rather good insulator. Sea ice (0.5% salinity) may have conductivity of 10^{-3} to 10^{-4} S/m (at -7°C to -24°C). The penetration depth, characterizes the ability of radio waves to penetrate the medium. It is the depth where the field strength has fallen to $1/e$ of its surface value. The skin depth is inversely proportional to the square root of the product of the conductivity and the operating frequency. At 100 kHz the penetration depth for sea water (5 S/m) is about 0.7 meters. With a layer of ice of 10 meters (3×10^{-4} S/m) the wave's surface field strength has been reduced only by 10%. It appears that about the same communication conditions exist with a submarine under a layer of ice as just under the sea level.

Recent investigations aimed at mapping the ground conductivity at high latitude have indicated the difficulty of such an effort. Ground conductivity in permafrost areas is heterogeneous and variable (in space and season), and thus an effective conductivity may not be assigned to a path of practical length.

Tropospheric Propagation

The propagation of radio waves is influenced by the atmosphere's refractive index, which may be expressed in terms of the atmospheric partial pressure, temperature and humidity. At the region near the receiver the signal path loss is dominated by the interference between the direct signal and surface reflected signal. The depth of the interference nulls depends on the surface reflecting roughness. Near the radio horizon the path loss is dominated by diffraction around the Earth's surface. The diffraction region is characterized by the ability of the radio wave to travel along the interface of dissimilar materials (earth's surface and atmosphere). At ranges far beyond the horizon, the path loss is dominated by tropospheric scatter, a mechanism by which EM energy is scattered from refractive heterogeneities at relatively high altitudes. At frequencies above 10 GHz gaseous absorption by oxygen and water vapor molecules is of importance. The first gaseous resonance is at 22 GHz (from water vapor). Such resonances (absorption peaks) offer limitation on communication ranges of frequencies but offer secure communication at available short ranges. Hydrometeors (principally rain) are of importance in attenuation of frequencies above 5 GHz and in the scattering of EM energy.

Anomalous propagation mechanisms are all associated with abnormal distribution of the refractive index. Depending on refractivity gradients, electromagnetic waves may be propagated via the subrefractive, standard, superrefractive, or trapping (ducted) modes; the latter may include surface-based ducts, elevated ducts or evaporation ducts. Such ducts offer the possibility of greatly extended detection ranges for radars (but also intercept) as well as opportunities for extended range communication (but also jamming).

High latitude regions are significantly different from the equatorial and temperate regions in that they have steeper surface temperature inversions during winter over large areas. Such inversions produce gradients and ducts and thus affect radio wave propagation.

Another tropospheric effect, especially at high frequencies, is precipitation. At high latitudes water precipitates as snow, ice crystals, rain, sleet and occasionally hail. Signal attenuation of radio signal traversing precipitation can be caused by absorption and/or scatter and by depolarization.

Ionospheric Propagation

The behavior of the ionosphere at high latitudes is characterized by its complex structure and extreme variability, mainly because it is exposed to the influence of disturbances in the interplanetary space and in the magnetosphere. The pressure of the solar wind confines the earth's magnetic field to a finite volume called the magnetosphere. At high latitudes geomagnetic field lines lead far from the earth, either to the outer magnetosphere or to interplanetary space. Charged particles from the sun or outer magnetosphere are guided earthwards towards the high latitudes and thus perturb the local ionosphere.

There are two major types of ionospheric influences brought about by interplanetary and magnetospheric events. The first involves energetic particles from the sun and outer magnetosphere which penetrate the atmosphere and create ionization at various altitudes, depending on the penetrating energy of the particles. The second involves a dynamo effect created by the blowing of the solar wind across the geomagnetic field lines. Besides accelerating some of the charged particles to high energy, the dynamo induces an electric field perpendicular to the magnetic field which causes ionization in high latitudes to drift horizontally and contributes to the formation of irregularities.

The important effects of the high latitude ionosphere on the performance of systems include:

- High energy charged particles (>20 keV electrons; ~10 MeV protons) penetrate to D-region heights and create extra ionization thereby increasing wave attenuation, sometimes causing blackouts.
- Lesser energy charged particles penetrate E- and F- region altitudes and create reflecting layers or produce irregular enhancement of electron densities.
- The F-region almost always contains small scale irregularities that scatter HF waves and which cause scintillations on transionospheric signals at VHF and above. These irregularities are due to precipitation at some places, but elsewhere may be due to plasma instabilities associated with electric fields.
- Variation in total electron content affect propagation time delay and, thus, affect ranging and satellite navigation systems.
- The produced electric field, along with aurorally produced ionization, gives rise to E-region irregularities that scatter radio energy at HF, VHF and UHF.

Conclusions

The uniqueness, variability and complexity of the high latitude propagation environment and its effects on radio systems is the subject of this lecture series. Modern technology and state-of-the-art research will permit communications/navigation/surveillance systems to adapt to the complex and rapidly changing medium. However, such adaptability depends to a large extent on:

- Improvement of prediction of auroral, ionospheric and magnetic disturbances.
- Understanding of the mechanisms responsible for the formation of ionospheric inhomogeneities and the propagation related effects.
- Obtaining long-term data base, and maintaining real time information flow on the natural electromagnetic and particle radiation background.

References

"Propagation Effects on Military Systems in the Hight Latitude Region,"
Ed. H. Soicher, AGARD-CP-382, 1985

THE HIGH-LATITUDE IONOSPHERE : GEOPHYSICAL BASIS

Dr. J.K. Hargreaves

Senior Research Fellow, Department of Environmental Science, University of Lancaster,
Lancaster LA1 4YQ, England.

1. P" POSE

This introductory lecture summarizes concepts of the ionosphere and the magnetosphere that are fundamental to our understanding of the high-latitude ionosphere. It begins with the basic theory of the ionosphere, particularly the processes of production and loss which lead to the existence of a permanent ionosphere and render the upper atmosphere electrically conducting. The structure of the magnetosphere, which strongly affects the polar regions because of coupling along the geomagnetic field lines, is then reviewed, including the form of the magnetosphere, and the plasma and energetic particles that are contained within the magnetosphere.

2. PRINCIPLES OF THE IONOSPHERE

2.1 Introduction

The ionized part of the atmosphere, the *ionosphere*, contains significant numbers of free electrons and positive ions. There are also some negative ions at the lower altitudes. The medium as a whole is electrically neutral, there being equal numbers of positive and negative charges within a given volume. Although the charged particles may be only a minority amongst the neutral ones they exert a great influence on the medium's electrical properties, and herein lies their importance.

The first suggestion of electrified layers within the higher levels of the terrestrial atmosphere go back to the 19th Century, but interest was regenerated with Marconi's well known experiments to transmit a radio signal from Cornwall to Newfoundland in 1901, and with the subsequent suggestions by Kennelly and by Heaviside (independently) that, because of the Earth's curvature, the waves must have been reflected from an ionized layer. The name "ionosphere" was coined by R. Watson-Watt in 1926, and came into common use about 1932.

Since that time the ionosphere has been extensively studied and most of its principle features, though not all, are now fairly well understood in terms of the physical and chemical processes of the upper atmosphere. Typical vertical structures are as shown in Figure 1. The identification of the regions was much influenced by their signatures on ionograms which tend to emphasize inflections in the profile, and it should be appreciated in particular that the various layers may not be separated by distinct minima. The main regions are designated D, E, F1 and F2, with the following daytime characteristics:-

D region, 60-90 km: $10^8 - 10^{10} \text{ m}^{-3}$ ($10^2 - 10^4 \text{ cm}^{-3}$)
 E region, 105-160 km: several 10^{11} m^{-3} (10^5 cm^{-3})
 F1 region, 160-180 km: several $10^{11} - 10^{12} \text{ m}^{-3}$ ($10^5 - 10^6 \text{ cm}^{-3}$)
 F2 region, maximum variable around 300 km: up to several 10^{12} m^{-3} (10^6 cm^{-3}).

The D and F1 regions vanish at night, and the E region becomes much weaker. The F2 region, however, tends to persist though at reduced intensity.

2.2 Physical aeronomy

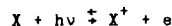
2.2.1 Principles

The ionosphere is formed by the ionization of atmospheric gases such as N_2 , O_2 and O . The energy comes from various sources, the most important globally being solar radiation in the Extreme Ultra-Violet (EUV) and X-ray parts of the spectrum. Once formed, the ions and electrons tend to recombine and to react with other gaseous species to produce other ions. Thus there is a dynamic equilibrium in which the net concentration of free electrons (which, following standard practice, we shall call the *electron density*) depends on the relative speed of the production and loss processes. In general terms the rate of change of electron density is expressed by a *Continuity Equation*:

$$\frac{dN}{dt} = q - L - \text{div}(N\mathbf{v}) \quad (1)$$

where q is the production rate, L the loss rate by recombination, and $\text{div}(N\mathbf{v})$ expresses the loss of electrons by movement, \mathbf{v} being their mean drift velocity. Plainly, one has to go into the details of these processes to understand the details of ionospheric formation, but a good deal can be learned from purely physical considerations that do not involve the details of the photochemistry. This is the approach of "Physical Aeronomy".

Following the "law of mass action", if we consider an ionization and recombination reaction:



then at equilibrium $[X][h\nu] = \text{const.} [X^+][e]$.
 Thus, since $[e] = [X^+]$ for electrical neutrality,
 $[e] = \text{const.} [X][h\nu]/[X^+]$.

During the day the intensity of ionizing radiation varies with the elevation of the Sun, and the electron density responds. At night the source of radiation is removed and the electron density decays. From this simple model one can also see that the ionosphere must vary with altitude, for the concentration of ionizable gas reduces with increasing height while the intensity of ionizing radiation increases. It is reasonable to anticipate from this that the electron density will pass through a maximum at some altitude.

2.2.2 The Chapman production function

The rate of production of ion-electron pairs can be expressed as the product of four terms:

$$q = \eta \sigma n I. \quad (2)$$

Here, I is the intensity of ionizing radiation at some level of the atmosphere and n is the concentration of atoms or molecules capable of being ionized by that radiation. For an atom or molecule to be ionized it must first absorb radiation, and the amount absorbed is expressed by the *absorption cross-section*, σ : if the flux of incident radiation is I (Joules/m²-s) then the total energy absorbed per unit volume of the atmosphere per unit time is $\sigma n I$. However, not all this energy will go into the ionization process, and the *ionization efficiency*, η , takes that into account, being the fraction of the absorbed radiation that goes into producing ionization.

From this simple beginning S. Chapman, in 1931, developed a formula which predicts the form of a simple ionospheric layer and of its variations with the time of day. At this stage we deal only with the rate of production of ionization (q), and the formula expressing this is the *Chapman Production Function*. The derivation makes some assumptions:-

- (a) the atmosphere is composed of a single species, exponentially distributed with constant scale height;
- (b) the atmosphere is plane stratified: there are no variations in the horizontal plane;
- (c) solar radiation is absorbed in proportion to the concentration of gas particles;
- (d) the absorption coefficient is constant: this is equivalent to assuming monochromatic radiation.

The Chapman production function is usually written in a normalized form as

$$q = q_{m0} \exp(1 - z - \sec \chi \cdot e^{-z}). \quad (3)$$

Here, z is the reduced height for the neutral gas, $z = (h - h_{m0})/H$, H being the scale height. χ is the solar zenith angle. h_{m0} is the height of maximum production rate when the Sun is overhead ($\chi = 0$) and q_{m0} is the production rate at h_{m0} , also when the Sun is overhead. Equation (3) can also be written

$$q/q_{m0} = e \cdot e^{-z} \cdot e^{-\sec \chi \cdot e^{-z}} \quad (4)$$

where the first term is a constant, the second expresses the height variation of the density of ionizable atoms, and the third is proportional to the intensity of the ionizing radiation.

The formula can be proved as follows. Referring to Figure 2, the intensity is given by $I = I_{\infty} e^{-\tau}$ where τ , the *optical depth* is the absorption coefficient times the number of absorbing atoms in a unit column down to the level being considered. I_{∞} is the intensity at a great height, effectively outside the atmosphere. Thus

$$\tau = \sigma(nH \sec \chi). \quad (5)$$

In an exponential atmosphere $n = n_0 e^{-z}$, n_0 being the particle concentration at the level where $z=0$. Thus we see that $q \propto e^{-z} \cdot e^{-K \exp(-z)}$, $K (= \sigma n_0 H \sec \chi)$ being independent of height.

By differentiating q with respect to z it is readily shown that q passes through a maximum when $K \cdot e^{-z} = 1$; that is, the production rate is greatest at the level where the optical depth is unity. This is a useful general result. Further, from Equation (5), $n = 1/\sigma H \sec \chi$. Putting $\sec \chi = 1$ (for overhead Sun) we obtain $n_{m0} = 1/\sigma H$ for the concentration of ionizable atoms at the level of maximum ion production when $\chi = 0$.

The production rate at this level is

$$q = \eta \sigma n I = \eta \sigma n_{m0} I_{\infty} e^{-1}. \quad (6)$$

Writing $n = n_{m0} e^{-z}$ in general, we obtain for the production rate at any level,

$$q = n n_{m0} e^{-z} I_{\infty} e^{-\sigma n_{m0} e^{-z}}.$$

The following properties of the Chapman production function are worth noting.

(a) The general shape of the production rate curves plotted in Figure 3. At a great height, where z is large and positive, $q \rightarrow q_{m0} e^{-z}$. Thus the curves merge above the peak, becoming independent of χ and showing an exponential decrease with height due to the reducing density of the neutral atmosphere. In the region well below the peak, when z is large and negative, the shape becomes dominated by the last term of Equation 4, producing a rapid cut-off. The production rate is limited by a shortage of ionizable gas at the greater altitudes and by a lack of ionizing radiation low down. On a plot of $\ln(q)$ against z all the curves are the same shape, but are displaced upward and to the left as the zenith angle, χ , increases.

(b) As proved above, the production rate maximizes where the optical depth is unity. An expression for the maximum production rate follows from Equations 4 and 6, giving

$$q_{m0} = n I_{\infty} / eH \text{ when } \chi = 0,$$

or, in the more general case of any solar zenith angle,

$$q_m = n I_{\infty} / eH \sec \chi. \quad (7)$$

(c) By differentiating Equation 3 it is readily proved that

$$z_m = \ln(\sec \chi) \quad (8)$$

where z_m is the reduced height of maximum production (the height at $\chi = 0$ being taken as zero). Substituting back into Equation 3 gives

$$q_m = q_{m0} \cos \chi \quad (9)$$

(essentially like Equation 7). These simple results are important in studies of the ionosphere because the maximum of a layer is the part most readily observed. From Equations 8 and 9 we see that a plot of $\ln(q_m)$ against z_m is effectively a plot of $\ln(\cos \chi)$ against $\ln(\sec \chi)$, obviously a straight line of slope -1. This line is shown in Figure 5.

The Chapman production function is important because it expresses fundamentals of ionosphere formation and of radiation absorption in any exponential atmosphere. Although real ionospheres may be more complicated, the Chapman theory provides an invaluable reference point for interpreting observations and a relatively simple starting point for ionospheric theory.

2.2.3 Ionization by energetic particles

The other source of ionization in the terrestrial ionosphere is energetic particles, which are not entirely absent at middle latitudes but are much more important at high latitudes where they frequently provide the dominant source of ionization. Two sources of major significance at high latitude are electrons associated with the aurora, and protons and, to a lesser extent, alpha particles emitted from solar flares.

Various methods have been used to calculate the rate of ion production by a stream of energetic electrons arriving from some source above the atmosphere. The most generally useful one relies on laboratory measurements of the range of electrons in air. The range, r_0 , is principally determined by the loss of energy due to excitation and ionization as an electron collides with the atoms and molecules in the neutral atmosphere. The total loss depends on the total number of gas particles encountered, and so the distance travelled varies in inverse proportion to the gas pressure.

An energetic particle entering the atmosphere from above travels into a medium of increasing density, and the altitude, h_p , to which it penetrates is such that the product of pressure and distance, integrated above h_p , is equal to the range r_0 . Obviously, this particle will ionize only above height h_p , and the total number of ion-electron pairs produced will depend on $E/\Delta E$ where E is the initial energy of the particle and ΔE is the energy required for each ionization (35 eV). We then have to take into account the distribution of ion production along the path, which is a function of the particle velocity. This is again done using results from laboratory experiments, expressed in terms of the atmospheric depth (the total mass of gas in a column of unit cross-section along the path of the particle, which in the atmosphere is the product of density and distance integrated down to h_p) in the form of an efficiency λ , a function of (z/R) , where z and R are the atmospheric depths at a point on the path and at the penetration altitude respectively.

The ion-electron production rate at depth z can be shown to be given by

$$q_z = \frac{E}{r_0 \Delta E} \lambda \left[\frac{z}{R} \right] \frac{n(z)}{n(R)}. \quad (10)$$

If the incident particles are mono-directional λ is maximum at $z/R = 0.4$. If the electrons arrive over a range of angles, as would be the case in the auroral regions, some

particles travel in a spiral path and thus cover a greater distance; in this case λ maximizes at a smaller value of z/R such as 0.1 or 0.2.

Figure 4 shows calculated production rates in a model atmosphere due to monoenergetic electrons of various initial energies. For a realistic spectrum of particles the production rate must be integrated over energy. The height of maximum production as a function of energy is given by Figure 5.

Significant ionization may also be caused by energetic protons, especially at high latitudes during *polar cap events* caused by proton fluxes released at the time of a solar flare. A lesser flux of alpha particles will generally arrive simultaneously. These particles, significantly more energetic than the auroral electrons discussed above, lose energy in colliding with the atmospheric gas and leave ionized trails. The gas concerned is principally that of the mesosphere with essentially the same composition as the troposphere, and the rate of energy loss in such a gas is well known from laboratory measurements. A graph showing the rate of energy loss against the distance travelled is called a *Bragg curve*. In the energy range of present concern the loss rate increases as the proton slows down because it then spends a longer time near each air molecule. Over the range 10-200 MeV the loss rate is almost inversely proportional to the energy, a typical value being 0.8 MeV/m of path in air at standard temperature and pressure when the energy is 100 MeV. The energy may be assumed to be used entirely in creating ion-electron pairs, each requiring about 35 eV.

A proton entering the atmosphere from space meets an atmosphere of increasing density, and, combined with the nature of the Bragg curve, this means that the ionization is very concentrated towards the end of the path; for example, a vertically incident 50 MeV proton loses half its energy in the last 2.5 km of the path and the last 10 percent in only 100 m. One consequence is that the penetration level does not depend strongly on the angle of incidence except near 90°. The altitudes at which protons and alpha particles of various energy stop are shown in Figure 6, and the production rate profiles for protons of different initial energy are given in Figure 7. For a given spectrum of energies the total effect would be calculated by appropriate summing over these curves at each height.

The same curves can be applied to alpha particles because they have almost the same range as protons of the same velocity, but the ionization rate is four times as great. Thus, for an alpha particle of 400 MeV we would use the 100 MeV curve of Figure 7 but multiply the production rates by four. This trick may be used down to energies of a few MeV.

2.2.4 Ion loss by recombination

Working out the rate of electron production is just the first step in calculating the electron density in an ionized layer, and the next step is to reckon the rates at which electrons are removed from the volume under consideration. These are represented in the continuity equation (1) by two further terms, one for the recombination between ions and electrons to reform neutral particles, and the other to account for movement of plasma into or out of the volume. We now deal with the principles of recombination.

First we assume that the electrons recombine directly with positive ions and that no negative ions are present: $X^+ + e \rightarrow X$. Then the rate of electron loss is

$$L = \alpha [X^+] N = \alpha N^2 \quad (11)$$

where N is the electron density (equal to the ion density $[X^+]$) and α is the recombination coefficient. At equilibrium, therefore,

$$q = \alpha N^2. \quad (12)$$

Taking the production rate q from the Chapman production function (Equation 3), we obtain

$$N = N_{m0} \exp\left\{\frac{1}{2}(1 - z - \sec \chi) e^{-z}\right\} \quad (13)$$

in which $z = (h - h_0)/H$. And from Equation 9 it is seen that the electron density at the peak of the layer varies as $\cos^{\frac{1}{2}} \chi$:

$$N_m = N_{m0} \cos^{\frac{1}{2}} \chi. \quad (14)$$

A layer with these properties is called an α -Chapman layer.

In the lower ionosphere there are also significant numbers of negative ions. Electrical neutrality now requires $N_e + N_- = N_+$, where N_e , N_- and N_+ are respectively the concentrations of electrons, negative ions and positive ions. Since the negative and positive ions may recombine with each other the overall balance between production and loss is now expressed by

$$q = \alpha_e N_e N_+ + \alpha_i N_- N_+ \quad (15)$$

α_e and α_i being recombination coefficients for the reactions of positive ions with electrons and negative ions respectively. The ratio between negative ion and electron

concentrations is traditionally represented by λ which in this instance has nothing to do with wavelength! In terms of λ , $N_- = \lambda N_e$ and $N_+ = (1+\lambda)N_e$, and thus

$$q = (1 + \lambda)(\alpha_e + \lambda\alpha_i)N_e^2 \quad (16)$$

which, in cases where $\lambda\alpha_i \ll \alpha_e$, becomes

$$q = (1 + \lambda)\alpha_e N_e^2. \quad (17)$$

In the presence of negative ions the equilibrium electron density is still proportional to the square root of the production rate but its magnitude is changed. The term $(1 + \lambda)(\alpha_e + \lambda\alpha_i)$ is often called the *effective recombination coefficient*.

If one is concerned particularly with electron loss, then attachment to neutral particles to form negative ions can itself be regarded as another type of electron loss process. In fact, as we shall see, this becomes the dominant type at somewhat higher levels of the ionosphere. Without specifying chemical details, the attachment type of reaction can be written $M + e \rightarrow M^-$, and the rate of electron loss is $L = \beta N$ where β is the *attachment coefficient*. The loss rate is now linear with N because the neutral species M is assumed to be by far the most numerous, so that removing a few of them has no significant effect on the total.

At equilibrium,

$$q = \beta N \quad (18)$$

and, taking q from the Chapman production function, as before, gives

$$N = N_{m0} \exp(1 - z - \sec \chi \cdot e^{-z}). \quad (19)$$

The peak electron density now varies as

$$N_m = N_{m0} \cos \chi. \quad (20)$$

Such a layer is β -Chapman layer.

This simple formulation assumes that β does not vary with height, though this restriction does not affect the validity of Equation (18) nor of (19) at constant z .

In fact β is expected to vary with height because it depends on the concentration of the neutral molecules (M), and this has important consequences for the form of the terrestrial ionosphere. It is known that electron loss in the F region occurs in a two-stage process:



in which A_2 is one of the common molecular species like O_2 and N_2 . The first step moves the positive charge from X to AX , and the second one dissociates the charged molecule through recombination with an electron, a *dissociative recombination reaction*. The rate of Equation (21) is $\beta[X^+]$ and that of (22) is $\alpha[AX^+]N$. At low altitude β is large, (21) goes quickly and all X^+ is rapidly converted to AX^+ ; the overall rate is then governed by the rate of (22), giving an α -type process because $[AX^+] = N$ for neutrality. At a high altitude β is small and (21) is slow and then controls the overall rate. Then $[X^+] = N$ and the overall process appears to be β -type. As height increases the reaction type therefore alters from α -type to β -type. The reaction scheme represented by Equations (21) and (22) leads to equilibrium given by

$$\frac{1}{q} = \frac{1}{\beta(h)N} + \frac{1}{\alpha N^2} \quad (23)$$

where q is the production rate as before. The change from α to β behaviour occurs at height h_t where

$$\beta(h_t) = \alpha N. \quad (24)$$

2.2.5 Vertical transport

The final term of the continuity equation (1) is to account for changes of electron and ion density at a given location due to bulk movement of the plasma. Such movements can have various causes and can occur in the horizontal and the vertical planes in general, but since our present emphasis is on the overall vertical structure of the ionosphere we shall concentrate here on the vertical component of movements in the F region. Assuming that photochemical production and loss are negligible by comparison with the effect of movements, the continuity equation (1) gives

$$dN/dt = -(Nv_z).$$

Taking vertical movement only,

$$dN/dt = -d(wN)/dh \quad (25)$$

where w is the vertical drift speed and h is the height. Supposing that this drift is due to diffusion we can put

$$W = -\frac{D}{N} \frac{dN}{dh} \quad (26)$$

D being the diffusion coefficient, given in its simplest form by $D = kT/mv$. Here k is Boltzmann's constant, T the temperature, m the particle mass and v the collision frequency.

This expression for D may be derived by equating the driving force due to pressure gradient to the drag force due to collisions as the minority gas diffuses through the stationary majority gas. However, for drift in the vertical direction the force of gravity also acts on each particle, so that the balance of forces becomes

$$-dP/dh = Nmg + Nvmw. \quad (27)$$

Since $P = NkT$, $D = kT/mv$, and $H_N = kT/mg$, this may be rearranged to give

$$Nw = -D(dN/dh + N/H_N),$$

and substitution into the continuity equation gives

$$\frac{dN}{dt} = \frac{d}{dh} (D(dN/dh + N/H_N)). \quad (28)$$

This is the equation that has to be satisfied by the time and height variations of the upper F region and the protonosphere where ion production and recombination are both relatively small.

In this equation the scale height H_N merely represents the value of (kT/mg) , and does not necessarily describe the actual height distribution. This is given by the distribution height,

$$\delta = \left(-\frac{1}{N} \cdot \frac{dN}{dh} \right)^{-1}$$

by definition. We can easily see that δ is equal to the scale height at equilibrium, since $dN/dt = 0$ gives $(dN/dh + N/H_N) = 0$, and hence $\delta = H_N$.

A plasma is composed of two minority species, ions and electrons. Initially the ions, being heavier, tend to settle away from the electrons, but the resulting separation of opposite charges produces an electric field, E , and a restoring force eE on each charged particle. To find the effect on the drift of the plasma, we write separate equations for each species:-

$$\text{electrons; } -dp_e/dh = Nm_e g + EeN + Nm_e v_e w = -kT_e dN/dh$$

$$\text{ions; } -dp_i/dh = nm_i g - EeN + Nm_i v_i w = -kT_i dN/dh.$$

Summing, $Nm_i g + Nm_i v_i w = -k(T_e + T_i)dN/dh$, it being assumed that $m_e \ll m_i$, $m_e v_e \ll m_i v_i$,

$N_e = N_i$, and $w_e = w_i$. Hence, for plasma,

$$Nw = -D_p(dN/dh + N/H_p) \quad (29)$$

$$\text{where } D_p = k(T_e + T_i)/m_i v_i \quad (30)$$

$$\text{and } H_p = k(T_e + T_i)/m_i g, \quad (31)$$

respectively known as *ambipolar* or *plasma diffusion coefficient* and *plasma scale height*.

In that part of the ionosphere where plasma diffusion matters the electron temperature usually exceeds the ion temperature. Taking $T_e = T_i$ by way of illustration we see that the plasma diffusion coefficient and scale height are double those of the neutral gas at the same temperature. Effectively the light electrons have the effect of halving the ion mass since the two species cannot separate very far. Equation (28) for a plasma becomes

$$\frac{dN}{dt} = \frac{d}{dh} (D_p(dN/dh + N/H_p)) \quad (32)$$

and at equilibrium $dN/dh = -N/H_p$ with the plasma exponentially distributed as

$$N/N_0 = \exp(-h/H_p)$$

with scale height H_p .

Note that this distribution is the same shape as a Chapman layer but with (about) twice the scale height.

If the plasma is not in equilibrium the distribution changes with time at a rate depending on the value of the diffusion coefficient, itself depending on the relevant collision frequency and therefore increasing with altitude. If H is the scale height of the neutral gas then the height variation of D can be written as

$$D = D_0 \exp(h-h_0)/H \quad (33)$$

where D_0 is the value of D at a height h_0 . Thus, diffusion becomes ever more important at greater heights as the photochemistry becomes less important.

2.3 Chemical aeronomy

2.3.1 Introduction

We have considered the physical principles governing the intensity and form of the ionospheric layer. To work out what the actual ionosphere should be like on Earth or any other planet requires a detailed consideration of many factors. We need to know the composition of the neutral atmosphere and its physical conditions such as density and temperature. We also need full information on the solar spectrum and any energetic particle fluxes able to ionize the constituents of the atmosphere. We would have to determine what gases could be ionized by the radiation incident, and then determine the ionization rate of each species, summing over all wavelengths and all gases to get the total production rate in a given volume. Then the loss processes, both chemical and by transport, have to be taken into account. Fortunately, for some regions major source and loss processes can be identified, though in others minor species are important and these are the regions that have proved the most difficult.

The neutral atmosphere is composed mainly of the nitrogen/oxygen mixture generally known as "air" up to about 100 km, and above that the atomic species O, He, and H progressively dominate the scene due to diffusive separation.

To be ionized a species must absorb a quantum of radiation whose energy exceeds the ionization potential, the values of which range between 9.25 eV for NO to 24.58 eV for He. The corresponding values of the maximum wavelength (1340 Å for NO to 504 Å for He), λ_{max} , immediately identify the relevant parts of the solar spectrum as the X-ray (1-170 Å) and extreme ultraviolet, EUV (170-1750 Å), emissions which come from the solar chromosphere and corona. Some are enhanced during flares. Figure 8 illustrates the solar spectrum up to 3000 Å (300 nm), including the major emission lines.

In the Chapman formulation the value of the absorption cross-section, σ , generally increases with increasing wavelength up to λ_{max} and then falls rapidly to zero. For a value $c \text{ m}^2$, a volume of 1 m^3 containing n particles per m^3 and irradiated by flux I will absorb an amount $I\sigma n$.

The efficiency with which the absorbed radiation leads to ionization is expressed by the ionization efficiency, η . With atomic species, all the absorbed energy goes into ion production at the rate of one ion-electron pair for about every 35 eV of energy. The energy is inversely proportional to the wavelength, and a convenient formula in terms of wavelength is

$$\eta = 360/\lambda(\text{Å}) \quad (34)$$

The Chapman theory shows that the production rate is a maximum at the level where the optical depth, $\sigma n H \sec \chi$, is unity. If the absorption at given wavelength is due to several species, then the condition for maximum production is

$$\sum \sigma_i n_i H_i \sec \chi = 1 \quad (35)$$

At that height the rate is given by Equation (7)

$$q_m = \eta \cos \chi / e H I_\infty$$

summed over several species if necessary.

The height of unit optical depth in the atmosphere, not the intensity of the ionizing radiation, is what determines the height of the ionospheric layers. The simple theory of Section 2.2 deals with the shape and intensity of an ionosphere produced by monochromatic radiation acting on a single gas. On a real planet the effect of all gases at a given wavelength has to be considered and then, since the ionosphere is in effect a number of overlapping Chapman layers, the production rate due to all relevant wavelengths has to be summed at each height.

2.3.2 E and F1 regions

Both the E region, which peaks at 105-110 km, and the F1 region at 160-180 km are fairly well understood. The F1 region is attributed to the most heavily absorbed part of the solar spectrum, between about 200 and 900 Å — the ionization limit of atomic oxygen is at 911 Å — for which the optical depth reaches unity from about 140 to 170 km. The primary reaction products are O_2^+ , N_2^+ , O^+ , He^+ , and N^+ , but subsequent reactions leave NO^+ and O_2^+ as the most abundant.

The E region is formed by the less strongly absorbed, and therefore more penetrating, parts of the spectrum. EUV radiation between 800 and 1027 Å (the ionization limit of O_2) is absorbed by molecular oxygen to form O_2^+ . The band includes several important emission lines. At the short wavelength end X-rays of 10-100 Å ionize all the atmospheric constituents. The main primary ions are N_2^+ , O_2^+ and O^+ , but the most numerous are again observed to be NO^+ and O_2^+ . The intensity of solar X-rays varies over the solar cycle and they probably make little contribution to the E region at solar minimum.

Direct radiative recombination of the type

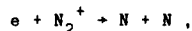
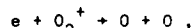


is slow relative to other reactions and is not significant in the E and F regions. Dissociative recombination, as

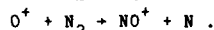
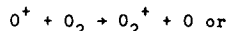


is 10^5 times faster (with a reaction coefficient of $10^{-13} \text{ m}^3 \text{ s}^{-1}$) and in both E and F regions the electron and ion loss proceeds via molecular ions.

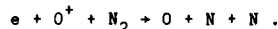
The main recombination reactions of the E region are therefore



In the F region the principal primary ion is O^+ , which is first converted to a molecular ion by a *charge exchange* reaction



The molecular ion then reacts with an electron as above, to give as the net result



In the F1 region the overall reaction is controlled by the rate of the dissociative recombination.

2.3.3 F2 region and protonosphere

At first sight the F2 region presents a puzzle because it peaks at 200-400 km whereas there is no band of radiation which has its maximum ionization rate at any height above 170 km. The answer is found in the height variation of the recombination rate, which forms the F2 region as an upward extension to F1 even though the production rate is now decreasing with height.

Taking O^+ as the major ion, the two stage recombination process is



As discussed above, the second reaction controls the overall rate at low altitude and the first is the rate determining step at high levels, the transition being where $\alpha N_e = \beta(h_t)$. Here h_t is the transition height, generally between 160 and 200 km. The appearance of the F1-ledge depends on h_t being above the height of maximum production rate, h_m : that is, on there being a production maximum within an α -type region.

To explain the F2 region we consider the upper part where the recombination is β type and β depends on the concentration of N_2 . On the other hand, the production rate depends on the O concentration. Thus, at equilibrium

$$N_e = q/\beta\alpha[O]/[N_2]$$

$$\propto \exp[-h/H(O) + h/H(N_2)]$$

where $H(O)$ and $H(N_2)$ are the scale heights for O and N_2 . Since the masses of N_2 and O are in the ratio 1.75:1, this rearranges to give

$$N_e \propto \exp \left[-\frac{h}{H(O)} \left(1 - \frac{H(O)}{H(N_2)} \right) \right] \\ = \exp[+ 0.75 h/H(O)] \quad (38)$$

This is a layer whose electron density increases with height because the loss rate falls off more quickly than the production rate. It is often called a *Bradbury layer*.

Since the Bradbury layer increases with height indefinitely it cannot explain the peak of the F2 layer. On the other hand, diffusion produces an electron density distribution that decreases with height. With increasing height, in-situ production and loss become less important but diffusion becomes more important because of the reducing air density. The F2 layer peaks where these two kinds of process are equally important. To decide the level at which this will occur we regard the two loss processes — 8-type recombination and transport — as being in competition, and compare their time constants for electron loss on the principle that the more rapid will be in effective control. This comparison places the peak where $8\sqrt{D/H'^2}$, in which D is the diffusion coefficient and H' is a typical scale height for the F2 region. The electron density at the peak is given by

$$N_m \sim q_m/8_m \quad (39)$$

At some level in the topside the ionosphere dominated by O^+ gives way to the protonosphere dominated by H^+ . The ionization potential is almost the same for these two ions (13.6 eV) and therefore the reaction



is rapid, and around the transition level there is equilibrium in which

$$[H^+][O] = \frac{9}{8} [H][O^+] \quad (41)$$

(The factor 9/8 arises for statistical reasons, and there is also a temperature dependence proportional to $(T_n/T_i)^{1/2}$). This reaction enables ionization to move readily between ionosphere and protonosphere, an important aspect of topside behaviour.

The transition effectively defines the base of the *protonosphere*. Below that level the H^+ distribution is determined by (41) and tied to the O^+ distribution by

$$[H^+] \propto [H][O^+]/[O] \\ = \exp \left[-\frac{h}{H(H)} \right] \cdot \exp \left[-\frac{h}{H(O^+)} \right] \\ \frac{\exp \left[-\frac{h}{H(O)} \right]}{\exp \left[-\frac{h}{H(H)} \right]} \\ = \exp[+ 7h/H(H)] \quad (42)$$

The strong upward gradient of H^+ concentration is apparent in the computed ionosphere/protonosphere profile shown in Figure 9. Above the transition the concentration of O^+ decreases rapidly, and the protonosphere when in equilibrium assumes an exponential profile with plasma scale height according to Equation (31). The corresponding change of gradient of the electron density profile is evident. As for the F2 peak, the transition level between ionosphere and protonosphere can be estimated by comparing time constants. This occurs at 700 km or above, which is always well above the peak of the F2 layer.

2.3.4 D region

The D region of the ionosphere does not include a maximum but is that part below about 90 km that is not accounted for by the processes of the E region. The D region is also the most complex part of the ionosphere from the chemical point of view. This is essentially due to the relatively high pressure, which causes minor as well as major species to be important in the photochemical reactions, and because several different sources of ionization contribute significantly to ion production.

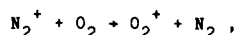
To treat the whole of the D region from 60 to 90 km over all latitudes one has to reckon with 6 ion production sources:-

- The Lyman- α line of the solar spectrum at 1215 Å penetrates below 95 km and ionizes the minor species nitric oxide (NO) whose ionization limit is at 1340 Å.
- The EUV spectrum between 1027 and 1118 Å ionizes another minor constituent, excited oxygen in the state $O_2(^1\Delta_g)$.
- EUV radiation also ionizes O_2 and N_2 , as in the E region.

- d) Hard X-rays of 2-8 Å ionize all constituents, most effect being therefore from the major species O_2 and N_2 .
 e) Galactic cosmic rays, which affect the whole atmosphere down to the ground, become a major ionization source in the lower D region. At this level the production rate increases downward in proportion to the total air density.
 f) Energetic particles from the Sun or of auroral origin ionize the D region at high latitudes, where at times they form the main source.

The relative contributions of these different sources varies with latitude, time of day, and level of solar activity. Computations for a mid-latitude site under typical daytime conditions show EUV as the dominant source down to 92 km (E region), Lyman-α important from 92 to 68 km (this depending on the NO model assumed), X-rays as the main source below 68 km and also at 81-85 km, and galactic cosmic rays assuming the major role below 61 km. $O_2(^1\Delta_g)$ contributes between 80 and 105 km but is never the major source. At greater solar zenith angles the contributions from Lyman-α and X-rays are reduced, cosmic rays becoming relatively more important below about 70 km. The X-ray flux varies strongly with solar activity (by a factor of a hundred to a thousand) and is probably not significant in the D region at sunspot minimum.

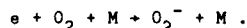
The primary ions are NO^+ , O_2^+ and N_2^+ , but the latter are rapidly converted to O_2^+ by the charge-exchange reaction



leaving NO^+ and O_2^+ as the major ions. However, below 80 or 85 km, apparently the level of the mesopause, rocket borne mass spectrometers find heavier ions which are hydrated species such as $H^+ \cdot H_2O$, $H_3O^+ \cdot H_2O$, and hydrates of NO^+ . These hydrates occur when the water vapour concentration exceeds about 10^{15} m^{-3} .

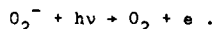
Where simple ions dominate, the loss process is dissociative recombination as in the E region, with a recombination coefficient of about $5 \times 10^{-13} \text{ m}^3 \text{ s}^{-1}$, the reaction of NO^+ being somewhat faster than that of O_2^+ . In total the situation is much more complex, as illustrated in Figure (10). This scheme includes O_2^+ , NO^+ , O_4^+ , hydrates and others, and has to be solved by means of a computer program. The significance of the hydrated ions is that, being large molecules, they have greater recombination rates than the simple ions, of the order of 10^{-12} to $10^{-11} \text{ m}^3 \text{ s}^{-1}$, depending on their size. Thus the electron density is relatively smaller in regions where hydrates dominate.

Below about 70 km by day or 80 km by night much of the negative charge is in the form of negative ions. The process begins with the attachment of an electron to an oxygen molecule, forming O_2^- . This is a three-body reaction involving any other molecule, M, whose function is to remove excess kinetic energy from the reactants:

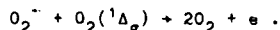


This is followed by further reactions forming other and more complex negative ions including CO_3^- , NO_2^- , NO_3^- and clusters such as $O_2^- \cdot O_2$, $O_2^- \cdot CO_2$ and $O_2^- \cdot H_2O$.

Because the electron affinity of O_2 is small (0.45 eV) the electron may be removed by a photon of visible light or near infra-red:



It is also detached in reactions with atomic oxygen to form ozone, and with the excited $O_2(^1\Delta_g)$:



However some of the negative ion species are very stable against detachment and these are called *terminal ions*.

The effect of negative ions on the balance between electron production and loss was included in Equations 15 to 17. Variations of electron density in the D region can be due to changes in the negative-ion/electron ratio, λ , as well as to production rate changes.

3. Electrical conductivity

3.1 Introduction

Whereas the troposphere is an excellent electrical insulator, the upper atmosphere becomes gradually more conducting with increasing height. Though never achieving the high conductivities of a metal, ionospheric conductivities are in the middle range typical of terrestrial materials like sea water and some rocks, and of laboratory semi-conductors. The upper atmosphere conductivity arises, of course, from the presence of free electrons and ions which can move readily under impressed forces and thereby act as efficient charge carriers.

We shall see that the ions and the electrons may respond to forces in different ways, so that ion and electron currents are not necessarily the same. If the positive and the negative particles move in opposite directions the ion and electron currents are simply added together. In the other extreme case the ions and the electrons might move exactly together; in this case the two currents cancel and there is no net current, but the plasma as a whole is in motion. This is called a *plasma drift*. The general situation is sketched in Figure 11: the drift is given by the vector sum of the ion and electron velocities, and the current by their vector difference, with suitable scaling in each case. Clearly the conductivity varies with altitude in direction as well as in magnitude.

Two different driving forces occur naturally in the upper atmosphere, and these act in somewhat different ways upon the medium. When an electric field is present the positive and the negative particles tend to be driven in opposite directions and one expects an electric current to be the first result. The other driving force is a wind in the neutral air. Through collisions some of the motion is transferred to the ionized species, initially driving them along in the same direction, as a plasma drift.

There are, however, two complicating factors. Collisions between the charged and the neutral particles is one. We can think of the collision frequency between two species as the number of times a selected particle of one kind collides with any particle of the other kind, though a more correct definition is based on momentum transfer, since particle mass m , relative velocity v , and collision frequency ν causes a drag force $m\nu v$. The collision frequency is a key parameter in conductivity considerations.

The other complicating factor is the geomagnetic field characterized by the gyrofrequency, the frequency at which a charged particle gyrates in the field, given by

$$\omega_e = Be/m_e \quad \text{for an electron,}$$

$$\text{and} \quad \omega_i = Be/m_i \quad \text{for an ion.}$$

Although the direction of gyration depends on the sign of the charge, our treatment takes the convention that all frequencies are considered positive. The gyrofrequency is the other key parameter, and an important consequence of the geomagnetic field is that all upper atmosphere motions and currents are anisotropic.

3.2 Particle motion in a magnetic field in the presence of collisions

To understand the conductivity structure of the upper atmosphere we must first appreciate how a charged particle in a magnetic field responds to a driving force when collisions with neutral particles also occur. The simplest case is when the force F acts along the magnetic field. The particle, mass m , initially accelerates at F/m , but if the collision frequency is ν it travels for a time of only $1/\nu$ and a distance of $F/2m\nu^2$ before colliding with a neutral particle. If we imagine that the particle stops for an instant at each collision, after which it is again accelerated by the force F , the overall speed will be $v = F/2m\nu$. However this is inexact because the particle may not stop on collision. The correct result is obtained, also more economically, by equating the driving force, F , to the drag force due to collisions, $m\nu v$, giving

$$v = F/m\nu. \quad (43)$$

The magnetic field has no effect in this case since it is parallel to the direction of motion.

Referring to Figure 12, consider now a force F_x directed along the x axis and acting on a positively charged particle at the origin. Initially the particle moves in the x direction, but as soon as it moves, with velocity v , it experiences a Lorentz force of magnitude Bev deviating it to the right, the magnetic field, B , being directed along the z axis. In vector notation, $\underline{F} = e\mathbf{v} \times \mathbf{B}$. If no collision occurs the particle will move in a loop, being retarded by F_x during the second part and coming to rest at a point further along the $-y$ axis. The average velocity in the $-y$ direction is approximately $F_x P/4m$ where P is the gyroperiod ($2\pi m/Be$). Thus an approximate expression for the drift speed is $v \approx \pi F/2Be$. The exact expression is $v = -F_x/Be$. A negatively charged particle drifts in the $+y$ direction since the Lorentz force acts in the opposite direction.

If collisions occur we can visualize their effect as to "stop" the particle every $1/\nu$ instead of every $P/2$ (provided $1/\nu < P/2$), and, as Figure 12 illustrates, this introduces a drift component in the x direction at the expense of motion along the y axis. If ν is large enough $v_x = F/m\nu$, as though the magnetic field were not present. To derive a general formula including the effects of both the magnetic field (introducing a Lorentz force) and collisions (introducing a drag force) we consider the vector equation balancing the various forces:-

$$\underline{F} \pm e\mathbf{v} \times \mathbf{B} - m\nu\mathbf{v} = 0. \quad (44)$$

Here the first term is the driving force, the second the Lorentz force (+ for a positive ion, - for an electron) and the third is the drag force due to collisions. Because of the cross product $\mathbf{v} \times \mathbf{B}$ the second term always acts at right angles to the third, and the vector diagram is a right angled triangle as sketched in Figure 13. Plainly, $\tan\theta = eB/mv$ and $\cos\theta = mvv/F$, from which may be derived the expressions for the velocity components for electrons and positive ions respectively:-

$$\begin{aligned} \text{Electron:} \quad v_y &= \frac{F_x}{eB} \cdot \frac{\omega_e^2}{v_e^2 + \omega_e^2} \\ v_x &= \frac{F_x}{eB} \cdot \frac{\omega_e v_e}{v_e^2 + \omega_e^2} \\ \text{Ion:} \quad v_x &= -\frac{F_x}{eB} \cdot \frac{\omega_i^2}{v_i^2 + \omega_i^2} \\ v_y &= \frac{F_x}{eB} \cdot \frac{\omega_i v_i}{v_i^2 + \omega_i^2} \end{aligned} \quad (45)$$

In these expressions ω_e and ω_i are the electron and ion gyrofrequencies and v_e and v_i are the respective collision frequencies. The electron charge, e , is considered positive. Since the fractions appear frequently it is convenient to express them by

$$\begin{aligned} f_1(e) &= \frac{\omega_e v_e}{v_e^2 + \omega_e^2} \\ f_2(e) &= \frac{\omega_e^2}{v_e^2 + \omega_e^2} \end{aligned} \quad (46)$$

with similar expressions for the ions. For motion along B or in the absence of a magnetic field

$$v_z = \frac{F_z}{mv_e} = \frac{F_z}{eB} \cdot \frac{\omega_e}{v_e}$$

and we define

$$f_0(e) = \omega_e / v_e \quad (47)$$

with a similar expression for ions. Recall that the angle between the force and the resulting velocity, θ , is given by

$$\tan\theta = \frac{\omega}{v} = f_0.$$

This ratio varies with height, being very small at low height and very large at a great height: thus θ varies between 0° and 90° .

3.3 Response to a neutral-air wind

The force due to a wind in the neutral air, U , is $F = mvU$ where v is the relevant collision frequency. First we consider that the wind blows perpendicular to the geomagnetic field. Substituting this value for F_x in Equations (45) then gives the resulting velocity components in the x and y directions (Figure 12).

Two limiting cases are of interest. At a sufficiently low height $v \gg \omega$, f_0 is small, $v_y \ll v_x$, and $v_x = mvU/eB \cdot f_0 = U$. The plasma is carried along with the wind as expected. At a great height $v \ll \omega$, f_0 is large, $v_x \ll v_y$; then

$$\begin{aligned} v_y &= \frac{mv_e U}{eB} = \frac{U}{f_0(e)} && \text{for electrons, and} \\ v_y &= -\frac{U}{f_0(i)} && \text{for ions.} \end{aligned}$$

The ions and electrons now move in opposite directions, comprising a current at right angles to the wind direction, though its value is relatively small because f_0 is large.

If $v = \omega$ the motion is at 45° to the wind. This occurs at about 75 km for electrons and 120 km for ions. Between these levels the ions move more or less with the wind whereas the electrons move nearly across it. This region, where the wind is most effective in producing an electric current, is the *dynamo region*. The principle reason for the existence of such a region is the mass ratio between the ion and the electron:

$$\omega_e/\omega_i = m_i/m_e = 1836 M_i$$

where M_i is the atomic weight of the ion.

Suppose now that there is a wind component along the geomagnetic field. In general this will be so, because the neutral air wind blows in the horizontal plane but the geomagnetic field is not vertical except at the magnetic poles. For simplicity assume that the wind, U , is in the magnetic meridian. If the dip angle is I , the neutral air component along the field is $U_{\parallel} = U \cos I$ — See Figure 14 — and the plasma moves in the same way. Compared to its vertical structure the ionosphere is relatively uniform in the horizontal plane. The principle effect of the field aligned drift, U_{\parallel} , is therefore a lifting or depression of the layer depending on the vertical component

$$w = U_{\parallel} \sin I = \frac{1}{2} U \sin 2I. \quad (48)$$

The effect is greatest where the magnetic dip is 45° . It can be shown that the effect of the neutral wind is to change the height of the layer maximum by

$$\Delta h_m \sim \frac{wH^2}{D} \sim \frac{w}{\beta}. \quad (49)$$

3.4 Response to an electric field

An electric field, E_x , exerts force $E_x e$ on a positive ion and $-E_x e$ on an electron. Replacing F_x by $E_x e$ and $-E_x e$ in Equations (45) respectively gives for a positive ion,

$$v_x = \frac{E_x}{B} \cdot f_1(i); \quad v_y = -\frac{E_x}{B} \cdot f_2(i);$$

$$\text{and for an electron, } v_x = \frac{E_x}{B} \cdot f_1(e); \quad v_y = -\frac{E_x}{B} \cdot f_2(e).$$

In each case, if $v \ll \omega$ then $v_x \ll v_y$ and $v_y = -E_x/B$. Therefore at high altitude the plasma as a whole drifts at velocity E_x/B in the $-y$ direction.

At a low level $v \gg \omega$ and $v_y \ll v_x$. Then for positive ions,

$$v_x = \frac{E_x}{B} \cdot f_0(i)$$

$$\text{and for electrons, } v_x = \frac{E_x}{B} \cdot f_0(e).$$

The electrons and ions move in opposite directions, representing currents in the same direction and parallel to applied electric field. However the currents are relatively small because f_0 is small at low altitude.

As before, the drifts are at 45° to the electric field when $v = \omega$ (i.e. $f_0=1$), and there is again a range of heights where the electrons tend to respond to the electric field but the ions remain more under the control of neutral air.

Table 1 summarizes the responses to wind and electric field in the three height regions.

3.5 Conductivity

Electrical conductivity is the ratio between current density (i in A/m) and electric field (E in V/m): $\sigma = i/E = Nev/E$, v being the velocity of the relevant particles, N their concentration and e the charge on each.

In the absence of a magnetic field, or if the electric field is along the magnetic field, $v = F/mv = Ee/mv$, from Equation (45). Thus,

$$\sigma = Ne^2/mv. \quad (50)$$

Table 1: Effects of Wind and Electric Field

<u>Altitude</u>	<u>Wind (U)</u>	<u>Electric Field (E)</u>
High ($f_0 \gg 1$)	Current $\perp U$	Plasma drift $\perp E$
Intermediate ($f_0(e) > 1$, $f_0(i) < 1$)	Ion current $\perp U$	Electron current $\perp E$
	Small electron current $\parallel U$	Small ion current $\parallel E$
Low ($f_0 \ll 1$)	Small plasma drift $\parallel U$	Small current $\parallel E$

Since the ion and electron currents are simply added, the conductivity due to both is

$$\sigma_0 = \left(\frac{N_e}{m_e v_e} + \frac{N_i}{m_i v_i} \right) e^2. \quad (51)$$

This is called the *direct* or *longitudinal* conductivity.

For electric fields (or electric field components) perpendicular to the magnetic field we define two conductivities to deal with currents flowing respectively parallel and perpendicular to the electric field. These are represented by the symbols σ_1 and σ_2 , called the *Pedersen* and *Hall* conductivities respectively

$$\begin{aligned} \sigma_1 &= (N_e f_1(e) + N_i f_1(i)) e/B = \left[\frac{N_e}{m_e v_e} \left(\frac{v_e^2}{v_e^2 + \omega_e^2} \right) + \frac{N_i}{m_i v_i} \left(\frac{v_i^2}{v_i^2 + \omega_i^2} \right) \right] e^2 \\ \sigma_2 &= (N_e f_2(e) - N_i f_2(i)) e/B = \left[\frac{N_e}{m_e v_e} \left(\frac{\omega_e v_e}{v_e^2 + \omega_e^2} \right) - \frac{N_i}{m_i v_i} \left(\frac{\omega_i v_i}{v_i^2 + \omega_i^2} \right) \right] e^2. \end{aligned} \quad (52)$$

When deriving and manipulating these expressions it should be borne in mind that $\omega_e = eB/m$.

A calculated height distribution of conductivity in the mid-latitude ionosphere at noon is shown in Figure 15. Note that the Pedersen and Hall conductivities peak in the E region whereas the direct conductivity continues to increase with altitude and is of much greater magnitude.

A complication of the real ionosphere is its spatial non-uniformity, which affects the currents through the continuity requirement. Latitudinal and time-of-day variations have some effect, but the horizontal layering of the ionosphere has greatest effect on vertical currents. At the magnetic equator the magnetic field is horizontal, which means that, in the terms of our convention, the medium is bounded in the y direction. (See Figure 16). Then, from our definitions of σ_1 and σ_2 ,

$$\begin{aligned} J_x &= \sigma_1 E_x + \sigma_2 E_y, \\ J_y &= -\sigma_2 E_x + \sigma_1 E_y. \end{aligned} \quad (53)$$

J_y must be zero because the y direction is vertical. Hence,

$$E_y = E_x \frac{\sigma_2}{\sigma_1},$$

and, by substitution,

$$J_x = \left(\sigma_1 + \frac{\sigma_2^2}{\sigma_1} \right) E_x = \sigma_3 E_x.$$

σ_3 is the *Cowling conductivity*. If the conductivity is due to only one species of particle, such as the electrons, it is easily proved that $\sigma_3 = \sigma_0$ (as though no magnetic field were present). This is analogous to the case of a metallic conductor in a laboratory; the conductivity is not affected by a transverse magnetic field, but a potential difference (the Hall Effect) appears across the other faces.

4. The Magnetosphere

4.1 Introduction - The Solar Wind

The magnetosphere is the region of the terrestrial environment where the geomagnetic field exerts the dominating influence. Generally (though there can be exceptions) the energy density of the magnetic field exceeds that of the plasma:

$$B^2/2\mu_0 > nkT$$

in MKS units, where B is the magnetic flux density, k is Boltzmann's constant, and the plasma contains n particles m^{-3} at temperature T . Below, the magnetosphere merges imperceptibly into the ionosphere and the division between them is more a matter of semantics than of physics. The outer boundary of the magnetosphere is determined by its interaction with the solar wind. Thus the magnetosphere can be regarded as the outermost part of the Earth.

Given the existence of the geomagnetic field, the form and structure of the magnetosphere are determined largely by emissions from the Sun, and the magnetosphere responds readily and rapidly to changes in the various solar emissions, particularly the solar wind. This stream of plasma that continuously leaves the Sun is composed mainly of electrons and protons, with a few percent ($\sim 5\%$) of alpha-particles and other heavier ions. The number density of positive ions varies between 3 and 10 cm^{-3} (3×10^8 to $10^7 m^{-3}$), the most typical value being 5 cm^{-3} and there are a similar number of electrons for bulk neutrality. The mean mass of solar wind particles is therefore almost half that of the proton, about 10^{-27} kg. Fluctuations as great as a factor of ten can occur in the solar wind in times of minutes and hours, implying irregularities with scales of 10^5 km and larger.

At the distance of the Earth's orbit the speed of the solar wind is usually between 200 and 700 or 800 $km s^{-1}$, on which is superimposed a random component of temperature $10^5 K$. The energy is more directed than random, and the plasma is considerably cooler than its directed velocity would suggest. The energy carried is about $10^{-4} Wm^{-2}$, approximately a tenth of that in the Extreme Ultra-Violet part of the electromagnetic spectrum which creates the ionosphere.

The solar wind carries with it a weak magnetic field amounting to a few nanoTeslas ($nT = 1$ gamma). The field is "frozen in" to the plasma because the electrical conductivity is very large, and the plasma controls the motion of the total magnetoplasma because it has the greater energy density (by a factor of about eight). The interplanetary magnetic field (IMF) was discovered in 1963 with a very sensitive magnetometer on IMP-1 (the Interplanetary Monitoring Platform), an eccentric orbit satellite with apogee at 32 R_E . Although the solar wind flows out almost radially from the Sun, the solar rotation gives the magnetic field a spiral form, as in Figure 17, often known as the *garden hose* effect. It happens that at the orbit of Earth the field lines run at about 45° to the radial direction: the radial and the east-west components are about equal.

In direction the IMF can be either inward or outward with respect to the Sun, and one of the most remarkable of the early results, which is also of great significance, was that distinct sectors may be recognized, the field being inward and outward in alternate sectors. Figure 18 shows some of the original measurements where four sectors — two inward and two outward — were present. However this is not always the case. The sector structure evolves with time; sometimes there are only two sectors, and sometimes the sectors are not all of the same width. Obviously, though the IMF originates in the Sun and is strictly part of the main solar magnetic field, the observations in the ecliptic plane between 0.3 and 10 A.U. show a form that is not dipolar. The resolution of this anomaly is achieved by inserting a current sheet in or near the equatorial plane, which effectively divides the outward field (above the plane) from the inward field (below it) as in Figure 19. If the solar magnetic dipole is tilted from the rotation axis, the current sheet will be tilted from the ecliptic plane and a spacecraft near the Earth will observe a two-sector structure as the Sun rotates. When more than two sectors are seen it is thought that the current sheet has developed undulations as in the skirt of a pirouetting ballerina; hence the concept of Figure 19 is often known as the *ballerina model*. Most solar wind measurements have been near the ecliptic plane, but spacecraft venturing out of the ecliptic plane have observed the disappearance of the sector structure — which is consistent with the ballerina model.

It is also possible that the more complex sector structures are due to a more complicated solar field, which when the sun is active could be due to localized plasma ejections, for instance from flares. The velocity of the ejected plasma will be greater than that of the ambient plasma and may be sufficient to produce a shock wave. This compresses the IMF and a turbulent region will form between the shock and the ejected matter. Within it the magnetic field appears to be strong and also well ordered, sometimes in the form of a loop or a helix. These *magnetic clouds* are typically 0.25 A.U. across at the Earth's orbit.

The solar wind is extremely important in solar-terrestrial relations, as the principal medium through which the activity of the Sun is communicated to the vicinity of the Earth. The interaction between the solar wind and the magnetosphere depends strongly on the orientation of the IMF.

4.2 The distorted geomagnetic field

4.2.1 Geomagnetic field near the Earth

To a first approximation the geomagnetic field at and close to the planet's surface can be represented as a dipole field. The poles of the dipole are at geographic latitudes and longitudes $79^\circ N$, $70^\circ W$ and $79^\circ S$, $70^\circ E$. The magnetic flux density is

given by

$$B(r, \lambda) = \frac{M}{r^3} [1 + 3 \sin^2 \lambda]^{\frac{1}{2}} \quad (54)$$

where M is the dipole moment, r the geocentric radial distance, and λ the magnetic latitude. This is accurate to about 30% at points within 2 or 3 Earth-radii of the surface. Although not very accurate, the dipole form is useful for making approximate calculations about the inner magnetosphere.

The field components in the r and λ directions are

$$\begin{aligned} B_r &= -2M \sin \lambda / r^3, \\ B_\lambda &= M \cos \lambda / r^3. \end{aligned} \quad (55)$$

Thus, by integration

$$r = r_0 \cos^2 \lambda. \quad (56)$$

For a selected value of r_0 , this is the equation of a field-line, the locus of the force on a single north pole. If $\lambda = 0$, $r = r_0$; r_0 is thus the radial distance to the field-line over the equator, and its maximum distance from the Earth.

It is convenient in the magnetosphere to use the radius of the Earth, R_E , as the unit of distance.

Putting

$$\begin{aligned} r/R_E &= R, \\ B(R, \lambda) &= \frac{0.32}{R^3} (1 + 3 \sin^2 \lambda)^{\frac{1}{2}} \end{aligned} \quad (57)$$

Gauss, 0.32 G being the flux density at the Earth's surface at the magnetic equator. In these terms, the field line equation becomes

$$R = R_0 \cos^2 \lambda \quad (58)$$

R and R_0 being measured in Earth-radii. The latitude where the field-line intersects the Earth's surface is given by

$$\cos \lambda_E = R_0^{-\frac{1}{2}}. \quad (59)$$

Figure 20 shows dipolar field-lines.

The displaced dipole model, in which the dipole is displaced 400 km from the centre, is a closer approximation to the real field than the centred dipole. However, for accurate work (not too far above the surface) the field is expressed as a series of spherical harmonics in which the magnetic potential, V , is given by

$$V = \sum_{n=1}^{\infty} (R_E/R^{n+1}) \sum_{m=0}^n (g_n^m \cos m\phi + h_n^m \sin m\phi) p_n^m(\cos \theta) \quad (60)$$

where g_n^m and h_n^m are coefficients, $p_n^m(\cos \theta)$ are associated Legendre functions, and R , θ and ϕ are spherical polar coordinates. The coefficients are derived by fitting the expression to measurements of the magnetic elements on the global scale, using magnetometers both on the ground and on satellites. The expression is applied as a computer program, the flux density being the gradient of the magnetic potential. Because the geomagnetic field changes with time a fresh set of coefficients, relating to a specific epoch, is published from time to time. Such representations are accurate to about 0.5% at and near the surface. The terms of higher order become less important at greater distances, and to an extent the field becomes more dipolar. However beyond 3 or 4 R_E a gross distortion due to the solar wind takes over.

The geomagnetic cavity, illustrated in north-south section in Figure 21, is formed because the solar wind is not able to penetrate the geomagnetic field, being swept around it and at the same time distorting the field.

4.2.2 Magnetopause

The form of the boundary between the geomagnetic field and the incident solar wind can be deduced by considering the pressure balance across the boundary. When the system is in equilibrium the pressure of the solar wind outside ($2Nm v^2 \cos^2 \psi$) is at every point of the surface equal to that of the magnetic field inside ($B^2/2\mu_0$), where the solar wind contains N particles m^{-3} , each of mass m kg, travelling at velocity v m/s and striking the surface at angle ψ from the normal. A simple calculation along these lines readily gives a realistic distance for the position of the boundary (10 R_E) along the Earth-Sun line and enables one to estimate how it varies with solar wind changes. A full computation is more complicated since the orientation of the boundary at each point is not known at the outset and an iteration procedure is required.

The resulting boundary, the *magnetopause* is included in Figure 21. The geomagnetic field is severely distorted and in particular:-

- (a) Field-lines originating at low latitude still form closed loops between northern and southern hemispheres, though there can be some distortion from the dipole form.
- (b) Lines emerging from the polar regions are swept back, away from the Sun; some of these would have connected on the day side in a dipole model.
- (c) Intermediate between these regions are two lines, one in each hemisphere, that go out and meet the magnetopause on the day side, though in fact their flux density falls to zero as they reach it; here, neutral points are formed.

In spacecraft observations the magnetopause is recognized by a sharp drop in magnetic field strength and the appearance of turbulence. Generally good agreement is obtained between calculated and observed shapes of the magnetopause, and Figure 22 illustrates this in the ecliptic plane. These measurements, having come from one spacecraft, were made over a period of time and the overall result is thus a long term average. In fact the magnetosphere varies considerably in response to changes in the solar wind.

4.2.3 Magnetosheath and shock

The region immediately outside the magnetopause is not in fact typical of the solar wind though it is composed mainly of solar material. As shown in Figures 21 and 22, a shock front is formed in the solar wind 2 or 3 R_E upstream of the magnetopause. In the region between the shock and the pause, which is known as the *magnetosheath*, the plasma is turbulent.

Tenuous though it may be by any ordinary standard, the magnetosphere is relatively a solid object in comparison with the solar plasma flow. Further, its velocity is "supersonic" at the orbit of Earth, meaning that the velocity exceeds that of any waves that can propagate within it. In the solar wind the speed of hydromagnetic waves, that is, the Alfvén speed, given in c.g.s. units by

$$v_A = B/4\pi\rho \quad (61)$$

where B is the magnetic flux density and ρ the particle density in gm/cm^3 , is about 50 km/s. At a solar wind speed of 400 km/s, therefore, the *Alfvén Mach number* is 8.

The situation is therefore similar to that of any solid object, a bullet or a fast aircraft for example, flying through the air supersonically, and a shock wave is formed. The existence and location of the shock were predicted from theory in the early 1960's and subsequently verified by observation. A shock wave represents a discontinuity in the medium of the solar wind, created when information about the approaching obstruction is not transmitted ahead into the medium. In crossing the shock, solar wind plasma is slowed down to about 250 km/s and the corresponding loss of directed kinetic energy is dissipated as thermal energy, increasing the temperature to 5×10^6 °K. Magnetosheath plasma is therefore slower than the solar wind proper but 5-10 times hotter.

4.2.4 Polar clefts

The simple models of the magnetosphere predict two neutral points on the magnetopause where the total field is zero. These points connect along field-lines to places on the Earth's surface near $\pm 78^\circ$ magnetic latitude. These are the only points that connect the surface to the magnetopause and all the field from the magnetopause converges to those two points. They are therefore regions of great interest where solar wind particles (from the magnetosheath) can enter the magnetosphere without having to cross field-lines. There is good direct evidence that this happens. Particles with energy typical of the sheath are observed over some 5° of latitude around 77° , and over 8 hr of local time around noon. Being more extended than points, these regions are now called the *polar clefts*. As regions where particles enter the magnetosphere, the clefts are significant in relation to the high-latitude ionosphere.

4.2.5 Magnetotail

In the anti-sunward direction the magnetosphere is extended into a long tail, usually known as the *magnetotail*, which is perhaps the most remarkable feature of the magnetosphere. Spacecraft magnetometers find that on the night side of the Earth the geomagnetic field beyond about $10 R_E$ tends to run in the Sun-Earth direction, with a reversal of direction across a central plane. The field points towards the Earth in the northern lobe, and away from the Earth in the southern. The tail is roughly circular, some $30 R_E$ (2×10^5 km) across, and of uncertain length though it has been detected downwind beyond 10^7 km.

Figure 21 shows the basic form of the magnetotail in the plane containing the magnetic poles. The flux density of the tail is about 20γ ($= \text{nT}$), though much weaker in the plane where the reversal occurs. In this region the magnetic pressure of the tail lobes ($B^2/2\mu_0$) is more or less balanced by an enhancement of the plasma density, the *plasma sheet*. In fact the tail, like the whole magnetosphere, is dynamic and an essential part of the magnetospheric circulation, to be considered in Lecture 7.

4.3 Particles in the magnetosphere

4.3.1 Principal populations

The geomagnetic field holds within it several distinct populations of charged particles.

(a) Deep within the magnetosphere (in the region often known as the inner magnetosphere) is the *plasmasphere*, closely linked to the mid-latitude ionosphere and comprising electrons, protons and some heavy ions, all having energies in the thermal range.

(b) Also trapped on closed field-lines are the energetic particles generally known as the *Van Allen particles* after their discoverer. Apart from cosmic rays and solar protons, which are merely passing through, the Van Allen particles are the most energetic in the magnetosphere and they make some contribution to the ionization of the upper atmosphere when precipitated out of the trapping region.

(c) The *plasma sheet* is associated with the magnetotail, essentially with the central region where the magnetic field reverses direction. Plasma sheet particles are energized within the magnetotail and they are important in auroral activity and the behaviour of the high-latitude ionosphere. Their energy is intermediate between those of the plasmasphere and the Van Allen belt. The inner edge of the plasma sheet supports the ring current that flows in the magnetosphere during magnetic storms.

(d) At the edges of the magnetosphere, and obviously connected with the physics of the magnetopause, are *boundary layers*. Their composition and energy are governed by the solar wind and magnetosheath plasma.

The locations of these particle populations are indicated in Figure 23. They should not be considered as merely incidental to the magnetosphere, but are in fact essential to its properties and behaviour.

4.3.2 Plasmasphere

Ionized particles in the upper ionosphere (F region and topside) have temperatures up to several thousand degrees Kelvin, and electron energies are therefore several tenths of an electron volt. The particle density is typically 10^{10} m^{-3} (10^4 cm^{-3}) at 1000 km altitude, reducing with increasing height — though not very rapidly because of the large scale height when atomic hydrogen is the principal ion. The theory of the protonosphere shows how ionospheric plasma flows up the field-lines to populate the protonosphere as far as the equatorial plane, provided the field-lines are closed. Some of this plasma flows back to lower levels at night where it helps to maintain the ionosphere during hours of darkness, but the plasmasphere nevertheless persists as a permanent feature of the inner magnetosphere.

By means of the *whistler* technique it is possible, from a suitably located ground-based station, to determine the variation of electron density in the equatorial plane, as in Figure 24. The remarkable feature of such plots, first observed by D.L. Carpenter in 1963, is that they often show a sudden drop in the electron density near 4 Earth-radii amounting perhaps to a factor of ten or more within a distance of $0.5 R_E$ or less. This is the *plasmopause*, sometimes also known as the "knee". If traced inward along the geomagnetic field the plasmopause is found to correspond approximately with the ionospheric main trough which effectively marks the poleward extent of the mid-latitude ionosphere. It is clear that the plasmopause occupies a doughnut-shaped region of the inner magnetosphere where the field-lines are not too distorted from the dipolar form.

Observations show the plasmasphere as a dynamic and variable region. There is a daily variation that includes a bulge in the evening sector (Figure 25), and the whole region contracts when geomagnetic activity increases, there being a gradual recovery in the few days following the storm. For most of the time it is found between 3 and $6 R_E$, though it has been detected as close to the Earth as $2 R_E$ (i.e. only one Earth radius above the surface).

4.3.3 Plasmasheet

Beyond the plasmopause the electron density is much smaller and the temperature is much higher, and this is clearly not the same population of particles which inhabits the plasmasphere. The electron density is only about 0.5 cm^{-3} and, for neutrality, the ion density is the same. Particle energies are 10^2 to 10^4 eV. The average energy of the electrons is about 0.6 eV and that of the protons about 5 keV. The total energy density of the particles is about 3 keV/cm^3 .

The plasma sheet is particularly associated with the central plane of the magnetotail and, to a first approximation, the pressure of the particles in the sheet balances the magnetic pressure in the lobes of the tail. Thus,

$$nkT = B_t^2/2\mu_0 \quad (62)$$

where B_t is the tail magnetic field outside the plasma sheet. As indicated in Figure 26 the plasma sheet follows the magnetic field down to lower altitudes in the vicinity of the auroral zone and also continues round to the day side of the Earth. In the equatorial plane there is an identifiable (though variable) inner edge near $7 R_E$ at midnight. The sheet is several Earth-radii thick (also variable) and it extends across the tail between the dusk and dawn sides.

The existence of a sheet of plasma between the two lobes of the magnetotail in which the fields run in opposite directions creates a curious and interesting physical situation. The configuration is far from the dipole form and thus it represents a store of energy which would be released if the two lobes could come together and allow the field to return to a dipolar shape. The magnetic merging in the neutral sheet of the magnetotail involves the mutual annihilation of field from the lobes, and this is the source of the energy that heats the plasma sheet particles. The process is not, in fact, a steady one, as we shall see in Lecture 7.

4.3.4 Boundary layers

As anticipated in the early magnetospheric theories, the cusps are regions where solar matter from the magnetosheath enters the magnetosphere. There is direct evidence for the entry: particles of the appropriate energy (< 1 keV) are observed over 5° of latitude centered about 77° and extending over 8 hours about noon. Further evidence is the enhanced electron density and temperature in the ionosphere beneath the cusps.

The structure of the cleft is illustrated in Figure 27. The magnetosphere circulation opens field-lines from lower latitudes which move poleward across the cleft and are then swept back over the poles into the tail. Magnetosheath particles flow down the newly opened field-lines, mirror in the stronger field near the Earth, and try to return to the sheath. But because of the convection of the magnetic field-lines some of this plasma finds itself on the open field-lines over the pole. This is the *plasma mantle*. There are also boundary layers at the equatorward side of the cusp, entrapped by eddy convection or diffusion.

4.3.5 Van Allen particles

The discovery of energetic particles trapped in the magnetosphere was the first major scientific result of the satellite era. The first reported measurements came from the Explorer 1 satellite, which on 1958 January 31 was the first to be successfully launched by the United States. The key observation was in fact somewhat peculiar. Being interested in cosmic rays, J.A. Van Allen's group at the University of Iowa had built for the satellite a Geiger counter with what should have been the appropriate sensitivity for cosmic ray detection. The measurements found the cosmic ray flux, but there were also times when the counting rate was very large and others when it fell below the expected cosmic ray level. This was interpreted as a particle flux so great as to cause a malfunction of the counter. Similar effects were seen on Explorer 3 in March 1958 and on the USSR's Sputnik 3. These Geiger counters gave little information as to the nature of the particles and they were at first thought to be electrons of energy 50 - 150 keV. However, Explorer 4, which was more fully instrumented, showed that they were actually protons of energy exceeding 30 MeV.

At the end of 1958, Pioneer 3 went out 107 400 km and found a double structure as in Figure 28. These and other early measurements gave rise to the idea that there are two distinct belts of trapped particles, the "inner" and the "outer" zones. In fact the total picture is more complicated than this because the distribution depends on the nature and energy of the particles.

The trapping of energetic charged particles arises from the interaction between a moving electric charge and a static magnetic field. The principles are best expressed in terms of a number of *adiabatic invariants*, which are quantities that do not change provided some other quantity (specifically the magnetic flux density) changes not at all or sufficiently slowly.

A charged particle of mass m and charge e gyrates in a magnetic field of flux density B at angular frequency, the *gyrofrequency*,

$$\omega_B = eB/m. \quad (63)$$

The radius of gyration is

$$r_B = mv/Be \quad (64)$$

where v is the particle velocity. If a particle in the magnetosphere has velocity v , normal to the magnetic field and v along it, the trajectory is a spiral. Provided no work is done on or by the particle, the magnetic flux through the orbit (ϕ_m) is constant.

Hence,

$$\phi_m = B \cdot \pi r_B^2 = 2\pi m E_\perp / e = \text{constant} \quad (65)$$

where E_\perp is the kinetic energy associated with the transverse velocity component, i.e.

$$E_\perp = mv^2/2.$$

Hence, E_\perp/B is constant. But this is also the magnetic moment of the current loop represented by the gyrating particle. This gives us the first adiabatic invariant of charged particle motion in a magnetic field:

the magnetic moment is constant.

This holds provided the magnetic field does not change significantly during one gyration period.

If the total velocity of the particle is v , then

$$v_{\perp} = v \sin \alpha$$

where α is the angle between the velocity vector and the magnetic field direction, the *pitch angle*. Hence, since the total kinetic energy, E , is constant,

$$E_{\perp}/B = E \sin^2 \alpha / B = \text{constant} . \quad (66)$$

Thus,

$$\sin^2 \alpha \propto B$$

As a particle moves from the equator towards higher latitude in a dipole field it encounters increasing B and therefore the pitch angle increases. Eventually, provided the atmosphere is not encountered first, $\alpha = 90^\circ$. Here the forward motion stops and the particle is reflected back along the field towards the equator. The point of reflection is called the *mirror point*. The total energy of the particle does not change during its motion because no acceleration mechanisms are at work. Hence the parallel energy falls to zero at the mirror point, as would be expected, and the changing pitch angle represents an alternation of kinetic energy between parallel and perpendicular components, the total remaining constant. It is the conservation of the first invariant within a non-uniform magnetic field approximating to a "magnetic bottle" that makes possible the trapping of energetic charged particles.

For a given particle the position of the mirror point is determined by the pitch angle as the particle crosses the equator (i.e. where the field is weakest), since

$$B_0/B_M = \sin^2 \alpha_0 \quad (67)$$

B_0 and B_M being the flux densities at the equator and at the mirror point respectively. The situation is sketched in Figure 29.

If the atmosphere is encountered before the mirror point, particles will be lost. The equatorial pitch angles of particles that will be lost to the atmosphere at the next bounce define the *loss cone*, which will be seen as a depletion within the pitch-angle distribution.

In addition to the gyration about the field-line and the oscillation between hemispheres, a trapped particle also drifts around the Earth. This is due to two mechanisms which are about equally important. The first is that the particle finds itself in a slightly weaker field when on that part of its gyration furthest from the Earth. The radius of gyration therefore changes and this introduces a lateral shift of the orbit. The second cause is the curvature of the field-line, which produces a centrifugal force to which the particle responds by drifting sideways. The combination of these two effects is called *gradient-curvature drift*. Gradient-curvature drift sends electrons to the east and protons to the west.

In a dipole field, gradient-curvature drift would move the particles around at the same distance from the Earth and would serve merely to distribute the particles to all longitudes. However in the actual field, which is not dipolar, the drift paths are not so obvious. The theory of trapped particles shows that the path may be determined from the *second adiabatic invariant*, also known as the *integral invariant*, which states that the *integral of the parallel momentum over one bounce between mirror points is constant*.

The second invariant can be written

$$I = \int_{\ell_1}^{\ell_2} (1 - B/B_M) d\ell \quad (68)$$

where ℓ is the distance along the field-line, and ℓ_1 and ℓ_2 are the mirror points at which the flux density is B_M .

This is a property of the field configuration and also of the mirror point (or equatorial pitch angle) of the particle, and it defines the surface, or *shell*, on which the particle remains as it drifts around the Earth. It holds provided the field does not change appreciably during one bounce period.

An important development from the second invariant is the L parameter introduced by C.E. McIlwain in 1961. L has the dimension of length taking one Earth radius as the unit. It is analogous to the distance to the equatorial crossing of a dipole field-line, to which it reduces in a dipole field. By analogy with a dipole field, an invariant latitude may be defined in terms of L :

$$\lambda = \cos^{-1}(1/L)^{1/2} . \quad (69)$$

" L " is commonly used to label field-lines, even at high latitude where L strictly has no meaning because particles cannot be trapped on field-lines that are not closed.

The *third adiabatic invariant* or *flux invariant* says that the *total geomagnetic flux enclosed by the drift orbit is constant*, and this enables the effect of very slow changes of magnetospheric structure on particle orbits to be calculated. The third invariant

is violated if changes occur in a time less than that taken for the particle to encircle the Earth; such violations are not infrequent, particularly during magnetic storms when conditions tend to change rapidly at the beginning but return to normal more slowly.

The morphology of the radiation belts involves four kinds of process:

- (a) injection of charged particles into the trapping region;
- (b) acceleration of particles to high energy;
- (c) diffusion within the region;
- (d) loss processes removing particles from the trapping region.

The source must either create particles in situ or introduce them by violating an invariant. In the so-called *inner zone*, within about $2.5 R_E$, the particles are created in situ by the decay of neutrons which themselves come from primary cosmic ray protons of very high energy. Calculation shows this to be a sufficient source for the inner zone. The loss process involves some kind of interaction with the atmosphere near the mirror points. The main inner zone loss processes are: retardation and charge exchange, particularly for the less energetic (<100 keV) protons; nuclear collisions, particularly for protons > 75 MeV; and scattering into the loss cone, particularly for electrons.

The question of how the particles of the outer zone ($L > 3$) are created does not have such a clearcut answer. The charged particles almost certainly come from the outer magnetosphere, and the main evidence for this is the increases of flux at times of enhanced geophysical activity. At geosynchronous orbit, which is well outside the maximum of the outer zone, the variations are very marked and are related to the velocity of the solar wind. The rate of decay shows a time constant of days to several days. Typical energy spectra are shown in Figure 30.

The particles probably enter the outer magnetosphere at the sunward cusps. Some will already be of high energy, but local acceleration in the magnetosphere is also required and it is not entirely clear how this happens. If a particle has to move nearer the Earth it will tend to gain energy because it is moving on to shorter field-lines and into a region of stronger field. There could also be scattering from shock waves in the magnetosphere. The drift to different L-shells is a process of radial diffusion resulting from the violation of the third (flux) adiabatic invariant when the magnetosphere changes in times smaller than the drift period.

Diffusion of pitch angle is the cause of particle loss from the outer zone. This involves the violation of the second invariant by varying fields or interaction with electromagnetic or electrostatic waves that act in times shorter than a bounce period. When particles diffuse into the loss cone they enter the atmosphere at the next bounce and are lost there. Figure 31 illustrates the observed spatial distribution of electrons and protons. The protons are also variable, though not to the same extent as the electrons.

The dependence of the spatial distribution on the energy of the particles is clear from Figure 31. In general the maximum occurs at greater distance for particles of lower energy, but the value of the maximum flux increases. The gap between the inner and outer zones is seen most clearly in the electron distributions and this feature is called the *slot*. It occurs generally between 3 and $4 R_E$ and its depth is a factor of 10 to a factor of 100 depending on energy. The slot tends to fill during periods of enhanced geophysical activity, with a gradual return to normality over the following days and weeks.

5. Ionosphere-magnetosphere coupling

At high latitude the ionosphere and the magnetosphere are linked in several ways, as will be clear from the preceding discussion. In the neutral atmosphere, stratification under gravity tends to isolate phenomena at different levels, but for the ionized component the geomagnetic field tends to couple the behaviour at different altitudes, so that changes in the ionosphere may affect the magnetosphere and vice versa. The physical reason for this coupling is that the conductivity is large along the field direction for electric currents, heat, and charged particle motion. This is particularly important at high latitude, first because solar effects (e.g. EUV ionization) are relatively weaker there, and second because field-lines passing through the high-latitude ionosphere go out well into the magnetosphere, extending to 4 Earth-radii and more in the equatorial plane. The high-latitude ionosphere therefore receives much of its ionization from particles energized in the magnetosphere, and its dynamics are largely governed by those of the outer magnetosphere. In both of these aspects, the solar wind provides the major driving force. To understand the high-latitude ionosphere it is necessary to understand the magnetosphere and its response to the solar wind, and to know the various coupling mechanisms.

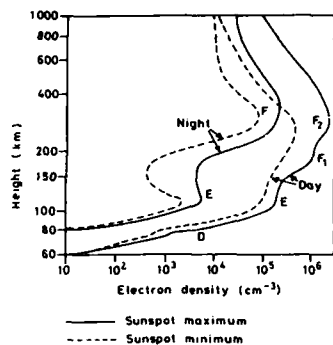


Fig. 1 Typical vertical profiles of electron density in the mid-latitude ionosphere (From wallchart, "Aerospace Environment", W. Swider, Air Force Geophysics Laboratory).

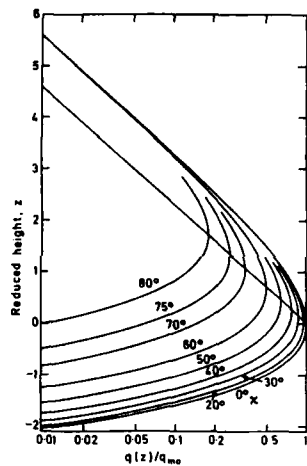


Fig. 3 Chapman production function (After T.E. Van Zandt and R.W. Knecht, Space Physics, Wiley, 1964).

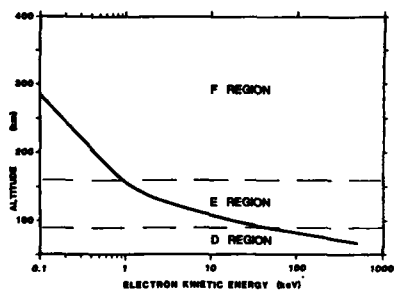


Fig. 5 Height of maximum ionization production by incident energetic electrons (J.A. Whalen (after M.H. Rees), private communication).

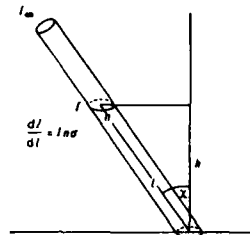


Fig. 2 Absorption of ionizing radiation in the atmosphere.

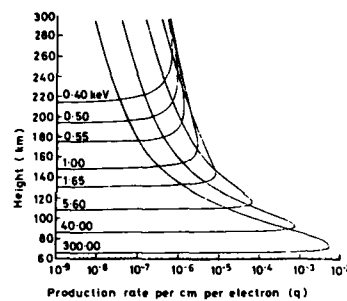


Fig. 4 Production rates due to monoenergetic electrons. (After M.H. Rees, Planet. Space Sci. 11, 1209, 1963).

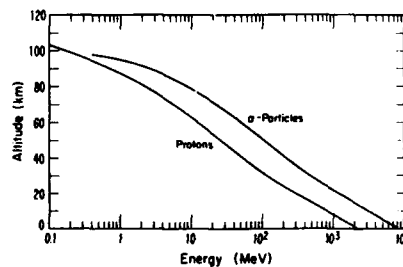


Fig. 6 Stopping heights of incident protons and alpha-particles. (G.C. Reid, Fundamentals of Cosmic Physics, 1, 167, 1974).

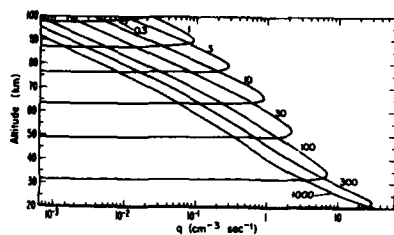


Fig. 7 Production rates due to incident monoenergetic protons. The initial energies are given in MeV, and the flux is 1 proton/cm²-sec-steradian. (G.C. Reid, Fundamentals of Cosmic Physics, 1, 167, 1974).

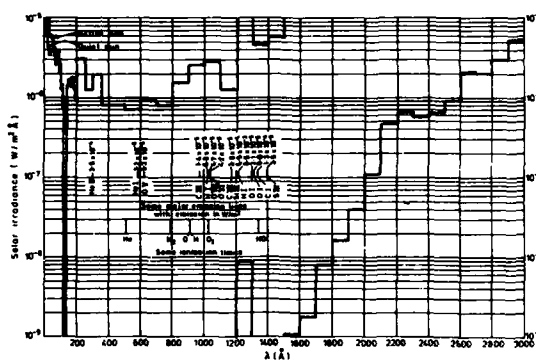


Fig. 8 Solar spectrum in the X-ray and UV regions. Note the change of scale over 1200-1500 Å. (Data from E.V.P. Seith and D.M. Gottlieb, Space Sci. Rev., 16, 77, 1974).

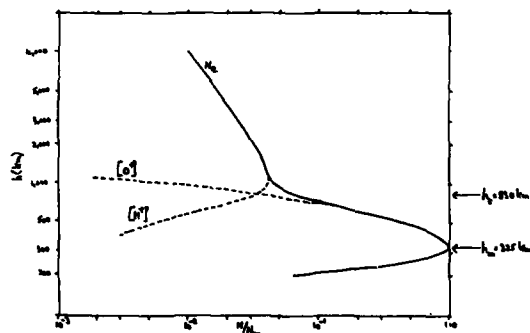


Fig. 9 Ionosphere model, showing transition between O⁺ and H⁺, for night, equinox at Boulder, Colorado.

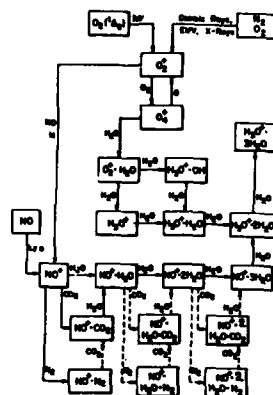


Fig. 10 Positive-ion chemistry of the D region. (J.R. Winick (after E.E. Ferguson), Solar-Terrestrial Physics, Reidel, 1983, p677).

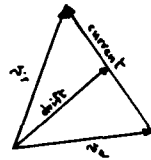


Fig. 11 Current and plasma drift due to electron and ion velocities.

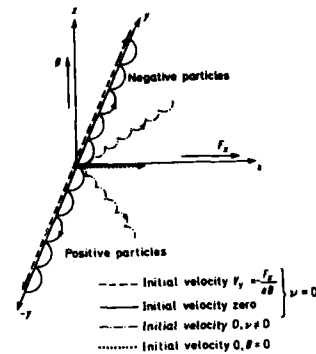


Fig. 12 Charged particle motions in a magnetic field.

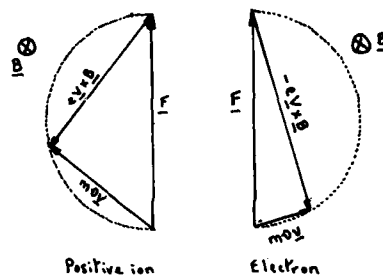


Fig. 13 Forces on electron and positive ion in presence of a magnetic field.

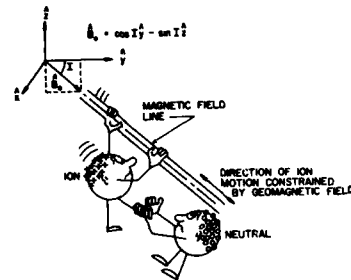


Fig. 14 Lifting effect of neutral wind and inclined magnetic field. (R.E. DuBroff et al., Report AFGL-TR-76-0143, University of Illinois, 1976).

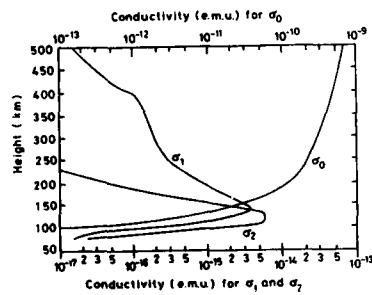


Fig. 15 Conductivity profiles calculated for middle latitude at noon. (S.-J. Akasofu and S. Chapman (after K. Maeda and R. Matsumoto), Solar-Terrestrial Physics, Oxford Univ. Press, 1972).

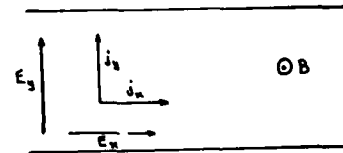


Fig. 16 Currents and fields in horizontal slab of ionization at the equator.

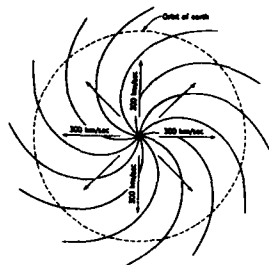


Fig. 17 Form of interplanetary magnetic field in solar equatorial plane due to solar wind of 300 km/s. (T.E. Holzer, *Solar System Plasma Physics*, Vol. 1, North-Holland, 1979, p103).

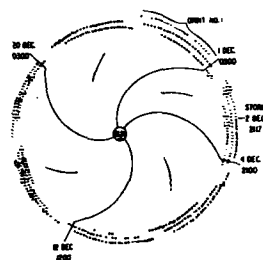


Fig. 18 Sector structure of the solar wind in late 1963. (J.M. Wilcox and H.F. Ness, *J. Geophys. Res.* 70, 5793, 1965).

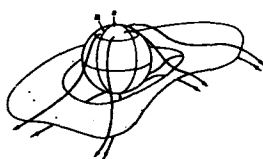


Fig. 19 Ballerina model of current sheet in solar wind. (E.J. Smith, *Rev. Geophys. Space Phys.*, 17, 610, 1979).

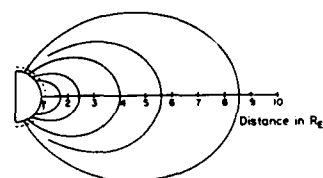


Fig. 20 Dipole field-lines. (D.L. Carpenter and R.L. Smith, *Rev. Geophys.*, 2, 415, 1964).

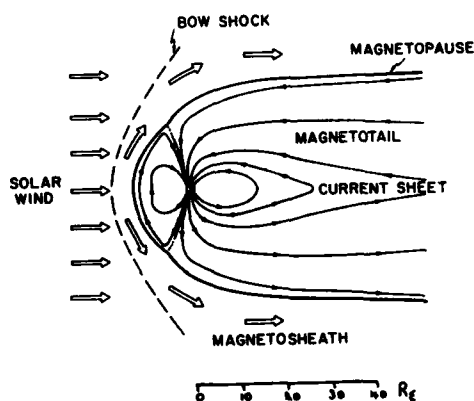


Fig. 21 Cross-section of the geomagnetic cavity and external plasma flow, showing magnetopause and shock. (After V.M. Vasyliunas, *Solar-terrestrial Physics*, Reidel, 1983, p243).

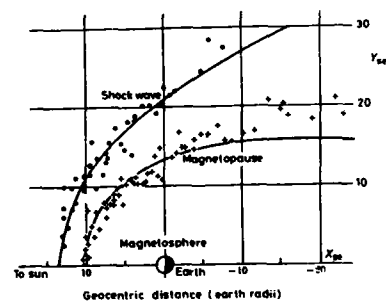


Fig. 22 Observed and calculated positions of magnetopause and shock in the solar equatorial plane. (After H.F. Ness et al., *J. Geophys. Res.* 69, 3531, 1964).

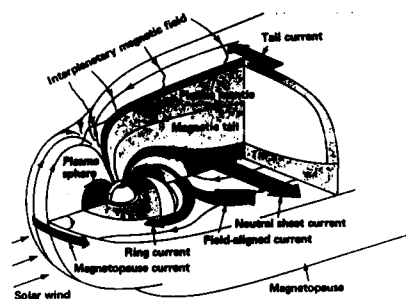


Fig. 23 Plasma populations and current systems of the magnetosphere. (T.A. Potemra, Johns Hopkins APL Tech. Digest, 4, 276, 1983).

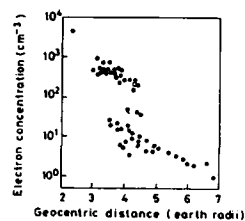


Fig. 24 Electron density in the equatorial plane determined from whistlers. (J.A. Ratcliffe (after D.L. Carpenter), An Introduction to the Ionosphere and Magnetosphere, Cambridge University Press, 1972).

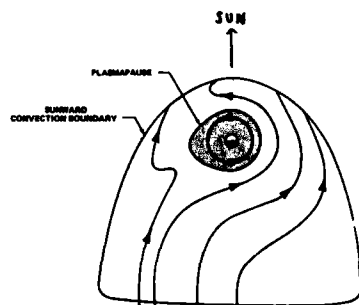


Fig. 25 Daily variation of the plasmapause in relation to the plasma convection in the magnetospheric equatorial plane. (After J.L. Burch, The Upper Atmosphere and Magnetosphere, National Academy of Sciences, Washington D.C., 1977, p.42).

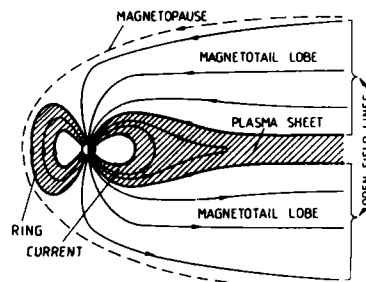


Fig. 26 Magnetospheric plasma sheet and ring current. (V.M. Vasyliunas, Exploration of the Polar Upper Atmosphere, Reidel, 1981, p.229).

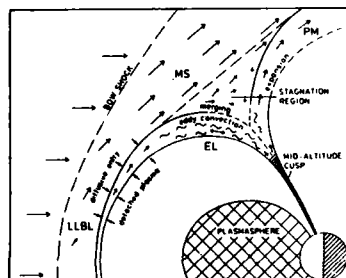


Fig. 27 Detail of the cleft: MS = magnetosheath, LLBL = low-latitude boundary layer, EL = entry layer, PM = plasma mantle. (G. Haerendel et al., J. Geophys. Res., 83, 3216, 1978).

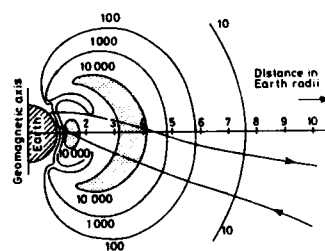


Fig. 28 Van Allen's first map of the radiation belts, showing counting rates of the Pioneer 3 Geiger counter. (After J.A. Van Allen and L.A. Frank, J. Geophys. Res., 64, 1683, 1959).

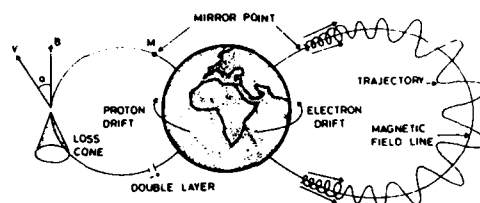


Fig. 29 Trajectories of particles trapped on closed field-lines.
(J. Lemaire, *Advances in Space Research*, 2, 3, 1982).

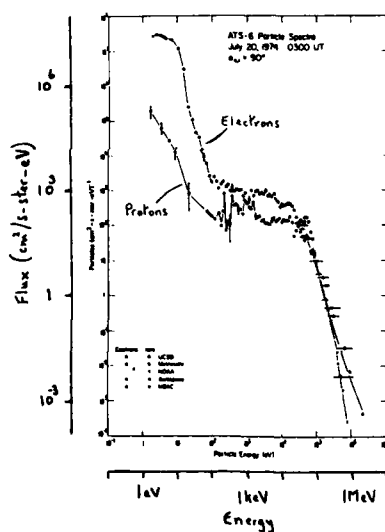


Fig. 30 Electron and ion spectra measured at geosynchronous orbit. (G.A. Paulikas and J.B. Blake (After T.A. Fritz et al.) *Quantitative Modeling of Magnetospheric Processes*, Am. Geophys. Union, 1979, p.180).

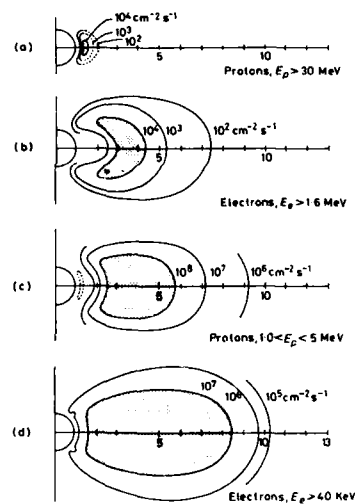


Fig. 31 Spatial distributions of trapped protons and electrons of higher and lower energy. (After W.N. Hess, *Radiation Belt and Magnetosphere*, Blaisdel, 1968).

TRANSIONOSPHERIC PROBING AND PROPAGATION

Dr. E.J. Fremouw
NorthWest Research Associates, Inc.
P.O. Box 3027
Bellevue, WA 98009-3027 USA

SUMMARY

The propagation of radio waves through the ionosphere is necessary for the operation of many C³I systems. Thus, the effect of the ionosphere on such waves is of practical interest. Moreover, analysis of propagation effects is used to characterize the medium in ionospheric research; that is, radio waves are used as probes of the intervening ionospheric plasma. Any signal at any frequency above the path critical frequency may be employed as such a probe. The most straight-forward analyses employ simple cw signals, preferably two or more coherent ones from which differential phase may be measured.

Effects of concern include absorption; dispersion; group delay; Faraday rotation; refraction; and phase, intensity, and angle scintillation. Each of these effects may be used as a diagnostic tool, the first five usually providing information on the bulk background ionosphere, while scintillation reveals characteristics of plasma-density structures. All information obtained is integral in nature, being accumulated along the ray path from transmitter to receiver.

In this talk, we shall review the aspects of magnetoionic theory that relate to transionospheric probing, dispensing rather quickly with the bulk-ionosphere effects and concentrating on the effects of spatially irregular total electron content and scintillation. Regarding the latter, we'll describe the signal statistics of scintillation and the channel parameters that describe those statistics. We'll go on to consider the geophysical parameters needed to characterize the plasma-density irregularities that produce scintillation. Our focus in this regard will be application to user-oriented computer models.

In addition to the foregoing, we'll briefly describe the experimental techniques used to employ scintillation as a diagnostic tool and the radio sources available for transionospheric probing. We'll conclude with a statement of current applications and open research questions.

1. INTRODUCTION

At the outset, it may be appropriate to add the words "of radio waves" to the title of this lecture. Traditionally these words would have been understood without statement, but ionospheric probing by rockets and satellites now is commonplace, and the propagation of waves from and through the ionosphere is of interest across the entire electromagnetic spectrum. Currently, the interaction of the ionosphere with infrared and ultraviolet waves is of particular defense interest, especially as regards structured emission therefrom. Still, the ionosphere's interaction with radio waves continues to be relevant to a far greater variety of systems, and that interaction will be our focus.

More specifically, we shall focus on radio waves that truly are "transionospheric" in behavior. We shall not consider communication and remote sensing by HF waves employed on ground-to-ground (or topside-to-topside) links, nor shall we consider that portion of a radar signal that may be backscattered from the ionosphere (e.g., auroral clutter). Moreover, we shall consider only effects of the ionosphere on the wave and not of the wave on the ionosphere (i.e., ionospheric modification). For the most part, these restrictions mean that we shall consider low-power waves at VHF and above.

We are interested in the physics and morphology of the high-latitude ionosphere and shall touch on these topics, but we'll leave a comprehensive treatment of them to Prof. Hargreaves. We'll also leave to him a discussion of dynamic models, limiting our consideration of models to those that are applications oriented.

While several practical details of the behavior of radio waves propagating through the ionosphere have still to be established firmly, and while the characteristics and dynamics of ionospheric structures that modify such waves are subjects of ongoing and systems-relevant research, the basics have been understood for quite a long time. We shall begin by revisiting a survey¹ of the most important propagation effects that is no less useful today than it was when it was conducted, almost a quarter century ago. We shall also find three more recent reports^{2,3,4} very useful for applying the basic concepts to modern systems. We shall describe effects on general types of systems, however, not on specific operational or planned systems.

2.0 EFFECTS OF INTEREST AND CONCERN

Fundamentally, the ionosphere can affect a passing radio wave in only three ways -- by altering its phase, its polarization, and/or its intensity. The first can lead to the second and third, and the latter can be imposed directly by absorption. All effects can be described by the classical equations of the magneto-ionic theory,⁵ in particular that for the complex refractive index, $\mu = i\chi$, in the approximation that the wave frequency is well above the plasma frequency. Moreover, at our frequencies of interest, the quasi-longitudinal approximation may be used, except for propagation almost precisely normal to the magnetic field, and the real part of the refractive index is quite close to unity.

Under the foregoing approximations, using rationalized mks units, we have

$$\mu = 1 - (\omega_p^2 / 2\omega^2) [1 \pm \omega_g (\cos \psi) / \omega] \quad (1)$$

$$\chi = (\omega_p^2 / 2\omega) [\nu / (\nu^2 + \omega^2)], \quad (2)$$

where

$$\omega_p = (Ne^2 / \epsilon_0 m)^{1/2} \quad (3)$$

is 2π times the plasma frequency,

$$\omega = 2\pi \times \text{wave frequency,}$$

$$\omega_g = eB/m \quad (4)$$

is the angular gyro frequency of an electron,

ψ = angle between wave normal and geomagnetic field,
 ν = electron collision frequency,
 N = plasma number density,
 e = electron charge,
 ϵ_0 = electric permittivity of free space,
 m = electron mass,
 and B = geomagnetic flux density.

We shall have repeated need for a particular combination of the foregoing physical constants, and so we define

$$d = e^2/2mc\epsilon_0 = 2\pi cr_e, \quad (5)$$

where

c = speed of light in vacuo,

and r_e = classical electron radius.

2.1 Absorption

As a VHF wave propagates through the ionosphere, a small fraction of its energy is lost to heating as the electrons it excites collide with neutral particles and ions. The absorption coefficient, in nepers per unit length, is

$$\gamma = \omega x/c. \quad (6)$$

The total absorption, A , in decibels (dB), suffered by the wave in passing through the ionosphere is the ionospheric path integral of γ . Since our frequencies of interest are well above the collision frequency, Eqns. (2) through (6) yield

$$A = d \omega^{-2} \int_0^P \nu N ds. \quad (7)$$

Thus, absorption is inversely proportional to the square of the wave frequency and proportional to the path integral of the product of the collision frequency and the plasma density. The latter, in particular, is a function of horizontal location as well as of height, especially at high latitudes and near the magnetic equator.

Lawrence et al.¹ employed typical height profiles of ν and N to illustrate that typical daytime (nighttime) values of absorption at 100 MHz and above are no more than a few hundredths (thousandths) of a dB. Even in the presence of increased D-region ionization levels due to solar-flare enhancement of ultraviolet and x-ray influx, absorption at such frequencies is no more than a few tenths of a dB.¹ Auroral absorption events associated with substorms⁶ also can produce VHF absorption of a few tenths of a dB when averaged over large portions of the sky. In isolated regions, auroral absorption may reach levels of a dB or so at 100 MHz.⁷ Employing 30-MHz zenith measurements, Pope and Leinbach⁸ extrapolated theoretically that VHF (137 MHz) absorption at low (10°) elevation angles could reach a few (4) dB during the first day of polar-cap absorption (PCA) events produced by solar proton influx. This is the maximum absorption expected to occur on transionospheric links at VHF.

2.2.0 Phase Shift in the Bulk Ionosphere

With the exception of absorption, all effects of the ionosphere on a passing VHF radio wave stem from the phase advance introduced by the plasma's imposition of a (real) refractive index less than unity. This fundamental effect produces other effects due to variations in that refractive index with respect to several independent variables: frequency (first and second derivatives with respect thereto), polarization state, transverse distance, and time.

The refractive index given by Eqn. (1) is the ratio of c to the phase velocity, or of the free-space wavelength to that in the medium. It exerts its influence by producing an ionospheric phase-path defect, which may be calculated by taking the path integral of μ through the ionosphere, subtracting the free-space value of the integral over the same path, and expressing the result in (negative) radian measure. At frequencies much larger than the gyro frequency, the result is

$$\phi = d \omega^{-1} \int_0^P N ds. \quad (8)$$

We shall find that many of the effects with which we are concerned are inversely proportional to the frequency or its square or cube and are proportional to the same constant. We shall find also that many of them are proportional to the integral of plasma density along the line of sight, in some cases weighted by another quantity, as for absorption (Eqn. 7) and Faraday rotation (Eqn. 15b).

Representative values for the path integral of plasma density, the so-called "total electron content" (TEC), range from less than 10^{16} el/m² (defined as 1 TEC unit) in the main ionospheric trough and in the pre-dawn hours to values in excess of 10^{18} el/m² in the daytime at solar maximum near the equatorial anomaly.⁹ Even the former value results in a phase-path defect of many times 2π at all frequencies of interest. Thus, the absolute value of phase shift imposed by the ionosphere always is many-fold ambiguous to direct measurement. We shall discuss means for resolving the ambiguity later.

2.2.1 Group Delay and Dispersion

The group velocity, with which energy and information are carried by a wave packet of finite bandwidth, is given by

$$v_g = d\omega/dk, \quad (9)$$

where the wave number, k , is 2π divided by the wavelength. Analogously to the phase refractive index in Eqn. (1), we may define a "group refractive index" as the ratio of c to the group velocity. That is

$$\mu' = c/v_g = c(dk/d\omega). \quad (10)$$

Since

$$k = \omega/v_p = \omega\mu/c, \quad (11)$$

we have

$$\mu' = \mu + \omega(d\mu/d\omega). \quad (12)$$

We find from Eqn. (1) that, at frequencies well above the gyro frequency,

$$\mu' = \mu + (\omega_p/\omega)^2 \approx 1 + (\omega_p^2/2\omega^2). \quad (13)$$

Thus, while the phase-path defect is negative, the "group-path defect" is positive (and of equal magnitude). We see from Eqns. (3), (5), (10), and (13) that the excess group delay is

$$\Delta T = d\omega^{-2} \int_0^P N ds. \quad (14)$$

Using the representative value of 10^{17} el/m² for the path integral of N , we obtain 1.34 μ sec for ΔT at 100 MHz, corresponding to 402 m of excess (one-way) range. Note that, while the phase-path defect goes inversely with frequency, group delay goes inversely with the square of frequency. This fact sometimes can be used to resolve the ambiguity that prevents direct interpretation of measured phase in terms of TEC.

Excess group delay stems from the difference in phase velocity between Fourier components in a wave packet. The difference is not constant for a given frequency separation between components, however, which leads to dispersive spreading and distortion of the packet. That is, the group velocity itself is a function of frequency, so the group does not travel as an unchanging unit. A useful criterion for the significance of dispersion is whether or not the difference in ΔT at the ends of the transmitted band is small or large compared with the group's original temporal width (comparable to the reciprocal of its bandwidth). By this criterion, dispersion through an ionosphere of a few times 10^{17} el/m² is significant at 100 MHz for groups narrower than about a μ sec (1% bandwidth)¹⁰. Note, however, that dispersion (the frequency derivative of group delay) goes inversely with frequency cubed. This provides an even greater opportunity than does group delay for resolving TEC ambiguity, to which we shall return in Section 3.1.

2.2.2 Polarization (Faraday) Rotation

Perhaps the most fundamental effect of ionospheric phase advance stems from its variation with the polarization state of the wave. The \pm sign in Eqn. (1) describes the fact that the ionospheric plasma is birefringent to radio waves, having a slightly (at VHF and above) different refractive index for two different characteristic polarizations. In the quasi-longitudinal approximation appropriate at our frequencies of interest, the characteristic polarizations are right-hand and left-hand circular. Any linearly polarized component of an input wave may be resolved into the two characteristic waves, which travel with slightly different phase velocities. Synthesis of the two resolved components at any subsequent point results in a wave whose linearly polarized component then has undergone "Faraday rotation" of its polarization vector.

The Faraday-rotation angle, Ω , in radians, is equal to half the differential phase-path defect between the two polarizations. By integrating the difference between the two values of Eqn. (1) along the ionospheric path, we find it to be

$$\Omega = (\pi/\lambda) \int_0^P (\mu_+ - \mu_-) ds \quad (15a)$$

$$= d\omega^{-2} \int_0^P \omega_g (\cos \psi) N ds. \quad (15b)$$

We see that Faraday rotation has the same frequency dependence as absorption, including the lead constant. Now, however, the weighting factor accompanying the plasma density, N , under the integral depends on the geomagnetic field strength, through the electron gyro frequency, rather than on the plasma temperature and neutral density, through the electron collision frequency.

Clearly, from the $\cos \psi$ factor in Eqn. (15b), the amount of Faraday rotation depends on the observing geometry relative to the magnetic field. It also can range through more than two orders of magnitude due to changes in integral plasma density. Typical values at VHF range from a small fraction of a radian at night to several complete rotations on some days. Lawrence et al.¹ cite about one complete rotation at 100 MHz for a typical value of the path integral of N (10^{17} el/m²).

2.2.3 Angular Refraction

The simplest practical effect of the ionospheric phase-path defect stems from spatial gradients in plasma density, N , and therefore in refractive index, μ . Gradients transverse to the propagation direction lead to gradients in phase-path defect, tilting the wavefront through an angle expressed as

$$\tau = (c/\omega)(d\phi/dx) = d c \omega^{-2} \frac{d}{dx} \int_0^P N ds. \quad (16)$$

An obvious case of such gradients is that produced by sunrise and sunset on the ionosphere. One may estimate from diurnal variations of TEC (e.g., Fig. 7-4 of Reference 9) that gradients associated with the morning terminator

are on the order of a few times 10^{13} el/m² per km. Such a value would produce a tilt angle on the order of a few tenths of a mrad at 100 MHz. It is quite comparable to the value quoted by Lawrence et al¹ for "wedge refraction." It is a few times larger than the estimates given in their Fig. 14 for the residual refraction encountered as a radio ray passes through a spherically stratified portion of the ionosphere, and a few times smaller than the "typical irregular refraction" shown in the same figure. The latter, based on radio-astronomy observations at middle latitudes, reaches a half degree or so at 100 MHz. (See Fig. 11 of the same reference for an example of such an extreme value.) We'll have more to say about irregular angle variations later, especially at high latitudes.

2.2.4 Differential (or Dispersive) Doppler Shift

Clearly, if a line of sight between a transmitter and receiver (or radar and target) scans across (or is scanned by) a gradient in TEC, the spatial gradient in phase represented by ω/c times Eqn. (16) is converted to a time rate of change of phase -- that is to a doppler shift that would be absent without the ionosphere. This excess doppler shift is referred to as "dispersive doppler." It is given by

$$\omega_d = v_s d\phi/dx = v_s d\omega^{-1} \frac{d}{dx} \int_0^P N ds, \quad (17)$$

where v_s is the line-of-sight scan velocity through the ionosphere (at a representative altitude of, say, 350 km).

As an example, if the line of sight to a satellite at 1000 km altitude were to scan directly across the representative morning terminator discussed in Section 2.2.3, a 100-MHz signal would experience a dispersive doppler shift of a few tenths of a Hz. Even without a physical ionospheric gradient, a dispersive doppler shift on the order of a Hz at 100 MHz is developed by the mid-latitude daytime ionosphere due to the changing ionospheric path length as a low-orbiting satellite overflies a station. This is very small (and opposite in sign) compared with the corresponding geometrical doppler, but it is useful for estimating TEC gradients.¹¹

2.3 Scintillation

We all know that stars scintillate in perceived intensity and apparent position due to refractive and diffractive scattering by refractive-index structures in the intervening atmosphere.¹² So do radio stars and other sources of radio waves beyond the ionosphere.¹³ Indeed, discrete-source radio astronomy owes its birth to this effect.¹⁴ The fundamental mechanism producing scintillation is spatially varying phase shift. In the case of radio waves, it is dispersive phase shift produced in the ionosphere.

Given spatial variations in phase on a wavefront exiting the ionosphere, there exist also spatial variations in all of the effects described in Section 2.2. Through focusing and defocusing and through the diffraction process, spatial variations in wave intensity also develop.^{15,16,17,18} When there is relative motion between the refractive-index irregularities and the radio line of sight, the spatial variations are translated into temporal variations. Taken together, all the aforementioned fluctuations in signal characteristics are called "radiowave scintillation." On frequencies of interest here, intensity scintillations can far exceed the immeasurably small variations that one might expect from spatially varying absorption. In much of the rest of this lecture, we shall deal in some detail with the characteristics of scintillation.

3.0 DISPERSIVE PHASE AND SCINTILLATION AS PROBES

In the present context, the great utility of radio waves as probes of a medium lies in the sensitivity of phase as a carrier of information. Small variations in refractive index produce readily measurable phase perturbations, and the latter can lead to strong perturbations in other observables. On the other hand, phase often is highly ambiguous.

3.1 Measurement of Total Electron Content (TEC)

Both the sensitivity and the ambiguity of phase are illustrated in Figure 1. What is shown are real-time outputs of VHF (138 MHz) phase and intensity from a satellite receiver locked to an S-band (2891 MHz) reference signal. Both the measurement and reference signals were transmitted from the DNA Wideband Satellite¹⁹, which was in a high-inclination circular orbit at 1000 km.

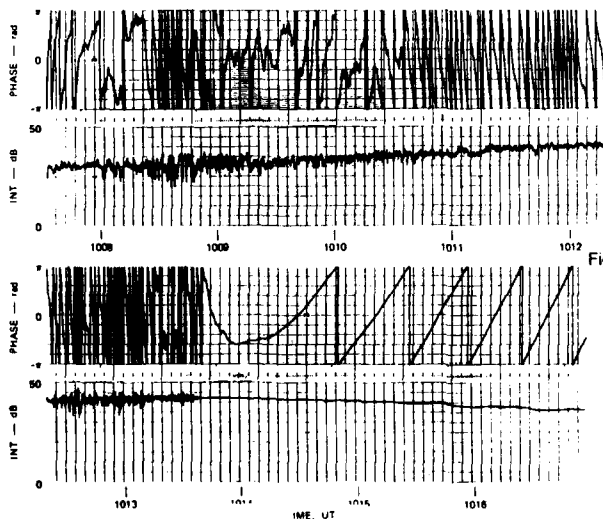


Fig. 1. Example of output from a satellite beacon receiver, strip chart of VHF (138-MHz) phase and intensity obtained at Poker Flat, Alaska, on 23 November 1976, just after local midnight (AST = UT - 10 hr). Note transition (subauroral scintillation boundary) from irregular to smooth, slab-like ionosphere as line of sight to the DNA Wideband Satellite scanned through about 64° N magnetic invariant latitude.

In such an experiment, the phase, ϕ_m , measured at the output of the coherent receiver is derived from the measurement signal's true phase, ϕ_t , and that of the reference signal, ϕ_r , as

$$\phi_m = \phi_t - \phi_r/n, \quad (18)$$

where n is the ratio of the reference frequency to the measurement frequency. Since the ratio of phase shift undergone by the two signals in free space also is n , the geometrical phase shift (as well as its time derivative, the geometrical doppler shift) is absent from the output. (For this reason, the absolute phase stability of the transmitter and the receiver is not important; what is important is that relative phase shifts between various signal paths in the instruments be small, or at least constant and measurable.) What Eqn. (18) actually represents is the difference between dispersive phase shift (Eqn. 8) at the measurement frequency and that at the reference frequency, the latter divided by n . Since the latter already is n^{-1} times the former, we have

$$\phi_m = (1 - n^{-2}) \phi, \quad (19)$$

where ϕ is evaluated at the measurement frequency. In the case of Figure 1, n^{-2} was of order 10^{-3} and quite negligible. Unless we note otherwise, we shall use ϕ_m and ϕ interchangeably in the rest of this lecture.

Thus, the phase chart in Figure 1 is a time record of Eqn. (8) as Wideband passed from north to south over the receiving station at Poker Flat, Alaska. We note that it ranges through 2π many times during the pass. The 2π crossings may be resolved in data processing, thus providing a continuous and very sensitive record of the change in TEC (the integral in Eqn. 8) along the changing ray path. There remains, however a many-fold ambiguity in the absolute phase value -- and hence in the deduced value of TEC -- at any point.

Now, Wideband also transmitted coherent signals at UHF (413 MHz \pm several sidebands). The phase on each of these received signals also is given by Eqn. (8), and one might hope to resolve the ambiguity by taking the phase difference between two of them, as follows

$$\Delta\phi = (d/2\pi) (\Delta f/f_1 f_2) N_T, \quad (20)$$

where f_1 and f_2 are the two frequencies employed, Δf is the difference between them, and N_T represents the integral in Eqn. (8). This is tantamount to employing the group velocity of the beat between the two signals as a measure of TEC (a variation of Eqn. 14).

The factor in parentheses is not small enough to remove the ambiguity, but one further step does so. If we now take the difference between two values of group delay as expressed by Eqn. (20), we have a measure of dispersion (curvature in the dispersion relation represented by Eqn. 1). This "second difference of phase" is given²⁰ by

$$\Delta_2\phi = (d/\pi) (f_m^2/f^3) N_T, \quad (21)$$

where f_m is the modulation frequency (Δf in Eqn. 20) and f is the carrier frequency (the center frequency of the triplet employed). The frequencies transmitted from Wideband were chosen to permit application of Eqn. (21) to resolving the ambiguity in Eqn. (8).

The multiplier in front of N_T is much smaller in Eqn. (21) than in Eqn. (8), which of course is why $\Delta_2\phi$ can be an unambiguous measure of N_T . By the same token, it is a much less sensitive measure. What is usually done in employing Eqn. (21) is to apply it to the average of an entire satellite pass (or some long observing period) to provide a reasonably accurate estimate of the absolute value of N_T . Eqn. (8) then is employed to obtain a much more precise measurement of relative TEC (changes in N_T during the pass or the observing period). In Figure 2, the bottom panel is a TEC record derived in such a way from the phase chart in Figure 1. After the record was "reconnected" at the $\pm\pi$ "fold-overs," it was smoothed to remove rapid fluctuations (phase scintillations) and converted to relative TEC by means of Eqn. (8). A triplet of UHF signals then was employed, via Eqn. (21), to establish the absolute (mean) level of TEC. The upper panel in Figure 2 is a smoothed version of the received signal intensity (with intensity scintillations removed), retaining the trend due to range-squared and antenna-pattern effects.

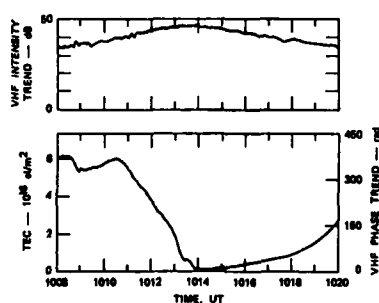


Fig. 2. The intensity and phase trends obtained from record displayed in Figure 1 by employing six-pole, Butterworth, low-pass software filters having 3-dB cutoffs at 0.1 Hz. The manifold 2π ambiguity in the starting point of phase was resolved by dispersion analysis of three UHF spectral lines.

The phase record, which was obtained just after local midnight in central Alaska, displays the path integral of plasma density in the auroral ionosphere to the north of the station early in the pass, giving way to much lower densities in the night-time trough to the south of the station. Part of the increase in measured N_T from mid-pass to pass end is due to the increase in path length through the ionosphere (about a factor of three for horizontal stratification without latitudinal gradients).

A more recent example of TEC derived from dispersive phase after ambiguity resolution by means of $\Delta_2\phi$ is shown in Figure 3. This is from a pass of the DNA Polar BEAR Satellite, again from north to south over Poker Flat, but

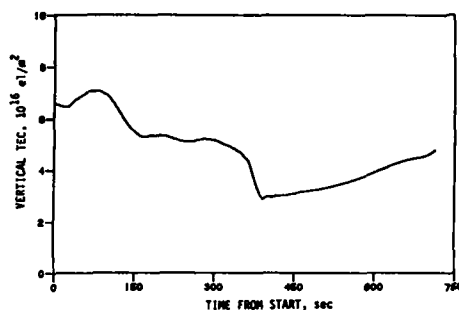


Fig. 3a. TEC record obtained from UHF phase trend recorded at Poker Flat on 17 April 1987, starting at 1537 GMT (about six hours after local midnight).

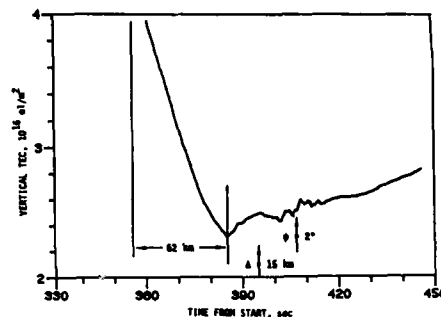


Fig. 3b. Enlargement of central portion of Figure 3a, showing sensitivity of dispersive phase to variations in TEC. Arrows mark times of closest approach of radio line of sight to (Δ) center of HIPAS HF heater beam and (ψ) alignment with geomagnetic field.

about six hours after midnight, when the subauroral trough has begun to fill in (and about one solar cycle later). Again there is some residual auroral ionization well to the north of the station. In this case, an attempt has been made to remove the path-length effect by dividing through by the secant of the ray-path incidence angle, computed at an altitude of 350 km. (The generally convex shape of the adjusted curve suggests that a somewhat different altitude might be more appropriate.) Figure 3b is an enlargement of the central portion of Figure 3a.

This pass was of special interest because the HIPAS HF heater was operating. At 394 sec after the start of the pass, the line of sight scanned within 15 km of the center of the HIPAS beam in the bottomside F layer. There is some evidence that the heater caused a slight depletion of ionization from the poleward edge of the residual trough and that some fine structure in plasma density may have developed on the equatorward edge of the depletion. Whether the heater actually did so is open to conjecture. This figure is shown in the present context to illustrate the sensitivity of dispersive phase as a means to measure TEC and variations therein. That sensitivity was enhanced in the present case for any plasma structures that might have been aligned along the geomagnetic field, a point to which we'll return later. At 408 sec after the beginning of this pass, the radio line of sight came within 2° of alignment with the field in the F layer.

Before leaving the topic of TEC measurement, we must point out that Faraday rotation (Eqn. 15b) also is used for this purpose. Because of its dependence on magnetic-field strength, its employment in conjunction with dispersive phase is useful for separating the contribution of different altitude regimes to TEC. For instance, Davies et al.²¹ have exploited this technique to estimate the contribution of the plasmasphere to mid-latitude TEC.

3.2 Phase and Intensity Scintillation

We turn now to several aspects of scintillation as a family of effects and as a probe. We noted in Section 2.3 that the term "scintillation" can include variations in group delay, polarization, and angle of arrival, as well as in dispersive phase and intensity. They are essentially derivatives of phase fluctuation, however, and there is little to be learned from them as probes that cannot be learned more directly from phase scintillation (given a coherent source). To some extent, the same is true of intensity scintillation, but we shall see that its dependence upon (free-space) propagation distance gives it some additional utility.

We already have encountered examples of scintillation, in Figures 1 and 3b. In the latter, the fine structure in TEC was obtained from measurement of phase fluctuations. The distinction between TEC variation and phase scintillation is somewhat arbitrary. All scintillations arise from fluctuations in TEC. When the resulting phase fluctuations are strong enough and/or of sufficiently small scale size to produce intensity scintillation by focusing and defocusing and/or diffraction, however, we treat the problem as complex-signal scintillation. Once such propagation processes have taken place, the observed phase pattern no longer possesses a faithful one-to-one correspondence to that emerging from the region of refractive-index structure, and its simple deterministic relation to TEC becomes blurred.

Strictly speaking, we define phase fluctuations as phase scintillations when and only when accompanied by intensity scintillations. In Figure 3b, we employed P.BEAR's UHF signal rather than its more sensitive VHF signal to obtain greater fidelity as a measure of TEC (due to the smaller Fresnel-zone size at UHF). In Wideband, we made the distinction between TEC variations and phase scintillations by setting the detrend cutoffs to just barely include all intensity scintillations (and, thereby, corresponding phase scintillations) to the extent practicable in routine data processing. Data from the DNA HiLat²² and P.BEAR²³ satellites currently in orbit are detrended with longer cutoffs, so as to obtain a broader-band picture of phase variations and the structures that produce them. Thus, some of the more recent phase scintillation spectra that we shall see include, at their low-frequency end, phase fluctuations that truly represent TEC variations.

Using the strict-definition detrender in the Wideband Experiment, we subtracted the trends in Figure 2 from the raw data in Figure 1 to produce the residual intensity and phase scintillations shown in Figure 4. We see now that as we move from TEC to scintillation, we leave the world of determinism and enter that of random processes and time series. Of geophysical note in Figure 4 is the abrupt cutoff of scintillation as the line of sight passed from the (diffuse) auroral ionosphere to the sub-auroral trough. This transition is termed the auroral (or sub-auroral) scintillation boundary.²⁴ It was evident already in Figure 1.

3.2.1 Signal Statistics

For systems applications, it is useful to have a reliable statistical characterization of complex-signal scintillation. In special cases (e.g., in the far zone of an irregular medium with an effective outer scale), sufficient moment calculations have been carried out²⁵ to completely define the first-order distribution of the complex signal (Rician), but a general treatment is not known to the author. Historically, there have been two heuristic views. The first applies the

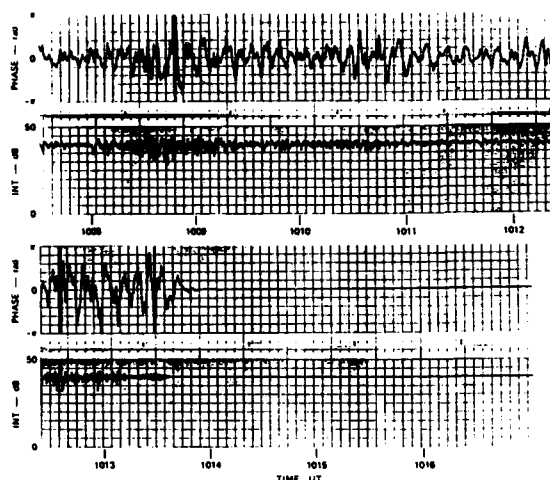


Fig. 4. VHF phase and intensity scintillations isolated from the record displayed in Fig. 1 by employing the trends displayed in Fig. 2 as the reference signal to a software coherent AGC processor.

central limit theorem to the random walk undergone by phase in traversing a structured medium, leading to a normal distribution. A natural extension, particularly convenient for application of the Rytov perturbation technique, was to suppose that the intensity obeys a log-normal distribution. The second view adds component phasors and applies the central limit theorem to the real and imaginary parts of the signal rather than to its logarithm.

An experimental investigation²⁶, using data from Wideband, found neither model adequate. Rather, a two-component model based on both views was necessary for a general description of first-order complex-signal statistics. Phase by itself, however, was well characterized by a normal distribution, and intensity by the Nakagami²⁷ distribution, which is a generalization of the Rice distribution (itself a generalization of the Rayleigh distribution). The result was quite consistent with the intensity behavior previously established by Whitney et al.²⁸

Typical signal behavior is illustrated in Figure 5, which displays, on the complex plane, a scatter plot of one of the UHF (379 MHz) signals received from Wideband at Ancon, Peru over an 80-sec time span shortly before local midnight on 3 March 1977. It also displays the time series of the phase, intensity, and quadrature components of the signal from which the scatter plot was developed. The "snail-shell" appearance of the scatter plot, stemming from correlation between the phase and intensity scintillations, is representative of the general statistical behavior of scintillating signals.

The results of hypothesis testing for intensity and phase distributions to characterize the signal in Figure 5 are displayed in Figure 6. At the top, we find that the log-normal hypothesis provides a good fit to phase but a too-peaked

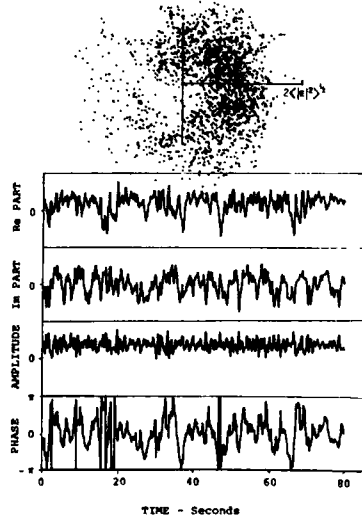


Fig. 5. Three representations of complex-signal scintillations observed at 379 MHz at Ancon, Peru, starting at 0420:19 GMT on 4 March 1977. Top to bottom: scatter plot on the complex plane; real and imaginary parts of the complex signal; amplitude and phase of the complex signal.

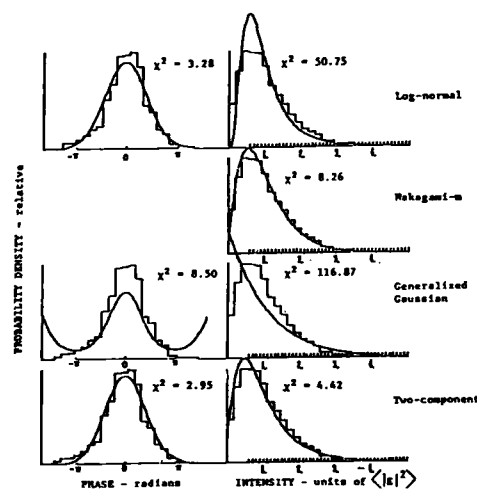


Fig. 6. Histograms of phase and intensity of the UHF signal shown in Fig. 5, compared with probability density functions calculated on the basis of four signal-statistical hypotheses.

distribution for intensity. Next, we see that the Nakagami-m distribution fits the intensity very well but has no theoretically based phase partner. Third, applying the central limit theorem to the observed quadrature components results in phase and intensity distributions quite useless for characterizing scintillation (except when it is very weak, for which all the hypotheses converge to the same distributions). Finally, at the bottom, we find that the two-component model provides satisfactory fits for both phase and intensity.

The two-component model²⁹ describes the total scintillating complex signal, E , as the product of a diffractively scattered component, E_s , and a refractively focused component, E_f , such that

$$E = A \exp(i\phi) = E_s E_f = (x_s + iy_s) \exp(x_f + i\phi_f). \quad (22)$$

It is postulated that E_s obeys complex gaussian statistics and that E_f obeys complex log-normal statistics. It is possible actually to isolate the two components by filtering. This processing was performed on the signal displayed in Figure 5, and the results are shown in Figure 7. The scatter plot in Figure 7a clearly shows the correlation between intensity and phase expected from geometrical-optics focusing and defocusing. That in Figure 7b also displays correlation between the quadrature components, which can be calculated from diffractive scatter theory.³⁰

The full range of signal behavior is illustrated in Figure 8. The middle row repeats the scatter plots from Figures 5 and 7. The top and bottom rows show corresponding plots for, respectively, the VHF (138 MHz) and L-band (1239 MHz) signals received from the same satellite (Wideband). The center and right-hand columns show the effect of (free-space) propagation distance and scattering strength. When the wave is in the near zone (L band), much closer than the focal plane and in which the Fresnel zone is smaller than the dominant irregularities, the focus component consists of almost pure phase variations, and the scatter component is largely imaginary. As the wave propagates through (UHF) and beyond (VHF) a kind of focal plane, refractive focusing occurs and then loses its correlation with phase as a broader and broader spectrum of intensity variations develops. Meanwhile, the scatter component has developed correlated real-component variations (UHF), which then lose their correlation with the imaginary component as the wave propagates beyond the Fresnel distance (VHF) and becomes more and more randomized.

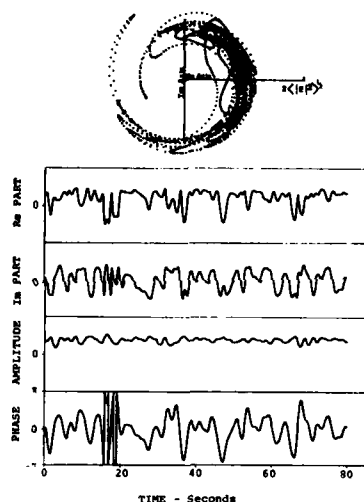


Fig. 7a. The "focus" component, E_f , of the signal shown in Fig. 5, containing phase and log-amplitude fluctuations with Fourier periods between 2.5 and ten seconds (isolated by means of a ten-pole, low-pass Butterworth filter).

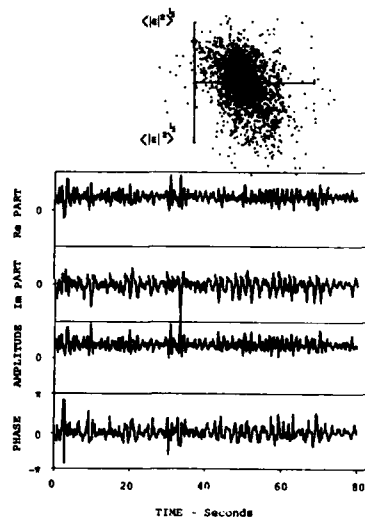


Fig. 7b. The "scatter" component, E_s , of the signal shown in Fig. 5, containing phase and log-amplitude fluctuations with Fourier periods shorter than 2.5 s (isolated by means of "dual detrending").

All of the foregoing behaviors can be calculated.³¹ So, too, can the other dominant characteristic of Figure 8, the increase with scattering strength as frequency decreases. Note that the composite signals (left-hand column) change from crescent shape, to the characteristic snail-shell shape, to Rayleigh-scatter behavior as the frequency decreases from L Band, through UHF, to VHF. This is the combined result of the behaviors described above and the increasing strength of scatter. The latter ultimately is traceable to Eqtn. (8), as we shall now see.

3.2.2 Propagation Theory

Consider an element of the integration path in Eqtn. (8). The phase shift undergone therein is

$$d\phi = (d/\omega) N(r) ds, \quad (23)$$

where N has been expressed as a function of vector position, r . As the wave propagates through a region of structured plasma density, the elemental phase shift along the ray path varies in proportion to N .

To obtain a statistical description of the resulting signal fluctuations, we begin with the two-dimensional spatial autocorrelation function of phase at the output plane of the structured region. If the spatial structures in N extend "deterministically" all the way through the region in the propagation direction, the result is obtained from "coherent" integration of Eqtn. (23) (expressed in Eqtn. 8) and is proportional to the corresponding two-dimensional

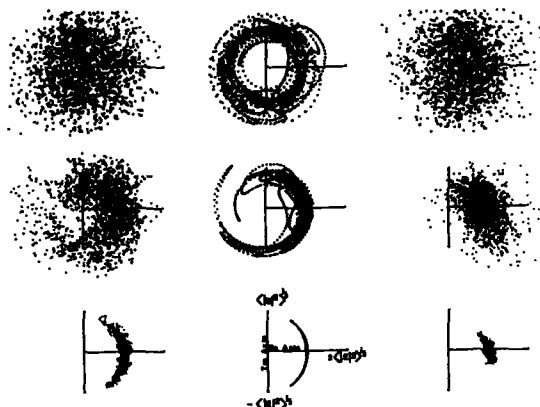


Fig. 8. Complex-plane scatter plots for VHF (top), UHF (middle), and L-band (bottom) signals received simultaneously at Ancon, Peru after transmission from a satellite in a 1000-km orbit above the equatorial ionosphere. Left: composite signal, E . Center: focus component, E_f . Right: scatter component, E_s .

autocorrelation function of N . That is, with H representing the thickness of the region in the direction of propagation, we have

$$R_\phi(\Delta r_1, H) = (d/\omega)^2 R_N(\Delta r_1) \left[\int_{-H/2}^{H/2} ds \right]^2 = H^2 (d/\omega)^2 R_N(\Delta r_1). \quad (24a)$$

where r_1 is the two-dimensional component of r transverse to the propagation direction. In this special case, the statistics of phase (or TEC) are the same as those that would be obtained for plasma density by means of an *in-situ* probe.

More generally, if the structured medium is more than one irregularity thick, the phase-path integration is at least partially "incoherent," with the result^{32,33,34} that

$$R_\phi(\Delta r_1, H) = H (d/\omega)^2 \int_{-H/2}^{H/2} [1 - (2|s|/H)] R_N(\Delta r_1, \Delta s) d(\Delta s), \quad (24b)$$

where $R_N(\Delta r_1, \Delta s)$ is the full three-dimensional autocorrelation function of plasma density. We note that for $\Delta r = 0$, the autocorrelation functions in Eqn. (24b) become variances, and the expression itself becomes the well-known one from sampling theory for the variance of the sample mean. It is as if different point measurements of phase (or TEC) on the output plane are (proportional to) estimates of the mean plasma density, obtained by integrating (or averaging) samples taken along different ray paths through the region.

Eqn. (24a) is the special case of Eqn. (24b) for a statistically thin region, in which R_N is constant (at its zero s -lag value) all along the integration path. The opposite limit is that for which the region is many irregularities thick (H very large compared with all s -lag values for which R_N is non-zero). Then the weighting factor in square brackets reduces to unity, and the integration limits go effectively to infinity. In this case, which is the one addressed in most scintillation theories, we have

$$R_\phi(\Delta r_1, H) = H (d/\omega)^2 \int_{-\infty}^{\infty} R_N(\Delta r_1, \Delta s) d(\Delta s). \quad (24c)$$

In this limit of a statistically thick region, all structure in the propagation direction is integrated up. It is important to note that R_ϕ is proportional to H^2 in the thin-layer case and to H in the thick-layer case. In general, the dependence on H may be intermediate between these two limits. This is pertinent in many applications because the ionosphere and its structures usually are at least approximately horizontally stratified. The dependence on H then dictates the zenith-angle dependence through the simple fact that

$$H = L \sec \Theta, \quad (25)$$

where L is the layer vertical thickness and Θ is the off-vertical incidence angle of the ray on the layer.

Early scintillation treatments used a specific form for R_N , almost always Gaussian because of its convenient Fourier self-transforming property. Although attempts at generalization were made,³⁵ a form is needed to make meaningful progress with the problem. Thus, experimental identification of an appropriate form in the early 70's was a significant contribution.³⁵ The form actually was established as the Fourier transform of R_N , the three-dimensional spatial power-spectral density (PSD) function of N , found to be a red power-law spectrum. In the late 70's, the form was generalized^{34,36} to describe three-dimensionally anisotropic irregularities elongated by a factor, a , along the magnetic field and a factor, b , in an orthogonal direction making an angle, δ , with the local geomagnetic L -shell.

The relation between the phase spectrum and the plasma-density spectrum is found by taking the two-dimensional Fourier transform of Eqn. (24c) and noting that the integral of R_N over Δs retains only the d.c. term of the s -direction spectrum. The relation, given in terms of an anisotropic transverse wavenumber, κ_1 , is

$$P_\phi(\kappa_1) = (d/\omega)^2 L \sec \Theta G(\alpha, \beta, \delta) P_N(\kappa_1, 0) \quad (26)$$

where

$$P_N(\kappa_1, 0) = K(\nu) \langle (\Delta N)^2 \rangle \alpha^3 / (1 + \alpha^2 \kappa_1^2)^{(p+1/2)}, \quad (27)$$

where

$$\begin{aligned} K(\nu) &= \text{a normalization factor,} \\ \langle (\Delta N)^2 \rangle &= \text{total plasma-density variance,} \\ \alpha &= \text{outer scale of the otherwise red spectrum,} \\ \text{and } (2\nu+1) &= \text{power-law index of the three-dimensional spectrum.} \end{aligned}$$

Thus, the three-dimensional plasma-density spectrum has been collapsed, without change to its spectral index, onto a two-dimensional phase screen.³⁷

The factor G in Eqn. (26) depends³⁶ on the direction of propagation as well as on the irregularity anisotropy parameters indicated. Together with the factor α^3 in Eqn. (27), it describes the efficiency of scatter. The fewer the number of independent scatterers along the path (i.e., the larger α for a given B , or L), the greater the degree of quasi-coherence the wave experiences in its phase shift along a given path and, therefore, the stronger the phase modulation on the output plane. The factor G describes the fact that the effective outer scale encountered by the wave depends upon the direction of propagation relative to elongation axes of the irregularities.

One seldom has an explicit measure of the layer thickness. It often happens, also, that the outer scale falls outside the measurement or processing window. If so, one cannot directly determine $\langle (\Delta N)^2 \rangle$ as the variance in Eqn. (27). In this common situation, a useful measure of the strength of Eqn. (26) is $C_k L$, where C_k is the strength of the plasma-density spectrum at a wavenumber of $2\pi/10^3$ rad/m (a wavelength of one km, hence the subscript k). It is given, from Eqn. (27) and because $\alpha > 10^3/2\pi$, by

$$C_k = (2\pi/10^3)^{-(2\nu+1)} \alpha^{(2-2\nu)} K(\nu) \langle (\Delta N)^2 \rangle \quad (28)$$

Then, from Eqns. (5), (26), and (27), we have

$$P_\phi(\kappa_1, L) = r_e^2 \lambda^2 G^* C_k L \sec \Theta \kappa_1^{-(2\nu+1)}, \quad (29)$$

where

$$G^*(a, b, \delta, \nu) = (2\pi/10^3)^{(2\nu+1)} G(a, b, \delta). \quad (30)$$

Thus, the PSD of phase scintillation is proportional to the square of the wavelength, the height-integrated spectral strength of the irregularities, and factors that depend on the three-dimensional shape of the irregularity spectrum and the geometry. An irregularity wavelength of one km is chosen³⁸ for the definition of C_k because it is representative of the scale size of scintillation-producing irregularities. (Note that the corresponding quantity, C_S , employed by Rino³⁹ was defined effectively at a wavelength of one meter, well outside the scintillation spectrum.)

A strip scan of the phase screen (or of its projection onto an observing plane such as the ground) is performed at zero lag in the dimension perpendicular to the scan. Such a scan is tantamount to integration, over that dimension, of the two-dimensional phase spectrum described by Eqn. (29), decreasing the spectral index by unity³⁷ to $p = 2\nu$. The corresponding temporal spectrum depends upon an effective (anisotropic) velocity, V_e , which is proportional to the rate at which contours of constant plasma-density autocorrelation are cut by the line of sight as it scans through the ionosphere perpendicular to itself.^{34,36}

The temporal PSD is given by

$$P_\phi(f_f) \approx T f_f^{-p}, \quad (31)$$

where the approximation stems from taking the infinite outer-scale limit in going from Eqns. (26) and (27) to Eqns. (28) and (29) and where

$$T = r_e^2 \lambda^2 K_1(p) G V_e^{(p-1)} C_k L \sec \Theta \quad (32)$$

is the strength of the temporal spectrum at a fluctuation frequency, f_f , of one Hz. The normalization factor in Eqn. (32) is given by

$$K_1(p) = \sqrt{\pi} \Gamma(p/2) / (10^3)^{(p+1)} \Gamma[(p+1)/2]. \quad (33)$$

Figure 9 shows an example of a temporal phase spectrum measured at VHF during ten seconds of a Wideband pass over Poker Flat. The power-law nature of the spectrum and the lack of an outer-scale (low-frequency) cutoff within the spectral window employed are evident. Note that the measured spectral index of 2.2 is a lower bound for application of phase-screen theory to estimation of the three-dimensional or one-dimensional (*in-situ*) spectral index of the plasma-density structures ($p+1 \approx 3.2$ and $p-1 \approx 1.2$, respectively). The theory does not account for diffractive effects on the phase spectrum. Wittwer (private communication) has pointed out that strong diffraction, which produces deep fades and attendant phase discontinuities, should drive the phase spectral index toward an asymptotic value of 2.0. A theoretical description of the process, however, has not been developed.

Spectral analysis is not always carried out. In that case, the standard deviation over some measurement window is computed from the temporal record for use as a phase-scintillation index. Its square, the variance, is equal to the integral under the phase power spectrum. For a spectrum described by Eqn. (31) and sharply cut off by a detrender with period t_c , the variance is given by

$$\sigma_\phi^2 = [2/(p-1)] T t_c^{(p-1)}. \quad (34)$$

Thus, the phase variance is proportional to $C_k L$, through T , but also depends upon a processing (or system) parameter, t_c .

Kilometer-scale structures are particularly relevant for defining C_k because such a size is comparable to that of the VHF Fresnel zone in the ionosphere. The Fresnel-zone size provides an effective cutoff of the intensity-scintillation spectrum.^{32,39} Moreover, at larger scales (lower frequencies), diffraction has no effect on the phase spectrum, which then accurately represents that of TEC fluctuations at the output screen. The former point is illustrated in Figure 10, which contains the intensity spectrum measured simultaneously with the phase spectrum shown in Figure 9. Since

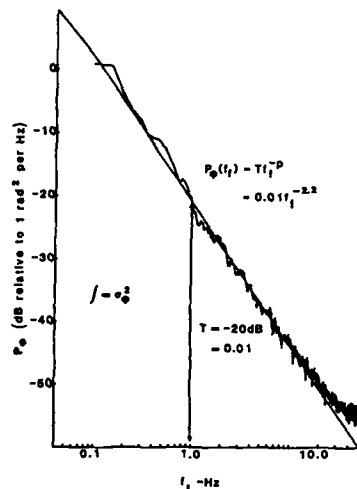


Fig. 9. Spectrum of VHF (138-MHz) phase fluctuations measured during ten sec of a pass of the Wideband Satellite over Poker Flat. Note power-law behavior and lack of an outer-scale (low-frequency) cutoff.

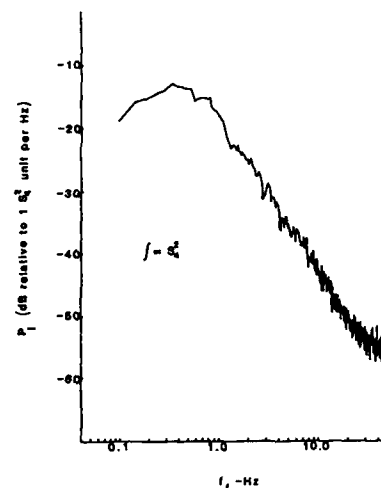


Fig. 10. Intensity spectrum corresponding to phase spectrum in Fig. 9. Note low-frequency cutoff below Fresnel frequency.

intensity scintillation owes its very existence to diffraction, it does not develop on scales much larger than (frequencies much lower than) the Fresnel-zone size (Fresnel frequency). This fact, coupled with the red nature of the irregularity and phase spectra, produces a strong peaking of intensity scintillation near the Fresnel frequency (for weak scatter).

Many of the references contain theoretical developments of the intensity-scintillation spectrum for weak (single) diffractive scatter. Among those that treat the problem more generally is that by Rino.⁴⁰ He explored effects of irregularity and phase spectra containing sufficiently strong large-scale structures that they can produce geometrical-optics focuses and defocuses, as well as effects of diffractive multiple scatter. In practice, *in-situ* spectra are such that the former effects seldom are very strong. The main effects of the latter process are to further "spoil" the focuses and to widen the angular spectrum. The angular spectrum,⁴¹ when translated to the temporal domain, is the doppler spectrum of the complex signal. Under increasingly multiple scatter, both undergo a random walk toward a gaussian shape. The intensity spectrum resembles the doppler spectrum, also broadening and approaching a gaussian.

The foregoing behaviors may be quite pertinent to system design. They also limit the utility of the intensity spectrum as a transionospheric probe, however. In the present context, we shall be content with its integral, the normalized (to the mean) standard deviation, S_4 ,⁴² of received signal power. In weak scatter, its square is given^{36,43} by

$$S_4^2 = K_2(p) \frac{T}{V_e(p-1)} \frac{F}{G} (\sqrt{Z})^{(p-1)} \quad (35a)$$

$$= r_e^2 \lambda^2 K_3(p) F (\sqrt{Z})^{(p-1)} C_{kL} \sec \Theta, \quad (35b)$$

where

$$F(a, b, \delta, p) = \text{"Fresnel filter factor,"}^{46}$$

and

$$\sqrt{Z} = \text{Fresnel-zone radius at penetration point of layer.}$$

We express the intensity scintillation index in the form of Eqtn. (35) to show its relationship⁴³ to the two commonly used phase scintillation indices, given in Eqtns. (32) and (34). Intensity scintillation is proportional to the height-integrated strength of irregularity, $C_k L$, through its dependence on T , but the dependence on V_e cancels out of Eqtn. (35). Instead of being cut off by the effective velocity and a detrended or other system parameter, as is the phase spectrum, the intensity spectrum is cut off by the Fresnel-zone size. In addition, G is replaced by a similar geometrical factor, F , which stems from the diffraction process and depends upon the sharpness of scattering gradients via p . There also is a different normalization factor, given by

$$K_3(p) = \left(\frac{2\pi}{10^3} \right)^{(p+1)} \frac{\Gamma[(5-p)/4]}{\sqrt{\pi}(p-1)\Gamma[(p+1)/4]}. \quad (36)$$

For most practical purposes, including applications-oriented modeling, the limitation of Eqtn. (35) to weak scintillation ($S_4 \leq 0.5$) is of little consequence. In the absence of strong geometrical-optics focusing and defocusing, the Nakagami distribution for intensity reduces to the Rice distribution. Under these circumstances, the intensity of the signal behaves as if the underlying complex-signal statistics are purely Rician (Rayleigh plus a steady, coherent component, which decreases with increasing scatter), with the result that

$$S_4^2 = 1 - \exp(-S_w^2). \quad (37)$$

In the (rare) presence of strong focusing, the Nakagami distribution approaches the Hoyt distribution, and S_4 can exceed unity. The largest value encountered experimentally by the author has been 1.3 (in equatorial scintillation).

3.2.3 Channel Parameters

The intensity and phase spectra and scintillation indices are in common use among those who employ scintillation as a probe. For their purposes, the observables of interest usually are T , p , σ_ϕ , and S_4 . There are several other signal parameters that are pertinent for characterizing the transionospheric communication channel for system designers. As identified schematically by Fremouw and Burns,⁴⁴ they consist of two-point correlation functions in the temporal, spectral, and spatial domains and their Fourier spectral partners.

Employment of some of these channel parameters has been specified and put into succinct form for Satellite C³ applications by Wittwer.² Perhaps the most useful of them is the channel's time-and-frequency (or space-and-frequency) mutual coherence function, familiar to radar designers as the signal ambiguity function. It has been related to the theory reviewed in Section 3.2.2 (with a less succinct but more lucid treatment of the geometry) also by Wittwer.^{3,4}

Space limitations preclude our addressing these points in detail. Suffice it to say that useful measures of the extent of the signal coherence function (to, say, its e^{-1} point) are the signal decorrelation time, τ_D , and its Fourier partner, the doppler spread, δf ; the coherence bandwidth, f_D , and its Fourier partner, the time-delay spread, δt ; and the signal correlation distance (on, say, a receiving aperture), ℓ_D , and its Fourier partner, the width of the angular spectrum, $\delta \gamma$. The first and last of these pairs are linked by the effective velocity, V_e .

The key points about the mutual coherence function are that it characterizes the complex signal and, unlike channel parameters relating exclusively to the phase or to the intensity, it is invariant during propagation in a homogeneous medium. As an example, let $E(r)$ represent the normalized complex signal received at point r , and let

$$\Gamma(\Delta r) = \langle E(r)E^*(r + \Delta r) \rangle \quad (38)$$

be the signal's space-and-frequency mutual coherence function evaluated at zero frequency lag. Its Fourier transform is the angular spectrum, which clearly is invariant in post-scattering propagation. If it is measured at the ground, it may be employed to infer the phase autocorrelation function at the ionospheric exit plane, where the following relation exists

$$\Gamma(\Delta r) = \exp [R_\phi(\Delta r) - R_\phi(0)]. \quad (39)$$

Thus, the exit-phase (and TEC) spectrum may be obtained without the diffraction effects that may be present in the phase spectrum measured directly at the ground.

3.2.4 Irregularity Parameters

Since the channel parameters observable in scintillating signals are established by scattering in ionospheric irregularities, we may use the theory described in Section 3.2.2 to deduce parameters that describe those irregularities. Perusal of the equations in that section identifies five parameters that may be obtained from scintillation measurements. They are

- $C_{\Sigma I}$, the height-integrated spectral strength of irregularity;
- $(2\nu + 1)$, the three-dimensional power-law spectral index;
- a , the along-field axial ratio of the irregularities;
- b , the cross-field axial ratio;
- δ , the orientation angle for three-dimensional anisotropy.

The final parameter, δ , is pertinent only in the event that the irregularities are aligned along a second axis (i.e., $b > 1$) as well as along the geomagnetic field ($a > 1$).

The foregoing five parameters fully describe the height-integrated spatial statistics of three-dimensionally anisotropic irregularities characterized by a power-law spectrum, except for

α , the outer scale

and for any inner scale that may be present (and buried in system noise). The outer scale often falls outside the processing window of scintillation measurements. For fast-moving sources, such as low-orbiting satellites, the window usually is limited by changing geometry. For slow-moving sources such as geostationary satellites and radio stars, the limitation is temporal change in the ionosphere, which may be less stringent.

In addition to the above, by employing spaced receiving antennas (i.e., performing radio interferometry), one may estimate

V_D , the vector drift velocity of the irregularities.

The velocity of scintillation-producing irregularities in the F layer is well approximated by the drift velocity of the bulk plasma, however, which often is available from other sources. One may also deduce

h , the effective centroid height of the irregular layer

from spaced-receiver measurements or from the ratio of intensity to phase scintillation. The latter is possible, in principal, because the intensity-scintillation index depends directly on the propagation distance through the Fresnel-zone size, whereas the phase scintillation indices are independent of the Fresnel-zone size. Care must be taken in the case of low-orbiting satellites, however, because an effective height dependence enters into the phase scintillation indices through V_e .

Table 1 displays an idealized order of analysis for determining the irregularity parameters listed at the top from the observations listed at the left. The author has employed the indicated order, with departures for various practical reasons, in applications-oriented scintillation modeling.^{45,46,47,48} We shall have more to say about the geometrical enhancement listed among the observables soon.

Table 1. An idealized order of analysis.

		Physical Parameters						
		\bar{V}_d	d	b	a	v	h	$C_k L$
Observables	Interferometer Measurements	\bar{V}_d	X					
	$R(\Delta r)$		X	X	X			
	Geometrical Enhancement		X	X	X			
	ρ					X		
	S_4/σ_ϕ						X	
	σ_ϕ or T							X

3.3.0 Experimental Methods

3.3.1 Single Receivers

The most straight-forward application of the propagation theory outlined in Section 3.2.2 is to signals received at a single antenna from satellites radiating coherently on more than one frequency. Such satellites currently in high-inclination orbits include the DNA HiLat^{22,49} and P.BEAR²³ Satellites and the constellations of Navy Navigation (Transit)⁵⁰ and Global Positioning (GPS)⁵¹ Satellites. That part of the following discussion pertaining to intensity scintillation applies also to the relatively limited ionospheric and channel information that one can glean from incoherent sources, including any satellite radiating at VHF and/or UHF (and/or, occasionally in equatorial regions near solar maximum, SHF).

We encountered examples of phase and intensity scintillation observed with HiLat's multi-frequency, coherent predecessor, Wideband, in Section 3.2.1 and their spectra in Section 3.2.2. Here, we look at the behavior of the two most commonly used scintillation channel parameters, σ_ϕ and S_4 , for a particular Wideband pass over Poker Flat. Figure 11 shows detrended strip charts of intensity and phase scintillation observed at VHF (138 MHz), UHF (413 MHz), and L Band (1239 MHz) about an hour after magnetic midnight. Phase excursions exceed $\pm\pi$ at VHF, and the inverse frequency dependence is evident. In addition, that the statistics of scintillation are not stationary over entire pass times is obvious. The intensity and phase scintillation indices for this pass are shown in Figure 12. The former, S_4 , ranges from near the minimum detectable level of about 0.02 at L Band to essential saturation near unity at VHF. The latter, σ_ϕ , tracks extremely closely from frequency to frequency.

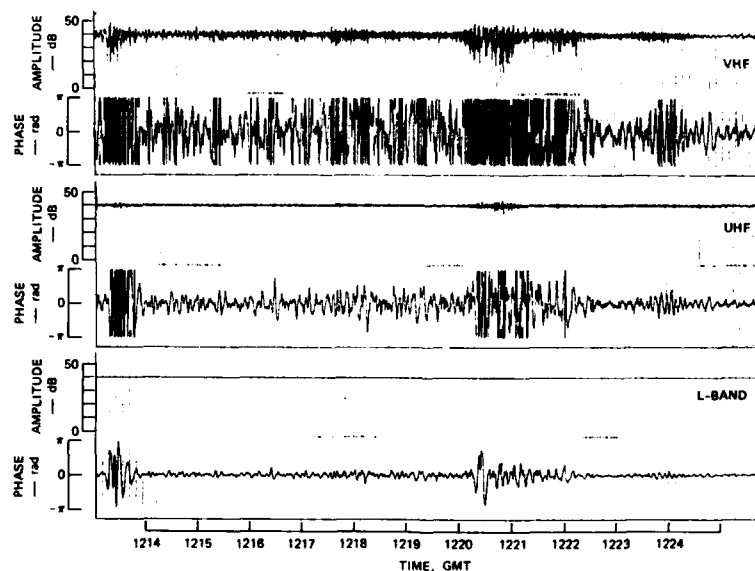


Fig. 11. Detrended VHF, UHF, and L-band strip charts from a Wideband pass recorded at Poker Flat on 29 May 1976.

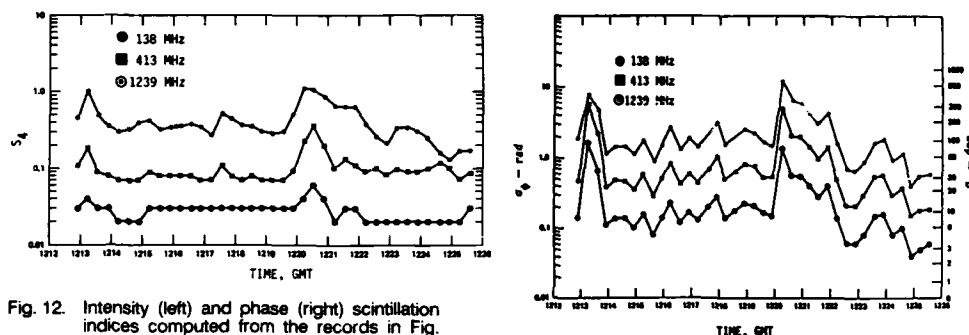


Fig. 12. Intensity (left) and phase (right) scintillation indices computed from the records in Fig. 11.

The frequency dependences for S_4 and σ_ϕ are shown respectively in Figures 13 and 14, for two time points in Figure 12. The former approximately follows an $f^{-1.5}$ dependence for $S_4 \leq 0.5$. This result is in accord with Eqn. (36) for an *in-situ* (one-dimensional) spectral index of 2.0 ($\nu = 1.5$), when one recalls that the Fresnel-zone area, Z , is proportional to λ . For larger S_4 values, the data are consistent with the saturation effect described by Eqn. (37).

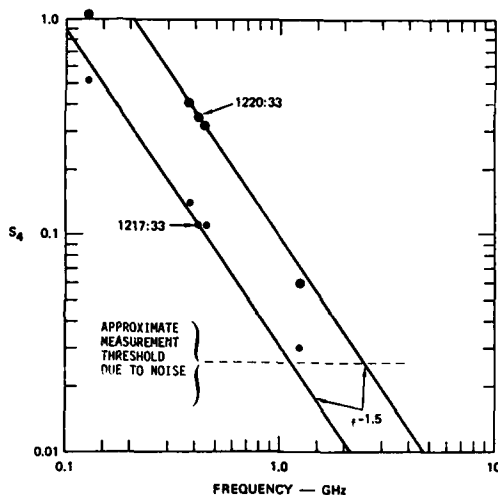


Fig. 13. Frequency dependence of intensity-scintillation index during two 20-sec periods (starting at the times noted) of the pass displayed in Fig. 11, compared with an $f^{-1.5}$ dependence.

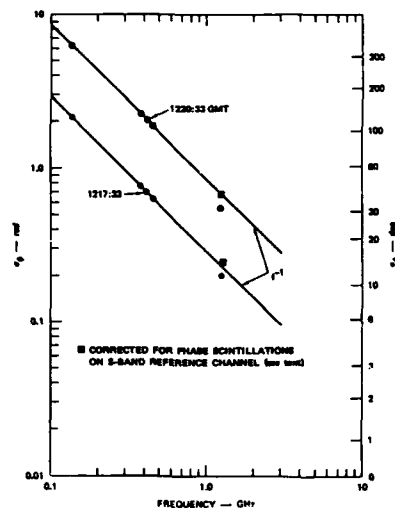


Fig. 14. Frequency dependence of phase-scintillation index during two 20-sec periods of the pass displayed in Fig. 11 compared with an f^{-1} dependence.

Figure 14 displays a remarkably strict f^{-1} dependence, in accord with Eqns. (32) and (34), except at L Band. The departure there stems from the difference between ϕ and ϕ_m in Eqn. (19) and the presence of phase scintillations on the S-band reference channel. The square points in Figure 14 are the results of correcting for this effect on the assumption that the L-band and S-band phase scintillations are fully correlated. Note that the strict adherence of the σ_ϕ frequency dependence to that predicted without regard for diffraction does not mean that there are no diffractive effects on the phase spectrum. Rather, it means that they are small in the aggregate spectrum, which is dominated by contributions from large-scale structures.

Part of the non-stationarity evident in Figures 11 and 12 arises from geometrical enhancement of scintillation, described by increases in $G(a, b, \delta)$ and $V_e(a, b, \delta)$ for phase and in $F(a, b, \delta)$ for intensity. When the line of sight is nearly aligned with an elongation axis of the irregularities, G and F increase due to increased quasi-coherence within the layer and an attendant increase in scattering efficiency. In addition, when the line of sight scans across a short dimension of the irregularities, the phase-scintillation temporal spectrum (Figure 9) shifts to the right due to an increase in the effective velocity, V_e . Both these effects increase the level of scintillation, doubly so for phase because scanning across a short dimension necessarily coincides with alignment with a long dimension.

Figure 15 shows other examples of geometrical enhancement observed at Poker Flat by means of Wideband. Such enhancement is expected at the magnetic zenith for axially symmetric, field-aligned irregularities. Figure 16, which indicates their observed location on a number of early Wideband passes, shows that the effect is not limited to the zenith. Rather, they were observed to occur anywhere along the intersection of the L-shell through the station with the F layer.³² The calculated behavior of the static (G and F) and dynamic (V_e) enhancement factors is consistent with such observations for irregularities aligned east-west along the L shell ($b > 1, \delta = 0$) as well as along the field ($a > 1$). Figure 17 shows the average phase-scintillation index, σ_ϕ , measured at Poker Flat vs. the angle between the line of sight and the local L-shell (computed at an altitude of 350 km) essentially throughout the nearly three-year lifetime of the Wideband experiment. Clearly, geometrical enhancement was a dominant effect.

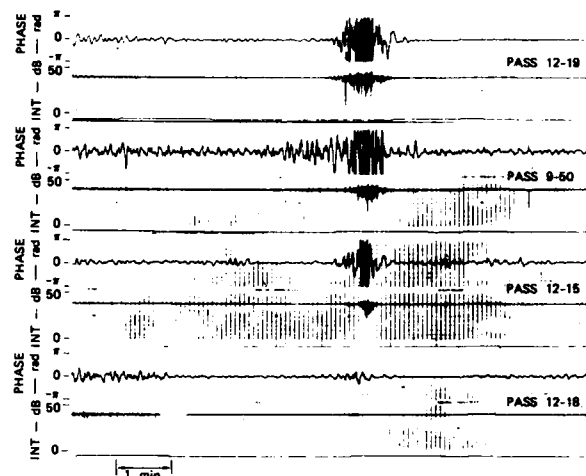


Fig. 15. Four examples of isolated phase-scintillation and intensity-scintillation enhancement. Recorded at Poker Flat, Alaska, during nighttime hours on (respectively, top to bottom) the 29th, 21st, 26th, and 27th of November 1976.

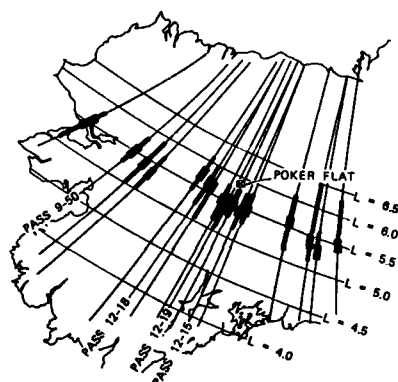


Fig. 16. Map of Alaska showing location of scintillation enhancement on 16 satellite passes observed from Poker Flat ($L = 5.5$) during the last two weeks of November 1976. Lines of constant L and penetration-point loci for the satellite line of sight were calculated for an altitude of 350 km.

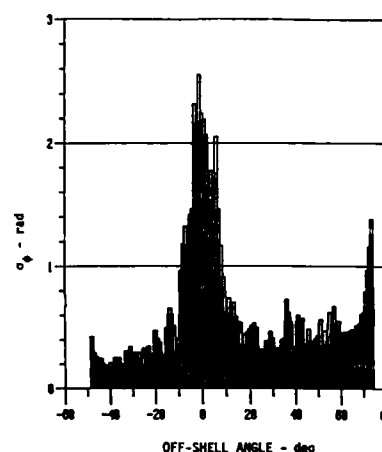


Fig. 17. Average values of VHF phase-scintillation index measured at Poker Flat over the nearly three-year lifetime of the Wideband experiment, as a function of angle between the radio line of sight and the intersection of the local L shell with the F layer.

Fremouw et al⁵² interpreted the foregoing scintillation enhancements as "evidence for either (1) a hitherto unrecognized irregularity enhancement or layer thickening in the subauroral ionosphere, or (2) longitudinally extended irregularity sheets." The latter interpretation regards the enhancement as geometrical in nature, supposing nothing unique about the L shell through Poker Flat. It happens, however, that Poker (as well as the nearby Chatanika, College, and Fairbanks) lies immediately beneath the equatorward edge of the diffuse aurora (scintillation boundary) on most nights of moderate geomagnetic activity. The point is illustrated in Figure 18, which contains plots of intensity and phase scintillation index and (slant) TEC for the four passes included in Figure 15. This unique location of Poker Flat required Fremouw et al⁵² to retain interpretation (1) as a possible explanation for the observations.

3.3.2 Spaced Receivers

Figure 17 attests to the persistence of the enhancement in a coordinate system based on observing geometry. Because the diffuse-auroral boundary also frequents the $L = 5.5$ shell, however, persistence alone is not sufficient to preclude a geophysical, as opposed to geometrical, interpretation of the enhancement. Rino et al⁵³ invoked spaced-receiver observations as confirmation of the hypothesis "that this enhancement is a purely geometric effect due to sheet-like ionospheric irregularity structures aligned along L -shells." Such observations permit direct measurement of the statistical shape of the radio diffraction pattern on the ground. Given reasonably homogeneous statistics of the scintillation-producing irregularities during an individual satellite pass, such measurements may be interpreted in terms of the three-dimensional shape of the irregularities.⁵⁴

The principle is illustrated in Figures 19 and 20, which are taken from Reference 54. Employing three or more antennas and cross-correlating the intensity and/or phase of the signals, one can deduce the elongation and orientation of a best-fit correlation ellipse on the ground. A series of such measurements made during a satellite pass

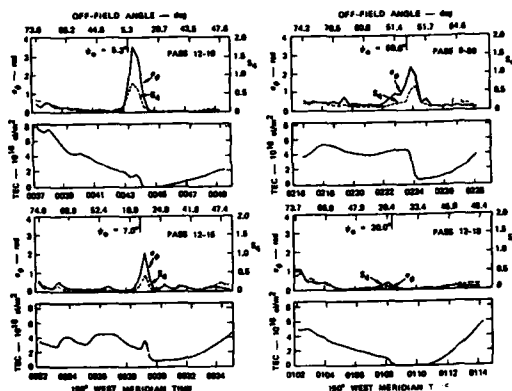


Fig. 18. Plots of phase-scintillation (S_ϕ) and intensity-scintillation (S_i) indices and slant total electron content (TEC) for the four satellite passes illustrated in Fig. 15. The minimum angle between the line of sight and the magnetic field is denoted by θ_0 .

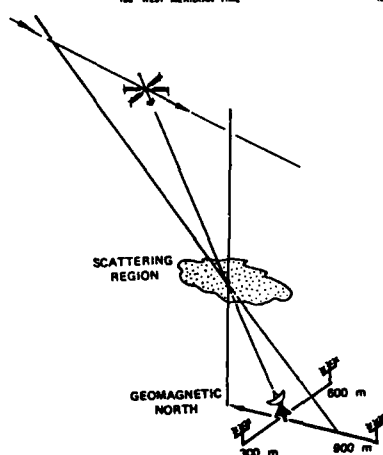


Fig. 19. Wideband spaced-receiver geometry. (From Ref. 54.)

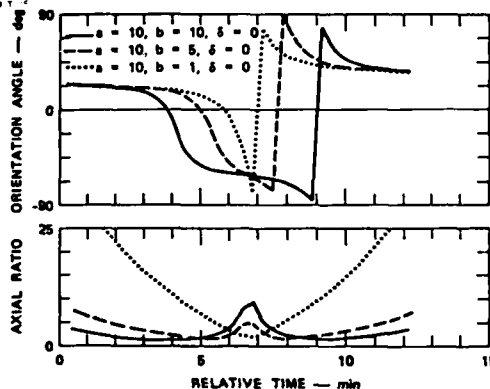


Fig. 20. Axial ratios and orientation angles computed for a high-elevation Wideband pass over Poker Flat by using different irregularity models. (From Ref. 54.)

will result in a time history of the axial ratio and orientation angle of the ellipse, which depends upon a , b , and δ , as indicated in Figure 20. Figure 21, also taken from Reference 54, shows such a time history for a Wideband pass over Poker Flat at about local magnetic midnight on 25 November 1976, compared with that expected for sheet-like irregularities elongated along the magnetic field and east-west in the L-shell by axial ratios of $a:b:1 = 10:10:1$. A series of such measurements led to the conclusion⁵⁵ that the near-midnight sector of the diffuse auroral oval is populated by such sheet-like and "wing-like" ($a > b > 1$) irregularities and that these three-dimensionally anisotropic structures give way to axially symmetric, field-aligned irregularities at higher latitudes. The synoptic picture presented in Reference 55, for moderate magnetic disturbance, is reproduced in Figure 22.

Spaced receivers may be thought of as a radio interferometer, a particularly apt view if phase coherence is maintained between the elements. In this case, one may glean some of the "phase" information contained in the signal from even an incoherent source, such as a radio star. That is, the interferometer is sensitive to phase differences between the signals received at its elements if the source is undergoing angular refraction or angle-of-arrival scintillations due to gradients in TEC and ionospheric exit phase. Indeed, the output of a radio interferometer is directly a measurement of the spatial mutual coherence function defined in Eqn. (38), where Δr represents the vector separation between elements.^{32,33}

An example of such measurements⁵⁶ is given in Figure 23, which contains strip charts of observations of the strong radio source in Cassiopeia made over about an hour and a half during the early morning hours of 4 May 1965. The three charts on the left are from a 68-MHz interferometer operating on east-west baselines of (top to bottom) 330, 220, and 110 meters. The two on the right are from (top) 137-MHz and (bottom) 223-MHz instruments operating on east-west baselines of, respectively, 220 and 218 meters. Intensity and phase-difference (angle) scintillations were experienced at 68 MHz throughout the period, as the source moved through the interferometer fringes.

For about 18 minutes during the middle of the period, the east-west coherence distance of the 68-MHz complex signal became shorter than 330 meters, so that the interferometer "fringe visibility" was totally lost on that baseline and reduced substantially over 220 meters. That is, the angular spectrum was broader than the fringe width for the former baseline and comparable to it for the latter. The signal retained its spatial coherence essentially fully across the 110-meter baseline, although scintillating strongly. Over the 220-meter baseline, fringe visibility was decreased somewhat at 137 MHz, but virtually not at all at 223 MHz.

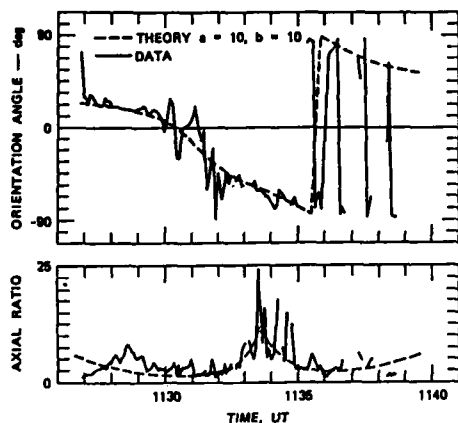


Fig. 21. Measured and calculated axial ratio and orientation angle, Poker Flat pass 12-11, November 25, 1976. (From Ref. 54.)

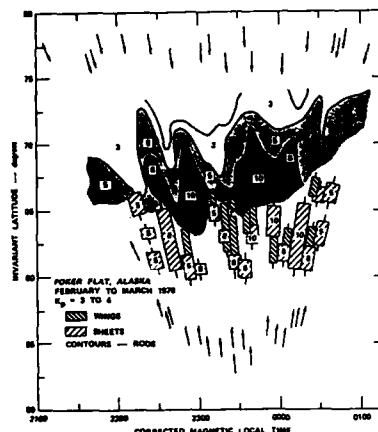


Fig. 22. Overall anisotropy pattern for moderate magnetic conditions (From Ref. 55.)

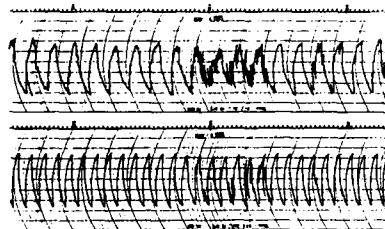
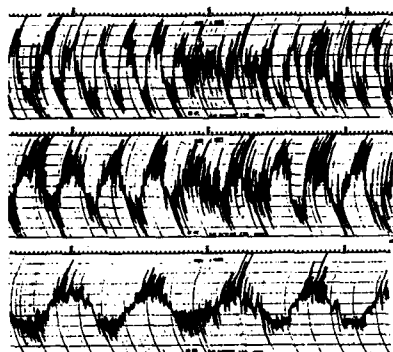


Fig. 23. A typical radio-star visibility fade. Left: 68 MHz with baselines of (top to bottom) 330, 220, and 110 meters. Above (top and bottom): 137 MHz, 220 meters; 223 MHz, 218 meters.

4.0 APPLICATIONS AND PROBLEMS

4.1 Descriptive Models for Application

There are two practical reasons for knowing about scintillation. The first is to design systems that are automatically or adaptively robust to its effects. The second is to schedule communications and other operations of less robust systems for times immune from those effects, or at least to recognize the effects so as to work around them. The former application requires primarily a knowledge of the signal statistics of scintillation, as described in Section 3.2.1. More particularly, it is aided by estimates of the channel parameters alluded to in Section 3.2.3. References 2, 3, and 4 can provide the systems designer with a description of the most relevant parameters.

The second application has been addressed in three ways. The first is exemplified by the work of Aarons et al.⁵⁷ In this approach, long series of observations of a particular parameter such as S_4 or some other convenient measure of scintillation strength are summarized by empirical equations relating the observations to some variable of interest such as time of day at a particular observing location and for a particular geometry such as the look angles to a geostationary satellite. A more fundamental approach⁵⁸ involves direct measurement of $\langle (\Delta N)^2 \rangle$ or C_N and ν *in situ* by means of satellite plasma probes and then application of the propagation theory outlined in Section 3.2.2 to calculate various channel parameters. This approach has the great advantage of permitting use of truly global data bases. It suffers, however, from lack of information on other irregularity parameters, particularly a , b , δ , and L .

The third approach^{31,45,46,47,48} is a hybrid of the first two. It employs scintillation measurements instead of *in-situ* measurements, thereby providing fully integral measures of irregularity strength ($C_N L$ instead of just C_N). It also permits identification of a , b , and δ by means of spaced-receiver observations or careful analysis of geometrical enhancements. It shares with the second approach direct use of the propagation theory for the purpose of separating geometrical from geophysical behaviors. Thus, it should permit reliable calculation of, say, the elevation angle and (geomagnetic) azimuth dependence of scintillation indices from a given station as well as of the (geomagnetic) latitude dependence of scintillation experienced at different stations.

Reference 31 describes an early model developed by the third approach and the computer program, IONSCNT, in which it was employed. That program provided outputs of several channel parameters. Based on the two-component signal-statistical model, calculation of some of those outputs was rather time-consuming. Accordingly, IONSCNT's successor, WBMOD, has been developed without provision for output of some channel parameters. Presently, it puts out only S_4 , T , p , and σ_ϕ . It will soon be augmented to provide L_o and τ_o . Computation of σ_ϕ is over a time span specified by the user as that over which the using system requires phase coherence. WBMOD is based on published scintillation results such as those summarized by Aarons⁵⁹ and, more particularly, on equatorial, mid-latitude, and auroral-zone data from Wideband (hence, the program name). It describes the known dependences

of the relevant irregularity parameters (primarily, but not solely, C_{KL}) on geomagnetic latitude, time of day, season, epoch of the solar cycle, and the state of solar-geophysical disturbance.

Figures 24 through 27 are examples of WBMOD outputs of σ_{ϕ} . The first three are compared with Wideband data from Poker Flat used in the modeling. The model also was tested successfully against subsets of the data not employed in the modeling effort. These three figures relate to latitudinal scans by a high-inclination satellite passing over a fixed station. In all nighttime cases (Figures 24 and 26), the geometrical enhancement is the most prominent scintillation feature. During the daytime (Figure 25), it occurs only on overhead passes (at the magnetic zenith). This behavior is reflected in WBMOD by a diurnal model for the cross-field axial ratio, b . A second prominent feature in Figure 26 stems from the observation of irregularities that develop at the F-layer projection of the plasmapause under magnetically disturbed conditions.⁶⁰ It is described in WBMOD by a sharp function of the planetary magnetic activity index, K_p .

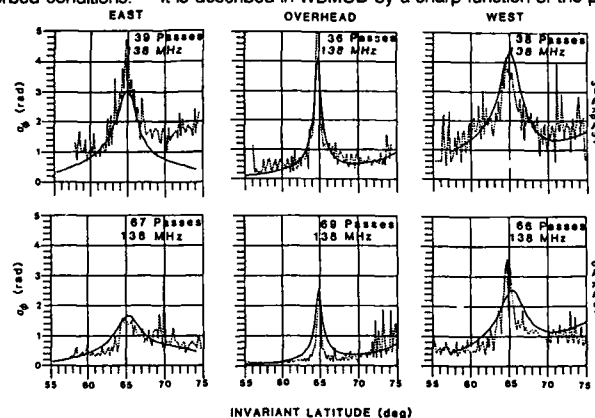


Fig. 24. Values of rms phase fluctuation over a ten-sec period for passage over central Alaska at night of a high-inclination satellite at 1000 km altitude, calculated (solid curves) by means of Program WBMOD. Dotted curves are values observed by means of the Wideband Satellite. Left, center, and right columns are for passes to the east, overhead, and west of the station, respectively. Lower row is for quiet magnetic conditions (K index $\leq 2+$); upper is for moderate activity ($3 \leq K$ index $\leq 5+$).

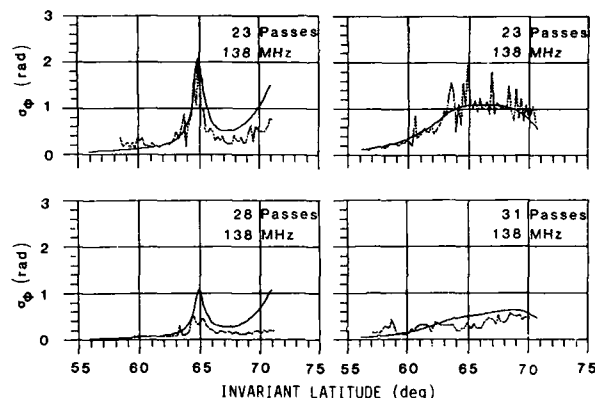


Fig. 25. Same as Fig. 24, except for daytime. Left column is for overhead passes, and right is for passes to the west. Again, lower row is for magnetically quiet conditions, and upper is for moderate disturbance.

Figure 27 is an example of a completely independent check on WBMOD. It compares outputs with 244-MHz observations from Goose Bay, Labrador.⁶¹ The two dashed curves are median diurnal variations observed in spring (upper) and fall (lower). The model, based on observations at different frequencies at different locations and for different observing geometries, reproduces the general level and diurnal variation in measured rms phase fluctuation quite well. What it does not reproduce is the seasonal variation, which is quite clear in the Atlantic (Labrador) sector and essentially nonexistent in the Pacific (Alaska) sector.

4.2 Open Questions for Research

Figure 27 is representative of the status of modeling of known scintillation behaviors. That is, the general level and variations are sufficiently well documented to have been committed to a reasonably reliable (and widely used) computer code, but the model is known to be incomplete. In the example here, a combined seasonal/longitudinal dependence of scintillation is known to exist at high latitudes, and a geophysical basis for it has been postulated,⁶² but it has not been fully documented or modeled. This and other high-latitude deficiencies soon will be remedied in WBMOD by means of data from HiLat and P.EFAR collected in Norway (Tromsø), Greenland (Søndre Strømfjord), and Canada (Churchill), as well as brief series of measurements in Alaska (Poker Flat and Barrow).

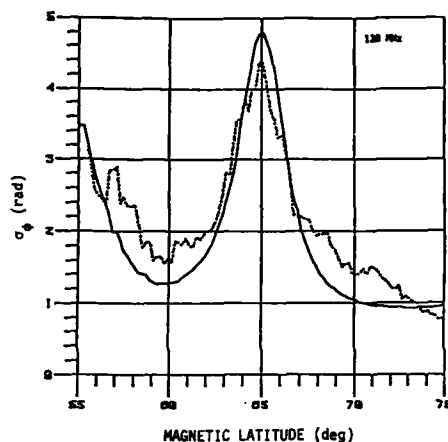


Fig. 26. Same as Fig. 24, except for all nighttime passes under highly disturbed magnetic conditions (K index 6-).

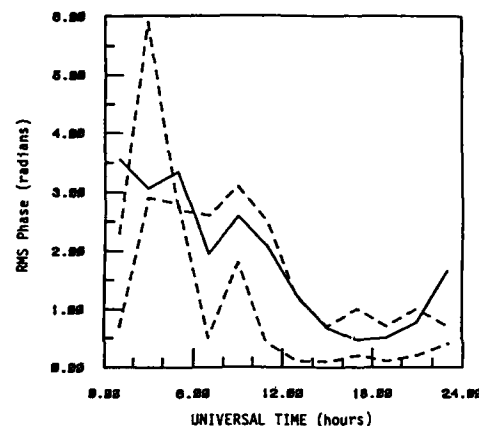


Fig. 27. Independent check on WBMOD output (solid curve) of 244-MHz rms phase to be expected at Goose Bay, Labrador. Comparison curves (dashed) are median values reported in Reference 61 for spring (upper) and autumn (lower).

Another known deficiency is in the seasonal/longitudinal variation at equatorial latitudes. WBMOD does include a description thereof, based on a published hypothesis⁶³ and general agreement of worldwide data therewith. Wideband data from the Marshall Islands (Kwajalein) and Peru (Ancon), however, are biased somewhat away from precise agreement, toward the local summer hemisphere, suggesting an additional controlling factor possibly related to thermospheric winds.

In this final section, we point out some remaining uncertainties in high-latitude scintillation behaviors and their underlying geophysical causes. First and foremost is need for an accurate assessment of the solar-cycle dependence of scintillation, at auroral and, more particularly, polar-cap latitudes. Again, this deficiency is being addressed by means of on-going observations of HiLat and P.BEAR, as well as of the Transits and GPS. Success depends upon continued health of the signal sources and continued commitment by funding sources.

On a more detailed level, questions remain about the three-dimensional spectrum of irregularities, both about the spectral shape itself and about its anisotropy. The shape appears often to be more complicated than the single-regime power law portrayed in Figure 9. A representative example of such a VHF phase spectrum from Wideband appears in Figure 28. Routine Wideband spectral processing did not include time-domain windowing. When a subset of 214 passes was more carefully analyzed⁶⁴ with windowing to suppress spectral leakage, 23% of them showed a downward spectral break at a fluctuation frequency of several Hz. Presumably, this break is the phase signature of a similar break seen *in situ* at spatial wavelengths of several hundred meters to a km.⁶⁵ We shall return to this point in Lecture #8. Suffice it to say here that the theory outlined in Section 3.2.2 needs to be (and is being) modified to permit a more general form, involving two spectral indices instead of just ν and a break scale, β , in addition to the outer scale.

The low-frequency, upward break in the spectrum shown in Figure 28 was observed in 77% of the more carefully analyzed data from Poker Flat, but it was not generally accepted as a meaningful feature because it included only the first few bins in the spectrum of Wideband detrended data. Subsequently, Livingston⁶⁶ reprocessed some of the raw Wideband data from Poker with a longer detrend cutoff (30 sec instead of 10 sec), finding 62% of the resulting spectra to show the upbreak. Moreover, routine processing of HiLat and P.BEAR data employs a 30-sec detrender, and it also reveals the upbreak, an example of which appears in Figure 29. Simultaneous incoherent-scatter data have prompted Livingston⁶⁶ to suggest that the enriched low-frequency portion of the spectrum arises from a contribution by large-scale arc structures in the E layer.

Livingston's suggestion provides an interpretation for another behavior observed in Wideband. It is illustrated in Figure 30, which shows the magnetic-latitude dependence of the phase spectral index routinely observed (best single-regime, log-linear fit) from Poker Flat at night, excluding the quietest magnetic conditions. Increased steepness (larger p) occurred at auroral latitudes, a behavior consistent with a contribution by E-layer arcs. Figure 30 does not complete the story, however, which becomes more complicated when the same data are displayed in two dimensions.

Figure 31 contains a contour plot of p values from essentially the same data population on a grid of angles between the line of sight and (y) the magnetic L-shell at 350 km and (x) the local magnetic meridian at the same altitude, which is similar to a magnetic latitude-longitude grid. The plot shows that, while the phase spectral index generally peaks near the L-shell through Poker Flat, it does not do so in a corridor including the magnetic zenith (0.0 at the center of the plot). We believe that the foregoing behavior results from a combination of (a) the enrichment of large-scale structures by E-layer (and possibly F-layer) arcs and (b) breakdown of the statistically thick-layer assumption. That is, large-scale structures increase the plasma-density spectral index, ν , in the vicinity of auroral-zone L-shells, but p is governed more nearly by Eqn. (24a) than by (24c) when the line of sight approaches field-alignment. Consistent with the latter point is that a decrease in phase spectral index has been found at the magnetic zenith in HiLat data from Churchill, as shown in Figure 32, again suggesting breakdown of the statistically thick-layer assumption. To treat this situation properly, the propagation theory needs to be generalized on the basis of Eqn. (24b). At least a portion of this task has been taken on by Franke,⁶⁷ but the result has not appeared in print as of this writing.

Breakdown of the statistically thick-layer assumption for field-aligned propagation is made at least plausible by Figure 33, which is displayed so that geomagnetic field lines appear vertical. It shows considerable spatial coherence from the bottomside to the topside of the F layer in contours of plasma density obtained⁶⁸ by means of the Chatanika incoherent-scatter radar, located near Poker Flat, at about local magnetic midnight on 20 February 1961. Note also

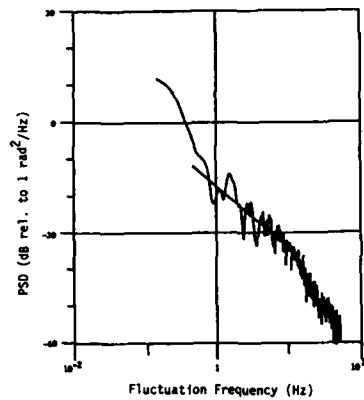


Fig. 28. Example of a fully developed, three-regime power-law phase spectrum, observed at VHF (138 MHz) by means of Wideband from Poker Flat just after local midnight on 29 November 1976.

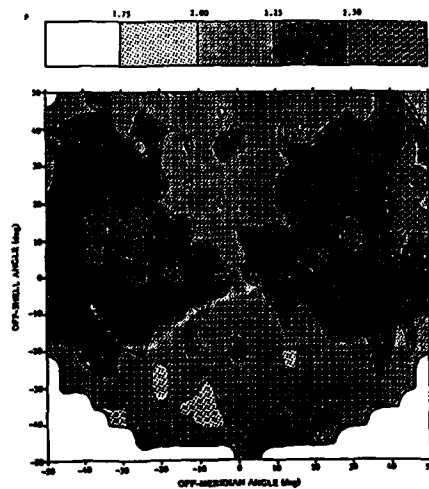
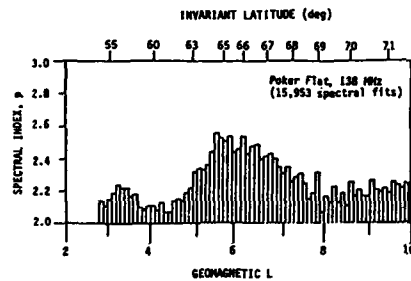


Fig. 31. Contour plot of VHF phase spectral indices measured by means of Wideband at night at Poker Flat, on a grid of angle between the radio line of sight and (y) the local L-shell in the F layer (350 km) and (x) the magnetic meridian at the same altitude.

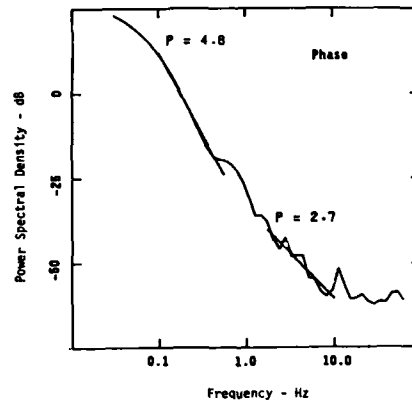


Fig. 29. Phase spectrum from HiLat pass over Sondre Stromfjord at 0235 GMT on 30 January 1987.

Fig. 30. Average values of phase spectral index observed at night during Wideband (except for local $K < 1$) from Poker Flat as a function of geomagnetic L value and latitude at the ionospheric penetration point of the VHF line of sight with the F layer (at 350 km).

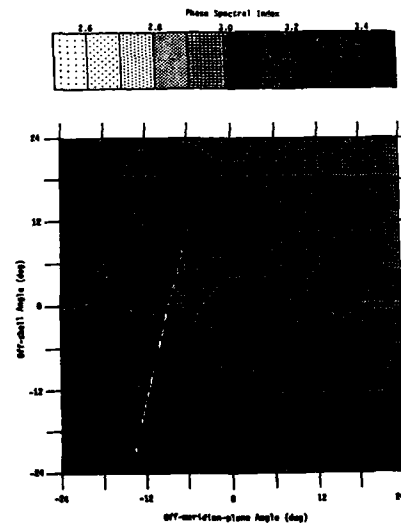


Fig. 32. Same as Fig. 30, except for HiLat data from Churchill collected over a period of about 33 months ending in mid-1987.

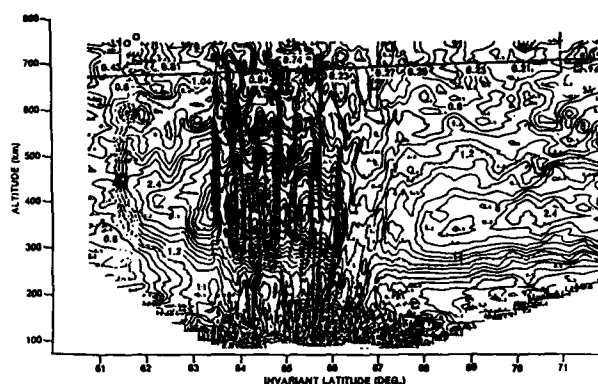


Fig. 33. Contours of plasma density on scale sizes large compared with scintillation-producing irregularities, observed at about magnetic midnight at Chatanika, Alaska, on 20 February 1981. Note considerable spatial coherence along field lines, which are displayed vertically. (From Ref. 68.)

that the coherent structures are confined to within a few degrees of the magnetic latitude of Poker Flat (65°). Thus, while the spaced-receiver observations of Rino et al.⁵³ indicated a geometrical interpretation for the L-shell-aligned scintillation enhancements reported by Fremouw et al.,⁵² L-shells in that region may still be unique as regards irregularity anisotropy. The relationship between three-dimensional anisotropy of scintillation-producing structures and that of larger structures is an open question. The author and Prof. Hargreaves have proposed a study of that relationship based on coordinated scintillation observations of HiLat from Tromsø and high-resolution incoherent-scatter measurements there.

In closing, we note that extensive efforts by the author to identify the geometrical signature of sheet-like irregularities in several years of HiLat scintillation data from Sondre Stromfjord have revealed no such signature. This, of course, is consistent with the idea that such a configuration is confined to the nightside diffuse auroral region. Surprisingly, however, equal efforts with HiLat data from Tromsø and Churchill, located at magnetic latitudes similar to that of Poker Flat, also have failed to disclose the signature. It may be that such a signature will emerge as data collection continues during the advancing solar cycle. At present, however, the apparent inconsistency between the Wideband results from Poker Flat and the HiLat results from Tromsø and Churchill is puzzling.

References

- ¹Lawrence, R.S., C.G. Little, and H.J.A. Chivers, "A Survey of Ionospheric Effects Upon Earth-Space Radio Propagation," *Proc. IEEE*, **52** (1), January 1964, pp 4-27.
- ²Wittwer, L.A., Defense Nuclear Agency, "Radio Wave Propagation in Structured Ionization for Satellite Applications," 1979, DNA 5304D.
- ³Wittwer, L.A., Defense Nuclear Agency, "A Trans-ionospheric Signal Specification for Satellite C³ Applications," 1980, DNA 5662D.
- ⁴Wittwer, L.A., Defense Nuclear Agency, "Radio Wave Propagation in Structured Ionization for Satellite Applications II," 1982, DNA-IR-82-02.
- ⁵Ratcliffe, J.A., *The Magneto-ionic Theory & Its Applications to the Ionosphere*, Cambridge University Press, London, 1959.
- ⁶Jelly, D.H., "On the Morphology of Auroral Absorption during Substorms," *Can. J. Phys.*, **48** (3), 1970, pp 335-345.
- ⁷Ansari, Z.A., "The Aurorally Associated Absorption of Cosmic Noise at College, Alaska," *J. Geophys. Res.*, **69** (21), November 1964, pp 4493-4513.
- ⁸Pope, J.H. and H. Leinbach, National Oceanic and Atmospheric Administration, "Effects of Polar Cap Absorption Events on Geostationary Satellite VHF Communications Systems," 1970, NOAA TR ERL 196-OD 5.
- ⁹Klobuchar, J.A., Air Force Cambridge Research Laboratories, "Total Electron Content Studies of the Ionosphere," 1973, AFCRL-TR-73-0098.
- ¹⁰Millman, G.H., "A Survey of Tropospheric, Ionospheric, and Extraterrestrial Effects on Radio Propagation between the Earth and Space Vehicles," *Propagation Factors in Space Communications*, ed. Blackband, AGARD Conference Proceedings No. 3, 1967, MacKay & Co, Ltd, London, pp 40-47.
- ¹¹Hook, J.L., Geophysical Institute, University of Alaska, "Electron Content Variations in the Auroral Ionosphere Determined from Satellite Radio Observations," 1963, UAG-R136.
- ¹²Little, C.G., "A Diffraction Theory of the Scintillation of Stars on Optical and Radio Wavelengths," *Mon. Not. Roy. Astr. Soc.* **111**, 1951, pp 289-302.
- ¹³Booker, H.G., "The Use of Radio Stars to Study Irregular Refraction of Radio Waves in the Ionosphere," *Proc. Inst. Rad. Eng.*, **46**, 1958, pp. 298-314.
- ¹⁴Hey, J.S., S.J. Parsons, and J.W. Phillips, "Fluctuations in Cosmic Radiation at Radio Frequencies," *Nature*, **158** 1946, p. 234.
- ¹⁵Booker, H.G., J.A. Ratcliffe, and D.H. Shinn, "Diffraction from an Irregular Screen with Applications to Ionospheric Problems," *Phil. Trans. Roy. Soc. A*, **242**, 1950, p. 579.

- ¹⁶Bramley, E.N., "The Diffraction of Waves by an Irregular Refracting Medium," Proc. Roy. Soc. A, 225, 1954, p. 515.
- ¹⁷Bowhill, S.A., "The Scattering of Radio Waves by an Extended Randomly Refracting Medium," J. Atmos. Terr. Phys., 20, 1961, pp 9-18.
- ¹⁸Booker, H.G. and G. MajidiAhi, "Theory of Refractive Scattering in Scintillation Phenomena," J. Atmos. Terr. Phys., 43, 1981, pp 1199-1214.
- ¹⁹Fremouw, E.J., R.D. Leadabrand, R.C. Livingston, M.D. Cousins, C.L. Rino, B.C. Fair, and R.A. Long, "Early Results from the DNA Wideband Satellite Experiment - Complex-signal Scintillation," Radio Sci., 13, (1), 1978, pp 167-187.
- ²⁰Burns, A.A. and E.J. Fremouw, "A Real-time Correction Technique for Transionospheric Ranging Error," IEEE Trans. Ant. Prop., 18, (6), November 1970, pp 785 - 790.
- ²¹Davies, K., R.B. Fritz, R.N. Grubb, and J.E. Jones, "Some Early Results from the ATS-6 Radio Beacon Experiment," Rad. Sci., 10 (8,9), August-September 1975, pp 785-799.
- ²²HiLat Science Team, "The HiLat Satellite Mission," Rad. Sci., 20 (3), May-June 1985, pp 416-424.
- ²³Fremouw, E.J., "The Polar BEAR Ionospheric Experiments: A Pre-Launch Overview," 1986, DNA-TR-86-156.
- ²⁴Aarons, J., J.P. Mullen, and H.E. Whitney, "The Scintillation Boundary," J. Geophys. Res., 74, (3), 1969, pp 884-889.
- ²⁵Mercier, R.P., "Diffraction by a Screen Causing Large Random Phase Fluctuations," Proc. Cambridge Phil. Soc., 58, 1962, pp 382-400.
- ²⁶Fremouw, E.J., R.C. Livingston, and D.A. Miller, "On the Statistics of Scintillating Signals," J. Atmos. and Terr. Phys., 42, 1980, pp 717 - 731.
- ²⁷Nakagami, M., "The m-Distribution - A General Formula of Intensity Distribution of Rapid Fading," Statistical Methods in Radio Propagation, Pergamon Press, New York, 1960, p. 3.
- ²⁸Whitney, H.E., J. Aarons, R.S. Allen, and D.R. Seemann, "Estimation of the Cumulative Amplitude Probability Distribution Function of Ionospheric Scintillations," Rad. Sci., 7 (12), December 1972, pp 1095-1104.
- ²⁹Fremouw, E.J., C.L. Rino, and R.C. Livingston, "A Two-component Model for Scintillation," Proc. of COSPAR Beacon Satellite Group Symposium on the Geophysical Use of Satellite Beacon Observations, Boston University, Boston, 1976, p. 463.
- ³⁰Rino, C.L. and E.J. Fremouw, "Statistics for Ionospherically Diffracted VHF/UHF Signals," Rad. Sci., 8 (3), 1973, pp 223-233.
- ³¹Fremouw, E.J. and C.L. Rino, "A Signal-statistical and Morphological Model of Ionospheric Scintillation," Operational Modelling of the Aerospace Propagation Environment, AGARD-CP-238-VOL. 1, 1978, p. 25.
- ³²Bramley, E.N., "Some Aspects of the Rapid Directional Fluctuations of Short Radio Waves Reflected at the Ionosphere," Proc. Inst. Elect. Engrs., 102, 1955, pp 533-540.
- ³³Fremouw, E.J., Geophysical Institute, University of Alaska, "Radiowave Scattering Structure in the Disturbed Auroral Ionosphere: Some Measured Properties," 1966, UAG R-180.
- ³⁴Rino, C.L. and E.J. Fremouw, "The Angle Dependence of Singly Scattered Wavefields," J. Atmos. and Terr. Phys., 39, 1977, pp 859-868.
- ³⁵Rufenach, C.L., "Power-law Wave Number Spectrum Deduced from Ionospheric Scintillation Observations," J. Geophys. Res., 77, 1972, p. 4671.
- ³⁶Rino, C.L., "Power-law Phase-screen Model for Ionospheric Scintillation: 1. Weak Scatter," Rad. Sci., 14, (6), November-December 1979, pp 1135-1145.
- ³⁷Cronyn, W.M., "The Analysis of Radio Scattering and Space-probe Observations of Small-scale Structure in the Interplanetary Medium," Astrophys. J., 161, 1970, pp 755-762.
- ³⁸Fremouw, E.J. and J.A. Secan, "Support of 'Rover' Ground Station for DNA's HiLat Satellite," Progress Report No. 7, Contract DNA001-85-C-0017, May 1986.
- ³⁹Rufenach, C.L., "Ionospheric Scintillation by a Random Phase Screen: Spectral Approach," Rad. Sci., 10, 1975, p. 155.
- ⁴⁰Rino, C.L., "A Power-law Phase-screen Model for Ionospheric Scintillation: 2. Strong Scatter," Rad. Sci., 14, (6), November-December 1979, pp 1147-1155.
- ⁴¹Booker, H.G. and P.C. Clemmow, "The Concept of an Angular Spectrum of Plane Waves and its Relation to that of the Polar Diagram and Aperture Distribution," Proc. Inst. Elect. Engrs., Pt. III, 97, 1950, p. 11.
- ⁴²Briggs, B.H. and I.A. Parkin, "On the Variation of Radio Star and Satellite Scintillations with Zenith Angle," J. Atmos. Terr. Phys., 25, 1963, p. 339.
- ⁴³Fremouw, E.J., "Geometrical Control of the Ratio of Intensity and Phase Scintillation Indices," J. Atmos. Sci., 42, 1980, pp 775-782.
- ⁴⁴E.J. Fremouw and A.A. Burns, "A Proposed Wide-band Satellite Transmission Experiment," Rad. Sci., 5 (6), June 1970, p.919.

- ⁴⁵Fremouw, E.J. and J.M. Lansinger, "A Computer Model for High-latitude Phase Scintillation Based on Wideband Satellite Data from Poker Flat," 1981, DNA Report 5686F.
- ⁴⁶Secan, J.A. and E.J. Fremouw, "Improvement of the Scintillation-irregularity Model in WBMOD," 1983, DNA-TR-81-241.
- ⁴⁷Fremouw, E.J. and R.E. Robins, "An Equatorial Scintillation Model," 1985, DNA-TR-85-333.
- ⁴⁸Robins, R.E., J.A. Secan, and E.J. Fremouw, "A Mid-latitude Scintillation Model," 1986, DNA-TR-86-381.
- ⁴⁹Fremouw, E.J., "Recent HiLat Results," Propagation Effects on Military Systems in the High Latitude Region, AGARD-CPP-382, 1985, paper 2.1.
- ⁵⁰Kersley, L., "Amplitude and Phase Scintillation at High Latitudes Over Northern Europe," The Effect of the Ionosphere on Communication, Navigation, and Surveillance Systems, ed. Goodman, 1987, Paper 5-7.
- ⁵¹Rino, C.L., M.D. Cousins, and J.A. Klobuchar, "Amplitude and Phase Scintillation Measurements Using the Global Positioning System," Effect of the Ionosphere on Radiowave Systems, ed. Goodman, 1981, pp 253-261.
- ⁵²Fremouw, E.J., C.L. Rino, R.C. Livingston, and M.C. Cousins, "A Persistent Subauroral Scintillation Enhancement Observed in Alaska," Geophys. Res. Letts., 4 (11), 1977, pp 539-542.
- ⁵³Rino, C.L., R.C. Livingston, and S.J. Matthews, "Evidence for Sheet-like Auroral Ionospheric Irregularities," Geophys. Res. Letts., 5 (12), 1978, pp 1039-1042.
- ⁵⁴Rino, C.L. and R.C. Livingston, "On the Analysis and Interpretation of Spaced-receiver Measurements of Transionospheric Radio Waves," Rad. Sci., 17 (4), July-August 1982, pp 845-854.
- ⁵⁵Livingston, R.C., C.L. Rino, J. Owen and R. T. Tsunoda, "The Anisotropy of High-latitude Nighttime F Region Irregularities," J. Geophys. Res., 87 (A12) 1982, pp 10,519-10,526.
- ⁵⁶Fremouw, E.J. and J.M. Lansinger, "Radio-star Visibility Fades in Alaska near Solar Minimum," J. Geophys. Res., 73 (11), 1968, pp 3565-3572.
- ⁵⁷Aarons, J., J. Mullen, H. Whitney, E. Martin, K. Bhavnani, and L. Whelan, Air Force Geophysics Laboratory, "A High-Latitude Empirical Model of Scintillation Excursions: Phase I," 1976, AFGL-TR-76-0210.
- ⁵⁸Basu, Su., Sa. Basu, and W.B. Hanson, "The Role of *In-situ* Measurements in Scintillation Modelling," Effects of the Ionosphere on Radiowave Systems, ed. Goodman, 1981, pp 440-449.
- ⁵⁹Aarons, J., "Global Morphology of Ionospheric Scintillations," Proc. IEEE, 70 (4), 1982, pp 360-378.
- ⁶⁰Houminer, Z., J. Aarons, and R. Rich, "Production and Dynamics of High-Latitude Irregularities during Magnetic Storms," J. Geophys. Res., 86 (A12), 1981, pp 9939-9944.
- ⁶¹Basu, Su., Sa. Basu, R.C. Livingston, E. MacKenzie, and H.E. Whitney, "Phase and Amplitude Scintillation Statistics at 244 MHz from Goose Bay Using a Geostationary Satellite," 1982, AFGL-TR-82-0222.
- ⁶²Basu, Su., "Universal Time Seasonal Variations of Auroral Zone Magnetic Activity and VHF Scintillation," J. Geophys. Res., 80 (34), 1975, pp 4725-4728.
- ⁶³Tsunoda, R.T., "Control of the Seasonal and Longitudinal Occurrence of Equatorial Scintillations by the Longitudinal Gradient in Integrated E Region Pedersen Conductivity," J. Geophys. Res., 90 (A1), 1985, pp 447-456.
- ⁶⁴Fremouw, E.J., J.A. Secan, and J.M. Lansinger, "Spectral Behavior of Phase Scintillation in the Nighttime Auroral Region," Rad. Sci., 20 (4), August 1985, pp 923-933.
- ⁶⁵Basu, Su., Sa. Basu, E. MacKenzie, W.R. Coley, W.B. Hanson, and C.S. Lin, "F Region Electron Density Irregularity Spectra Near Auroral Acceleration and Shear Regions," J. Geophys. Res., 89 (A7), 1984, pp 5554-5564.
- ⁶⁶Livingston, R.C., "High-Latitude Phase Spectral Shape," Minutes of HiLat/P.BEAR Science Team Meeting, ed. Fremouw, May 1987.
- ⁶⁷Franke, S.J., "Modeling of High Latitude Scintillation Spectra," The Effect of the Ionosphere on Communication, Navigation, and Surveillance Systems, ed. Goodman, 1987, paper 5-10.
- ⁶⁸Muldrew, D.B. and J.F., "High-latitude F Region Irregularities Observed Simultaneously with ISIS 1 and the Chatanika Radar," J. Geophys. Res., 87 (A10), 1982, pp 8263.

"Ground/Lower Atmospheric Consideration"

H. Jeske

Meteorological Institute of Hamburg University

Abstract:

The ground-wave propagation of electromagnetic waves in the frequency range below 30 MHz is especially influenced by the ground characteristics (electrical constants, roughness, obstacles) along the path. For frequencies above 30 MHz the main propagation mechanisms are determined by the vertical stratification of the refractive index in the lowest part of the non-ionized atmosphere. The effects are hardly frequency-dependent. The paper will discuss the characteristics of the involved media (ground, troposphere) and their influences on electromagnetic wave propagation with special emphasis to anomalies due to the complex environment of polar regions.

1. Introduction

Electromagnetic waves in the frequency range from VLF to EHF (wavelengths between 100 km and 1 mm) are used for all kinds of communication, navigation, and remote sensing techniques. The physical effects of the transmission medium on electromagnetic wave propagation, which are hardly frequency dependent, are the same all over the world and well known. The interaction between waves and medium include the mechanisms of diffraction, refraction, reflection, ducting, scatter, attenuation, and polarization changes causing supports or limits for electronic systems. In high latitude regions the waves propagate in a particularly complex environment which differ decisively from that at lower latitudes. A very rugged terrain and tremendous differences in electrical ground constants with large seasonal variations hinder the development of prediction methods for ground-wave propagation. Extreme climatic conditions producing low temperature, low absolute humidity and a special stable stratification of the lower troposphere are responsible for propagation anomalies of UHF and higher frequencies.

Some general properties of the propagation medium, which consists of the ground and the troposphere in high latitudes, will be given and a description of their influence on radiowave propagation will be discussed. The paper is divided in two main parts, on the one hand the influence of the earth's surface characteristics on ground-wave propagation and on the other hand the influence of the troposphere on UHF and microwave propagation.

2. Some fundamental considerations of electromagnetic wave propagation

The electromagnetic wave propagation is governed by Maxwell's equations taking account of the material equations which define the electromagnetic material constants of a medium which are essential to a study of wave propagation.

ϵ dielectric constant (permittivity) in $F \cdot m^{-1}$, μ permeability in $H \cdot m^{-1}$, and σ specific conductivity in $S \cdot m^{-1}$. For ϵ and μ often the relative values ϵ_r , μ_r are used referred to their values in vacuum (free-space conditions) $\epsilon_0 = 8.8542 \cdot 10^{-12} F \cdot m^{-1}$ and $\mu_0 = 4\pi \cdot 10^{-7} H \cdot m^{-1}$. Assuming harmonic time dependence Maxwell's equations for a lossy homogeneous medium become ($\mu_r = 1$ for non-magnetic material)

$$\text{curl } \underline{H} = \sigma \underline{E} + i\omega \epsilon \underline{E} = i\omega \epsilon_0 \epsilon_r \underline{E} = \underline{J}_{\text{total}} \quad (1)$$

$$\text{curl } \underline{E} = -i\omega \mu_0 \underline{H}, \quad \text{where} \quad (2)$$

$$\epsilon_r = \epsilon'_r - \frac{i\sigma}{\omega \epsilon_0} = \epsilon'_r - i60 \lambda_0 = (\epsilon'_r - i\epsilon''_r) e^{-i\phi} = \epsilon'_r - i\epsilon''_r \quad (3)$$

is the relative dielectric constant (λ in m, σ in $S \cdot m^{-1}$). It is common practice to use ϵ'_r and ϵ''_r to represent the real and imaginary part of ϵ_r ; ϵ'_r is connected with the phase of the wave and ϵ''_r with its attenuation. The total current $\underline{J}_{\text{total}}$ in Eq. (1) is given by a conducting current $\sigma \underline{E}$ and a displacement current $i\omega \epsilon \underline{E}$. The expression $\tan \delta = 60 \lambda_0 \epsilon''_r / \epsilon'_r$ is known as the loss tangent. For a low-loss medium yields $\tan^2 \delta \ll 1$ (displacement currents large against conducting currents), and for a high-loss case (conducting medium) is $\tan^2 \delta \gg 1$. Often instead of ϵ_r the complex refractive index of a medium is introduced ($\mu_r = 1$)

$$\underline{n}^2 = \epsilon_r = \epsilon'_r - i\epsilon''_r \quad (4a)$$

$$\underline{n} = n - i\kappa \quad (4b)$$

The real refractive index n is optically defined as

$$n = \frac{c}{c_0} \quad (4c)$$

where c and c_0 are the velocity of light of the medium and in vacuum, respectively; κ is called the absorption index. The connection with the material constants ϵ and σ may be found by setting

$$\epsilon'_r - 60 \lambda_0 = n^2 - \kappa^2 - i2n\kappa \quad (5a)$$

This complex equation corresponds to the two equations

$$\begin{aligned} n^2 - \kappa^2 &= \epsilon'_r \\ n\kappa &= 30 \lambda_0 \end{aligned} \quad (5b)$$

A general solution can be obtained

$$n = \pm \sqrt{\frac{1}{2} \left[\epsilon'_r + \sqrt{\epsilon_r'^2 + (60 \lambda_0)^2} \right]} \quad (6a)$$

$$\kappa = \pm \sqrt{\frac{1}{2} \left[-\epsilon'_r + \sqrt{\epsilon_r'^2 + (60 \lambda_0)^2} \right]} \quad (6b)$$

The vacuum is characterized by ϵ_0 , μ_0 , and $\sigma = 0$, an ideal homogeneous dielectric by $\epsilon'_r = \text{const}$, $\mu = \mu_0$, $\sigma = 0$. For low-loss media ($\epsilon'_r \gg 60 \lambda_0$) or a high-loss media ($\epsilon'_r \ll 60 \lambda_0$) simplified equations may be used:

$$n \approx \sqrt{\epsilon'_r}, \quad \kappa \approx \frac{60 \lambda_0}{2 \sqrt{\epsilon'_r}} \quad (\text{low-loss media}) \quad (7a)$$

$$n \approx \sqrt{30 \lambda_0}, \quad \kappa \approx \sqrt{30 \lambda_0} \quad (\text{high-loss media}) \quad (7b)$$

Note the wavelength dependence of the absorption index κ . So the same media may act for long waves as conductor and for microwaves as a dielectric (Fig. 1).

A simple solution of Maxwell's equations for a homogeneous medium are plane waves. For a dielectric (lossless media) holds for a wave propagating in z -direction

$$\underline{E}(z, t) = \underline{E}_0 \exp i(\omega t \pm k z) = \underline{E}_0 \exp i\omega \left(t \pm \frac{n z}{c_0} \right) \quad (8)$$

Eq. (8) represents two waves propagating in opposite directions along the z -axis with time phase ωt and space phase kz , where k is the wavenumber

$$k = \frac{2\pi}{\lambda} \text{ and } \lambda = \frac{v}{c_0}, \quad \omega = 2\pi \nu \text{ (frequency)}, \quad \frac{\omega}{k} = v = \left(\epsilon_r \mu \right)^{-1/2} = c_0 \left(\epsilon_r \mu_r \right)^{-1/2} = \frac{c_0}{n} \quad (8a)$$

For a lossy media ($\sigma \neq 0$) the plane wave solution becomes

$$\begin{aligned} \underline{E}(z, t) &= \underline{E}_0 \exp i \left(\omega t \pm \omega \left(\mu \epsilon \right)^{1/2} z \right) = \underline{E}_0 \exp i\omega \left(t \pm \frac{n z}{c_0} \right) \\ &= \underline{E}_0 \exp i\omega \left(t \pm \frac{n - i\kappa}{c_0} z \right) = \underline{E}_0 \exp \mp \frac{\omega \kappa}{c_0} z \exp i\omega \left(t \pm \frac{n z}{c_0} \right) \end{aligned} \quad (9)$$

It follows from Eqs. (8) and (9) that the plane-wave solution for lossless and lossy media differs by a real exponential factor of the form $\exp \mp \alpha z$ which accounts for the attenuation present in the lossy media. The relation between \underline{E} and \underline{H} may be found by inserting \underline{E} -solutions into Maxwell's equations as

$$\underline{E} = \left(\frac{c_0}{\mu} \right)^{1/2} \left(\underline{k} \times \underline{H} \right), \quad (10)$$

$$Z = \left(\frac{\mu}{\epsilon} \right)^{1/2} \quad (11)$$

is called the intrinsic impedance of a medium. If ϵ is complex as in a lossy media furthermore a phase difference between the \underline{E} - and \underline{H} -field follows ($\exp -i \arctan \kappa/n$).

As a measure of conductivity of a medium it's common practice to use the skin depth or penetration depth δ following from the attenuation term in Eq. (9) as that distance $z = \delta$ over which the field strength amplitude decreases by a factor of $1/e$:

$$\delta = \frac{c_0}{\omega \kappa} = \frac{\lambda}{2\pi \kappa}, \quad (12)$$

$$\delta \approx \frac{\sqrt{\epsilon'_r}}{60 \pi n} \quad \text{for low-loss media (n in } S m^{-1}) \text{ and} \quad (12a)$$

$$\delta \approx \frac{1}{2\pi} \sqrt{\frac{\lambda}{30 \sigma}} \quad \text{for high-loss media (k in m, } \sigma \text{ in } S m^{-1}) \quad (12b)$$

δ is divided by a factor 2 if the decrease in signal power is considered.

Generally, the skin depth increases (less absorption) with increasing wavelength and decreases with increasing conductivity of the medium. This effect is well known in submarine reception or as skin effect in copper conduction. The skin depth of the earth's crust varies typically from a few centimeters at VHF and UHF to 100 m at VLF. Often the name penetration depth is used in connection with effective values of the material constants of the

ground which take into account the stratification of the ground or its roughness.

For the theory of radio wave propagation near the surface of the earth it is essential to know the ground characteristics along the path and the electrical constants of the atmosphere near the surface (in the lower troposphere). For frequencies below 3 MHz ($\lambda > 100$ m) especially the conductivity for the underlying surface layers are essential, at least down to the penetration depth, for frequencies above 30 MHz ($\lambda < 10$ m) the structure of the troposphere governs the propagation properties. The ground constants determine the transmission of the surface- or ground-wave and the magnitude and phase of reflection coefficients being used for propagation of line-of-sight links. The spatial and temporal structure of the troposphere determines the tropospheric propagation mechanism as refraction, ducting, reflection, scatter, and attenuation.

3. Characteristics of the earth's surface and its influence on electromagnetic wave propagation

3.1 General remarks

The earth's surface will absorb, reflect, guide, diffract, and scatter electromagnetic waves. The main influences may be divided into three classes:

- The influence of the smooth (homogeneous) surface, characterized by ϵ , μ , σ , for line-of-sight transmission as for beyond-the-horizon propagation. This incorporates ground-wave propagation (surface-wave and diffracted field) and interference between direct and reflected rays within the horizon. The effects are strongly wavelength-dependent.
- The influence of rough surfaces where "rough" is meant in the sense of the Rayleigh-criterion of optics.
- The influence of topographical obstacles as rugged and mountainous terrain.

In high latitudes there are special problems associated with snow, ice, permafrost and Arctic tundra connected with a strong annual and interannual variability.

3.2 Electrical properties of the ground

Generally, the ground possesses properties as a semiconductor having a dielectric constant ϵ as well as a conductivity σ . For the permeability μ mostly the free-space value μ_0 is assumed. The two relevant parameters depend to a great extent on the nature of the terrain which is particularly complex in high latitudes. In order to get an overlook on the bandwidth of values for different surface materials and the wavelength dependence Fig. 2 may be consulted, supplemented by Table 1a and 1b. Generally, a strong dependence from the water content of the medium is observed [Albrecht, 1970; Großkopf, 1970]. The interesting values for the conductivity lies between about 5 Sm^{-1} (sea water) and 10^{-6} Sm^{-1} (Arctic tundra) and that for the dielectric constant ϵ , between 2 (dry snow, very dry soil) and 100 (pure ice). An approximate value for the dielectric constant (lower frequencies) may be obtained for the most ground materials from an average relationship between this quantity and the ground conductivity [Albrecht, 1965]

$$\epsilon' = 180 K (\sigma)^{1/2} e^{-0.001 \sigma} \quad (13)$$

where t is the ground temperature (°C) and K a factor depending on the type of ground and varying between 0.5 and 1.5, average value = 1.0 in Sm^{-1} .

The conductivity for most materials is constant for frequencies below 30 MHz ($\lambda > 10$ m), however, the conductivity for fresh-water ice varies over the whole frequency range and it is expected that sea ice has a similar variation. Fig. 3 demonstrates the differences in ϵ' and ϵ'' (see Eq. (3)) of four types of sea ice in the microwave range gained by a dielectric mixing model [Ulaby et al., 1986]. The differences depending on the ice type are a consequence of the fact that sea ice is a heterogeneous mixture of ice, salt, brine pockets, and air bubbles. The relative levels of the dielectric constant curves among the four ice types is (above all) a direct result of their relative salinity. The salinity of the first-year ice ($\approx 5\%$) is typically 5 times that of multi-year ice. Arctic ocean water has a salinity of the order of 32‰. Especially for ϵ'' a strong decrease as function of temperature is given (first-year ice $\approx -10^\circ\text{C}$, multi-layer ice $\approx -20^\circ\text{C}$). Further influences are coming from ice density (first-year ice 0.87 g cm^{-3} , multi-year ice 0.77 g cm^{-3}) and brine pockets [Ulaby et al., 1986]. Fig. 4 presents curves and ranges of values of the penetration depth for microwaves of pure ice, first-year ice, and multi-year ice. As the ice thickness vary from young ice to multi-year ice between about 20 cm and 3 m the effect of the underlying water is completely masked by the ice for frequencies higher than 10 GHz due to small penetration depths. For LF and MF conductivity, values of Table 2 may be used.

Snow is a mixture of ice and air (dry snow) and free (liquid) water (wet snow). Some values for LF and MF regions may be found in Table 2. The low conductivity of snow corresponds to a low-loss media (insulator properties). The frequency dependence of ϵ' and ϵ'' in the microwave region with wetness as a parameter is given in Fig. 5. Measured values of the real part of the dielectric constant contains Fig. 6. The ϵ' -values may approach the value of air ($\epsilon' = 1$) Fig. 7 shows penetration depths for some frequencies as function of snow wetness.

By satellite remote sensing of snow and ice cover and permafrost areas, more and more information of their geographical distribution and its annual variation is available [Hall et al., 1985] but values of the ground constants in high latitudes are still very rare. A great spatial inhomogeneity and the strong seasonal variations of structure and composition of snow, ice, permafrost, and soil complicate the situation. The CCIR collects ground values and has published a first edition of a world atlas of ground conductivities. Fig. 8 gives an example showing the deficiencies in high latitudes. In any case the conductivity in the interior of polar regions is extremely low (10^{-6} Sm^{-1}).

3.3 Ground-wave propagation

Ground-wave propagation includes the surface wave, the direct and reflected wave within the horizon, and the diffracted field around the horizon of the curved earth. If ground-wave fieldstrength are to be calculated, it is essential to know the ground characteristics along the path. Formulas or computer programmes are available for practical use. The most important electrical characteristic of the earth for frequencies below 10 MHz is the conductivity. The CCIR has published two atlases of ground-wave propagation curves for a vertical transmitting dipole as function of frequencies (between 10 kHz and 10 GHz) and different heights of transmitting and receiving antennas above the ground for sets of constant which are representative for propagation over sea water and over land (smooth and homogeneous surface). The mentioned CCIR world atlas of ground conductivities also in-

clude propagation curves for the frequency range 30-3000 kHz. This type of propagation is utilized above all in the VLF, LF, and MF region for world-wide navigation systems or stable communication far behind the horizon without the assistance of the ionosphere. The influence of conductivity may be seen from Fig. 9 for a frequency of 700 kHz ($\lambda = 430$ m). Included are curves for mixed path (land and sea). At 200 km a difference of fieldstrength of about 60 dB results for conductivities between 4 and $\leq 10^{-4}$ Sm $^{-1}$.

However, also for propagation of UHF and higher frequencies beyond the horizon the diffracted fieldstrength is of importance. It determines the signal level which is permanently present. At larger distances behind the horizon tropospheric scatter from atmospheric irregularities (see below) is the principal mechanism for frequencies greater than 30 MHz. The transmission loss for diffraction paths increases rapidly with decreasing wavelength (see Fig. 10). For mm- and cm-waves practically no energy is received behind the horizon via this mechanism.

Concerning high latitudes it should be noted that ground-wave propagation over sea ice is anomalous [Bourne et al., 1970; Hill et al., 1981]. The presence of a low conductivity ice layer over high conductivity sea water supports a trapped surface-wave or "Elliott mode" [Elliott, 1956]. This mode dominates at short ranges where the field may exceed the free space value. At intermediate distances the surface-wave interferes with the normal ground-wave (both are of comparable magnitudes) and may produce rapid variations of fieldstrength and phase. At longer ranges the usual ground-wave modes are dominant. An example for 10 MHz [Hill et al., 1981] may be shown in Fig. 11. Theoretical and experimental results for a 1.7 MHz-path are reported by Bourne et al. [1970]. Furthermore, the phenomenon was studied theoretically by Wait [1962]. It's obviously a speciality of highly inductive surfaces, i.e. not necessarily involving ice or sea water.

Dry new snow with very low conductivities of 10^{-9} to $3 \cdot 10^{-11}$ Sm $^{-1}$ acts as a rather good insulator. Therefore, a LF-, MF- and even HF-antenna may be laid directly on soft new snow with successful results.

3.4 Line-of-sight propagation

3.4.1 Smooth earth

This type of propagation is a characteristic feature of UHF and microwave propagation where the antennas are located several wavelength above the ground and the field within the horizon is built up by the interference of a direct ray and a reflected ray (geometric optics). To calculate the fieldstrength in this "interference" zone (behind the horizon lies the diffraction of shadow zone) it is necessary to know the reflection coefficient R of the surface ($R = R \exp - i \Phi$). If specular reflection can be assumed Fresnel's formulas are used. The fieldstrength then may be estimated by

$$E = E_0 \sqrt{1 + R^2 + 2R \cos \left(\Phi + \frac{2\pi \Delta}{\lambda} \right)}, \quad (14)$$

where E_0 is the free space fieldstrength, Φ the reflection coefficient phase angle and $2\pi \Delta / \lambda$ the phase angle resulting from the path-length difference of the direct and reflected rays. The path-length difference is

$$\Delta = \frac{2h_1 h_2}{d}, \quad (14a)$$

h_1, h_2 antenna heights, d distance between transmitter and receiver. For small grazing angles ψ ($R \rightarrow 1, \Phi \rightarrow 180^\circ$) Eq. (14) is reduced to

$$E = 2E_0 \sin \left(\frac{2\pi h_1 h_2}{\lambda d} \right) \quad (14b)$$

and the interference pattern (with maxima ($2E_0$) and nulls) as function of height or distance becomes obviously (see example in Fig. 12). The reflection coefficients, remarkably different for horizontal and vertical polarization, are again a sensitive function of the electrical ground constants as may be derived from Fig. 13. As in the UHF and microwave region the difference of the real dielectric constant at the boundary is the dominating factor, the reflection coefficient may become very small because ϵ_r of dry snow may approach the value of air (perhaps filled with drift-snow). This means that significant transmission across the boundary takes place. During geodetic distance measurements with microwaves this effect was confirmed, i.e. the reflected component ("swing") vanished [Hofmann, 1964]. Often the detection range of the instruments (tellurometer) was (although within optical range) only 1-2 km. The reasons may be ray deflection due to an decrease of temperature with decreasing height (measured below the instrument) together with lacking reflection. Also difficulties with radar altimeters (frequency 450 MHz) above snow covered surfaces are known.

3.4.2 Rough surfaces

In the UHF and microwave range the reflection properties are more determined by the roughness of the surface than by the ground constants. For rough surfaces the specular reflection of smooth surfaces is reduced, the reradiation is distributed in other than specular directions. To distinguish between the two types of reradiation (specular or diffuse) the well-known Rayleigh-criterion of optics may be used for a first-order classification. For smooth reflection yields:

$$h < \frac{\lambda}{8 \cos \Theta_i}, \quad (15)$$

where h is the standard deviation of the surface height variation, λ the wave length, and Θ_i the angle of incidence. It is assumed that a phase difference between two reflected rays at levels one standard height deviation apart is less than $\pi/2$ radians. A more stringent criterion adopt the limit used to define the far-field distance of an antenna which requires a phase difference between rays from the centre and the edge of an antenna less than $\pi/8$. In Eq. (15) then stands 32 instead of 8 [Ulaby et al., 1982]. It is seen that the greater the wavelength or the angle of incidence Θ_i , the less important is the influence of roughness. As the roughness increases the expected lobe structure of line-of-sight paths may be destroyed more and more, i.e. the nulls will be filled up suggesting the forward reflection decreases.

The problem of predicting the reflection or scattering of rough surfaces has not been fully solved but a number of useful models are available [Beckmann et al., 1963; Ulaby et al., 1982; Miller et al., 1984]. Surface parameters necessary for model calculations are (above all) the Rayleigh parameter ($h \sin \psi / \lambda$), i.e. the standard deviation of surface height h , and the surface correlation length l . The slope of the surface irregularities is then h/l . Such parameters will be made available - also for high latitudes - by modern remote sensing techniques. Microwave radar altimeters, laser altimeters, imaging radars, multi spectral scanners and scatterometers (which measures the scattering function, too) have been flown on aircrafts or satellites [Carsey et al., 1981]. Complicated is the situation near the ice margin, with ice of different evolution stages, and also for summer ice with melt ponds or frozen melt ponds.

In HF and VHF ground-wave propagation across a rough surface an additional transmission loss due to roughness is estimated by the concept of effective surface impedance depending on the spatial height spectrum of the surface [Barrick, 1971].

In rugged and mountainous terrain additional diffraction effects (knife-edge diffraction) complicate field-strength estimations. Progress is being made by means of multiple knife-edge diffraction models using topographic data base available from survey ordnance maps or digital terrain mapping [e.g. Loew et al., 1983]. Practical application of the method, which is capable to predict the median values of fieldstrength, was made for determining service areas in mobile UHF radio.

4. The role of the troposphere for electromagnetic wave propagation

4.1 The refractive index of the troposphere

The effects of the troposphere are most important for frequencies above the HF band ($\lambda < 10$ m), and they are most pronounced for transmission at low elevation angles. The propagation properties are governed by the radio refractive index only, which is real and non-dispersive for frequencies below 10 GHz ($\lambda < 3$ m), or higher (100 GHz) if the zones around the absorption regions of oxygen (60 GHz and 119 GHz) and water vapor (22 GHz and 183 GHz) will be excepted. The refractive index n is very close to unity and is therefore expressed commonly in N-units (refractivity) where

$$N = (n - 1) \cdot 10^6 \quad (16)$$

The refractivity N depends upon atmospheric pressure, temperature, and humidity and may be given by a half-empirical formula after Smith and Weintraub, rewritten in a "dry" (D) and a "wet" (W) term.

$$N = D + W = \frac{77.61 p}{T} + \frac{37.31 \cdot 10^3 e}{T^2} \quad (17)$$

where p total pressure (mb), e partial pressure of water vapor (mb), and T temperature (K). The verified ranges of validity are $-20^\circ\text{C} < T < 60^\circ\text{C}$, $200 \text{ mb} < p < 1100 \text{ mb}$, and $e < 100 \text{ mb}$. The surface value N_s varies geographically from about 400 N-units in humid tropical regions to about 300 N-units in desert climates or for a time, in high latitudes, too. As humidity is the most critical parameter (highly variable, difficult to measure especially in high latitudes) for high precision geodetic or geophysical applications, therefore, light transmission is preferred to microwaves. The optical refractive index is practically only a function of pressure and temperature due to the disappearance of the effect of orientation polarizability of the polar water vapor for such high frequencies. All other atmospheric gases are nonpolar gases.

For the transition region near absorption bands Liebe [1981] has developed a practical calculation procedure up to 300 GHz. Besides the frequency-independent refractive index outside the absorption regions some frequency-dependent terms which are mainly due to the dispersion and absorption properties within the resonance zones have to be taken into account. An example of the behaviour of refractive dispersion Δn (deviation of n from the frequency-independent term, see Eq. (17)) and attenuation for microwaves under different meteorological conditions (warm/humid and cold/dry) is given in Fig. 14. Note the influence of humidity on attenuation and refractive index.

The sensitivity of the normally used refractivity (Eq. (17)) to the atmospheric parameters p , T , e may be derived from

$$dN = \frac{\partial N}{\partial p} dp + \frac{\partial N}{\partial T} dT + \frac{\partial N}{\partial e} de \quad (18)$$

The determination of the coefficients $\partial N/\partial p$, $\partial N/\partial T$, $\partial N/\partial e$ under mean conditions ($p = 1013 \text{ mb}$, $T = 288 \text{ K}$, $e = 10.2 \text{ mb}$), arctic summer (1010 mb, 273 K, 7 mb), and arctic winter (1020 mb, 248 K, 0.5 mb) leads to

$$\Delta N = 0.27 \Delta p - 1.27 + 4.5 \Delta e \quad (19a)$$

$$\Delta N = 0.28 \Delta p - 1.31 \Delta T + 5.0 \Delta e \quad (19b)$$

$$\Delta N_{\text{opt}} = 0.31 \Delta T - 1.31 \Delta T + 8.1 \Delta e \quad (19c)$$

A decrease of N is connected with an increase of temperature (inversion) and a decrease of water vapor. The comparison with the optical refractive index (mean conditions) shows the 100 times stronger influence of humidity on the radio refraction index.

$$\Delta N_{\text{opt}} = 0.27 \Delta p - 0.95 \Delta T - 0.04 \Delta e \quad (19d)$$

The correspondent N -values for the given typical conditions and the optical value are 319, 322, 322, 273, respectively.

With the aid of formulas like Eq. (17) the refractive index may be computed at any point in space at which the meteorological parameters p , T and e are observed. For the surface refractivity N_s world charts of monthly mean values are available [Bean et al., 1968]. However, for latitudes higher than 75° the material is scanty. Characteristic annual mean values of N_s for different climates may be taken from Table. 3.

4.2. Refractive index stratification

The height variation of N is approximately exponential and may be written

$$N(h) = N_s \exp\left(-\frac{h}{H}\right). \quad (20)$$

CCIR recommends as an average exponential decrease a surface value $N_s = 315$ and a scale height $H = 7.35$ km. Below 1500 m, a linear height dependence exists:

$$N(h) = 315 - 40h \quad (h \text{ in km}), \quad (20a)$$

i.e. a vertical gradient of 40 N-units per km. From this linear model the concept of an effective earth radius $r_{eff} = k r_0$ (r_0 true earth radius) was derived; under the given conditions r_{eff} is 4/3 times the actual radius (4/3-earth). In the lower atmospheric boundary layer ($h < 50$ m) the linear model cannot be used, here a more or less logarithmic height dependence is characteristic.

The model of an effective earth allows propagation to be considered as rectilinear above a hypothetical earth of effective radius $k r_0$ with an effective curvature

$$\frac{1}{k r_0} = \frac{1}{r_0} + \frac{1}{n} \frac{dn}{dh}. \quad (21)$$

The vertical gradient of n gives the ray bending ($1/\rho$) for an approximately horizontal path ($\mu = 0$). Generally yields

$$\frac{1}{\rho} = \frac{1}{n} \frac{dn}{dh} \cos \phi, \quad (21a)$$

where ϕ is the angle of the path with the horizontal at the point considered. The variability of the n -gradient determines the variability of the ray curvature (bending). Eq. (21) means that the curvature of the ray is incorporated in the effective curvature of the earth ($1/k r_0$) and the ray remains a straight line ($\mu = \infty$). The curvature factor k can be derived from vertical profiles of n (see Eq. (21)). With this model all refraction effects may be handled by using the effective radius of the earth $k r_0$ instead of r_0 , for example, estimating the horizon distance, the diffraction field behind the horizon, or the pathlength difference between the direct and reflected rays for line-of-sight propagation. Frequency distributions of k were made from meteorological soundings. It varies usually between 0.9 and 3. But note the assumption for the k -model (linear decrease of n , horizontal path).

A general accepted standard profile (of the form of Eq. (20)) of refractivity for high latitudes is not available. Based on the 1966 given U.S. Standard Atmosphere Supplements, McClatchey et al. [1978] published an atmosphere for a latitude of 75° north (summer and winter). From these models a N -gradient between surface and 1 km of 52.6 N-units follows for the summer ($N_s = 339.7$) and of 40 N-units for the winter ($N_s = 316.9$). The correspondent values of the curvature factor k in the effective earth model are 1.50 and 1.34. The derived model parameters for the exponential model of Eq. (20) are $N_s = 340$ and $H = 6.9$ km (summer) and $N_s = 317$ and $H = 7.5$ km (winter).

For the marine environment statistics of N_s and ΔN may be found in the Naval Ocean Systems Center's Technical Document 573 [Patterson, 1982]. From 84 stations between 60° and 70° values of N_s and ΔN , subdivided into winter (January-March) and summer (July-September) are given in Table 4. The data show only less deviation from standard refraction conditions.

Generally, caution should be exercised in the use of given mean values or profiles of N from standard atmospheres because of the great variability of the parameters (see world charts of monthly values of $\Delta N = N_s - N_{1km}$ in Bean et al. [1968]). Like the standard atmosphere used in meteorological sciences the correspondent N -models may describe only the gross structure of the atmospheric refractive index field. Under special climatic conditions - even for stationary conditions - also the mean structure with its annual variation may show a complete different height distribution, for instance within the trade wind inversion region. Of course, synoptic variations as fronts, ground inversions, elevated inversions and other inhomogeneities are also not included. Especially the situations connected with inversions are of interest for propagation problems as they give rise to anomalous propagation mechanisms due to reflection or ducting.

Under the influence of subsidence effects, advection, surface heating or radiative cooling there is a tendency for stratification of the lower troposphere. This takes the form of refractivity layering. Layers of ducting gradients ($\Delta N/\Delta h < -0.157$ N-units per km) of only a few hundred meters or often less, superrefraction layers ($-0.157 < \Delta N/\Delta h < 80$ N-units/km) or subrefraction layers ($\Delta N/\Delta h > 80$ N-units/km) are possible. These layers can be horizontally extensive (to hundreds of kilometers). In the case of ducts the gradients are less than -157 N/km, i.e. the ray curvature exceeds the earth's curvature and trapping of rays occur. To identify such trapping layers the modified refractivity M is very useful. M is defined by

$$M = N + \left(\frac{h}{r_0}\right) 10^8 = N + 0.157h, \quad (22)$$

where h and r_0 in meters. Here the earth is flat and a modified ray bending is introduced (a radio ray will be bend upwards). A trapping-gradient layer is then defined by a negative slope of M (M -inversion). Three types of ducts exist in the lower atmosphere (Fig. 15). A surface-based duct (the M -inversion begins at the surface), a surface duct with an elevated M -inversion, and an elevated duct (with elevated M -inversion). A special type of the surface-based duct is the evaporation duct of the lower boundary above the sea which is a nearly permanent feature above the oceans due to a rapid decrease of moisture immediately above the sea surface (see Chap. 4.3).

The central Arctic shows a meteorological situation which may be connected with strong stratifications in the boundary layer, namely the Arctic stratus clouds. During the summer season, low-level stratiform clouds - almost entirely attributed to Arctic stratus clouds - are the prevalent feature in the central Arctic. Monthly-averaged low cloud cover amounts show a steep increase during April to a broad maximum of nearly 70% for the summer

months of May through September. After that follows a rapid decrease during October to the winter value of 20%. The clouds occur below about 3000 m (typically 1000 m) with a thickness of a few hundred meters (typically 300 m), frequently comprised of two or more separate layers, and sometimes accompanied by an underlying fog. These persistent low-level cloud cover is interpreted as an air mass modification phenomenon on which variations in cloudiness due to synoptic activity are superimposed. At lower levels, warm air is advected over the pack ice, and is cooled by some combination of radiation and eddy turbulence to produce condensation. A unique feature of the Arctic stratus is the presence of strong temperature inversion and humidity decrease overlying a frequently stable boundary layer. By this a reflecting layer (ΔN -jump), an elevated duct or a surface duct may result with considerable consequences for VHF, UHF and microwave transmission. Two characteristic examples of radiosonde ascents (Fig. 16a, b) may illustrate the situation and serve to estimate the relevant refractive index parameters. The profiles stem from the MIZEX-experiment 1984 (at about 80° north and 2° west) with research vessel POLARSTERN, organized by the Alfred-Wegener-Institute for Polar Research (Bremerhaven, FRG). On June 23rd, 23.30 an elevated inversion exist with $\Delta N = 10.5$ N-units between 500 and 550 m which gives an elevated duct of 120 m between 550 and 430 m. Also other superrefraction gradients exist (between 0-25 m: 0.089 m or between 550 and 600 m: 0.112 m). On July 1st, 18.30 there are nearly a ground-based duct between 0 and 25 m ($\partial N/\partial z = 0.151/m$) and a reflecting layer between 250-300 m ($\partial N/\partial z = 0.142/m$ or $\Delta N = 7.1$). If we remember the limitation in the response time of the radiosonde sensors some more trapping gradients should exist. The humidity profile (%) shows a strong variation, but note that the absolute humidity only varies between about 3 g/kg (surface) and 2 g/kg at 1000 m.

Long-term statistics of ducts from radiosonde stations of the Arctic region, as for example given in Table 5, show very low occurrence of ducts. But the results from climatological data based upon routine measurements must be considered very sceptical because of their insufficient height- and time-resolution. To get an impression on the annual variation of temperature and absolute humidity in high latitudes in Fig. 17a, b time-height sections for 1984 of the Georg-von-Neumayer-Station (70.5°S, 8.3°W) are presented. One major feature are the low temperatures and low absolute humidities in winter time. In the central polar regions the level would be still essentially lower.

4.3. The lower boundary layer (Prandtl-layer)

As mentioned the lower boundary layer (say up to some decameters) has its own physics. The fundamental laws are the same for air-water interaction as for air-ice or air-snow interaction as long as ice ridges and other roughness elements will be absent. Within this layer strong gradients exist due to a more or less logarithmic height distribution of meteorological parameters. The boundary layer formalism to determine profiles, gradients, fluxes, or stability parameters is to-day fully developed and generally accepted (see e.g. Brunner [1984]). In radio-meteorology this formalism is the key for evaluating the evaporation duct thickness above the sea from simple meteorological measurements near the ground (see e.g. Richter [1986]). The open water regions bordering the Arctic ocean show significantly different evaporation duct height statistics. In Fig. 18a, b duct heights in the Bering Sea and the Norwegian Sea are presented in order to show magnitudes for high latitudes (further evaporation duct statistics see Patterson [1982]). The thickness lies mostly for below 6 m. The higher occurrences of larger duct heights for the Norwegian Sea is probably due to the influence of the Gulf Stream. Propagation anomalies caused by ducting so are possible only for very high frequencies (> 10 GHz).

The characteristic feature of the boundary over ice and snow is its extreme thermal stability, especially during the dark season. The stability parameters as the Richardson number are mostly far beyond the critical value (~ 0.2) used for a verified boundary layer theory. Beyond this critical number no definitive profile form is known. In these quasi non-turbulent conditions the gradient are no more the result of eddy diffusion. The temperature profile obviously is governed by radiative effects.

Nevertheless, the conditions for ducting gradients ($\partial N/\partial z < -0.157/m$) are frequently given as we know from direct mass measurements. From Eq. (19a, b) we may deduce ($\Delta z = 0$):

$$\frac{\partial N}{\partial z} < -0.157 \text{ m}^{-1} < -0.042 \text{ m}^{-1} - 1.3 \frac{dT}{dz} \quad (23)$$

$$\frac{dT}{dz} > 0.089 \text{ m}^{-1} \quad (23a)$$

this means to get a dry duct the temperature gradient must exceed $8.9/100$ m. Such conditions are no rarity within the central polar regions, above all during the winter time. Examples are shown in Fig. 19 [Lettau et al., 1977]. Long-term statistics are not yet available.

Special difficulties arise in the Arctic marginal ice zone. This area is characterized by strong horizontal variability due to the differences in the roughness and thermal characteristics of the underlying surface (open water, thin ice, sea ice, polynyas, pack ice) and the development of (horizontal inhomogeneous) internal boundary layers over the water or the ice surface correspondent to wind direction. Such features limits any operational prediction of propagation conditions.

4.4. Refraction effects

4.4.1 General remarks

It's common to differentiate between four types of refractive conditions, namely trapping ($\partial N/\partial h \leq -0.157 \text{ km}^{-1}$), superrefraction ($-0.157 < \partial N/\partial h \leq -0.79 \text{ km}^{-1}$), "standard" ($-0.79 < \partial N/\partial h < 0$), and subrefraction ($\partial N/\partial h > 0$). For standard and superstandard refractivity gradients, a radio ray will refract downward toward the earth's surface, but with a curvature less than that of the earth. Under trapping conditions (ducting) the ray curvature exceeds the earth's curvature. If the gradients are positive ($> 0 \text{ N/km}$), a radio ray will bend upwards. Fig. 20 illustrates the relative curvature for each. For $k > 1$ ($\partial N/\partial h < 0$) the distance of the horizon d_H , given by

$$d_H = \left(2 k r_e h \right)^{1/2} \quad (h: \text{height}) \quad (24)$$

is extended with increasing k -values (increasing negative gradient of refractivity). In the presence of a trapping layer, the concept of horizon no longer has any precise meaning, and very distant points may be "in line-of-sight".

4.4.2 Fieldstrength alteration

For within-the-horizon propagation, the interference structure of fieldstrength (i.e. the position of maxima and minima) is changed. At a fixed distance a downward displacement occurs if $k > 1$, and upward displacement if $k < 1$ (substandard). In practice pace-diversity systems are used for correction. For fixed antenna-heights the interference pattern is shifted towards the horizon (for $k > 1$).

The diffraction field is enhanced with increasing k -values (Fig. 21). Remarkable effects only set in if superrefraction conditions ($k > 2$) are given. As we learned from Table 4, the k -values in polar regions are mostly below 1.5 and so no specific effects will occur for this transmission mode.

4.4.3 Elevation angle error, height error

Since the rays in the atmosphere normally are bent downwards all observed points or targets within or without the atmosphere are elevated above the straight-lined connection between observer and target, i.e. a difference between the apparent and true (geometrical) direction occurs, the elevation angle error (see Fig. 22 for definitions). For space targets this error corresponds to the total ray bending ϵ , for targets within the atmosphere the error corresponds to the terrestrial refraction error ϵ' (approximately half of the total ray bending, $\epsilon \approx \epsilon'$ only for earth-space links). Fig. 23a gives values for the elevation angle errors computed for an averaged exponential atmosphere, Fig. 23b includes values calculated for the arctic and subarctic winter and summer with 100% humidity. Obviously the bending effect falls off rapidly as the ground elevation angle increases. The maximum value for a horizontal path amounts to $0.8''$.

When layers exist which have steeper N -gradients than standard gradients additional bending will occur. Layers close to the surface are much more effective in increasing ϵ and ϵ' than higher layers. An impression may give Fig. 24. Above a ground elevation of 5° even trapping layers will cause no additional bending.

For waves > 75 cm (400 MHz) the influence of the ionosphere has to be taken into account [Millmann, 1965].

4.4.4 Range errors

Because radio waves travel slower in the atmosphere than in vacuum and since radio range calibration are mostly made using the vacuum velocity (or another fixed velocity) measured ranges are slightly larger than actual. A further smaller effect (typically $< 10\%$ of the total error) is given by the curvature of the radio ray. Fig. 25 shows values for a standard atmosphere with 0% and 100% humidity with ground elevation angle as parameter. The limits (for a space target) are 381 ft (100% humidity) or 290 ft (0%).

Also the Doppler velocity (Doppler frequency) of a moving target is measured incorrectly due to refraction effects. The error results from the fact that the direction of the refracted ray at the target differs slightly from the direction of the line-of-sight path [Millmann, 1965].

4.5. Ducting

The most dramatic nonstandard effects are caused by ducts in the lower atmosphere (existing also in high latitudes). Propagation ranges far exceeding the normal horizon (superdetection ranges) or correspondent fieldstrength enhancements are possible, but also areas where the signal level is very low (radio holes) occur. As in the wave guide theory the atmospheric ductpropagation is coupled with a critical wavelength (or cut-off frequency). Above this wavelength the trapping effect for a given duct thickness falls off markedly. Typical values are 10 m for a duct thickness of 700 m, 1 m for a thickness of 130 m, 10 cm for 20 m, 3 cm for 10 m, or 1 cm for 6 m. The duct effect will also decrease rapidly if the penetration angle exceeds about 1° . Elevated ducts and ground-based ducts due to advection or subsidence are mostly relatively thick, say > 50 m and can affect propagation for frequencies above approximately 100 MHz ($\lambda < 3$ m). The N -stratification in connection with the Arctic stratus clouds may be effective for these frequencies.

The evaporation duct due to turbulent diffusion processes (especially water vapor transport) can affect frequencies above 3 GHz ($\lambda < 10$ cm). The evaporation duct heights vary generally between 0 and 40 m with a long-term mean value of about 8 m at northern latitudes. It is to note that an antenna need not to be in the evaporation duct to benefit from signal enhancement of the duct (which is strongly dependent on frequency and duct thickness) because the atmospheric ducts are very leaky ducts. Also an antenna above the duct will still receive signals very much enhanced over nonducting conditions.

The optimum frequency to achieve extended ranges via an evaporation duct appears to be around 18 GHz ($\lambda = 1.6$ cm). Although the ducting effect extends beyond this frequency, absorption of atmospheric gases and extra attenuation due to a rough sea surface begin to counteract the benefits of the duct [Hitney et al., 1985]. As in high latitudes the thickness of evaporation ducts are below or around 5 m, no remarkable effects are to be expected.

Some examples may illustrate the preceding statements. Fig. 26 gives a correlation between fieldstrength (path loss) and duct thickness for an 18 GHz-link (distance 81 km, antenna 20 m and 11 m above sea level). The solid oscillating curve is the theoretical dependence based on wave guide modelling (smooth sea) with the successful operating "Integrated Refractive Effects Prediction System (IREPS)" described by Hitney et al. [1976]. The observed values are mostly somewhat below the theoretical curve. The agreement would be better if the sea surface roughness is incorporated. This may demonstrate an attempt of [Rotherman 1974] given in Fig. 27. Furthermore, the variation of the N -profile as function of stability may give an effect in the right direction. Another gap in the field of wave guide modelling are the consideration of horizontal inhomogeneities, effects which are remarkable at coastlines or near the marginal ice zone (formation of internal boundary layers).

4.6. Reflection

Another mechanism giving occasion to an increase of fieldstrength or superdetection ranges is the reflection of electromagnetic energy at atmospheric layers (inversions). As the reflection coefficient for an horizontal layer of definite thickness decreases strongly with increasing ratio layer thickness/wavelength this type of propagation is favoured for longer wavelengths. It may be sometimes in high latitudes (ΔN -values are not too high) of significance for waves above 1 m [Großkopf, 1970].

4.7. Tropospheric scatter

At ranges far beyond the horizon, the field strength is dominated by the mechanism called troposcatter (curve 3 in Fig. 21). Propagation in the troposcatter region is the result of scattering of electromagnetic waves from refractive heterogeneities at relatively high altitudes, which are line-of-sight to both the transmitting and receiving antennas. The scattering coefficient is proportional to the spectrum of spatial refractive index fluctuations due to temperature and humidity fluctuations. The intensity of such fluctuations depends upon climate and weather conditions. If the spectrum in the medium is known transmission parameters can be calculated. The rate at which the path loss increases with range (within the troposcatter region) is considerable less than the rate in the diffraction region. No special features in high latitudes are known, the fluctuation intensity will be relatively low.

4.8. Attenuation by gases and precipitation

Oxygen and water vapor molecules in the atmosphere absorb some energy from radio waves and convert it to heat. The amount of the resonance absorption is highly dependent on the radio frequency and is negligible, compared to all other propagation considerations, below 20 GHz. The absorption spectrum was shown in Fig. 14 for different water contents of the atmosphere. The total attenuation of an earth-space path for Arctic summer and winter (75 N) is given in Fig. 28. The plots show the attenuation for different elevation angles for frequencies between 20 and 50 GHz. It's generally low during winter time and increases with frequency. Extinction (absorption and scattering) by rain drops and other forms of precipitation can be important for some meteorological situations in polar regions, too. However, a main feature of these regions is a low precipitation rate. Furthermore, the most part of precipitation are falling as snow or ice crystals having a very low attenuation rate (due to the low imaginary part of refractive index of ice or dry snow). An overlook may be deduced from Fig. 28, for the same precipitation rate the attenuation coefficient of dry snow is about 20 to 50 times smaller than that of rain. Note that a snowfall of 10 mm/h is a maximum value. The attenuation of melting snow, however, has been observed to be substantially larger than that of rain [Atlas, 1964].

5. References

- Albrecht, H. J., On the relationship between electrical ground parameters, Proc. IEEE 53, 1965, 544
- Albrecht, H. J., Geographical distribution of electrical ground parameters on navigation systems, AGARD/NATO Conf. Proc., no. 33, 1970, 327
- Atlas, D., Advances in Radar Meteorology, Adv. in Geophys., 10, 1964, 318
- Barrick, D. E., Theory of HF and VHF propagation across the rough sea, Radio Sci 6 (5), 1971, 527
- Barton, D. K., ed., Radars, Vol. 2, Artech House Inc., 1974, 219
- Bean, B. R., Dutton, E. J., Radio Meteorology, New York, Dover Publ., 1968
- Beckmann, P., Spizzichino, A., The scattering of electromagnetic waves from rough surfaces, New York, Pergamon Press, 1963
- Bourne, I. A., Ross, D. B., Segal, B., Phase instability in radio waves propagating across ice-covered seas, AGARD/NATO Conf. Proc. no. 33, 1970, 319
- Brunner, F. K., ed., Geodetic refraction, Berlin, Springer-Verlag, 1984
- Burrows, C. R., Attwood, S. S., Radio wave propagation, New York, Academic Press Inc., 1949
- Carsey, F. D., Zwally, H. J., Remote sensing as a research tool, in N. Untersteiner (ed), The Geophysics of Sea Ice, NATU-ASI Series B, Phys. Vol. 146, New York, Plenum Press, 1986
- David, P., Voge, J., Propagation of waves, New York, Pergamon Press, 1969
- Elliott, R. S., Spherical surface wave antennas, IRE Trans. Ant. Prop., A. P.-4, 1956, 422
- Großkopf, J., Wellenausbreitung I, Hochschultaschenbücher, Nr. 141/141 a, Mannheim, Bibliogr. Inst., 1970
- Grube-Lenhard, M., The meteorological data of the G. v. Neumayer Station for 1933 and 1984, Rep. 38, 1987, Alfred-Wegener-Institut f. Polar- u. Meeresforschung, Bremerhaven, FRG
- Hall, D. K., Jaroslav, M., Remote sensing of ice and snow, London, Chapman and Hall, 1985
- Hill, D. A., Wait, J. R., HF radio transmission over sea ice and remote sensing possibilities, IEEE Trans. Geosci. and Remote S., GE-19 (4), 1981
- Hitney, H. V., Richter, J. H., Integrated Refractive Effects Prediction System (IREPS), Nav. Eng. J. 88 (2), 1975, 257
- Hitney, H. V., Richter, J. H., Pappert, R. A., Anderson, K. D., Baumgärtner, Jr., G. B., Tropospheric radio propagation assessment, Proc. IEEE 73 (2), 1985, 265
- Hofmann, W., Nortarp, K., Die geodätische Lagemessung während der Sommerkampagne 1959 der Int. Glaziol. Grönlid-Exp., M. O. G. Bd 173, Nr. 6, Kopenhagen 1964
- Kruspe, G., Personal Communication 1988, Max-Planck-Institut f. Meteorologie, Hamburg

- Lettau, H., Riordan, A., Kuhn, M., Air-temperature and two-dimensional wind profiles in the lowest 32 meters as a function of bulk stability, Antarctic Res. Ser., 25, A. G. U., 1977
- Liebe, H. J., Modeling attenuation and phase of radio waves in air at frequencies below 1000 GHz, Radio Sci 16 (6), 1981, 1183
- Loew, K., Lorenz, R. W., Determination of service areas for mobile communication with a topographical data base, IEEE, ICC '83, A 2.3, 1983, 54
- McClatchey, R. A., Fenn, R. W., Selby, J. E. A., Volz, F. E., Garing, J. S., Optical properties of the atmosphere, in W. Driscoll (ed), Handbook of Optics, New York, McGraw-Hill Book Comp., 1978
- Miller, A. R., Brown, R. M., Vegh, E., New derivation for the rough-surface reflection coefficient and for the distribution of sea-wave elevations, IEE Proc. 131, Pt. H (2), 1984
- Millman, G. H., Atmospheric effects on radio wave propagation, in R. Berkowitz, Modern Radar, New York, J. Wiley, 1965
- Patterson, W. L., Climatology of marine atmospheric effects, Naval Ocean Systems Center, San Diego, TD 573, 1982
- Paulus, R. A., Practical application of an evaporation duct model, Radio Sci. 20 (4), 1985, 887
- Reed, H. R., Russell, C. M., Ultra high frequency propagation, London, Chapman and Hall (Science Paperbacks), 1966
- Rex, D. F. (ed), Meteorological aspects of radio-radar propagation, Norfolk, Virginia, U.S. Navy Weather Res. Facilities, 1960
- Richter, J. H., Review of recent developments in evaporation ducting assessment, AGARD/NATO, CP-407, 11-11-9, Ottawa 1986
- Rotherham, S., Beyond the horizon propagation in the evaporation duct - inclusion of a rough sea, Marconi Tech. Rep. MTR 74/33, May 1974
- Stokke, K. N., World atlas of ground conductivities with particular emphasis on the high latitude region, AGARD/NATO Conf. Proc, no 382, 1985, 8.4-1-84 - 11
- Wait, J. R., Electromagnetic waves in stratified media, Oxford, Pergamon Press, 1962
- Ulaby, F. T., Moore, R. K., Fung, A. K., Microwave remote sensing, Vol. II, London, Addison-Wesley Publ. Comp., 1982
- Ulaby, F. T., Moore, R. K., Fung, A. K., Microwave remote sensing, Vol. III, 610 Washington St., Artech House, Inc., 1986
- Zimmerman, D. L., Providakes, G. F., Post, D. L., Talbot, S. H., SHF/EHF bending, AGARD/NATO Conf. Proc, no 382, 1985, 2.8-1-2.8-6

Tab. 1 a: Ground conductivities σ and dielectric contents ϵ_r
(David et al., 1969)

Wavelength	> 3 m		10 cm		3 cm		1 cm	
	ϵ_r with respect to vacuum	σ^* mho/m	ϵ_r	σ	ϵ_r	σ	ϵ_r	σ
Sea water	80	1-5	69	6.5	65	16	22	50
Fresh water	80	0.001-0.1						
Humid soil, clay	30	0.01-0.02	24	0.6				
Fertile cultivated soil	15	0.005						
Grass, meadow, race courses, sports grounds				0.05 3-6-0.11				
Rocky ground	7	0.001						
Urban areas, large towns	5	0.001						
Dry soil	4	0.01						
Very dry soil, deserts	4	0.001-0.0001	2	0.03	about 3	0.007 -0.1		

* σ is sometimes given in e.m. c.g.s. units, which are equivalent to 10^{11} mho/m; the conductivity of the sea is then $(1.5) \times 10^{-11}$ e.m.u.

(CCIR Rep. 879) Tab. 1 b: Expected ground conductivities

Ground conductivity (S/m)	Type of ground
5	Sea water
10^{-2}	Very moist soil, cultivated soil, fresh water
10^{-3}	Dry soil, clay, forest soil, desert soil, soil in mountainous areas, fresh sea ice
10^{-4}	Granite, dry gravel and sand, mountainous areas in cold regions, old sea ice
10^{-5}	Dry glacier in mountainous areas, permafrost in northern polar areas

Note. - For areas in the interior of Antarctica, where the absolute humidity is very low, the conductivity may be of the order of 10^{-6} S/m.

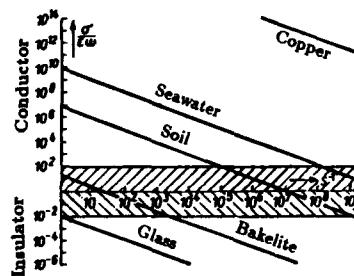


Fig. 1: The denotation "insulator" or "conductor" depends upon the frequency.

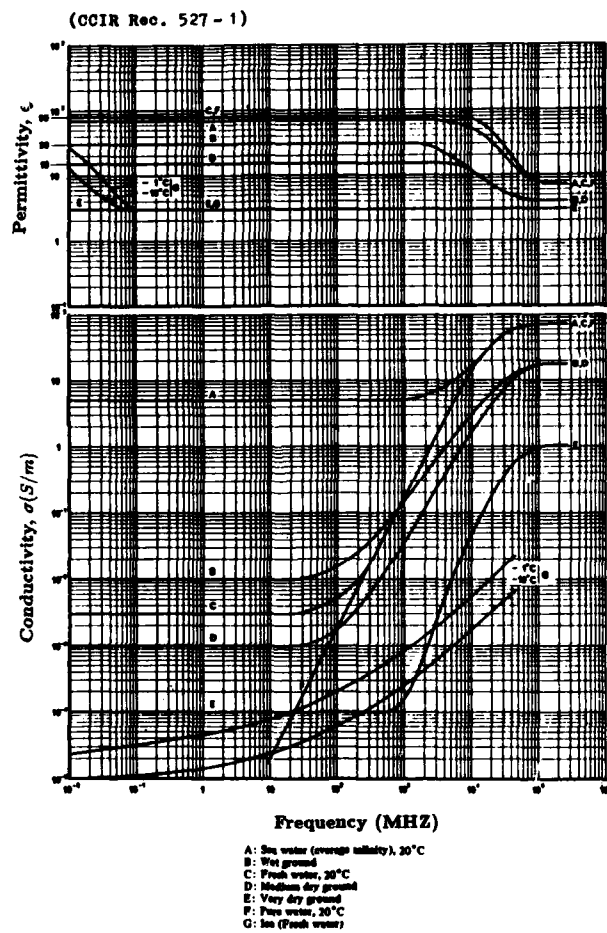


Fig. 2: Variation in conductivity and dielectric constant (permittivity) with frequency for different materials.

Tab. 2: Conductivities and permittivities for ice and snow
(Stokke, 1985)

Material	Temperature °C	Conductivity S/m	Relative permittivity
Pure ice	-10	10^{-7}	95
	-40	3×10^{-9}	105
Soft new snow 0.13 g/cm ³	-10	10^{-9}	4
	-40	3×10^{-11}	4
Granular snow 0.4 g/cm ³	-10	10^{-7}	15
	-40	10^{-9}	15
Glacial snow	0	5×10^{-7}	120
Sea ice	-7	10^{-3}	4
0.5% salinity	-24	10^{-4}	4

Tab. 3: Typical average values of the dry and wet components
of N for arctic, temperate, and tropical locations
(Bean et al., 1968)

Station and climate	D_0	W_0	N_0
Isachsen (78°50' N), arctic	332.0	0.8	332.8
Washington, D.C. (38°50' N), temperate	266.1	58.5	324.6
Canton Island (2°46' S), tropic	259.4	111.9	371.3

Tab. 4: Statistics of surface refractivity N_s
and refractivity gradient (N/km) between
ground and 1 km for polar stations after
Patterson, 1982

Year	Jan./March	July/Sept.
	N_s (N-units)	
317	322	315
	dN/dz (N/km)	
42.2	45.9	38.8
	k	
1.37	1.41	1.33

Tab. 5: Annual percentage of ducts from arctic radio-
sonde stations (Patterson, 1982)

Location	Surface ducts Day/Night	Elevated ducts Day/Night
Jan Mayen, Norway 70.93 N, 8.67 W	0/0	1/2
Alert, N.W.I., Canada 82.50 N, 62.33 W	1/1	1/2
Eureka, Canada 80.00 N, 85.93 W	0/0	1/1
Fairbanks, Alaska 64.82 N, 147.87 W	8/6	1/3
Barrow, Alaska 71.30 N, 156.78 W	3/2	7/10
Ostrov Vrangeljja, USSR 70.97 N, 178.53 W	0/1	1/1
Ostrov Hejsa, USSR 80.62 N, 58.05 E	0/1	0/0

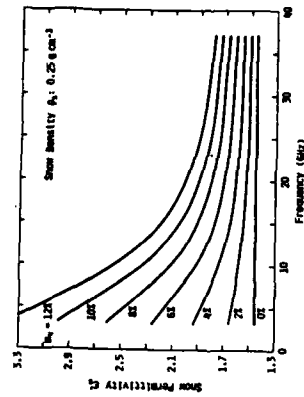


Fig. 2: The spectral variation of the permittivity of wet snow with snow volume fraction. The curves are based on the modified Debye-like model given by (E.96).

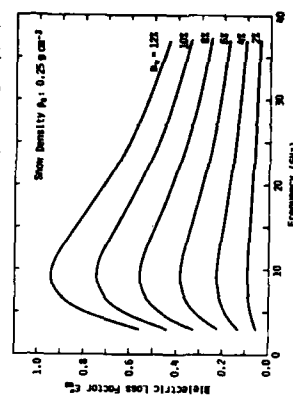


Fig. 3: Dielectric constants of four types of sea ice as function of frequency, computed with a refractive dielectric mixing model (Ulaby et al., 1986).

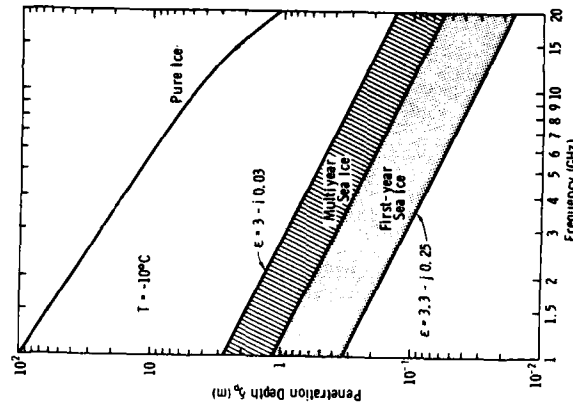


Fig. 4: Penetration depth in pure ice, first-year ice, and multi-year ice. Shaded areas correspond to the range of values of dielectric constant commonly reported in the literature (dependent on salinity and density), (Ulaby et al., 1986).

Fig. 5: The variation of the dielectric constant of wet snow as function of frequency, parameter: snow wetness; (a): real dielectric constant (ϵ'), (b): loss factor (ϵ''). The curves are based on a half-empirical, Debye-like model (Ulaby et al., 1986).

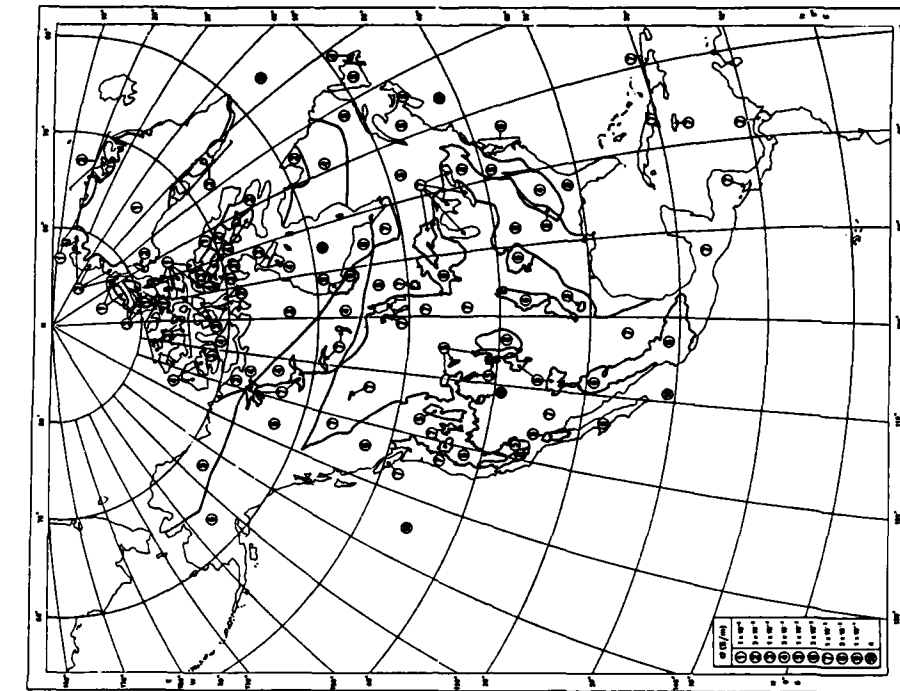


Fig. 8: Example of conductivity map (North America) in the world atlas of ground conductivities (effective values), (CCIR Doc 5/382, 1986).

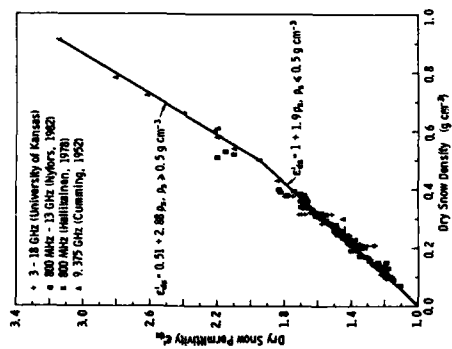


Fig. 6: Measured dielectric constant of dry snow (Ulaby et al., 1986).

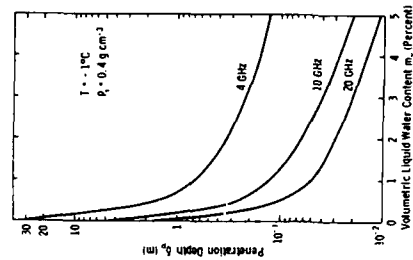


Fig. 7: Penetration depth of snow as function of liquid water content (Ulaby et al., 1982).

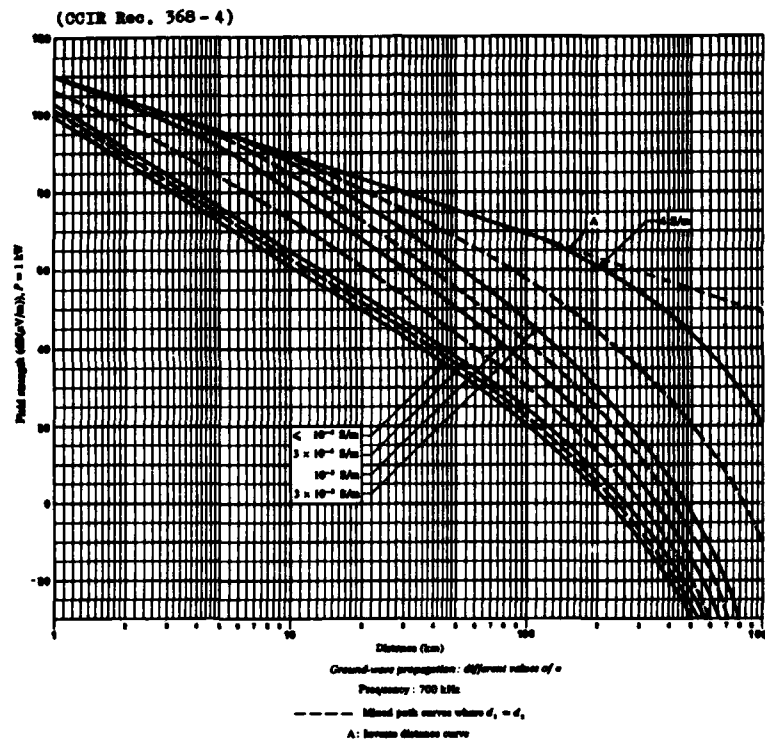


Fig. 9: Ground-wave fieldstrength curves for different conductivities at 700 kHz ($\lambda = 430 \text{ m}$) as function of distance; included are the inverse distance curve and curves for mixed paths ($d_1 = d_2$), (CCIR Rec. 368-4, 1982).

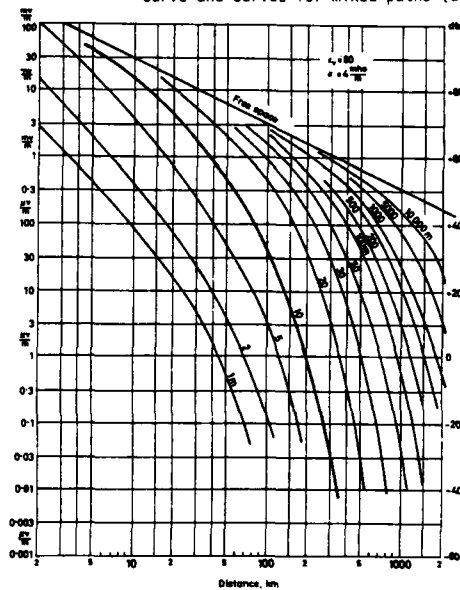


Fig. 10: Decrease of fieldstrength in the diffraction zone over sea for various wavelengths (stations at ground level, radiated power 1 kW), (David et al., 1969, see also Fig. 21).

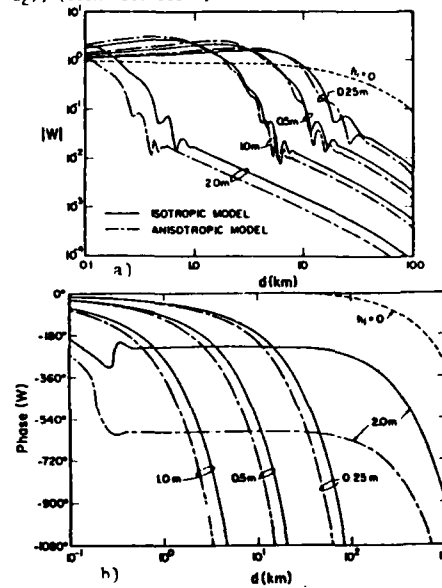


Fig. 11: Magnitude (a) and phase (b) of ground-wave attenuation function W (frequency 10 MHz) for various sea-ice thickness as a function of range ($\sigma_w = 1 \text{ S/m}$, $\epsilon_w/\epsilon_0 = 80$, $\epsilon_i/\epsilon_0 = 6$, and $\sigma_i/\epsilon_i \omega = 0, 1$), (Hill et al., 1981).

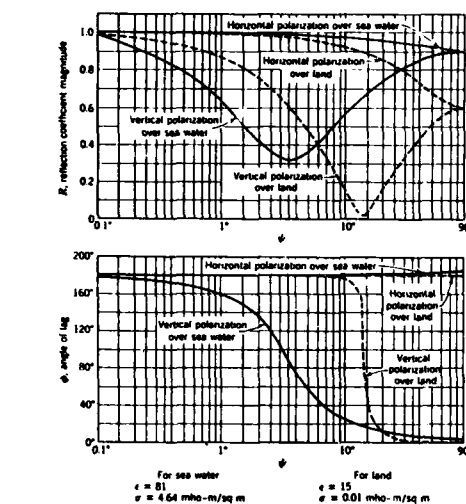
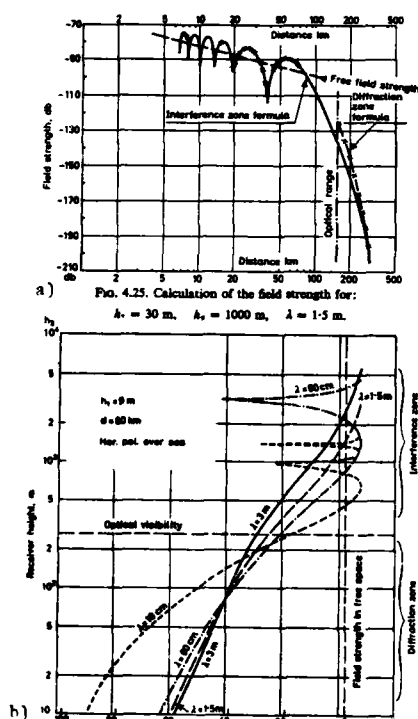


Fig. 13: Theoretical reflection coefficients over land and over water, frequency 328.2 MHz, horizontal and vertical polarization (Reed et al., 1966).

Fig. 12: Interference pattern for "fieldstrength-distance" (a) and "fieldstrength-height" (b) dependence over sea (Burrows et al., 1949).

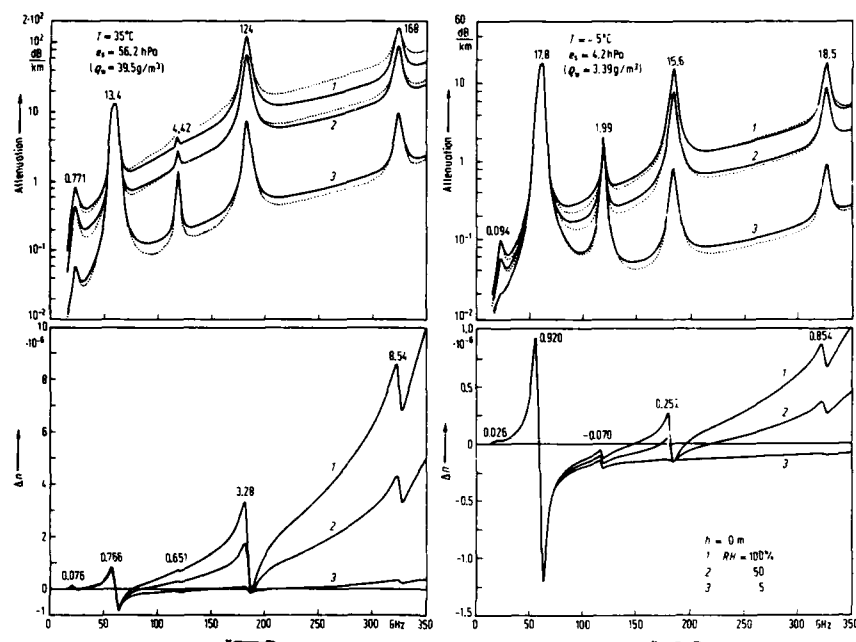


Fig. 14: Attenuation and refractive dispersion Δn (deviation from the frequency-independent term of dry (curve 3), humid (curve 2) and saturated (curve 1) air at sea level for temperatures of -5°C and 35°C over the frequency range of 15 - 350 GHz ($\lambda = 20 - 0.86$ mm); e_s saturation pressure, ρ_w absolute humidity. Solid and dotted curves refer to different mode's of the additional contributions of the continuum spectrum (Liebe, 1981).

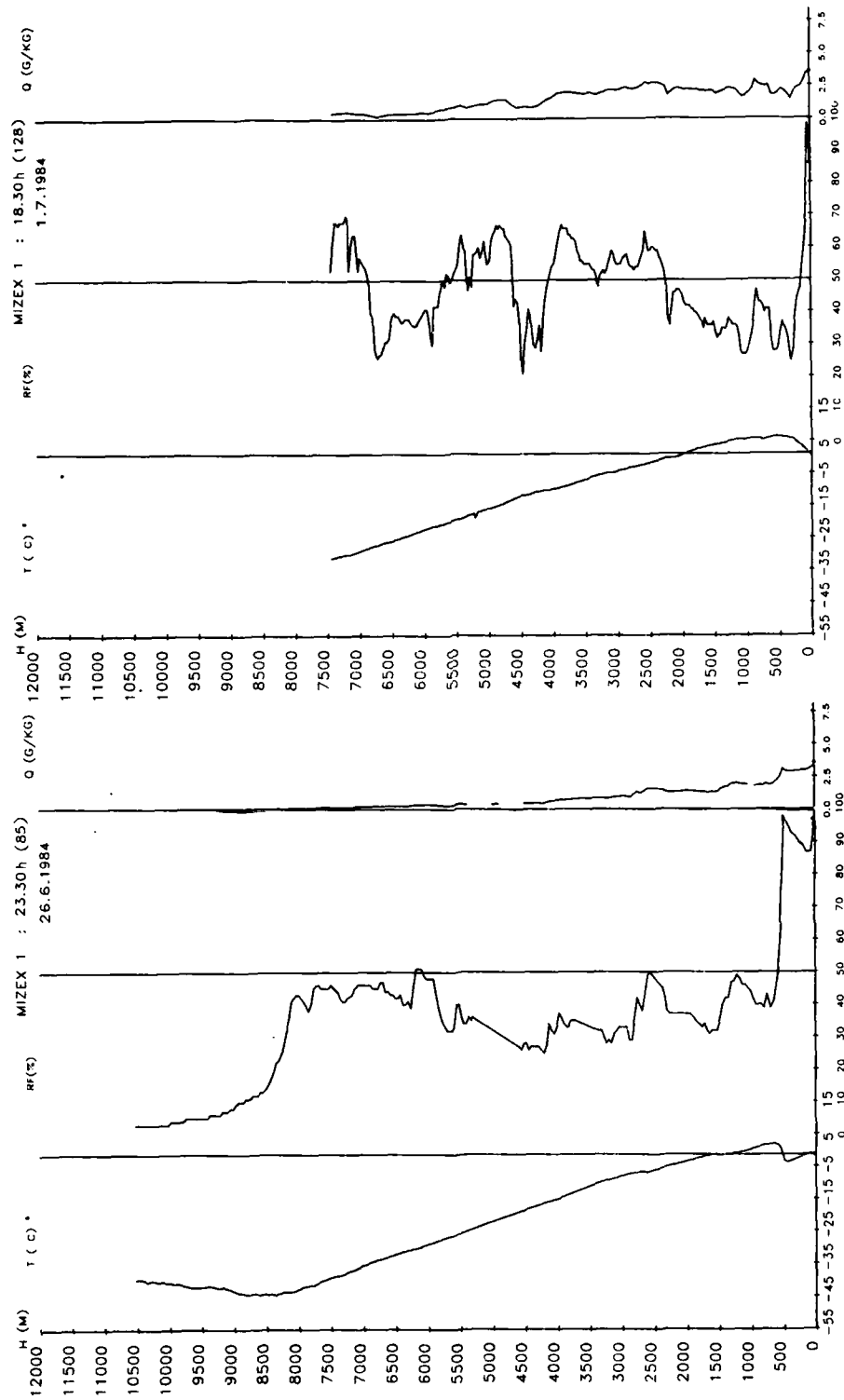


Fig. 16: Vertical profiles of temperature (T), relative humidity (RH), and specific humidity (Q) from radiosonde soundings (Vaisala-Omega-System) during MIZEX 1984, (a) 26.6.1984, 23.30 h, (b) 1.7.1984, 18.30 h (Kruspe, 1988).

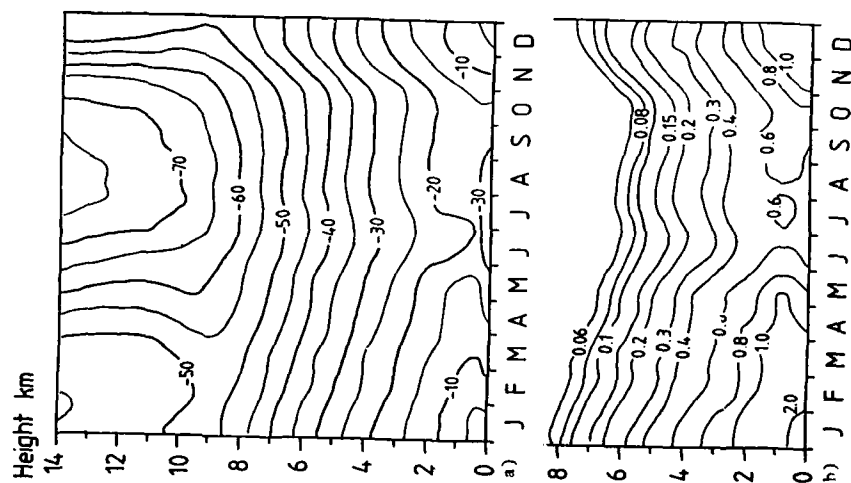


Fig. 17: Time-height sections of temperature in K (a) and specific humidity in g/kg (b) from daily radiosonde soundings 1984 at the Georg v. Neumayer Station (70.5°S, 8.3°W), (Grube-Lenhard, 1987).

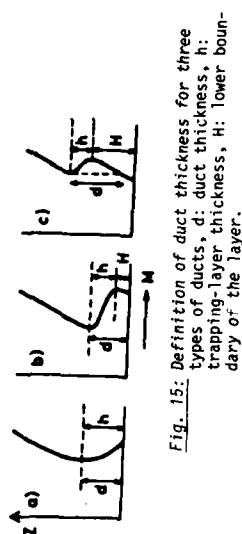


Fig. 15: Definition of duct thickness for three types of ducts, d: duct thickness, h: trapping-layer thickness, H: lower boundary of the layer.

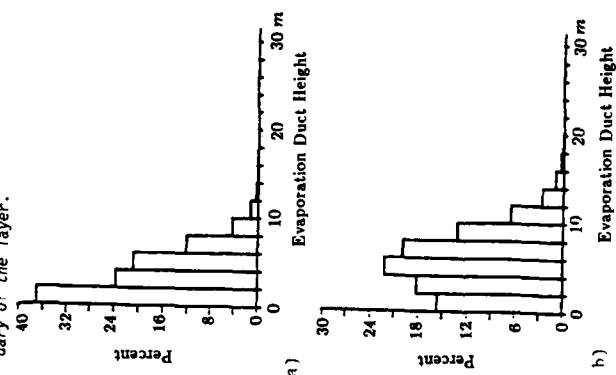


Fig. 18: Evaporation duct height statistics, (a) in the Bering Sea (65°N, 165°W), (b) Norwegian Sea (65°N, 5°W), (Patterson, 1982).

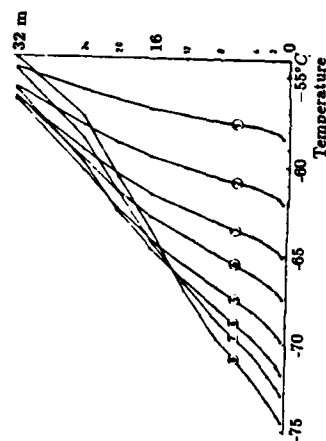


Fig. 19: Mean temperature profiles between 0 and 32 m for different classes of stability during the dark season 1967 at Plateau Station (79.2°S, 40.5°E), (1) slightly unstable, (8) strongly stable conditions (Lettau et al., 1977).

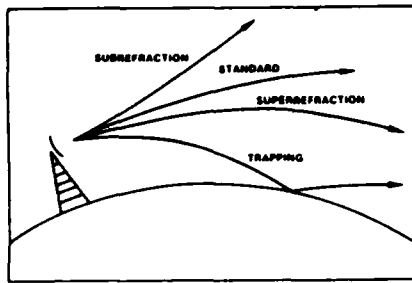


Fig. 20: Relative bending for each of the four refractive types.

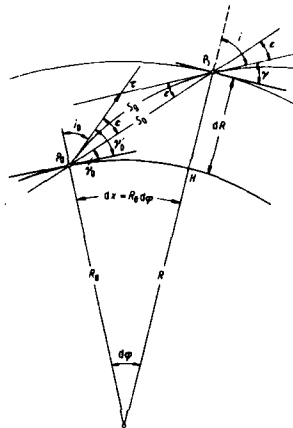


Fig. 22: Geometry of the refraction of electromagnetic waves, α total bending, ϵ terrestrial elevation angle error.

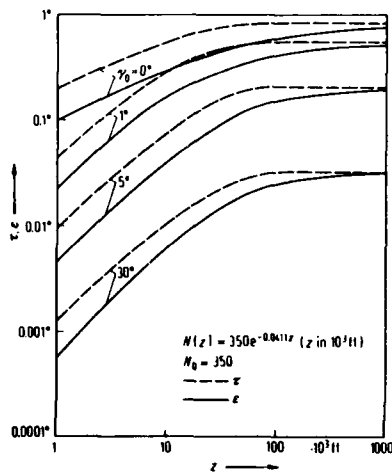


Fig. 23 a: Total atmospheric bending ϕ and terrestrial elevation angle error ϵ for an exponential refractive index model as function of target height z for various ground elevation angles b_0 (Rex, 1960).

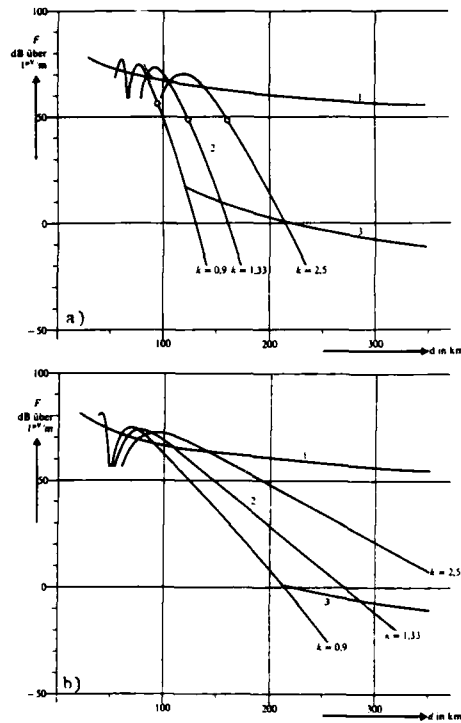


Fig. 21: Fieldstrength E as function of distance d for different effective earth radii kR_0 (circles give the radio optical horizon). Curve 1 represents free-space propagation and curve 3 troposcatter propagation, (a) $\lambda = 0.1$ m, (b) $\lambda = 3$ m, (Großkopf, 1970).

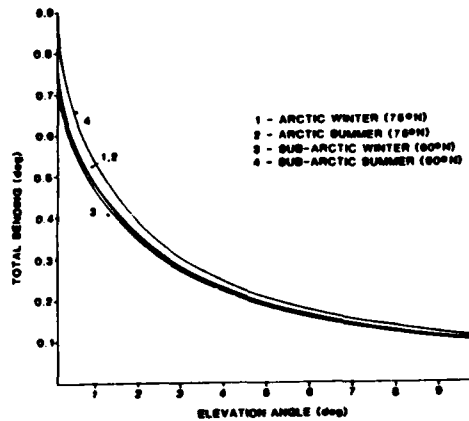


Fig. 23 b: Total bending as function of elevation angle for high latitudes (100 % humidity), (Zimmermann et al., 1985).

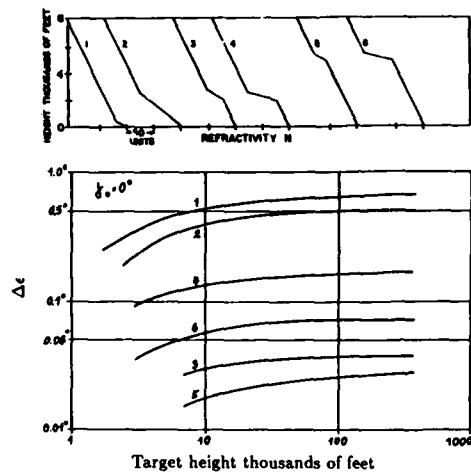


Fig. 24: Excess elevation angle error $\Delta\epsilon$ due to different layers as function of target height, ground elevation $\gamma_0 = 0^\circ$ (Rex, 1960).

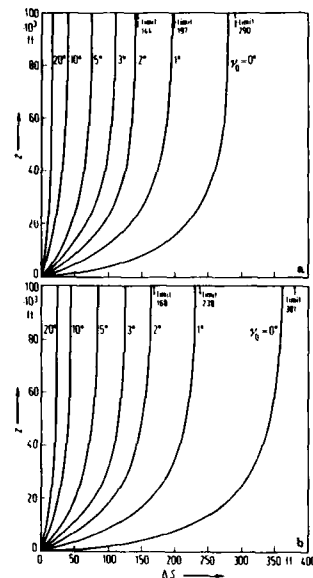


Fig. 25: Tropospheric range errors ΔS for a standard atmosphere one-way transmission path for various ground elevation angles γ_0 , (a) with 0% relative humidity, (b) with 100% humidity (Millman, 1965).

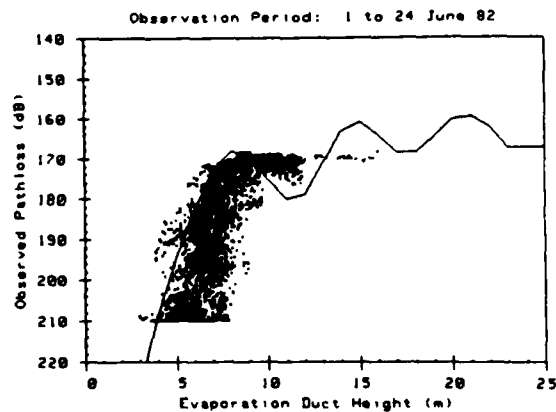


Fig. 26: Comparison of experimental measurements (18 GHz) to waveguide prediction (Paulus, 1985).

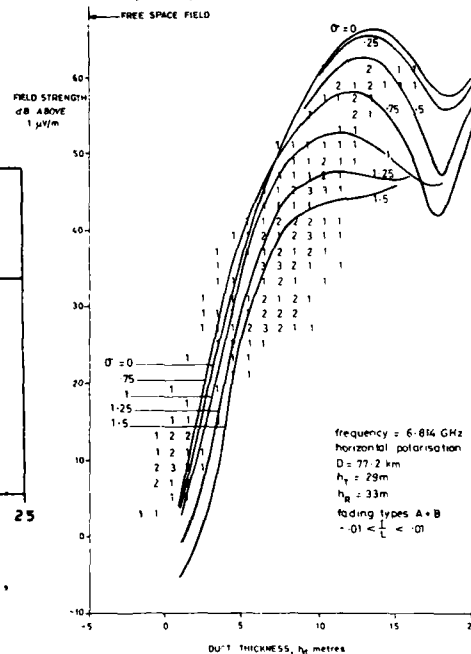


Fig. 27: Theoretical and experimental "fieldstrength-duct thickness" relations during near-neutral stability for different surface-roughness reflection coefficients ($R = R_0 \exp(\theta^2/2)$, $\theta = 2k \sin \theta$, θ is the rms bump height, and θ the angle of incidence at the surface), (Rotherham, 1974).

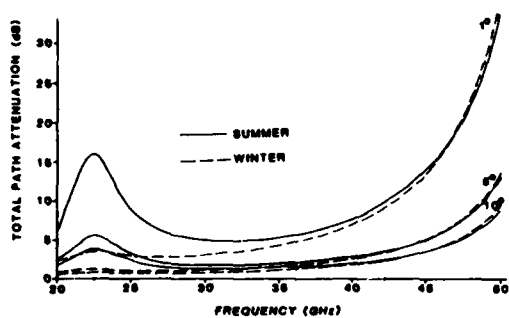


Fig. 28: Total atmospheric attenuation of gases at 1°, 5°, and 10° elevation angles for arctic summer and winter (75°N, 100% humidity), (Zimmerman et al., 1985).

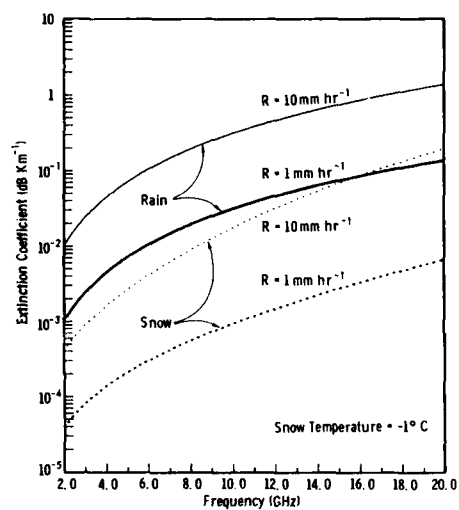


Fig. 29: Attenuation of rain and snow as a function of frequency, based on a summary of experimental data (Barton, 1974).

HF Communications and Remote Sensing in the High Latitude Region

John S. Belrose
Radio Propagation Laboratory
Communications Research Centre
P.O. Box 11490, Station H
Ottawa, Ontario, K2H 8S2
Canada

Preface

Observations at high latitudes are essential for modern research in space physics, for it is there that the interplanetary magnetic field lines approach the Earth at a high angle, and direct observations are possible of the behaviour of plasma boundary layers caused by the interaction between magnetic fields of the Earth and the "solar wind" energy pervading the solar system. Recent observations in Alaska, Canada, Greenland, Svalbard and Finland are making significant advances in understanding the nature of the magnetosphere that surrounds the earth. Studies of the polar atmosphere have recently revealed features of significance to the world as a whole.

The weakly ionized upper atmosphere, or ionosphere, is strongly influenced by the Earth's magnetic field at high latitudes, one spectacular visual effect is the aurora, and these disturbances propagate across lower latitudes between north and south regions. The disturbances have important effects on communications, surveillance, navigation and are of great practical importance to both military and civilian, as well as being of great scientific interest.

The low level of available solar energy (in places less than one-tenth that at the tropics), the extreme summer-to-winter variation, the fact that water is commonly in solid form, and the extensive area of permanently frozen peat moss, and muskeg or arctic tundra has significant effect on the performance of equipment, on the propagation of ground waves and on the performance of antennas.

Canada is a northern nation. Two-thirds of the country has a natural environment which is "arctic" by any definition of the term. The north magnetic and geomagnetic poles lie in Canada, and the auroral belt extends to low geographic latitudes in Canada. The military and geopolitical importance of the Canadian Arctic has increased during the closing decades of the twentieth century, since Canada is sandwiched between two super powers. This has not only brought new technologies to the north, from the now obsolete (about to be refurbished) DEW line, to under-the-sea submarines, to advances in satellite surveillance, it has moved many areas of important scientific arctic research away from the influence of organizations and interests primarily concerned with the North to that of interests and organizations primarily concerned with military power and global strategies, and it has increased the requirement for strategic communications, and for a renewed effort to improve the reliability of HF communications in the high latitude region.

It is not surprising therefore that radio communications in Canada can be difficult, and that the author's background and experience and the background and experience of his colleagues have been concerned with research into methods to minimize some of the problems with HF radio communications; this is the subject of this lecture.

Paraphrased (in part) from: Canada and Polar Science, * March 1987

Overview

Good HF propagation requires the ionosphere to be well defined and horizontally stratified. The HF wave must not be abnormally attenuated during its passages through the D-region, to reach its reflection height in the E- or F-regions of the ionosphere. A further most important requirement is that the HF channel be free of interference and that radio noise (local man-made noise and atmospheric noise from distant thunderstorms) be low. At mid-latitudes, while the ionosphere exhibits marked solar control, it is possible to relate propagation, MUF, LUF, etc., to the solar zenith angle of the sun, and to a solar activity index, and to predict propagation with some degree of certainty. This is not to say that the propagation media is undisturbed. Certainly there are significant changes associated with geomagnetic storms, and there are marked day-to-day changes in the MUF and the strength of the received wave, particularly in winter. The winter day of "anomalous absorption" is a well known phenomenon, that affects MF and low HF. But ionospheric absorption is not catastrophic, to the point where no signal is received (radio blackout). By proper choice of operating frequency mid-latitude HF communications can be very reliable.

The high latitude ionosphere is affected by two major phenomena: (1) energetic particles from the sun and from the outer magnetosphere penetrate the atmosphere and create abnormal ionization and irregularities at various altitudes; and (2) the solar wind induces an electric field perpendicular to the magnetic field which causes ionization drift, and this contributes to the formation and transport of ionization irregularities, particularly through the polar cap. Some of the ionospheric propagation anomalies include: auroral and polar cap absorption; sporadic-E (particularly auroral-E or night-E); small and large scale irregularities in the F-region (which are particularly marked in the auroral zone) giving rise to scattering and fading; effects of magnetic sub-storm activity; electron density troughs; and large sheets of field-aligned ionization. The auroral oval is a region of particular irregularity. In this zone the electron density may become extremely complex, with ionization irregularities of scales from tens of metres to hundreds of kilometres.

* Canada and Polar Science (ed. W.P. Adams, P.F.B. Barnett, M.R. Gordon and E.F. Roots), a Study Commissioned by the Circumpolar and Scientific Affairs Directorate, Department of Indian and Northern Development, Ottawa, Ontario, K1A 0H4

While it is not the purpose of this lecture to discuss the physics and morphology of the high latitude ionosphere (this is the subject of the lecture by John Hargraves), it is not possible to discuss media effects on HF communications and remote sensing, without beginning by a brief overview, or mini-review of the special properties of the high latitude ionosphere that affect radio communications.

An outline of the lecture follows:

1. The Renaissance of HF Communications
2. High Latitude Disturbance Zones and Magnetic Co-ordinates
3. The Propagation Media in the High Latitude Region
 - 3.1 The Auroral Oval
 - 3.2 The Polar Cap
 - 3.3 Modelling and Prediction of HF Propagation
 - 3.3.1 Prediction of the Solar Cycle
 - 3.3.2 Long Term Trends in Geomagnetic Activity
 - 3.3.3 HF Propagation Prediction Techniques
 - 3.4 Ground Effects
 - 3.5 Radio Noise and Interference
4. Some results of HF Communications, Direction Finding, Surveillance and Remote Sensing at High Latitudes
 - 4.1 HF Communications
 - 4.1.1 Polar cap communications
 - 4.1.2 Trans-Auroral communications
 - 4.1.2.1 Multipath and Scatter
 - 4.1.2.2 Auroral Absorption
 - 4.1.2.3 Some results of HF transmission tests for auroral zone paths
 - 4.2 HF Direction Finding
 - 4.3 Transionospheric HF Propagation
 - 4.4 OTH Surveillance Radars
 - 4.5 Remote Sensing
5. Closing Remarks

1. The Renaissance of HF Communications

Communications among NATO Nations has always been a challenge, since the area to be covered stretches from high arctic to the equator, in different longitude sectors, the Pacific, the Atlantic and the European sectors. Whether by land, sea, beneath the sea, or by air, communications between decision making centres and military outposts demands the utmost reliability. While satellite communications offers the ultimate, in terms of quality of communications and channel capacity, satellite communications is potentially vulnerable. HF communications, which fell into disfavour for a decade or more, while satellite communications was being developed, is regaining a vital role in providing a flexible and resilient communications capability, for the local area to connectivity paths, ensuring minimal essential communications in both tactical and strategic scenarios [Kelly, 1987, Smith and Werner, 1988]. The author has always been amused by the expression often stated that "HF is dead but it won't lie down." The fact is HF never did die.

The increasing need to provide more reliable HF communications has stimulated renewed research into a better understanding of the high latitude ionosphere, on which HF communications depends, and on the development of adaptive HF communication systems, particularly those that depend on real time channel evaluation (RTCE) and networking for improved performance [Perl, 1987]. A renewed interest in HF radars is also emerging. HF OTH skywave radars were abandoned in the late 70's, after trials showed that acute ionospheric variations in the high latitude region made HF "impractical". Certainly there are almost insurmountable problems with north-looking radars, because of the backscatter from the auroral zone ionosphere, however OTH radars located to the south of the auroral zone are coming into operational use: for example, the USAF OTH-B radar in Maine, USA [Boutacoff, 1985]; and a new OTH radar system is planned for the Aleutian Island chain [Wylde, 1987]. North looking, research HF backscatter radars are in operation in Europe and Canada; and new experiments are planned for the SRI WAFB OTH radar, located in the San Joaquin Valley, California, which will employ beacons at Ft. Langley and Ft. Smith in Canada.

The potential of ground wave HF over-the-horizon (OTH) radars for ocean and ice mapping, and for ship and aircraft detection is also being actively explored [see the special issue of the IEEE J. of Oceanic Engineering, April, 1986].

In recent years the AGARD Electromagnetic Propagation Panel presented two lecture series on HF communications [LS No. 127 and 145], in 1983 and 1986; and HF systems were specifically addressed at an AGARD symposium on Propagation Effects on Military Systems in the High Latitude Region, held in Fairbanks in June 1985 [Conf. Proc. No. 382]. The CCIR, recognizing the special nature of the high latitude ionosphere and the affects of the high latitude media on radio communications has published a report on the subject [CCIR Report 886, 1986]. Jones [1987] has briefly overviewed the subject of high latitude propagation. The IEE hosted its Fourth International Conference on HF Radio Systems and Techniques, London, UK, 11 - 15 April, 1988.

Circuit reliabilities in the arctic are certainly not 100 percent, but HF communications is more reliable in the high latitude region than some authors and communicators would have one believe. These reliabilities can be further improved by adaptive frequency management and adaptive networking, based on concepts which date back 30 years or more, but which are now possible with today's technology employing microprocessor controlled radio communication systems.

2. High Latitude Disturbance Zones and Magnetic Co-ordinates

The behaviour of the high latitude ionosphere differs from the lower latitudes because it is exposed to the influence of disturbances in interplanetary space and the magnetosphere. The pressure of the interplanetary plasma, which is in motion away from the sun (the solar wind), distorts the earth's magnetic field, and confines it to a finite volume, called the magnosphere (see Fig. 1). At low latitudes, a magnetic field line, followed upward, passes horizontally over the magnetic equator not far from the earth and returns to the earth in the opposite hemisphere, remaining within the inner magnetosphere. At high latitudes, on the other hand, field lines lead far from the earth, either to the outer magnetosphere, where they may eventually close but at a great distance in the anti-sun direction, or to interplanetary space. Since electrically charged energetic particles can move easily along magnetic field lines, but only with difficulty across them, the low latitude ionosphere is to a great extent protected from events far from the earth, while the high latitude ionosphere is not. A recent review of the complex nature of magnetosphere - ionosphere interactions has been published by Falthammer [1986].

Since the morphology of the high latitude ionosphere is controlled to a great extent by the earth's magnetic field, a most important parameter is the magnetic latitude. There are several forms of magnetic latitude in use: early work employed a dipole centred "geomagnetic" latitude. Later "corrected" geomagnetic latitudes (CGLs) were employed [c.f. Hakura, 1965 and Gustafsson, 1970], which better represents the real earth's field (see Fig. 2). A corresponding corrected geomagnetic latitude local time (CGLT) is defined, which is similar to ordinary local time, except it is based on the corrected geomagnetic latitude pole rather than the geographic pole. "Invariant" latitude Λ is a still more sophisticated coordinate [McIlwain, 1966], which is used primarily for studies of energetic trapped particles. At the earth's surface it is almost identical to corrected geomagnetic latitude.

For points well away from the region between the geographic and geomagnetic poles, the two types of local time are approximately equal. In each hemisphere, a magnetic "latitude - local time" frame (CGLT) reference is fixed wrt a line from the magnetic pole to the sun. In this reference, the observer on the earth is on a moving platform that passes beneath phenomena that are (statistically) stationary in space. One important exception is the solar terminator, which is fixed wrt the geographic pole, at a given time of year. In magnetic co-ordinates the solar terminator moves diurnally toward and away from the sun. All this is a bit hard to realize in 3-dimensional space, and to aid determination of regions on the earth subject to different kinds of disturbances as a function of space and time, Whalen [1970] has developed a monograph for determining corrected geomagnetic local time, latitude and longitude for high latitudes in the northern hemisphere. This information has been transposed, together with the location of various disturbance regions/or ovals on a plastic disc, with a transparent geographic map overlay (see Fig. 3).

On this figure the UT line reference has been set to 05 CGLT, a situation which results in the equatorward edge of the auroral oval (to be described) and the associated auroral D (a belt where statistically radio wave absorption is high) reaching to rather low geographic latitudes in eastern Canada. On this map five regions are evident: (1) a low latitude region which lies below the shaded areas on the map; (2) the trough region, a belt of low electron density; (3) the auroral D region; (4) the auroral oval; and (5) the polar cap, which is sometimes defined as the region poleward of the upper edge of the auroral oval. However, polar cap absorption (to be discussed later) occurs at lower latitudes than this boundary, to about 60° CGL. The auroral oval, the position and width of which is based on a statistical analysis by Feldstein and Stariv [1967], corresponds to periods of moderate magnetic activity ($Q=3$). When magnetic activity is high the lower latitude edge moves as much as 5° equatorward [c.f. Gussenhaven and Hardy, 1987]. The upper edge can move as much as 2° poleward. The lower latitude edge of polar cap absorption also moves equatorward when magnetic activity is high.

3. The Propagation Media in the High Latitude Region

At low latitudes, the ionosphere is primarily controlled by the absorption of ultra violet radiation in the production of ionization, and by recombination collisions and vertical transport in the loss of ionization. At high latitudes the ultra violet source becomes secondary, and null during night time, which can be weeks or months long during the northern hemisphere winter when the distribution of ionization in the ionosphere is primarily determined by convection and particle precipitation.

On Fig. 4, taken from Knudsen [1974] we illustrate the convection flow pattern of the ionosphere at mid and high latitudes, resulting from a combination of earth rotation and magnetospheric convection. See also Knudsen et al. [1977], and the more recent study by Soika and Schunk [1988]. At lower latitudes the ionosphere simply corotates with the earth. Near the lower latitude limit of convection flow, the flow is more complex than shown on the figure. Slow and even reverse flow on the afternoon and prenight side account for prolonged recombination. This results in a region of low electron density in the F-region, referred to as the main trough, located equatorward of the auroral belt (Fig. 3). On Fig. 4 the time between dots on the flow lines is 1-hour. Ionization and irregularities at high latitudes are normally created in one place and carried to other places where they can affect communications. The sources are ultra violet radiation at mid-latitudes and particle precipitation in the auroral zone.

3.1 The Auroral Oval

There are two kinds of particle precipitation in the auroral oval, a hard type on the night side and a soft type on the day side. On the day side, solar wind particles can enter the magnetosphere directly in the region called the "Cusp" (see Fig. 1). These consequently penetrate down to near the F-region peak density. Here they generate ionization enhancements, heat [Whitaker, 1976] and irregularities in the F-region.

Energetic particles precipitating in the auroral oval originate in the tail of the magnetosphere. They enter the tail by diffusion of the solar wind through the magnetosphere boundary or by upward diffusion of thermal H^+ ions (polar wind). They are accelerated downward into the ionosphere by magnetic field motion due to convection and/or complex-field aligned electric fields. These mechanisms can cause greater acceleration and more intense fluxes during times of enhanced magnetic (solar wind) activity.

The nighttime particles have energies up to 10 keV, and tend to precipitate on the poleward side of the nighttime auroral oval. Intense electron "spikes" [McDiarmid and Burrows, 1965] of energy > 40 keV are shown on Fig. 5. The location of several occurrences are shown as function of local time and CGL. They were observed with Alouette 1 at a height of 1000 km. Intense electron "bursts" [Fritz and Gurnett, 1965] at energies > 10 keV observed with INJUN 3 are also shown on Fig. 5. Hardy et al. [1985] have made a detailed statistical study of auroral electron precipitation as a function of magnetic local time, magnetic latitude and geomagnetic activity. Their paper includes as well a useful reference to previous work. The study clearly shows the two average energy maximum: one post midnight ($E < 600$ eV) and the other prenoon ($E \geq 600$ eV). The "hot" electron region ($E \geq 600$ eV) is generally not continuous in CGLT but shows a gap between 1200 and 1800 CGLT. These are the electrons that carry most of the energy flux into the oval. The energy flux on the nightside increases with K_p , while the level in the pre-noon period increases with K_p when K_p is small ($K_p = 0$ to $K_p = 3$), but is approximately constant for higher K_p . Particles of these energies are absorbed in the D-, E- and F₁-regions. F₂-region ionization enhancements can result not only from increased F₁ ionization diffusing upward, but also by heating followed by expansion [Whitaker, 1977]. E-region ionization enhancements result in abnormal increases of peak densities in the E region [McNamara, 1969], "auroral E or night E" [Robinson and Vondrak, 1985], which can be used for communications, particularly if frequencies well above those that are typical of regular conditions can be employed [Jull et al. 1962]. D-region ionization density enhancements results in absorption of HF radio waves, since HF waves are reflected at heights above the D-region.

Local ionization enhancements, created both in the daytime cusp region and on the poleward side of the nighttime auroral oval convect antisunward into the nighttime auroral oval where N-S motion is small. The ionization rotates roughly with the earth (between about 60° and 70° CGL) to the day side. Abnormal ionization enhancements are therefore in effect stretched in the EW direction, and this dimension is long compared with the dimension in the NS direction. The auroral zone surrounding the polar cap is thus a region of intense irregularities and enhanced ionization in the D, E and F regions. Auroral absorption is correlated with geomagnetic activity. The occurrence pattern is zonal in contrast with polar cap absorption (see Fig. 3), with a statistical width of 5° - 8° of magnetic latitude. At a fixed site the observer sees absorption events typically from a minute to several tens of minutes in duration. Absorption is greatest in two regions, near midnight, and in the morning. The midnight absorption occurs in brief, intense events, which are associated directly with local sub storm (break up) aurora. Miller and Vondrak [1985] have developed a phenomenological model of auroral electron precipitation and ionospheric effects, based on riometer absorption and satellite spectrometric observations of auroral emissions. The morning absorption commences about an hour after a substorm, and is more spread out in space and time. It is not associated with local aurora.

An early plot (on polar coordinates of dipole centred geomagnetic latitude and time) by Hartz, et al. [1963] shows the percentage of time for which absorption exceeds 1 dB (Fig. 6). The midnight absorption region does not appear because events are brief. However, the midnight maximum in occurrence of absorption is clearly evident on Fig. 7, which show data for Canadian and USSR longitudes for different solar cycles [after Foppiano and Bradley, 1985].

Auroral absorption (AA) events are smaller in magnitude compared with polar cap absorption (magnitudes up to about 10 dB [c.f. Belrose, 1983] on a 30 MHz zenith riometer, compared with PCA events > 20 dB), but nevertheless absorption on an HF oblique circuit can exceed 100 dB, and radio blackout associated with AA frequently occurs.

3.2 The Polar Cap

The F region, when sun lit, and in the absence of energetic particle precipitation, owes its existence to solar radiation. Even when the sun is close to the horizon, it produces ionization at a rate comparable with that due to precipitation in the noon sector of the auroral oval, where F-region particle production is greatest [Whitaker, 1977]. Horizontal drift moves this ionization into the dark part of the polar cap. In general, the polar cap is a region of low ionospheric density compared with the auroral zone, but during daytime the ionization densities as a function of space and time are quite regular.

When most of the polar cap is in darkness (near winter solstice), and when the geomagnetic pole is on the side of the geographic pole away from the sun the F region is more variable in space and time than otherwise. Under these conditions penetration frequencies are commonly low, 2 - 3 MHz [Whiteaker et. al., 1978], but have occasionally been observed to go below 1 MHz. The lowest densities tend to occur at local midnight in the polar cap [Timleck and Nelms, 1969; Nelms and Chapman, 1978; and Brinton et. al., 1978].

The regularity of the polar ionosphere, however, provides good long range communications over paths that lie entirely within the polar cap. On occasion communications is disrupted by polar cap absorption (PCA), which is often called a solar proton event (SPE), since SPEs are caused by certain solar X-ray (SXR) flares that emit energetic (MeV) protons. These MeV protons freely enter the polar cap, because of the geometry of the earth's field (Fig. 1) where they cause significant increases in the ionization densities in the D-region [see Belrose, 1983]. At HF, and particularly over oblique paths, the absorption can be hundreds, perhaps thousands of dB thus HF communication is blacked out [c.f. Jelly, 1963].

PCA events are of long duration compared with auroral absorption, and the absorption is quite uniform over the whole of the polar cap, down to $\lambda \sim 60^\circ$. If a PCA event begins at a time when a strong geomagnetic storm is in progress (due perhaps to a previous solar disturbance), the absorption is observed at even lower latitudes (the low latitude boundary can move 5° or so equatorward). A first clear example of this was the great SPE of 12 November, 1960 which began almost coincident with a geomagnetic storm [Belrose and Ross, 1962]. PCA events can last for 1 - 3 days, however durations up to 10 days have been observed in their effect on VLF/LF propagation. The effect of PCA is rather catastrophic for HF communication, however statistically, over an 11-year solar cycle, PCA does not decrease the overall circuit reliability significantly. Occurrence varies from 0 - 1 event per year during the one-to-three year solar minimum, to 15 - 20 per year during a strong solar maximum [Collins et. al., 1961; Bailey, 1964; Jelly and Collins, 1962; and Jelly, 1963]. The overall outage due to PCA during the relatively active 1949 to 1958 solar cycle was 4 to 5%. Typical outage during a year at solar maximum is 5%, although in 1958, the worst recorded year, outage due to PCA occurred 10 - 15% of the time. PCA events are to some degree predictable, on the basis of solar observations which can provide warnings from several hours to one day in advance of the actual onset of absorption [c.f. CCIR Report 727].

There is a marked diurnal variation in the magnitude of the PCA absorption (by as much as 4:1), and HF communication may be possible at night.

3.3 Modelling and Prediction of HF Propagation

The subject of HF propagation modelling and prediction is a topic in itself, that can only be briefly discussed here. Current methods for propagation prediction are semi-empirical, that is they depend upon a large data base of ionospheric observations combined with physical models of the ionosphere, and of radio wave propagation through the medium. In addition models of noise and interference environment, and system parameters (antenna, ground conductivity in front of the antenna, transmitter power, required signal-to-noise, etc.) are required. Finally, since the optimum frequency and the expected signal strength are strongly dependent on solar and magnetic activity it is necessary to be able to predict these parameters.

The prediction of solar activity (sunspot numbers or solar flux) and of ionospheric disturbances (solar flares, geomagnetic storms and solar proton events, or polar cap absorption events) are also a subject that an entire lecture could be devoted to. The accuracy in predicting the end of a solar cycle and the amplitude of a new cycle is not good even though historically we have data on solar activity (sunspot numbers) for 22 (11-year) cycles since 1740. Unfortunately the solar cycle appears to be highly variable in its behaviour, perhaps even chaotic. The state of art of modelling and prediction of HF propagation has been reviewed in a previous lecture series by Thrane [1986].

3.3.1 Prediction of the Solar Cycle

A wide variety of methods have been used to predict the amplitude of the solar cycle prior to the previous solar minimum [c.f. Thompson, 1987]. Prediction into the future is obviously dependent on the behaviour in the past. On Fig. 8 we have plotted the yearly-averaged sunspot number since 1930 (dashed line). Clearly, excepting for Cycle 20, there appears, judged on these data, to be a long-term trend in solar activity (so called "secular cycles"). That is the amplitude of the maximum for cycles 17 and 18 progressively increased, reaching an all time high for cycle 19, and thereafter solar activity appears to decrease. However, prediction based on similar cycles have had limited success in the past.

Even the length of the sunspot cycle is variable. The average is 10.7 years, but there have been cycles as short as 7.3 years and as long as 17.1 years.

The actual data points are not shown on the Fig. 8, nevertheless it would appear that the yearly-averages of sunspot numbers trace out a rather smooth curve. There is, however, a marked day-to-day variability, and the monthly high-and-low values can be as large as the change of the mean values over the solar cycle (see Fig. 9).

On this figure is plotted the solar flux index, a number associated with measured radio noise coming from the sun at 2800 MHz (10.7 cm). The measurements were made at Ottawa, Canada at 17 UT.

Before leaving the subject of the long term trend in solar activity let us look at some of the forecasts into the future. Thompson [1987] has summarized the results of various estimates for the amplitude of Cycle 22. These range from 109 - 190, reaching peak values in 1990 - 1991. Paul [1986] has looked into his crystal ball with longer range glasses than most, and he has predicted the solar sunspot number for the next five sunspot cycles (see Fig. 10). Kopesky [1987] on the other hand has seen a different future in his cup of tea, he has

forecast abnormally high sunspot numbers (as high as 300) in the first half of the 21 century. He also discusses the consequence of such abnormally high solar activity for processes on the earth: changes in climate, anomalous propagation of radio waves, increased effect of the density of the upper atmosphere on orbits of man-made satellites, in seismicity, and etc.

3.3.2 Long Term Trends in Geomagnetic Disturbances

The prediction of geomagnetic disturbances is important if one wants to predict the reliability of HF propagation at high latitudes, since auroral absorption is a substorm related phenomenon, and auroral absorption limits the reliability of HF communications for trans-auroral zone paths.

There are basically two types of geomagnetic storms: 1) those that occur sporadically, associated at least on some occasions, with a prior disturbance on the sun; and 2) a recurrent type of geomagnetic disturbance that exhibit a strong 27-day periodicity. The irregular type occurs most frequently during active sun years. The 27 day periodicity in geomagnetic activity can be found at any phase of the solar cycle, but is particularly evident during the declining years of a solar cycle; and ends fairly abruptly with the beginning of a new cycle, see Fig. 11 [after Sargent, 1985]. This indicates that the predictive capability breaks down just at the time when one expects activity levels to be highest. Its breakdown during periods of high solar activity emphasizes the necessity of having real time interplanetary plasma and field parameters for effective prediction of magnetospheric substorm activity [Rostoker, 1988] and some progress has been reported on the development of a model of the high latitude ionosphere covering the polar cap and auroral zone latitudes using such parameters as input [Akasofu, 1985].

The connection between recurrent geomagnetic disturbances in the declining phase of a solar cycle has been used to predict the strength of the next solar cycle [c.f. Thompson, 1987]. On Fig. 8 we have plotted the variation of geomagnetically disturbed days since 1932 (the solid line), together with the variation of the yearly averaged sunspot numbers (the dashed line). For this plot a day was considered to be disturbed if the magnetic Ap index was greater than 24. The number of disturbed days appears to vary with two components. Firstly there is a component which is approximately in phase with the solar cycle. Secondly there is a component which peaks in the declining phase of some, but not all cycles. For example, two of the largest peaks on Fig. 8 occurred in 1951 - 1952, just before cycle 19 the highest on record; and in 1973 - 1974 just before cycle 21 which was the second largest on record. The disturbances in these peaks exhibited a very strong tendency for recurrence. Both peaks were characterized by "monster" solar wind streams giving rise to two equally spaced disturbances during each solar rotation. These streams were long lived, lasting for more than a year. In contrast, the declining phase prior to relatively weak cycle 20, showed evidence of a very small peak of recurrent geomagnetic activity in 1963.

The frequency of occurrence of geomagnetic activity above a given threshold intensity varies not only with the solar cycle but also exhibits a seasonal effect. Geomagnetic disturbances occur most frequently during equinoctial months and less frequently during solstitial months. The effect is most pronounced for the largest disturbances (see Fig. 12) and least pronounced for the weaker disturbances [Thompson, 1985].

3.3.3 HF Propagation Prediction Techniques

During the past 20 years, a number of computer programs have been developed for predicting the long term performance of HF skywave circuits. Notably among these are ITSA, HFMUFES in several versions, IONCAP, CANPRED, MUFFY, FTZ, HFML0S and SKYWAVE. The earliest programs predicted only ionospheric parameters (MUFs, LUFs, etc); the later ones permitted the inclusion of system parameters [c.f. CCIR Report 892]. Communications using long term prediction schemes for HF frequency selection have experienced difficulty achieving reliable communications during periods of strong solar and geomagnetic activity, and particularly at high latitudes. To improve the reliability of communications the alternatives are: 1) the use of a relatively simple ionospheric prediction scheme updated in real time with information from an oblique incidence sounder operated on the desired or different (control) paths; 2) the development of new prediction techniques based on a more sophisticated model, and the use of real time interplanetary and magnetospheric parameters as input; and 3) recognizing that the accuracy of predictions is poor in the high latitude region, to restrict use of prediction schemes to long term planning and frequency management, and to undisturbed days. Operationally the HF communications system, under microprocessor control, would employ channel sounding and adaptive networking, to change operation of a link or HF network automatically to suit prevailing conditions without reference to any prediction scheme.

Let us consider the first alternative, which is being used on some HF systems operated by the military, c.f. Elvy [1985]. Harnish and Hagn [1985] have examined this strategy for predicting the appropriate frequency to optimize communications. Since a first requirement is the availability of a micro-computer based prediction program, let us first discuss the availability of such prediction programs.

The program MICROPREDIC developed by Petrie et. al. [1986] computes both the maximum usable frequency (MUF) and the E-layer screening frequency for any terrestrial HF path. The optimum working frequency (OWF) and the lowest usable frequency (LUF), based on these are also calculated. System parameter are not (at present) included. Petrie and Timleck [1988] have compared these predictions with those actually measured over oblique sounding circuits and with predictions made by other available microcomputer prediction programs.

On Fig. 13 we compare observed and predicted MUFs for the high latitude circuit Resolute Bay to Ottawa (RE-OT), see Fig. 2, for a summer month (August) and a winter month (December) in a year of high solar activity (1960). The scatter plots are the individual values taken twice hourly. MICROPREDIC under predicts the high midday maximum in winter.

As noted above, to predict circuit reliability it is necessary to predict skywave field strength [c.f. CCIR Report 252], radio noise [c.f. CCIR Report 322], and as well it is necessary to include antenna parameters [CCIR Report 891]. The CCIR method of predicting auroral absorption is particularly relevant to high latitude communications. This method is based on an analysis by Foppiano and Bradley [1985]. These authors analysed 30 MHz riometer absorption measured for solar cycle 19, in several longitude sectors, Alaska, Canada, USSR and Norway. The model devised is a function of latitude, longitude, time-of-day and solar activity. The reported dependence on solar activity is perhaps questionable since auroral absorption is correlated with geomagnetic activity, and geomagnetic activity is not well correlated with solar activity (at least not in a simple direct way as we have discussed above). Indeed, the recent study by Hargraves et al. [1987], who also analysed riometer absorption (in the European sector) revealed, as might be expected, a poor correlation with solar activity. The correlation with magnetic activity was much better. These observations were made from 1972 to 1983, during the declining phase of cycle 20 and during the increasing phase of cycle 21. Why this difference between these two sets of data?

The explanation is clear if we look at Fig. 8. The number of geomagnetically disturbed days per year and the yearly averaged sunspot number were well correlated for cycle 19, corresponding to the data analysed by Foppiano and Bradley. However the peak in the occurrence of geomagnetic disturbances occurred in the declining phase of the solar cycle, in the period between cycle 20 and 21 in the period analysed by Hargraves et al. In fact there was a minimum in geomagnetic activity around 1980 when solar activity was a maximum. Clearly, the CCIR method of predicting auroral absorption needs to be revised.

The riometer absorption data discussed above were the percent of time that the absorption at 30 MHz exceeded 1 dB. An unpublished companion paper referenced in the Foppiano and Bradley [1985] paper apparently shows how riometer absorption can be related to HF absorption at vertical and oblique incident.

Finally, consider the second alternative. Over the years major improvements have been and are being made to the various prediction methods, particularly at high latitudes. Since the ionosphere is highly variable in time and location monthly medians of propagation parameters may not always be useful to the communicator. The prediction of signal strength is particularly difficult, since signal strength is a non-linear function of ionospheric parameters, and a median ionosphere does not necessarily give a correct median value for the signal strength. We have shown that the state of the ionosphere depends on solar activity, but the dependence is very complicated because events on the sun are coupled through the interplanetary medium to the ionosphere in most complex way. Since most prediction methods use smoothed sunspot numbers as a driving function to determine propagation parameters, one would intuitively expect that the accuracy of the predictions would deteriorate markedly as the latitude increased, and that the uncertainties would be great in particular zones such as the main trough region and the auroral oval.

It is for these reasons that recent attempts to operationally model HF propagation at high latitudes are based on a more realistic physical model that uses interplanetary and magnetospheric parameters as input. It is too early to say whether such techniques will be useful or practical for operational modelling, but certainly progress is being made [Akasofu, 1985; Watkins et al., 1985; Quegan et al., 1985]. Predictions have been made [Fuller - Rowell et al., 1988] with and without self-consistent neutral winds, temperature and composition which are derived by coupling the model to a global thermospheric model. The results have been tested for periods of constant interplanetary magnetic field (IMF) orientation [Quegan et al., 1988] and for periods of variable IMF, when the input model of the convective pattern must be specified with much higher time resolution [Ettemadi et al., 1988].

3.4 Ground Effects

We have discussed above some of the special properties of the high latitude ionosphere affecting radio communications. In this section we shall consider the effect of the finite conductivity of the ground which affects the performance of HF antennas. Ground conductivity in the north is low and can be very low, and this limits the distance range to which HF propagation by ground wave is possible.

The lossy ground plane beneath antennas, affects performance. If ground conductivity is low it is better to employ horizontal polarization, rather than vertical polarization, since horizontally polarized radio waves are less affected by the finite conductivity of the ground in front of the antenna.

For perfectly conducting ground the voltage reflection coefficient for horizontally polarized waves equals -1 for all angles of incidence. A horizontal current element thus has a reflected image in which the current flows in the opposite sense and ground reinforcement occurs at angles of elevation for which the path difference between direct and reflected waves is one-half a wavelength. The dominant parameter determining the pattern is the mean height of the active part of the antenna above ground. If the ground is not a perfect conductor, the reflection coefficient at small launch angles has a smaller value, but the phase remains near 180°, so the pattern is scarcely changed. The actual reflection coefficient may lead to a loss of gain, usually less than 1 dB. At large launch angles the reflection coefficient falls and the loss is correspondingly greater, up to 3 dB; but even here the directive gain remains 3 dB higher than it would if the ground reinforcement were absent. The launch angle depends on the height of antenna, and the antenna type. For a horizontal dipole at heights of 0.2λ, 0.4λ, 0.5λ, λ, 2λ, and 3λ the launch angle changes from 90°, 40°, 30°, 14°, 7°, to 4.7° respectively. For a 5-element yagi the launch angles will be 32°, 25°, 22°, 12°, 7° and 4° respectively.

For vertical polarization the effects are more complex. For highly conducting ground, the reflection coefficient is approximately 1. A vertical current element above the ground has a reflected image in which the current flows in the same sense, so ground reinforcement occurs at low launch angles. When the conductivity is finite, the phase of the complex reflection coefficient changes by 180° at small launch angles. Over sea this happens at launch angles of a degree or two above the horizon, and the formation of the low angle maximum is scarcely affected. Over land, the phase change occurs at launch angles around 15°, and the reflection

coefficient falls to a low value in the region of the change. The angle which this occurs is called the Brewster angle. Antenna performance is seriously affected, particularly as the minimum reflection coefficient occurs at angles which are comparable with the most probable angle of arrival of HF skywaves for long distance communications. For propagation paths > 2000 km the optimum launch is angle $< 15^\circ$. A vertical monopole must be fed against a radial ground system or against an elevated radial ground system, or counter poise, and ground conductivity effects the design of the ground system.

Thus, while vertical polarization offers the possibility of a low radiation angle, unless the launch direction is over sea water horizontal polarization is preferred; but an optimum design is not always practical. As noted above, the antenna height for a dipole must be $> \lambda$ if the launch angle desired is $< 15^\circ$, and this is certainly not practical when low HF frequencies are employed. For example a 30 m mast is practical. For a frequency of 10 MHz this mast height corresponds to one wavelength, and so the launch angle for a dipole at this height would be 14° . However, at 4 MHz it would be necessary (for the same launch angle) to employ a mast height of 75m, which is quite impractical. Thus, in spite of the fact that the performance of a vertical monopole is poor at low launch angles, it may well out perform a horizontal dipole at low height, particularly for communications to distances near the limiting range for a one hop sky-wave. On Fig. 14 we compare the gain for horizontal dipoles at 60 and 100 feet, with a quarter wave monopole, for good and poor ground conductivity. The various curves for the monopole are for different numbers of radial wires comprising the ground system. For low ground conductivities, characteristic of high latitudes, it is better to employ insulated wires lying on the ground, or elevated wires for the ground system. Four-radial wires each $\lambda/4$ long is sufficient if the radials are elevated.

The presence of ice on a sea surface can seriously reduce the accuracy of MF radio navigation systems that depend upon ground waves. Bourne et. al. [1970] showed that changes in the ice thickness can produce instability in the phase of the received wave; more over, even if the ice thickness remains constant, the phase velocity can be a rapidly varying function of the position of the receiver. It was found that a decrease in the wave frequency will increase the useful range of a system and the thickness of ice that can be tolerated.

3.5 Radio Noise and Interference

In the author's experience man-made radio noise and interference can be an even greater problem than radio propagation variability affecting the reliability of HF radio communications. The farther north one goes, unless a very directional antenna is employed, the wider becomes the horizon for radio interference, and radio noise generated locally in northern communities can be a problem.

Northern communities are very closely confined. Power is usually generated by a diesel driven alternator. Power-line distribution system hardware generated radio noise can be a problem, particularly in coastal communities. This is because of inadequate electrical and radio frequency grounds. Rock and arctic tundra make for poor earth connections, and insulators and hardware collect a thin film of salt due to moist air from the sea. The wind in a tree-less, open terrain shakes everything loose. Tightening the hardware on the poles, or spraying the insulators with silicone spray will cure a problem, at least until next time. The noise is variable because the load on the line is variable, and weather conditions are variable. When radio noise is bad, the levels can be up to 30 dB greater than the normal "quiet" background levels. Rain washes the insulators, and so power line noise is worse on dry days. Heavy loading on the line will sometimes cause the power line noise to disappear. For example, when everyone gets up in the morning, or at meal preparation time, the extra load on the line due to electric water heaters and stoves can cause the noise to disappear. The construction season in the North is rather short, and hence radio noise during the brief arctic summers can be bad, due to extensive use of power tools and electrical machinery. One might tend to think that northern communities would be "quiet", from a radio point of view since there are no electric elevators, neon signs, arc welders and other electrical sparking and switching machinery. However this is not usually the case. The radio site should be located on the fringes of the community, in fact better still at the end of a power line extension beyond the outer edge of the community.

Electromagnetic compatibility (EMC) is not generally a problem, but EMC must not be ignored. For example in Canada an omni-directional MF radio beacon is usually operating on the fringes of northern communities and there may be other HF installations in the community. EMC can be an important problem for northern/arctic military communication exercises, since multiple transmitters and receivers are operated in close proximity and the site configuration is usually less than ideal. The subject of radio noise and interference was discussed at a recent AGARD/EPP Specialists' meeting [AGARD Conf. Proc., 1988].

4. Results of HF Communications, Direction Finding, Surveillance and Remote Sensing at High Latitudes

4.1 HF Communications

From the discussions above it should be clear that propagation problems at HF in the high latitude region cannot be eliminated, but may be alleviated by proper system design and by development of suitable forecast and warning systems. There are basically three problems: 1) the variability of the propagation media; 2) absorption or blackout (and the problems are different for circuits within the polar cap and for circuits which traverse or are near to the auroral zone); and 3) Multipath and scatter, which is particularly a problem for circuits within, or for circuits which cross, the auroral zone.

4.1.1 Polar Cap Communications

Except for PCA events, HF is a reliable means of communications for circuits which lie entirely within the polar cap. Ten-watt battery-operated, portable radios with simple dipole antennas are extensively used in Canada for reliable remote-outpost radio communications.

Jenkins [1977] measured circuit reliability on two polar cap links, but his experiments were conducted during the autumn of 1975 and the winter of 1976, when solar activity was a minimum. FSK teletype transmissions, employing an 85 Hz frequency shift were employed, and measurements were made on Alert-Resolute Bay (AL-RB) and Alert-Inuvik (AL-IN) circuits (see Fig. 2).

The HF communication tests employed an experimental channel evaluation and calling (CHEC) system, similar to the one described by Steven [1968]. The CHEC system employed 6-channels in the 5 - 15 MHz frequency band. Typical values of circuit reliability for 60 WPM radio teletype are given in Table 1.

Table 1

	Polar Cap Circuits	
	Alert - Resolute (percent)	Alert Inuvik (percent)
Equinoxial Day	98	92
Equinoxial Night	95	93
Winter Day	95	90
Winter Night	84	90

Antenna diversity was not employed, and some other system parameters were not optimized.

HF communication systems that depend on the high latitude ionosphere as a part of the propagation medium suffer outages during PCA events. In the MF and lower-HF bands all ionospherically propagated radio waves, including atmospheric noise and interfering signals can be completely attenuated or "blacked out" due to high absorption in the D region. This absorption is a maximum in the frequency range 0.5 - 3 MHz, typically reaching values of several hundred or even thousands of dB during PCA. Such values have been deduced from vertical incidence absorption measurements (at 30 MHz), assuming the absorption varies as $1/(1 + f_H^2 \cos^2 \theta)$, where f is the wave frequency, f_H the gyrofrequency and θ the angle between the direction of propagation and magnetic field. While such a law does not apply if the absorption occurs at very low heights where the collision frequency can become large wrt the wave frequency, nevertheless the absorption can be catastrophic. Since the absorption decreases rapidly with increase in frequency, the highest possible frequency should be employed. An operating frequency that is sufficiently high to avoid black out may however not be possible.

Notwithstanding PCA is not a principle factor that limits circuit reliability. For example, even during the most active solar cycle on record, as we have noted above significant PCA occurred about 4% of the time over the 11-year period. Furthermore during a PCA event, there is a significant drop in PCA during hours of darkness [Collin et al, 1961; Jelly and Collins, 1962; Jelly, 1963]. A polar cap HF circuit may then be operative during these hours.

While statistically PCA is not a principle cause of poor circuit reliability, one may want to communicate when PCA is present. If so the only possibility to communicate may be to employ VLF/LF, or VHF/UHF relay employing low power battery operated repeaters. VLF/LF radio waves are never "blacked out" no matter how severe the solar proton event, since reflection occurs from the abnormal D-layer that is responsible for the HF absorption. VHF/UHF relay is a reliable alternative, a technology that has been developed for the Canadian environment. The problems here are not with the propagation medium, although propagation studies are needed for circuit design [c.f. Butler, 1985], but with operating repeaters in a severe environment, cold, icing/hoar frost and wind, and with battery charging.

MF ground wave has been suggested as an alternative to HF skywave [Hagg, private communication, 1974]. Intuitively one might reject such a suggestion, because the ground conductivity is very poor, and the communications range would be limited to short to medium range; particularly in northern Canada where propagation for many circuits will be over land paths. But on the other hand we do not know since MF communication systems have not been designed for optimum launch of ground waves.

If a communications system were designed for ground wave, signal reception during a strong PCA might in fact be improved, since in the absence of local site noise, the only detectable noise and interference in the frequency range say 0.3 - 3 MHz would be the thermal noise generated in the antenna and in the receiver. Hagg proposed a feasibility study (which was never carried out) of a so-called black-out free ground wave/skywave medium frequency (0.3 - 3 MHz) radio communication system for point-to-point operation in the Arctic. His mini-study concluded that such a system appeared capable of providing uninterrupted radio communication to distances of 400 to 1600 km using transmitter powers of 100 to 1000 watts in conjunction with a

low-noise receiver site and directional antennas optimized for ground wave transmission. The antenna he recommended was a long (4λ) Beverage array of the type described by Belrose et. al. [1983].

While such a communications system may be feasible, it has not been tested.

4.1.2 Trans-Auroral Communications

The ionospheric E and F regions in the auroral zone and the auroral D-region are very irregular in space and time. We have pointed out the usefulness of frequency flexibility and path diversity for avoiding problems during disturbance. We will discuss here in a bit more detail the problems in HF propagation, and conclude with a summary of results for some trans-auroral communications circuits.

4.1.2.1 Multipath and Scatter

It was mentioned above that soft particle precipitation in the cusp region and hard precipitation in a region near the poleward edge of the night-time auroral oval are responsible for generating F-layer ionization irregularities. One form of irregularity, called a "blob", has a horizontal size of tens of kilometers with an electron-density enhancement of up to a factor of 10 over the background [Vickrey et. al., 1980]. Instabilities occur at the steep density gradients at the edge of the blob, resulting in small-scale irregularities (tens of meters) which can scatter HF waves. Thus even in the absence of auroral absorption, which like PCA can cause radio blackout, propagation on paths which traverse the auroral belt is frequently less than ideal for good long-range communications.

An example of a very irregular ionosphere is illustrated in Fig. 15. These figures give contours of electron density as a function of height and invariant latitude (Λ) as obtained by an incoherent scatter radar at Chatanika, Alaska. On Fig. 15a a series of density enhancements or blobs can be seen from $\Lambda = 63.5^\circ$ to 66° , and between 250 and 700 km height. On Fig. 15b, recorded about 15 minutes after Fig. 15a, it can be seen that although the blobs have changed in detail, the main features are still present and they have convected equatorward by about 1° in latitude. These figures were recorded coincidentally with the passage of the ISIS topside sounder satellite. An intense electron precipitation event was in progress about 1145 UT and recorded by the ISIS satellite near the time the end of Fig. 15a was being recorded and the start of recording of Fig. 15b. The estimated location of the precipitation, determined from consecutive ISIS ionograms was found to be about 69.5° . Comparing Figs. 15a and 15b, it can be seen that a density enhancement is forming at 69° latitude, between 200 and 300 km in Fig. 15b. This appears to be the birth of a blob [Muldrew and Vickrey, 1982], caused by intense precipitation. The blobs illustrated on the figures can bend HF waves greatly from the great circle bearing. For example, a blob having a density increasing from 4×10^5 to $6 \times 10^5 \text{ cm}^{-3}$ in 300 m horizontally could refract a 10 MHz wave by 80° (about 40° in bearing at each end of the path) and a 15 MHz wave 34° (about 17° in bearing). These represent increases in path length over great-circle paths of about 30% and 5% respectively, which for a 2000 km path would give rise to multipath spreads of about 2.0 and 0.3 ms respectively. Multipath propagation (auroral flutter) is a characteristic of transauroral propagation.

Off-great circle scatter from the F-region auroral irregularities have been observed on E-W circuits near the auroral belt by several authors. Hagg and Rolfe [1963] received aurorally scattered signals at 41.5 MHz over a London (UK) - Ottawa path. These signals deviated 7° in bearing a remarkably large amount considering the frequency. The signals were similar in strength to the great-circle one-hop F trans-Atlantic path, but about 25 dB weaker than the two-hop path. Aurorally scattered signals were commonly observed at 5, 9 and 11 MHz, for 2000 km E-W paths between Ottawa and the N-W Atlantic [Jenkins et. al., 1979]. Arrival directions up to 40° north off the great-circle bearing were typical.

Measurements on N-S transauroral circuits [Venier, 1980a, 1980b] indicate that large off-great circle auroral reflections occur less often for the N-S direction. This difference may be explained by the shape of the blobs. Incoherent scatter observations [J.F. Vickrey, M.C. Kelley, R.T. Tsunda and M.A. McCready, private communications, 1982] show the blobs to be more extended in the E-W direction than in the N-S direction. Thus the surfaces of constant electron density will be tilted much more in N-S direction than in the E-W direction giving rise to larger off-great-circle reflections for E-W paths. Transauroral direction-finding measurements to be described below provide evidence for such tilts [Venier, 1980b]. The bottomside ionospheric tilts associated with the auroral blobs can affect N-S transauroral propagation in another way, by altering the directions of ionospheric reflected signals within the plane of propagation. Thus a signal may be scattered from several points along the irregular ionospheric path, and arrive at the same ground point, giving rise to multipath interference and a small amount of time dispersion. Of more serious consequence the blob-related tilts can be expected to block propagation between two fixed points, on many occasions.

The large horizontal density gradients associated with blobs are often unstable and decay by generating small-scale (tens of meters) irregularities [Kelly et. al., 1982]. These irregularities scatter HF signals propagating through them. The small-scale irregularities have dimensions which are much longer along the magnetic field direction than across it. The Fourier component with the appropriate wave length in the direction perpendicular to the magnetic field direction will Bragg-scatter the HF wave.

The night-time scatter region is centred on about 65° CGL. During the day-time the main scatter region is the cusp region where the magnetic field lines are open to the solar wind. At noon this is centred at about 80° CGL. There is another scattering region equatorward of the night-time auroral oval, probably extending to the equatorward limit of the convection flow lines. References and a short discussion of these regions can be found in Muldrew [1983].

4.1.2.2 Auroral Absorption

Auroral absorption is the most frequent cause of radio blackout, since these events frequently occur irregularly over the entire solar cycle. However, the magnitude of the peak absorption and the frequency of occurrence change with the solar cycle. At a fixed site the observer sees absorption events typically lasting from a minute to tens of minutes in duration. Absorption is greatest in two regions, near midnight and in the morning although isolated events can occur at any time of the day.

Hartz et. al. [1963] carried out a study of auroral absorption (based on 30 MHz riometer absorption), during a 2-year period that covered a medium and high sunspot number period (summer 1959 to summer 1961). The 12-month running average sunspot numbers were from 157 to 102 for the first 12 months and from 98 to 56 for the next 12 months. Their results were based on measurements made on a N-S chain of six riometers from Resolute Bay in the north to Ottawa in the south. The results were presented in percentage of time the 30 MHz auroral absorption was ≥ 1 dB, and plotted against geomagnetic latitude (Fig. 6). They also studied the location in geomagnetic latitude of auroral absorption based on time percentage of occurrence for different values of magnetic activity (daily sum of the geomagnetic index Kp) (Fig. 16).

Hagg [private communications, 1974] has used these results to predict the reliability for HF communications on a long trans-auroral circuit (Alert - Ottawa). This is a 2-hop path in which the first and second passages through the D-region are well north of the auroral absorption zone; but the third and fourth passages are within the auroral absorption zone (Fig. 16). His predictions are summarized in Table 2.

Table 2

Level of Magnetic Activity	Expected occurrence in % time absorption ≥ 1 dB Alert - Ottawa Circuit
Severe	29
Moderate to severe	18
Slight to moderate	9

The averaged expected occurrence of auroral absorption ≥ 1 dB for the period studied by Hartz, et. al. was 7%. These predictions will be compared with circuit reliability measurements for this path in the next section.

4.1.2.3 Results of HF transmission tests for auroral zone paths

Inside the auroral oval the ionosphere is characterized by irregularities in the F-region (the normal reflecting layer) and by irregularly-occurring increases in ionization densities in the D-region. The F-region irregularities may be large-scale (which deflect radio waves) or small scale (which scatter radio waves). Enhanced D-region ionization absorbs radio waves. Auroral absorption is most prominent during pre-midnight and early morning hours and, since low HF frequencies must be used during night-time hours, AA can make HF communications during nighttime extremely difficult.

Another relevant feature of the auroral ionosphere is sporadic-E ionization, which in contrast to the above-mentioned features, can be used to benefit. Sporadic E consists of localized, short-lived patches of ionization in the E-region of the ionosphere, which provide highly coherent, non-dispersive radio wave reflection at frequencies which can be much higher than would be propagated by the normal F-layer reflection.

Jull et. al. [1962] were perhaps the first to demonstrate the advantages of using oblique sounding and the auroral Es as an aid to communication over auroral paths. They were concerned with air-ground paths. On Fig. 17 we show the path taken by the aircraft for a particular flight into the auroral zone south of Greenland. On Fig. 18 we show the maximum and lowest frequencies observed with the airborne sounding equipment, for the outgoing flight. A geomagnetic storm was in progress at the time (magnetic Kp index 6), and the North Atlantic

Quality Figures were 2 - 3 (a severe disturbance). Clearly frequencies well above those predicted for a normal night were observed, and it was possible to communicate effectively using channel assignments in this frequency band.

Channel sounding is the preferred system since if only a limited selection of channels is available there is no use sounding on someone else's channel if that channel cannot be used. The CHEC system relies on a measurement of the signal-to-noise ratio. The RACE system, although conceptually close to CHEC performs the frequency selection based on a bit error rate (BER) measurement [McLarnon, 1982]. A completely adaptive HF system should perform both the frequency management function and the connectivity achievement function (adaptive networking) [Nourry and Mackie, 1988]. This latter is based on the concept that a network of HF stations is available, and alternate adaptive routing is employed to achieve the highest reliability possible for high latitude communication. A so-called technology break through that could improve system reliability. This system and others, which employ adaptive packet-switched technology, are a result of the renaissance of HF communications that we referred to above.

While these concepts for improving HF have been around for some 30 years, there are only a few reported experiments on circuit reliabilities for high latitude paths. These were short in duration (about one year) compared with a solar cycle (11 years). Below are results of some HF transmission tests made in Norway and in Canada on paths in and near to the auroral zone, and on a path which traversed the auroral zone.

The purpose of the Norwegian tests [Thrane, 1983, 1986] was to investigate the importance of frequency flexibility and space diversity for circuits in and near the auroral zone. On Fig. 19 we show the path geometry. The long path (1250 km) normally had its reflection well to the south of the auroral oval, whereas the short path (459 km) lies inside the auroral oval. A simple digital test signal was transmitted on 4 frequencies (2.5, 3.5, 8.1 and 15 MHz) over both circuits, and the error rate of the received signals was recorded for selected times of day and season. The data were divided into periods with different degrees of auroral absorption, as measured by a 30 MHz riometer. The results from measurements on the 4 frequencies and over the two paths were combined to simulate different systems. Computations were made for 5-cases to find:

- The reliability when only one path and one frequency are available (two cases: long and short path);
- The reliability when 4-frequencies and one path are available, always the best frequency (two cases, long and short path); and
- The reliability when two paths and 4-frequencies are available, using the best frequency and best path at any time. This situation simulates a relay system in which a message may be transmitted B to R via A (assuming a 100% reliability from B to A).

Table 3

	Quiet	Moderate	Disturbed
System/absorption	0 - 0.1 dB	0.2 - 2 dB	> 2 dB
Single Frequency Short Path (3.5 MHz)	73%	51%	15%
Four Frequencies Short Path	78%	72%	37%
Single Frequency Long Path (8.1 MHz)	71%	71%	40%
Four Frequencies Long Path	88%	85%	54%
Four Frequencies Two Paths	90%	89%	62%

The results clearly show that during disturbed conditions (judged by the auroral absorption measured by a riometer), a substantial improvement in circuit reliability may be achieved by means of frequency flexibility and relaying (this is space diversity). However, the result is an over estimate since a 100% reliability was assumed for channel from B to A.

Jenkins [1977] carried out channel-evaluation-aided circuit-performance measurements from February 1975 through February 1976 on an Alert-Ottawa (AL - OT) HF circuit (Fig 2). The two-hop Alert-Ottawa path was found capable of supporting reliable communications only during daylight hours (Table 4) and the reliabilities recorded for this circuit during winter night were significantly lower than expected from predictions based upon expected signal-to-noise ratios. Doppler shifts in transmitted frequency, multi-mode time dispersion effects, auroral absorption, and scattering and shielding by the ionospheric trough in electron density, which exists to the south of the auroral zone are undoubtedly causes for the discrepancy.

Table 4
Typical Values of Circuit Reliability
(percent) at 60 WPM

	Trans-Auroral Circuit Alert-Ottawa
Equinoxal Day	86
Equinoxal Night	52
Winter Day	85
Winter Night	37

The circuit reliabilities given on Table 4, may be compared with the predictions, based on 30 MHz riometer absorption, as discussed above. The mean predicted outage of 7% corresponds to a circuit reliability of 93%. The predicted performance was based on a simple analysis of riometer absorption measured during the maximum of solar cycle 19, a cycle of exceptionally high sunspot numbers. The measured circuit reliabilities were made during a solar minimum period (winter 1975 to winter 1976).

Measurements were made for 3-data rates: 60, 100 and 150 WPM. The transmissions (as previously noted) were standard FSK employing an 85 Hz frequency shift. The circuit reliabilities decreased with increase in data rate.

4.2 HF Direction Finding

The CRC HF sampled aperture receiving array (SARA) was perhaps unique in the world. This subsection will be concerned with results obtained using that facility. SARA was a sophisticated radio receiving facility with a large antenna aperture. It could be operated in a number of modes for receiving and recording both cooperative and non-cooperative transmissions. The in-phase (I) and quadrature (Q) components of signals received by individual antenna elements were separately processed through individual receivers, and sequentially (later simultaneously) recorded for subsequent computer analysis. The large aperture provided fine azimuthal resolution. A high-resolution-analysis-ranging capability was also provided for radar and path delay measurement when a transportable frequency-modulated continuous wave (FMCW) transmitter was used. The experimental arrangement was ideally suited for adaptive antenna research, however only a little work was done in that area.

The antenna array was used mainly for HFDF studies (since 1972). Most of the work involved measurements employing a transportable transmitter which could be operated in an FMCW mode, and a number of propagation paths across, parallel to, and to the south of, the auroral zone were studied for the purpose of measuring and identifying the effects of the Canadian ionosphere on the accuracy of HFDF and to gain some insight into techniques for reducing DF errors. Its configuration was a crossed array of lengths 1943 m by 236 m. The long arm comprised 62 elements, the short arm 32 elements. The equipment associated with the array included a 90 channel phase-stable receiving system, and a computer controlled data acquisition and data processing system [Rice and Winacott, 1977]. Both swept and fixed frequency operation were provided so as to make possible, when used with a transportable transmitter, the separation of ionospheric modes and the collection of ionograms.

Errors in DF occur because the ionospheric reflecting layers are not smooth concentric reflecting surfaces. They are sometimes rough, and the surface is usually tilted due in part to the latitude dependence of solar ionizing radiation which is particularly severe at dawn and dusk. Sometimes travelling ionospheric disturbances (TID's) can be observed which cause periodic changes in bearing error. The irregularity of the high latitude ionosphere is particularly troublesome at Canadian latitudes and for this reason studies were directed toward the measurements on paths having different geometrical arrangements with respect to the auroral zone.

Signals propagated via the ionosphere can be Doppler-shifted, particularly during periods of ionospheric disturbance and near sunrise and sunset. The same time-varying ionospheric characteristics which produce Doppler shifts, also produce bearing errors. Hence the occasions when there are appreciable Doppler shifts are occasions which most need bearing improvement. Also, it is known that signals propagated via F-region modes are much more likely to exhibit appreciable Doppler shift than are signals propagated via E-region modes. Thus, at least on 1-hop mid-latitude paths, E and F mode signals can often be separated on the basis of their differing Doppler characteristics. Once they are thus separated, it may be possible to recognize and select those signal components giving the most reliable bearings.

As an example, Figure 20 shows the result of a Doppler analysis of a 4.1 MHz CW signal after propagation over the (911 km) Sept Iles - Ottawa (SI-OT) path (Fig. 2) during a sunrise period. A stable, unshifted E-mode signal can be identified, together with an F-mode component which first appears with a Doppler shift of about +0.7 Hz, and then approaches zero Doppler on a time scale of about 45 minutes. This behaviour is associated with the build-up of F-region ionization density at sunrise. In the experiment, mode identification was confirmed by oblique ionograms which were made over the same path at 20-minute intervals, during the times noted as "no data" on the figure.

Figure 21 shows the corresponding bearing behaviour for the two Doppler-resolved signal components. The unshifted E-mode component is seen to provide reliable bearings throughout the period. In contrast, the Doppler-shifted F-mode component provides bearings which are in error by as much as 11 degrees.

The results on Figures 20 and 21 were taken from data collected during an 8-day trial. Statistical analysis of this data showed that, when both E- and F-mode signals were present, they could be separated by a Doppler analysis of 0.05 Hz resolution, about 65% of the time. There is thus a significant probability of bearing improvement by Doppler analysis, in cases in which the signals have sufficient coherence to permit such analysis.

The FMCW signals allow the investigation of the angle variations of individual propagation modes, such as E, low angle F, high angle F and as well, multiples of these wave hop modes and mixed modes. Venier [1980a, b] employed this technique and he compared results obtained employing mode separation by Doppler techniques for two high latitude paths (see Fig. 2): Iqaluit (Frobisher Bay) - Ottawa (IQ - OT) and Churchill - Ottawa (CH - OT). The experiments covered a variety of ionospheric conditions. E-mode propagation over these paths provided good azimuth accuracy, the RMS error from the great circle direction was $0.3 - 0.4^\circ$ for E and E_s (Fig. 22). The F-mode spreading in range occurred a significant percentage of the time in contrast with lower-latitude paths. This spreading was accompanied by large departures in angle of arrival for this mode from the great circle direction. The RMS errors for low-angle-F-mode were $0.5 - 1.2^\circ$, for high-angle-F-mode $0.5 - 1.5^\circ$, and for spread-F-mode were $1 - 10^\circ$ (Fig. 23). Multiple and combination modes gave RMS errors in between these limits. These are the values that were found after the removal of cases with highly non-planar phase fronts.

As noted above, Venier [1980a, b] used the Doppler processing technique for mode separation. Two azimuth-estimation techniques were tested in the fixed-frequency data. One used a phase-front planarity test and averaging over relative frequent samples, while the other was based on separation of modes by Doppler. The former technique was found to provide slightly better results than the latter on these data and its accuracy was, in most cases, close to that which could be obtained from the best mode when separated using swept frequency data.

Rice [1982] made a detailed study of HF direction finding by phase front testing in a fading signal environment. He supported the experimental study by theoretical calculations of the probability of observing various degrees of phase front nonlinearity, for two and three signals incident from different directions upon a phase measuring array. Before summarizing these results, we should discuss some qualitative considerations of time scales in direction finding. Traditionally, HFDF has been performed using time constants of the order of a second or so. This is done by correlating signals from two or more antennas over times of this order, or by beam forming using a circular array and a goniometer spinning several times per second. With current technology employing a computer for system control and for data acquisition, and in particular with the development of sample and hold techniques, it is possible to sample the incident wave field at an array of antennas in times much less than 1 ms. This might be expected to lead to major changes in DF techniques and usage because the time constant of sampling can be of the order or less than other important time constants of the signal, of the interference and of the noise. By sampling at the right time it should be possible to improve direction finding accuracy in the presence of multiple modes, multiple signals and noise, since these parameters fade or change in an uncorrelated way. Such fading may provide periods of a basically plane wave condition at the receiving site, if techniques to accept bearings, based on phase-front testing can be adopted, such that bearing measurements are accepted only at times when propagation conditions appear to be unimodal. It was found that the time domain behaviour of the instantaneous samples of wave front linearity varied slowly when an unmodulated signal was received (CW or FMCW), with an observed fading rate expected for an ionospheric channel. On the other hand, when the transmitted signal was single side band, the time scale of changes in wave front non-linearity changed significantly. It was commensurate with that of the modulation [Rice et al, 1978].

Rice [1982] studied the cumulative distributions for the rms phase deviations measured on a six-element interferometer-array. He showed that distortions in the linearity of the phase fronts similar to those observed would be expected theoretically. An important part of the work was substantiating that wave front tests could be utilized to improve the accuracy of DF measurements.

The FMCW data collected in the interferometer experiment were computer-processed to provide angle-of-arrival standard deviation statistics for each mode which could be isolated by virtue of its separation in time delay. The bearing was taken as equal to the incident angle measured with respect to the array axis, a good approximation since the transmitter was located broadside to the array (the Sept Isles - Ottawa (SI - OT) path). Table 5 shows the mean standard deviation of the bearing for each mode for each of two days. Each standard deviation contributing to the mean is based on a 1 hour measurement interval. Standard deviations range from about 0.3° for the E-mode to 1.36° for the $F_2(o)H$ mode (F_2 layer, ordinary magnetoionic component, high angle).

Table 5

Standard Deviation of Bearings, Classified by
Ionospheric Mode for Range-Resolved FMCW Data

Mode of Propagation	Standard Deviation, (deg.)	
	Day 167	Day 168
EL	0.33	0.40
EH	0.27
E _s	0.67
F1(o)L	1.18	0.93
F1(o)H	1.05	0.84
F1(x)H	0.86
F2(o)L	1.07
F2(o)H	1.36

Dots indicate insufficient observations. Modes are designated as follows: E is ionospheric E layer; E_s is sporadic E; F1 is ionospheric F1 layer; F2 is ionospheric F2 layer; L is low-angle ray; H is high-angle ray; (o) is ordinary magnetoionic component; and (x) is extraordinary magnetoionic component.

Table 6 shows the results of a similar analysis performed on CW and SSB signals. A bearing was derived from the average of all those phase front measurements which passed a 10°-threshold test within each 5-second segment. The bearing standard deviations were then calculated from these values in 1-hour batches, and the hourly figures averaged, to produce the results shown. The bearing standard deviations for the wave front test data range from 0.6° to 0.9°, and thus are within the range for the separated modes as shown in Table 5.

Table 6

Standard Deviation of Bearings from Scan-by-Scan
Wave Front Test with a Phase Threshold of 10° rms

	Standard Deviation, deg.	
	Day 167	Day 168
CW signal	0.73	0.60
SSB signal	0.91	0.76

A pertinent question is the DF performance of an interferometer that uses a wave-front test. Unfortunately, the experimental work described above was not optimum to answer this question because only a single linear array was used. Measurements using two orthogonal arrays offer the potential benefit of sorting by elevation angle, so the performance in that case could approach that available via the mode which provides the best angular accuracy. Without elevation sorting, the error in measured bearing should, at best, lie somewhere within the range of values provided by the modes in isolation. This in fact is what was observed (see Tables 5 and 6).

In the summer of 1977 a signal of opportunity was observed, which was subsequently identified as a USSR OTH radar located near Kiev. This 7200 km path passed twice through the auroral zone to reach the receiver site at Ottawa. Some interesting results were obtained during a short period of observation made on that signal. Fig. 24 shows the relative occurrence of direction of arrival as a function of time. On the expectation that the OTH radar signals did originate from Kiev, this great circle bearing is marked on the figure. The data were divided according to fading rates (> 1 Hz black, < 1 Hz white). The data fall clearly into four types which are interpreted as:

- (1) Northern scatter (shaded black) with rapid fading rates and an instantaneous spread in direction. The diurnal variation strongly suggests that the signals are scattered from the disturbed F-region zone that is associated with the auroral oval; presumably this is auroral scatter;

- (2) Great-circle propagation typified by low fading rates and little spread in angle of arrival. This is the dominant mode in the daytime;
- (3) Ground side scatter. This is observed arriving from well to the south at nighttime; and
- (4) Propagation in the presence of ionospheric tilts. These signals are similar to the great-circle signal, but arrive up to a few degrees off great circle. They are tentatively identified as due to ionospheric tilts.

The top part of Table 7 shows the percentage of the total observation time that propagation of each of the above types was observed. The bottom table shows the percentage of time that northern scatter was the strongest. It is of interest that near midnight the northern scatter signal exhibits the properties of spread F (i.e. rapid fading, spread in angle of arrival, disappearance of the great-circle coherent signal) suggesting that auroral-zone spread F and auroral side-scatter are basically the same phenomenon. It is clear from the results in Table 7 that spread F (northern scatter) is a major problem for direction-finding on this circuit also.

Table 7

Percentage of measurements for which the four types of propagation defined above were seen, as a function of time-of-day.

Time (EST)	No. of Measurements	Percentage of measurements for which propagation is seen via			
		1. northern scatter	2. great-circle reflection	3. ground side-scatter	4. tilted reflection
0300-0600	89	69%	48%	9%	17%
0600-0900	88	11%	94%	3%	6%
0900-1200	246	19%	86%	0%	24%
1200-1500	186	48%	87%	0%	6%
1500-1800	101	47%	79%	0%	9%
1800-2100	46	70%	0%	0%	17%
2100-2400	18	78%	0% *	78% *	39% *

* Based on 18 measurements only, from a single 30 minute time period.

Percentage of measurements for which northern scatter was the strongest, or equal to the strongest, mode of propagation, as a function of time-of day.

Time (EST)	Percentage of Measurements
0300-0600	56%
0600-0900	6%
0900-1200	15%
1200-1500	23%
1500-1800	36%
1800-2100	70%
2100-2400	78% *

* Based on 18 measurements only, from a single 30 minute time period.

Another important parameter for DF is the dependence of bearing accuracy on aperture size. Montbriand [1981] has carried out such a study employing transmissions from Sept. Isles - Ottawa (911 km) and San Antonio (Texas) - Ottawa (2654 km). An FMCW sounding mode was employed, which made it possible to resolve modes differing in arrival time by ≥ 20 μ sec. Nine different aperture sizes were tested. The "goodness" of the bearing was judged by the RMS phase deviations from a straight line fit to the phases along the array. For the shorter path, the standard deviation at 100 m and 1000 m aperture size were 1.0 and 0.4° for the E-mode; 2.5 and 1.5° for the F₁-mode and 2.5 and 2.0 for the F₂-mode. For the longer path, these standard deviations were 0.2 and 0.2° for the F₁-mode, 0.8 and 0.5° for the F₂-low-angle-mode; 1.5 and 1.3° for the F₂-high-angle-mode; and 1.0 and 0.5° for the 2E_s-mode.

From January 27 to February 4, 1976, the SARA receiving array near Ottawa was used to record HF transmissions from a USAF Geophysics Laboratory aircraft 2000 km away over the northwest Atlantic on four evening flights. Geomagnetic conditions ranged from quiet to active. Signals from individual array elements were separately recorded, and later analyzed to provide the Doppler shift and direction of the signal. Also used were oblique ionograms recorded on the aircraft for a similar path [Jenkins et al, 1979].

The F-mode MUFs were below 5 MHz for the major portions of all evening flights. However, several weaker modes were observed to be present at much higher frequencies. They were examined for their potential utility in extending HF communications and surveillance:

- (1) Sporadic-E was a persistent feature on the oblique records. A vertical ionosonde on board the aircraft did not see the same phenomenon. This mode had a path centred close to great-circle with typical spreads in bearing of 8 degrees (see Fig. 25);
- (2) Skip-distance-focused ground sidescatter to the south was persistently present (see Fig. 26). Position estimates of the scatterers made from Doppler and direction measurements imply severe multi-path for this mode which sometimes limit data rates to less than 25 baud;
- (3) A mode involving scatter from auroral irregularities was observed which was extremely variable in time and generally weaker than the other modes; and
- (4) Occasional reflections from the northern edge of the main trough in ionospheric electron density were seen, but were limited to frequencies of less than 1 MHz above the F-mode MUF.

It was concluded that Sporadic-E and skip-distance-focused ground-sidescatter modes present an opportunity for limited HF operations in the subauroral region during evening hours, when very low F-mode MUFs would otherwise make such operations impossible.

The unmodulated HF signals transmitted from the aircraft over the ocean showed a Doppler-spread component 15-25 dB less than the normal coherent component (Fig. 27b). By interpreting the spread component as caused by nonspecular scatter from the ocean, both the aircraft ground speed and the velocity component in the direction of the observer could be derived without prior knowledge of the exact frequency of transmission [Jenkins, 1979]. The results using this technique agreed with values determined from the aircraft log within a median difference of six percent (Fig. 27C).

4.3 Transionospheric HF Propagation

The ISIS II spacecraft carried a pulse transmitter-receiver system which was primarily intended for sounding the topside ionosphere. Sounding could be carried out on a swept frequency basis, or at any one of six selectable fixed frequencies. The 9.303 MHz fixed-frequency pulse transmissions (the highest frequency available) were recorded on the ground using the HF sampling array (SARA) at the Communications Research Centre. Measurements were made in July-September 1979, in December 1981 - January 1982, June 1982 and September - October 1982. We will consider here the initial set of measurements. Montbriand and Rice [1986] have made a more detailed analysis.

The SARA array configuration for these observations consisted of two linear arms, each of length 236 m, which provided a beam width of 7° near the zenith.

At night, the observations showed a distinct lower boundary to the high latitude region of ionospheric irregularity. The data were plotted in two ways. Figs. 28 and 29 show results as a function of ray elevation angle as observed at the ground. Similar plots were made for the same data as a function of aspect angle with respect to the magnetic field.

Both aspect angle and ray elevation would be expected to have effects on the level of scintillation. The magnetic dip angle varied from 80° at the northern end of a pass observed at Ottawa, to about 60° at the limit of southern coverage. The magnetic field direction is thus within 10 to 30° of vertical, and it was not possible to clearly separate elevation angle and magnetic field aspect angle effects. However, there was less spread in the data when plotted as a function of ray elevation angle. It should be noted that these data indicated a minimum in scintillation level when the direction of propagation is near field alignment which is the opposite of behaviour noted at VHF [c.f. Cranc, 1977].

Besides this irregular behaviour at high latitudes, and the relatively abrupt latitudinal transition from the small regular fluctuations at low latitudes to larger fluctuations at high latitudes, we would expect a regular mean departure in the vertical component of the DOE as the line-of-sight to the spacecraft departs from overhead due to refraction of the ray in traversing the ionosphere. This leads to the concept of an ionospheric iris, that is an elevation-angle cone beyond which it is not possible to receive signals on the ground from a source above the ionosphere. Fig. 30 shows ray tracing results which illustrate the effect. It was assumed that the ionosphere was horizontally invariant (not a good assumption for the ionosphere north of Ottawa). For a radio frequency of 9.3 MHz, the wave refraction as a function of ray elevation angle is shown for various values of f_oF_2 . Results are shown for both ordinary (o) and extraordinary (x) magnetoionic components. The region in which the refraction increases rapidly with decreasing elevation angle defines the edge of the iris. On the figure are plotted experimental values of direction of arrival (DOA) error vs ray elevation. The numbers correspond to the rounded value of f_oF_2 applicable to the particular value. The agreement between measured data and the theoretical curves is rather poor. The points are very spread and there is an asymmetry in the plotted data as compared to the theoretical contours. In the north, the plotted DOA errors for points coded 4 MHz are spread along a curve (interpolated) near to 7 MHz. In the south the reverse holds. Points coded 4 MHz are spread along a curve (interpolated) near to 3 MHz. This asymmetry can be explained by an equatorward gradient in the electron density isopleths in the F2 layer over Ottawa which would be expected for a location on the equatorward side of the ionization trough.

4.4 OTH Surveillance Radars

In addition to its usefulness as a communications medium, the HF frequency band offers a potential for target detection to ranges of several thousands of kilometers. Both ground wave [Sherman, 1983] and skywave [Headrick and Skolnik, 1974] OTH radars have been proposed and skywave surveillance radars are in operational use [Boutacoff, 1985]. A number of propagation studies have been conducted to evaluate the potential of HF skywave OTH radars at middle [Sweeney et al., 1983] and at high latitudes. The high latitude experiments have involved research type OTH radars located in the polar cap, in the auroral zone [Greenwald et al., 1985], and at latitudes below the auroral zone [Montbriand, 1988]. In all cases the radars were looking north, although the north-looking beam(s) could be directed over a range of angles within a north-directed sector.

In a joint USAF-Canada experiment conducted in the mid-1950s a monostatic OTH radar was installed at Hall Beach (HB), NWT (Fig. 2), which employed a narrow beam antenna array directed toward the north (Fig. 31). A second receiving station installed at Cambridge Bay (CB) made possible an evaluation of the bistatic mode of operation, and an examination of signals scattered from ionospheric irregularities outside the main beam of the Hall Beach radar. The Cambridge Bay receiver employed an antenna array permitting both direction-selectable wide angle receive patterns (a Beverage rosette array), and a single-direction narrow beam receive pattern (a 32-element array of Beverage elements).

An important feature of this polar cap location was the proximity of the auroral zone, which surrounds the radar and its intended field of view, since the auroral oval is a source of ionization irregularities which are potential scatterers. For an OTH radar scanning the polar cap, signals backscattered from strong ionospheric irregularities in the auroral zone to the rear and sides of the field of view may compete with wanted signals from targets of interest. Therefore, in order to be effective any operational radar would be required to have sufficient back and side-lobe rejection to reduce signals from the auroral scatterers to a level above which the wanted target signals can be seen.

The experiments involved the operation of several ground-based transponders. The principal one for the study was located at Alert (AL), N.W.T. Riometers and ionosondes at Churchill and Resolute Bay provided synoptic data on ionospheric conditions and on the occurrence of auroral absorption (AA) and polar-cap absorption (PCA). The transponder experiments themselves provided direct evidence of backscatter, since the background level was set most of time by energy backscattered from ionospheric irregularities. Typical percentages of detection of the Alert transponder at Cambridge Bay were 80% for summer daylight hours, 40% for equinoctial daylight, and 15% for equinoctial and winter darkness. These variations are not unlike those observed with more direct communications experiments. Signal detection is dependent on propagation conditions over the path (in the present experiment two slightly different propagation paths are involved), the frequencies available and the response of the antenna systems particularly at the low range of HF. A diurnal variation was noted in the median background level and this varied with season: about 20 dB for summer months, 30 dB for equinoctial months and 15 dB for winter months. A minimum at local noon occurred in all seasons. The seasonal variation in median background level for local noon was found to be approximately 30 dB, with a minimum during summer months.

There was a strong anti-correlation between median background level and 30 MHz auroral absorption measured by the Churchill riometer. This implies that much of the time the background is set by backscatter from ionospheric irregularities in the auroral zone and that this contribution is sometimes reduced by auroral absorption.

The majority of the scatterers of large apparent cross-section were seen during local night and were found within the auroral zone (Fig. 32). However, an appreciable number of lower-apparent-cross section scatterers were found to exist in the polar cap as well (Fig. 33). Many of these were within the main beam of the Hall Beach radar. The inference that scatterers from the polar cap and from the auroral zone are both present came not only from direction and delay, but from their range-time behaviour. Ionospheric motions in the polar cap are dominantly in the anti-sun direction [Heppner, 1972], while those in the auroral zone are normally E-W or in the sunward direction.

The John Hopkins University, Applied Physics Laboratory HF coherent backscatter radar at Goose Bay (GB), Labrador is providing new information on the small-scale structure in the high-latitude ionosphere. This is an auroral zone location at a CGL of 65°. Although coherent scatter studies of the high latitude F region were performed nearly a quarter of a century ago [Bates, 1959, Bates and Albee, 1970] there is currently a renewed interest in the operation of high latitude sophisticated HF radar systems. For example currently an HF radar is operated in northern Scandinavia [Hanuise et al., 1981, and Hanuise, 1983], and a new French facility is operated at Schefferville, Quebec. This radar provides a capability for "stereoscopic" observations with the Goose Bay radar. A third HF radar will be installed at Halley Bay, Antarctica (CGL = 60.8°). Recent studies with the Labrador radar include: an analysis of irregular drift patterns [Hanuise et al., 1985]; coordinated radar-satellite studies of processes in the dayside cleft region [Baker et al., 1986]; observations of drift velocity pulsations in the high latitude ionosphere [Walker et al., 1986]; co-ordinated observations with the SRI International incoherent scatter radar at Sondre Stromfjord, Greenland [Ruohoniemi et al., 1987]; and a statistical survey of the backscatter observed with the Labrador radar [Baker et al., 1988]. The detailed physics emerging from these comprehensive studies is more pertinent to the overview in the lecture given by Bower [reference this Lecture Series].

Coherent scatter from F-region irregularities in the polar cap is a complicated subject. The range of structure sizes and the magnitude of the electron density irregularities ($\Delta N/N$) is much less than found in the auroral zone and the earth's magnetic field is even more vertical. The irregularities are most certainly field aligned, and present an appreciable cross-section for backscattering only if the sampling radar wave is nearly perpendicular to the local field lines. This will only occur at or near the height of reflection for waves obliquely incident on the ionosphere, hence the backscatter seen will be strongly dependent on ionospheric

conditions at the time of the observations. A further limitation and complicating factor is concerned with the use of horizontal log-periodic antennas (vertically polarized antennas are not recommended for places where the ground conductivity is poor). The vertical pattern is a function of frequency. There are nulls at certain launch angles, and antenna heights are usually less than optimum at the low frequency end of the band of frequencies employed; e.g. the antenna array employed at Goose Bay is not very high (15.2 m) and so the antenna response does not favour long distance one-hop propagation. With an antenna at this height, which is 0.55λ at 10.8 MHz the launch angle will be about 22° (which is the optimum launch angle for a path length of about 1250 km). This factor will limit the maximum range of the observed backscatter (which in some of the early observations was reported to come from irregularities located at distances of 900 - 1200 km).

A curious observation, in the author's view, is the reported early results using the Goose Bay phased array to receive HF transmissions from a transmitter at Thule, Greenland [Sales et. al., 1985]. These authors observed only 2-hop skywaves.

The coordinated observations employing the Goose Bay OTH radar and the incoherent scatter radar at Sondre Stromfjord, Greenland [Ruohoniemi et. al., 1987] reveal a correspondence between the measured irregularities and ion drift that is consistent with the supposition that the motion of the irregularities is dominated by convective drift of the ambient plasma. This observation supports the conclusion reached much earlier by Canadian work, and with the accepted model of F-layer drift [c.f. Whiteker, 1977].

Finally, we will conclude this brief overview with a summary of observations made by Montbriand [1988]. He made HF bistatic recordings of auroral scattering sources north of Ottawa during 1980-81 using the SARA array of the CRC, and swept frequency CW transmissions from the RADC facilities at Rome, NY. Doppler-frequency spreads of ± 100 Hz (corresponding to scatter motions of 2200 m/s) were obtained at least 35% of the time. The peak of the Doppler-frequency distribution was sometimes shifted from zero by as much as 50 Hz (Fig. 34), and significant contributions often occurred at Doppler-frequencies greater than 150 Hz. It is the Doppler-frequency spread which can make difficult detection of aircraft, since backscatter from aircraft is identified and extracted from the clutter by the regular doppler return from the moving target.

Signals received on the two arm SARA array were used to identify the specific elevations and bearings of the backscatter signals. A detailed study of a particular hour long period was reported. Based on elevations and bearings obtained from data recorded at different times (minutes apart), from Doppler-frequencies and different delay times, a number of "apparent" auroral backscatter sources were identified. All the sources were thought to be located in the F layer. The source regions were elongated mainly in the N-S direction and extended over at least 3 degrees in latitude. Between such sources, N-S corridors were found in which echo returns were either absent or very weak. The aspect sensitivity nature of the backscatter return is apparent (Fig. 35), since all sources identified were found to lie within the contour where the angle between the line-of-sight and the normal to the magnetic field lines at 300 km height as seen from Ottawa was $< 12^\circ$. The location of the Feldstein auroral oval for $Q=2$ is also marked on the figure.

The OTH radar is able to detect ships over very large ocean areas, but ship detection poses a whole new set of problems. Basically a ship is detected in the Doppler-spectrum of the radar echo providing its spectral line is not masked by the sea clutter. The theoretical limitations on ship detection have been studied by Maresca and Barnum [1982] who derived performance curves and defined blind speeds which depend on several parameters: radar cross section and radial speed of ships, sea state, operating frequency, coherent integration time and spatial resolution of the OTH radar. In this work Maresca and Barnum did not consider ionospheric multipath effects and smearing of the sea echo, which was a serious omission that further limits the detection capability. Sometimes the operating frequency can be chosen to illuminate a given patch of the sea without or with weak multipath contamination, but it is more difficult to avoid smearing of the sea echo. One kind of smearing of the sea echo occurs when the ionospheric Doppler shift varies during the acquisition time period, which can be significant, particularly for the F2-modes when integration times of 20 - 30 seconds are employed. The subject of ship detection is still under investigation. Barnum [1986] in a more recent paper has recognized the problems associated with ionospheric multi-path, and Bourdillon and Gauthier [1987] have proposed the use of a maximum entropy spectral analysis of sea scatter Bragg lines, to correct the phase of the signal before performing the classical Fourier transform processing. The improvement is said to sharpen the spectral peaks and so improve ship detection by OTH radar.

Research on ship detection employing HF OTH skywave radars at high latitudes has not been conducted (that the author knows about). However research on remote sensing of sea state at high latitudes has been carried out by Canadian workers. Since all the difficulties mentioned above were experienced, it is likely that ship detection would be difficult if not impossible. The measurement of sea state by skywave OTH radar is the subject of the following section.

4.5 OTH Measurement of Sea State

The potential of HF OTH radar for remote sensing sea state was recognized by Crombie [1955], who observed and identified the distinctive features of the sea-echo Doppler spectra. Barrick [1972 a, b], and Lipa and Barrick [1986] have developed the exact theoretical formulation that expresses the HF sea-echo Doppler-spectrum in terms of ocean-wave height, directional spectrum and surface current velocity. They presented mathematical methods for interpretation of HF OTH radar measurements by narrow-beam and wide-beam systems. Narrow-beam systems were developed for OTH radar detection and tracking of military targets. There use for remote observation of the sea surface is now recognized (c.f. the special issue of the IEEE J. of Oceanic Engineering, OE-11, No. 2, on HF radar for ocean and ice mapping and ship location). Large skywave radars such as WARF at SRI in the United States and JINDALEE in Australia are used for military applications, however these same skywave radars can be used for ocean-surface windfield and wave parameter measurements (c.f. Anderson [1986] and a paper by French scientists Parent and Gafford [1986]).

Narrow beam ground-wave radars with ranges to ~ 150 km, are being used in the UK, Australia and France, c.f. the overview paper by Shearman [1986]. Broad beam ground wave radars are being applied in Canada, West Germany and the U.S. HF radar iceberg observations were reported by Walsh et. al. [1986] of Canada and Arctic ice-pack breakup and velocity tracking were reported by Lipa et. al. [1986].

Only the Canadian observations [Winacott, 1986] are described here since these reveal the difficulties experienced in measuring sea state by an HF skywave radar operated at a latitude near the auroral zone. Bradley et. al. [1983, 1985] have discussed the ionospheric factors affecting the performance of HF sky-wave sea-state radars at high latitudes, but these authors have not actually tried to use such radars at high latitudes.

The Canadian skywave radar program made use of the SARA array, previously described, at Ottawa, and the US RADC transmitting facility at Rome, NY. The RADC facility provides compatible FMCW transmissions at power levels up to 100 kw, although due to limitations of the transmitting antenna used, levels of 5 - 10 kw were employed. A horizontally polarized log periodic antenna was employed (60° beam width) directed north east to cover the area of interest, viz. the Gulf of St. Lawrence, and the Newfoundland coastal areas from Sable Island and the Hibernia Oil field northward to the Labrador Sea, and the adjacent ocean areas (Fig. 36).

Two factors make the study unique. The first is that the area is relatively high in geomagnetic latitude, so that ionospheric contamination of sea-induced Doppler spectrum was expected to be more severe than has been the case in other studies. The second factor is the much greater significance of ice as a hazard to sea operations in the area. For this reason, part of the objective was to study the extent to which the pack ice along the Labrador coast and in the Gulf of St. Lawrence could be detected and mapped. However, the study did not succeed in detecting sea ice.

The efforts of the Communications Research Centre team were complemented by a university-related research group at the Centre for Cold Ocean Resources Engineering (C-CORE) in St. John's, Newfoundland. The C-CORE group had responsibility for the final processing of some of the data, for the interpretation of the radar data in terms of sea-state parameters, and for the collection of truth data from shipping observations and other sources. C-CORE also operated a transponder for calibration purposes during radar operating periods.

The derivation of sea-state parameters from the radar signal involves the interpretation of a rather complex Doppler spectrum. The spectrum consists of two lines offset from zero by the so-called Bragg frequency. These two "first-order" lines are superimposed upon a continuum which is called the "second order" spectrum. The ratio of the amplitudes of the two Bragg lines gives the wind direction (with a left-right ambiguity about the radar look direction). The amount of power in the second order spectrum increases with increasing ocean wave height. The ratio of this second-order power to the power in a narrow spectral region encompassing the dominant Bragg line, gives a measure of rms ocean wave height. The entire spectrum is less than 2 Hz wide; integration times of 1 minute or so were necessary to delineate the fine details. The entire spectrum may be frequency shifted by the effects of surface currents or by ionospheric motion. If the radar cell includes an island or coastal area, there will be a third Doppler line at zero frequency.

Almost all of the results were obtained by means of reflections from the F2 layer, with a few returns from the F1 layer during a period of moderate ionospheric disturbance. E layer reflections were in general not observed. A considerable fraction of the analysis procedures had to be directed towards averaging and alignment of the sea-state spectra, in an attempt to reduce the degradation caused by ionospheric Doppler effect and smear. This problem was aggravated by the necessity for relatively long observing periods (50 - 100 seconds) to provide adequate resolution in the sea-state spectra, in the presence of the short times of ionospheric variations, usually only a fraction of a second to a few seconds. A manual acceptance technique had to be employed since acceptance criterion developed by others was found to reject virtually all the Canadian data.

The Doppler spectrum obtained with the CRC facility involved a detailed, somewhat subjective data processing, carried out in a number of steps. First, a 102.4 second record was subdivided into three 50-percent overlapping records of 51.2 seconds each. Each segment was windowed with a Blackman - Harris window, and Fourier transformed. Ninety-six spectra from an observing interval were then averaged in groups of twelve: three "overlapped" spectra from each of four contiguous range cells (Fig. 37a). Next, each subgroup of twelve spectra was averaged, to generate an averaged spectra representing one, of a group of eight of four range cells each for the entire observation period. The group shown in Fig. 37a produced spectrum number 3 in Fig. 37b. From these eight "unconditionally" averaged spectra four were selected (in this case spectra 1, 2, 3 and 6) for alignment, normalization and final averaging. The resulting spectrum (Fig. 37c) was analysed for wave direction and wave height. This analysis yielded a wave direction of 23.4 degrees, and a wave height of 3.3 metres, both of which agreed closely with hindcast surface data. The final result is a spectral estimate applicable to an ocean area of about 72 km (along the radar look direction) by 77 km (defined by the 2.5° receiving array beam width). The amount of averaging indicated is typical of that necessary to produce low variance spectral estimates because of ionospheric contamination.

The CRC analysis was focussed on derivation of wave height; in fact, any spectrum that yielded an acceptable measure of wave height also yielded wave (wind) direction. Radar-wave-height results obtained on 8 April, 1982, during a storm period, are compared in Fig. 38 with hindcast ship reported data. The radar results were averaged data recorded between 14 - 20 UT, the hindcast wave height data were based on ship reports for 12 UT. The wave heights shown within the land area of northern Newfoundland, thought to be the result of side-lobe responses, were in agreement with the low wave heights near the tip of the island.

The corresponding wind field map is shown in Fig. 39, where the radar data recorded between 14 - 20 UT are compared with hindcast meteorological isobars measured at 18 UT. The inherent right/left ambiguity of the radar results was resolved by comparison to the meteorological data. Again, wind directions over land areas agreed with wind directions over nearby ocean areas.

From the limited amount of data analysed, it was concluded that wave direction was the easiest parameter to measure. The manual technique derived valid results even from unconditional averages of the spectra. Accurate measurement of low waves (heights 2 or 3 metres) was found difficult because of the sensitivity to multipath contamination. Although the scope of the work was insufficient to estimate the reliability of the technique to routinely monitor sea state, obviously reliability would not be high. The problem of finding good operating days during the execution of the experiment suggest that there would be significant gaps in coverage by an operational radar. In fact the results analysed were selected because they were successful. Therefore, not unlike high-latitude communication difficulties described above, successful use of the technique would be dependent upon a capability for on-line real time analysis, which permitted the observer to persist until he succeeds, and upon freedom of choice of operating frequency.

5. Closing Remarks

Propagation problems at HF in the high latitude region cannot be eliminated, but may be alleviated by proper system design and by the development of suitable forecast and warning techniques. Frequency flexibility and path diversity can minimize outages due to auroral absorption, which statistically is the most frequent cause of disruption of HF communications. One problem limiting the reliability of HF communications is interference from other users of the HF band, and this could be chaotic if communicators were allowed to jump frequency freely. Real time channel evaluation is a powerful tool for avoiding such interference and for adapting rapidly to changing ionospheric conditions.

In spite of employing methods such as adaptive networking, to minimize HF blackout, an ionospheric channel will not always be available. During strong natural disturbances such as a solar X-ray-flares and PCA events, or after nuclear explosions in the upper atmosphere, complete HF blackout may occur for relatively long periods of time over wide areas.

Meteor burst communications has been suggested as a back-up for HF [c.f. Forsyth et. al., 1957], and because meteor burst propagation has a high degree of inherent resistance to jamming and interception [Oetting, 1980], this makes it attractive for military applications. At high latitudes, however, off-path auroral scatter contribute to multipath modes which limit the data rate for simple signalling systems. During periods centred on the maximum epoch of the solar cycle, polar cap and auroral absorption at these latitudes can cause effective signal blackouts, not only at the frequencies normally used (40 - 50 MHz), but even at the highest frequencies so far employed (100 MHz) [Maynard 1968]. Notwithstanding, meteor burst communications over high latitude paths is currently being reassessed [Cannon et. al., 1985 and Ostergaade et. al., 1985]. Brown [1985] has developed a physical meteor burst propagation model.

If all else fails, and satellite links are not available, there is still one fall back for terrestrial communications over high latitude paths - VLF/LF communications. Paths which traverse the Greenland (or Antarctic) ice cap should be avoided. Otherwise, in the author's experience VLF/LF propagation over trans-auroral or over polar cap paths is never disrupted, even for the largest of natural disturbances during the largest so-far-recorded solar cycle [Belrose, 1968]. This is not to say that VLF/LF is not affected by high latitude disturbance, in fact VLF/LF propagation particularly the received phase provides a very sensitive tool for the synoptic monitoring of high-latitude-disturbances. However, the received signal amplitude is never smaller than the normal signal in summer at midday and the received signal amplitude can, in fact, be markedly enhanced. The phase delay is decreased, particularly for solar X-ray-flare events and solar proton events, which affect long range navigation systems such as OMEGA [Swanson, 1982].

Acknowledgement

The author wishes to acknowledge discussions with his colleagues, particularly with Robert Jenkins and Donald Muldrew, who provided unpublished papers and memoranda.

References

- Akasofu, S.I. [1985] Solar terrestrial relationship in the high latitude region, AGARD CP 382, I.1-1-1.1-17.
- Anderson, S.J. [1986] Remote sensing with the JINDALEE skywave radar, IEEE J. Oceanic Engr. QE-11, No. 2, 158 - 163.
- Bailey, D.K. [1964] Polar-Cap Absorption, Planet. and Space Sci., 12, 537.
- Baker, K.B., Greenwald, R.A., Walker, A.D.M., Bythrow, T., Potemra, A., Hardy, D.A., Rich, F.J. and Rino, C.L. [1986] A case study of plasma processes in the dayside cleft, J. Geophys. Res., 91, 3130.
- Baker, K.B., Greenwald, R.A. and Villain, J.P. [1988] HF-radar backscatter from decameter ionospheric irregularities at high latitudes: A statistical survey, submitted to J. Geophys. Res.
- Barnum, J.R. [1986] Ship detection with high resolution HF skywave radar, IEEE Oceanic Engr. Soc., QE-11, No. 2, 196 - 209, April, 1986.
- Barrick, D.E. [1972a] First order theory and analysis of MF/HF/VHF scatter from the sea, IEEE Trans. Ant. Prop., AP-20 2 - 10.

- Barrick, D.E. [1972b] Remote sensing of sea state by radar, in Remote Sensing of the Troposphere, V.E. Derrid., Washington DC; GPO, 1972, Chap. 12.
- Bates, H.F. [1959] The height of F-layer irregularities in the arctic ionosphere, *J. Geophys. Res.*, **64**, 1257.
- Bates, H.F. and Albee, P.R. [1970] Aspect sensitivity of F-layer HF backscatter echoes, *J. Geophys. Res.*, **75**, 165.
- Belrose, J.S. [1968] Low and very low frequency propagation, AGARD Lecture Series XXIX, Lecture No. 4.
- Belrose, J.S. [1982] The Propagation Medium: An overview, AGARD Conf. Proc. No. 305, Paper No. 1.
- Belrose, J.S., Litva, J. and Stevens, E.E. [1983] Beverage antennas for amateur communications, *QST*, **22** - 27, Jan. 1983.
- Bourdillon A. and Gauthier, F. [1987] Use of maximum entropy spectral analysis to improve ship detection by OTH radar, *Radio Sci.*, **22**, 313 - 320.
- Bourne, I.A., Ross, D.B., and Segal, B. [1970] Phase instability in radio waves propagating across ice-covered seas, in Phase and Frequency Instabilities in EM wave Propagation, AGARD CP No. 33, 318 - 330, Technivision Series, Slough, England.
- Boutacoff, D.A. [1985] Backscatter radar extends early warning times, *Defense Electronics*, August, 71 - 83.
- Bradley, P.A., Bramley, E.N., Gibson, A.J. and King J.W. [1983] Ionospheric factors affecting the performance of HF sky-wave sea-state radars, AGARD Conf. Proc. No. 345, Paper No. 13.
- Bradley, P.A., Gibson, A.J., Schlobohm, J.C. and Westover, D.E. [1985] Ionospheric factors affecting the performance of HF sky-wave sea-state radars at high latitudes, AGARD Conf. Proc. No. 382 Paper No. 4.1.
- Brinton, H.C., Grebowsky, J.M. and Brace, L.H. [1978] The high latitude winter F-region at 300 km: Thermal plasma observations from AE-C, *J. Geophys. Res.*, **83**, pp 4767 - 4776.
- Brown, D.W. [1985] A physical meteor-burst propagation model and some significant results for communication system design, *IEEE J. on selected Areas in Communications*, **SAC-3**, 745 - 755.
- Butler, R.S. [1985] The NW Passage propagation experiment: Report of the 1983 - 1984 Measurement Program, CRC Report No. 1391, Dept. of Communications, Canada.
- Cannon, P.S., Dickson, A.H. and Armstrong, M.H. [1985] Meteor burst radio communications at high latitudes, AGARD Conf. Proc. No. 382, paper No. 9.1.
- Collins C., Jelly, D.H., and Matthews, A.G. [1961] HF radio-wave blackouts at medium and high latitudes during a solar cycle, *Can. J. Phys.*, **39**, 35 - 52.
- Crane, R.K. [1977] Ionospheric scintillations, *Proc. IEEE*, **65**, 180 - 199, February, 1977.
- Crombie D.D. [1955] Doppler spectrum of sea echo at 13.56 MHz, *Nature*, **175**, 682.
- Driatskiy, V.M. [1966] *Geomagn. Aeron.*, **6**, 828.
- Etemadi, A., Cowley, S.W.H., Lockwood, M., Bromase, B.J.I. Willis, DM and Luhr, H. [1988] The dependence of high-latitude dayside ionospheric flows on the N-S component of the IMF: a high time resolution correlation analysis using EISCAT "Polar" and AMPTE UKS and IRM data, *Planet. Space Sci.* (to be published).
- Elvy, S.J. [1985] A design for an automatic HF system, *Radio Sci.*, **20**, 261 - 268.
- Falthammer, C. [1986] Magnetospheric - ionosphere interactions - near Earth manifestations of the plasma universe, *IEEE Trans. Plasma Sci.*, **PS-14**, No. 6, pp 616 - 628.
- Feldstein, Y.I. and Stanov, G.V. [1967] Dynamics of auroral belt and polar geomagnetic disturbances, *Planet and Space Sci.*, **15**, p.p. 209 - 229.
- Foppiano, A.J. and Bradley P.A. [1985] Morphology of background auroral absorption, *J. Atmos. Terr. Phys.*, **47**, 663 - 674.
- Forsyth, P.A. Vogan, E.L., Hansen, D.R., and Hines C.S. [1957] The principles of JANET - A meteor burst communications system, *Proc. IRE*, **45**, 1642 - 1657, Dec. 1957.
- Fritz, T.A. and Gurnett, D.A. [1965] Diurnal and Latitudinal Effects Observed for 10 Kev Electrons at Low Satellite Altitudes, *J. Geophys. Res.*, **70**, pp 2485.
- Fuller-Rowell, T.J., Rees, D., Quegan, S., Bailey, G.J., and Morfett, R.J. [1988] Interaction between neutral thermospheric composition and the polar ionosphere using coupled-ionosphere-thermosphere model, *J. Geoph. Res.*, (to be published).

- Greenwald, R.A., Baker, K.B., Hutchins, R.A., and Hanuise, C. [1985] An HF phased-array radar for studying small scale structure in the high latitude ionosphere, *Radio Sci.*, 20, 63 - 79.
- Gustafsson, G. [1970] A revised corrected geomagnetic coordinate system, *Arkiv for Geofysik*, 5, p.p. 595 - 617.
- Gussenhoven M.S. and Hardy D.A. [1987] The equatorward boundary of auroral ion precipitation, *J. Geophys. Res.*, 92, 3273 - 3283.
- Hagg, E.L. and Rolfe, W. [1963] A study of Trans Atlantic Radio Propagation at 41.5 Mc/s., *Can. J. Phys.*, 41, 220.
- Hakura, Y. [1965] Tables and maps of geomagnetic co-ordinates corrected by the higher order spherical harmonic terms, *Rep. Ion. and Space Res., Japan*, 19, 121 - 157.
- Hanuise, C., Villain, J.P. and Crochet, M. [1981] Spectral studies of F region irregularities in the auroral zone, *Geophys. Res. Lett.*, 8, 1083.
- Hanuise, C. [1983] High-latitude ionospheric irregularities: A review of recent results, *Radio Sci.*, 18, 1093.
- Hanuise, C., Greenwald, R.A. and Baker, K.B. [1985] Drift motions of very high latitude F region irregularities: Azimuthal Doppler analysis, *J. Geophys. Res.*, 90, 9717.
- Hardy, D.A., Gussenhoven, M.S. and Holeman, E. [1985] A statistical model of auroral electron precipitation, *J. Geophys. Res.*, 90, 4229 - 4248.
- Hargraves, J.K., Feeney, M.T., Ranta, H. and Ranta, A. [1987] On the prediction of auroral radio absorption on the equatorial side of the absorption zone, *J. Atmos. Terr. Phys.*, 49, 259 - 272.
- Harnish, L.O. and Hagn, G.H. [1985] A comparison of MOF factors and frequency of optimum transmission bands observed using oblique-incidence sounder-update PROPHET predictions for a one-month test in continental US during the geomagnetically active summer of 1982, *Radio Sci.*, 20, 269 - 279.
- Hartz, T.R., Montbriand, L.E. and Vogan, E.L. [1963] A study of auroral absorption at 30 MHz, *Can. J. Phys.*, 41, 581 - 595.
- Hartz, T.R. and Brice, N.M. [1967] *Planet. Space Sci.*, 15, 301.
- Headrick, J.M. and Skolnik, M.I. [1974] Over-the-horizon radar with HF band, *Proc. IEEE*, 62, No. 6, 664 - 673.
- Heppner, J.P. [1972] Electric field variations during substorms: OG0 - 6 Measurements, *Planet. Spac. Sci.*, 20, 1475 - 1498.
- Jelly, D.H. and Collins, C. [1962] Some observations of Polar-cap absorption in the northern and southern hemispheres, *Can. J. Phys.*, 40, 706 - 718.
- Jelly, D.H. [1963] The effects of Polar-Cap Absorption on HF oblique circuits, *J. Geophys. Res.*, 68, 1705 - 1714.
- Jenkins, R.W. [1977] HF channel evaluation trials of trans-auroral and polar cap circuits, CRC Report No. 1302, Ottawa, ON.
- Jenkins, R.W. [1979] A doppler technique for measuring an aircraft's velocity from the spectrum of its HF transmissions, *IEEE Trans. Ant. Prop.*, AP-27 No. 6, 885, November 1979.
- Jenkins, R.W., Hagg, E.L. and Montbriand, L.E. [1979] Direction and doppler characteristics of medium and long-path HF signals within the night-time sub-auroral zone, AGARD Conf. Pub. No. 263.
- Jones, T.B. [1987] HF propagation at high latitudes, *IEE Conf. Proc.* No. 274 (ICAP 87), 155 - 169.
- Jull, G.W., Doyle, D.J., Irvine, G.W. and Murray, J.P. [1962] Frequency sounding techniques for HF communications over auroral zone paths, *Proc. IRE*, 50, 1676 - 1682.
- Kelley, M.C., Vickrey, J.F., Carlson, C.W. and Torbert, R. [1982] On the Origin and Spatial Extent of High-Latitude F Region Irregularities, *J. Geophys. Res.*, 87, p.p. 4469.
- Kelley, W.D. [1987] HF communications: New life for an old friend, *Signal*, August p.p. 89 - 94.
- Knudsen, W.C. [1974] Magnetospheric convection and the high-latitude F2 ionosphere, *J. Geophys. Res.*, 79, p.p. 1046.
- Knudsen, W.C., Barks, P.M., Winningham, J.D. and Klumpp, D.M. [1977] Numerical model of the convecting F2 ionosphere at high latitudes, *J. Geophys. Res.*, 82, 4784 - 4792.
- Lipa, B.J. and Barrick, D.E. [1986a] Extraction of sea-state from HF radar sea echo: Mathematical modelling, *Radio Sci.*, 21, 81 - 100.

- Lipa, B.J., Crissman, R.D. and Barrick, D.E. [1986b] HF radar observations of Arctic pack-ice breakup, *IEEE J. Oceanic Engr.*, QE-11, No. 2, 270 - 275.
- McLarnon, B.D. [1982] Realtime channel evaluation in automatic HF radiotelephone system, *IEE 2nd Conf. on HF Communication systems and Techniques*, p.p. 46 - 50.
- McDiarmid, I.B. and Buitows, J.R. [1965] Electron Fluxes at 1000 kilometers Associated with the Tail of the magnetosphere, *J. Geophys. Res.*, 70, p.p. 3031.
- McIlwain, C.E. [1966] Magnetic coordinates, *Space Sci.*, 5, 585 - 598.
- McNamara, A.G. [1969] Rocket measurements of plasma densities and temperatures in visual aurora, *Can. J. Phys.*, 47, 1913 - 1927.
- Maynard, L.A. [1968] Meteor burst Communications in Ionospheric Radio Communications (ed. K. Folkestad), 165 - 173, Plenum Press, NY.
- Maresca, J.W. and Barnum, J.R. [1982] Theoretical limitation of sea on the detection of low Doppler targets by OTHR, *IEEE Trans. Ant. Prop.*, AP-30, 837 - 845.
- Miller, K.L. and Vondrak, R.R. [1985] A high-latitude phenomenological model of auroral precipitation and the ionosphere, *Radio Sci.*, 20, 431 - 438.
- Montbriand, L.E. [1981] The dependence of direction finding accuracy on aperture size, *CRC Report No. 1343*, June 1981.
- Montbriand, L.E., Auroral backscatter observations at HF from Ottawa [1988], *Radio Sci.*, on press.
- Montbriand, L.E. and Rice D.W. [1986] Ground-based reception of ISIS-I and ISIS-II transmissions: Final Report, Communications Research Centre, Tech. Memorandum, DRC-86-05.
- Moresca, J.N. and Barnum, J.R. [1982] Theoretical limitation of the sea on the detection of low Doppler targets by OTH radar *IEEE Trans. Ant. & Prop.*, AP-30, 837.
- Muldrew, D.B. [1983] Alouette-ISIS radio wave studies of the cleft, the auroral zone, and the main trough and of their associated irregularities, *Radio Sci.*, 18, p.p. 1140.
- Muldrew, D.B. and Vickrey, J.F. [1982] High Latitude F Region Irregularities Observed Simultaneously with ISIS-I and the Chatanika Radar, *J. Geophys. Res.*, 87, 8263.
- Nelms, G.L. and Chapman, J.H. [1970] The high latitude ionosphere results from the Alouette/ISIS topside sounders. *The Polar Ionosphere and Magnetospheric Processes*, 233 - 269 (Ed. G. Skovli), Gordon Breach Pub. Co., NY.
- Nourry, G.R. and Mackie, A.J. [1988] The design and performance of an adaptive packet switched HF data terminal, in *Effects of Electromagnetic Noise and Interference on Performance of Military Radio Communications systems*, AGARD CP, Paper No. 11 (on press).
- Oetting, J.D. [1980] An analysis of meteor burst communications for Military applications, *IEEE Trans. Com.*, COM-28 September, 1980.
- Ostergaard, J.C., Rasmussen, J.E., Sowa, M.J., Quinn, J.M., and Kossey, P.A. [1985] characteristics of high latitude meteor burst propagation parameters over the 45 - 104 MHz band, *AGARD Conf. Proc. No. 382*, Paper No. 9.2.
- Parent, J. and Gaffard, C. [1986] Detection of meteorological fronts over the North Sea with Valensole skywave radar, *IEEE J. Oceanic Engr.* QE-11, No. 2, 174 - 179.
- Paul, A.K. [1986] NOSC Scientist predicts Sunspot Activity, *Technical Briefs*, Naval Ocean Systems Centre, 17 February, 1986.
- Perl, J.M. [1987] A real time HF adaptive communications system, *Signal*, August p.p. 81 - 86.
- Petrie, L.E., Goudie, G.W., Ross, D.B., Timleck, P.L. and Chow, S.M. [1986] MICROPREDIC: An HF prediction Program for 8086/8088 - based computers, *CRC Rep. 1390*, Ottawa.
- Quegan, S., Gill, R.S., and Lockwood, M. [1988] Comparisons between EISCAT observations and model calculations of the high latitude ionosphere, *J. Atmos., Terr. Phys.*, (to be published).
- Rice, D.W. and Winacott, E.L. [1977] A sampling array for HF direction finding, *CRC Report No. 1310*, CRC, Dept. of Communications, Canada.
- Rice, D.W., Venier, G.O. and Atkinson, G. [1978] The effect of signal modulation in the application of wave front linearity test in HFDF, *Proc. of the 1978 NRL-ONR Symp. on the Effect of the Ionosphere in Space and Terrestrial Systems*, Arlington, VA, 24 - 26 Jan. 1978, Paper 3 - 12.

- Rice, D.W. [1982] HF direction finding by wave front testing in a fading signal environment, *Radio Sci.*, **17**, 827 - 836.
- Robinson, R.M. and Vondrak, R.R. [1985] Characteristics and sources of ionization in the continuous aurora, *Radio Sci.* **20**, 447 - 455.
- Ruohoniemi, J.M., Greenwald, R.A., Baker, K.B. and Villain, J.P. [1987] Drift motions of small scale irregularities in the high latitude F region: An experimental comparison with plasma drift motions, *J. Geophys. Res.*, **92**, 4553 - 4564.
- Sales, G.S., Cormier, R.J., Greenwald, R.A. and Baker, K.B. [1985] High latitude spatially adaptive propagation experiment, AGARD CP 382.
- Sargent, H.H. [1985] Recurrent geomagnetic activity: Evidence for long-lived stability in solar wind structure, *J. Geophys. Res.*, **90**, 1425 - 1428.
- Sherman, E.D.R. [1986] A review of methods of remote sensing of sea surface conditions by HF radar and design considerations for narrow-beam systems, *IEEE J. Oceanic Eng.*, **QE-11**, 150 - 157.
- Smith, G.F. and Werner, W.L. [1988] The renaissance of HF communications, *Signal*, January, 55 - 62.
- Sojka, J.J. and Schunk, R.W. [1988] A model of how electric field structures affect the polar cap F region, *J. Geophys. Res.*, **93**, 884 - 896.
- Stein, K.J. [1982] Backscatter Radar Unit enters production phase, *Aviation Week & Space Tech.*, 16 August.
- Stevens, E.E. [1968] The CHEC sounding system, *Ionospheric Radio Communications* (ed. K. Folkestad), Plenum Press, p.p. 359 - 369.
- Swanson, E.R. [1982] OMEGA, AGARD Conf. Pub. No. 305, Paper No. 36.
- Sweeney, L.E., Washburn, T.W., Zavoli, W.B. and Barnum, J.R. [1983] Target detection and tracking with OTH radar: A review of WARF results, AGARD CP 345.
- Thompson, R.J. [1985] The seasonal distribution of geomagnetic disturbances, IPS Radio and Space Services, Tech. Rep. IPS-TR-85-05, Darlinghurst, NSW, Australia.
- Thompson, R.J. [1987] The amplitude of solar cycle number 22, IPS Radio and Space Services, Tech. Report IPS-TR-87-03, Darlinghurst, NSW, Australia.
- Thrane, E.V. [1983] Propagation II : Problems in HF Propagation, AGARD LS 127, p.p. 11-1 - 11 - 17.
- Thrane, E.V. [1986] Propagation I: State of the art of modelling and prediction of HF Propagation AGARD LS 145, p.p. 5 - 1 - 5 - 21.
- Timleck, J.E., and Nelms, G.L. [1969] Electron densities less than 100 cm^{-3} in the topside ionosphere, *Proc. IEEE*, **57**, 1164 - 1171.
- Venier, G.O. [1980a] An investigation of HFDF accuracy on the Churchill - Ottawa auroral zone path, Commun. Res. Centre, Tech Note 702.
- Venier, G.O. [1980b] An investigation of HFDF accuracy on the Frobisher Bay - Ottawa path auroral zone path, Commun. Res. Centre, Tech. Note 703.
- Vickrey, J.F., Rino, C.I., and Potemra, T.A. [1980] Triad observations of unstable ionization enhancements in the auroral F region, *Geophys. Res. Let.*, **7**, 789.
- Walker, A.D.M., Greenwald, R.A. and Baker, K.B. [1986] HF radar observations of pulsations near the magnetospheric Cusp, *J. Geophys. Res.*, **91**, 8919.
- Walsh, J., Dawe, B.J. and Srivastava, S.K. [1986] Remote sensing of icebergs by ground wave Doppler radar, *IEEE J. Oceanic Engr.*, **QE-11**, No. 2, 293 - 295.
- Watkins, B.J., Akasofu, S.I. and Fry, C.D. [1985] Progress in modelling the polar ionosphere from solar and magnetospheric parameters, AGARD CP-382, 7.2-1 - 7.2-4.
- Whalen, J.A. [1970] Auroral oval plotter and monograph for determining corrected geomagnetic local time, latitude and longitude for high latitudes in the Northern Hemisphere, AFCRL, Report No. A FCRL-70-0422, Environmental Research Paper No. 327, AD713170 (available from Defense Technical Information Centre, Cameron Station, Alexandria, VA 22314, USA).
- Whitaker, J.H. [1976] The magnetospheric cleft - ionospheric effects, *J. Geophys. Res.*, **81**, 1279 - 1288.

Whitaker, J.H. [1977] *The transient response of the topside ionosphere to precipitation*. Planet. and Space Sci., 25, p.p. 773 - 786.

Whitaker, J.H., Shepherd, G.G., Anger, C.D., Burrows, J.R., Wallis, D.D., Klumpar, D.M. and Walker, J.R. [1978] *The winter polar ionosphere*, J. Geophys. Res., 83, 1503 - 1518.

Winacott, E.L. [1986] *An experimental investigation of skywave sea-state radar techniques at a latitude near the auroral zone*, IEEE J. Oceanic Engr., OE-11, No. 2, 187 - 195.

Wylder, J. [1988] *The frontier of sensor technology*, Signal, March, 73 - 76.

Bibliography

Radiowave Propagation, AGARD LS XXIX, 1968. Avail: NTIS (Ref. NASA Acces. No. N68-37825).

Ionospheric Radio Communications (in the Arctic) (ed. K. Folkestad), Plenum Press, NY, 1968.

Medium, Long and Very Long Wave Propagation (at frequencies less than 3000 kHz) (ed. J.S. Belrose), AGARD CP 305, 1982. Avail: NTIS (Ref. NASA Acces. No. N82-27613).

Modern HF Communications, AGARD LS 127, 1983. Avail: NTIS (Ref. NASA Acces. No. N83-30862).

Propagation effects on Military Systems in the High Latitude Region (ed. H. Soicher), AGARD CP 382, 1985. Avail: NTIS (Ref. NASA Acces. No. N86-27566).

The energy budget campaign 1980, Special issue of J. Atmos. Terr. Phys., Jan. - March, 1985.

Propagation impact on modern HF communication system design, AGARD LS 145, 1986. Avail: NTIS (Ref. NASA Acces. No. N86-27531).

HF Radar for Ocean and Ice Mapping and Ship Location, Special issue of IEEE J. Ocean Eng., OE-11, No. 2, April, 1986.

Effects of Electromagnetic Noise and Interference on performance of Military Radio Communication Systems, AGARD CP, 1988 (on press).

CCIR Reports, Vol. VI, Propagation in Ionized Media, Geneva, 1986

- Special properties of the high latitude ionosphere, CCIR Report 886.
- Long-term ionospheric propagation prediction, CCIR Report 255.
- Short-term prediction of solar induced variations of operation parameters for ionospheric propagation, CCIR Report 727.
- Man-made radio noise, CCIR Report 258.
- Characteristics and applications of atmospheric radio noise, CCIR Report 322.
- Antenna characteristics important for analysis and prediction of skywave propagation, CCIR Report 891.
- Computation of reliability for HF systems, CCIR Report 892.
- Operational modelling of HF radio propagation conditions at high latitudes, CCIR Rep. 1012.
- Second CCIR computer based interim method for estimating skywave field strength and transmission loss at frequencies between 2 and 30 Mhz, Supplement to CCIR Report 252.

Postscript

In Section 3.3.3 we noted that recent progress is being made in modelling the high latitude ionosphere using interplanetary parameters as input. This topic was highlighted at a recent AGARD Symposium, on "Ionospheric Structure and Variability on a Global Scale and Interaction with Atmosphere, Magnetosphere", held in Munich, FRG, 16 - 20 May, 1988 [reference AGARD CP 441, to be published]. Particular reference should be made to the papers by Lemaire, Rostoker (local cite), on solar terrestrial relations and on magnetospheric substorms as signatures of the solar terrestrial interaction; and, on the subject of modelling, the papers by Schunk and Soja, Szuszczewicz, and Carlson. Also see a special issue of Annales Geophysicae, (Atmospheres, Hydrospheres and Space Sciences), 6, February 1988, which describes first results from an international solar-terrestrial research programme that combines theoretical and empirical modelling with co-ordinated ground-based and satellite-borne measurement programmes. This campaign began in October 1984, and is planned to continue during the ascending phase of the current solar cycle.

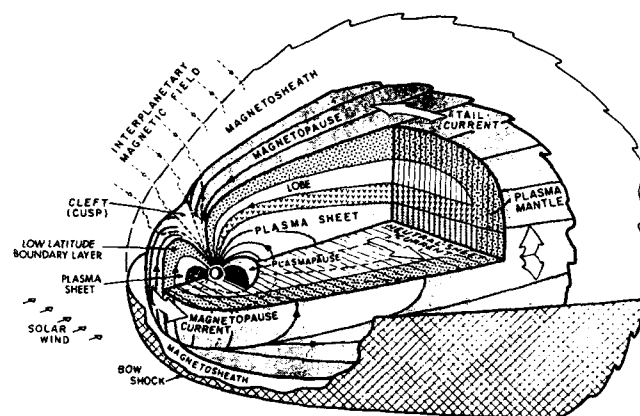


Fig. 1 The particle and magnetic field regimes of the earth. The plasma sheet boundary layer at the high-latitude edge of the (central) plasma sheet maps to the high-latitude ionosphere where dynamic auroral activity is found [after Rostoker, 1988].

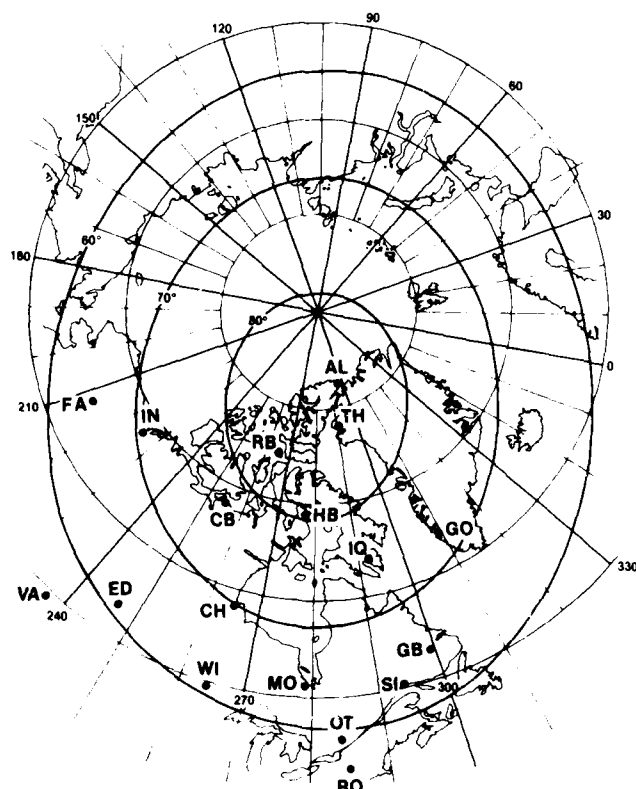


Fig. 2 Corrected geomagnetic latitude in the northern hemisphere (geographic latitude and longitude and place names are marked for reference).

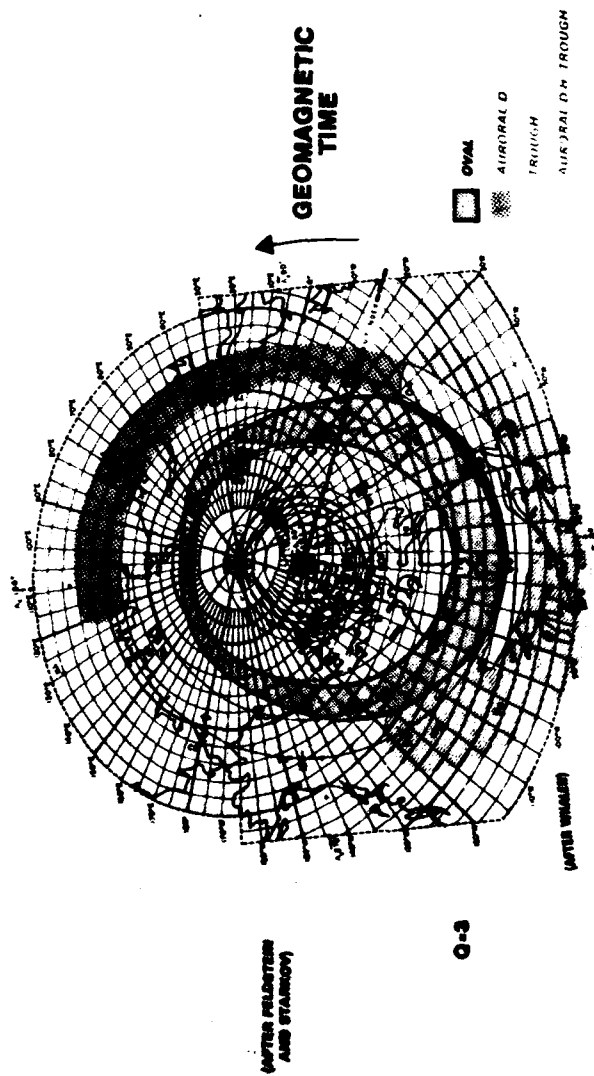


Fig. 3 Photograph of a northern hemisphere map on which boundaries of high latitude disturbance zones (or ovals) have been plotted (co-ordinates are CGL and local magnetic time) with a clear plastic overlay on which a map in geographic co-ordinates has been drawn. To determine the diurnal movement of say the (auroral) oval relative to a point on the earth rotate the overlay through one revolution (24-hours). For the photograph the UT index line has been set to 05 hours [after NSA, Washington, DC, 1986].

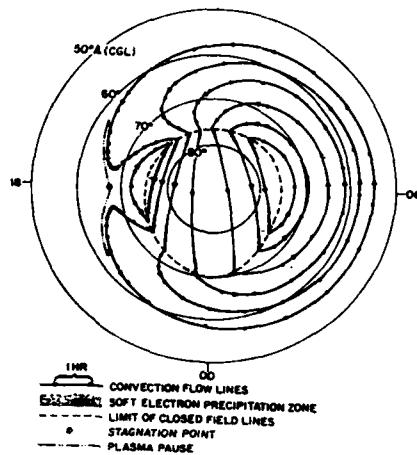


Fig. 4 Corrective flow paths of F-layer ionization implied by models of the magnetospheric electric field [after Krudsen, 1974].

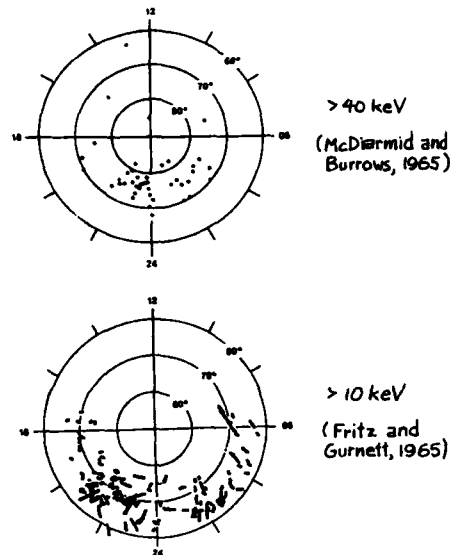


Fig. 5 The distribution in invariant latitude and local time of: a) intense electron spikes (energies > 40 keV) observed at a height of 1000 km by Alouette 1 [after McDiarmid and Burrows, 1965]; and intense electron fluxes (energies > 10 keV) observed with INJUN 3 [after Fritz and Grunett, 1965]. See Hartz and Brice [1967].

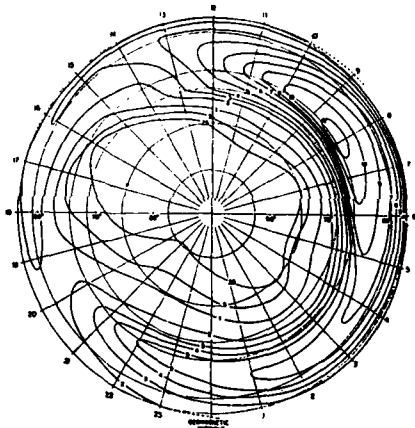
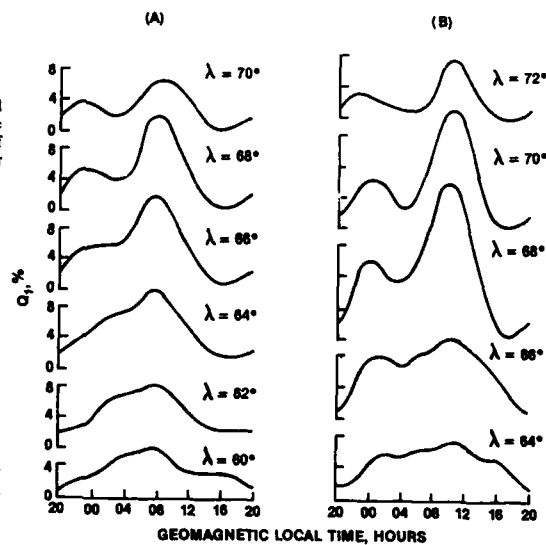


Fig. 6 The percentage of time that auroral radio wave absorption of 1.0 dB or more occurred at 30 MHz plotted as a function of "simple" geomagnetic latitude and time [after Hartz and Brice, 1967].

Fig. 7 The percentage of time that auroral radio wave absorption of 1.0 dB or more occurred ($Q_1\%$) at 30 MHz plotted as a function of geomagnetic local time and corrected geomagnetic latitude. a) Data from Canadian sector given by Hartz et. al. [1963] for the period July 1959 - June 1961 (mean $R \sim 100$); and b) Data from the USSR sector given by Driatskiy [1966] for the period December 1963 - November 1964 (mean $R \sim 10$) [after Foppiano and Bradley, 1985].



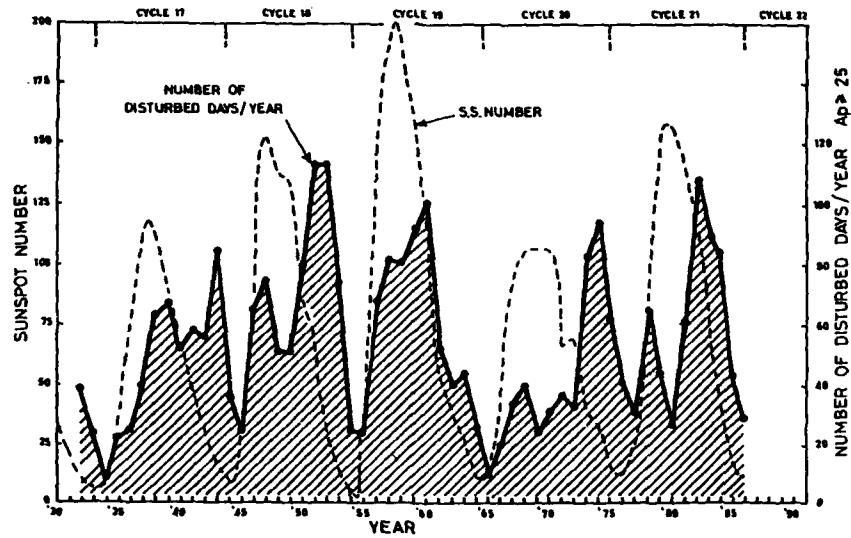


Fig. 8 The variation of the yearly-averaged sunspot number since 1930 (dashed line) and the variation in the number of geomagnetically disturbed days since 1932 (solid line) [after Thompson, 1987].

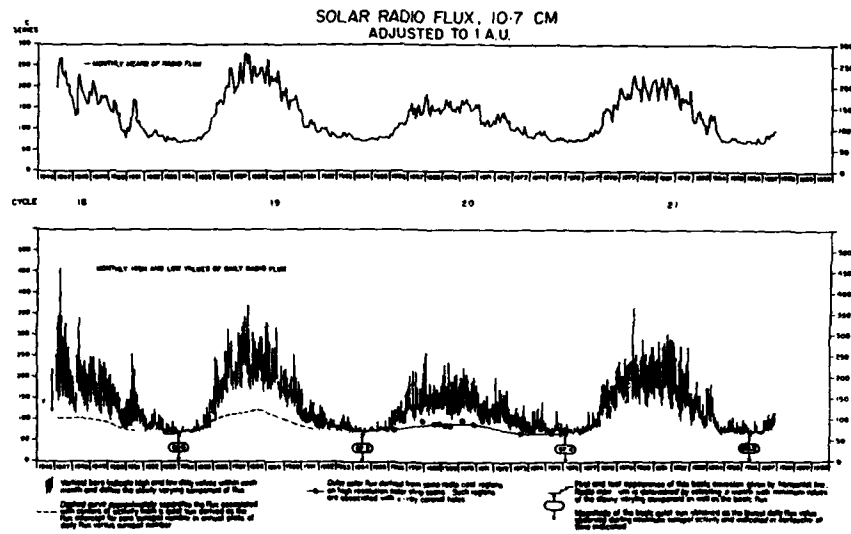


Fig. 9 Monthly high and low values and monthly mean values of daily solar radio flux for 1947 to 1985 (measured at Ottawa).

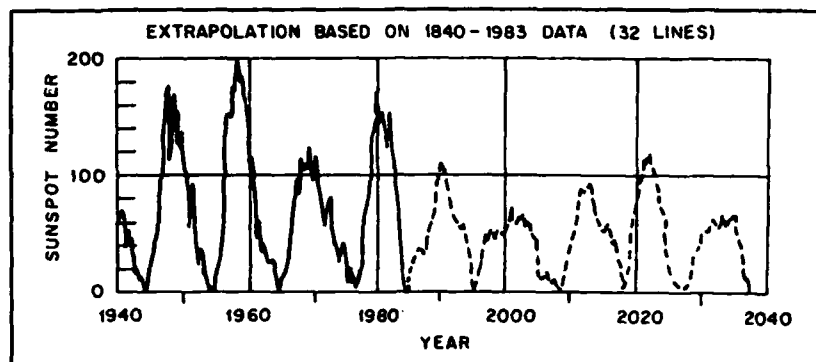


Fig. 10 Solar sunspot number prediction for the next five cycles [after Paul, 1986].

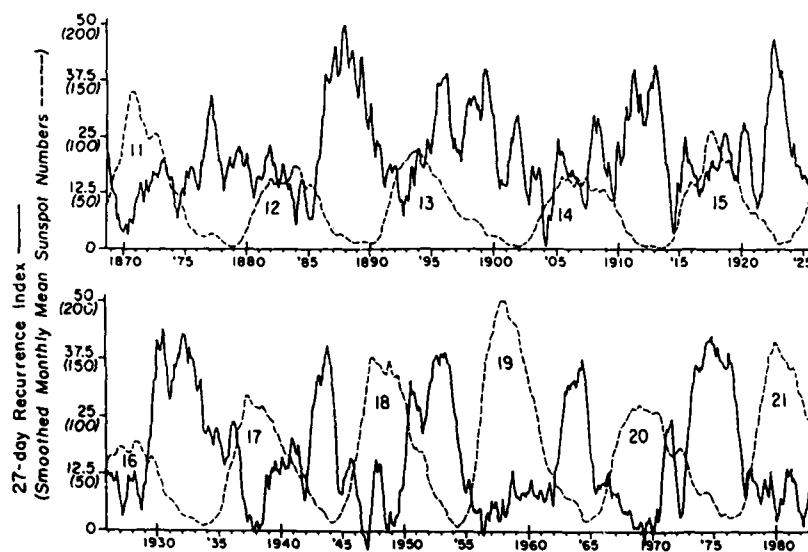


Fig. 11 Twenty-seven day recurrence index (solid line) and smoothed mean sunspot numbers (dashed line) from 1868 to present [after Sargent, 1985].

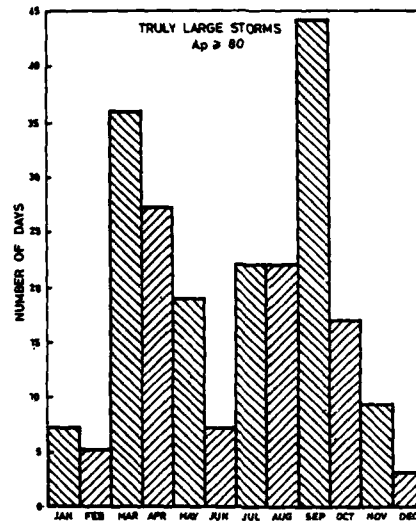


Fig. 12 Seasonal distribution of truly large geomagnetic storms, 1932 - 1984 [after Thompson, 1985].

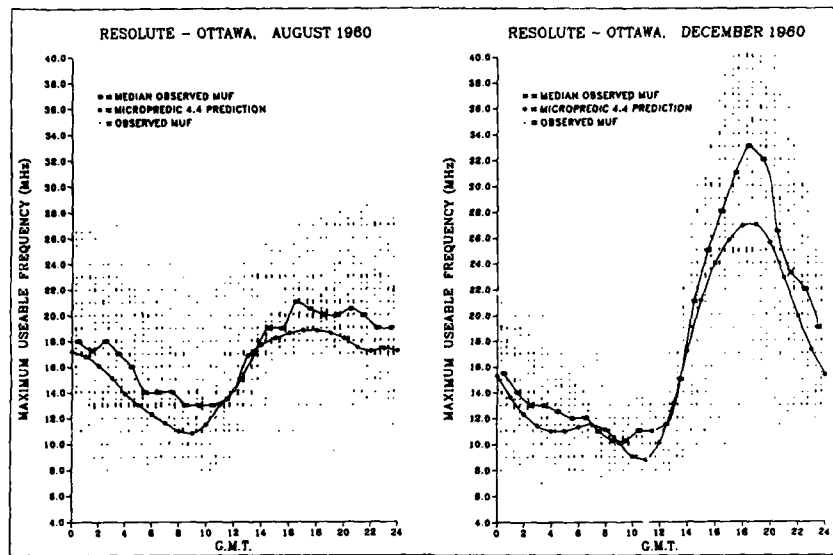


Fig. 13 Scatter plot of individual observed values of maximum useable frequency (MUF) taken twice hourly for the circuit Ottawa-Resolute Bay, August 1960 (summer); December 1960 (winter), on which are superimposed curves of the predicted and the observed median values.

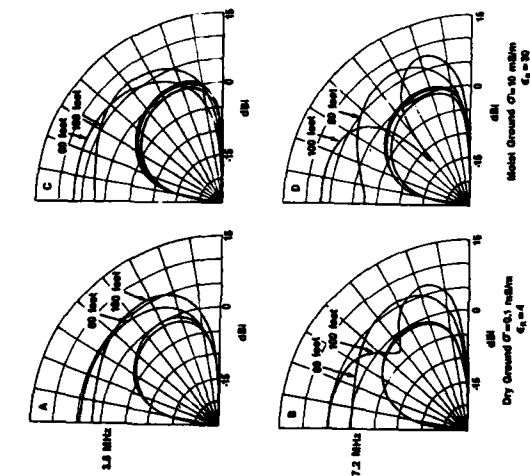


Fig. 14 Theoretical gain for a horizontal dipole at two heights (60 and 100 feet), two ground conductivities (dry and moist ground) and two frequencies (3.8 and 7.2 MHz), compared with a quarter wave vertical monopole with radials a quarter wave length long (after Breakall, private communications, 1986).

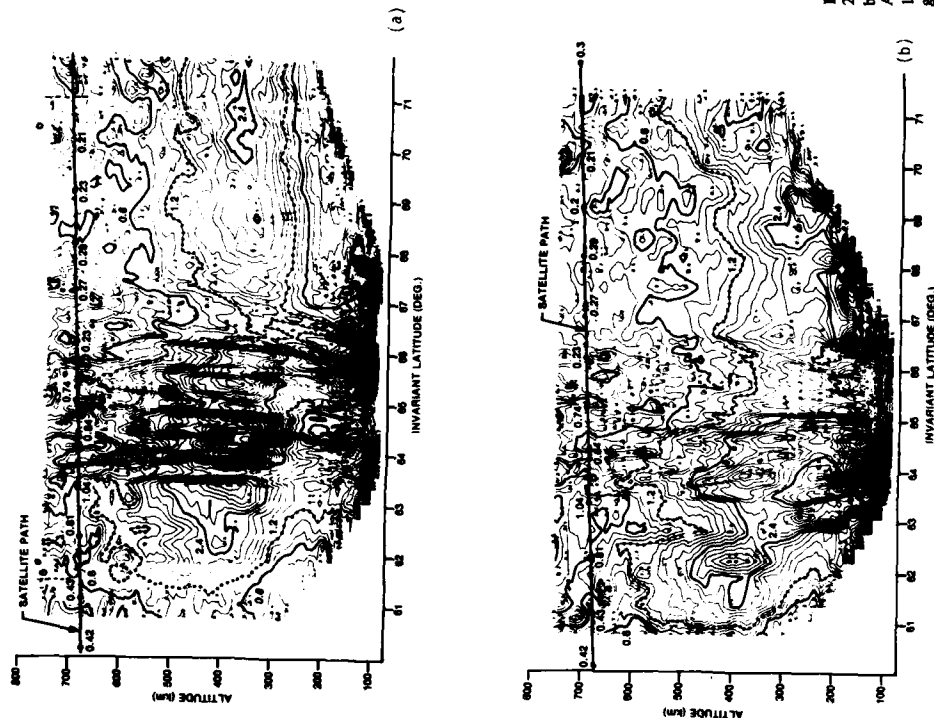


Fig. 15 a) Electron density contour map obtained with the Chatanika radar on 20 February 1981, between 1130:25 and 1144:25 UT. The contours are separated by $0.2 \times 10^5 \text{ cm}^{-3}$. Enhanced contours are given at 0.6 , 1.2 and $2.4 \times 10^5 \text{ cm}^{-3}$. A near-coincidence ISIS 1 satellite path near 700 km is shown about 1142 and 1146 UT. The electron density in units of 10^5 cm^{-3} obtained from ionograms is given along the path. b) the same as (a) between 1144:50 and 1157:28 UT (after Muldrew and Vickrey, 1982).

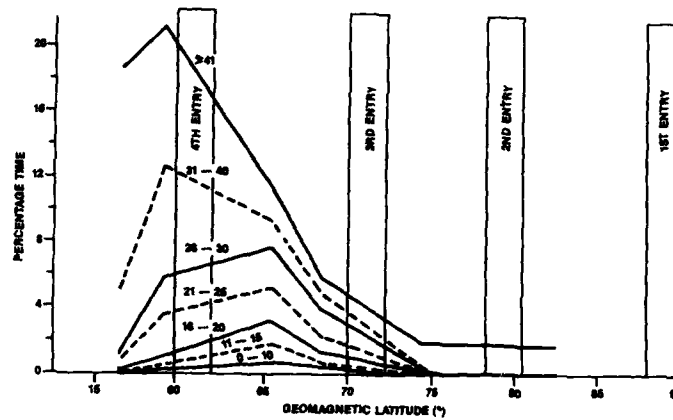


Fig. 16 The percentage of time (solid line) for which auroral absorption equaled or exceeded 1 dB as a function of geomagnetic latitude for different values of the daily sum of planetary geomagnetic indices (K_p). The pedestals are the approximate locations for passage through the D-region, for a 2-hop circuit Alert-Ottawa.

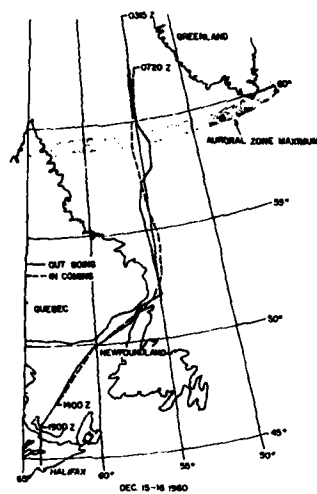


Fig. 17 Flight path for ground-air trials, December 15 - 16, 1960 [after Jull et al., 1962].

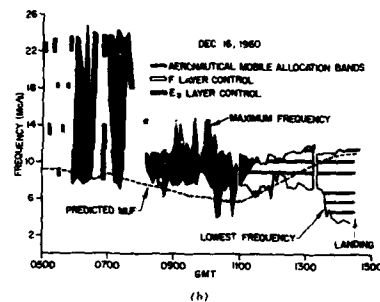
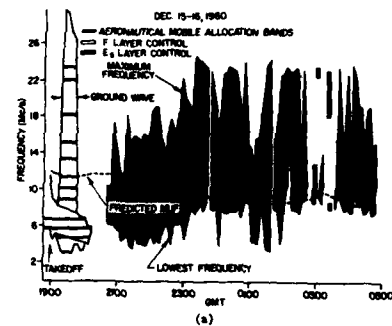


Fig. 18 The maximum and lowest observed frequencies with airborne sounding equipment, for ground-air trials, December 15 - 16, 1960 [after Jull et al. 1960].

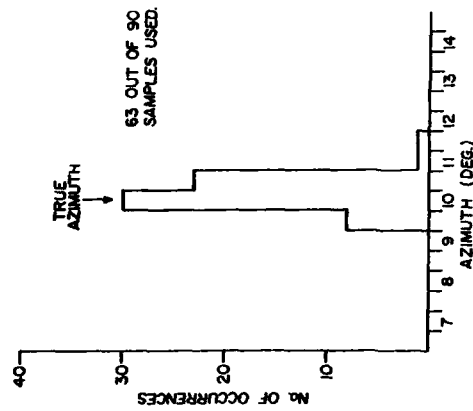


Fig. 22 Histogram of azimuth for the E and E_s modes (range separated modes) for the path Frobisher Bay (Igloolik) - Ottawa (Day 338 23:05 to Day 339 00:59 December, 1976) [after Venier, 1980b].

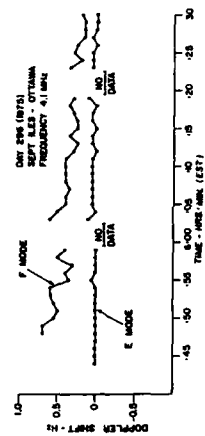


Fig. 20 Mode separation by Doppler (mode identified by oblique ionograms).

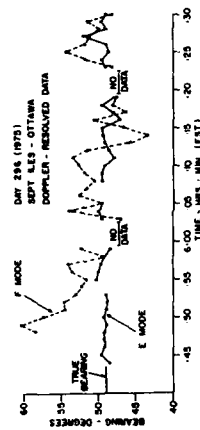


Fig. 21 Bearing as measured for the E and F-reflections (modes Doppler resolved).

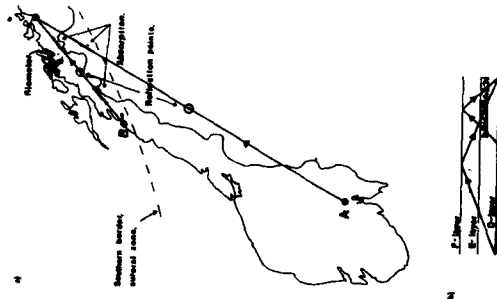


Fig. 19 a) The two transmission paths used in tests in Norway. b) Schematic representative of the wave paths through the disturbed auroral D-region [after Thrane, 1983, 1986].

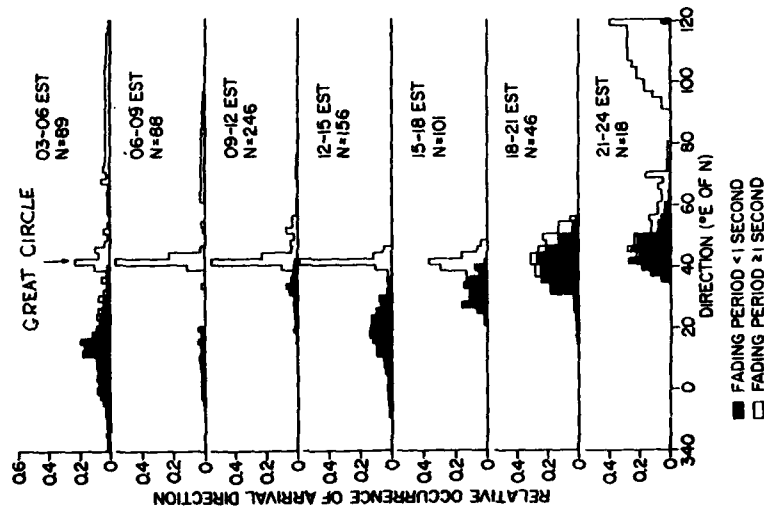


Fig. 24 Distribution of observed directions of arrival of USSR OTH radar signals received at Ottawa for various times of day, August 1977, divided on the basis of observed fading. On the expectation that the signals originated from Kiev, this great circle bearing is marked on the upper graph.

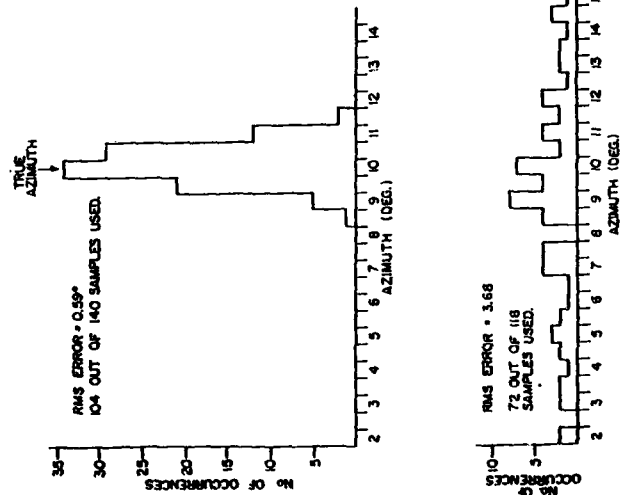


Fig. 23 Histograms of azimuth estimates for low-angle F-mode (range separated modes), for the path Frohisher Bay (Iqaluit) - Ottawa, December 1976. Upper graph day 329, 11:45 to 15:32, normal-F; Lower graph day 352, 20:35 to 22:35, spread F (after Venier, 1980b).

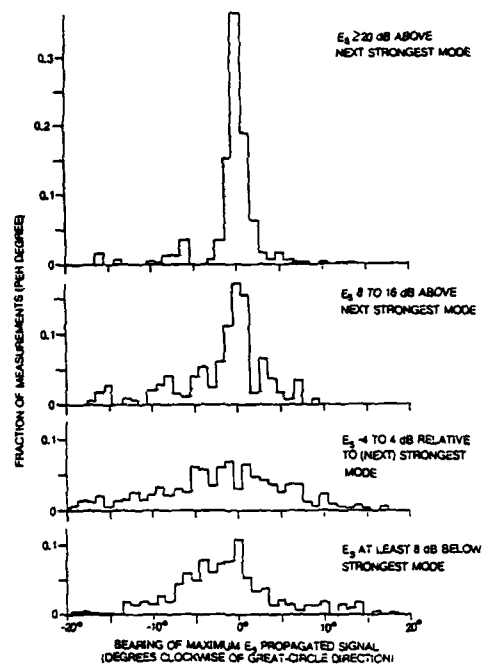


Fig. 25 Distributions of maximum-signal direction for the Es mode arranged according to strength of the Es mode relative to other modes present [after Jenkins et. al., 1979].

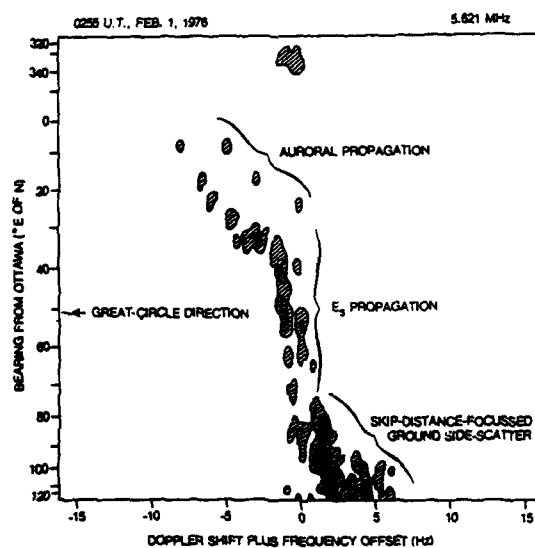
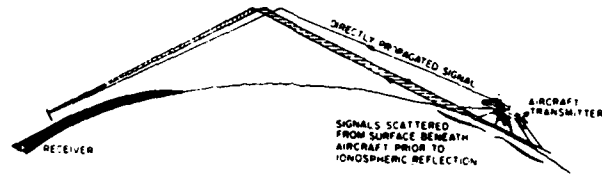
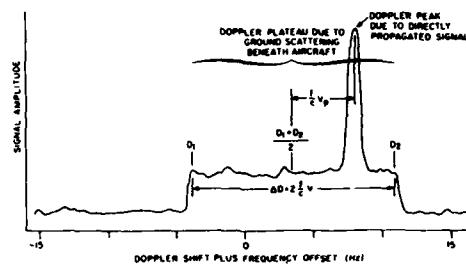


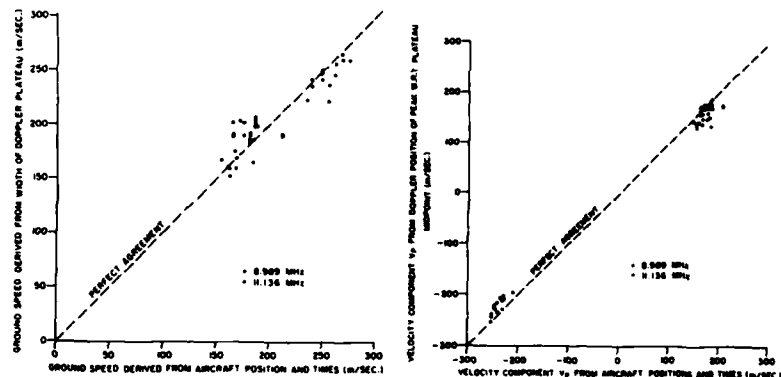
Fig. 26 Contour plot taken from a line printer display of received signal strength vs. doppler shift and bearing. 8 dB contour levels shown [after Jenkins et. al., 1979].



(a)



(b)



(c)

(d)

Fig. 27 a) Proposed propagation model for Doppler plateau signals involving non-specular scattering from ocean surface in vicinity of aircraft; b) Idealized Doppler spectrum in great circle direction showing both Doppler peak and plateau; c) Comparison of aircraft ground speeds derived from width of observed Doppler plateau with those derived from logged aircraft position and times; and d) Comparison of aircraft velocity components in receiver direction derived from frequency of coherent peak signal relative to midpoint of Doppler plateau with those derived from logged aircraft positions and times [after Jenkins, 1979].

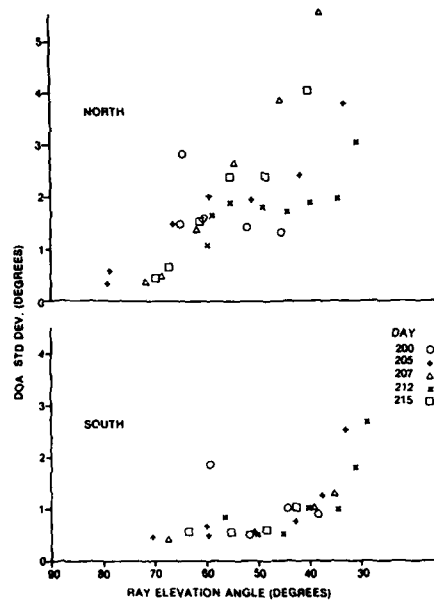


Fig. 28 Direction of arrival (standard deviation) vs ray elevation for 9.303 MHz pulsed transmissions from ISIS-II satellite received on the SARA facility, Ottawa, July - September 1979.

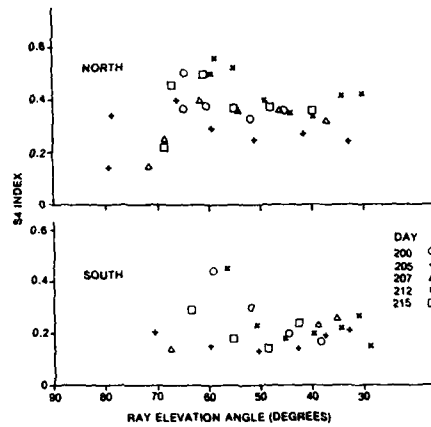


Fig. 29 Scintillation S4 Index of the amplitude measurements vs ray elevation angle for the 9.303 MHz pulse transmissions from the ISIS-II satellite, received on the SARA facility, Ottawa, July - September, 1979.

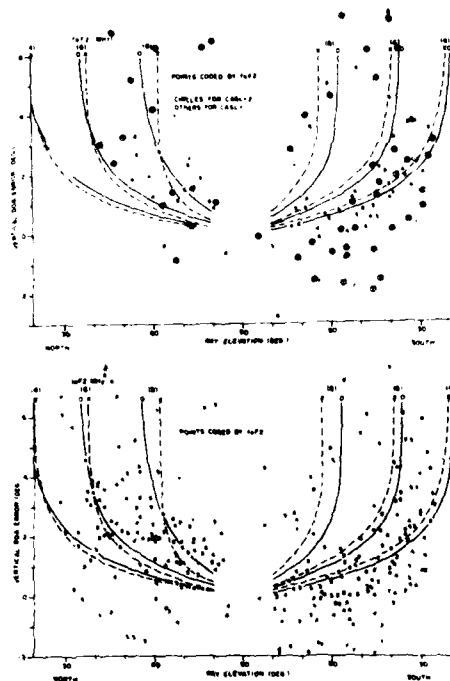


Fig. 30 Vertical DOA error vs. ray elevation. Contours are theoretical departure from line of sight based on a horizontally invariant ionosphere. Upper graph: times when cone angle scintillation index equalled 1 (uncircled) and 2 (circled) dB. Lower graph: times for all levels of direction of arrival scintillation index [after Montbriand, 1986].

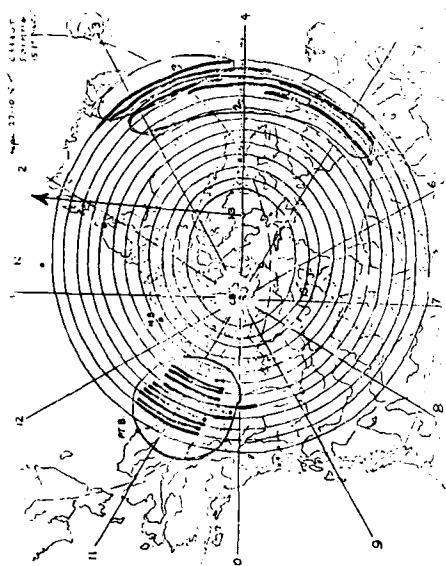


Fig. 32 Sample side-lobe-epiry plot for the Hall Beach - Cambridge Bay bistatic OTH radar experiment. Ellipses of constant range from Cambridge Bay, and the 12-directions of the Beverage Rosette Array are shown.

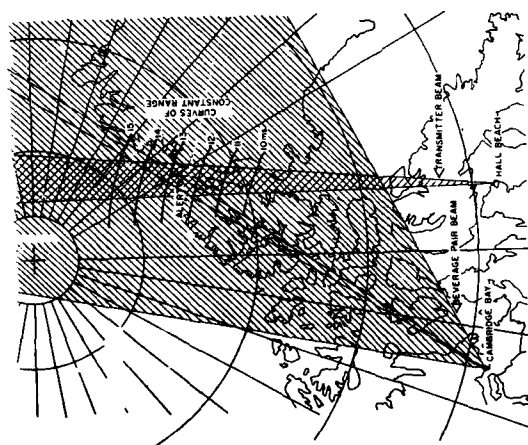


Fig. 31 Transmitting and receiving antenna beams for the Alert direction and 9.2-MHz operating frequency. The Cambridge Bay receiver had a wide directional beam and a narrow fixed beam.

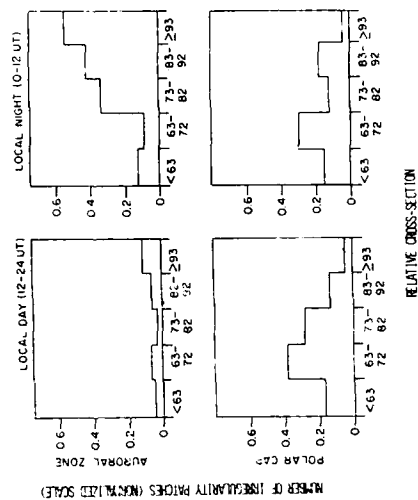


Fig. 33 Diurnal dependence of auroral and polar cap scatterers for the Hall Beach - Cambridge Bay bistatic OTH radar.

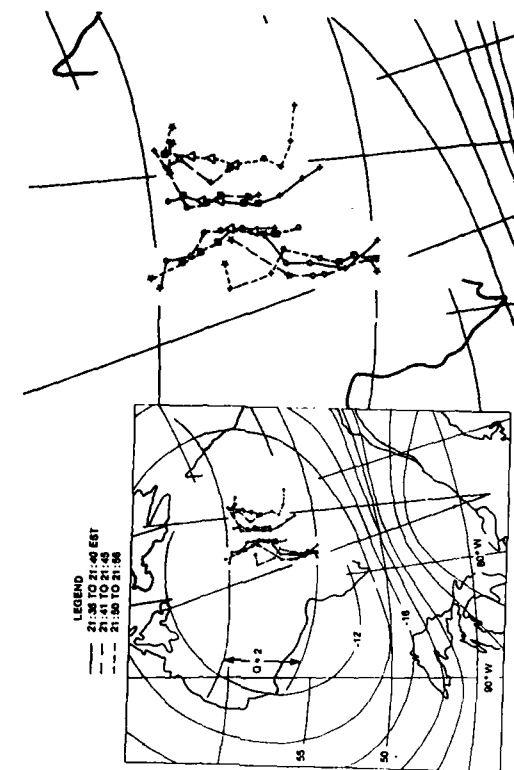


Fig. 35 Geographical location of sources identified during period 21:35 to 21:56 EST on 30 April, 1981. Auroral oval for $Q = 2$ and transmitter beam are shown. Data points are occurrence coded as indicated on legend. The contours give the angle between the L-O-S and the normal to the magnetic field lines at 300 km as seen from Ottawa (after Montbriand, 1988).

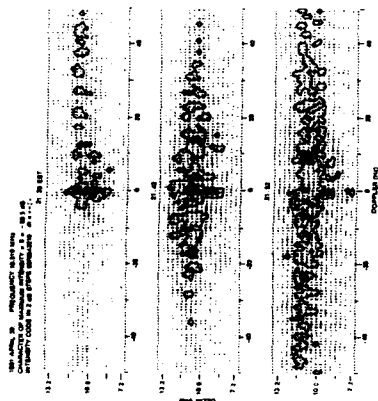


Fig. 34 Signal strength of Doppler shifted auroral backscatter. Black areas include signals -6 dB from the maximum, white contours include signals -16 dB from the peak (after Montbriand, 1988).

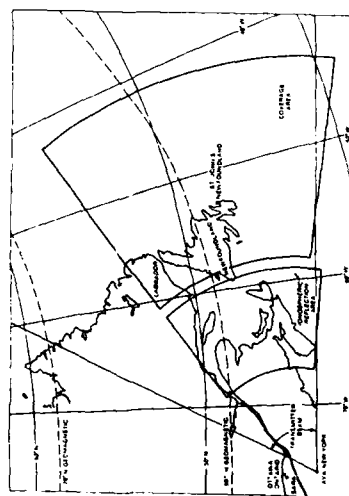


Fig. 36 Coverage map of the Canadian OTH radar experiment for remote sensing of sea state.

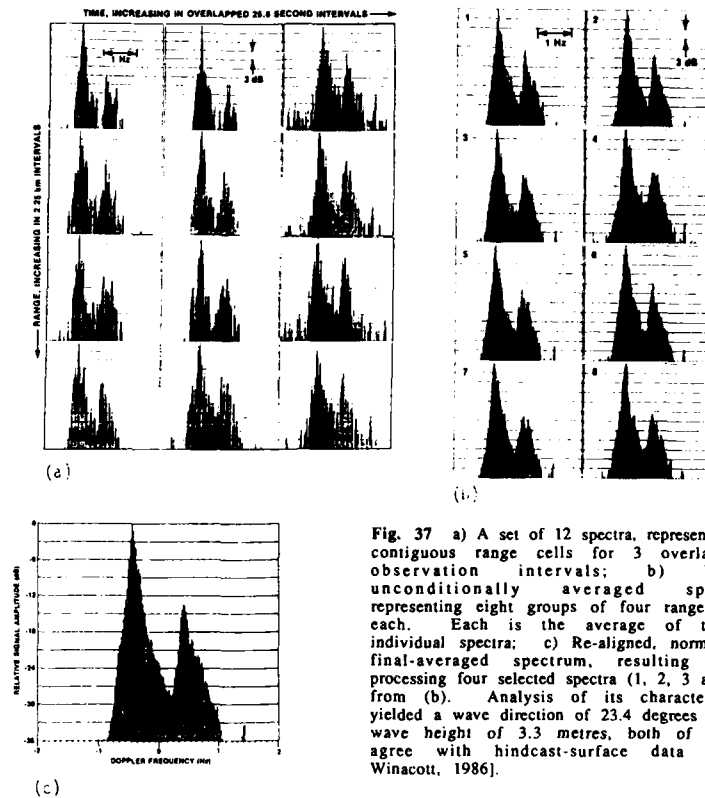


Fig. 37 a) A set of 12 spectra, representing 4 contiguous range cells for 3 overlapping observation intervals; b) Eight unconditionally averaged spectra representing eight groups of four range cells each. Each is the average of twelve individual spectra; c) Re-aligned, normalized final-averaged spectrum, resulting from processing four selected spectra (1, 2, 3 and 6) from (b). Analysis of its characteristics yielded a wave direction of 23.4 degrees and a wave height of 3.3 metres, both of which agree with hindcast-surface data [after Winacott, 1986].

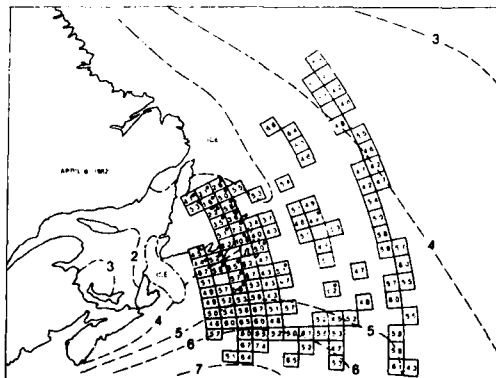


Fig. 38 Wave-height map for 8 April, 1982. The cells marked with an asterisk displayed significant land echoes [after Winacott, 1986].

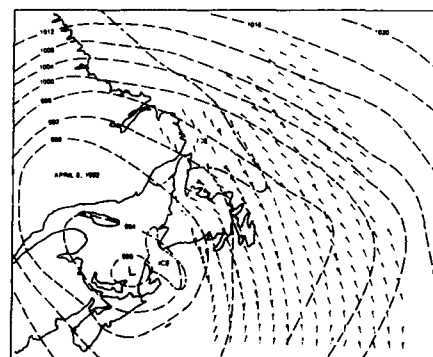


Fig. 39 Wave-direction map for 8 April, 1982. The double arrows display two self-consistent sets of wave directions which indicate a change in the weather during the 6-h period of data acquisition [after Winacott, 1986].

H.F. RADAR PROBING (INCLUDING MODIFICATION)

P. Bauer
 Directeur de Recherche
 Service d'Aéronomie du CNRS
 BP 3 91371 Verrières-le-Buisson Cedex, France

ABSTRACT

At high magnetic latitudes (auroral and polar regions), the ionospheric plasma is governed by i) the geometry of the magnetic field, ii) the existence of particle precipitations (from 100 MeV solar protons to keV electrons), iii) large and small scale convection electric fields, and iv) strong atmosphere ionosphere coupling processes. As a result, the various forms of free energy sources feed the growth of plasma instabilities which through non linear mechanisms lead to a turbulent cascade of ionospheric inhomogeneities from the regional scale to the scale of the ion Larmor radii.

The scales of the irregularities encompass the wavelengths ranges of HF systems, thus providing natural targets for HF radars. While highly horizontally stratified in the D and E layers, the targets are essentially aligned along the magnetic field in the F region.

HF radar techniques making use of these properties include :

- partial reflection systems (D and lower E region)
- E region auroral radars
- F region auroral and polar radars

These techniques afford to characterize :

- the irregularities and the underlying instabilities
- the high latitude plasma convection
- the middle atmosphere motions (gravity waves and tides)

A better understanding of the basic plasma processes is also provided by HF ionosphere modification experiments performed from the D up to the F region through the excitation of resonant frequencies and through the local change of macroscopic properties such as the electron temperature or the electron density.

INTRODUCTION

Free or bounded electrons in the Earth environment constitute the natural scattering targets for radio waves. Two basic classes of scattering can be distinguished at HF frequencies : - the resonant backscattering occurring whenever the wave frequency approaches a natural frequency of the plasma such as the electron plasma frequency, - the Bragg scattering occurring whenever the half wavelength is matched by a spatial Fourier component in the electron concentration distribution. The first process for which a strong interaction of the electromagnetic wave with the ionospheric plasma develops lays the ground for HF modification experiments. The second process gives rises to signal returns varying over a very large dynamical range according to the physical processes enhancing the spatial Fourier component : from plasma thermal fluctuations to plasma instabilities.

This lecture will first address the problem of plasma irregularities which naturally develop in the high latitude regions. It will then consider the various HF radar configurations which have been developed. It will later deal with their application to the study of the plasma and atmospheric processes. It will finally consider the natural plasma laboratory aspect of HF modification experiments.

I. HIGH LATITUDE IRREGULARITIES

Sources of free energy compete at high latitudes, either directly or through cascading processes, in order to create ionospheric irregularities :

- turbulent phenomena in the neutral atmosphere,
- atmospheric gravity waves,
- particle precipitations,
- electric currents parallel and perpendicular to the magnetic field,
- electromagnetic waves (whistlers),
- plasma instabilities.

Scales sizes range from hundred of kilometers to meters and therefore encompass the High Frequency wavelengths (few MHz to few tens of MHz).

I.1. MESOSPHERIC (D REGION) IRREGULARITIES

In the mesosphere (~ 60-90 km), the irregularities in the electron concentration result from atmospheric turbulent processes. Indeed atmospheric waves originating from the lower

atmosphere tend to amplify when they propagate upward through a less and less dense air. Above a certain amplitude, the waves become unstable and generate turbulence. Several authors have discussed the exact nature of the resulting turbulent layers, e.g. [1], [2], [3], [4], [5]. It seems that at low altitude (below 80 km) they consist in thin stratified layers (< 2 km thick) with large horizontal scales and that above, thick turbulent like layers are observed. An example of turbulent layers observed by the MU radar [5] is shown on figure 1.

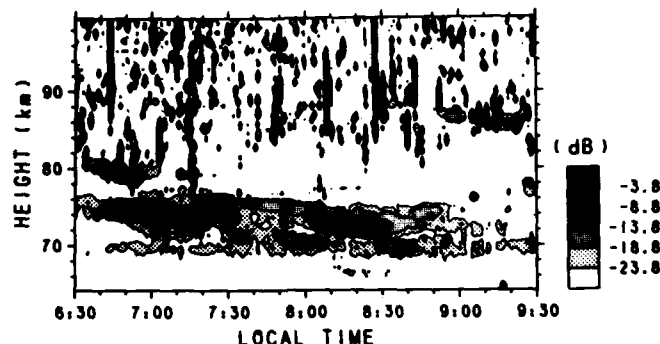


Figure 1. Time-height section of the mesospheric echo in the vertical beam direction on June 21, 1984. The echo power is in an arbitrary unit, and contours are drawn at 5 dB intervals. [5]

The turbulent atmospheric activity is mirrored by the electron concentration which in turn is responsible for partial reflexion echoes observed in the lower range of HF frequencies (2-4 MHz) called also MF range.

1.2. HIGH LATITUDE E REGION IRREGULARITIES

Observations of high latitude E region irregularities have been made as early as 1938 [6] and this phenomenon has been extensively reviewed [7], [8], [9], [10], [11], [12], [13]. These irregularities are characterized by scale sizes of meters to hundred of meters. They are closely associated with the electrojet [14], [15]. They are located between 100 and 130 km of altitude and have thicknesses ranging between 2.5 and 20 km.

One primary source of the irregularities arises from the two stream instability, called Farley-Buneman instability [16], [17]. Indeed, whenever the electron drift velocity relative to the ions exceeds the ion acoustic velocity, ion acoustic waves are generated. The necessary condition is fulfilled in the case of strong auroral electrojets currents flowing across the geomagnetic field lines in response to large convection electric fields.

A second source of irregularities is the gradient drift instability which develops when strong electric fields perpendicular to the magnetic field are combined with large electron concentration gradients [18].

E region field aligned currents inducing ion acoustic waves and ion cyclotron instabilities have also been proposed as sources of irregularities [18], [19].

Finally, thermal plasma instabilities created by whistler waves are invoked as a source of irregularities [20].

In all cases, non linear processes are involved which lead to a cascade from large and medium scales irregularities to small scales.

1.3. HIGH LATITUDE F REGION IRREGULARITIES

At F region heights (above 120 km), collisions of charged particles with neutrals diminish with altitude while the influence of the magnetic field on the plasma plays gradually a major role. These two facts result in a large diffusivity of the plasma along the magnetic field lines (above 200 km) and a very low diffusivity of the plasma across the field lines. The plasma is then "frozen" in the magnetic field and moves with the magnetic field lines so that in the local reference frame of the plasma, the external electrostatic field is always null. As a consequence, similar free energy sources to those acting in the E region lead to different classes of irregularities.

A first source of energy naturally spatially structured is given by particle precipitations in the energy range 10^2 to 10^3 eV. Indeed, such fluxes of electrons exist over the whole high latitude region which deposit their energy in the F region. They create field

aligned plasma enhancements on spatial scales of few tens of kilometers [21], [22], in turn cascading processes lead to smaller scales (down to meter scales) [23]. An example of plasma enhancements observed in the auroral F region with the Chatanika radar is given on figure 2 [23].

A second source is given by the crossfield ($E \times B$) gradient drift instability which develops when the plasma is convected by the electric field E in the presence of a density gradient perpendicular to the magnetic field line. The process, similar to the Rayleigh-Taylor instability which occurs when a heavy fluid lies on top of a lighter one, is illustrated on figure 3 [12]. On this figure, the magnetic field is directed along z , the background electric E_0 field is along $-x$ and there exists a density gradient directed towards the y direction. A sinusoidal perturbation of the isocontour of the plasma density, as shown on the figure, induces polarization charges due to the relative drift of the ions and the electrons in the direction of E_0 , associated with the Pedersen current existing in the F region. The Lorentz Force associated with the local electric field E' caused by the charges tends to enhance the initial density perturbation which is characteristic of an unstable situation. A numerical simulation performed by Keskinen and Ossakow [24] shows on figure 4 how a small initial perturbation evolves with time.

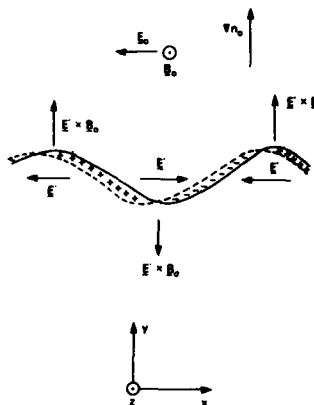


Figure 3. Physical mechanism of F region $E \times B$ gradient drift instability. [12]

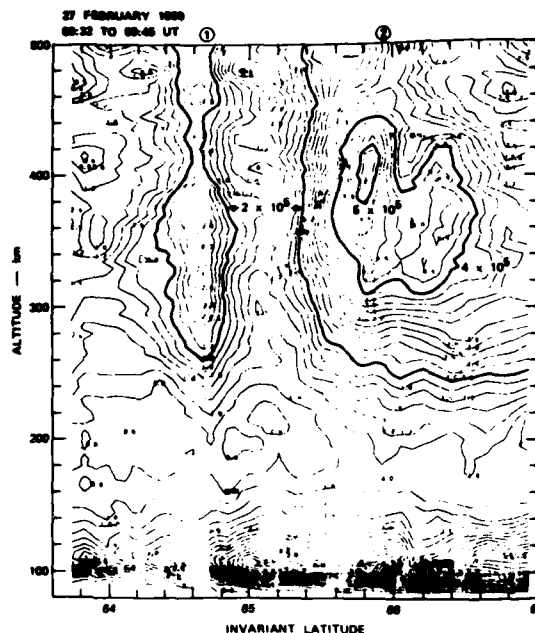


Figure 2. Altitude/latitude variation of electron density on February 27, 1980, from 0932 to 0945 UT. [23]

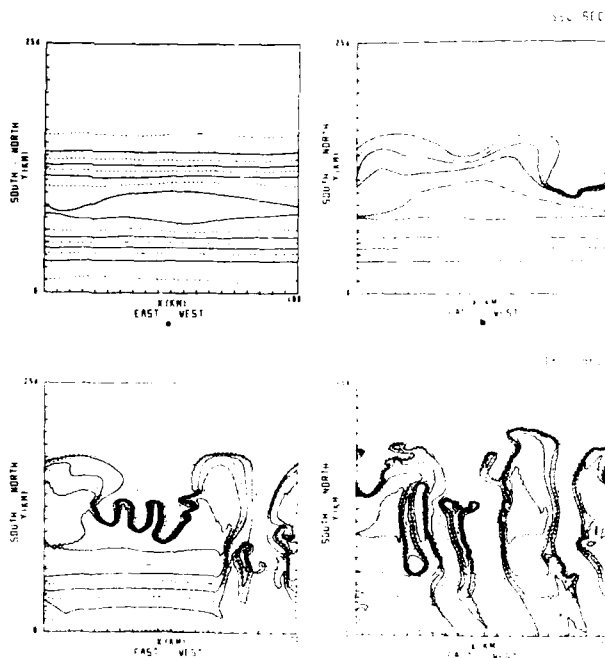


Figure 4. Real space plasma isodensity contour plot of $[n_e(x, y) + \delta n(x, y)] / N$ at (a) $t = 0$ s, (b) $t = 550$ s, (c) $t = 1000$ s, and (d) $t = 1800$ s. The y axis is compressed by a factor of 2.38. The distance between tick marks in the x direction (y direction) is 5 km (12.8 km). Eight contours are plotted in equal increments of 1.25 beginning at 1.25. The observer is looking upward along the magnetic field lines. [24]

Similarly density gradients couple to magnetic field aligned current to give a current convective instability, e.g. Chaturvedi and Ossakow [25]. Field aligned currents can also drive ion cyclotron instabilities.

Other high latitude plasma processes include :

- temperature gradient drift wave instabilities arising from colinear density and temperature gradients perpendicular to the magnetic field ;
- highly structured electric fields ;
- anisotropic ion velocity distributions due to ion-neutral charge exchanges in the presence of large electric fields ;
- thermal plasma instabilities created by whistler waves...

A last source of instabilities (scales of 100 km to few 1000 km) lies in the wavy nature of the high latitude atmosphere (gravity waves). Indeed Joule heating, particle precipitations and momentum transfer from the plasma feed gravity waves which are mirrored by fluctuations in the plasma. These fluctuations can in turn trigger smaller scale irregularities.

II. HF AND MF HIGH LATITUDE RADAR SYSTEMS

Radar backscatter echoes can be obtained from free or bounded electrons in the Earth environment whenever the half wavelength of the transmitted wave in the medium (λ) matches one spatial Fourier (λ_p) component of the electron distribution along the radar beam :

$$(1) \quad \lambda_p = \lambda / 2$$

In the more general case of bistatic radar systems equation (1) becomes :

$$(2) \quad \lambda_p = \lambda / (2 \sin \theta/2)$$

where θ is the angle between the transmitted and the scattered wave vectors.

The wavelength λ of the transmitted wave is related to the wavelength λ_0 in free space through the equation

$$(3) \quad \lambda = \lambda_0 \left[1 - \frac{f_p^2}{f^2} \right]^{-1/2}$$

where f_p is the local electron plasma frequency and f the frequency of the radar signal. The refractive properties, which manifest themselves when f decreases toward f_p , are exploited for geometrical and ionospheric heating purposes.

II.1. PARTIAL REFLECTION (MF) SYSTEMS

Mesospheric irregularities (60-90 km) constitute the targets for partial reflection systems operating around 3 MHz. They consist in backscatter radars making use of the differential absorption of ordinary and extraordinary waves [26], [27], for the purpose of electron vertical profile measurements and in spaced antenna arrays [28], [29] aiming at wind measurements.

Several such systems have been developed at middle and high latitudes. Only the high latitude ones are dealt with here. Table I gives the main characteristics of the high latitude partial reflection systems currently in use.

TABLE I - High Latitude Partial Reflection Systems

	PRE	PARK RADAR	KUHLUNGSBORN	SCOTT BASE
Location	Ramfjordmoen (Norway) 69.6°N, 19.02°E	Saskatoon (Canada) 52°N, 107°W	Juliusruh (GDR) 55°N, 13°E	Scott Base (Ross Island) 77.8°S, 166.7°E
Type	Backscatter	Backscatter & Antenna Array	FM - CW Backscatter	Antenna Array
Frequency MHz	2.75	2.22	3.18	2.9
Peak Power kW	40	100	1	60

The geometry of the Park Radar is shown on figure 5 [30]. The fading records obtained at the different receiving sites allow, through a correlation analysis, to recover the mesospheric horizontal winds.

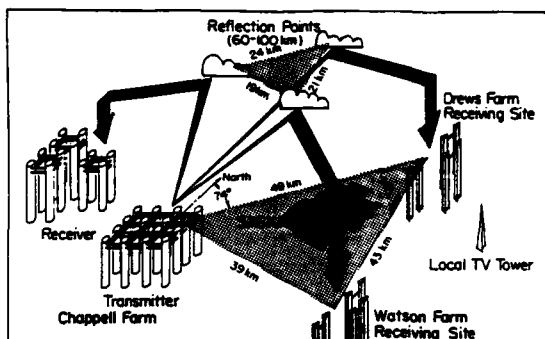


Figure 5. Geometry of spaced radio sites. [30]

II.2. HF DOPPLER RADARS

E and F region irregularities have the property of scattering electromagnetic waves transmitted in the HF frequency range ($\sim 6-30$ MHz) since their characteristic scales include decametric wavelengths.

However, both in the E and F regions, geometry considerations of the radar beam with respect to the medium have to be made. Indeed, the targets are "aspect-sensitive" due to the way in which they are created. In the E region, the geometry of the electrojet as well as the one of the magnetic field have to be considered. The irregularities generated by the various types of instabilities are essentially magnetic field aligned and are distributed along the electrojet. As a consequence, radar returns are only obtained when the beam is nearly perpendicular to the magnetic field in the scattering region. Furthermore, the radar cross section as well as the spectral characteristics of the signals are fairly sensitive upon the angle between the radar beam and the electrojet jet.

In the F region, the geometry is only governed by the magnetic field. As in the case of the E region, the irregularities are field aligned and the radar beam is due to reach perpendicularity to the magnetic field line.

At high latitude in free space, perpendicularity can only be achieved in the E region when the radar is located at a large distance equatorward and perpendicularity cannot be reached in the F region. The refractive properties of the ionosphere at HF frequencies (see eq. 3) open a large range of possibilities with however the drawback of making the localization of the scattering region more difficult. These possibilities are illustrated on figure 6 extracted from Hanuise [13]. It can be seen from it that perpendicularity can be reached at closer equatorward ranges in the E region. The F region becomes accessible. Perpendicularity can be achieved poleward of the scattering region as well as eastward or westward.

Table II gives the main characteristics of the high latitude HF radars in use or operated in the recent past. The field of view of EDIA is given as an example on figure 7 [31]. Similarly, the field of view of the

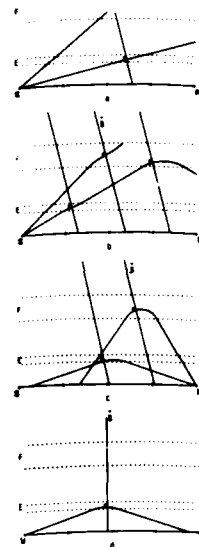


Figure 6.
a) Propagation in free space, perpendicularity for E region only ; b) c) d) Refraction of HF waves allows to reach perpendicularity in E and F region for radars located equatorward b), poleward c), eastward or westward d). [13]

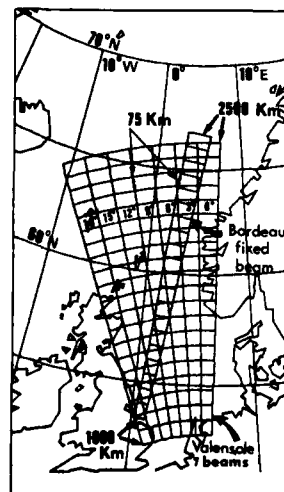


Figure 7.
Intercept zone of the beams of Valensole and Bordeaux. The seven beams used at Valensole are indicated. The resolution cells are drawn for a 3 dB beamwidth at a frequency of 15 MHz and for a transmitted pulse length of 500 μ s. [31]

TABLE II - High Latitude HF Radar Systems

	SAFARI	EDIA	SONDRE STROMFJORD	CLEARY	APL/SHERPA
Location	64.4°N, 18.7°E 65.0°N, 25.5°E	43.8°N, 6.0°E 44.4°N, 0.9°W	67.0°N, 50.6°W	65.1°N, 147.6°W	53.15°N, 60.2°W 54.5°N, 67.0°W
Type	pulsed	pulsed	CW	Pulsed	Pulsed
Frequency MHz	7 - 30	10 - 20	12.3	10 - 30	8 - 20
Peak Power kW	1.6	100, 30	0.35	4	2

APL/SHERPA radar together with a radar image obtained in an initial configuration (APL part of the system) is shown on figure 8 [32].

III. HIGHLIGHTS OF SOME RESULTS OBTAINED WITH HF AND HF HIGH LATITUDE RADARS

III.1. D REGION DATA

Backscatter data have played a unique role in monitoring electron density profiles from 60 to 90 km. Very significant results on seasonal variations, e.g. [33], on the effects of dynamics on the electron concentration profile, e.g. [34], on the electron loss coefficient, e.g. [35], and on the effects of electron precipitations, e.g. [36], [37], have been obtained.

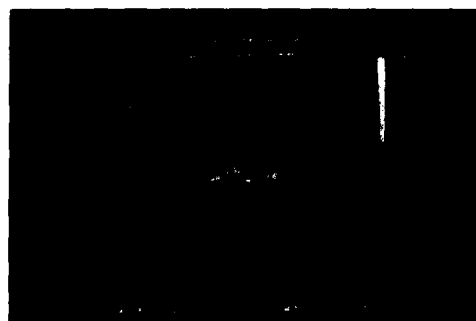


Figure 8. Backscatter power image obtained with the Goose Bay radar at 1920:00 UT (~1600 MLT) on 19 March 1985. [32]

However, it should be mentioned that some difficulties are sometimes experienced when the vertical electron concentration profiles are compared with data from other techniques. Such an example is given on figure 9 [38] which shows a comparison between PRE data and rocket data. It seems difficult to give an account of the discrepancy observed on the sole basis of spatial variations.

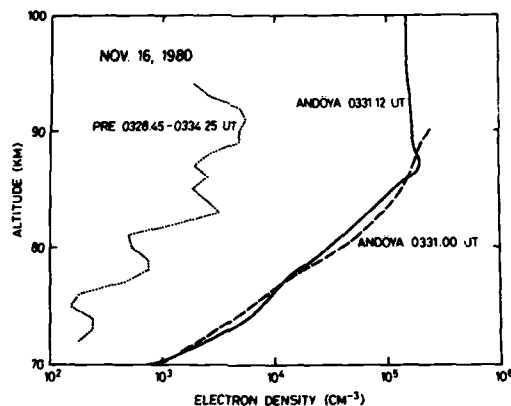


Figure 9. Electron density profiles observed by the partial reflection technique from Ramfjordmoen and by the Faraday rotation technique by a rocket from Andoya. [38]

A major contribution to the study of middle atmosphere dynamics from short periods to planetary waves has been provided in recent years by the HF antenna array technique. An example of short periods measurements obtained at Saskatoon is shown on figure 10 [39]. These types of data are invaluable as far as characterizing the turbulent processes acting in this region of the atmosphere. The capability of the same system in order to determine mean zonal and meridional winds is illustrated on figure 11 [40] which displays isocontours of these quantities for the year 1982 as a function of altitude.

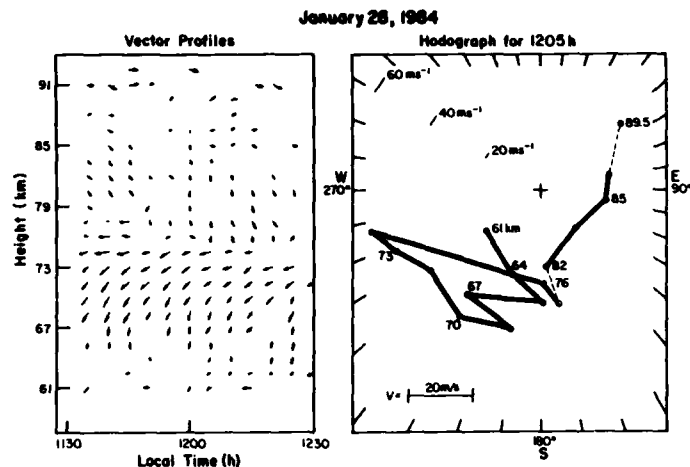


Figure 10. Wind vectors for one hour : up is northward, left is westward. [39]

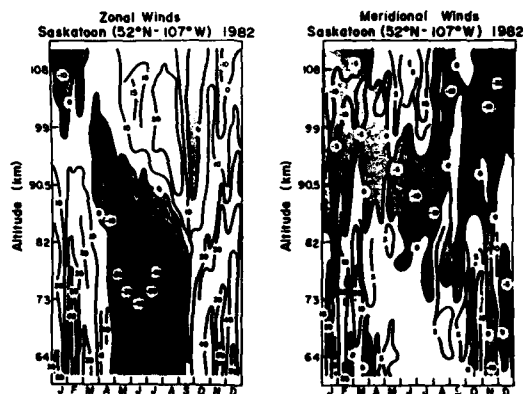


Figure 11. Zonal and meridional winds for 1982. [40]

III.2. E REGION DATA

- HF radar data serve two scientific purposes in the E region :
- they allow to characterize the irregularities of the plasma and the energy sources which feed them, through the spectral shape of the signals ;
 - they give a determination of the dynamical state of the plasma through doppler shift measurements.

These aspects are illustrated on figure 12 and 13 [41]. The data were collected by the SAFARI Radar before, during and after a strong disturbance. Several features are worth noticing :

- rapid changes in signal strength,
- rapid changes in doppler shift.

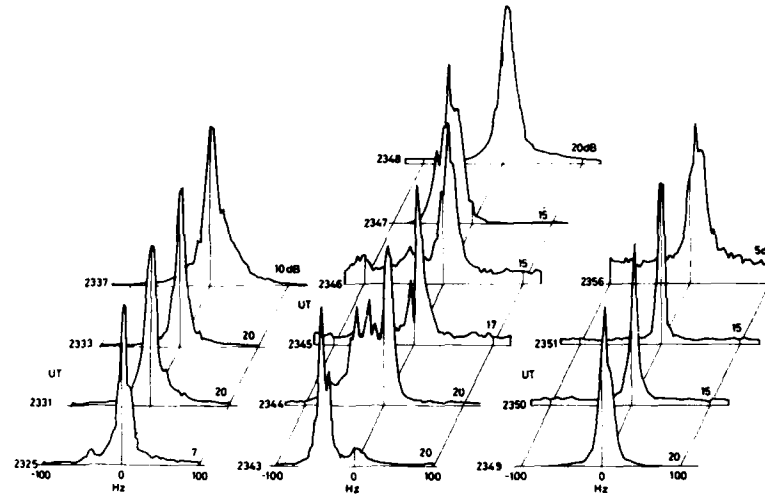


Figure 12. Doppler spectra from SAFARI radar at a range of 360 km (Kiruna). The spectral signal to noise ratios are indicated in dB. The spectra are normalised to constant peak height. The central group of spectra were obtained during a strong geomagnetic disturbance (+ 600 γ). [41]

Figure 13 displays as a function of range the observed velocities. The extent of the observations shows that irregularities are developed on a range of at least 225 km. Two sharp velocity peaks are observed corresponding to northward motions.

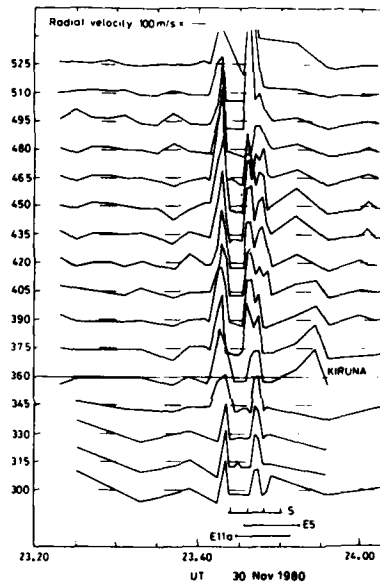


Figure 13. Doppler velocities of 10 m irregularities measured by SAFARI radar (positive velocities towards north). S, times of STARE data. Flight times of rockets E1a and E5 are indicated. The latitude of Kiruna is shown. [41]

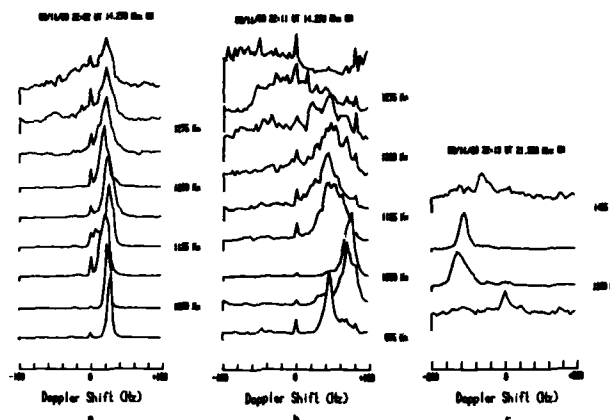


Figure 14. Doppler spectra from F region irregularities observed northward from Lycksele, Sweden, with the SAFARI experiment. Note the large spatial and temporal variations in radial velocity. [42]

III.3. F REGION DATA

A very promising possibility which has emerged in the last few years is the global monitoring at HF frequencies of F region irregularities and plasma velocities by using the refractive properties of the ionosphere. Initial measurements performed with EDIA [31] at subauroral latitudes and SAFARI [42] in the auroral zone, have immediately demonstrated the interest of such systems. Figure 14 [42] exhibits the first F region spectra obtained with SAFARI. On a time scale of few minutes, the signal strength varies rapidly reflecting the temporal changes in small scale irregularities (7 to 10 m wavelengths). The doppler shifts associated with north south motions indicate velocities of up to 800 m/s with sharp variations both in time and space. Narrow spectral widths are observed at short ranges (doppler broadenings of 100 to 300 m/s) changing to multi-component broad spectrum for larger ranges. Figure 15 [31] shows EDIA data obtained at subauroral latitudes (geographic latitudes of 59 to 62°N) as a function of time during a substorm. Very large westward velocities are observed immediately after the onset of the substorm.

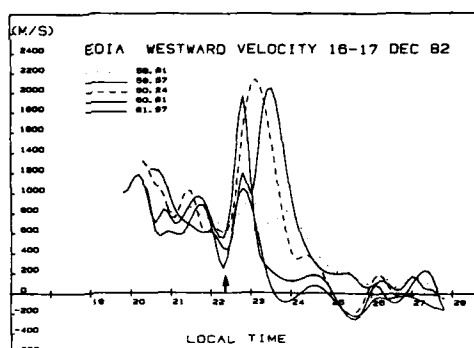


Figure 15. Westward component of the velocity of F region irregularities (lower panel) versus local time (LT=UT+10 min). The H component of the magnetic field at Tromsø (upper panel) shows onset of a substorm at 2225 UT which correlates with an increase of the westward velocity. [31]

These initial observations, as well as those performed by Greenwald with the CLEARY Radar laid the ground for an ambitious project the APL/SHERPA system consisting of two identical phased array radars built respectively by the John Hopkins University at Goose Bay, Canada, and by the CNRS (Centre National de la Recherche Scientifique) at Schefferville, Canada. The purpose of this system is to yield two dimensional maps of F regions irregularities and plasma drift vectors over Greenland at auroral and polar cap latitudes.

Figure 16 [32] shows data obtained with the Goose Bay APL multibeam systems in the polar cap in the magnetic midnight sector. Spectra from 3 magnetic azimuth are displayed. They are generally broader than those observed with SAFARI at auroral latitudes and their doppler shifts are consistent with flows of the plasma out of the polar cap.

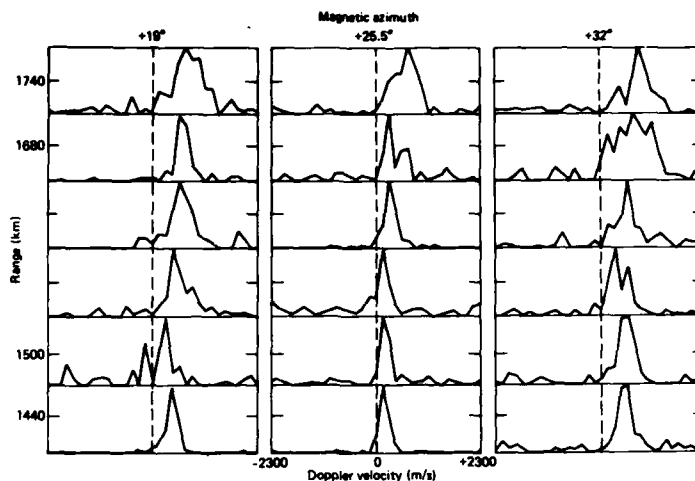


Figure 16. Examples of Doppler spectra that were obtained at 0311 UT (magnetic midnight) on 30 April 1985 at a frequency of 10.7 MHz. Note that the spectra are appreciably broad and that they have Doppler shifts consistent with irregularity flow out of the polar cap. [32]

IV. HF IONOSPHERIC HEATING

The effects of high power radio waves on the ionosphere were identified in 1933 with the discovery of the Luxembourg effect [43]. Early experiments were conducted at middle latitudes (see e.g. CARLSON and DUNCAN [44]). More recently, taking account of the interesting geometry of the magnetic field at high latitudes and of the opportunity provided by the EISCAT Incoherent Scatter project at Ramfjordmoen near Tromsø, Norway, the Max Planck Institut für Aeronomie in cooperation with the University of Tromsø decided to build a powerful heating facility on the EISCAT site. The system operates since 1980 in CW at a power of 1.5 MW in the frequency range 2.5 to 8 MHz. The antenna arrays together with the other instruments available on the site are sketched on figure 17 [45]. An extensive review of the experiments performed up to 1984 has been given by Stubbe et al. [46].

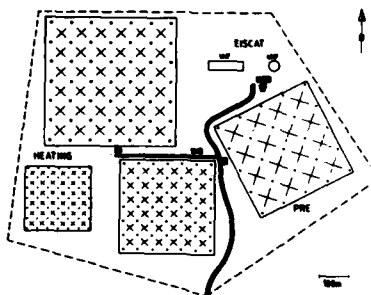


Figure 17. View of the research installations at Ramfjordmoen showing the three heating antenna arrays (2.5-4, 3.85-5.65, and 5.5-8 MHz), the EISCAT UHF (933 MHz) and VHF (224 MHz) radars, and the PRE (partial reflection experiment) array (2.75 MHz). [45]

IV.1. D REGION EFFECTS

When operating the heater on the extraordinary (X) or on the ordinary mode, it has been observed [47] that the echo strength of the PRE partial reflection radar decreased markedly due to an enhancement of the D region absorption associated with an electron temperature

increase. Subsequent changes in the ion chemistry are also indirectly observed by the PRE system. This is illustrated on Figure 18 [47] which shows significant PRE amplitude decreases after the switch on of the heater.

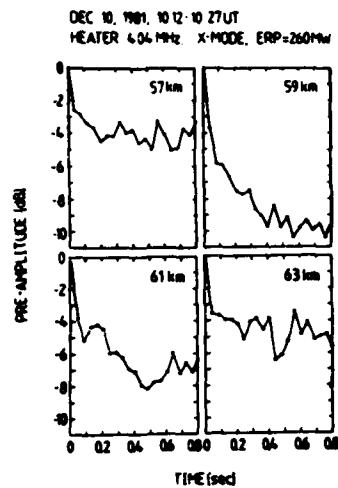


Figure 18. D region absorption of partial reflection radar at Tromsø. [47]

IV.2. E REGION EFFECTS

The auroral electrojet can be efficiently modulated by the heater. Indeed heating of the electrons brings a change in electron recombination rate and consequently in the conductivity. As a result, the electrojet can be modulated from VLF to ELF frequencies. An example of pulsations induced by the heater is shown on figure 19 [46]. Ground based H magnetometer data shows the effect of the modulated current. E regions irregularities can be excited by the heater. The O mode is particularly efficient. The development of the irregularities have been observed by the STARE radar [46].

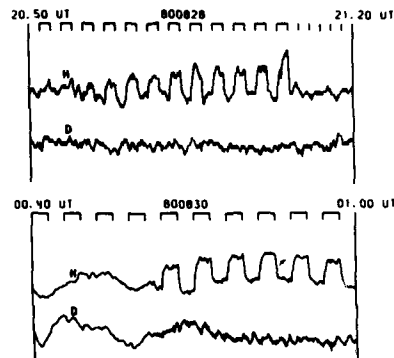


Figure 19. H and D components of ground-based magnetometer showing heater-induced pulsations. The heater-on times are indicated by bars. The heater operated in the X-mode at 4.04 MHz with ERP = 130 MW. [46]

IV.3. F REGION EFFECTS

F region small scale irregularities induced by the heater have been observed by the SAFARI Radar and two other similar instruments operated from Sweden [48], [49]. Figure 20 [48] shows the development of backscatter signals when the transmitter is switched on in the O mode. The recovery after the switch off of the transmitted is more rapid for the larger frequency (smaller wavelength) indicating the time evolution of the F region striations. No such striations are observed in the X mode. Indeed the striations are expected to be generated at the height where the heater frequency matches the upper hybrid frequency and the X mode is reflected before reaching this height.

It is possible to excite Langmuir waves in the F region and the geometry of the high latitude magnetic field appears as favorable for this purpose. The detection of such waves can be made with an Incoherent Scatter radar which detects a considerable enhancement of the plasma lines. Such experiments were performed [50] and showed surprisingly that, after a very strong initial overshoot of the plasma lines, these tended to disappear few hundred milliseconds later. A typical spectrum obtained at a time near the heater turn on time is shown on figure 21 [50]. It shows very clearly the cascade of modes at odd numbers of the ion acoustic frequency.

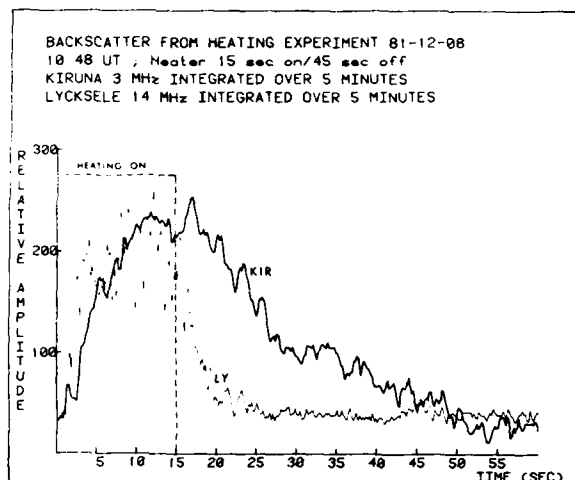


Figure 20. Growth and decay of the backscatter echoes at two different frequencies, 3 MHz (heavy line) and 14 MHz (thin line). [48]

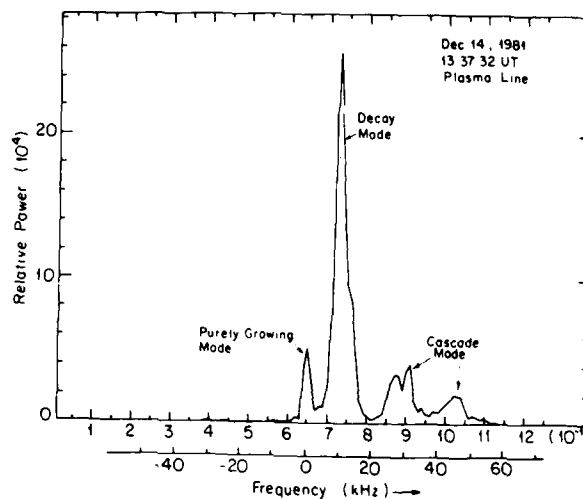


Figure 21. Typical observed power spectrum encompassing the heater turn-on time, for the height gate containing the maximum signal. [50]

Stimulated electromagnetic emissions obtained with the heater in the O mode have been observed within ± 100 kHz of the heater frequency [51]. Figure 22 [51] gives examples of stimulated emissions when the heater is on for 15 s. These stimulated emissions give one possibility of diagnostic of the F region plasma.

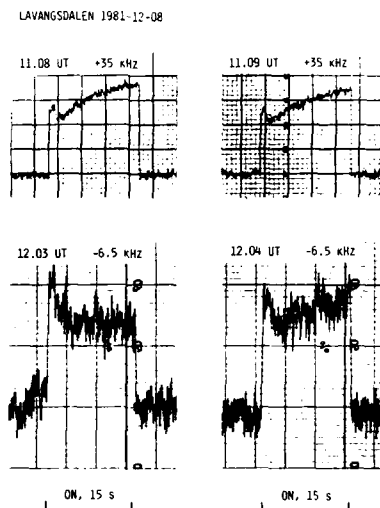


Figure 22. Examples of temporal behavior of the power (logarithmic scale) in the sidebands induced by Heating transmitting a sequence of 15-s pulses on 5423 kHz as received at Lavangsdalen December 8, 1981. The upper two curves depict the power in the upper sideband at $+35$ kHz. The temporal pattern, with a long-term increase in power except for the more rapid changes during the first 1.5 s, shows a very high degree of repeatability, as can be seen in the two curves recorded at 1108 UT and 1109 UT. No clear temporal repeatability is found for the lower sideband power received at -6.5 kHz even though this component sometimes shows a certain tendency for decrease in power with time as can be seen in the lower left-hand curve recorded at 1203 UT. [51]

V. CONCLUSION

HF radar techniques provide a powerful tool for the understanding and the monitoring of atmospheric processes (60 - 90 km) and ionospheric processes (D - E - F regions). In particular, they allow to characterize the dynamical state of the atmosphere and of the plasma and give access to small scale basic plasma processes. Their usefulness can be asserted in terms of fundamental research (plasma physics, neutral dynamics) as well as in terms of applications (propagation effects).

REFERENCES

- (1) GREGORY J.B., Radar wave reflections from the mesosphere 1. Heights of occurrence. *J. Geophys. Res.*, **66**, 1961, 429-445.
- (2) FRASER G.J., R.A. VINCENT, A study of D-region irregularities, *J. Atmos. Terr. Phys.*, **32**, 1970, 1591-1607.
- (3) MANSON A.H., C.E. MEEK, Partial reflection D-region electron densities, *MAP Handbook*, vol. 13, 1984, 113-123.
- (4) FRAZER G.J., Partial reflection spaced antenna wind measurements, *MAP Handbook*, Vol. 13, 1984, 233-247.
- (6) HARANG L., W. STOFFREGEN, Scattered reflections of radio waves from a height of more than 100 km, *Nature*, **142**, 1938, 832.
- (7) HULTQVIST B., A. EGELAND, Radio aurora, *Space Sci. Rev.*, **3**, 1964, 27-78.
- (8) LANGE-HESSE G., Radio aurora in Aurora and airglow, Ed. by B.M. Mc CORMAC, Reinhold, New York, 1967, 519-562.
- (9) UNWIN R., W.J. BAGGLEY, The radio aurora, *Ann. Geophys.*, **28**, 1972, 111-127.

- (10) GREENWALD R.A., Studies of currents and electric fields in the auroral zone ionosphere using auroral backscatter, in Dynamics of the magnetosphere, D. Reidel, Hingham, Mass., 1979.
- (11) FEJER B.G., M.C. KELLEY, Ionospheric irregularities, Rev. Geophys. Space Phys., 18, 1980, 401-454.
- (12) KESKINEN M.J., S.L. OSSAKOW, Theories of high-latitude ionospheric irregularities : a review, Radio Sci., 18, 1983, 1077-1091.
- (13) HANUISE C., High latitude ionospheric irregularities : a review of recent radar results, Radio Sci., 18, 1983, 1093-1121.
- (14) GREENWALD R.A., W.L. ECKLUND, B. BALSLEY, Auroral currents, irregularities and luminosity, J. Geophys. Res., 78, 1973, 8193-8203.
- (15) TSUNODA R.T., R.I. PRESNELL, Y. KAMIDE, S.I. AKASOFU, Relationship of radar aurora, visual auroral, and auroral electrojets in the evening sector, J. Geophys. Res., 81, 1976, 6005-6015.
- (16) FARLEY D.T., A plasma instability resulting in field-aligned irregularities in the ionosphere, J. Geophys. Res., 68, 1963, 6083-6097.
- (17) BUNEMAN O., Excitation of field aligned sound waves by electron streams, Phys. Rev. Lett. 10, 1963, 285-287.
- (18) D'ANGELO N., Type 3 spectra of the radio aurora, J. Geophys. Res., 78, 1973, 3987-3990.
- (19) VOLOSEVICH A.J., V.A. LIPEROVSKY, Generation of small scale inhomogeneities in a turbulent plasma and radio auroras, Geomagn. Aeron., 14, 1975, 58-61.
- (20) LEE M.C., J. BUCHAU, H.C. CARLSON, J.A. KLOBUCHAR, E.J. WEBER, Formation and detection of high latitude ionospheric irregularities.
- (21) REES M., Auroral ionization and excitation by incident energetic electrons, Planet. Space Sci., 11, 1963, 1209-1218.
- (22) KELLEY M.C., J.F. VICKREY, C.W. CARLSON, R. TORBERT, On the origin and spatial extent of high latitude F region irregularities, J. Geophys. Res., 87, 1982, 4469-4475.
- (23) VICKREY J.F., C.L. RINO, T.A. POTEMRA, Chatanika/Triad observations of unstable ionization enhancements in the auroral F region, Geophys. Res. Lett., 7, 1980, 789-792.
- (24) KESKINEN M.J., S.L. OSSAKOW, Non linear evolution of convective plasma enhancements in the auroral ionosphere, 1. Long wavelength irregularities, J. Geophys. Res., 87, 1982, 144-150.
- (25) CHATUVERDI P.K., S.L. OSSAKOW, The current convective instability as applied to the auroral ionosphere, J. Geophys. Res., 86, 1981, 4811-4814.
- (26) GARDNER F.F. AND J.L. PAWSEY, Study of the ionospheric D-region using partial reflections, J. Atmos. Terr. Phys., 3, 1953, 321-344.
- (27) MANSON A.H. and C.E. MEEK, Partial reflection D-region electron densities, MAP Handbook n°13, Pub. ICSU/SCOSTEP, Univ. of Illinois, 1984, 113-123.
- (28) FRASER G.J., The measurement of atmospheric winds at altitudes of 65-120 km using ground-based radio equipment, J. Atmos. Sci., 22, 1965, 217-218.
- (29) FRASER G.J., Partial reflection spaced antenna wind measurements, MAP Handbook n°13, Pub. ICSU/SCOSTEP, Univ. of Illinois, Radio Sci., 20, 1985, 1363-1382.
- (30) MEEK C.E., I.M. REID, A.H. MANSON, Observations of mesospheric wind velocities. I. Gravity wave horizontal scales and phase velocities determined from spaced wind observations, Radio Sci., 20, 1985, 1363-1382.
- (31) BOURDILLON A., Spectral characteristics of high frequency waves backscattered by small scale F region irregularities : Evidence of strong sub-auroral ion flow, AGARD Conference Proceedings n° 382 "Propagation effects on military systems in the high latitude region", 1985, 4.2-1-4.2-16.
- (32) GREENWALD R.A., K.B. BAKER, Observations of very high latitude ionospheric irregularities with the GOOSE BAY HF Radar, AGARD Conference Proceedings n°382 "Propagation effects on military systems in the high latitude region", 1985, 4.5-1-4.5-17.
- (33) CHAKRABARTY P., C.E. MEEK, D.K. CHAKRABARTY and A.H. MANSON, Results inferred from electron density measurements at Saskatoon, Canada (L = 4.4) by a partial reflection technique. I. Variations of nitric oxide in the D-region during quiet periods, J. Atmos. Terr. Phys., 44, 1982, 952-962.

- (34) MEEK C.E. and A.H. MANSON, Comparisons between time variations in D region winds and electron densities at Saskatoon, Canada (52°N ; 106°W), J. Atmos. Terr. Phys., 40, 1978, 1267-1274.
- (35) MONTELAND L.E. and J.S. BELROSE, Diurnal and seasonal variations of the steady state loss coefficient in the D region, J. Geophys. Res., 84, 1979, 1921-1929.
- (36) RASTOGI P.K., A. BREKKE, O. HOLT and T. HANSEN, Variability of D-region electron densities at Tromso, J. Atmos. Terr. Phys., 44, 1982, 313-323.
- (37) CHAKRABARTY P., C.E. MEEK, D.D. CHADRABARTY and A.H. MANSON, Results inferred from electron density measurements at Saskatoon, Canada (L = 4.4) by a partial reflection technique. II. Ion production rates and nitric oxide in the D-region during post storms periods, J. Atmos. Terr. Phys., 45, 1983, 303-308.
- (38) BREKKE A., O. HOLT, P.H.G. DICKINSON, M. FRIEDRICH, T. HANSEN, P. STAUNING and E.V. THRANE, Development of D-region electron and ion densities under various auroral conditions during the energy budget campaign (EBC), J. Atmos. Terr. Phys., 47, 1985, 101-121.
- (39) MANSON A.H. and C.E. MEEK, Small scale features in the middle atmosphere wind field at Saskatoon, Canada (52°N ; 107°W). An analysis of MF Radar data with rocket comparisons, J. Atmos. Sci., in press.
- (40) MANSON A.H. and C.E. MEEK, Dynamics of the middle atmosphere at Saskatoon (52°N ; 107°W) : A spectral study during 1981, 1982, J. Atmos. Terr. Phys., 48, 1986, 1039-1055.
- (41) DICKINSON P.H.G., R. GRABOWSKI, C. HANUISE, D.J. MACKINNON, E. NIELSEN, E.V. THRANE, J.P. VILLAIN, H. WOLF and O. ANDREASSEN, Simultaneous observations of E region irregularities by ground-based and rocket-borne techniques, J. Atmos. Terr. Phys., 47, 1985, 265-281.
- (42) HANUISE C., J.P. VILLAIN and M. CROCHET, Spectral studies of F-region irregularities in the auroral zone, Geophys. Res. Lett., 8, 1981, 1083-1086.
- (43) TELLEGEN, B.D.H., Nature, 131, 1933, 840.
- (44) CARLSON H.C. and L.M. DUNCAN, HF excited instabilities in space plasmas, Radio Sci., 12, 1977, 1001.
- (45) STUBBE P. and H. KOPKA, Summary of results obtained with the Tromso heating facility, Radio Sci., 18, 1983, 831-834.
- (46) STUBBE P., H. KOPKA, M.T. RIETVELD, A. FREY, P. HOEG, H. KOHL, E. NIELSEN, G. ROSE, C. LA HOZ, R. BARR, H. DERBLUM, A. HEDBERG, B. THIDE, T.B. JONES, T. ROBINSON, A. BREKKE, T. HANSEN, O. HOLT, Ionospheric modification experiments with the Tromso heating facility, J. Atmos. Terr. Phys., 47, 1985, 1151-1163.
- (47) STUBBE D., H. KOPKA, H. LAUCHE, M.T. RIETVELD, A. BREKKE, O. HOLT, T.B. JONES, T. ROBINSON, A. HEDBERG, B. THIDE, M. CROCHET, H.J. LOTZ, Ionospheric modification experiments in Northern Scandinavia, J. Atmos. Terr. Phys., 44, 1982, 1025-1041.
- (48) HEDBERG A., H. DERBLUM, B. THIDE, H. KOPKA and P. STUBBE, Observations of HF backscatter associated with the heating experiment at Tromso, Radio Sci., 18, 1983, 840-850.
- (49) HANUISE C., A. HEDBERG, J. OKSMAN, E. NIELSEN, P. STUBBE and H. KOPKA, Comparison between the ionospheric plasma drift and the motion of artificially induced irregularities as observed by HF backscatter radars, Ann. Geophys., 4, 1986, 49-54.
- (50) HAGFORS T., W. KOPFMAN, H. KOPKA, P. STUBBE and T. ALJANEN, Observations of enhanced plasma lines by EISCAT during heating experiments, Radio Sci., 18, 1983, 861-866.
- (51) THIDE B., H. DERBLUM, A. HEDBERG, H. KOPKA, P. STUBBE, Observations of stimulated electromagnetic emissions in ionospheric heating experiments, Radio Sci., 18, 1983, 851-859.

ACKNOWLEDGEMENTS

The author is very thankful to A. Brekke, G. Fraser, C. Hanuise, R. Munsucker, T.B. Jones, A.H. Manson, P.C.E. Meek, P. Stubbe, R.A. Vincent for providing very valuable inputs to this lecture.

THE HIGH-LATITUDE IONOSPHERE: DYNAMICAL ASPECTS, AND MODELS

Dr. J.K. Hargreaves

Senior Research Fellow, Department of Environmental Science, University of Lancaster, Lancaster LA1 4YQ, England.

Abstract

Whereas the inner magnetosphere co-rotates with the Earth, the outer region circulates in a pattern determined by the solar wind. These motions are communicated along the geomagnetic field-lines to the high-latitude ionosphere, causing F-region plasma to drift bodily and producing electric currents in the E region. The dynamics of the polar ionosphere are characterized by trans-polar drift from day to night and a return flow around the auroral zone. The neutral thermospheric wind is driven by solar heating, and this also flows across the polar caps from day to night sectors.

Models are becoming increasingly important in upper-atmosphere geophysics. The extensive data sets now available have enabled empirical models to be compiled. These are essentially mathematical representations of the data in a form suitable for a computer. Where the theory is sufficiently well developed it is worthwhile to develop a mathematical model based on the fundamental equations governing the phenomenon. The output from such models obviously needs to be checked against data, and they offer a useful technique for studying the fundamentals of complex phenomena. Models — some empirical, some mathematical, and some mixed — have been produced for the structure of the neutral atmosphere, the winds and tides of the thermosphere, the ionosphere, the magnetosphere, and for ionospheric radio propagation.

1. Circulation of the magnetosphere1.1 Circulation patterns

We have seen that the general form of the magnetopause can be derived by assuming that the solar wind exerts a pressure against the surface but otherwise flows past smoothly. This must be a dubious assumption, however, because most objects flying through a fluid experience some friction, and we might expect something similar of the magnetosphere as the solar wind travels past super-Alfvénically. This is an important point because any friction at the boundary would provide a mechanism for transferring energy from the solar wind into the magnetosphere.

In 1961, W.I. Axford and C.O. Hines suggested that momentum is transferred from the solar wind into the magnetosphere by some unspecified process equivalent to friction, and that the whole system was caused to circulate. Experimental evidence was adduced from a study of the S_q current system, whose behaviour can be derived from observations with magnetometers at medium and high latitudes. S_q is the polar part of the basic S_q system, the upper atmosphere current related to the solar day under quiet conditions. Its basic form, illustrated in Figure 1, is a current flowing over the poles from night to day with return currents at lower latitudes. It is characteristic of the dynamo region of the ionosphere that positive ions move with the neutral air but electrons with the magnetic field. S_q can therefore be explained by a motion of magnetic field-lines opposite to the current flow in Figure 1. Projected to the magnetosphere, this implies that the field-lines circulate over the poles from the day to the night sectors of the Earth with a return flow around the dawn and dusk sides. The resulting circulation is similar to that within a falling raindrop, in which the fluid is swept back at the surface and returns inside the drop. Figure 2a shows the magnetospheric circulation pattern in a section through the equatorial plane. Figure 2b takes account of the Earth's rotation which carries the inner part of the magnetosphere with it.

The difficulty with the *viscous interaction* theory was the nature of the frictional force, since friction is usually associated with collisions and the solar wind is so tenuous that collisions are virtually absent, the mean free path being some 10^9 km! Attention therefore moved to an alternative mechanism, based on the work of J.W. Dungey which supposed connections between the interplanetary magnetic field (IMF) and the geomagnetic field. Figure 3 depicts a distorted dipole field representing the geomagnetic field in polar section, with the addition of (a) a northward IMF and (b) a southward IMF. In the second case, neutral points are formed in the equatorial plane and some lines of the IMF connect to geomagnetic lines. This is not so in the first case. In fact the IMF tends to lie in the solar-ecliptic plane and be oriented at the "garden hose" angle, but there is usually a north-south component as well and this, when directed southward, is what may connect to the geomagnetic field.

The IMF is frozen into the solar wind and is therefore carried along with it. When geomagnetic field-lines are connected to those from the IMF they are dragged over the poles from the sunward neutral point, as in Figure 3c, and thereby transported from the day to the night side. While over the polar caps the field-lines are open in the sense that they do not connect back to the other hemisphere in any simple or obvious manner. In the tail these lines reconnect and move back towards the Earth.

The above picture is of course a simplified one. Figure 4 shows a more realistic version which includes a degree of connection when the IMF is northward.

Since both the driving mechanisms predict rather similar circulations there has been some doubt as to their relative importance. There is direct evidence for the merging of magnetic fields, and other observations demonstrate that major effects are associated with a southward IMF component:

- (a) the dayside magnetopause moves inward;
- (b) the auroral zone and the dayside cusps are displaced equatorward;
- (c) the magnetic flux in the tail lobes is increased;
- (d) substorms occur more frequently.

All of these argue that a southward IMF increases the magnetospheric circulation. There is also an effect of the east-west IMF component on the symmetry of the polar convection — the Svalgaard-Mansurov effect. However geomagnetic activity does not cease altogether when the IMF has a northward component, indicating that the circulation does not stop. Current opinion is that both viscous interaction and magnetic merging operate but that merging is considerably the more important during periods of southward IMF. Figure 5 indicates how the two mechanisms may co-exist: here, merging drives the flow over the poles involving open field-lines, and "friction" pushes closed field-lines within a limited depth along the flanks of the magnetosphere.

Despite remaining problems there can be no reasonable doubt about the fact of magnetospheric circulation and its significance in geospace. It is a concept that has made it possible to comprehend many of the phenomena that have been observed and well substantiated in geospace research, and is one of the foundation stones of modern magnetospheric theory.

1.2 Field merging

In the dynamic magnetosphere open field-lines from the polar regions reconnect in the centre of the magnetotail and then contract towards the Earth. Satellite observations reveal the presence of a small north-south magnetic component across the reconnection region, showing that, as in Figure 6, the field-lines are not strictly parallel. This *X-type neutral line* cannot be a static configuration because the tension in the field-lines will produce net forces towards the Earth and into the tail. But there can be a dynamic equilibrium, in which that depletion is replaced by other field-lines moving over the poles from the dayside and through the lobes towards the neutral sheet. It would also be possible to have a *Y-type neutral line*, where the field continues to converge on the tailward side, the earthward side being as in Figure 6. The velocity of the field-lines towards the Earth is estimated as about 100 km/s and the drift towards the neutral sheet as about 10 km/s. However it is more likely that the tail reconnection occurs not steadily but intermittently in limited regions, and this will be taken up again later.

The principal region of connection between the IMF and magnetospheric field-lines is on the dayside. When connection occurs a geomagnetic flux tube has to break and connect with an IMF tube. This causes a characteristic magnetic signature which has been sought with spacecraft. The results of such measurements show that during periods of southward IMF dayside connection events (often known as *flux transfer events*) occur frequently (1-2/hr) but that they are of short duration (approx. 5 min.) and relatively small in spatial extent.

1.3 Magnetospheric electric fields

There is an equivalence between an electric field and moving magnetoplasma. If an electric field E is applied across a magnetoplasma with magnetic flux density B , the magnetoplasma moves at velocity

$$v = E \times B / |B|^2 \quad (1)$$

Conversely, it may be shown that if magnetoplasma moves at velocity v with respect to a stationary observer, the observer will measure an electric field

$$E = v \times B \quad (2)$$

Electric field and motion of magnetoplasma are equivalent in highly conducting plasmas such as the magnetosphere and the solar wind.

An equivalent description of the dynamic magnetosphere can therefore be given in terms of electric fields (as seen by a stationary observer). The general circulation of the outer magnetosphere is equivalent to an electric field across the magnetosphere directed from the dawn to the dusk side. The magnitude is about 0.3 mV/m, though considerably variable, giving a total potential difference of some 60 kV across the magnetosphere.

The source of this electric field can be appreciated by considering the magnetosphere as a magneto-hydrodynamic generator, in which a jet of plasma is forced across a static magnetic field and an electric potential is developed by dynamo action. If the magnetosphere were static the solar wind would blow across the field-lines and

an electric field would be generated. The magnitude of this field is just that required to produce the circulation. The total potential drop is given by

$$V_T = vLB_n \quad (3)$$

where v is the solar wind speed, L is the width of the magnetosphere, and B_n is the magnetic flux density normal to the boundary. B_n is estimated from the magnetic flux leaving the polar caps (approximately the regions within the auroral ovals) which ultimately connects to the IMF. For a polar cap of radius R_p and magnetic flux density B_p , a magnetotail of length S_T and radius $R_T (= L/2)$:

$$B_n = \pi R_p^2 B_p / 2\pi R_T S_T \quad (4)$$

Taking reasonable values gives $V_T \sim 60$ kV.

The co-rotation of the inner magnetosphere can also be represented by an electric field, E_c . Rotation at angular frequency ω produces to a stationary observer in the equatorial plane an electric field of magnitude $r\omega B$, where B is the magnetic flux density at radial distance r . The electric field is directed radially inward. In terms of the L value, the radius of the Earth (R_E) and the equatorial flux density at the surface,

$$E_c = LR_E \omega B_E / L^3 = R_E B_E \omega / L^2 = 14.4/L^2 \text{ mV/m} \quad (5)$$

2. Substorms in the magnetosphere

2.1 Consequences of intermittent merging

The circulation of the magnetosphere is driven (mainly) by magnetic merging on the sunward side of the magnetopause, but its continuity depends on reconnection in the tail plasmasheet. Figure 7 follows the history of a selected field-line: connecting with the IMF, convecting over the poles as open lines, reconnecting in the tail, and returning to a nearly dipole form in the earthward return flow. If R_m and R_r are the connection rates at the magnetopause and in the tail respectively, T is the rate of transport of open lines into the tail, and r is the rate at which closed flux is returned from the tail to the closed magnetosphere, $R_m = T = R_r = r$ implies a state of steady circulation. Over a long enough period of time it must still be true that $R_m = T = R_r = r$. On the other hand, intermittent merging will cause an imbalance. When the IMF turns southward, the connection rate increases and for a while $R_m > R_r$. More open field is then being produced than removed, and this is why the auroral oval moves equatorward. If $R_r > R_m$ there is a net loss of open field because the tail reconnection rate exceeds the merging rate at the magnetopause; the auroral oval then shrinks again.

We have seen that magnetopause connection proceeds as a series of discrete, limited but frequent "flux transfer events". Connection in the tail goes in less frequent but more cataclysmic events, and this is the basis of the substorm. The substorm was originally identified from ground-based studies of the aurora and three phases have been identified:

- the growth phase,
- the expansion phase, and
- the recovery phase.

In the magnetosphere the growth phase corresponds to increased erosion from the front of the magnetosphere, and at this time the plasma sheet becomes thinner as illustrated in Figure 8. The expansion phase begins with the formation of a neutral line nearer to the Earth than during quiet times (Figure 9). Satellites at geosynchronous distance observe an increase in the flux of energetic electrons, and the geomagnetic field becomes more dipolar. The sequence of events is illustrated in Figure 10. Note that the region of the tail between the two neutral lines is ejected along the magnetotail as the recovery phase begins; this is known as a *plasmoid*. The thinning of the plasma sheet in the expansion phase can be detected as a loss of particle flux by a satellite near the neutral sheet. The expulsion of the plasmoid is seen by satellites at 20 or 30 R_E in the tail as a burst of energetic particles moving away from the Earth.

2.2 Substorm triggering and the influence of the IMF

The general sequence of events in the substorm is well established, but the question of substorm triggering is not so clearly answered. Presumably the right conditions must be there, but even so we have to ask whether it is triggered by some identifiable feature, for instance in the solar wind, or whether, on the other hand, it might be a spontaneous phenomenon without apparent cause.

Important factors are certainly the energy flux of the solar wind and the efficiency with which the energy is coupled into the magnetosphere. The index AE, a geomagnetic activity index indicating the activity level of the northern auroral zone, is well correlated with a quantity

$$\epsilon = vB^2 \sin^4(\theta/2) L_0^2 \quad (6)$$

where

v = solar wind speed,
 B = IMF magnitude,

R_0 = a length related to the cross section of the magnetosphere ($7 R_E$), and
 θ = angle of IMF seen from the Earth (as in Figure 11).
 If $B_z > 0$ (northward), $\theta = \tan^{-1} |B_y/B_z|$, and if $B_z < 0$ (southward), $\theta = 180^\circ - \tan^{-1} |B_y/B_z|$.
 The magnetic energy reaching the magnetosphere per unit time is proportional to $v B^2 R_0^2$, the magnetic power of the solar wind. The expression $\sin^4(\theta/2)$ represents the fraction of this power coupled into the magnetosphere. It gives a gradual transition between full coupling when the IMF is fully southward ($\sin^4(\theta/2) = 1$) and zero coupling when it is fully northward ($\sin^4(\theta/2) = 0$). If $B_z \ll B_y$, $\theta/2 = 45^\circ$, and the coupling factor is 0.25.

Some other expressions based on different combinations of solar wind parameters also correlate with substorm occurrence, though ϵ is perhaps the best (Figure 12). That substorms occur most frequently when B_z is southward has been known for some years, and it is found that the beginning of the substorm often coincides with a southward turning of the IMF. But there are also cases when the substorm begins as the IMF turns northward, having previously been southward for an hour or two. In such a case it appears that southward IMF puts energy into the magnetosphere and then the shock of the northward turning triggers its release in the substorm.

3. Magnetospheric current systems

The combination of plasma and electric field in the magnetosphere also allows electric currents to flow. Several current systems can be identified:

the magnetopause current;
 the tail current;
 the ring current;
 Birkeland currents.

3.1 The magnetopause current

Magnetic fields and electric currents are fundamentally related through the Biot-Savart law. The magnetopause is the outer boundary of the geomagnetic field, and the current flowing at the magnetopause is such that its magnetic field cancels the geomagnetic field outside the boundary. In the inner magnetosphere, where the field is almost dipolar, the contribution from the magnetopause current is small compared with that from the Earth's internal dipole. The form of the magnetopause current is shown in Figure 13a.

3.2 The tail current

The down (solar) wind extension of the magnetosphere into a tail indicates the presence of a current flowing across the plasma sheet from the dusk to the dawn side. But the tail is also bounded, and this requires a tail current in the form of a double solenoid, as in Figure 13c. Referring to Figure 14, if the current density over the surface of the tail is i_t A/m (that in the plasma sheet being $2i_t$), the magnetic flux density in the tail is

$$B_T = \mu_0 i_T. \quad (7)$$

The tail current and the tail magnetic field are therefore simply related. Since $B_T \sim 20$ nT, $i_t \sim 1.6 \times 10^{-2}$ A/m. In the sheet the current density is about 3×10^{-2} A/m. Assuming a reasonable length for the tail, the total tail current comes to some 10^6 A, and, taking the cross-tail potential difference as 60 kV, the power extracted from the solar wind by the tail amounts to 6×10^9 kW (6000 GW).

3.3 The ring current

The ring current may be detected by ground-based magnetometers at the lower latitudes. It has long been known that under magnetic storm conditions the magnetic field at the Earth's surface may be depressed for hours or days. This depression is due to a ring current in the magnetosphere, flowing round the Earth from east to west (clockwise as seen from over the north pole), as in Figure 13b. The magnetic field due to this current acts to oppose the geomagnetic field. A depression of 30 nT at the surface, which would be moderate storm, could be explained by 10^6 A at geocentric distance $4.5 R_E$. The simple relation between current and field is

$$\Delta H = 2\pi I(A)/10r(km), \quad (8)$$

but currents induced in the ground increase the effect by an amount depending on the ground conductivity but which typically amounts to a factor of about 3/2. Thus, an approximate relation is just

$$\Delta H \sim 3\pi I/10r \sim I/r. \quad (9)$$

The distance, r , cannot of course be determined from ground-based observations alone, though satellite measurements can do so. For example a satellite-borne magnetometer inside the ring current will observe an effect in the same sense as is seen at the ground; if the satellite is outside the ring current the effect will be in the opposite sense.

A clockwise ring current is produced by the drift of trapped particles since protons drift to the west and electrons to the east. The particles responsible are mainly protons of 10 to 100 keV. Generally the current is located between 4 and 6 R_E , close to the inner edge of the plasma sheet and to the outer edge of the trapping zone. Although H^+ is the major ion in the ring current, heavier ions, such as O^+ , He^+ , He^{++} , and O^{++} , are also present. The energy density of the ring current can exceed that of the geomagnetic field ($2 \times 10^{-8} \text{ J/m}^3$ at $5R_E$) and then the field becomes distorted. This is called *inflation* of the geomagnetic field.

3.4 Birkeland currents

For many years it was assumed that ionospheric currents flow only horizontally; the current systems derived from ground-based magnetograms were really *equivalent current systems* only, since the possibility of vertical current had been excluded. Nevertheless, the conductivity along the geomagnetic field far exceeds that across the field, and thus the idea that some current flows along the field cannot be lightly dismissed. The first suggestion of *field-aligned currents* was put forward by K. Birkeland in 1908, but the idea lay dormant for many years for lack of evidence. It began to return to favour on theoretical grounds in the 1960's, but it was not until quite recently that solid evidence was found.

The convincing observations came from magnetic measurements on satellites in the early 1970's. When the satellites crossed the auroral zone there were magnetic signatures such as that in Figure 15, which shows a westward magnetic field extending over $2-3^\circ$ of latitude (200-300 km). To explain this it is necessary to suppose that the satellite had passed through a double sheet of electric current, with a magnitude of about $5 \times 10^{-7} \text{ A/m}^2$ and directed downward at the higher latitude and upward at the lower. Other satellite observations since then have plotted the statistical distribution of the currents and filled in many other details.

The currents are nearly always present, with typical distributions as in Figure 16; they intensify and move equatorward with increasing disturbance level. The components into and out of the ionosphere change places (almost) between the evening and the morning sectors. By convention, the region on the poleward side is called "region 1" and the equatorward one is "region 2", irrespective of the direction of the current flow. The current density in each region depends on the time of day; region 1 dominates on the day side of the Earth, and the regions are about equally intense around midnight. There is a transition at midnight where the flow occurs in three regions, one upward between two downward. The current density varies almost linearly with the magnetic activity index K_p . The total current in the Birkeland system is 10^6 to 10^7 A , and a budget of the currents in the various regions and sectors indicates that, within the accuracy of measurement, the total current flowing into the ionosphere is equal to that flowing out.

3.5 Substorm currents

When the tail collapses at a neutral point the cross-tail current must be reduced in that region. The current is diverted along the field-lines into the auroral ionosphere, where the circuit is completed by an *electrojet*, as in Figure 17a. This E-region current flows in a region where the conductivity is enhanced by particle precipitation. Some of the particles accelerated by the collapsing field become trapped to enhance the ring current, at least some of which is partial and does not encircle the Earth. As the particles drift away from the injection region in the midnight sector some are lost to the atmosphere, and thus the westward ring current tapers off towards the day side. All the current must be accounted for, and the partial ring current is thought to be completed by Birkeland currents to the ionosphere and an eastward current in the ionosphere. A circuit diagram of the substorm currents is given in Figure 17b. Figure 18 indicates the likely connection between various current components in a substorm. This is consistent with the observation that during a substorm the Birkeland currents are enhanced most strongly in the night sector.

4. Features of the high-latitude ionosphere

4.1 Dynamics

We have seen that the magnetosphere circulates as two regions, an inner one rotating daily with the Earth, and an outer one circulating under the influence of the solar wind. The polar ionosphere is connected by the geomagnetic field lines to this outer region, and — since the field lines are (almost) equipotentials — its circulation is essentially a projection of that of the outer magnetosphere.

In the F region, where the ion-neutral collision frequency is small relative to the gyrofrequency, it is obvious that the plasma will move with the magnetic field lines. More correctly — and to give an alternative picture — we should say that the electric field which the solar wind generates across the magnetosphere is mapped into the F region along the equipotential field lines. The polar-cap electric field so created (as measured by a stationary observer) then acts as the driving force for the F-region plasma. The integral of the electric field gives the total electric potential across the polar cap. This is nearly equal to the total potential across the magnetosphere between its dusk and dawn sides, and is an important parameter for the behaviour both of the magnetosphere and of the polar ionosphere. Its magnitude is around 60 kV.

The basic flow pattern caused by the polar-cap electric field is simply from the noon sector to the midnight sector directly over the pole, as sketched in Figure 19a. There is a return flow around the low-latitude edge of the polar cap, in the vicinity of the auroral oval, and that corresponds to the sunward flow of closed field lines at the flanks of the magnetosphere. However the co-rotation effect, conveniently represented by the co-rotation electric field, must also be included, and it distorts the flow pattern as shown in Figure 19b. The two circulation cells are now different, with marked distortion in the evening cell where the return flow and the co-rotation act in opposite directions. Some field lines now follow long, complicated paths, while others may circulate endlessly in small vortices — except that the whole pattern must in any case be constantly changing in response to variations of the solar wind.

The interplanetary magnetic field (IMF) also exerts a major influence. Because of stronger coupling at the magnetopause, the magnetosphere circulates most strongly when the IMF has a southward component. The east-west component also affects the circulation, presumably because of shifting connection regions at the magnetopause, and in particular it alters the relative size of the polar circulation cells.

There is also some interaction with the neutral air if the plasma and the neutral air are moving at different velocities. This is similar to the effect of the thermospheric wind on the ionosphere except that the field lines are being driven instead of the air. Assuming the air is stationary or moving more slowly than the field the interaction tends to lift the F region as it approaches the magnetic pole from the day side, and depress it as it moves to lower latitude on the night side. We have to remember that the neutral air is already in motion with the solar tide and it is the relative motion which counts. If a certain plasma circulation is maintained for long enough the neutral air will tend to catch up, causing a polar tide to be added to the solar one.

4.2 Polar Wind

The polar circulation carries field lines through regions where they are open to the solar wind or go deep into the tail of the magnetosphere. Since the scale height for light ions is very large the absence of an effective upper boundary means that plasma can flow away from the ionosphere. This "polar wind" includes the ions H^+ , He^+ and O^+ . In principle the flow can even reach supersonic speeds, but the details depend on the flow speed at the outer boundary: the term "polar wind" is sometimes restricted to the supersonic regime and then subsonic flow would be called a "polar breeze".

4.3 Polar Cusps

On the day side of the Earth are two regions, one in each hemisphere, where the geomagnetic field lines provide a direct connection between the ionosphere and the magnetosheath. In static models of the magnetosphere these correspond to the neutral points on the surface of the magnetosphere, marking the division between the closed field-lines at lower latitudes and those at higher latitudes that are swept back into the magnetotail. In the dynamic picture they are where the dayside field lines open before being swept over the poles. The unique structure of these cusps make them very interesting regions of the magnetosphere, but they also have significant effects within the ionosphere.

At ionospheric heights the cusp regions are recognized from two signatures:

- (1) The appearance of charged particles with energies similar to those in the magnetosheath. The cusps are typically located near $\pm 78^\circ$ geomagnetic latitude, and are about 5° wide. According to the particle observations the cusps extend over all daylight hours and merge into the auroral oval. There is also a second, smaller region extending only a few hours from local noon. The particle flux from the magnetosheath is highly variable over short times (or over small distances, since these observations come from orbiting satellites).
- (2) The enhancement of 6300 Å luminous emissions, indicating low-energy excitation of the upper atmosphere, and a reduction of those emissions typical of the aurora. This latter feature is sometimes called the *noon gap*. The photometric observations have shown a considerable variation in the latitude of the cusp, from 84° under very quiet geomagnetic conditions to 61° when they are very disturbed.

The influx of particles from the magnetosheath enhances the density and temperature of the ionosphere in the cusps, and there is a greater degree of irregularity. Some ionospheric plasma also flows out to high altitudes where its ionospheric origin has been recognized from its temperature and composition.

4.4 Troughs

One of the consequences of the polar circulation is that the ionosphere tends to be depleted between the mid-latitude and high-latitude regions. Figure 20 shows the locations related to the polar circulation and to the auroral oval. The *main trough*, alternatively called the *mid-latitude trough*, was first detected with orbiting ionospheric satellites in the 1960's, when it was known as the "Canadian border effect" since it appeared in many cases to coincide with the border between Canada and the U.S.A. Subsequent work, both satellite- and ground-based, has amply confirmed the main trough as a major feature of the ionosphere — and one by no means confined to the western

hemisphere! There are several aspects. As observed in the ionosphere the trough is a night-time occurrence at latitudes between 60 and 65° geomagnetic. It occurs in both hemispheres and in all seasons, though in summer it is only seen near midnight. The trough moves gradually towards lower latitude during the night. It also moves equatorward under storm conditions. The latitude of the trough minimum is given empirically (to 2° accuracy) by

$$\Lambda = 65.2^\circ - 2.1 K_p - 0.5 t, \quad (10)$$

where Λ is the invariant latitude of the minimum, K_p is the global 3-hour index of magnetic activity, and t is the time from local midnight in hours reckoned positive after midnight and negative before.

The detailed structure of the main trough varies considerably; Figure 21 illustrates typical features. The whole structure is quite broad, but the poleward edge, which is adjacent to the auroral oval, tends to be sharp and for some techniques is the most readily observed feature. The electron temperature is enhanced in the trough.

The trough is related in a general way to the plasmopause. Both are consequences of the change of circulation pattern between the inner and outer magnetospheres, but the correspondence is not exact because the immediate cause of the trough is the decay of ionization on flux tubes that have been away from the sunlit side of the Earth for too long a time. For example, the evening bulge in the plasmasphere does not show in the latitude of the trough. The "hole" marked on Figure 20 is a depletion at higher latitude, not connected with the plasmopause but due to field-lines circulating only in darkness so that the ionization lost by recombination is not replenished. At high altitudes, where H^+ is the principal ion, the trough is still observed. This *light-ion trough* usually occurs by day as well as by night. There are relationships, in some cases ill defined, with the heavy-ion trough and with the plasmopause. These relationships are necessarily complicated, since they depend on the production and loss of ionization and on its flow between ionosphere and protonosphere, as well as on the polar circulation pattern, all of which depend to at least some extent on the state of geophysical disturbance. On the theoretical side, this is a topic which, because of its complexity, is ideally suited to computer modelling.

4.5 Auroral phenomena

The aurora is the most readily observed consequence of the dynamic magnetosphere and the most obvious characteristic of the high-latitude ionosphere. Mankind must have been looking at the northern and southern lights in the night sky, the *aurora borealis* and the *aurora australis*, for thousands of years, which surely puts them amongst the oldest known geophysical phenomena; though only in the last part of the 20th century has any proper explanation become possible. The term "aurora borealis" dates from 1621, and there are detailed reports of auroral displays dating from 1716.

The aurora comprises a group of upper-atmosphere phenomena, not just the emission of light. Each is a direct or an indirect consequence of the entry of energetic particles from the magnetosphere to the atmosphere:

- (a) luminous aurora;
- (b) radar aurora, the reflection of radio signals from ionization in the auroral region;
- (c) auroral radio absorption, the absorption of radio waves in the auroral ionization;
- (d) auroral X-rays, generated by the incoming particles and detected on high-altitude balloons;
- (e) magnetic disturbances, due to enhanced electric current flowing in the auroral ionization and detected on magnetometers;
- (f) electromagnetic emissions in the very-low- and ultra-low-frequency bands, generated in the magnetosphere by wave-particle interactions, and propagating to the ground for detection with a receiver or a sensitive magnetometer.

The auroral phenomena have several features in common. They are all related to solar activity in a general way, though usually without specific association with any particular solar event. The term *M region* was used from the 1930's to denote an unseen solar region causing aurora and magnetic storms, and then the auroral phenomena could be described as those due to *M regions*. It is now understood, of course, that the connection from the Sun is via the solar wind.

In general the auroral phenomena are highly structured in both space and time, with occurrence patterns that are essentially zonal. The classical picture of auroral occurrence (Figure 22) shows 100% occurrence at the peak of a zone centred between geomagnetic latitudes 65 and 70°, with the rate falling off on both the equatorward and the poleward sides. But in 1963, Y.I. Feldstein, analysing data from the International Geophysical Year (1958-9), pointed out that the locus of the aurora at a fixed time is oval, not circular (Figure 23). The maximum is near 67° at midnight, increasing to about 77° at noon, and the classical zone is the locus of the midnight sector of the oval as the Earth rotates underneath it. To a first approximation the oval is fixed with respect to the Sun.

The third common feature of the auroral phenomena is that they all show sub-storm behaviour. They tend to occur in bursts, each lasting perhaps 30-60 min., separated by quiet intervals of several hours. In each substorm the auroral oval first becomes

active in the midnight sector, and the activity then spreads in latitude and also to other local times. The auroral substorm is of course a consequence of the substorm in the magnetosphere, whose behaviour has been discussed.

4.6 Summary

Figure 24 summarizes the dominant features of the high-latitude ionosphere, most of which owe their existence to the coupling along the geomagnetic field between the polar atmosphere and the outer magnetosphere.

5. Models

5.1 Introduction

Although we do not yet have a full understanding of the magnetosphere-ionosphere system, there is a lot of information from direct observations and much of the theory about its behaviour is well advanced. The ready availability of computers during the last few years has made it practical to develop "models" of the ionosphere and magnetosphere, which take the accumulated knowledge in some area and employ the power of the computer to process it, with the object of making a prediction.

There has been something of a boom in ionospheric modelling in recent years. It might even be said that models have become rather fashionable, and, if that is so, we should approach them with some caution. This is not to impute modelling as an activity, for it has a valuable role to play in developing the science of a complex environment. The warning is, rather, that the output from a model can be no better than the input, and the danger is in believing results just because they come out of a computer.

5.2 Types of model

There is more than one kind of model. *Empirical models* are based on data compilations. For example, the set of measurements from an incoherent-scatter radar of the ionospheric electron density will include variations with height, time of day, season, sunspot number and magnetic activity. If the electron density can be represented as a function of these variables by a mathematical expression, then that expression can be used as a model to predict the electron density under specified conditions. The value of the prediction will depend on how well the expression fits the input data (i.e. on the magnitude of the "noise") and on whether any unrecognized factors are at work. A purely empirical model does not contain any physics, except perhaps as a general guide to the likely form of variation. For example, a daily component would probably be fitted by a sinusoidal 24-hour fundamental plus a number of harmonics.

The second general type of model is the *mathematical model* based on theory. This starts from the basic physics of the situation, and the procedure solves the relevant equations under the relevant imposed conditions, to achieve a prediction of the quantity of interest. Usually a numerical solution technique will be required. In the example of ionospheric electron density, one would require a knowledge of the solar spectrum, the composition of the neutral atmosphere, the photochemistry of ionized and neutral species, and the wind system in the thermosphere, at least. The equations for continuity, momentum, and heat flow would have to be solved numerically, to give a time-varying electron density distribution. This is obviously a powerful method, since a mathematically correct answer is obtained from a given input. But there are some dangers as well:-

- (a) The physics is complicated and, therefore, so is the mathematics needed to describe the real atmosphere. In an ionosphere model, for example, one has to include not only ion production and loss, but also transport along the field-lines which involves interaction with the protonosphere above, and the effect of neutral-air winds.
- (b) The program may require an excessive amount of computer time. This is a real problem with the more comprehensive models. Sometimes there are factors that have only a minor effect on the result, and it may be possible to omit them; but if too much is left out the model may be inadequate in some circumstances. Experimentation and a certain amount of finesse may be required in deciding the balance.
- (c) Even if we have a mathematically complete model, and can afford to run it, the answers might still be unreliable because the input parameters are not well enough known. In the ionosphere the neutral-air wind and the polar-cap electric field are both changeable and not well known in detail, yet they certainly affect the ionosphere.

Mathematical modelling is certainly a valuable technique in ionospheric science, as a means to investigate the importance of candidate mechanisms or to derive unknown parameters from observations. Its value to the forecaster depends very much on how well the model has been validated by trial and error. For someone who just wants to know the answer, the empirical model, if available, may be more accurate. In some cases, mixed models have been constructed, in which theory has been used to help fill gaps in an empirical data set.

5.3 Modelling activities

Various aspects of the geospace environment have been the subject of modelling activities. These are summarized in Table 1. Most of the categories contain several models, some devised by individuals or groups and others constructed through organized

international collaboration. Some models include or subsume earlier ones. Some have been developed within organizations primarily for their own use, while others may be commercial products offered for sale.

The overall picture being complicated, and the author's information being almost certainly incomplete, no attempt will be made at a comprehensive review. Instead, selective comments will be offered to illustrate the models available and the work being done in the various areas.

5.4 Empirical models

The principal empirical models are those describing the neutral atmosphere and the ionosphere on the basis of observations, and these are fundamental to modelling in general because they contain basic facts needed by practically all models however constructed.

5.4.1 MSIS

The "Mass-Spectrometer-Incoherent-Scatter" model, the most recent version of which is MSIS-86, is based on work at the Goddard Space Flight Center (Hedin¹, 1983). It deals with the neutral atmosphere from 50 to 2500 km altitude, taking data from various rockets, satellites, and incoherent scatter radars. The polar regions are included. For input values of latitude, longitude, local time, day of year, altitude, 10.7 cm flux and A_p , the model gives values for the number densities of O, N_2 , O_2 , He, Ar, H and N, the total mass density, and the neutral air temperature.

There is, in addition, a considerable body of information in various Standard and Reference atmospheres such as the U.S. Standard Atmosphere, 1976, and COSPAR International Reference Atmospheres (CIRA) from 1965 on. These are presented as tables of temperature, density, pressure, scale height, composition, wind, etc. (Champion et al.² 1985).

5.4.2 Empirical models of the ionosphere - the I.R.I.

The "International Reference Ionosphere" is the internationally recommended model of the ionosphere, developed by a joint URSI/COSPAR working group since the late 1960's. One of its vital elements is a "map" of critical frequencies taken from ionosonde data. Jones and Gallet³ (1962) took data from the international ionosonde network (Figure 25) and carried out a spherical harmonic analysis (including 788 coefficients per map) on each set of monthly median values over 24-hours of the day and for a range of sunspot numbers. The set of maps was thereby represented by a (large) set of coefficients, and particular values of the critical frequency, corresponding to specified conditions, could be retrieved as required. The distribution of ionosondes over the Earth's surface is very uneven, and some form of interpolation is needed to fill the gaps. These maps have been adopted by the C.C.I.R. as the basis for HF propagation predictions. Figure 26 shows an example.

However, the IRI aims to be more comprehensive (Bilitza⁴, 1986). It includes the profile of electron density (composed of 6 sections, as in Figure 27), electron temperature, ion temperature and ion composition. It is planned to add ion drift and electron collision frequency. The input parameters are altitude, location, time of day, month, and solar activity. In addition to the ionosonde data represented by the CCIR maps, data have been taken from incoherent scatter radars, radio absorption measurements, and in-situ measurements by satellites carrying topside sounders and probes, and from rockets.

There are several restrictions. The values are "mean" ones which do not include any day-to-day variation ($\pm 25\%$), though there is an option to use a measured critical frequency instead of that from the CCIR map. Solar activity is only represented up to a value of 130; above that value saturation is assumed. Irregularities such as spread-F, sporadic-E, and magnetic storms, are not included. And, most limiting for the polar ionosphere, the model does not include auroral latitudes. Earlier versions of the IRI are restricted to 1000 km altitude, but the protonosphere is to be included in future versions.

The IRI is a major enterprise in empirical ionospheric modelling, but its results should not be accepted uncritically. Comparisons between the model and new data have shown some marked discrepancies, for example at low latitudes and in electron content.

5.4.3 Electron content modelling

For trans-ionospheric propagation, for example satellite tracking, the integrated electron density, or electron content, is the important quantity. The basis for empirical electron content models is a compilation of topside-sounder measurements published by Bent and Llewellyn⁵ (1973). This is a tabular model, which has also been incorporated into later models; the topside in the IRI, for example, is based on the Bent and Llewellyn model. The usual approach to electron content modelling has been to integrate the Bent model or the IRI along the propagation path. The agreement with new observations is not always as good as might be wished (Figure 28).

Empirical electron content models have the same difficulty as critical frequency models regarding the day-to-day variability. At high latitude, in particular, the

electron content is structured in dynamic patches; it is difficult to see how this fact could be handled empirically.

5.5 Propagation models

A propagation model is constructed by adding a ray tracing routine to an ionospheric model in order to predict propagation quantities such as maximum usable frequency, signal strength, propagation mode, angle of arrival, time delay, etc., over a given path. Many such programs have been developed (Table 2). Some of the most widely used, including ITS-78 and IONCAP are described by Dandekar⁶ (1985).

In most cases the ionospheric representation depends on an empirical input of C.C.I.R. or other coefficients, and the propagation models therefore tend to be weak in equatorial and polar regions, and to omit day-to-day variability, spatial irregularities, and storms. The D region of the ionosphere may not be included, and this, of course, has a effect on signal strength, possibly a large effect at high latitude.

Some attempts are being made to overcome these weaknesses. For example the ICED model of the U.S. Air Weather Service (Tascione et al.,⁷ 1987) is making use of energetic particle precipitation and photography from orbiting satellites to obtain the position of the auroral oval and auroral electron densities. Essentially the ICED model is still based on a set of coefficients, but these are modified by other inputs. There are separate algorithms for the low- and mid-latitude ionosphere, the main trough, the auroral zone, and the polar cap, and in each region the F2, F1, and E layers are included. There is no D region. Ionization patches within the polar cap are not represented, though work is proceeding to express polar convection in terms of the interplanetary magnetic field and geomagnetic activity.

The AMBCOM model of IRI International Inc. (Smith and Hatfield⁸, 1987) includes models of the auroral oval and the main trough depending on K_p , and auroral absorption, again depending on K_p . Auroral absorption is a sporadic phenomenon, and predictions are of a statistical nature only.

An international Workshop held in 1986 included amongst its recommendations on propagation predictions that better estimates are needed for the high latitude and equatorial regions; that variability as well as mean behaviour is required; and that short-term disturbance predictions, possibly using solar wind observations, should be developed (C.M. Rush, private communication).

5.6 Mathematical models

Several aspects of the geospace environment have been subjected to mathematical modelling based on numerical solutions of time-varying equations. The neutral atmosphere, the ionosphere, and the magnetosphere have all been so treated, though often some parts of the model have to be empirical. Several groups are working in each area, and there is now a trend to connect models together to make a larger and more comprehensive model. One long-term objective is to be able to model the whole solar-terrestrial system sufficiently to predict terrestrial effects from solar causes.

5.6.1 Thermosphere dynamics

The dynamics of the neutral atmosphere and their consequences may be treated by solving numerically the equations for momentum, energy, continuity, and mean mass. The models are global and cover altitudes from below the mesopause to the exosphere. The system is driven by the heating from solar UV and EUV radiation and from energetic particles, Joule heating from ionospheric currents, and convection due to the electric field across the polar cap. Cooling is by infra-red radiation.

For computational purposes the atmosphere is represented on a grid covering geographic latitude and longitude, and atmospheric pressure. The grid rotates with the Earth, and the time-varying quantities of neutral wind, total energy density, and mean molecular weight are evaluated at each point. The vertical wind, the temperature, the heights of the pressure surfaces, the density, and the concentrations of atomic oxygen and molecular nitrogen are also calculated. The solutions also describe many other quantities, such as the horizontal and vertical heat conduction, the transport of the major species, and ion drag effects.

These models — the description above is based on Fuller-Rowell and Rees⁹ (1980) and subsequent work — are very sophisticated and, at least in some instances, they appear to reproduce experimental data quite well. Figure 29 shows an example. Their major role is in helping to understand how the thermosphere works, though increasing validation and speedier running will make them progressively more useful as practical representations of the thermosphere under various conditions.

5.6.2 Mathematical models of the ionosphere

These are based on time-dependent solutions of the continuity and momentum equations for the relevant ions (usually O^+ and H^+ , possibly with He^+ as well). Ion production and loss are based on known chemistry, and may be varied to take account of seasonal changes in the neutral species. Electron and ion temperatures may be input from a temperature model or computed from the ionization rate. Ion flow is constrained along the geomagnetic field, and the neutral air wind may add a contribution through

air drag. The transition between O^+ and H^+ at the base of the protonosphere enables the protonosphere to build up during the day and to act as reservoir to the heavy-ion ionosphere by night. At low and middle latitudes it is possible to include both hemispheres, and thereby model the effects of photo-electrons from the conjugate ionosphere (Figure 30). Electrodynamic lifting is important at equatorial latitudes.

In mathematical models of the high-latitude ionosphere the procedure is to follow the drift paths of the tubes of force, updating the plasma density, composition and temperature as the element proceeds through the system. Auroral ionization rates would be taken from a satellite-based empirical model.

The high-latitude ionosphere is affected by the neutral wind which tends to reinforce the plasma drift over the pole and affects the composition of the neutral air by bringing in species from lower latitude. Thermosphere and ionosphere models have been coupled together in order to study the high-latitude behaviour in a self-consistent manner (Fuller-Rowell et al.,¹⁰ 1987). Results from a coupled model must be more reliable than those from one in which only the ionosphere is treated mathematically. For example, it has been shown that the heating of the auroral zone by particle precipitation increases the concentration of molecular species in the F region, and, by increasing the loss rate, this tends to prevent the large increase of F-region electron density that would otherwise be expected.

The principal use of mathematical ionospheric models at the present time is in studying the behaviour of the ionosphere and deciding the important physical processes. Some results are, however, being included in empirical models to fill deficiencies in the data base. In general, computation times are too long for the mathematical model as such to be useful in practical propagation prediction.

5.6.3 Magnetosphere models

There are many aspects of the magnetosphere that can usefully be modelled, the most obvious being the form of the distorted geomagnetic field, the magnetospheric electric fields, and the particle fluxes. The magnetic field will be made up of several components — the Earth's main field, the field related to the Chapman-Ferraro currents, and those due to the ring current and to the tail current. The electric field is a consequence of the convection, and there may be provision for actual measurements to be incorporated, such as the potential drop across the polar cap. Empirical relations with other measured indices such as K_p may also be involved. The same is true of particle fluxes, which are of interest to satellite operations. It is possible to compute the drift paths of trapped particles in a model magnetosphere, and thus direct measurements can be incorporated if available (Freeman et al.,¹¹ 1987).

The most comprehensive and ambitious projects in this area are attempting to establish a connection from the Sun to the high-latitude ionosphere. One scheme (Watkins and Akasofu¹², 1987) is shown in Figure 31. Such a model is made up of several main parts. First in the logical sequence is a prediction of solar wind parameters using solar flare observations as input. This section is on the left in Figure 31. The solar wind velocity, and the magnitude and orientation of the interplanetary magnetic field are then applied to the magnetosphere model, which gives the position and size of the polar cap, and the polar cap electric field. The empirical formula of Equation (6), relating the cross polar cap potential to the ϵ parameter, is employed here. The electric field gives the polar convection pattern (Figure 32). An auroral zone, somewhat arbitrarily related to the edge of the polar cap, is included, and the particle precipitation in the auroral zone represents typical values. The ionospheric section of the model solves the continuity and momentum equations for O^+ ions, loss by recombination and by outflow at high altitude (polar wind) being included. A sequence of computed electron density contours every two hours during a simulated storm (of greatest intensity between 0400 and 0600 UT) is shown in Figure 33. These are polar plots out to 50° latitude, for summer (May) conditions with local noon at the top. They clearly show a tongue of ionization being carried across from the day side during the storm.

5.7 Conclusion

Ionospheric modelling in its various aspects is now a major activity, both for helping to understand the ionosphere and in bringing that knowledge and the information accumulated over many years of measurements into the practical business of radio propagation.

A useful statement of the recent position was produced at the conclusion of the URSI Workshop on Ionospheric Modelling in 1986, and this is reproduced as an Appendix.

References

1. A.E. Hedin: A revised thermospheric model based on mass spectrometer and incoherent scatter data: MSIS-83. *J. Geophys. Res.* **88**, (1983) 10170.
2. K.S.W. Champion, A.E. Cole and A.J. Kantor: Standard and Reference Atmospheres. Handbook of Geophysics and the Space Environment (ed. A.S. Jursa). Air Force Geophysics Laboratory (1985) p.14-1.
3. W.B. Jones and R.M. Gallet: The representation of diurnal and geographical variations of ionospheric data by numerical methods. *Telecommun. J.* **29**, (1962) 129.

4. D. Bilitza: International reference ionosphere: recent developments. *Radio Science* 21, (1986) 343.
5. R.B. Bent and S.K. Llewellyn: Documentation and description of the Bent ionospheric model. Report AFCL-TR-73-0657, Hanscom, Mass., (1973).
6. B.S. Dandekar: Ionospheric Radio Wave Propagation (Ionospheric Modelling), Handbook of Geophysics and the Space Environment (ed. A.S. Jursa). Air Force Geophysics Laboratory (1985), p.10-38.
7. T.F. Tascione, H.W. Kroehl and B.A. Hausman: ICED - A new synoptic scale ionospheric model. Proc. Symposium on "The Effect of the Ionosphere on Communications, Navigation, and Surveillance Systems", Springfield, Virginia, May 1987, paper 4A-1.
8. G. Smith and V.E. Hatfield: AMBCOM User's Guide for Engineers. Report from S.R.I. International, Menlo Park, California (1987).
9. T.J. Fuller-Rowell and D. Rees: A three-dimensional, time-dependent, global model of the thermosphere. *J. Atmos. Sci.* 27, (1980) 2545.
10. T.J. Fuller-Rowell, D. Rees, S. Quegan, R.J. Moffett and G.J. Bailey: Interactions between neutral thermospheric composition and the polar ionosphere using a coupled ionosphere-thermosphere model. *J. Geophys. Res.* 92, (1987) 7744.
11. J.W. Freeman, R.A. Wolf, G.-H. Voigt, R.W. Spiro, R.V. Hilmer and J. Shade: Project for the development of a magnetospheric specification model. Proc. Symposium on "The Effect of the Ionosphere Communications, Navigation, and Surveillance Systems", Springfield, Virginia, May 1987, paper 4A-4.
12. B.J. Watkins and S.-I. Akasofu: A numerical prediction of ionospheric conditions after an intense solar flare. Proc. Symposium on "The Effect of the Ionosphere on Communications, Navigation, and Surveillance Systems", Springfield, Virginia, May 1987, paper 6-4.

APPENDIX

1.8. URSI WORKSHOP ON IONOSPHERIC MODELLING^(*)

Boulder, Colorado, USA, 12-14 August 1986

Report by Charles M. Rush

The Workshop on Practical Aspects of Ionospheric Modelling was held at the National Center for Atmospheric Research in Boulder, Colorado from 12 to 14 August 1986. It was attended by 33 scientists from 5 countries. Its purpose was to bring together ionospheric model builders and ionospheric model users to exchange ideas, review current work and develop recommendations for further activity. To this end, the workshop has to be considered a success. Scientists and practitioners whose experience and expertise spanned the range from theoretical ionospheric modelling to development of ionospheric propagation prediction programmes met for 3 days and discussed the various aspects of ionospheric modelling in an atmosphere that can accurately be described as open and constructive.

The following topics were discussed: Neutral Atmospheric Modelling, Theoretical Ionospheric Modelling, Empirical Ionospheric Modelling, Propagation System Prediction Requirements, Data Needed to Verify/Quantify Models.

The major points that emerged from the discussions are listed below.

1. Both global and localized neutral atmospheric models were needed for ionospheric modelling applications. The global models are needed better to understand the overall physics and dynamics of the upper atmosphere. The localized models are needed to interpret specific ionospheric features and observations.
2. An improved ionospheric model is needed in the Thermospheric General Circulation Model. In particular, a direct coupling between the ionospheric model and the thermospheric model is required in the computer simulations.
3. Values of the global distributions of thermospheric winds have been developed for specific time periods and expressed in terms of vector spherical harmonics (VSH). There was a general feeling that VSH coefficients for standard periods, i.e. equinox, solstice, solar minimum and solar maximum are required for incorporation into theoretical ionospheric models.
4. Theoretical ionospheric models were felt to be extremely useful in interpolating observations into regions where measurements are sparse or non-existent.
5. Theoretical ionospheric models should be used to test the sensitivity of calculated output parameters (electron density, electron temperature,

^(*)Extract from URSI Information Bulletin No. 239, December 1986.

etc.) to changes in input parameters (production rates, loss rates, etc.). These results are extremely important for deciding where to make investments for measurements of required parameters that can lead to better ionospheric predictions.

6. There is a need for semi-empirical models of the high latitude ionosphere that are based on the output of theoretical ionospheric models.
7. The International Reference Ionosphere (IRI) has been extensively studied and outstanding developments have been made. Further work is needed in order to bring the results of the IRI closer to reality. In particular, the high latitude part of the model needs to be improved.
8. The IRI is particularly geared for aeronomy applications; for telecommunication purposes, it may be overly specific. Further work addressing the applications of the IRI for telecommunication system performance predictions is needed.
9. Further improvements to the existing global maps of ionospheric parameters, particularly foF2, need to be accomplished in order to lead to better predictions of the performance of ionospheric-dependent telecommunication systems.
10. Observations of the mean behaviour of the ionosphere and the variability about the mean continue to be needed. Furthermore, both the mean and the variability must be quantified for inclusion into performance prediction methods in order that the prediction methods yield results that are of value to the telecommunication system user.
11. There is a need to have a standardized set of data that can be used to verify ionospheric models. These data should be independent of the models that are being verified. The data need to be representative of the entire range of season, solar, and geomagnetic activity variations that is observed in practice.
12. It must be appreciated by both ionospheric model builder and ionospheric model user that the usefulness of a model or a prediction method is dependent upon how long into the future the prediction or the model can be applied with accuracy.

There were a number of recommendations made at the workshop that addressed the points enumerated above. These recommendations, along with descriptions of specific issues related to ionospheric model development and use are provided in the full report of the workshop that will be available shortly.

Table 1Modelling activities

<u>Topic</u>	<u>Quantities</u>	<u>Examples</u>
Neutral atmosphere	Temperature, density, composition	MSIS CIRA
Thermosphere dynamics	Winds and tides, temperature, density, composition.	Uni. College, London. NCAR
Ionosphere (mathematical)	Electron and ion densities, flows, temperatures.	Uni. of Sheffield Utah State Uni.
Ionosphere (empirical)	Electron density, conductivity, electron content, irregularities, electric fields.	IRI Bent
Propagation	Max. usable frequency, signal strength, noise, angle of arrival, etc.	ITS-78 IONCAP ICED AMBCOM (see Table 2)
Magnetosphere	Convection, particles	Rice Uni.
Comprehensive	Solar wind + ionosphere	Uni. of Alaska

Table 2Mainframe computer prediction models for ionospheric characteristics, MUF's, noise and system performance

<u>MODEL</u>	<u>PROGRAM NAME</u>	<u>SOURCE ORGANISATION</u>
IONOSPHERIC CHARACTERISTICS	WOMAP	CCIR
	HRMNTH	CCIR
MUF's	MUFFY	CCIR
	MINIMUMUF 3.5	NOSC
NOISE	NOISEY	CCIR
SYSTEM PERFORMANCE	HFMUFES	ITS
	IONCAP	ITS
	APPLAB	RAL
	PROPHET	NOSC
	AMBCOM	SRI
	CCIR 252	CCIR
	CCIR SUP252	CCIR
	REP 894	CCIR

ITS - Institute for Telecommunication Sciences, Boulder, Colorado
 NOSC - Naval Ocean Systems Center, San Diego, California
 RAL - Rutherford Appleton Laboratory, Didcot, Oxon
 SRI - SRI International, Menlo Park, California.

(Table from P.A. Bradley, private communication)

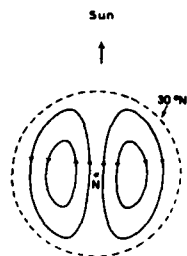


Fig. 1 S_q current system due to the motion of the feet of magnetospheric field-lines over the pole. (From J.A. Ratcliffe, *An Introduction to the Ionosphere and Magnetosphere*, Cambridge University Press, 1972).

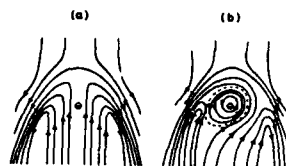


Fig. 2 Patterns of magnetospheric circulation in the equatorial plane: (a) due to "friction" at the magnetopause; (b) including the effect of the Earth's rotation. (After A. Mishida, *J. Geophys. Res.* **71**, 5669, 1966).

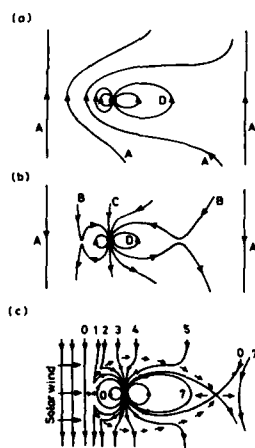


Fig. 3 Terrestrial and solar-wind fields in polar section: (a) northward IMF; (b) southward IMF; (c) circulation due to flow of solar wind (After C.T. Russell, *Critical Problems of Magnetospheric Physics*, 1972, and R.H. Levy et al., *Am. Int. Astronaut. Astronaut J.* **2**, 2065, 1964).

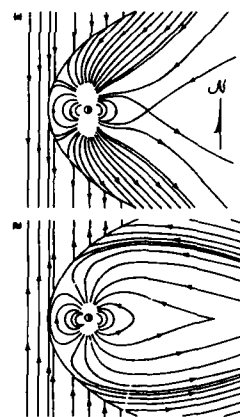


Fig. 4 Magnetic field topology with IMF (a) southward, (b) northward. (T.A. Potemra, *Johns Hopkins APL Tech. Digest*, **4**, 276, 1983).

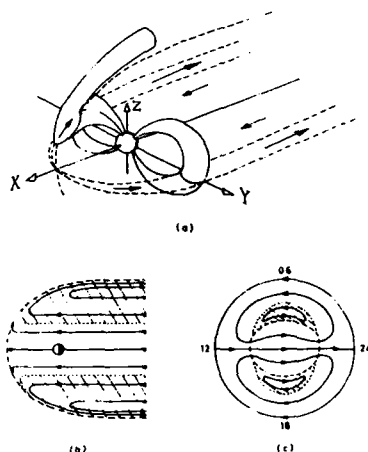


Fig. 5 Circulation due to viscous and magnetic drag in combination: (a) flux tube motions; (b) equatorial plane; (c) northern polar region. The hatched region is driven by the boundary layers. (S.W.H. Cowley, *Rev. Geophys. Space Phys.*, **20**, 531, 1982).

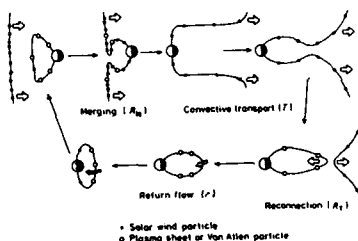


Fig. 7 History of a selected field-line. (After S.-I. Akasofu, Chapman Memorial Lecture, 1973).

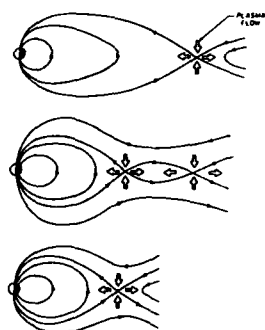


Fig. 9 Formation of second neutral line in a substorm. (J.L. Burch, *The Upper Atmosphere and Magnetosphere*, Nat. Ac. Sci. Report, Washington, D.C. 1977, p.42).

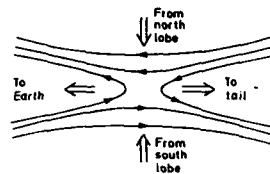


Fig. 6 X-type neutral line in the magnetotail.

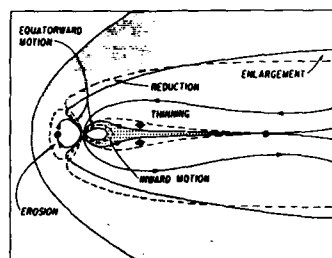


Fig. 8 Changes in the magnetosphere during the growth phase of a substorm. (R.L. McPherron et al., *J. Geophys. Res.* **78**, 3131, 1973).

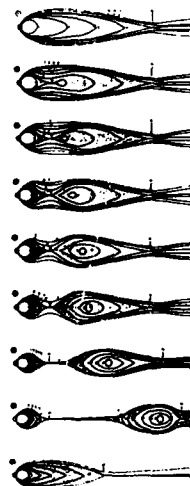


Fig. 10 Sequence of events in the magnetotail during a substorm. (R.L. McPherron (after E.W. Hones), *Rev. Geophys. Space Phys.* **17**, 657, 1979).

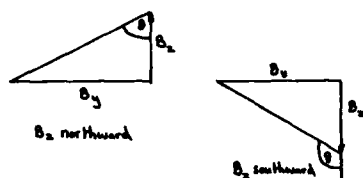
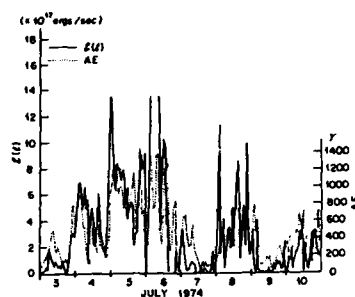
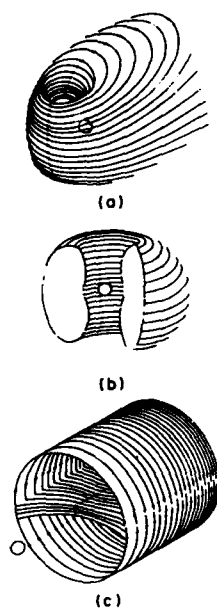
Fig. 11 Definition of θ for Equation (6).Fig. 12 Correlation between AE and ϵ for a storm in July 1974. (S.-I. Akasofu, Planet. Space Sci., 27, 429, 1979).

Fig. 13 Magnetospheric current systems: (a) magnetopause (Chapman-Ferraro); (b) ring; (c) tail. (W.P. Olsen, Adv. Space Res., 2, 13, 1982).

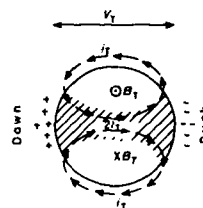


Fig. 14 Tail current as seen from the Earth. (After L. Svalgaard, NASA Report SP-366, 1975).

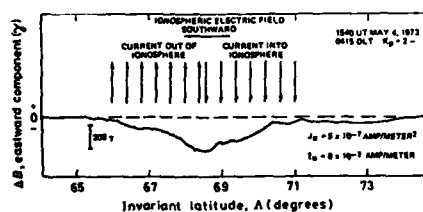


Fig. 15 Magnetic signature of a Birkeland current. (A.J. Zmuda and J.C. Armstrong, J. Geophys. Res., 79, 4611, 1974).

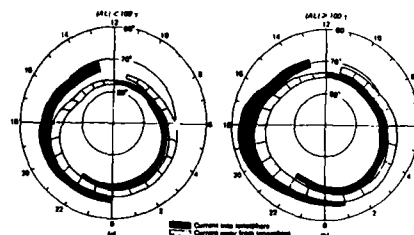


Fig. 16 Distribution of Birkeland currents during (a) quiet and (b) active disturbances (T. Iijima and T.A. Potemra, J. Geophys. Res., 83, 599, 1978).

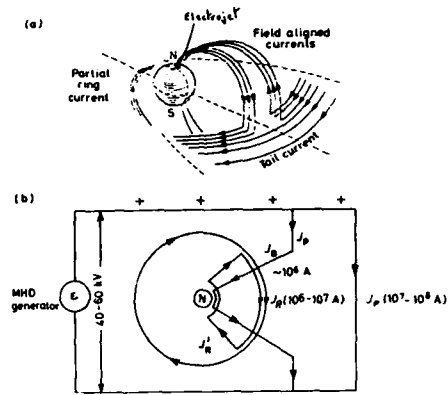


Fig. 17 Substorm currents: (a) pictorial; (b) schematic. (After L. Svalgaard, NASA Report SP-366, 1975, and W.J. Heikila, J. Geophys. Res. **79**, 2476, 1974).

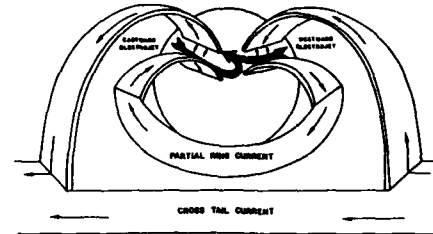


Fig. 18 Relation between ionospheric and magnetospheric currents. (D.W. Swift, Rev. Geophys. Space Phys. **17**, 681, 1979).

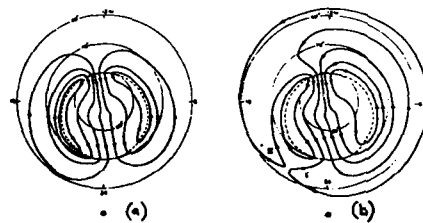


Fig. 19 Polar convection patterns (a) without and (b) with co-rotation field. (R.W. Spiro et al., J. Geophys. Res., **82**, 4255, 1978).

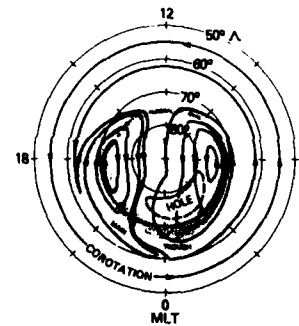


Fig. 20 Troughs in relation to drift pattern. (R.J. Moffett and S. Quegan, J. Atmos. Terr. Phys. **42**, 315, 1983).

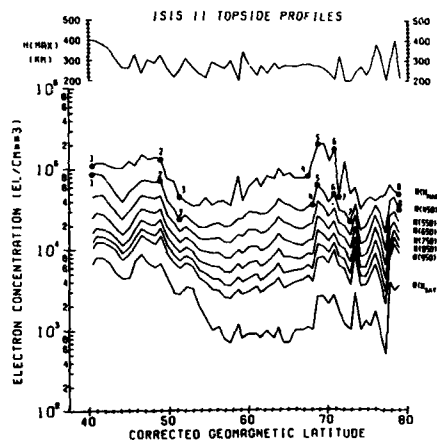


Fig. 21 Features of the main trough from topside sounder data. 4-5 denotes the poleward edge. (M. Mendillo and C.C. Chacko, J. Geophys. Res. **82**, 5129, 1977).

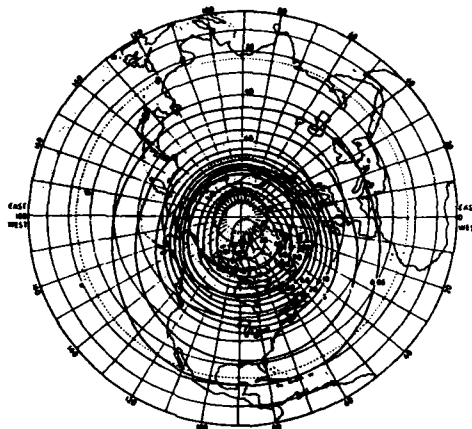


Fig. 22 Northern auroral zone, showing the percentage of good observing nights when aurora may be seen (From D.R. Bates, *Physics of the Upper Atmosphere* (Ed. J.A. Ratcliffe), Academic Press, 1960).

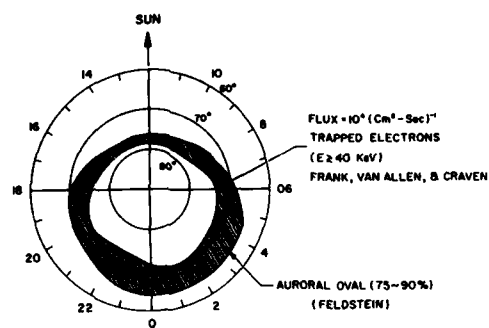


Fig. 23 Auroral oval in relation to the 40 keV trapping boundary (S.-I. Akasofu, *Polar and Magnetospheric Substorms*, Reidel, 1968).

THE HIGH-LATITUDE IONOSPHERE
PHENOMENOLOGY, IRREGULARITY DISTRIBUTIONS, TRANSPORT AND
MAGNETOSPHERIC COUPLING

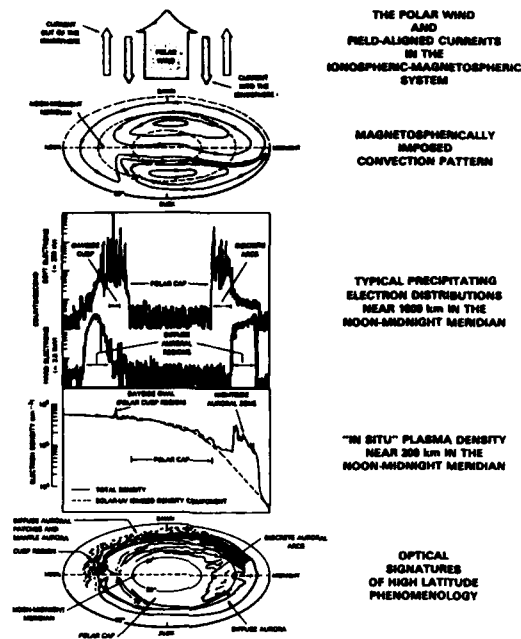


Fig. 24 A summary of the high-latitude ionosphere.
 (E.P. Szuszczewicz, Artificial Satellites 22,
 143, 1987).

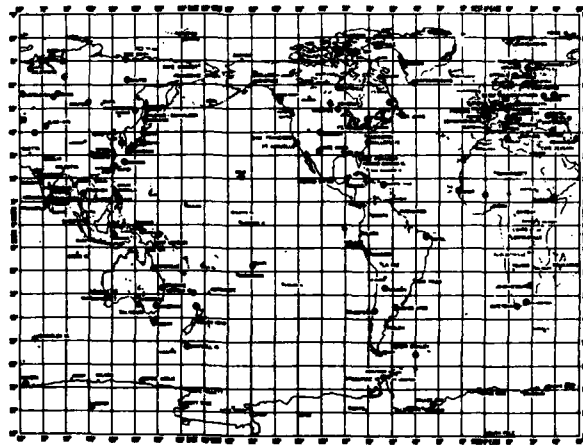


Fig. 25 World-wide distribution of ionosondes. (K. Davies, Artificial Satellites 22, 167, 1987).

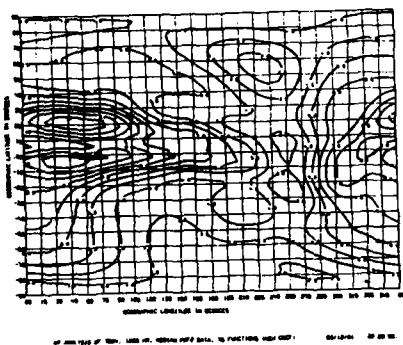


Fig. 26 Predicted monthly median critical frequencies. (K. Davies, *Artificial Satellites* 22, 167, 1987).

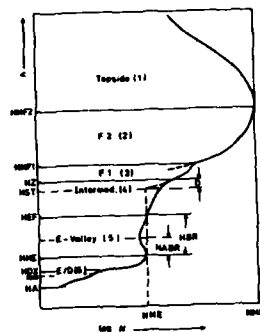


Fig. 27 Segments of the International Reference Ionosphere. (D. Billets, *Proc. Modelling Workshop*, Boulder, 1986, p33).

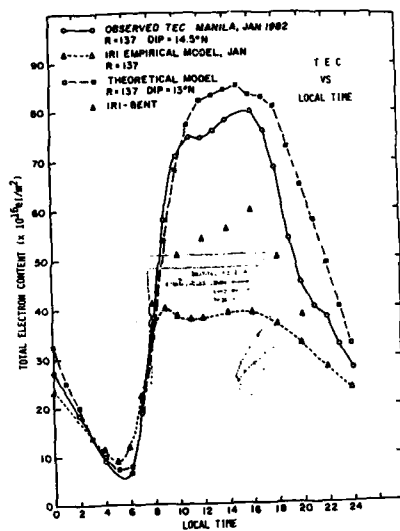


Fig. 28 Predicted and observed electron content over Manila. (D.N. Anderson, *Proc. Modelling Workshop*, Boulder, 1986, p19).

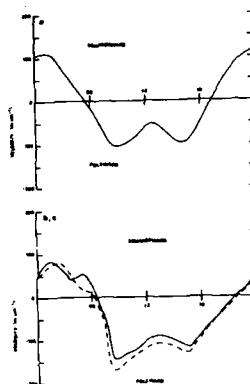


Fig. 29 Observed (a) and computed (b,c) meridional wind for winter, 45° latitude, 300 km altitude. (a) is from Ameyo (1974); (b) dashed line takes solar heating only; (c) solid line adds an electric field. (T.J. Fuller-Rowell and D. Rees, *J. Atmos. Sci.* 27, 2545, 1980).

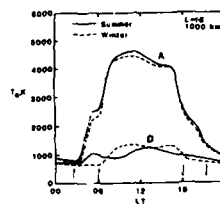


Fig. 30 Computed electron temperature at 1000 km altitude with (A) and without (D) the heating by photoelectrons. (G.C. Sethia et al., 22, 321, 1985).

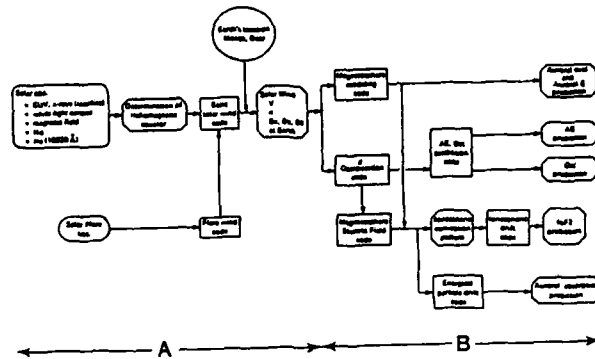


Fig. 31 A scheme for predicting geomagnetic storm effects. (B.J. Watkins and S.-I. Akasofu, Proceeding of Symposium on "The Effect of the Ionosphere on Communication, Navigation and Surveillance Systems", Virginia, U.S.A., (1987), paper 6-4).

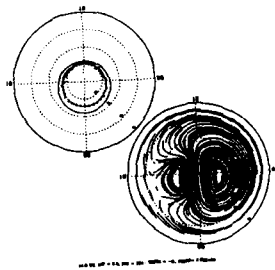


Fig. 32 Auroral oval and polar convection pattern. (B.J. Watkins and S.-I. Akasofu, as figure 31).

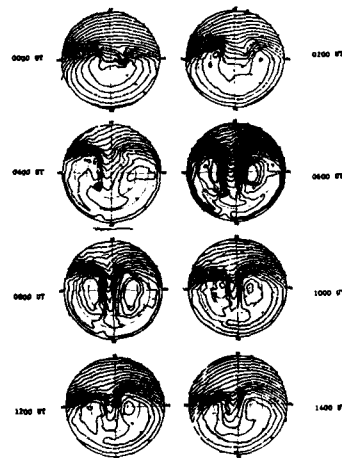


Fig. 33 Computed electron density contours during a simulated storm. (B.J. Watkins and S.-I. Akasofu, as figure 31).

SATELLITE IN-SITU PROBING

E.J. Fremouw
NorthWest Research Associates, Inc.
Bellevue, WA 98040-3207 USA

SUMMARY

The theme of this lecture series directs our attention to radiowave propagation media at high latitudes. Of those various media that affect radio propagation, the one that can be probed *in situ* by means of satellites is the ionosphere. The portion of the ionosphere that can be so probed repeatedly over long periods of time is the F layer. In this talk, we'll focus on phenomena that affect and/or can be sensed in the F layer. Specifically, we'll review techniques for, and some recent results on, the two major phenomena identified in the series theme as affecting the high-latitude ionosphere: (1) particle precipitation and its resulting ionization and (2) ExB drift and the plasma-density irregularities that result therefrom, especially those that produce radiowave scintillation.

Regarding particle precipitation, we'll confine our attention to electrons in the range of a few tens of eV to a few tens of keV, excluding other species and energies that produce ionization lower than the E layer. We'll also be concerned with upwelling electrons and the question of balance between currents flowing into and out of the ionosphere, insofar as they can be sensed on board a satellite in the F layer. Thus, we shall consider measurement of the magnetic field, especially the local perturbation field. We'll also indicate the utility of optical remote sensing, in the form of imaging from a platform in the F layer, for providing a "plan view" related to point measurements on the platform.

Primarily we'll consider *in-situ* measurements of the F-layer thermal plasma, mainly its electron and total ion density, temperature, and drift, giving little attention to the identification of ion species. Accordingly, we'll briefly review the measurement principles of the Langmuir probe, the retarding-potential analyzer, and the ion drift meter. Our consideration of the *in-situ* electric field will be limited primarily to the d.c. convection field, but it will include structure therein.

By way of example, we'll describe in some detail the complement of instruments on board the DNA HiLat and Polar BEAR satellites and results therefrom. This example will be augmented by consideration of certain of the instruments on and results from the Atmospheric and Dynamics Explorers and ARCAD-3, as well as from operational spacecraft of the Defense Meteorological Satellite Program. We'll emphasize results bearing on densities and drifts of the F-layer plasma and its gradients, which lead to scintillation-producing irregularities.

1. INTRODUCTION

In Lecture 3, we considered the effects of the ionosphere on radio waves propagated through it and the use of such transionospheric waves as probes for research. For assessing the effects, the waves themselves provide the most direct probe. As does any technique, however, such probing has its limitations. Others must be invoked to provide the comprehensive description needed for understanding the ionospheric medium well enough to make detailed predictions about it.

In Lecture 9, Dr. Bauer will describe the remote sensing that is possible by means of radio backscatter, including the powerful incoherent-scatter technique. Here, we consider those techniques employed aboard satellites in the medium itself. Some of what they tell us can be inferred also by means of incoherent scatter. Among their advantages over that technique are availability of (1) substantially finer resolution and (2) essentially global coverage. Among their relative disadvantages is the fact that they cannot provide sustained measurements in a given locale. As contrasted with transionospheric radio probing, they (1) can provide information on additional physical variables, and (2) are not affected by diffraction as are radio waves. They also augment the path-integral information imposed on the transionospheric waves with point measurements along a track in the medium.

Primarily, we'll consider *in-situ* probes employed in the F layer, at altitudes of several hundred to a thousand km or so. Many of the same techniques are suitable at higher altitudes in the magnetosphere, but we'll limit our attention to the ionosphere, where the main interaction with radio waves takes place. They may also be employed in the E layer, near 100 km altitude. Drag limits the continuity and repeatability of satellite probing there, however, and rocket probing is more common. We'll limit our E-layer attention to optical remote sensing of it from the same satellites used for *in-situ* sensing of the F layer above.

Of primary interest for application to problems of radio propagation are measurements of plasma density. The *in-situ* techniques for that purpose measure either electron or ion density, the two being equal on all scale sizes of interest. Some also can provide estimates of the density of individual ion species, but we shall not consider this point since it is of little direct consequence to radio propagation. What is of consequence is an understanding of the processes by which the ionospheric plasma may develop structure on scale sizes of many tens of meters to a few tens of km, which can refract and diffract passing radio waves. Foremost among the drivers of such structuring are the local electric and magnetic fields, which largely control the dynamics of the F-layer plasma. Electron and ion temperature also are of interest, dynamically, through control of collision frequency and also as indicators of the age of the plasma.

Thus, the plasma-electrodynamical measurements with which we shall be concerned primarily are those of the following parameters: plasma density, N ; electron and ion temperature, T_e and T_i ; and the magnetic and electric fields, B and E . (Boldface denotes vector quantities.) The last of this set (E) may be inferred from the plasma drift velocity, V , which also is of inherent interest, and we shall deal with it primarily in the latter form. We are interested both in the general level of these parameters and in their spatial variations, which are recorded as temporal fluctuations while the satellite moves through a measurement region. Plasma-density fluctuations are of concern directly because they represent variations in radio refractive index. Magnetic-field variations may be interpreted in terms of local currents, and variations in V or E reveal regions of plasma-velocity shear.

In addition to the foregoing, we are concerned with energetic electrons passing through the measurement region (i.e., electrons with energy exceeding that of the thermal electrons in the ambient plasma). They are of interest in our context because, through collisions with the background neutral gas, they can produce additional plasma locally and in the E layer beneath the satellite. To a good approximation for many purposes, geomagnetic flux tubes behave as highly conducting surfaces of constant electrostatic potential. The plasma density in the E layer exerts dominant control on conductivity between flux tubes and thereby influences the electrodynamics in the F layer. The final important influence on the dynamics of F-layer plasma is that of collisions with the neutral gas. A complete treatment would consider techniques for probing the density of the latter and its velocity (thermospheric winds), but time constraints prevent our doing so in this talk.

2.0 MEASUREMENT TECHNIQUES

In this section, we describe common methods for measuring the foregoing parameters, limiting our discussion mainly to one instrument type for each. As examples of instrument types, we'll use those currently in orbit on the DNA HiLat¹ and Polar BEAR² Satellites.

2.1 Plasma Density and Temperature

Measurement of plasma density and temperature in space is performed by essentially the same methods employed in the laboratory. Aside from radio-frequency resonance techniques, most instruments exploit the "Langmuir characteristic" between the current drawn from a plasma to a probe placed in it and the potential applied to the probe.³ The current-voltage curve for an idealized Langmuir probe is presented in Figure 1, in which negative (i.e., electron) current increases upward. Owing to the large mass difference between ions and electrons and the consequently greater thermal velocity of the latter, satellites typically acquire a net electronic charge that places them at a negative potential, ϕ_s , on the order of minus one volt relative to the plasma. A probe maintained at this "floating potential" will draw an ion current that just balances the thermal electron current, the net current then being zero.

If a more negative potential is applied to the probe, all electrons are retarded and a positive current is drawn from the resulting thin ion "sheath" surrounding it. In this negative (by more than about a volt) potential range, the current measured is proportional to the number density, N_i , of positive ions in the plasma being traversed by the satellite. If a positive potential (relative to the plasma) is applied to the probe, the opposite happens. Local ions are repelled, and a negative current is drawn from a thin electron sheath. Here, the measured current is proportional to electron density, N_e . Since $N_e = N_i$ in the undisturbed plasma, either "saturation" condition may be employed to measure the plasma density.

For slightly negative voltage, between the floating and plasma potentials, increasing the voltage toward zero results in rapidly increasing current. In this range, the first incremental increase in voltage permits the most energetic electrons in the thermal plasma to reach the probe, while retarding the rest. Each further increment accepts electrons of decreasing energy, until all are participating in the measured current at the upper knee of the curve. The slope of the transition between the two saturation currents is an inverse measure of the spread in energy, or temperature, T_e , of the electron gas.

For various practical reasons, individual instruments usually are designed to measure only a portion of the Langmuir characteristic curve. On HiLat, for instance, a Langmuir probe was flown as an electron sensor intended primarily to record fine structure in plasma density. Its characteristic is illustrated in Figure 2, in which the horizontal scale now is the potential, ϕ_p , applied to the probe relative to the spacecraft "ground" potential, ϕ_s . The solid curve is the theoretical response given⁴ in the retarding region, by

$$I = -\lambda_f e N_e v_e \exp(-e\phi/kT_e), \quad (1)$$

where

- λ_f = effective probe area, including efficiency, etc.,
- e = electronic charge,
- v_e = most probable electron speed = $(2kT_e/m_e)^{1/2}$,
- $\phi = \phi_p + \phi_s$,
- k = Boltzman's constant,
- and m_e = electronic mass.

In the acceleration region near saturation, it is given⁴ by

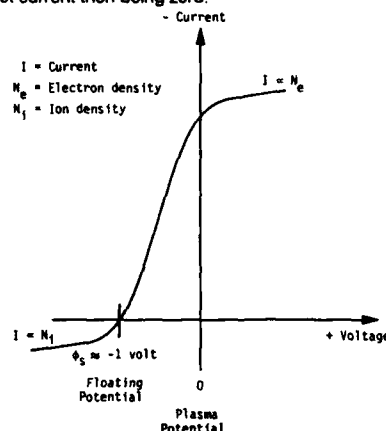


Fig. 1. "Langmuir characteristic" relating current drawn from a probe imbedded in a plasma to the potential applied to it.

$$I = -A_f e N_e v_e [1 + (e\phi/kT_e)] . \quad (2)$$

Note that when (1) is plotted in semi-logarithmic coordinates, as in Figure 2, the slope of the curve is inversely proportional to T_e . In fact, for the Langmuir probe on HiLat,⁴ the logarithmic slope is $5040^\circ\text{K}/T_e$.

Two departures from the ideal Langmuir characteristic are indicated by the dots in Figure 2. First, two thermal-electron populations are indicated, a relatively dense and cold population and a second less dense and warmer population. Such a situation is a complication, especially for automated data processing, but it does not represent a defect in the technique. The up-turn of data points at the lower left of the figure, however, does represent a limitation, due to locally produced electrons that reach the collector. Specifically, it is possible for photoelectrons and other secondaries to reach the collector from other parts of the apparatus.

As it turned out, the Langmuir probe was the only instrument damaged during HiLat's launch and/or orbital insertion, and it has not been used. Its counterpart ion sensor, a retarding potential analyzer (RPA)⁵, was not damaged, and it continues to operate well. This type of instrument, which also sometimes is called an "ion trap,"⁶ separates the functions of sampling and collecting.³ HiLat is three-axis stabilized, and its RPA employs a Faraday cup, shown in Figure 3, which faces the ram direction and which has a circular aperture of 2.54 cm diameter. All ions pass through the aperture freely as the spacecraft moves supersonically through the ion gas, the ground plane and aperture grids ensuring straight trajectories by virtue of their electrostatic uniformity. Internally, a suppressor grid is biased substantially negative to exclude electrons and to accelerate ions. Between the aperture and suppressor grids is the retarding grid, which is swept with a retarding potential to separate ions according to energy, including that gained by virtue of the satellite potential and motion. Any satellite undergoes variations in its potential relative to that of the surrounding plasma as the plasma density varies and due to charging by energetic electrons. Steps have been taken on HiLat to isolate the RPA and its companion Ion Drift Meter (IDM) from these variations.

An ion sensor has a more complicated current-voltage characteristic than does an electron sensor, owing to the different masses of multiple ion species. For each species, there is a characteristic similar to that described for electrons by (1) and (2). Careful analysis permits separation of information for different species, but this is not attempted in synoptic processing carried out routinely on HiLat data. Moreover, the satellite velocity enters into the characteristic since it is large compared with ion thermal and drift velocities. One result⁴ is that, for $\phi \geq 0$, the argument of the exponential in (1) is replaced by the negative of

$$x_i^2 = [v_r - (2e\phi/m_i)^{1/2}]^2 v_i^{-2} , \quad (3)$$

where, in the earth reference frame,

$$v_r = v_n - v_{sn} ,$$

v_n = component of bulk plasma velocity normal to aperture,

v_{sn} = component of satellite velocity normal to aperture,

v_i = most probable ion thermal speed = $(2kT_i/m_i)^{1/2}$,

and m_i = mass of the ion species.

When $\phi < 0$, the corresponding quantity in (2) is replaced by

$$x_i = v_r/v_i . \quad (4)$$

The full characteristic, for one singly charged species, is⁴

$$I = A_f e N_i (\pi^{1/2} v_r [1 + \text{erf}(x_i)] + v_i \exp(-x_i^2)) , \quad (5)$$

with x_i defined by (3) or (4) depending on the sign of ϕ .

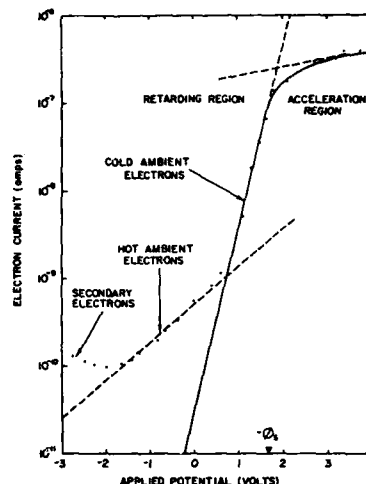


Fig. 2. Example of current-voltage characteristic for Langmuir probe flown on HiLat. Solid line represents theoretical response. Dots represent data points during an applied-voltage sweep. (From Ref. 4.)

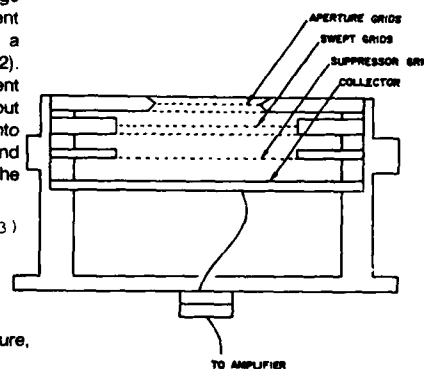


Fig. 3. Cross-section of Retarding Potential Analyzer (RPA) on HiLat Satellite. (From Ref. 4.)

With the aperture oriented in the ram direction, v_{sn} is negative, and v_r is positive and large compared with v_i . The characteristic curve in Figure 1 thereby is effectively biased to the right. With zero applied potential, the exponential term is negligible, and the error function is near unity. The current, proportional to $v_r N_i$, results from the flux of all ions swept up by the ion trap in its motion through the plasma. As a retarding potential is applied, increasingly energetic ions are rejected. Again the rate of change of current as the potential is swept depends upon temperature. In the presence of several ion species, plateaus of constant current can be interpreted in terms of relative abundance. In general, considerable information on the ion gas can be extracted by careful least-squares fitting of the characteristic curve.

2.2 Plasma Drift Velocity

In the topside F layer, collision frequencies are smaller than the ion gyro frequency. Accordingly,⁷ the electrons and ions tend to move together with an \mathbf{ExB} drift perpendicular to both the largely constant magnetic field and the much more variable electric field. Measurement of either the drift or the electric field, then, can be interpreted in terms of the other, and the drift velocity itself is important as regards generation of plasma-density structures. Since orbital considerations render the satellite velocity known in the earth frame, evaluation of v_r in (3), (4), and (5) by means of an RPA permits partial determination of plasma drift velocity in that frame, namely evaluation of the component normal to the instrument aperture. This can be done by noting the applied potential at which the ion current undergoes an inflection, at which point $x_i = 0$ in (3) and (5). Two or more such points (due to two or more ion species) permit determination of both the instrument floating potential and v_r . Once v_r is determined, N_i can be evaluated from the saturation current.

Typically, as on HiLat, the remaining two velocity components (in the aperture plane of the RPA) are determined by means of a mutually aligned ion drift meter (IDM). The IDM also employs a Faraday cup with aperture and suppressor grids, but it does not require a retarding grid, and its collector is split to permit measurement of the angle of arrival of the ions it traps. Both RPA's and IDM's were employed in the Atmosphere Explorer^{5,8} (AE) and Dynamics Explorer⁹ (DE) programs. The IDM principal is illustrated in Figure 4, which shows the configuration used on HiLat⁴ and on spacecraft in the Defense Meteorological Satellite Program¹⁰ (DMSP). The upper view is from either above or below the spacecraft. A stream of ions entering through the aperture at a horizontal angle, α , from the normal is intercepted by a larger area on one half of the collector than on the other half. A view from the side would be identical except that α would represent a vertical angle. The lower view is from the front or back of the spacecraft looking at the square aperture (crosshatched) and the four segments (A, B, C, D) of the collector.

The angle is determined by connecting segments A and B to one electrometer and segments D and C to another and then measuring the ratio of the currents to the two electrometers. The two currents are given by

$$I_{AB} = (\lambda_f/w) e N_i v_r (w/2 - d \tan \alpha) \quad (6a)$$

and

$$I_{CD} = (\lambda_f/w) e N_i v_r (w/2 + d \tan \alpha) \quad (6b)$$

Clearly, one can determine $\tan \alpha$ from the ratio of the currents since the width, w , of the aperture and the depth, d , of the Faraday cup are known. Moreover, with v_r and v_n determined from the RPA, the component of plasma drift velocity parallel to the line separating segments A and D from segments B and C may be computed from the angle. Obviously the same procedure can be followed to obtain the remaining orthogonal component (parallel to the line separating A and B from C and D) by connecting segments A and D to one electrometer and segments B and C to the other and measuring the ratio of those currents. Thus, the combination of an RPA and an IDM yields the complete vector drift velocity of the plasma in three orthogonal spacecraft coordinates. Given information on spacecraft attitude, the vector can then be expressed in any desired external coordinate system.

The total current collected by an IDM is the same as the saturation current collected by an RPA with zero retarding voltage applied and is proportional to $N_i v_r$. Thus, if either N_i or the ram velocity, v_r , is available from another source such as an RPA, the IDM also can yield the other. In routine processing of data from HiLat, in fact, reasonably good first approximations to N_i and the cross-track velocity components are obtained by employing the negative of the satellite velocity for v_r , temporarily neglecting the relatively small part of the ram velocity actually due to plasma drift. By the same token, accurate determination of attitude is important for finally determining the vector drift velocity, because of the preponderance of the satellite velocity in the ram direction. Another useful approximation may be achieved by taking the component of plasma drift along the magnetic field to be zero, reducing the vector velocity problem to two dimensions. For this problem, the two components measured by the IDM are sufficient.

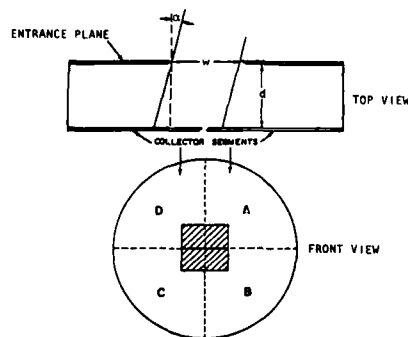


Fig. 4. Collector and aperture configuration of the ion drift meter (IDM) on HiLat. (From Ref. 4.)

2.3 Magnetic Fields and Electric Currents

A rather complete set of plasma-electrodynamical parameters is represented by the number density and temperature of electrons and ions, together with the electric and magnetic fields and electric currents therein. We have now discussed all but the final two. They are linked together even more fundamentally than are the electric field and plasma velocity. On many spacecraft, magnetometers are employed to measure both the background vector magnetic field and the perturbations to it caused by local electric currents. For instance, HiLat and Polar BEAR both carry three-axis fluxgate magnetometers.

Fluxgate magnetometers are essentially electrical transformers with saturable cores.¹¹ The primary winding typically is driven at a frequency of some kHz, driving the core into saturation for a portion of each half cycle. Any externally applied magnetic field causes an asymmetry in the voltage output from the secondary, which is proportional to the time rate of change of magnetic flux in the core. The asymmetry produces a harmonic of the input frequency, the magnitude of which depends upon the offset established by the external field, and the phase of which depends upon the direction of the external field's component along the core axis. A synchronous detector referenced to the primary senses both the intensity and phase of the harmonic, and three such devices with orthogonal cores constitute a three-axis vector magnetometer. The magnetometer on Polar BEAR¹² measures 20 such vectors per second with a resolution of 15.2 nT.

2.4 Energetic Electrons

The foregoing three subsections describe the principles of measurement of the main electrodynamical parameters of the F-layer plasma. Here we describe one method for detecting, counting, and analyzing energetic particles streaming through that plasma. As an example, we use the electron energy spectrometer on HiLat. Several techniques have been used, starting at the dawn of the space age, for measuring particle radiation from a variety of sources. The choice of technique in a given application hinges, aside from charge, largely on the flux and energy ranges. In our context, primary interest centers on electrons with energies above thermal (a few eV) to a few tens of keV. These energies are among the very lowest possessed by "particle radiation", but the fluxes involved (up to, say, 10^{10} el/cm²/sec/sr) are among the larger encountered in space measurements.¹³ The low energies require minimizing (preferably, reducing to zero) the amount of material that must be traversed in the instrument by the electrons to be counted before they reach the detector.

In HiLat, the foregoing requirement is achieved by means of a "channeltron." The channeltron is a curved glass tube, the inner surface of which is coated with a material from which secondary electrons can be emitted upon the impact of primaries. A voltage difference is applied to the two ends of the tube, producing an electric field therein. The curvature ensures that primary electrons entering at the input end impact the wall and produce secondaries, which then are accelerated toward the output end by the field and which also collide with the wall. Several secondaries are released by the impact of each primary in the energy band of interest, and subsequent, multiple impacts result in an overall number gain of several orders of magnitude. The output, which is proportional to the input flux, then is amplified and processed.

By itself, the channeltron provides no energy discrimination within the broad band of primaries that it is capable of multiplying and detecting. In HiLat, energy spectrometry is performed by means of electrostatic analyzers¹⁴, two of which are shown in Fig. 5. Each consists of (1) a collimating aperture system, (2) a pair of curved plates across which a stepped potential difference is applied, and (3) a channeltron employed as a multiplier/detector. The aperture system restricts the range of angles from which arriving electrons are admitted, to within a few degrees of normal to the

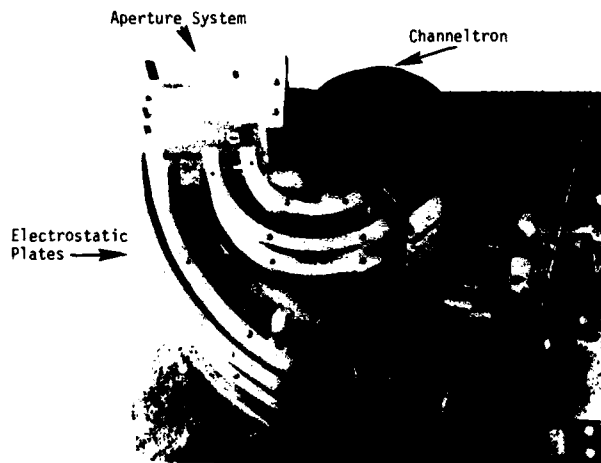


Fig. 5. One of three pairs of electrostatic analyzers used for energy spectrometry of precipitating and upwelling electrons on HiLat. (From Ref. 14.)

aperture plate. The two analyzers shown cover two different energy ranges. The one with plates having the smaller radii of curvature permits electrons with energies between 20 and 632 eV to reach the channeltron, the instantaneous energy range depending upon the potential difference between its plates. Electrons arriving with too great an energy are lost to the exterior plate, and those with too small an energy are accelerated to the interior plate. The larger-radius analyzer admits primaries with energies between 632 eV and 20 keV. The potential difference between plates in each analyzer is stepped through four values, yielding a total of eight logarithmically spaced energy bins between 20 eV and 20 keV.

On HiLat, there are three such pairs of electrostatic analyzers. One pair looks upward toward the zenith, one downward toward the nadir, and the third at an angle of 40° to the nadir. Pitch angle of precipitating electrons is not a central issue in the HiLat mission, but the third sensor pair does provide a modicum of pitch-angle information. The nadir-directed pair is intended to detect electrons upwelling from the E layer or the peak of the F layer beneath the satellite. The electron spectrometer can be operated in any of three modes, by command from the ground. In Mode 3, all three pairs of sensor are operated. In Mode 2, both analyzers of the zenith-directed pair are operated with a faster electrostatic sweep to provide greater time resolution by means of the same telemetry allotment. In Mode 1, only the low-energy analyzer of the zenith pair is operated. In this mode, 24 eight-point spectra are telemetered per sec, providing an along-track spatial resolution of between 300 and 400 meters. For many satellite-borne experiments, the element limiting resolution is telemetry capacity, especially when there is no on-board recording capability (as on HiLat).

2.5 Photometric Imaging & Spectrometry

Photometry and spectrometry of the aurora and airglow from space are well established. Imaging of the aurora also has been conducted by several techniques and at several wavelengths. One of the most helpful recent developments has been of the capability to do so at vacuum ultraviolet (vuv) wavelengths, on such satellites as DE, HiLat, Viking, and Polar BEAR. The advantage of vuv observations is that solar backscatter from the earth and the atmosphere is extremely low at these wavelengths, permitting the recording of auroral and airglow emissions on the day side as well as on the night side of the earth. Here, we briefly describe the combined visible/vuv imaging spectrophotometer on Polar BEAR, which is called AIRS, for Auroral/Ionospheric Remote Sensor.

The AIRS instrument¹⁵, which is illustrated in Figure 6, consists of a vuv spectrometer and a pair of photometers operating in the visible and near-uv band, all augmented with a telescope and a rocking mirror to produce images. The lower portion of the figure shows the spectrometer unit, the photometer unit appearing in the upper portion. Light is provided to both via the common telescope unit in the middle, behind which is located the rocking mirror. The system can operate in any one of three modes, two with the mirror fixed and one with the mirror scanning. First, the spectrometer can operate by itself, with the mirror fixed, to scan over the vuv band between approximately 118 and 180 nm every three sec, with a spectral resolution of 3 nm. With both the mirror and the spectrometer grating fixed, AIRS becomes a four-wavelength photometer. In this mode, it produces photometric records at any pair of wavelengths separated by 24 nm in the vuv band plus a pair of records at 630.0 and 391.4 nm or at 337.1 and 225.0 nm.

In the third mode, the mirror rocks to produce line scans essentially from horizon to horizon at the two selected vuv wavelengths and at the two selected visible/near-uv wavelengths. Each three-sec scan produces 326 pixels in each of the four colors. Like HiLat, Polar BEAR has no on-board recording capability, and data are telemetered in real time to several high-latitude receiving stations. An overhead pass of about 12 minutes duration produces four images roughly 6000 km across the track by 5000 km along the track, centered on the receiving station. Shorter images are produced by lower-elevation passes.

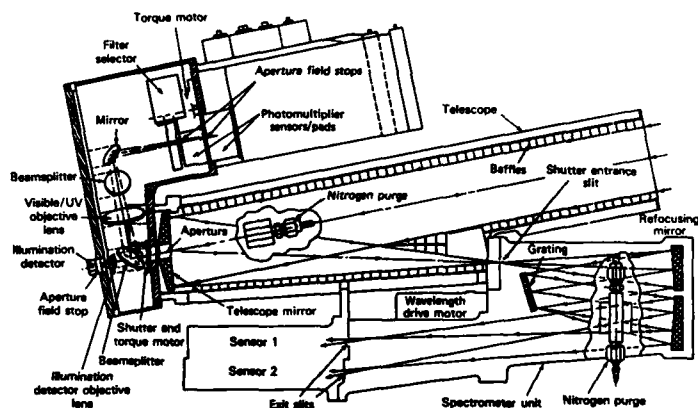


Fig. 6. AIRS optical schematic. (From Ref. 15.)

The visible and near-uv sensors are useable for auroral and airglow observations only on the night side of the earth, because of solar backscatter from the dayside atmosphere. The combined angular and temporal resolution of the photometers in this band produces a footprint in the E layer of about 23 km across the satellite track by about 35 km along the track, with a design sensitivity of about a kilorayleigh. Airglow and auroral spectra, photometric records, and images in the vuv band can be obtained on the day side as well as on the night side of the earth. In this band, the photometric footprint is about 6 by 24 km, and the design sensitivity is about 30 rayleighs.

3.0 MEASUREMENT EXAMPLES

In this section, we present measurement examples from most of the instrument types described in Section 2. To give some impression of the relevance to radiowave propagation, we begin in Figure 7 with combined data from the radio-frequency beacon^{16,17} on HiLat and two of its on-board sensors. (The reason that HiLat and Polar BEAR carry no on-board recording capability is that receiving stations exist anyway for their beacon propagation experiments.) All quantities are plotted vs. geomagnetic latitude at the relevant location. For the on-board sensors, the relevant location is that of the satellite (at approximately 800 km altitude). For the beacon parameter, the latitude employed at a particular time is that of the intersection between the ray path from satellite to receiver and the approximate peak of the F layer (taken as 350 km altitude).

The top plot shows the total flux of electrons recorded by HiLat's zenith-directed energetic-electron spectrometer in its four low-energy bins (i.e., between 20 and 632 ev). The low-energy range of precipitating particles was selected because they deposit a substantial fraction of their energy in the F layer, via collisions, and can produce plasma there.

Indeed, the poleward wall of the main plasma trough coincides with the latitudinal onset of the precipitation recorded. The trough wall is evident as the abrupt change near 59° magnetic latitude in the second plot, which shows the ion density in the topside F layer. The ion density was measured by the IDM every two sec, providing a spatial resolution of approximately 15 km. The third plot is of the cross-track (approximately east-west) plasma velocity measured at the satellite altitude by the IDM, with a resolution of approximately four km.

The bottom plot displays a measure of phase-scintillation strength. The parameter, derived from spectral analysis of the VHF (138-MHz) phase record, is the power spectral density of phase at a fluctuation frequency of 1 Hz (F-layer scale size on the order of a km), corrected for varying path length. Because of the effective altitude difference between the *in-situ* and beacon measurements, the latter cover a narrower latitude range than do the former. The steep trend in scintillation near the low-latitude trend of the beacon trace, however, is consistent with the well-known auroral (or sub-auroral) scintillation boundary^{18,19}. In this case, it appears to be co-located with the poleward trough wall (equatorward edge of the auroral F layer). Interestingly, the plasma density measured by the IDM reaches trough-like low densities in at least one depletion poleward of the boundary without a corresponding decrease in scintillation. Thus, the existence of the scintillation boundary does not stem simply from an increase in the amount of plasma interacting with the radio wave but also from an increase in the relative irregularity of that plasma.

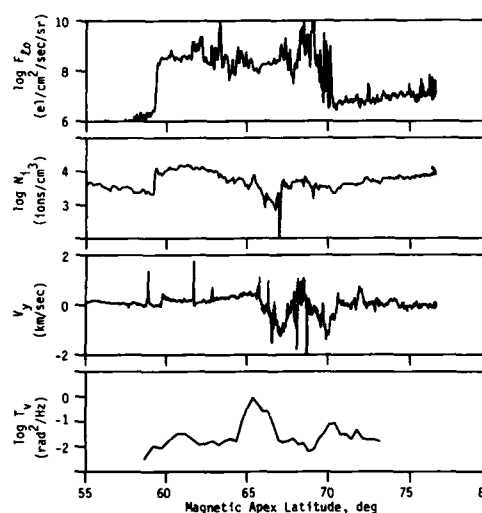


Fig. 7. Data from a HiLat pass over Poker Flat, Alaska, beginning at 0014 local (150° west meridian) time on 4 April 1987. Top to bottom: flux of low-energy (20 - 632 ev) precipitating electrons; plasma density at 800 km; cross-track plasma velocity; VHF phase-scintillation strength.

Indeed, the strongest scintillation observed during this pass occurred in a region of substantial equator-directed ion-density gradient, a region likely to be structured by the ExB instability. The region also experienced substantial velocity shear, which may produce structure by the Kelvin-Helmholtz (KH) instability. As a complication, scintillation in that location also was subject to geometrical enhancement if the scattering irregularities were aligned along L shells. It is not our intent here to sort out geometrical from geophysical effects nor the relative importance of the ExB and KH instabilities in the formation of scintillation-producing irregularities. Rather, we seek to indicate the utility of *in-situ* plasma measurements in such endeavors.

Even without coincident beacon observations, *in-situ* measurements can contribute to understanding of plasma characteristics and dynamics pertinent to transionospheric propagation. Figure 8 contains high-resolution plasma-density measurements from ARCAD 3, which has contributed to investigation of the irregularities causing equatorial spread F and scintillation.²⁰ The figure is from a study of data obtained by ARCAD at high latitudes, which has disclosed a rich variety of plasma waveforms.²¹ The figure shows a potentially important characteristic of one type of

waveform and corresponding power spectra. The upper left panel shows data obtained over one second, and the other two upper panels contain enlargements of portions thereof. The pertinent point is the "sawtooth" nature of the plasma waveform, with very abrupt changes alternating with lesser reversed gradients. Such behavior is reminiscent of the one-sided "steepening" of barium-ion clouds undergoing gradient-drift instability. The lower panels show power spectra of the upper waveforms, with best-fit power-law spectral indices and spectral breaks that may be carried over into the behavior of scintillating signals.

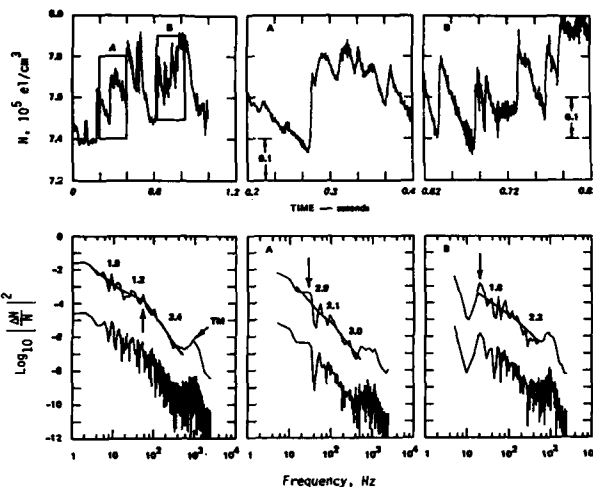


Fig. 8. High-resolution measurements of plasma density made at high latitude during Orbit 2112 of ARCAD-3 at 2103 GMT on 28 February 1982. Upper left panel shows one sec of data. Other two upper panels contain enlargements of sections A and B thereof. Note "sawtooth" character of plasma waveform. Lower panels contain corresponding power spectra. (From Ref. 21.)

Finally, we illustrate by example the utility of remote imaging in providing a "plan view" for guiding propagation studies. Figure 9 contains a copy of the central portion of a vuv image developed by AIRS during a pass by Polar BEAR through the midnight sector of the auroral oval on 24 January 1987. The brightest auroral forms lie mainly at the northern and southern edges of the oval and are clearly visible in the black-and-white figure. On the original false-color image, weaker luminosity appears between them, but we shall not be concerned with that portion of the image. The land mass in the upper middle is Greenland. The cross hairs mark the center of the image, and the satellite moved through it from south to north. The beacon/telemetry receiving station is at Sondre Stromfjord on the west coast of Greenland left of the cross hairs and just north of the aurora. The line to the left of the cross hairs marks the penetration scan of the radio line of sight through the E layer at 100 km altitude, with superposed minute ticks. We see that the E-layer penetration point scanned through the northernmost auroral arc during a few minutes early in the pass.

Figure 10 shows the effect of the E-layer arc on the HiLat beacon signals.²² In the bottom panel is the UHF dispersive-phase record, converted to the line-of-sight integral plasma density, or TEC (total electron content). The dashed line includes a correction for change in path length with zenith angle. There is more ionization to the south (in the aurora) than to the north (in the polar cap). The local increase in TEC between about 0209 and 0211 GMT coincided with the E-layer scan through the northernmost arc, which is indicated by the shaded bar in the upper panel. The incoherent-scatter radar at Sondre Stromfjord verified that the majority of plasma density in this region indeed was in the E layer and coincident with the arc.

The upper plot shows that the rms phase fluctuation experienced by the VHF (138-MHz) signal during the pass was greatest during the scan of the arc. The third prominent peak may have been enhanced geometrically, but the others should not have been so affected. Detailed analysis, yet to be completed, may show that the phase scintillations stemmed primarily from relatively large-scale gradients associated with the E-layer aurora rather than from km-scale scattering structure in the F layer. The point here is that coincident auroral imagery permits

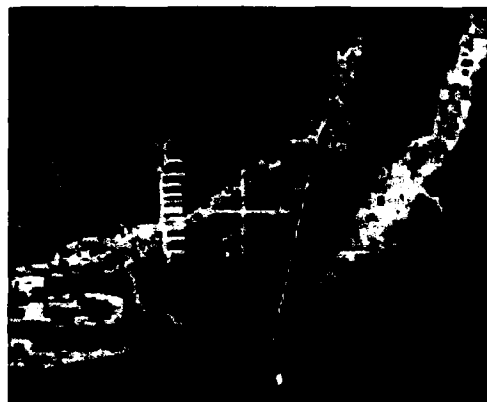


Fig. 9. Portion of a vuv image developed by AIRS during a pass by Polar BEAR over Greenland, starting at 0219 GMT on 24 January 1987. Line with minute ticks indicates scan through the E layer by the line of sight between the satellite and the beacon/telemetry receiving station at Sondre Stromfjord. (From Ref. 22.)

quick identification of situations in which this may be the case and, thereby, provides valuable guidance in analysis of scintillation and other data.

4.0 CONCLUSION

The full significance of techniques for *in-situ* probing by satellite hopefully will become apparent during the course of other lectures in this series. We have attempted here to introduce the nonspecialist to the techniques most often used in applications relating to transionospheric radio propagation. These techniques, together with satellite-borne radio probing and ground-based methods, currently are being used quite actively at high latitudes by several groups.

Coordination of techniques and of group efforts is returning considerable information and, we believe, is leading to increased understanding of the ionospheric processes that affect a wide range of radio propagation at high latitudes. Such coordination and cooperation should yield both increased applications payoff and research challenge as we move into the forthcoming years of growing solar/geophysical activity.

Acknowledgement

I hereby gratefully acknowledge the financial support extended by the Defense Nuclear Agency of the U.S. Dept. of Defense to my research efforts on topics of ionospheric physics and radiowave propagation, currently under the HiLat/Polar BEAR Satellite Program and Contract DNA001-88-C-0001.

References

- ¹HiLat Science Team, "The HiLat Satellite Mission," *Rad. Sci.*, **20** (3), May-June 1985, pp 416-424.
- ²Fremouw, E.J., Northwest Research Associates, "The Polar BEAR Ionospheric Experiments: A Pre-Launch Overview," 1986, DNA-TR-86-156.
- ³Giraud, A. and M. Petit, *Ionospheric Techniques and Phenomena*, D. Reidel Publishing Company, Dordrecht, 1978, Chapter V.
- ⁴Rich, F.J. and R.A. Heelis, Air Force Geophysics Laboratory, "Preliminary Data Processing Plan for the Thermal Plasma Experiment on the HiLat Satellite," 1983, AFGL-TR-83-0091.
- ⁵Hanson, W.B. and R.A. Heelis, "Techniques for Measuring Bulk Gas Motions from Satellites," *Space Science Instrumentation 1*, D. Reidel Publishing Company, Dordrecht, 1975.
- ⁶Carignan, G.R., "Ion and Electron Sensors," *Geoscience Instrumentation*, ed. E.A. Wolff and E. P. Mercanti, John Wiley & Sons, Inc., New York, 1974, p 337.
- ⁷Ratcliffe, J.A., *An Introduction to the Ionosphere and Magnetosphere*, Cambridge University Press, Cambridge, 1972, Chapter 7.
- ⁸Hanson, W.B., D.R. Zuccaro, C.R. Lippincott, and S. Sanatani, "The Retarding-potential Analyzer on Atmosphere Explorer," *Rad. Sci.*, **8** (4), April 1973, pp 333-339.
- ⁹Hoffman, R.A., "Dynamics Explorer," *Space Science Instrumentation 5*, D. Reidel Publishing Co., Dordrecht, 1981, pp 503-521.
- ¹⁰Rich, F., M. Smiddy, R.C. Sagalyn, W.J. Burke, P. Andersen, and W.P. Sullivan, Air Force Geophysics Laboratory, "In-flight Characteristics of the Topside Ionospheric Monitor (SSIE) on the DMSP Satellite Flight 2 and Flight 4," AFGL-TR-80-0152, 17 April 1980.
- ¹¹Skilman, T.L., "Magnetic Field Sensors," *Geoscience Instrumentation*, ed. E.A. Wolff and E.P. Mercanti, John Wiley & Sons, Inc., New York, 1974, pp 353-354.
- ¹²Bythrow, P.F., T.A. Potemra, L.J. Zanetti, F.F. Mobley, L. Scheer, and W.E. Radford, "The Polar BEAR Magnetic Field Experiment," *Johns Hopkins APL Tech. Dig.*, **8** (3), July - Sept. 1987, pp 318-323.
- ¹³Reagan, J.B., "Particle Radiation Sensors," *Geoscience Instrumentation*, ed. E.A. Wolff and E.P. Mercanti, John Wiley & Sons, Inc., New York, 1974, pp 366-386.
- ¹⁴Hardy, D., A. Huber, and J.A. Pantazis, "The Electron Flux J Sensor for HiLat," *Johns Hopkins APL Tech. Dig.*, **5** (2), April - June 1984, pp 125-130.
- ¹⁵Scheckel, F.W. and B.S. Ogorzalek, "Auroral Images from Space: Imagery, Spectroscopy, and Photometry," *Johns Hopkins APL Tech. Dig.*, **8** (3), July - Sept. 1987, pp 308-317.
- ¹⁶Cousins, M.D., R.C. Livingston, C.L. Rino, and J.F. Vickrey, "The HiLat Satellite Multifrequency Radio Beacon," *Johns Hopkins APL Tech. Dig.*, **5** (2), April - June 1984, pp 109-113.
- ¹⁷Fremouw, E.J., Northwest Research Associates, "Transionospheric Probing and Propagation," Lecture No. 3, This Lecture Series.
- ¹⁸Aarons, J., J.P. Mullen, and H.E. Whitney, "The Scintillation Boundary," *J. Geophys. Res.*, **74** (3), 1969, pp 884-889.

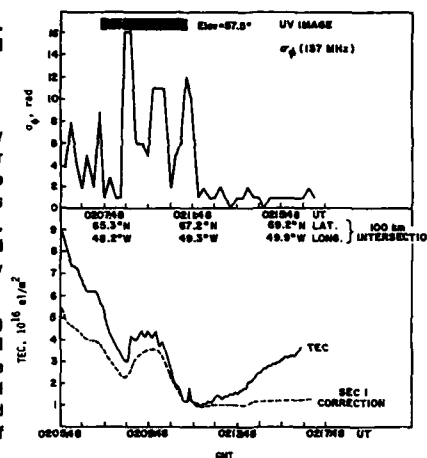


FIG. 10. Beacon data obtained during Polar BEAR pass illustrated in Figure 9. Bottom panel shows total electron content (TEC) deduced by dispersion analysis of UHF signals. Upper panel shows rms phase scintillation experienced at VHF during overlapping 30-sec computation windows. Bar at top indicates time span during which beacon line of sight scanned northern auroral arc. (From Ref. 22.)

- ¹⁹Fremouw, E.J., R.L. Leadabrand, R.C. Livingston, M.D. Cousins, C.L. Rino, B.C. Fair, and R.A. Long, "Early Results from the DNA Wideband Satellite Experiment - Complex-signal Scintillation," Rad. Sci., 13 (1), 1978, pp 167-187.
- ²⁰Beghin, D., R. Pandey, and D. Roux, "North-south Asymmetry in Quasi-monochromatic Plasma Density Irregularities Observed in the Night-time Equatorial F-Region," Adv. Space Res., 5 (4), 1985, pp 209-212.
- ²¹Tsunoda, R.T., "ARCAD-3 Experiment Results," Minutes of HiLat/P.BEAR Science Team Meeting, 18 November 1987, ed. Fremouw, Northwest Research Associates, Bellevue, 1987.
- ²²Basu, Su. and R. Eastes, "Polar BEAR UV Images, Ground ASIP," Minutes of HiLat/P.BEAR Science Team Meeting, 18 November 1987, ed. Fremouw, Northwest Research Associates, Bellevue, 1987.

INCOHERENT / COHERENT SCATTER

P. Bauer
 Directeur de Recherche
 Service d'Aéronomie du CNRS
 BP 3 91371 Verrières-le-Buisson Cedex, France

ABSTRACT

Coherent and Incoherent VHF and UHF radars provide a means for studying, in three dimensions, some of the basic physical properties of the atmosphere (from the troposphere up to the thermosphere) and of the ionosphere.

The term coherent refers here to pulse to pulse "phase coherent" integration of the scattered radar signals. This technique is applicable whenever the scattering process is stationary over the interpulse period. It is the case for the scattering of electromagnetic waves arising from turbulent atmospheric fluctuations and from ionospheric irregularities. On another hand, incoherent integration has to be used when the scattering occurs from plasma thermal fluctuations in the ionosphere.

Mesosphere - Stratosphere - Troposphere (MST) coherent radars give access to atmospheric dynamics (wind and turbulence). Aspect sensitive coherent radars allow to map the ionospheric electric field and to characterize E region plasma instabilities, whenever such instabilities are sufficiently developed. Incoherent scatter radars provide three dimensional measurements of the electron and ion temperatures, of the electron concentration and of the ion drift vector over the whole ionosphere.

Coherent and incoherent radar facilities have now been implemented on a large scale at high northern latitude when they provide a unique means of studying the intricate atmosphere-ionosphere-magnetosphere coupled system.

The implementation of major radar facilities in Antarctica is contemplated.

I. INTRODUCTION

VHF and UHF radars can collect signal returns from targets located at short distances (\sim km) up to few thousand kilometers. As in the case of HF radars [1], the targets consist in free or bounded electrons. Echoes are obtained whenever the electron density fluctuations contain the spatial Fourier component corresponding to the geometry of the radar system and to the operating wavelength. Figure 1 illustrates the condition to be met for a given incident wave vector k_i and a given scattered wave vector k_s . Scattering occurs from stratified fluctuations characterized by a vector $k = k_s - k_i$.

The radars operate coherently or incoherently according to the degree of stationarity of the medium as measured on a time interval T corresponding to the interpulse period. In practical terms, a phase coherent integration of the signals from pulse to pulse is possible when the Doppler broadening of the signals (Δf) is small as compared to T^{-1} . The interest of coherent integration lies in the possibility of adding amplitudes rather than powers. As a result, the signal to noise ratio after m coherent integrations is enhanced by a factor m : indeed the broadband noise power level increases (in the addition process) as m while the narrow band signal power level increases as m^2 .

Density fluctuations due to atmospheric turbulence (mesosphere, stratosphere, troposphere) or to E region irregularities satisfy the criterium for coherent operation. Thermal plasma fluctuations lead in general to incoherent scattering of electromagnetic waves.

The lecture deals first with the various kinds of high latitude UHF/VHF radars and then reviews some of their scientific achievements.

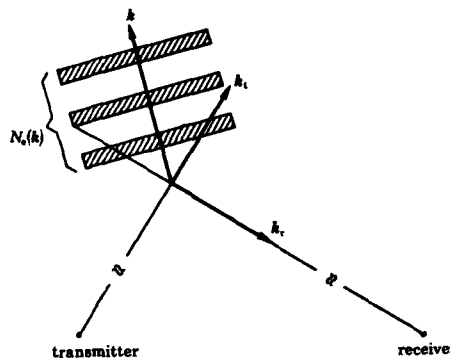


Figure 1. Geometry of radar scattering.

II. UHF/VHF HIGH LATITUDE SYSTEMS

These radars operate in the frequency range 30 MHz to 1.3 GHz. The coherent echoes are generally much stronger than the incoherent ones and this results in practice in systems which are much smaller and easier to handle for coherent use than for incoherent use. In turn, incoherent radars can also in most instances be used in a coherent mode.

II.1. MESOSPHERE - STRATOSPHERE - TROPOSPHERE RADARS (MST)

Scattering of electromagnetic waves by bound and free electrons in the atmosphere can be expressed after [1] in terms of the fluctuations in refraction index n :

$$(1) \quad n - 1 + \frac{3.73 \times 10^{-1} P_v}{T^2} + \frac{77.6 \times 10^{-6} P}{T} - \frac{N_e}{2 N_c}$$

where T is the temperature in K, P_v is the water vapor partial pressure in mb, P the atmospheric pressure in mb, N_e is the electron concentration in m^{-3} and $N_c = 1.24 \times 10^{12} f^2$ (f = frequency of the wave in Hz). Eq.1 is valid as long as the second, third and fourth terms on the right hand side are small with respect to 1. The second and third terms of the right hand side correspond respectively to contributions of bound electrons associated with fluctuations of water vapor and dry air. The fourth term corresponds to free electrons. Humidity fluctuations dominate in the lower troposphere, dry air contributions play a major role from the upper troposphere to the stratosphere, free electrons constitute the main target above 50 km. In all cases, the fluctuations are strongly dependent upon the dynamical (turbulent) properties of the atmosphere either in volume or in thin horizontal layers.

MST radars operate indifferently at all latitudes since the basic scattering processes are independent of the geomagnetic geometry. They have been initially developed at low and middle latitudes (Jicamarca, Peru; Sunset, Colorado; Arecibo, Puerto Rico...). However for the purpose of this lecture, only the high latitude ones are mentioned here. Table I lists the main characteristics of the high latitude facilities (in operation or operated until a recent date).

TABLE I - High Latitude MST Radars

	POKER FLAT	CHATANIKA	SONDRESTROMFJORD	EISCAT
Location	65.1 N, 147.4 W	65.1 N, 147.4 W	67.0 N, 51.0 W	69.6 N, 19.2 E
Type	Phased dipole array 200 m x 200 m	Parabolic Antenna Ø 27 m	Parabolic antenna Ø 27 m	Dual system UHF/VHF UHF-Tristatic 32 m dishes VHF-Parabolic cylinder 40m x 120m
Frequency MHz	49.9	1300	1300	933 (UHF) 224 (VHF)
Peak Power MW	6.4	4	4	2 (UHF) 5 (VHF)
Remark	- in operation since 1980	-operated until 1982 and transferred to Sondrestromfjord -mainly used for incoherent scatter studies	-in operation since 1982 -mainly used for incoherent scatter studies	-UHF system in operation since 1981 -VHF system in operation since 1986 -mainly used for incoherent scatter studies

Figure 2 extracted from Balsley and Gage [1], gives the lay out of the Poker Flat MST radar. It shows in particular how the two crossed dipole fields allow for a transmission in two orthogonal polarizations. It also indicates that through phasing of the arrays, it is possible to steer the antenna beam within 15° of the zenith.

An example of spectra obtained at Poker Flat from the troposphere to the mesosphere is given on figure 3. the spectra (normalized) were obtained for two pointing directions. The signal to noise ratio (S/N) expressed in dB is indicated on the right hand side. Valid data are obtained whenever S/N exceeds - 14 dB. The observed doppler shifts are used to determine wind profiles. The signal strength and/or the spectral width are related to the turbulent state of the atmosphere characterized by the refractivity turbulent structure constant C_n^2 .

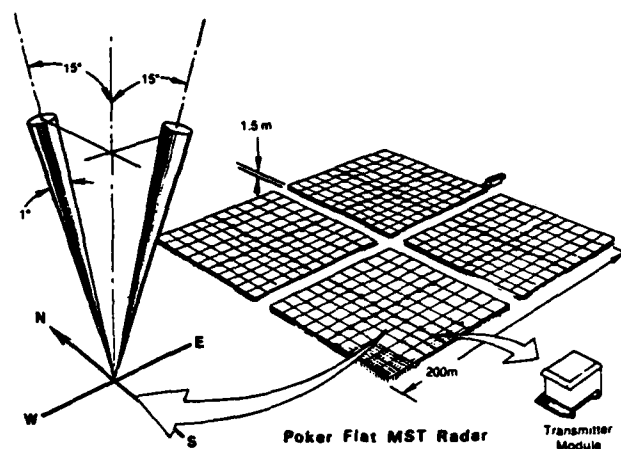


Figure 2. Artist's conception of the Poker Flat MST radar. [1]

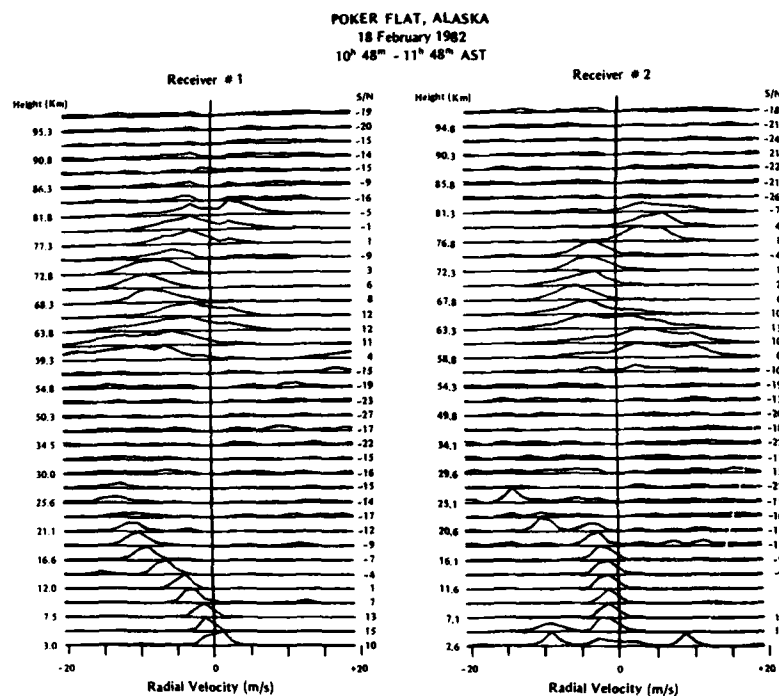


Figure 3. Sample of on-line cathode ray tube display of Doppler spectra from two polarizations (antenna beam directions) as a function of height. Height intervals are 2.2 km. Note stratospheric echoes to about 27.8 km and mesospheric echoes from about 56.6 km to 81.8 km altitude. [2]

II.2. E REGION UHF/VHF COHERENT RADARS

The field aligned irregularities which develop in the high latitude regions in the altitude range 100 to 130 km in association with the electropjet current (see e.g. [3]) scatter UHF and VHF electromagnetic waves when the wave vector k of the radar configuration (figure 1) is perpendicular to the magnetic field. The radar echoes have been classified in two types : diffuse echoes and discrete echoes. The most common are the diffuse echoes which last over long periods of time, are extended in space, and are characterized by stable spectral shapes. Discrete echoes are obtained from regions of small spatial extension and are short lived. Radar echoes are only obtained when the electric field exceeds a threshold of some 10 to 30 mV/m depending upon the radar frequency : the larger the frequency, the larger the threshold. Such electric field strengths correspond to $E \times B$ drift electron velocities of 200 to 600 $m s^{-1}$.

Table II lists the main characteristics of high latitude UHF / VHF E region coherent radars (extracted from [4]).

TABLE II - High Latitude UHF/VHF E Region coherent radars

	HONOLULU	STARE	SABRE	DAR	SLOPE POINT	ANCHORAGE	AKIAK	ITHACA	SASKATOON
Location	59.7 N, 151.5 W	63.4 N, 10.4 E	58.4 N, 3 W	63 N, 34 E	46.75, 169.0 E	61.3 N, 149.6 W	61.5 N, 150.6 W	42.4 N, 76.5 W	52.2 N, 106.6 W
Type	Pulsed	Pulsed	Pulsed	Pulsed	Pulsed	Pulsed	Pulsed	Pulsed	CV
Frequency MHz	139; 398; 1210	140 ; 143.8	140	88	53.5	49.9	49.9	49.9	42.1
Peak Power kW	6.5 ; 40 ; 37	60	60	75	15	30	7	10 - 20	0.05

Figure 4 [5] illustrates the field of view of the SABRE radars. These multibeam radars constitute a twin system to the STARE radars [6]. The complementary fields of view of STARE and SABRE are shown on figure 5.

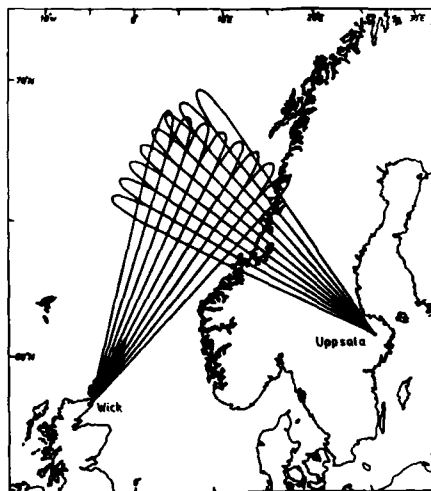


Figure 4. Illustrating the location and field of view of the SABRE radars at Wick in Scotland, and at Uppsala in Sweden. [5]

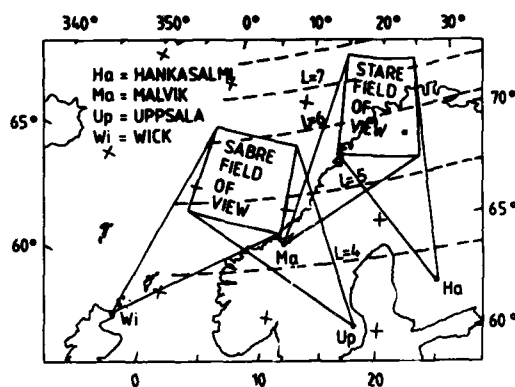


Figure 5. The geographical location of the STARE and SABRE radars of their viewing regions. The solid circles denote magnetometer sites.

Spectral shapes and doppler shifts are the two basic sources of information. Their interpretation is however not always straightforward since they depend upon the nature of the irregularities responsible for the scattering of the radio waves. The essential facts which have to be kept in mind are :

- the importance of the geometry of the observations ; indeed, in order to meet perpendicularity to the magnetic field lines, the radar systems are located far from the scattering regions in such a way that essentially no height resolution can be achieved in the E region (between 100 and 130 km) and that, as a result, simultaneous scattering from different layers will appear as superimposed in the data,
- the existence of various types of irregularities observed on different spatial scales ; as a consequence, the radar spectral signatures will be different for different wavelengths (UHF, VHF),
- the difficulty of interpretation of the doppler shift ; indeed, the doppler shifts reflect phase "velocities" which are not always directly related to plasma velocities.

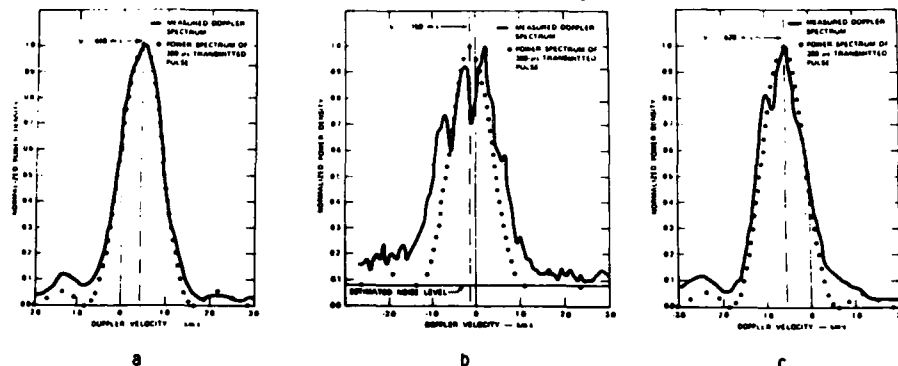
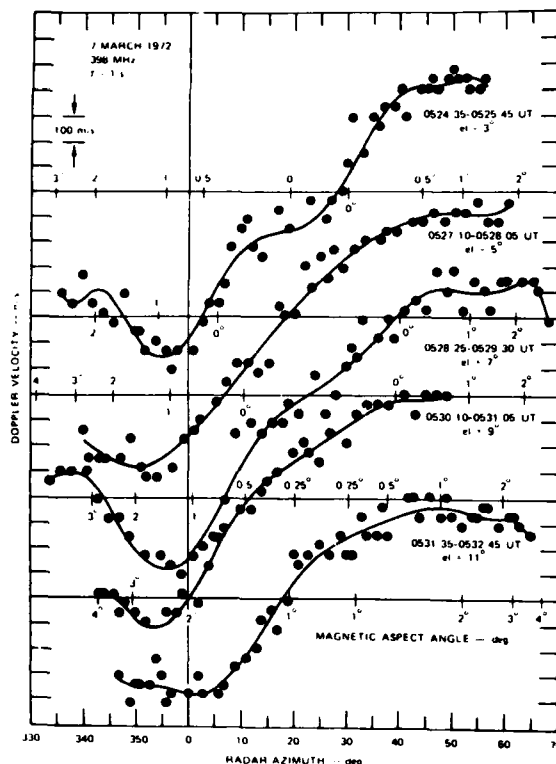


Figure 6. Doppler spectra observed at 398 MHz with the Homer radar. Elevation was 3° and azimuth was (a) 52 E, (b) 19 E and (c) 2 W. The velocity changes from negative to positive when the antenna moves from east to west. Spectra observed at extreme azimuths are narrower than near geomagnetic north. [7]

Some of these aspects are illustrated with data obtained with several radars. Figure 6 [7] shows UHF spectra collected with the HOMER radar for three different aspect angles of the radar with respect to the electrojet. These correspond to diffuse echoes. It can be seen first that the spectral width narrows down when the radar beam is steered away from perpendicularity to the current flow (perpendicularity is approximately achieved in figure 6 b). The doppler shift evolves from positive to negative values as one would expect from a westward motion. However, looking at the variation of the doppler shift over a wide range of azimuths, indicates, as illustrated in figure 7 [7], that instead of undergoing a sinusoidal variation, as expected from a uniform motion, it reaches two limits for eastward and westward azimuths. These limiting values correspond to phase velocities close to the ion acoustic velocity. This feature shows that relating coherent radar E-region doppler shifts to plasma motions is intricate.

Figure 7. Azimuthal variation of the Doppler velocity measured at 398 MHz, showing a region of nearly constant velocity at extreme azimuths (plateau) and a transition region with monotonically varying Doppler shift. [7]



Higher velocities being occasionally observed at VHF frequencies, it was thought for sometime that VHF doppler shifts did not suffer from the same limitations. A thorough study by Nielsen and Schlegel [8] combining incoherent scatter velocity measurements and STARE data has shown in fact that the same limitation at the ion acoustic velocity does exist but that this ion acoustic velocity itself varies as a function of the electron drift velocity due to plasma heating processes (heating by unstable plasma waves associated with the two stream instability).

Figure 8 [9] shows different types of spectra observed at VHF frequencies with the Saskatoon CW radar : diffuse (wide) spectra with a doppler shift always smaller than the one corresponding to the ion acoustic velocity, discrete spectra consisting in the sum of narrow spectra, narrow spectra with a doppler shift corresponding to the ion acoustic velocity. The small component systematically observed for zero doppler shift is spurious and certainly corresponds to ground clutter echoes.

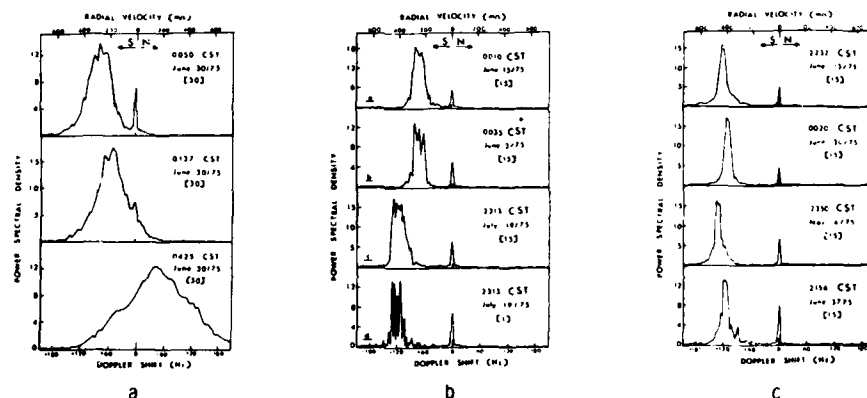


Figure 8. Auroral spectra observed with the Saskatoon CW radar showing (a) the diffuse type with a time varying velocity, (b) the discrete type made up from a few specular components and (c) the ion-acoustic type. The numbers between brackets indicate the number of individual spectra averaged. [9]

Short lived (20 ms) double peaked spectra have been observed with the Saskatoon radar during a strong geomagnetic event. These are displayed on figure 9 [10]. Peaks corresponding to the ion acoustic velocity C_s alternate with peaks corresponding to a higher phase velocity. Other observations have also identified peaks corresponding to ion-cyclotron doppler shifts.

These results indicate that many of the instability mechanisms envisaged in [3] operate in the E-region : two stream instability, gradient drift instability, ion-cyclotron instability...

It was mentioned above that it was initially believed that VHF experiments did not suffer from the limitation of the doppler shift to the ion acoustic ones. In fact, examination of the conditions to be met for the generation of irregularities [11] shows that there exists a minimum electron velocity (relative to the ions) which is frequency dependent : the higher the frequency, the higher the velocity. In practical terms, this velocity is close to the ion acoustic velocity C_s at UHF frequencies and significantly lower at VHF frequencies. As a consequence,

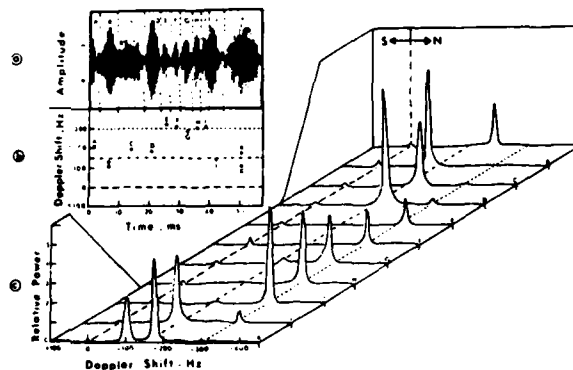


Figure 9. Result of maximum entropy analysis of short-lived (20 ms) signal bursts detected with the CW Saskatoon radar. The strong peak at C_s alternates in time with a weaker peak at a higher velocity. [10]

observations can only be made at UHF frequencies when the velocity is near or above C_s and therefore the observed doppler shifts always reach their limiting values. At VHF frequencies, irregularities can develop for velocities smaller than C_s and this leads to a constricted situation in which for small velocities, the doppler shift corresponds effectively to the electron drift and for larger velocities saturates to the ion acoustic one.

In short, and this will be further developed in chapter III, E region coherent VHF/UHF radar constitute powerful means of study of the plasma irregularities and of the dynamics of the E region ionosphere.

II.3. INCOHERENT SCATTER RADARS

We have seen that sources of free energy create instabilities which in turn lead to magnetic field aligned irregularities. In addition to those and independently of the geometry, natural fluctuations always exist; they are simply due to the random thermal motion of the particles. As early as 1928 Fabry [12] envisaged the scattering of electromagnetic waves by free electrons in a manner similar to the Rayleigh scattering of the light by the atmospheric molecules. However, the expected power level was so small that one had to wait for the availability of powerful radars to attempt to detect echoes from free ionospheric electrons.

Such an experiment was finally proposed in 1958 by Gordon [13]. The first echoes detected, while of the same order of magnitude as expected, were characterized by a much narrower doppler broadening than the one which would have resulted from the thermal motions of the electrons. These results initiated a large number of theoretical studies and led to a complete quantitative understanding of the processes involved (see e.g. [14] for a review). The main point raised by the initial observations was that the thermal fluctuations of the electrons are dominated by the collective behavior of the plasma (ions and electrons) due to Coulomb interactions.

This holds true as long as the scattering wavelength is larger than the Debye length λ_D , or shielding distance, which is equal to the ratio of the electron thermal velocity N_e to the electron plasma frequency f_p . For smaller wavelengths, the plasma cannot sustain a collective behavior since the plasma waves at the plasma frequency would have then a phase velocity smaller than the thermal velocity N_e . In this latter case, the incoherent scatter spectrum reflects effectively the random independent motions of the free electrons (maxwellian velocity distribution). The collective behavior which is generally observed at VHF and UHF frequencies in the ionosphere can be described through the use of the dispersion relation for plasma oscillations. Two basic modes are of interest:

- the pseudo acoustic mode which can be viewed as sound waves of a gas consisting of particles having the mass of the ions and the sum of the energies of both the ions and the electrons,
 - the plasma mode corresponding to electrostatic waves at a frequency close to f_p .
- These modes give rise to two basic spectral components:
- the ion line approximately centered on the transmitted frequency,
 - two plasma lines located respectively at approximately $\pm f_p$ from the transmitted frequency.

Figure 10 shows schematically the incoherent scatter ion and plasma spectral lines for positive angular frequencies. The origin of the frequency axis corresponds to the frequency of the transmitter. K refers to the Boltzman constant, T the plasma temperature, k the wave number, m_i the ion mass, m_e the electron mass, ω_p the angular plasma frequency. A symmetrical situation is found for negative values of ω . It appears consequently that the ion line is double peaked. From it, several basic ionospheric parameters can be extracted:

- the total power yields the electron concentration N_e ,
 - the spectral shape gives, through a least square fitting procedure the electron and ion temperature (T_e , T_i), the mean ion mass $\langle m_i \rangle$, the ion drift component V_{ik} along the wave vector \vec{k} (figure 1), the ion neutral collision frequency ν_{in} (at low altitudes).
- The plasma lines give an independent estimate of the electron concentration N_e and an estimate of the electron velocity V_{ek} along \vec{k} .

The first high latitude incoherent scatter radar was installed at Chatanika in Alaska (Table I). This radar was ultimately moved to Sondrestromfjord in Greenland at an higher geomagnetic latitude.

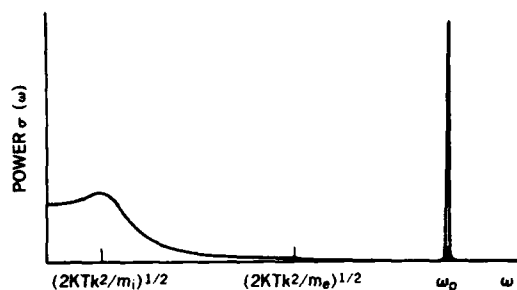


Figure 10. Incoherent scatter ion and plasma lines.

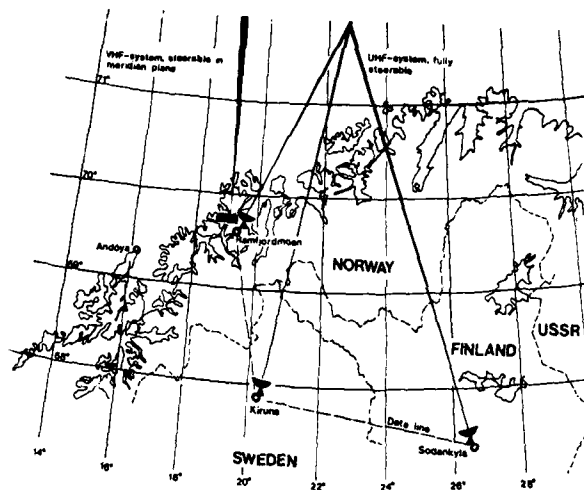


Figure 11. Sketch map of the EISCAT installations.

EISCAT (Table 1) is a dual system (VHF-UHF) built in Northern Scandinavia as illustrated in figure 11. The UHF system includes a transmitter at Ramfjordmoen (Norway) associated with a fully steerable 32 m diameter antenna functioning as a monostatic radar; two identical receiving antenna at Kiruna (Sweden) and Sodankylä (Finland) give a tristatic configuration and allow for full velocity vector measurements. The VHF system is located at Ramfjordmoen and operates monostatically.

The Millstone Hill radar, built in 1960 at middle latitudes (42.6°N, 71.5°W) near Boston was later upgraded so as to reach far ranges and contribute in this way to high latitude studies.

As will be shown in Chapter III, the high latitude incoherent scatter systems play a unique role in monitoring several of the basic ionosphere - magnetosphere couplings.

III. SCIENTIFIC RESULTS

III.1. TROPOSPHERE - STRATOSPHERE DYNAMICS

The Chatanika radar was used in three different ways to determine the vertical wind. The results are displayed on figure 12 [1]. The "large" vertical velocities (up to about 1 m s^{-1}) correspond to a local situation and are certainly associated to a lee wave. The turbulence is the second aspect for which valuable contributions can be obtained from radar measurements. The echo power strength is one way to approach the turbulence. This is illustrated in figure 13 [1] which shows how at a fixed altitude of 12 km, the turbulence varies horizontally on a scale of few kilometers. The results are obtained by rotating the Chatanika antenna by 360°.

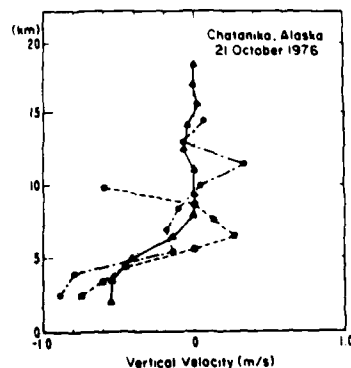


Figure 12. Vertical profiles of the vertical wind inferred from Chatanika radar data. The dashed lines refer to azimuth-scan data (VAD), dashed-dotted lines to elevation-scan data, and the solid line to data obtained with the antenna directed vertically. [1]

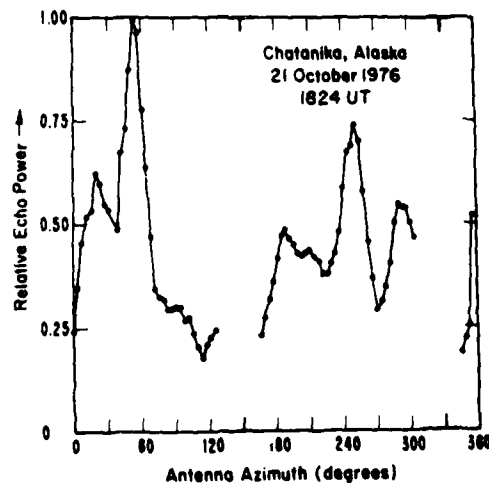


Figure 13. Spatial variation of relative echo power (αC^2) observed at a height of 12 km by the Chatanika radar. These data were obtained by observing the echo power at one range as the antenna rotated 360°. [1]

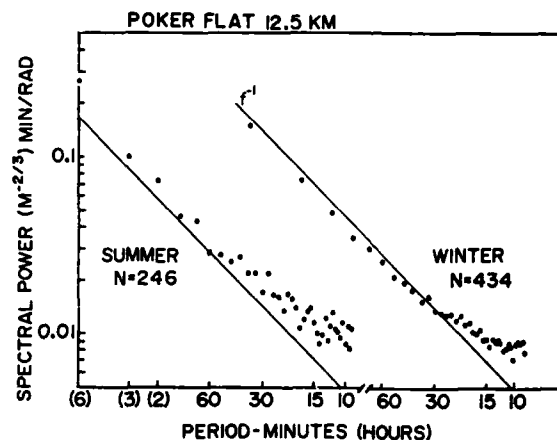


Figure 14. Power spectrum of $\log C^2$ at 12.5 km at Poker Flat during summer (May-August) and winter (October-April), over the range of periods from about 9 minutes to 6 hours. [15]

Further characterization of the turbulence is given by the variance power spectrum of $\log C^2$ determined at Poker Flat at 12.5 km for summer and winter. This is shown on figure 14 [15]. The observed law in f^{-1} is not yet fully understood.

The spectrum of atmospheric motions can be also obtained from doppler measurements. This is illustrated on figure 15 [16]. It exhibits wind speed power spectra obtained at 8 km with the Poker Flat MST radar. One can observe this time a power law in $f^{-5/3}$ attributable to quasi two-dimensional turbulence and corresponding to a universal spectrum of buoyancy waves [17].

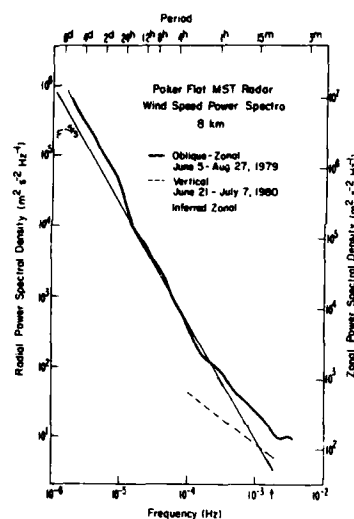


Figure 15. Power spectrum of zonal wind observed by Poker Flat, AK MST radar. [16]

III.2. MESOSPHERIC DYNAMICS

Radars have played a major role in investigating the largely unknown dynamical behavior of the mesosphere particularly in its lower part. Long term averages of the vertical wind and of the meridional wind are shown on figure 16 a [16]. Upward vertical velocities of few 10 cm s^{-1} are observed in the altitude range 75-92 km around winter solstice while downward winds appear around summer solstice. Figure 16 b exhibits meridional wind

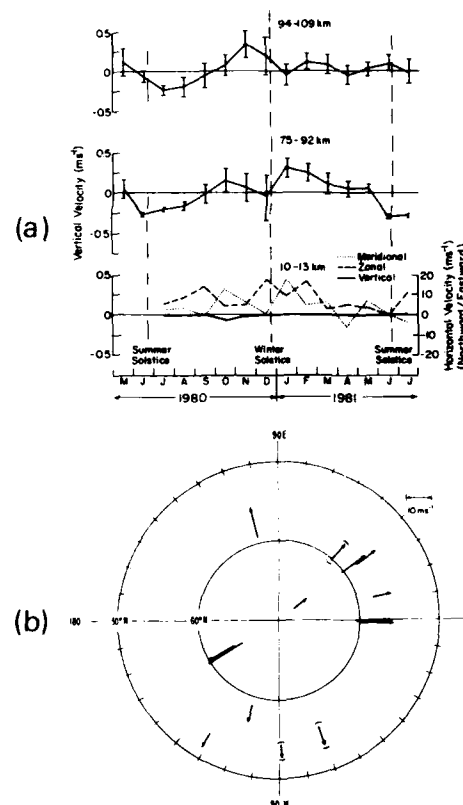


Figure 16. Monthly averaged vertical winds for the period May 1980 to July 1981 at Poker Flat (a) ; Mean meridional winds in June at 90 km over the Northern hemisphere (b). Data are from Doppler radar, meteor radar and partial reflection/radio drift. [16]

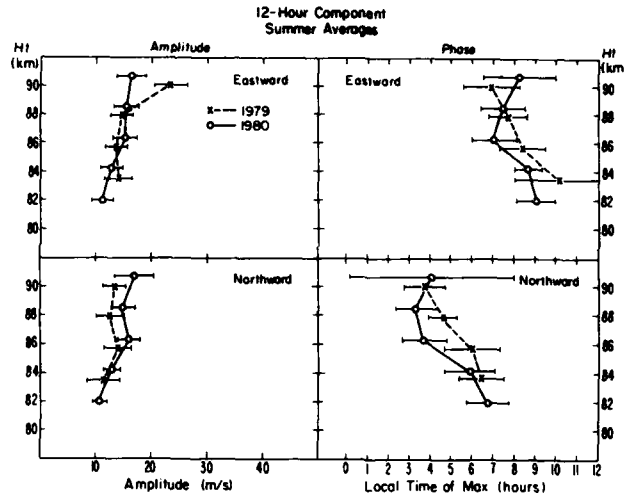


Figure 17. The semi-diurnal component of the summer wind field at Poker Flat. [16]

Similarly, gravity waves propagating upward play an important role in the mesosphere in as much as they tend to have a break up in this region and in this way dissipate locally their energy and produce small scale turbulence.

Gravity waves observed at Poker Flat are shown on figure 18 [16]. The downward propagating phase is characteristic of an upward propagating wave. The above mentioned breaking of gravity waves is illustrated on figure 19 [16] which shows the variability of wind field for short periods as a function of altitude. Such variability, associated to wave activity, should increase exponentially for non breaking waves (energy conservation in an atmosphere decreasing exponentially with altitude). It appears clearly that the variability is rather constant with height and that therefore wave energy is dumped.

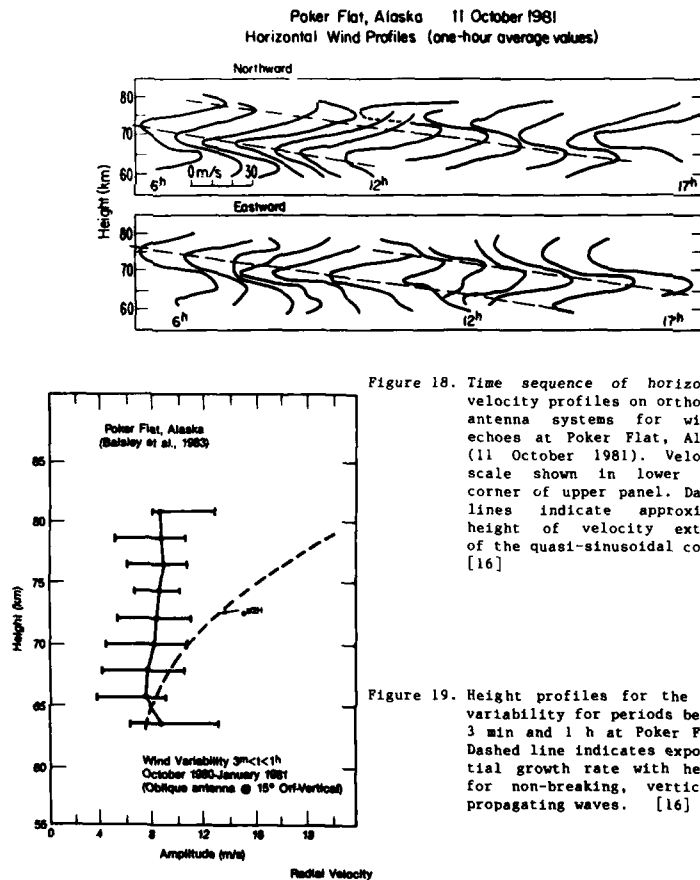


Figure 18. Time sequence of horizontal velocity profiles on orthogonal antenna systems for winter echoes at Poker Flat, Alaska (11 October 1981). Velocity scale shown in lower left corner of upper panel. Dashed lines indicate approximate height of velocity extrema of the quasi-sinusoidal contours. [16]

Figure 19. Height profiles for the wind variability for periods between 3 min and 1 h at Poker Flat. Dashed line indicates exponential growth rate with height for non-breaking, vertically propagating waves. [16]

data obtained at 90 km in June at various locations in the northern hemisphere. It is interesting to notice that the flow is away from the summer pole. Tidal motions of the atmosphere carry a significant part of the atmospheric kinetic energy towards higher altitude. This aspect is illustrated on figure 17 [16] which exhibits the vertical profiles of the amplitude and phase of the zonal and meridional semidiurnal wind component measured in summer at Poker Flat between 82 and 91 km.

III.3. STRUCTURE AND DYNAMICS OF THE THERMOSPHERE

The incoherent scatter radar provide a unique means of study of the thermosphere. Indeed, the strong couplings which exist between the neutrals and the plasma are reflected in the parameters measured by the radars : ion collision frequency, electron and ion temperatures, ion composition, ion velocity. The data obtained in such a way at high latitudes are particularly important to characterize the processes involved in the couplings between the magnetosphere and the atmosphere (energy, dynamics).

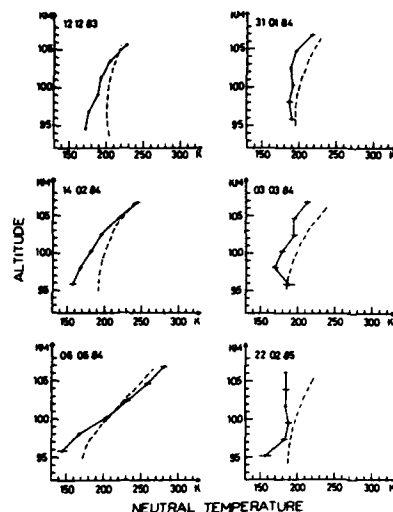


Figure 20. Neutral temperature measured with EISCAT (continuous lines) compared to the MSIS-83 model (dashed lines). [18]

Figure 20 [18] exhibits neutral temperature profiles in the E region obtained with EISCAT. These profiles when compared to the MSIS 83 model [19] show a trend for systematically lower values. Similarly, figure 21 [20] shows the height distribution of the ion neutral collision frequency for one day in February 1984 measured by EISCAT between 90 and 140 km. This profile is directly related to the neutral concentration. Also shown for comparison is the CIRA 1972 model. The Chatanika radar has provided for summer days a very elaborated set of wind data [21] in the lower thermosphere. The data have been organized into average (zonal and meridional) components, diurnal and semi-diurnal tidal components. The average components are shown on figure 22 together with MST radar data from Poker Flat, partial reflection data from Saskatoon and incoherent scatter Millstone Hill data. While a summer to winter meridional flow deflected towards the west by the Coriolis force is expected on the basis of EUV heating, on the contrary up to about 115 km, the opposite trend is observed (zonal component). The eastward flow is in fact a confirmation of the importance of the breaking of gravity waves in the mesosphere with a subsequent transfer of momentum decelerating the mesospheric jet [22].

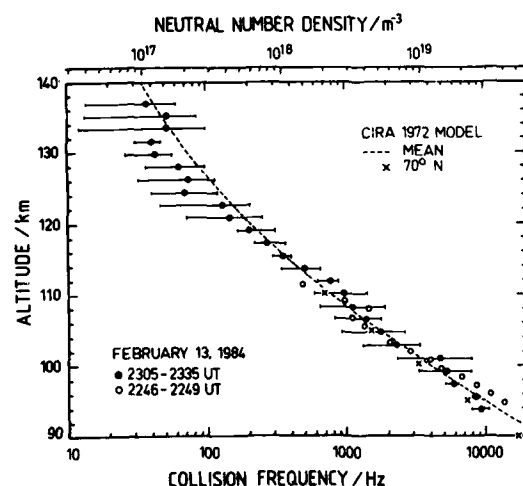


Figure 21. Ion neutral collision frequencies deduced from vertical ion speeds and from the shape of the scattered spectrum. [20]

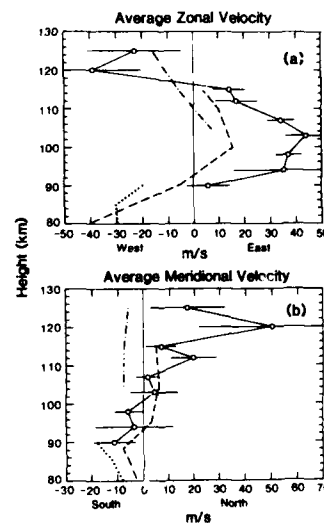


Figure 22. Solid curves correspond to the Chatanika data. The dotted curve shows comparable results obtained with the Poker Flat radar, while the dashed and dot-dashed curves show results from the Saskatoon partial reflection and Millstone Hill incoherent scatter radars. [21]

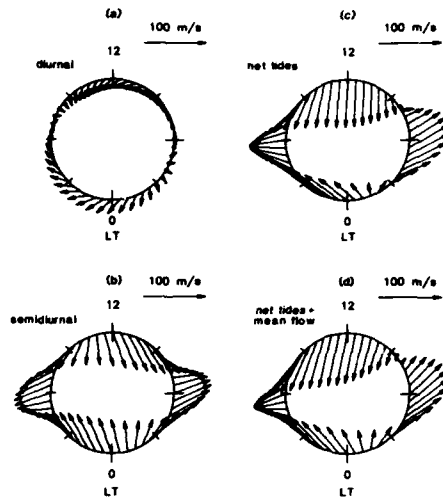


Figure 23. Polar plot showing the diurnal (a), semidiurnal (b), net tides (c), and tides plus mean flow (d) calculated from the least-squares fit to the average neutral wind velocity at 115 km. LT is provided, along with a vector length scale. [21]

The neutral flow at 115 km is shown on polar plots on figure 23 [21]. Successively are plotted the diurnal, semidiurnal, net tidal and overall flows. Strong polar flows around noon and midnight are balanced by equatorward flows at dawn and dusk.

The previous Chatanika data correspond to magnetically quiet periods. The effect of magnetic storm at 115 km is illustrated on figure 24 [21]. Strong departures up to 400 m s^{-1} are observed on the zonal component between 14 and 22 UT, i.e. 4 to 12 LT.

Gravity wave activity is also observed in the thermosphere corresponding either from wave leakage from the mesosphere or from energy deposition in the thermosphere due to particle precipitations and Joule heating. An example of gravity wave observed with EISCAT [23] is given on figure 25. The data correspond to the field aligned ion velocity which is directly related to the north south neutral wind component.

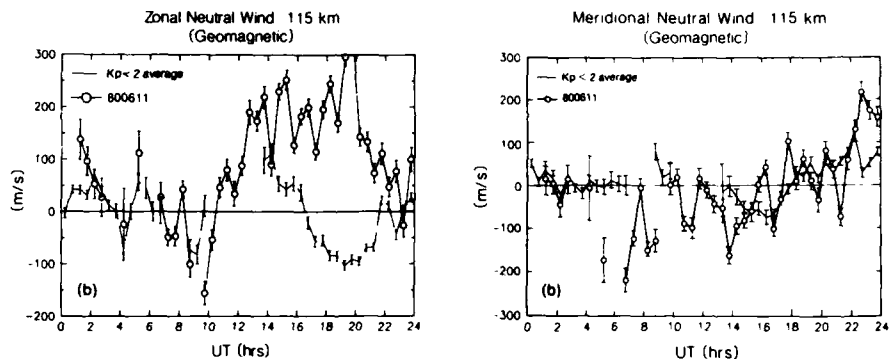
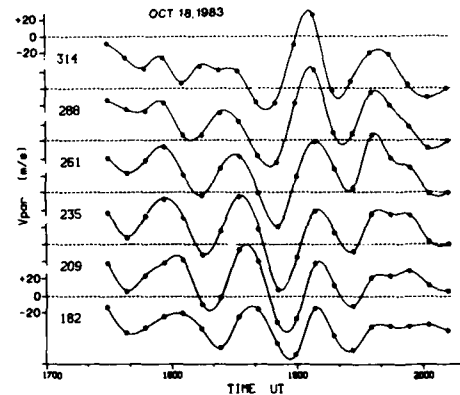


Figure 24. Zonal (left) and meridional (right) neutral velocities in geomagnetic coordinates at 115 km observed on June 11, 1980 (circle symbol) compared with $K_p < 2$ average (thin solid line). The weighted average uncertainty is indicated by error bars for each half-hour interval. [21]

Figure 25. Example of wave-like oscillations in v_z at 6 different altitudes (182-314 km) which are regarded as a signature of a gravity wave with a dominant wave period of $T = 35 \text{ min}$. [23]



One clearly sees the similarity of the oscillations between 182 and 314 km, with their characteristic downward propagating phase. The capability of mapping the neutral wind field is illustrated on figure 26 [24]. Wind vectors obtained from EISCAT data are plotted between 60 and 72.5°N on a polar diagram for June 27, 1984 at 325 km. It appears that strong winds directed essentially sunward develop in the early afternoon and around dawn.

Heating due to particle precipitations and Joule heating associated with the ionospheric current constitute a very large energy source in the lower thermosphere during strong magnetospheric events. These quantities can be inferred from the electron production rates (particle precipitations) and from the measurements of the currents and of the ionospheric conductivity. Figure 27 [25] exhibits height profiles of the heating rates for January 19, 1984 obtained with EISCAT operated in a scanning mode.

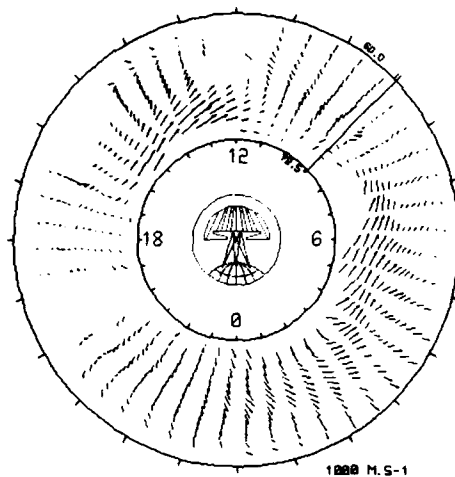


Figure 26. Neutral wind vectors at 325 km altitude, deduced from EISCAT CP-3 observations on 27 June 1984. [24]

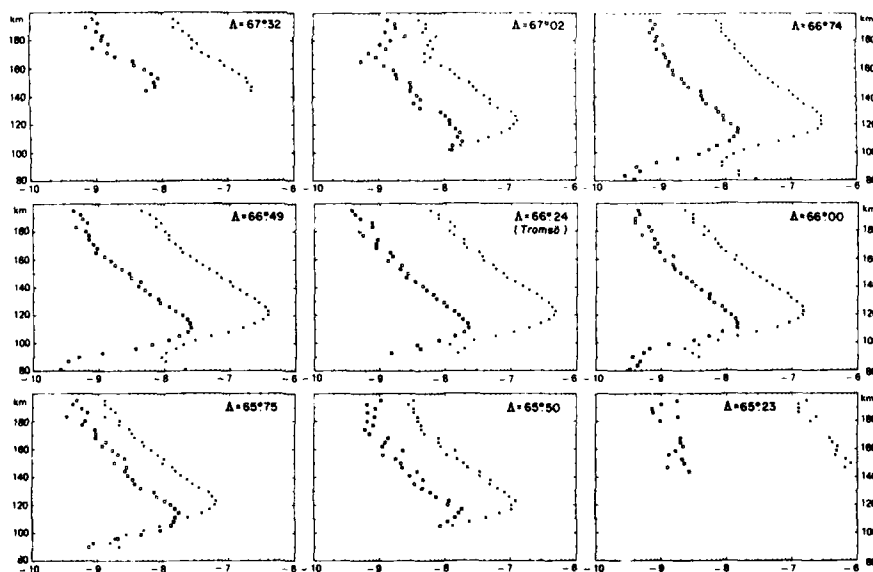


Figure 27. Altitude profiles of heating rates measured during the scan between 0250 et 0300 MLT on 19 January 1984. Each panel corresponds to a step during the scan, at the indicated invariant latitude A at the 130 km level. The squares show the particle heating rate values, the crosses the Joule heating rates. The abscissa are in $W m^{-3}$. [25]

III.4. HIGH LATITUDE PLASMA PROCESSES

The solar wind magnetosphere interaction is at the origin of a large scale dynamo electric field. This field feeds a global electric circuit which dumps its energy in the high latitude atmosphere at ionospheric heights. Incoherent and coherent scatter radars allow a monitoring of the electric field on a large scale as well as in small (space and/or time) scale structures like discrete auroral arcs.

The large scale mapping of the magnetospheric electric field using EISCAT is illustrated on figure 28 [26]. It shows a polar map of the ionospheric potential obtained with EISCAT, together with the projection of the geostationary orbit of GEOS along the magnetic field lines at ionospheric level. The full lines correspond to the evening and morning convection cells while the dashed lines correspond to a region dominated by corotation (plasmasphere). The thick line corresponds to the crossing by GEOS 2 of the plasmasphere while the dotted thick line is the part of the GEOS 2 orbit outside the plasmasphere. The collocation of the boundaries seen by GEOS and EISCAT indicate the overall consistency of the two sets of data. It should be noticed at last that the morning convection cell appears to be much more developed than the evening one.

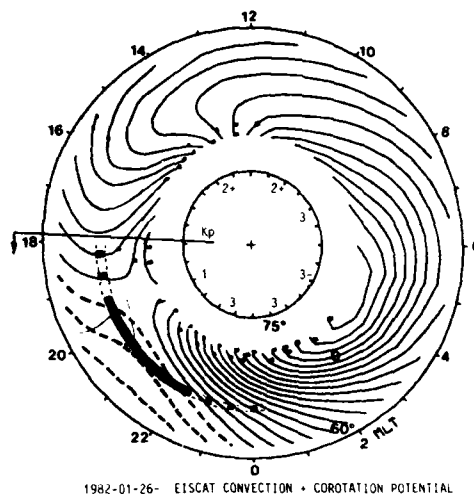


Figure 28. 26 January 1982. Ionospheric potential pattern at 325 km on a polar diagram versus magnetic local time and invariant latitude. The equipotential lines are drawn at 2 kV contour intervals. The thick curve represents the ionospheric projection of the geostationary orbit in the dusk sector. [26]

STARE-SABRE DRIFT VELOCITY PLOTS

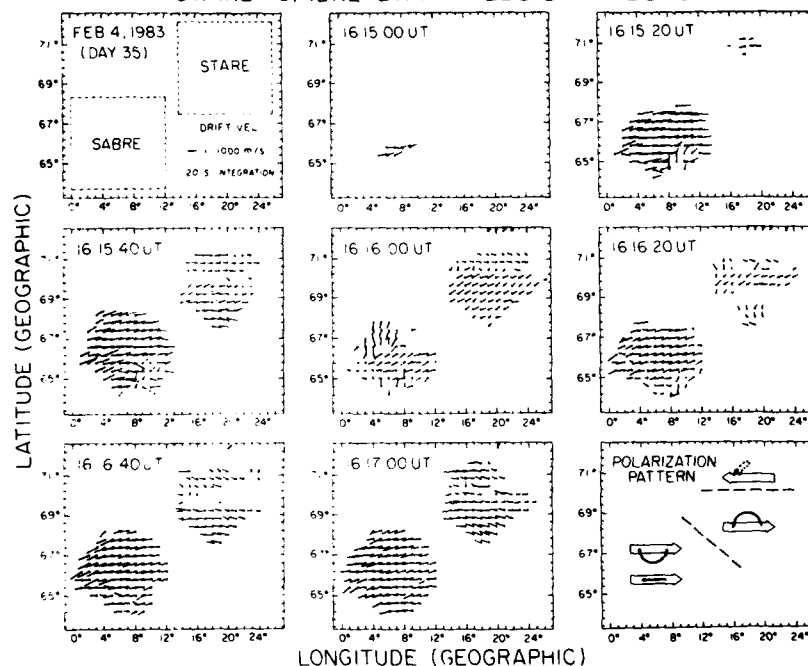


Figure 29. The STARE and SABRE drift velocity plots for the February 4, 1983, storm sudden commencement. [27]

The capability of coherent radar in determining map of the electric field with a high time resolution is demonstrated on figure 29 [27] showing simultaneous STARE and SABRE drift measurements every 20 seconds at a time of a sudden storm commencement. Prior to the event, the electric field is below the instability threshold so that the coherent radar does not detect any echo. The SABRE data is the first to detect a signal return and show an eastward flow (opposite to the usual sunward flow). A westward flow appears next at the highest latitudes near by STARE. Then essentially an eastward flow is seen by SABRE and STARE (except at the highest latitudes). Finally, the flow reverses everywhere to westward, rotating clockwise in the south and anticlockwise in the north.

The same two radars are also able to detect geomagnetic pulsations as seen on figure 30 [28]. East-west and north-south flow velocities driven by the electric field averaged over 1° longitude in the STARE and SABRE data exhibit well organized oscillations, essentially at all latitudes, with periods of few minutes. The phase propagates in opposite direction above and below 68° .

Very high latitude arcs resulting from particle precipitations have been observed at Sondrestromfjord at invariant latitudes around 73° and near local dawn. Two types of arcs corresponding to different precipitating energy populations are generally observed: in the south, localized ionization enhancements at low altitude (~ 115 km) created by 5-10 keV electrons, in the north arc segments extending over several degrees of latitude with ionization peaks around 180 km due to low energy electron fluxes (100 eV - 1 keV). An example of such arcs is shown on figure 31 [29]. Two elevation scans give electron density distributions between 71° and 77° invariant latitude in the altitude range 100 to 200 km. On figure 31 a, the two arcs appear clearly. The electric field data exhibits a strong southward excursion at the northern boundary of the low altitude arc. On figure 31 b, 16 minutes later, the low altitude arc is still present and the electric field behaves in the same manner.

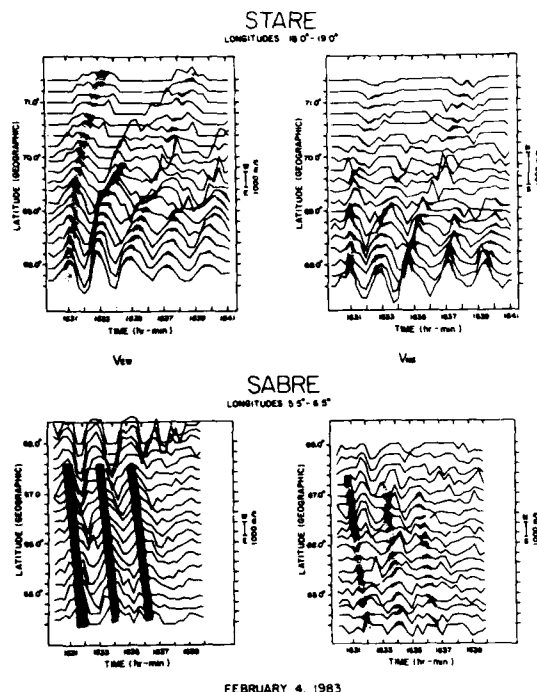


Figure 30. Time and latitude variations of the two orthogonal flow components for each radar system during the pulsation. [28]

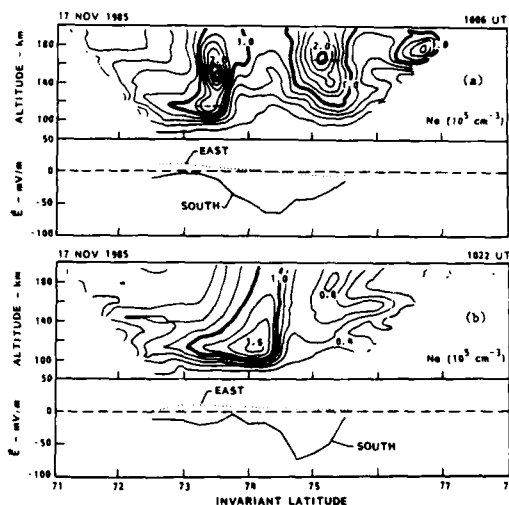


Figure 31. Electron density and electric fields measured by the Sondrestromfjord radar during two scans beginning at a) 1006 UT and b) 1022 UT. [29]

IV. CONCLUSION

Coherent and incoherent scatter radar constitute a means to monitor and study the global behavior of the atmosphere and of the ionosphere at high latitudes. While incoherent scatter radars are highly expensive and will only exist in few limited sites (including possibly an antarctic one), the coherent radar systems can virtually offer a complete coverage of the high latitude regions. These two types of systems are in fact complementary since :

- on one hand, the incoherent scatter systems give a continuous time coverage of many parameters which allow for establishing a quantitative understanding of basic dynamical and plasma processes taking place in the thermosphere and the ionosphere in conjunction with magnetospheric activity,
- on the other hand, the coherent radar are a unique way to monitor the dynamics of the low and middle atmosphere and have, at higher altitude, when the threshold conditions are satisfied, the capability of mapping on very large spatial scales and with very high time resolutions the ionospheric electric field and the E-region plasma irregularities.

REFERENCES

- (1) BALSLEY B.B., K.S. GAGE, The MST Radar technique : Potential for middle atmospheric studies, *Pure Appl. Geophys.*, **118**, 1980, 452-493.
- (2) BALSLEY B.B., Poker Flat MST Radar measurement of winds and wind variability in the mesosphere, stratosphere and troposphere, *Radio Sci.*, **18**, 1983, 1011-1020.
- (3) BAUER P., HF Radar probing (including modification). This volume.
- (4) HANUISE C., High-latitude ionospheric irregularities : A review of recent radar results, *Radio Sci.*, **18**, 1983, 1093-1121.
- (5) JONES T.B., J.A. WALDOCK, E.C. THOMAS, C.P. STEWART, T.R. ROBINSON, SABRE Radar observations in the auroral ionosphere, AGARD Conference Proceedings n° 382, Propagation effects on military systems in the high latitude region, 1985, 6.4-1 - 6.4-15.
- (6) GREENWALD R.A., W. WEISS, E. NIELSEN, N.R. THOMSON, STARE, a new radar auroral backscatter experiment in northern Scandinavia, *Radio Sci.*, **13**, 1978, 1021-1039.
- (7) TSUNODA R.T., Doppler velocity maps of the diffuse radar aurora, *J. Geophys. Res.*, **81**, 1976, 425-435.
- (8) NIELSEN E., K. SCHLEGEL, Coherent radar doppler measurements and their relationship to the ionospheric electron drift velocity, *J. Geophys. Res.*, **90**, 1985, 3498-3504.
- (9) HALDOUPIS C., G. SOFKO, VHF doppler spectrum of 42 MHz CW auroral backscatter, *Can. J. Phys.*, **54**, 1976, 1571-1584.
- (10) HALDOUPIS C., G. SOFKO, Short term characteristics of ion acoustic type radio auroral echoes, *Can. J. Phys.*, **56**, 1978, 292-301.
- (11) GREENWALD R.A., Diffuse aurora and the gradient drift instability, *J. Geophys. Res.*, **79**, 1974, 4807-4810.
- (12) FABRY C., Remarques sur la diffusion de la lumière et des ondes Hertziennes par les électrons libres, *C.R. Hebd. Séance Acad. Sci., Paris*, **187**, 1928, 777-781.
- (13) GORDON W.E. Incoherent scattering of radio waves by free electrons with applications to space exploration by radar, *Proc. I.R.E.*, **46**, 1958, 1824-1829.
- (14) BAUER P., Theory of waves incoherently scattered, *Phil. Trans. R. Soc. Land. A.*, **280**, 1975, 167-191.
- (15) NASTROM G.D., The frequency spectrum of C^2 from MST Radar data, *MAP Handbook*, vol. 20, ICSU/SCOSTEP Ed., Urbana, Illinois, 1986, 211-215.
- (16) GAGE K.S., B.B. BALSLEY, MST Radar studies of wind and turbulence in the middle atmosphere, *J. Atmos. Terr. Phys.*, **46**, 1984, 739-753.
- (17) VAN ZANDT T.E., A universal spectrum of buoyancy waves in the atmosphere, *Geophys. Res. Lett.*, **9**, 1982, 575-578.
- (18) KOFMAN W., C. LATHUILLIERE, B. PIRARET, Neutral atmosphere studies in the altitude range 90-110 km using EISCAT, *J. Atmos. Terr. Phys.*, **48**, 1986, 837-847.
- (19) HEDIN A.E., A revised thermospheric model based on mass spectrometer and incoherent scatter data : MSIS-83, *J. Geophys. Res.*, **88**, A12, 1983, 10170-10188.
- (20) HUUSKONEN A., T. NYGREN, L. JALONEN, T. TURUNEN, J. SILEN, High resolution EISCAT observations of the ion-neutral collision frequency in the lower E-region, *J. Atmos. Terr. Phys.*, **48**, 1986, 827-836.

- (21) JOHNSON R.M., V.B. WICKWAR, R.G. ROBLE, J.G. LUHMANN, Lower-thermospheric winds at high latitude : Chatanika radar observations, *Ann. Geophys.*, 5, 1987, 383-404.
- (22) GARCIA R.R., S. SOLOMON, The effect of breaking gravity waves on the dynamics and chemical composition of the mesosphere and lower thermosphere, *J. Geophys. Res.*, 90, 1985, 3850-3868.
- (23) SCHLEGEL K., The study of tides and gravity waves with the help of field-aligned velocities measured by EISCAT, *J. Atmos. Terr. Phys.*, 48, 1986, 879-886.
- (24) ALCAYDE D., J. FONTANARI, Neutral temperature and winds from EISCAT CP-3 observations, *J. Atmos. Terr. Phys.*, 48, 1986, 931-947.
- (25) DUBOIN M.L., Heating rates measured by EISCAT : Latitudinal variations, *J. Atmos. Terr. Phys.*, 48, 1986, 921-930.
- (26) FONTAINE D. S. PERRAUT, D. ALCAYDE, G. CAUDAL, B. HIGEL, Large scale structures of the convection inferred from coordinated measurements by EISCAT and GEOS 2, *J. Atmos. Terr. Phys.*, 48, 1986, 973-986.
- (27) McDIARMID D.R., E. NIELSEN, Coherent radar observations of a storm sudden commencement having a preliminary reverse impulse, *J. Geophys. Res.*, 92, 1987, 159-167.
- (28) McDIARMID D.R., E. NIELSEN, Simultaneous observation of monochromatic and variable period geomagnetic pulsations, *J. Geophys. Res.*, 92, 1987, 4449-4457.
- (29) ROBINSON R.M., R.R. VONDRAK, Electrodynamic properties of very high latitude aurora. NSF Grant ATM8508129, Space Sciences Laboratory, Lockheed Palo Alto Laboratories, 1987.

ACKNOWLEDGEMENTS

The author is very thankful to C. Hanuise, E. Nielsen, B. Balsley, T.B. Jones, R.M. Robinson for providing very valuable inputs to this lecture.

PROPAGATION MEDIUM ADAPTIVE TECHNIQUES
FOR ADVERSE COMMUNICATIONS AND FOR REMOTE SENSING

by
Dag T Gjessing
Royal Norwegian Council for Scientific and Industrial Research
Environmental Surveillance Technology Programme
PO Box 25 - N-2007 Kjeller
NORWAY

SUMMARY

In general terms, an object probed by electromagnetic waves can be characterized by the distribution of scatterers along and transverse to the propagation direction, the chemical surface structure of the object, the surface temperature and the motion pattern.

A unified set of first order expressions derived from basic physical principles characterizing the scattering object is presented. From these it is shown how the propagation medium affects the results of the various remote sensing techniques. In exactly the same way the factors which characterize the propagation medium in relation to communications are derived.

It is shown that in regard to the influence of the propagation medium, the problems related to communications are very much unified with those of remote sensing.

1 INTRODUCTION

With recent advances in radio science and growing interest in environmental monitoring, remote sensing based on electromagnetic waves has become an important field of study. Using a radar system in which the illuminating frequency can be controlled by a computer system and likewise the receiving system can be "matched" to the backscattered signal, a system which adapts itself both to the transmission medium and to the target of special interest can be designed.

From information theory it is well known that the more information one requires per unit time, the wider must the bandwidth of the communication channel be. In terms of radar terminology, what it means is that the more information we require about the target, the more widebanded must the illuminating radar be, and as a consequence of this, we must make use of a transmission medium with sufficient bandwidth capability. We know from experience, however, that the propagation medium in general varies both in space and in time. In order, therefore, to optimize the system performance, our remote sensing system must adapt itself so as to make optimum use of the conditions prevailing. We must, therefore, "code" or "pre-tailor" the radar wave so as to allow it to pass through the intervening propagation medium with a minimum of distortion and at the same time, upon reflection by the object of interest, give optimum information about this object.

It does not take much imagination or experience to realize that an object can be characterized in several "signature domains" and that the propagation medium influences these signatures in different ways. We are, as a consequence of this seeking a remote sensing system which makes use of a set of preferably orthogonal signatures which are not only orthogonal in the sense that they all contribute to the description of the target; it should be such that the propagation medium degrades the information content in the signature domains in different ways and at unequal times.

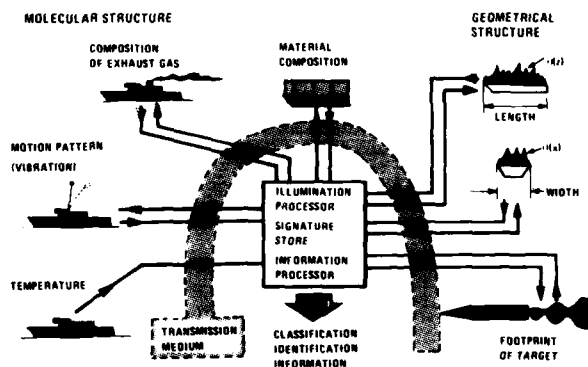


Figure 1.1 An object or a phenomenon can be characterized in several signature domains. Influence of the propagation medium may have different effects on these signatures (1).

Figure 1.1 illustrates this "mult. sensor remote sensing data fusion system". The figure illustrates in the form of an artist's conception a set of detection/identification methods based on several signature domains; surface temperature distribution based on Planck's law of radiation, motion pattern from Doppler analysis of reflected radio-wave, shape and size from measurements of space and frequency coherence properties

of reflected radio wave, measurement of material composition or composition of exhaust gas by spectroscopy methods, etc.

It is evident from this example that the propagation medium influences the various remote sensing signatures in a very different manner: precipitation blanks out most of the signatures based on optical and infrared spectroscopy methods. Severe turbulence causing refractive index regularities in the transmission medium and multipath phenomena may give rise to severe distortion and "blurring" when we base our detection/identification on scattering of microwaves or millimeter waves.

Remote sensing techniques based on surface- or gas-spectroscopy are considered as being outside the scope of this contribution. Likewise we shall not consider in any degree of detail thermal emission. We shall confine ourselves to the more classical topics related to scattering and absorption of radio waves. We should in passing note, however, that fundamentally it is not in this context very meaningful to make a very clear distinction between radio waves and optical waves. Both suffer absorption through the atmosphere to a larger or smaller extent, both are subjected to diffraction and refraction phenomena.

It does not take much imagination to see the analogy between the factors of importance for remote sensing and those affecting communication systems. This analogy is visualized in Table 1.1.

TRANS- MISSION MEDIUM CHARACTERIZATION	COMMUNICATION CIRCUIT	REMOTE SENSING
Bandwidth Width of delay function	<ul style="list-style-type: none"> - Spread spectrum processing gain - Rate of information transfer - Frequency diversity efficiency 	Longitudinal (z) resolution of target (Blurring in range)
Discrete multipath (Lobing of delay and bandwidth functions)	<ul style="list-style-type: none"> - Rate of information transfer - Crosstalk in FDM and TDM systems 	Ambiguous position measurements
Wavelength dependence (Frequency selective absorption)	Influences the choice of frequency band, distortion of TDM and FDM signals	Limits spectroscopic measurements of gases and reflecting surfaces
Temporal correlation properties (Motion pattern of transmission medium)	<ul style="list-style-type: none"> - Limits usable bandwidth - Length of spread spectrum code in time domain - Limits integration time 	<ul style="list-style-type: none"> - Limits resolution of target motion pattern - Limits detection range by blurring coherency of the radar signal
Horizontal correlation of field strength	Horizontal space diversity efficiency	Horizontal (x) resolution of object. Blurring in the x direction
Vertical correlation of field strength	Vertical space diversity efficiency	Vertical (y) resolution of object. Blurring in the y direction
Antenna-to-medium coupling loss	Degrades S/N ratio	Degrades S/N ratio
Polarization properties of medium	Affects antenna-to-medium coupling	Limits the possibility of object characterization by polarization
Time variation of polarization properties	Limits polarization diversity efficiency	Reduces S/N ratios

Table 1.1 Remote characterization of objects (remote sensing) is very analogous to information transfer in a communication system

2 MULTISENSOR CHARACTERIZATION OF TARGETS

Characterization of a scattering object by studying the properties of backscattered radio waves (inverse scattering)

Under this heading there are fundamentally three cases (3 degrees of freedom). The first concerns the case when we have at our disposal an electromagnetic radiator capable of illuminating the object of interest in a prescribed manner (composite spectrum of radio wavelength). The second deals with the situation when we have at our disposal one illuminating frequency and an array of spatially distributed receiving elements capable of determining the spatial wave pattern (correlation properties in space of the scattered wave). Thirdly, we can consider the polarization characteristics of the scattering object.

In this brief survey of remote sensing (inverse scattering) methods in relation to the limiting influence of the propagation medium, we shall confine ourselves to the two first cases. We should note, however, that we at least in principle will have one set of case 1 and case 2 signatures for each set of polarization combinations (vertical transmission V_T , vertical reception V_R ; $H_T H_R$ and $V_T H_R$). These polarization domains may, however, conceivably give redundant information.

2.1 Measurement of object size and shape based on a multi-frequency system

We first consider detection/identification on the basis of an electromagnetic radiator capable of illuminating the object of interest in a prescribed manner (composite spectrum of wavelengths). Consider first the simplest of all targets consisting of two reflection points spaced Δz longitudinally along the direction of wave propagation. We shine a wide spectrum of frequencies on this object, and analyze the set of interfering waves received. We note that as the difference in frequency is changed, the situation arises when the waves reflected from the two reflection points arrive in antiphase at the receiving site, causing a minimum in the frequency spectrum. If the distance in depth between the two reflecting elements is Δz , the phase angle between the waves reflected from the two reflectors is given by

$$\phi = 2\pi \frac{2\Delta z}{\lambda_1} = 2\pi \frac{2\Delta z F_1}{c} \quad (2.1)$$

for the frequency F_1 . To change the phase angle ϕ through 180° so as to move from constructive interference to destructive interference requires a frequency change to F_2 such that

$$\phi + 2\pi = 2\pi \frac{2\Delta z F_2}{c} \quad (2.2)$$

The distance in frequency between two successive interference minima is then given by

$$F_2 - F_1 = \Delta F = \frac{c}{2\Delta z} \quad (2.3)$$

Then consider the more general situation with an object in the form of a periodic structure (a tree with a set of equally spaced branches). We express the size of the object as Δz , and the fine-scale structure as δz (exponential damped sinusoidal oscillation). The object is a distance z_0 from the transmitter. We illuminate this object with a set of correlated frequencies. The source is a large number of frequency generators which are derived from a common source. When this set of electromagnetic waves is coupled to the general object shown, the reflected wave is decorrelated frequency-wise as shown in Figure 2.1: the maximum of the correlation envelope is shifted a distance $\frac{c}{2\delta z}$ (where δz is the finest structure of the object under investigation). The width of the correlation envelope is determined by $\frac{c}{2\Delta z}$ where Δz is the size of the object. Finally, under the envelope of the correlation function there are periodic oscillations stemming from the fact that the system delay function is nonsymmetrical, resulting in a complex autocorrelation function in the frequency domain. In analyzing the fine scale oscillation of the correlation function, we find a period which is given by

$$\frac{c}{2z_0} \quad (2.4)$$

where z_0 is the distance to the target.

In conclusion, the autocorrelation in the frequency domain (the "bandwidth") of a scattered/diffracted electromagnetic wave is determined directly from the Fourier transform of the object's delay function. Knowing the position, the size and the shape of the object, the correlation function in the frequency domain is determined (2).

Figure 2.2 shows a plot of essentially eq (2.4) for various object shapes. Note that since the bandwidth function is determined by the Fourier transform of the object shape, the proportionality factor will be affected by the object shape. Specifically, if the scattering coefficient varies exponentially along the axis of propagation through the object, $\Delta F_y = 0.16 \frac{c}{\Delta z}$. If we are dealing with a Gaussian object, the factor is 0.37. For a rectangular one it is 0.44, for a triangular one 0.64, and for an object consisting of two discrete scatterers it is 0.25.

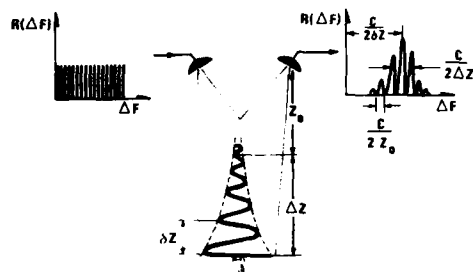


Figure 2.1 Illuminating the object with a set of electromagnetic waves with different frequencies, the correlation function in the frequency domain of the reflected wave gives information about the distance to the object, the size of the object and its shape (2)

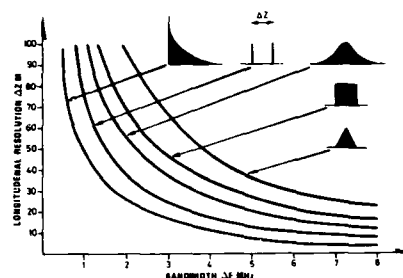


Figure 2.2 The bandwidth required to resolve a given object is determined by the shape and size of the object

2.2 Measurement of object shape and size based on spaced receiving antennas

In the same way as above where the distribution in depth of an object is determined by the autocorrelation function of the scattered field in the frequency domain, the transverse distribution of the object is determined by measuring the spatial correlation properties transversely to the scattered wave. This property of the scattered field is depicted in Figure 2.3. Two scattering elements a and b spaced Δx apart along a direction normal to the propagation direction of the scattered field, give rise to a spatially periodic interference pattern at the receiver. Measuring the spatial period of this interference pattern gives information about the transverse size Δx of the object. It can be shown (see reference (2)) that if $\sigma(x)$ is the spatial distribution of the object in the x-direction, then the spatial autocorrelation function of the field along the x-direction at the receiving site is given as the Fourier transform of the $\sigma(x)$ function normalized with the distance R to the object.

Thus, in order to measure the "transverse shape" of an object, we shall need a set of spaced antennas (a broadside array). Figure 2.3 shows such an array system coupled to a microprocessor.

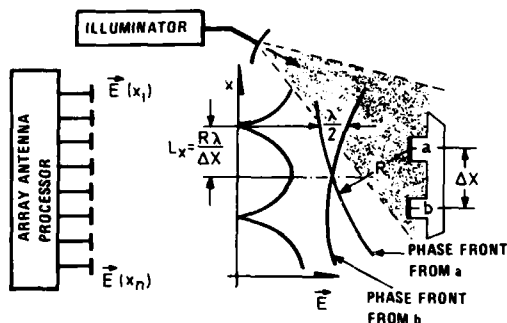


Figure 2.3 Transverse distribution of field strength. The size (width) Δx of the object manifests itself as a "transverse interferogram".

If one wants to resolve the fine-scale structure of the object, the phase relationship between distant antennas should be observed. On the other hand, if the interest is focused on the large-scale properties of the object, this information is obtained from antenna elements which are closely spaced. This is in direct analogy with the case discussed above with spaced frequencies. Note that the principal of the side-looking radar relies on the spatial property of a scattered electromagnetic wave.

As we have seen, the transverse resolution Δx is given in terms of array width L_x , the range R and the wavelength λ as

$$\Delta x = \frac{R\lambda}{L_x} = \frac{cR}{FL_x} \quad (2.5)$$

where F is the carrier frequency.

Note, in contrast to section 2.1 above that the longitudinal resolution Δz is given by

$$\Delta z = \frac{c}{2\Delta F}$$

Hence, the longitudinal resolution Δz is proportional to the bandwidth ΔF whereas the transverse resolution Δx is proportional to the carrier frequency F.

For Δx to be the same as Δz , we have

$$\frac{\Delta F}{F} = \frac{L_x}{2R} \quad (2.6)$$

2.3 Classification of environmental state parameters by motion pattern mapping

In order to identify an environmental object on the basis of its motion pattern, we shall have to rely on the Doppler principle. Illuminating a body which is in motion by electromagnetic waves, the wave upon reflection is subjected to a Doppler shift f . This Doppler shift is characterized by the well-known Doppler equation stating that the Doppler shift $f = \frac{1}{2\pi} \cdot \vec{K} \cdot \vec{V}$ where \vec{K} is the wave vector of the electromagnetic field ($\vec{K} = \vec{k}_i - \vec{k}_r$, the vector difference between the incident and the reflected wavenumber). \vec{V} is the velocity of the object. Observing then both the Doppler shift and the Doppler spread, we obtain information about the mean systematic velocity of the object, as well as information about the velocity distribution. As an example, we use this Doppler principle to investigate the motion pattern of ocean waves. Studying the time history of the correlation between two radio frequency lines, we obtain information about the motion pattern of a particular ocean wavelength. The wavelength L which the experiment selects is given by

$$L = \frac{c}{2\Delta f} \quad (2.7)$$

where Δf is the frequency spacing of the radiowaves.

3 FUNDAMENTALS OF RADIOWAVE PROPAGATION THROUGH THE ATMOSPHERE IN RELATION TO REMOTE SENSING AND COMMUNICATIONS

From the preceding chapters we have seen that in order to resolve the fine-scale structure of a target, we shall have to illuminate this with broadbanded electromagnetic waves, and we shall have to maintain amplitude and phase coherence across the target.

It is the purpose of the following section to analyze a set of practical propagation media with a view to obtaining analytical expressions providing information about:

- path loss
- bandwidth (resolution capability longitudinally, rate of information transfer)
- spatial coherence (resolution capability transversely, space diversity reception)
- temporal coherence (fading, integration time)

We shall endeavour to offer a unified set of theoretical expressions based on simple first principle physics. The aim is to present theoretical expressions which lend themselves to further analysis, so as to form the basis for adaptive manipulations and thus maximize system performance. Furthermore, we shall base our theoretical approach on the concepts derived above, where we presented the basic concepts for scattering/diffraction.

3.1 Line-of-sight propagation

Figure 3.1 shows the distance dependence of a radio field for various propagation mechanisms. Within line-of-sight, the power density decreases with distance as R^2 and in terms of transmitted power P_T , gain of transmitting antenna G_T , area of receiving aperture A , and distance between transmitter and receiver R , the received power P_R is given by

$$\frac{P_R}{P_T} = \frac{G}{4\pi R^2} A \quad (3.1)$$

The received power decreases gradually as the distance increases; for a given power and beam configuration there is no parameter which can be altered in order to improve the situation.

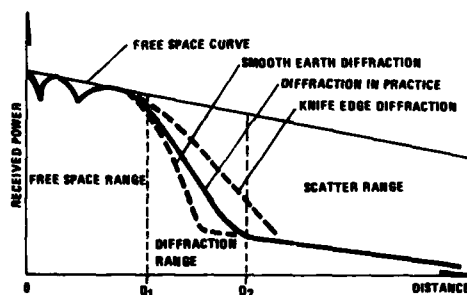


Figure 3.1 Factors determining the path loss in tropospheric propagation

shown in Figure 3.1. Similarly, if the phase angle is equal to 2π , we have constructive interference and we get a maximum. Accordingly, in order to change a maximum to a minimum without altering the geometry, i.e. the position of the transmitter and the receiver, the wavelength will have to be changed by a factor 2.

Then let us consider what happens if part of the transmitted energy is illuminating the ground surface and is reflected into the direct wave. If now H_T is the height above the reflecting surface of the transmitting antenna, and H_R is the corresponding height of the receiving antenna, then the difference in path length of the direct wave relative to that of the reflected wave is given by

$$\Delta = \frac{2H_T H_R}{R}$$

Phase angle ϕ between the two waves is therefore

$$\phi = \frac{4\pi H_T H_R}{\lambda R}$$

such that when $\phi = \pi$ the two waves appear in antiphase, giving rise to a minimum in the plot of received power versus distance, as shown in Figure 3.1. Similarly, if the phase angle is equal to 2π , we have constructive interference and we get a maximum. Accordingly, in order to change a maximum to a minimum without altering the geometry, i.e. the position of the transmitter and the receiver, the wavelength will have to be changed by a factor 2.

Now let us assume that we would like to adjust the height of the receiving antenna in such a way as to achieve constructive interference. As seen from the above expression, this is achieved by shifting the receiving antenna vertically through a distance

$$\Delta H_R = \frac{\lambda R}{4H_T} \quad (3.2)$$

Hence, if we are dealing with a target of vertical extent ΔH_{TARGET} , we shall have to control the propagation parameters so as to ensure that $\Delta H_R \geq \Delta H_{\text{TARGET}}$

Then let us, in terms of bandwidth, consider the properties of a propagation circuit involving ground reflections. Having already calculated the delay function related to our transmission circuit, the bandwidth is readily obtained as a function which is proportional to the inverse of delay. Specifically, if the delay function, as in our case, consists of two δ -functions with separation

$$\Delta = \frac{2H_T H_R}{R}$$

the correlation properties in the frequency domain of the reflected signal are given by the Fourier transform of a cosine relationship. The half-power bandwidth of the first order is therefore given by (2)

$$\Delta F = 0.25 \frac{c}{\Delta} \quad (3.3)$$

Introducing the geometrical expression for Δ above, we find that the bandwidth is given by

$$\Delta F = \frac{c \cdot R}{8H_T H_R} \quad (3.4)$$

This is plotted in Figure 3.8.

The simple formulas above are based on the assumption that radio rays propagate along straight lines. If the atmosphere is not homogeneous as regards refractive index, this is not the case. If we are dealing with a vertical profile of refractive index, we shall experience bending (refraction). Knowing the refractive index profile, we can calculate the ray bending from Snell's law (3). We are thus able to calculate the total bending to which a ray is subjected when propagating from the radar to the target (and back along the same path).

So far, we have restricted the discussion to the case where the spatial small-scale fluctuations in refractivity were negligible; we shall thus experience refraction only and no scattering. We shall now consider an atmosphere which is characterized by small-scale spatial refractivity fluctuations and the effect of these on line-of-sight propagation.

As a consequence of the fact that irregularities in the atmospheric refractive index structure lead to multipath phenomena and delay variations when an electromagnetic wave passes through the irregular transmission medium, we suffer a loss in bandwidth. We shall now give some theoretical results, which are well confirmed experimentally, giving information about the amplitude covariance as a function of frequency separation (i.e. bandwidth properties of the medium) and as a function of spatial separation.

Before referencing the results of comprehensive calculations, we shall, as above, give some quantitative results for the purpose of ensuring a physical understanding of the basic physics involved.

Referring to the simple geometrical sketch of Figure 3.2, we see that there are two extreme paths through which the electromagnetic waves can travel from the transmitter T to the receiver R. One is the shortest direct way from T to R, the other is via a path which is half a wavelength longer than the direct route. The result of these two waves is the vector sum of two signals with a 180° difference in phase causing destructive interferences.

To the first order, therefore, we would expect the width θ of the angle of arrival spectrum at the receiving point to be given by

$$\tan^{-1} \theta = \frac{\sqrt{\lambda d}}{d} \quad (3.5)$$

$$\theta = \frac{\sqrt{\lambda d}}{d}$$

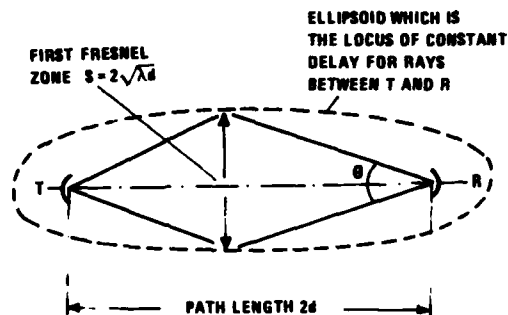


Figure 3.2 The geometry of line-of-sight propagation

Knowing the angular power spectrum (the beamwidth), the correlation distance in a plane through the location of the receiver normal to the line T-R can be calculated. We have shown in section 2 above that this spatial correlation of field strength is the Fourier transform of this angular power spectrum.

If this power spectrum is a $\frac{\sin x}{x}$ function, then the Fourier transform is a rectangular function. If the width of this, i.e. the correlation distance of field strength, be L , then we have the following relationship between the half-power width of the beam θ_h and the correlation distance L

$$\theta_h = \frac{0.88 \lambda}{L} \quad (3.6)$$

where λ is the wavelength of the electromagnetic wave.

In passing, note that this is the same expression as that relating antenna beamwidth θ_h to the antenna aperture diameter L . This is not surprising since the antenna radiation pattern (the $P(\theta)$ function) is the Fourier transform of the illuminating field strength distribution over the antenna aperture.

From equations (3.5) and (3.6) above, therefore, we have

$$\frac{0.88 \lambda}{L} = \frac{\sqrt{\lambda d}}{d} \quad (3.7)$$

i.e. correlation distance $L = 0.88 \sqrt{\lambda d}$.

Thus, the correlation distance of field strength transverse to the line of propagation is comparable with the first Fresnel zone.

Then let us calculate the bandwidth Δf . From section 2 above we have learnt that the bandwidth function (autocorrelation function in the frequency domain) is obtained by Fourier transforming the delay function.

For simplicity, let us again assume that the delay function is of the $\frac{\sin x}{x}$ form with a half-power width $\Delta \tau = (\lambda/2)/C$. The bandwidth function $P(\Delta f)$ or the correlation function in the frequency domain $R(\Delta f)$, would then be a rectangular function, the width of which is

$$\begin{aligned} \Delta f &= \frac{1}{\Delta \tau} = \frac{2C}{\lambda} \\ &= \frac{1}{2} \text{ frequency of the electromagnetic wave} \end{aligned} \quad (3.8)$$

These were the approximate results. Lee and Harp (4) have performed rigorous calculations based on a general expression for the spatial distribution of refractive index. For details the reader is referred to ref (4) and also to ref (5).

Summing up this section on line-of-sight propagation mechanisms in relation to remote sensing, the following should be noted:

- The path loss can be minimized by adjusting the height of the transmitting antenna or the wavelength.
- The vertical coherence distance of field strength can likewise be maximized by adjusting the antenna height. The lower the antenna height, the larger is the coherence distance.
- If we are dealing with a homogeneous refractive index structure, the bandwidth of the line-of-sight circuit can be optimized by decreasing the height of the transmitting antenna.
- Spatial fluctuations in refractive index resulting from atmospheric turbulence impose severe limitations on bandwidth as well as on the vertical coherence distance. There is nothing we can do in order to improve this situation, except noting that the turbulent transmission medium is very variable. Given sufficient time, there will be a time interval where conditions are very much better than the average conditions.

3.2 Propagation mechanisms involving scattering and reflection

As the demand for reliable broad-band communication circuits/high-resolution adaptive radar systems increases, so does the need for detailed information about the transmission medium.

The multitude of new demands leads to a very versatile and sophisticated usage of the transmission medium. This, in turn, calls for a very comprehensive description of the medium. The transmission medium constitutes the limiting factor in many interesting and potentially powerful communication and radar techniques.

Basic relationships in over-the-horizon scatter propagation, a brief summing up

When discussing the characteristic properties of a scattered (or diffracted) wave in relation to radar and communication systems, it is useful to have a physical understanding of the basic principles involved.

With reference to section 2 above and earlier works (5,6) a brief sketch of some of the more important derivations will be given.

Consider a volume element $dv = dx dy dz = d^3\vec{r}$ within the scattering volume V , this scattering volume being confined to the spatial region in the troposphere illuminated by the transmitting antenna and "seen" by the receiving antenna. If the permittivity (refractive index squared) within the elementary volume differs by an amount $\Delta\epsilon$ from the average value of the permittivity ϵ_0 , the element of dielectric becomes polarized, giving rise to a dipole moment $d\vec{p} = \Delta\epsilon dv \vec{E}_0$ when under the influence of an electric field \vec{E} . At distance R from the scattering element the dipole moment results in a polarization potential dv , and provided $k^2 \vec{r} \gg \nabla \nabla \cdot \vec{r}$ (which requires $R \gg V^{1/3}$), the scattered field strength $\vec{E}_s = k^2 \vec{r}$, where \vec{k} is the wavenumber of the electric field. The scattered field resulting from the integral of elementary scattering elements is then given by

$$\vec{E}_s = \frac{k^2}{4\pi R} \int_V \vec{E}_0(\vec{r}) \epsilon(\vec{r}, t) e^{-j\vec{k} \cdot \vec{r}} d^3\vec{r} \quad (3.9)$$

where $\vec{k} = \vec{k}_0 - \vec{k}_s$, \vec{k}_0 and \vec{k}_s being the wavenumbers of the incident and the scattered fields, respectively, such that $|\vec{k}| = (4\pi/\lambda) \sin \theta/2$, where θ , the scattering angle, is the angle between \vec{k}_s and \vec{k}_0 .

In exactly the same way, $\vec{E}_0(\vec{r})$ describes the spatial variations in the electric field within the scattering volume.

From the basic equation above, we see that there are two limiting cases:

- (a) If the field $\vec{E}_0(\vec{r})$ is constant within the scattering volume (or varies slowly in space in comparison with the $\epsilon(\vec{r})$ function), then

$$\vec{E}_s = \frac{k^2 \vec{E}_0}{4\pi R} \int_V \epsilon(\vec{r}) e^{-j\vec{k} \cdot \vec{r}} d^3\vec{r}$$

which states that the scattered field \vec{E}_s is proportional to the Fourier transform of the spatial variation in refractive index within the scattering volume V .

- (b) If $\epsilon(\vec{r})$ is constant within the scattering volume, then the equation tells us that the diffraction field \vec{E}_D is the Fourier transform of the spatial variation in field strength within the scattering volume V (see section 3.3)

$$\vec{E}_D = \frac{k^2 \epsilon}{4\pi R} \int_V \vec{E}_0(\vec{r}) e^{-j\vec{k} \cdot \vec{r}} d^3\vec{r}$$

The intermediate conclusions are visualized in Figure 3.3.

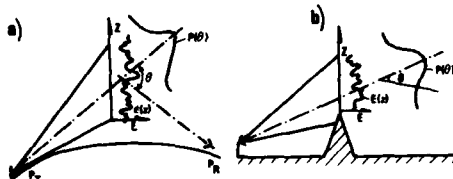


Figure 3.3 a) The scatter field is the Fourier transform of the spatial variations in refractive index $\epsilon(z)$
b) The diffracted field is the Fourier transform of the spatial variation in the illuminating field $E(z)$

Now let us concentrate on the scattered field associated with spatial variations in refractive index $\epsilon(r)$.

We shall need information about the scattered power P as a function of scattering angle θ . To obtain this we multiply \vec{E}_s by its complex conjugate \vec{E}_s^* obtaining the scattering cross-section σ given by

$$\sigma(\theta) = (\pi k^4/2) \phi(\vec{k}) \quad (3.10)$$

where $\phi(\vec{k})$ is the spatial "power spectrum" of the refractive index irregularities such that $\phi(\vec{k})$ is the Fourier transform of the spatial autocorrelation function of $\epsilon(\vec{r})$. The scattering cross-section σ is defined as the mean power in the scattered wave per unit

power density of the incident wave in the scattering volume, per unit solid angle in the direction of k_s , per unit scattering volume.

Note that the power spectrum $\Phi(\vec{k})$ is the Fourier transform of the spatial autocorrelation function of refractive index fluctuation.

Many forms of the $\Phi(\vec{k})$ function have been suggested. The more important ones are associated with the following names: Obukhoff-Kolmogorov, Booker-Gordon, Bolgiano, Willers-Veisskopf, Norton.

In this brief discussion of the subject, a detailed discussion of the relative merits and justification for the various $\Phi(\vec{k})$ functions does not seem justified. There is good justification (2, 6) for writing the power spectrum in the form

$$\Phi(\vec{k}) = K^{-n} \quad (3.11)$$

where n is a number that, depending on the atmospheric conditions, may vary between approximately 2 and 7. Many theories predict $n = 11/3$.

Based on the refractive index spectrum expressed in the form $\Phi(K) = K^{-n}$ we shall now calculate some of the characteristic parameters of a long-distance over-the-horizon remote sensing radar. There are many such, of which should be mentioned: time-delay spectrum, bandwidth, horizontal and vertical correlation distance of field strength, antenna-to-medium coupling loss. These will now be considered.

Calculation of pulse distortion in terms of radiometeorological parameters

Our task is now to calculate the delay function (pulse distortion) and subsequently the bandwidth on the basis of information about the refractive index structure $\epsilon(r)$ as expressed by its spatial power spectrum $\Phi(K)$, written in the form $\Phi(K) = K^{-n}$.

Using a wide-beam antenna so that the multipath transmission is governed by the scattering mechanism rather than by the beam geometry, we first seek an expression relating ϵ and the position in space of the scattering element; i.e. we require an expression relating ϵ and the scattering angle θ (see Figure 3.4). If d is the length of the chord between T and R, then simple geometrical calculations give the required results, namely

$$\theta = 2 |(\epsilon/d)^2 - 1|^{1/2}$$

If we transmit a short radio pulse, the power that reaches the receiver has travelled through a wide spectrum of different paths.

By substituting for θ in the expression for the angular power spectrum ($P \sim \theta^{-n}$), we get the spectrum relating power and path length. Normalizing this power with respect to the power received via the shortest propagation path ϵ_0 , namely that determined by the earth's tangent planes, we get

$$\epsilon_0 = d |1 + (d/2a)^2|^{1/2}$$

(where a is the effective earth radius), the power spectrum takes the form

$$|P(\epsilon)/P(\epsilon_0)| = \left(\frac{4a^2}{d^2}\right)^{-n/2} |(\epsilon/d) - 1|^{-n/2}$$

Expressing this spectrum in terms of the path length $\Delta\epsilon$, which is in excess of the minimum

path length ϵ_0 (i.e. writing $\epsilon = \epsilon_0 + \Delta\epsilon$), we find that the power spectrum referred to ϵ_0 is given by

$$|P(\Delta\epsilon)/P(\epsilon_0)| = \left|1 + \left(\frac{8a^2}{d^2}\right)\Delta\epsilon\right|^{-n/2}$$

And since $\Delta\epsilon = rC$, where C is the velocity of light, the delay function referred to τ_0 (the shortest time delay) is given by

$$|P(\tau)/P(0)| = \left|1 + \frac{8a^2 r C}{d^2}\right|^{-n/2} \quad (3.12)$$

The 1/e width of this delay function is then given by

$$\Delta\tau = \left(\frac{d^2}{8a^2 r C}\right) (e^{2/n} - 1) \quad (3.13)$$

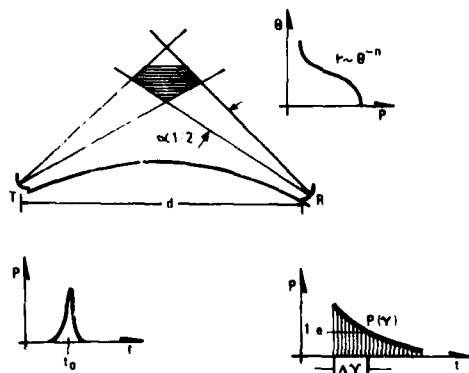


Figure 3.4 The delay spectrum is determined by the variation in path length

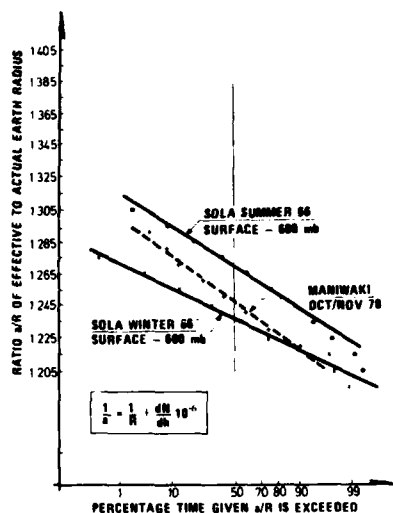


Figure 3.5 Distribution of the ratio of effective to actual earth radius, based on radiosonde observations at Sola, Norway and Maniwaki, Canada (6)

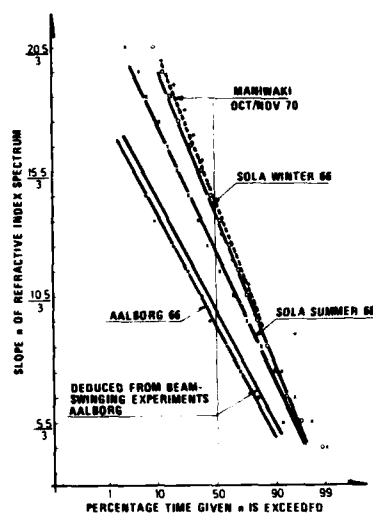


Figure 3.6 Distribution of the slope of the spectrum of refractive index irregularities as deduced from radiosonde observations and beam-swinging experiments (6)

If, on the other hand, the antenna beams are narrow such that the spread in the path length is determined by beam geometry rather than by the $\phi(K)$ function (i.e. the beams are so narrow that $\phi(K)$ can be considered constant when θ varies within the scattering volume), then we can find a simple expression for the delay spectrum in terms of geometrical parameters. Under these conditions the delay function will have a width $\Delta t/C$ given by (6)

$$\Delta t = \frac{d}{2C} \left(\frac{d}{a} B + B^2 \right)$$

where β is the beamwidth.

We have noted that the pulse distortion is determined by the geometry of the transmission circuit and by the atmospheric parameters "a" and "n".

As we have already noted, the parameter "a" is the effective earth radius and is determined by the mean decreases with height of the refractive index. The parameter "n" describes the irregularity structure of the atmosphere in that it gives the slope of the refractive index spectrum when expressed in the form $\phi(K) = K^{-n}$.

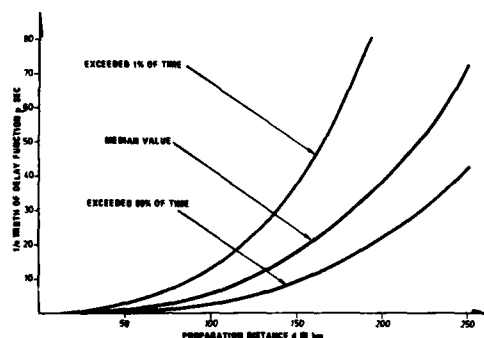


Figure 3.7 The pulse distortion is determined by the length of the transmission path and by the atmospheric refractivity conditions

Note furthermore that both "a" and "n" vary with time and with geographical location. Before we can calculate the pulse distortion, therefore, we shall need information about the variability of "a" and "n". Sets of such distributions are shown in Figures 3.5 and 3.6.

Based on these and on equation (3.13), we can calculate the pulse distortion as a function of propagation distance. This is shown in Figure 3.7.

Having expressed the delay function in terms of geometrical and radio-meteorological parameters, we shall now apply a similar method to calculate the bandwidth of the transmission channel.

Calculation of bandwidth

We transmit a set of radio waves having different frequency. We now make sure that all these frequencies are correlated in amplitude and phase. This is, as an example, achieved by amplitude modulating a carrier, thus obtaining two sidebands $2f_{AM}$ apart, if f_{AM} is the frequency of the modulating wave. These sidebands obviously are correlated in amplitude and phase. At the receiving end we pick up the two sidebands and correlate one with the other (i.e. we form the cross-correlation function $R_{12}(\gamma)$). The more narrow-banded the transmission channel, the poorer is the correlation. (Transmitting many correlated waves spread over a frequency band, we can find the complete autocorrelation function $R(\Delta F)$ in the frequency domain, as discussed in section 2 above.) As we shall see in the following, this is very analogous to the power spectrum of the transmission channel.

By analyzing the first alternative first, we can use the results of simple network theory to obtain a simple approximate result. We know that the response to a delta pulse of a network is known as the impulse response $V(\tau)$ of the network. Furthermore, the Fourier transform of the impulse response is known as the transfer function $F(\omega)$ of the network. By multiplying this transfer function with its complex conjugate, we obtain the power spectrum we are seeking. From the previous section we obtain the expression for the impulse response by taking the square root of equation (3.12). Analyzing this function, we find that it closely resembles an exponential function of the form $P(\tau) = \exp(-a\tau)$. The $1/e$ width of the impulse response is given by

$$\Delta\tau = d^3(e^{4/n} - 1) / 8aC \quad (3.14)$$

To simplify the Fourier transformation, we assume an exponential impulse response such that $\Delta\tau = 1/a$ (when we introduce only a small error). The Fourier transform of the exponential impulse response $\exp(-a\tau)$ is given by

$$F(\omega) = (a + j\omega)^{-1}$$

The power spectrum is then given by

$$\begin{aligned} W(\omega) &= F(\omega) F^*(\omega) \\ &= (a^2 + \omega^2)^{-1} \end{aligned}$$

Substituting for a as obtained from equation (3.14) and normalizing the resulting equation for $\omega = 0$, we find that the $1/2$ power width of the power spectrum is given by

$$\Delta\omega = 8a^2 Cd^{-3} (e^{4/n} - 1)^{-1} \quad (3.15)$$

This expression is plotted as a function of propagation distance in Figure 3.8. Note that, as in the case of pulse distortion, we are dealing with a time variable transmission medium as shown in Figures 3.5 and 3.6. We shall therefore make use of a statistical description.

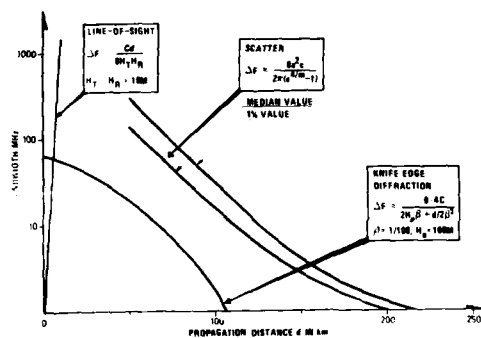


Figure 3.8 The bandwidth of the transmission medium is determined by the geometry and by the propagation medium, the troposphere.

Correlation distance of field strength

In this section attention is focused on the spatial field-strength correlation properties of a scattered radio wave. We have a wide-beam transmitter radiating its power essentially in a horizontal direction. The scattered wave resulting from this transmitter impinges on two nearly identical, small-aperture receiving antennas positioned beyond the horizon relative to the transmitter. The antennas are spaced vertically or horizontally such that the centre line through the receiving antennas is normal to the centre line through the transmitter T and the receivers R . We measure the normalized complex correlation of the voltages induced in the antennas.

As indicated in section 2 above, this spatial field-strength correlation function is the Fourier transform of the angular power spectrum of the wave reaching the receiving antennas. Specifying the angle of arrival of a particular scattered wave by an elevation angle α (relative to the centre line through T and R) and an azimuth angle β (relative to a great circle plane through T and R), we have in the same manner as above, that a refractive index spectrum $\phi(K) \sim K^{-n}$ gives rise to an angular power spectrum of the form

$$P(\alpha, \beta) \sim (g^2 + \alpha^2)^{-n/2} \quad (3.16)$$

The horizontal correlation of field strength is thus obtained by a Fourier transformation of P with respect to β , whereas the vertical correlation is obtained from the $P(\alpha)$ relationship.

A rigorous Fourier transformation of expression (3.16), however, lends itself to numerical computations only. In our case, we need a simple approximate expression. This can

be obtained if we approximate $P(\alpha)$ and $P(\beta)$ by a $\sin x/x$ function, thus giving us a simple expression for the Fourier transform. This is a procedure well known in antenna theory. From antenna theory we know that if L is the width of the illuminating field-strength distribution, then the $1/2$ power width of the resulting angular power spectrum (beam width) is given by

$$\theta_{1/2} = 0.88 \lambda/L \quad (3.17)$$

where λ is the radio wavelength. By applying these results to our problem, we find that the 3-decibel width of the scattered beam as measured in the vertical plane is given by

$$P_{1/2}/P_0 = 1/2 = (\alpha_0 + \alpha_{1/2}/\alpha_0)^{-n} \quad (3.18)$$

where $\alpha_{1/2}$ is the 3-decibel beamwidth of the scattered beam, $\alpha_0 = d/2a$, d is the path length, and a is the earth radius.

By solving for $\alpha_{1/2}$ and substituting this in equation (3.17), we find that the vertical correlation distance of field strength is given by

$$L_v/\lambda = 0.44 \left(\frac{a}{d}\right) (2^{1/n} - 1) \quad (3.19)$$

Similarly, the horizontal correlation distance is given by

$$L_H/\lambda = 0.44 \left(\frac{a}{d}\right) (4^{1/n} - 1)^{1/2} \quad (3.20)$$

These approximate expressions are in very good agreement with the results based on rigorous numerical transformations of the scattered angular power spectra (7).

Note that the correlation distance is only very weakly related to the spectrum slope and that refraction effects play a dominating role.

Pulse distortion, bandwidth, horizontal and vertical correlation distance of field strength are important parameters in relation to remote sensing in that they determine the spatial resolution capability of any remote sensing system, as emphasized in section 2 above. There are several more, such as antenna gain degradation, wavelength dependence, absorption by gases and by precipitation.

In this condensed survey we shall limit ourselves to the most important parameters discussed and summarize the main expressions related to the remaining factors. These are given in Table 3.1. Note that the propagation medium is characterized by the shape n of the refractive index spectrum $n(\beta(K) - K^{-n})$ and the refraction parameter a (effective earth radius).

Since we are interested in the statistics of the various limiting factors constituted by the propagation medium, such as the bandwidth, we need the statistical distribution functions for "a" and "n". Obviously, these are determined by geographical location.

Some examples are given in Figures 3.5 and 3.6. For details, the reader is referred to (6).

In summing up this section on propagation mechanisms involving scattering and reflection, the following should be noted. The parameters characterizing the transmission medium exhibit dramatic variations with time. When illuminating a target through this variable propagation medium, one should bear in mind that the propagation conditions can be favorable during small time intervals only. To achieve maximum radar target resolution therefore, we shall have to take many "snapshots" and select the data sets which give optimum resolution (contrast).

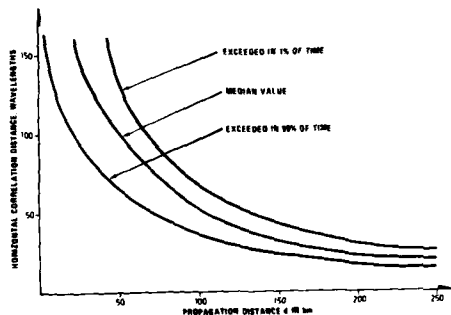


Figure 3.9 Horizontal correlation distance of field strength as a function of distance

COMMUNICATION CIRCUIT PARAMETER	RELATION BETWEEN CIRCUIT PARAMETER AND RADIOSET PARAMETER
WIDTH OF DELAY SPECTRUM	$\Delta\gamma = \frac{d}{8a^2c} (2^{1/n} - 1)$
BANDWIDTH	$\Delta f = \frac{8a^2c}{d} (2^{1/n} - 1)^2$
GAIN LOSS	$G_L = \frac{5.4d^2}{\lambda a^2} (2^{1/n} - 1)(4^{1/n} - 1)^2$
HORIZONTAL FIELDSTRENGTH CORRELATION DISTANCE	$L_H = \frac{0.44\lambda a}{d(2^{1/n} - 1)^{1/2}}$
VERTICAL FIELDSTRENGTH CORRELATION DISTANCE	$L_V = \frac{0.44\lambda a}{d(2^{1/n} - 1)}$
WAVELENGTH	$\frac{P(\lambda_1)}{P(\lambda_2)} = \left(\frac{\lambda_1}{\lambda_2}\right)^{n-1}$

Table 3.1 Some relationships characterizing the propagation medium for an over-the-horizon remote sensing circuit

3.3 Propagation medium involving diffraction by terrestrial obstacles

A review on propagation and remote sensing is not complete unless diffraction by obstacles is included. In order for the presentation to be unified in the sense that the same physical/mathematical concepts are used whenever possible, we shall pursue the approach introduced in Figure 3.10 using Fourier representations.

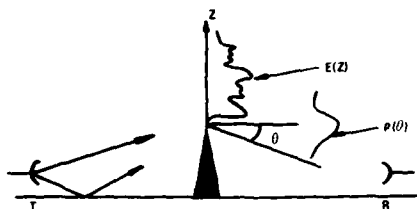


Figure 3.10 Geometry of the diffraction problem

Basic theory of diffraction

Our problem is the following:

The transmitter illuminates a region above the obstacle. This gives rise to a distribution of field strength along a vertical direction above the obstacle. This distribution is determined by multipath effects, by the ground reflection coefficient, and by the radiation properties of the antenna. On the basis of knowledge about $E(z)$, we want to calculate the angular power spectrum $P(\theta)$ of diffracted wave.

We now use exactly the same approach as for the scatter propagation discussed above and derive the following expression for the secondary field E_s (scattered field or diffracted field as the case may be)

$$E_s(K) = \frac{k^2}{4\pi R} \int E_0(z) \epsilon(z) e^{-jKz} dz \quad (3.21)$$

where the symbols are as defined in Figure 3.10.

The angular distribution (K distribution) of the secondary field is the Fourier transform of the $E_0(z) \epsilon(z)$ product. Thus, if we want to calculate the transmission loss resulting from a given obstacle, the procedure is in short the following:

- (1) Calculate the field strength distribution along a vertical direction over the obstacle, considering the influence of ground reflections, etc.
- (2) Having obtained an expression for $E_0(z)$, we compute the Fourier transform of $E_0(z)$, thus obtaining the angular field strength distribution $E_s(\theta)$ of the diffracted wave. In order to obtain the angular power distribution $P(\theta)$, we shall have to multiply $E_s(\theta)$ with its complex conjugate $E_s^*(\theta)$.
- (3) Having obtained the angular power spectrum $P(\theta)$, we shall essentially have to repeat step number one in order to obtain the desired expression for the power received at a given point in the diffraction zone behind the obstacle.

In order to obtain simple, comparatively general and in particular physically interpretable expressions for the field-strength distribution above the obstacle (first step in the procedure) we shall have to idealize the problem and in doing so make certain approximations. Let us consider the case with one direct and one reflected wave.

We then see that the most striking feature of the vertical field-strength distribution is the periodicity. We clearly have a component of field strength which varies in a sinusoidal fashion with height.

Our diffraction problem will therefore be based on the following field strength profile:

- a constant term E_1
- a damped sinusoidal term given by $E_2(z) = E_2 e^{-\alpha z k} \sin \beta z k$

Note that the vertical coordinate z is measured in terms of number of wavelengths $\beta = \lambda/L$, L being the vertical period of field strength variation.

The angular spectrum of the diffracted field is obtained by Fourier transforming the $E(z)$ function.

Performing this, we get the following results (2)

$$F(\theta) = F_2(\theta) + F_1(\theta) \\ = \frac{\beta E_2}{a^2 + \beta^2 - \theta^2 + 2j\alpha\theta} + \frac{E_1}{j\theta} \quad (3.22)$$

The angular power spectrum is then obtained from the following

$$P(\theta) = F(\theta) \cdot F^*(\theta)$$

This function has a pronounced maximum for a certain direction, mainly the direction corresponding to

$$\theta = \pm \sqrt{\beta^2 + \alpha^2}$$

If we have no damping, i.e. if $\alpha = 0$, then we have a Dirac delta function for $F_2(\theta)$ centered at

$$\theta = \beta \quad \text{i.e. at } \theta = \frac{\lambda}{L}$$

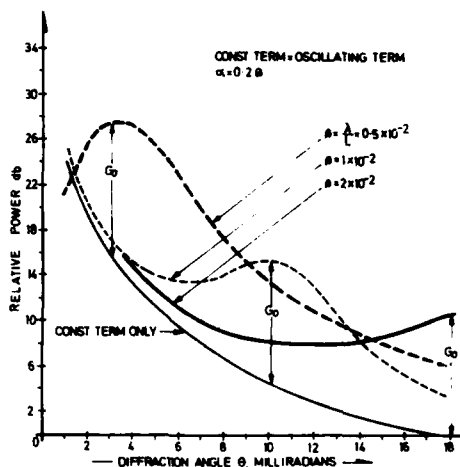


Figure 3.11 Angular diffraction spectrum for various periods of field-strength oscillations

We know that a single ground reflected component interfering with the direct wave will give a field strength distribution above the obstacle of the form given in equation (3.22) above. The damping factor α will then be determined by the rate at which the ground reflection coefficient decreases with increasing angle of incidence to the ground. The period of oscillation L is given by the geometry. Let R be the distance between transmitter and knife-edge obstacle, h the height of the transmitter above the flat earth and λ the radio wavelength; then the period L is given by

$$L = \frac{\lambda R}{2h} \quad (3.23)$$

In this case we will thus have maximum energy diffracted in a direction given by

$$\theta = \frac{2h}{R} \quad (3.24)$$

Thus, by adjusting the height h of the transmitting antenna, we can beam the diffracted wave in the desired direction. This is visualized in Figure 3.11.

Bandwidth limitations of a transmission path involving diffraction

Having formed the basis for calculating the path loss and obstacle gain, we shall now consider the bandwidth limitations of a transmission path involving diffraction. Like in the sections above, the aim is to provide a method which first of all is physically interpretable and which makes it possible to form an opinion as to the relative importance of the various factors involved. Secondly, the aim is to form the basis for approximate calculations.

In section 2 above, we saw that the bandwidth of a transmission circuit is directly determined by the delay function. Knowing the delay function, the bandwidth function (power spectrum) is obtained directly from the delay function by a simple Fourier transformation process. Referring now to Figure 3.12 we see that if the illuminated area above the obstacle is wide, the delay function will be correspondingly wide, and the bandwidth function will be narrow. We shall now consider the case where the illumination is limited to the antenna pattern of width β with elevation angle $\theta/2$ such that the total diffraction angle for symmetrical path will be θ .

From simple geometry we see that the path length difference is given by

$$\Delta l = d/2(\theta\beta + \beta^2)$$

$$\theta = \frac{4H_0}{d}$$

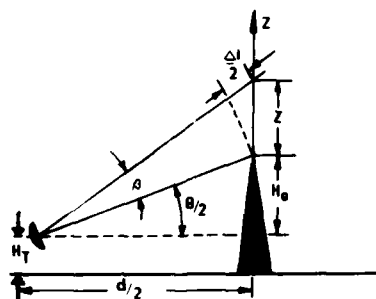


Figure 3.12 Simple path geometry for a transmission path involving knife-edge diffraction

and

$$\delta = \frac{2z}{d}$$

$$\Delta l = \frac{2}{d} (2H_O z + z^2) \quad (3.25)$$

Let us again assume that the field strength distribution above the obstacle is characterized by a damped sinusoidal oscillation superimposed on a unit step function.

Let us denote the spatial period of the oscillations as δz and the damping function Δz . As we have seen in the foregoing section, two limiting cases are of particular interest. First we assume that the ground reflections are such that the oscillating term E_2 dominates over the constant term E_1 . In this case we essentially have a diffracting grating with line spacing δz . The object now is to calculate the bandwidth of such a diffraction circuit. As we have noted from the previous sections, the centre frequency in the bandpass filter is

$$F_O = \frac{c}{\delta l}$$

where δl is the increase in path delay associated with a vertical displacement δz . Making use of this, we find that the centre frequency of our filter is given by

$$F_O = \frac{c}{\frac{2}{d} (2H_O \delta z + \delta z^2)} \quad (3.26)$$

As we have seen in the sections above, we can calculate δz directly from the path geometry. If H_T be the height of the transmitting antenna above the reflecting plane, then

$$\delta z = \frac{\lambda d}{4H_T} \quad (3.27)$$

Making use of this relationship, the expression for the centre frequency of our bandpass filter becomes

$$F_O = \frac{c H_T}{H_O \lambda + \frac{\lambda^2 d}{8H_T}} \quad (3.28)$$

Then let us calculate the width of this bandpass filter. As we have already seen in section 2 above, if the delay function is an exponentially damped sinusoidal with $1/e$ width equal to Δl , and the half-power width of the resulting bandpass filter is equal to

$$\Delta F_{1/2} = 0.16 \frac{c}{\Delta l} \quad (3.29)$$

accordingly, we find the bandwidth $\Delta F_{1/2}$ in the same way as we found the centre frequency F_O above by substituting for Δl using the appropriate value for Δz .

If the geometry is such that

$$2H_O \delta z \gg \delta z^2 \quad (3.30)$$

which requires

$$H_O H_T \gg \frac{\lambda d}{8}$$

then the expression for the centre frequency F_O (equation (3.30) above) reduces to

$$F_O = \frac{c}{\lambda} \frac{H_T}{H_O} \quad (3.31)$$

If we then express the width of the exponential damping function Δz in terms of the relation period δz as

$$\Delta z = n \cdot \delta z$$

our bandwidth becomes

$$\Delta F_{1/2} = \frac{0.16}{n} \frac{c}{\lambda} \frac{H_T}{H_O} \quad (3.32)$$

Note that the factor n is determined by factors such as the rate at which the reflection coefficient of the ground decreases with increasing angle of incidence. This is shown in Figure 3.10.

From the two preceding sections we have shown that it is possible to minimize the transmission loss by adjusting the height of the transmitting antenna (measured in wavelengths) so as to "beam" the diffracted wave in the desired direction. We have also shown that we can adjust the geometry so as to optimize the bandwidth of the transmission circuit. It remains to study the spatial correlation properties of the scattered field. In chapter 2 we have shown that if we are to analyse an object, we shall have to produce an illuminating field which is coherent both as regards phase and amplitude across the object. This means that if the height of the target to be analysed is ΔH , we shall have to organize ourselves so as to produce an illuminating field which is coherent over the vertical region ΔH .

In order to calculate the spatial correlation properties of the scattered field, we shall make use of the results from chapter 2 above.

Here we saw that there is a direct relationship between the angle of arrival spectrum at the receiving site and the spatial correlation of field strength. The spatial correlation, in fact, is the Fourier transform of the angular distribution of the waves impinging on the receiver.

Making direct use of the approach adopted earlier, we find the collection distance of field strength behind a knife-edge obstacle from simple geometrical considerations (8).

3.4 Absorption phenomena

So far, we have concerned ourselves with the influence of the atmosphere in regard to remote sensing and propagation. We have been focusing attention on scattering and diffraction phenomena giving rise to contrast loss, to blurring. We have so far neglected the effect of atmospheric absorption and assumed that the free space attenuation loss is governed by the inverse square law.

A survey on the effect of propagation phenomena on remote sensing is, however, incomplete unless mention is also made of absorption phenomena. This subject has been covered in great detail over the years (9, 10). For the purpose of keeping the current contribution within a reasonable volume, therefore, we shall here limit ourselves to a reference to the mentioned contributions.

4 ADAPTION TECHNIQUES IN RELATION TO THE VARIOUS PROPAGATION MECHANISMS, AN ILLUSTRATING EXAMPLE IN THE FIELD OF COMMUNICATIONS

A communication circuit should ideally adapt itself to allow for maximum information transfer. This means that at any given time the information rate (bandwidth) should make full use of the instantaneous bandwidth of the transmission medium. To achieve this, one has to use the results of the chapter above, where we have characterized the propagation medium in a way which is meaningful in relation to information transfer. If our task is to transmit a certain amount of information from point A to point B, we shall need a buffer store at A and one at B. Between A and B a set of "pilot tones" is transmitted. By the aid of these, the channel parameters of the communication medium are measured continuously. Information about the communication medium is returned to the transmitter, and the system is coded in order to transmit the message at an optimum rate and in a manner which makes optimum use of the available bandwidth. Figure 4.1 illustrates the general scheme.

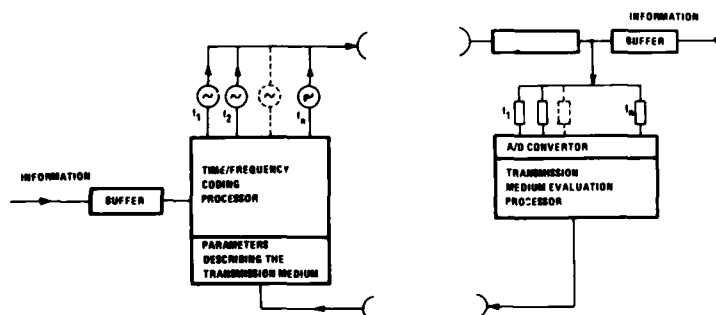


Figure 4.1 A schematic diagram of a propagation medium adaptive communication system. A set of pilot frequencies is transmitted through the propagation medium. The characteristic properties of the transmission medium are assessed by a processor. Information regarding the propagation medium is used to program the time/frequency coding processor of the transmitting system in an adaptive manner.

Note that this scheme is passive in the sense that it only adjusts the information rate so as to be harmonized to the prevailing conditions. We use the same radio carrier frequency, and we confine ourselves to an adjustment of the rate at which the message is transferred on this carrier.

We can also improve the propagation conditions by e.g. changing the carrier frequency.

To illustrate this, we shall confine ourselves to a very specific and well defined transmission mode, namely, one which is based on the spread spectrum concept. This is visualized in Figure 4.2. For this application there are two propagation parameters which are of dominating importance. The first is, obviously, the instantaneous bandwidth of the propagation medium.

Another important parameter describing the propagation medium is the correlation distance in space. We transmit a single wave at point A. At the receiving point B we have a set of vertically spaced receiving antennas. We measure the complex field strength (amplitude and phase) and we compute the spatial autocorrelation function. The antenna separation corresponding to a $1/e$ correlation coefficient, we define as the spatial correlation distance. In the general case where we want both to match to the available bandwidth and take the spatial correlation properties of the propagation medium into consideration, we need a set of transmitters which is capable of transmitting a set of electromagnetic waves with different frequencies in an adaptive manner as illustrated in Figure 4.1 and this set of electromagnetic waves carrying the information to be transferred, should be passed through a computer controlled array element antenna, capable of shaping the wave-front (directing the antenna beam) adaptively so as to minimize the adverse effect of the propagation medium. By means of such a system, we can do more than merely adjusting our information transfer rate to match the available bandwidth. We can adjust our system parameters so as to improve, at any one given instant, the usable bandwidth conditions.

In a practical situation there are many propagation modes to which our system should be capable of adapting, such as:

- propagation phenomena involving ground reflections and line-of-sight
- propagation with ground reflection and no direct path
- propagation conditions involving diffraction shadowing effects
- propagation through refractive irregularities in the troposphere, scattering

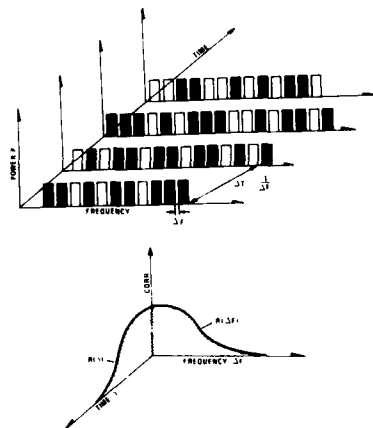


Figure 4.2 A simple schematic coding diagram of a frequency-time adaptive communication system. The information is coded in both frequency and time domain in a manner determined by the propagation medium (the $R(\Delta F)$ and the $R(\Delta t)$ functions)

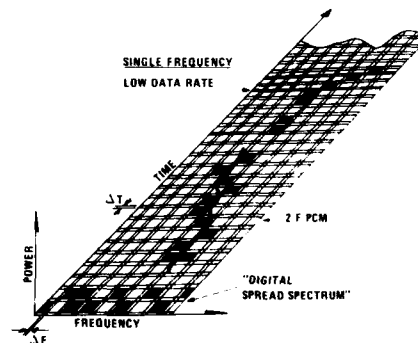


Figure 4.3 Frequency-time-power plot of a self-adaptable communication system. The system adapts itself from wide band spread spectrum through two frequency PCM to a single frequency low data rate system. The total information transfer is proportional to the time-frequency integral.

As an example consider the following.

Adaptivity requirements in relation to line-of-sight propagation with added ground reflections

In chapter 3 we established some simple relationships in connection with line-of-sight propagation. We saw that, by altering the height of the receiving antenna relative to the reflecting plane, a considerable improvement in signal strength is achieved. We also saw that by changing the frequency of the carrier wave, the propagation loss can likewise be minimized. What we want, therefore, is a communication channel which first changes the carrier frequency so as to optimize the conditions from the point of view of transmission loss, and thereafter adjusts the bandwidth for maximum information transfer rate. As an example, with reference to the schematic diagram of Figure 4.1, we shall consider a "spread spectrum or holograph" communication channel. Let us assume that we have at our disposal a large number N of discrete frequency generators on the transmitting end, and these can be switched on and off by a microprocessor. Let us assume that the information word is composed in a binary fashion by switching the frequency generators on and off such that N frequency generators give us an N -bit word as depicted in Figure 4.2. At the receiver, there are N narrow-band filters which are tuned to the corresponding set of transmitting generators. If now the bandwidth of the transmission medium is large enough so as to take care of all the N frequency lines simultaneously, our "message frame" can contain N bits of information. If now the frequency spacing between the channels is ΔF , then we can transmit another N -bit frame after a time interval

$$\Delta T > \frac{1}{\Delta F}$$

(see Figure 4.2).

Then let us assume that the ambient noise level increases such that the noise intensity within each of the N frequency channels exceeds the signal level. To improve this signal-to-noise situation, we must know something about the correlation properties both in frequency and in time of this noise. If the correlation distance in time of the noise is γ_0 , and we can integrate the signal in each frequency slot over a period T , and we receive a signal/noise enhancement proportional to $\sqrt{T/\gamma_0}$, this is the same as repeating the N -bit information frame n times, where $n = T/\Delta T$. We have thus obtained an n -fold redundancy in the time domain.

Then let us do the same in the frequency domain. Let us reduce the information content in our information frame by a factor r such that the information is contained in N/r frequency slots. We have then the possibility of transmitting the same message at the same time in other portions of our available frequency spectrum. With this ratio r between the message bandwidth, we obtain an r -fold redundancy, and the corresponding processing gain. This means that we can increase the ambient noise level correspondingly without altering the error rate of our circuit.

If now the bandwidth of the communication channel decreases whereas the ambient noise level remains constant, then we must confine our "spread spectrum message" or "holographic message" to a set of frequency slots within which we have correlated conditions. This reduces our redundancy potential, and also correspondingly our processing gain.

Now note that we cannot always treat the frequency domain and the time domain separately. When we have "frequency selective fading" resulting from multipath phenomena, then there is a direct relationship between the correlation distance in the frequency domain, and the correlation distance in the time domain (Fourier transforms). For a given coding in the frequency domain, therefore, there is a corresponding one in the time domain. In the general case, however, with "power fading" as well as multipath fading, some improvements in system performance can apparently be achieved by coding both in the frequency domain and the time domain as indicated in Figure 4.2.

To visualize this, Figure 4.3 is presented. This is a sketch of an adaptive communication system which adapts itself both to bandwidth and to centre frequency for maximum field strength. This system can adapt itself from a digital large-bandwidth spread spectrum to a "single frequency" low data-rate channel.

REFERENCES

- (1) Gjessing, Dag T: "Directions in Remote Sensing, Past, Present and Future". In: Processes in Marine Remote Sensing, Eds F J Vernberg and F P Diemer. University of South Carolina Press (1981).
- (2) Gjessing, Dag T: Adaptive Radar in Remote Sensing. Ann Arbor Science Publishers Inc. (1981)
- (3) Bean B R and Dutton E J: Radio Meteorology. US Department of Commerce, National Bureau of Standards, Monogr 92. US Government Printing Office (1966)
- (4) Lee R W and Harp J C: Weak scattering in random media. J IEEE 57 (1969) p 375.
- (5) Gjessing, Dag T: Remote Surveillance by Electromagnetic Waves for Air - Water - Land. Ann Arbor Science Publishers Inc. (1978)
- (6) Gjessing, Dag T and McCormick K S: On the prediction of the characteristic parameters of long-distance tropospheric communication links. IEEE Trans Comm 22 (1974) p 9.

- (7) Grosskopf J: Investigation of the receiving field for scatter propagation. AGARD Conf Proc 37 (1968) pp 22-1 to 22-11.
- (8) Gjessing Dag T: "Propagation Effects in Relation to Remote Sensing". In: Proceedings of the IEE Third International Conference on Antennas and Propagation ICAP 83 (1983).
- (9) Gordy W: "Microwave Spectroscopy". In: Handbuch der Physik. Berlin: Springer-Verlag (1957) p 28.
- (10) Ryde J W: The Attenuation and Radar Echoes Produced at Centimeter Wavelengths of Various Meteorological Phenomena. The Physical Society, London (1946).

BIBLIOGRAPHY

- 1 Gjessing, Dag T: Scattering of radio waves from regular and irregular time varying refractive index structures in the atmosphere. AGARD Conference Proceedings No 37 (August 1968)
- 2 Gjessing, Dag T: Scattering mechanisms and channel characterization in relation to broadband radio communication systems, AGARD Conference Proceedings No 244 (October 1977)
- 3 Früchtenicht H W: Characteristics and applications of line-of-site duct propagation. NATO Advanced Study Institute Series: Modern topics in microwave propagation and air/sea interaction. Ed: A Zanca (1973)
- 4 Gjessing, Dag T: On the use of forward scatter techniques in the study of turbulent stratified layers in the troposphere. *Boundary-Layer Meteorology* 4 (1973) pp 377-396.
- 5 Wait J R: A note on VHF reflection from a tropospheric layer. *Radio Science* 7 (1964) pp 847-848.
- 6 Gjessing, Dag T, Kjelaas A G, Nordø J: Spectral measurements and atmospheric stability. *Journal of Atmospheric Sciences* 26, 3 (May 1969) pp 462-468.
- 7 Grosskopf J: Investigation of receiving field for scatter propagation. AGARD Conference Proceedings 37 (1968) pp 22.1 - 22.11.
- 8 Gjessing, Dag T: Environmental remote sensing. Part I: Methods based on scattering and diffraction of radio waves. *Physics in Technology* 10 (December 1979) pp 266-271.
- 9 Hagfors T: Investigation of the scattering of radio waves at metric wavelengths in the lower ionosphere. *Geophysica Norwegia* 21, 2 (1959).
- 10 Hagfors T: Some properties of radio waves reflected from the moon and their relation to the lunar surface. *Journal of Geophysical Research* 66, 3 (1961) pp 777-785.
- 11 Hjeltnad J; Skaug R: Spread Spectrum Communications with Military Applications. Peter Peregrinus Limited (IEE, London) (1985).
- 12 Ishimaru A: Wave Propagation and Scattering in Random Media. New York: Academic Press (1978).
- 13 Waterman A T, Gjessing D T, Liston C L: Statistical analysis of transmission data from a simultaneous frequency- and angle scan experiment. Contribution to the URSI Spring Meeting, Washington DC (1961).
- 14 Gjessing, Dag T: Target Adaptive Matched Illumination Radar. Principles and applications. Peter Peregrinus Limited (IEE, London) (1986).

SELECTIVE BIBLIOGRAPHY

This bibliography with abstracts has been prepared to support AGARD Lecture Series No.162 by the Scientific and Technical Information Division of the US National Aeronautics and Space Administration, Washington, D.C. in consultation with the Lecture Series Director, Dr Haim Soicher, Department of the Army, Fort Monmouth, New Jersey.

UTTL: A method to correct HF skywave backscattered signals for ionospheric frequency modulation
 AUTH: A/PARENT, JACQUES; B/BOURDILLON, ALAIN
 PAA: B/(Paris VI, Université, France) IEEE Transactions on Antennas and Propagation (ISSN 0018-926X), vol. 36, Jan. 1988, p. 127-135. Research supported by Meteorologie Nationale.

ABS: A method is described to correct HF signals reflected by the ionosphere and backscattered by the sea surface for ionospheric frequency modulation, which produces spectral-line smearing. The statistical mean of the time derivative of the phase of the signal, weighted by the signal energy, is proposed as an estimator of this modulation. The accuracy of the estimator is measured and the efficiency of the signal processing is tested by synthetically contaminating high-quality signals obtained via sporadic E-layer propagation. Examples of data corrected for F2-layer ionospheric perturbations are shown. 88/01/00 88A33500

UTTL: The adaptive suppression of interference in HF ground wave radar

AUTH: A/MADDEN, J. M.
 PAA: A/(Ministry of Defence, Air Systems Div., London, England) IN: Radar - 87; Proceedings of the International Conference, London, England, Oct. 19-21, 1987 (A88-33301 13-32). London and New York, Institution of Electrical Engineers, 1987, p. 98-102.

ABS: The feasibility of the concept of interference suppression in the high-frequency ground wave radar using adaptive null steering in polarization space is demonstrated. The described system uses a horizontal auxiliary aerial that feeds a least mean squares estimation filter to generate an estimate of the interference affecting the radar's performance. Subtraction of this estimate from the affected radar signal results in suppression of the interference. Skywave interference-to-noise levels were reduced by up to 30 dB. The performance depends upon there being a detectable horizontal component of the interference signal's polarization. 87/00/00 88A33318

UTTL: Radar of the '80s and beyond - An update

AUTH: A/BROOKNER, ELI
 PAA: A/(Raytheon Co., Equipment Div., Weyland, MA) IN: International Conference on Radar, 1st, Nanjing, People's Republic of China, Nov. 4-7, 1986, Record (A88-33176 13-32). Beijing, China Academic Publishers, 1986, 20 p.
 ABS: This paper provides an update of a paper by Brookner (1986). Since then the construction of two new PAVE PAWS radars has started. Also a solid state UHF phased array upgrade of the Thule, Greenland BMEWS radar has started. A production run of 92 B-18 X-Band phased array radars has been initiated. The Patriot C-Band phased array radar, which is in production, has been ordered by West Germany, Japan and the Netherlands. The AEGIS S-Band phased array radar has gotten well into its production phase. 16

systems having been ordered. Considerable progress has been made on the development of MMIC for radar from L-Band to X-Band. All the VHSIC Phase 1 contractors have developed working chips. The new adaptive-adaptive array processing technique has been developed which reduces the processing complexity and transient time of adaptive array processing by orders of magnitude. 86/00/00 88A33300

UTTL: Solid state transmitters for modern radar applications

AUTH: A/HOFT, DONALD J.; B/AGI, FUAT
 PAA: B/(M/A-COM, Inc., Burlington, MA) IN: International Conference on Radar, 1st, Nanjing, People's Republic of China, Nov. 4-7, 1986, Record (A88-33176 13-32). Beijing, China Academic Publishers, 1986, p. 775-781.

ABS: To exemplify the advancing state-of-the-art in radar SS transmitters, this paper describes in some detail three major systems covering a broad range of frequencies: HF, UHF and L-band, which utilize SS transmitters. At HF a 200 kW CW transmitter is described which is applicable in an over-the-horizon radar application; at UHF the Pave Paws (AN/FPS-115) long-range phased array radar transmitter (over 0.5 megawatt PK power per face) is presented; and finally at L-band an 80 kW pulsed transmitter for shipboard and ATC surveillance applications is described. 86/00/00 88A33282

UTTL: HF sky-wave backscatter over-the horizon radar

AUTH: A/WANG, JUN; B/WU, CHANGGEN
 PAA: B/(Nanjing Research Institute of Electronic Technology, People's Republic of China) IN: International Conference on Radar, 1st, Nanjing, People's Republic of China, Nov. 4-7, 1986, Record (A88-33176 13-32). Beijing, China Academic Publishers, 1986, p. 84-89.

ABS: HF sky-wave backscatter over-the horizon radar detects over-the-horizon targets from the ionospheric reflection of HF radio waves. In this paper, the configuration, properties and some testing results of an experimental prototype of the OTH-B radar system which has been operating for three years, are presented. An experimental prototype of OTH-B radar system was built for the study of the OTH-B radar. It is a monostatic PD pulse radar with separate transmitting and receiving antennas and ionosounder. 86/00/00 88A33182

UTTL: Cross-correlation analysis and interpretation of spaced-receiver measurements

AUTH: A/COSTA, EMANUEL; B/FOUGERE, PAUL F.; C/BASU, SANTIMAY
 PAA: A/(Emmanuel College, Boston, MA); C/(USAF, Geophysics Laboratory, Hanscom AFB, MA) Radio Science (ISSN 0048-6604), vol. 23, Mar.-Apr. 1988, p. 141-162.

ABS: The results of two algorithms which provide a statistical treatment of the estimation parameters in the cross-correlation analysis of spaced-receiver data are compared. The observations are found to be consistent with a previous morphological model for anisotropy of high

Latitude nighttime F region irregularities. It is suggested that a possible dependence of the results of the spaced-receiver measurements on the receiver baselines may be responsible for the relatively small values of the anisotropy of the diffraction pattern noted in Hlat satellite measurements. A procedure for estimating the anisotropy of the in situ irregularities from the anisotropy of the diffraction pattern is proposed.
88/04/00 88A33146

UTTL: A study of gravity waves ionospheric electron content at $L = 4$

AUTH: A/HUNSUCKER, ROBERT D.; B/HARGREAVES, JOHN K.
PAA: A/(Alaska, University, Fairbanks); B/(Lancaster, University, England) Journal of Atmospheric and Terrestrial Physics (ISSN 0021-9169), vol. 50, Feb. 1988, p. 167-172.

ABS: Using satellite radio beacon transmissions, traveling ionospheric disturbances have been observed in the electron content at $L = 4$. Waves are a common feature at this latitude, present for at least 98 percent of all daylight hours. The amplitude is usually 1-4 percent of the mean electron content, and periods range between 15 and 90 minutes. Simultaneous observation of two satellite beacons, giving an effective east-west separation of 350 km, indicated apparent east-to-west velocities of 200-700 m/s. A search was made for a likely source of the waves, using data from magnetometers and riometers, from incoherent scatter radar measurements of Joule heating, and from orbiting satellite measurements of electron influx, but no definite source could be established. It is also shown that traveling disturbances are closely related to occurrences of spread-F on ionograms at high latitudes.
88/02/00 88A29350

UTTL: The spatial coherence of Schumann activity in the polar cap

AUTH: A/HULTHAM, P. M.; B/MCASKILL, B. J.
PAA: B/(Defence Research Establishment Pacific, Victoria, Canada) Journal of Atmospheric and Terrestrial Physics (ISSN 0021-9169), vol. 50, Feb. 1988, p. 83-92.

ABS: The spatial coherence of the first two Schumann resonant modes has been studied at two locations in the polar cap separated by 1100 km. Measurements were made at Assistance Bay and Mould Bay, which have geomagnetic latitudes of 83 and 79 deg, respectively, and satellite time-keeping was employed to accurately synchronize the field stations. The coherence was found to be high, typically 95 percent for the first Schumann mode, and was unaffected by changes in Kp, a storm sudden commencement, or a solar flare event. Polarization rotations were observed between the two stations, which could most likely be attributed to the coastline effect. The results are consistent with a stable propagation of Schumann activity from midlatitudes to high latitudes that is relatively unaffected by changes in the polar cap ionosphere.
88/02/00 88A29343

UTTL: On the potential of a system of transionospheric sounding by geostationary satellites

A/SERAFIMOVA, M. K.; B/SERAFIMOV, K. B.
PAA: A/(Bulgarska Akademiia na Naukite, Geofizicheski Institut, Sofia, Bulgaria); B/(Bulgarska Akademiia na Naukite, Tsentraina Laboratoriia po Vissha Geodeziia, Sofia, Bulgaria) Bolgarskai Akademiia Nauk, Doklady (ISSN 0366-8681), vol. 40, no. 12, 1987, p. 29-32.

ABS: Transionospheric sounding is a novel technique of satellite/ground-based investigation for the entire ionosphere, using satellite ionosondes of the Intercomos-19 satellite type. Attention is presently given to a system based on this technique that employs three geostationary satellites. The accurate determination of the sounding 'portion frequency' requires a ground ionosonde for automatic calculation of the satellite's maximum usable frequency, conducted by a microprocessor controller of the ground transmitter.
87/00/00 88A28622

UTTL: Low-frequency waves and electric fields in the magnetospheric current sheets

A/HRUSKA, A.
PAA: A/(National Research Council of Canada, Herzberg Institute of Astrophysics, Ottawa) Journal of Geophysical Research (ISSN 0148-0227), vol. 93, Feb. 1, 1988, p. 1002-1006.

ABS: Low-frequency disturbances in a plasma immersed in a force-free magnetic field B0 characterized by a zero-order field-aligned current J are analyzed in the short-wave approximation. A parallel electric field often substantially modifies the properties of waves in the typical current sheets in the near-earth magnetosphere. The mode of oscillations corresponding in the limit $J = 0$ to the Alfvén mode is partly or totally absorbed on the auroral oval field lines. Conditions under which optimum absorption occurs are pointed out. The second mode of oscillations, which correspond to the compressional wave in the limit $J = 0$, is not substantially affected by the magnetospheric current sheets.
88/02/01 88A25897

UTTL: Errors of the inverse problem of transionospheric sounding

A/DANILKIN, N. P.; B/DENISENKO, P. F.; C/LEVCHENKO, I. F.
PAA: C/(Institut Prikladnoi Geofiziki, Moscow; Rostovskii Gosudarstvennyi Universitet, Rostov-on-Don, USSR) Geomagnetizm i Aeronomiia (ISSN 0016-7940), vol. 27, Nov.-Dec. 1987, p. 916-920. In Russian.

ABS: Error sources for the inverse transionospheric-sounding problem are considered in connection with the ill-posedness of this problem. It is shown that the dispersion of the initial data is determined by errors of three measured parameters: the group paths of the transionogram, the effective heights of the topside-sounding ionogram, and the critical frequency.

- Since the critical-frequency errors depend on energy losses in the ionosphere, an estimate is made of the spatial attenuation and absorption of radio waves necessary in the planning of experiments on transionospheric sounding. 87/12/00 88A25581
- UTTL: HF propagation at high latitudes
- AUTH: A/JONES, T. B.
PAA: A/(Leicester, University, England) IN: International Conference on Antennas and Propagation, 5th, York, England, Mar. 30-Apr. 2, 1987, Proceedings, Part 2 (A88-17501 05-32). London, Institution of Electrical Engineers, 1987, p. 155-169.
- ABS: A review of problems associated with HF propagation at high latitudes is presented. Disturbances and electron densities are greater in the ionosphere in the auroral oval than in other parts of the polar ionosphere. The high latitude ionosphere is characterized by a marked absorption of radio waves traveling through the region, particularly during geomagnetically disturbed periods. In a high latitude HF circuit, a large number of modes can be supported. The general turbulence, tilts, and field-aligned irregularities present in the polar ionosphere can produce multiple ray paths between the transmitter and the receiver, leading to destructive interference in the composite received signal. 87/00/00 88A17636
- UTTL: Experimental measurement and characterization of ionospheric and multipath errors in differential GPS
- AUTH: A/SENKOWITZ, J. W.; B/PIETRASZEWSKI, D.
PAA: A/(Bradley University, Peoria, IL); B/(USCG, Research and Development Center, Groton, CT) IN: Institute of Navigation, National Technical Meeting, Anaheim, CA, Jan. 20-23, 1987, Proceedings (A88-17326 05-04). Washington, DC, Institute of Navigation, 1987, p. 168-172.
- ABS: Propagation decorrelation errors and local multipath errors in real-time differential GPS are estimated on the basis of extensive two-frequency P-code and integrated Doppler data collected over 150 and 1500 km. The estimation scheme treats multipath errors and carrier-code offsets as state variables; the resulting Kalman filter yields the very precise carrier observation, corrected to carrier-code offset. The day-to-day repeatability of multipath errors is illustrated, and the decorrelation of ionospheric errors across short and long baselines is evaluated. The present study was conducted in an effort to help establish an error budget for any monitor station network that the U.S. Coast Guard would consider for a nationwide system. 87/00/00 88A17343
- UTTL: Characterizing the multipath and Doppler spreads of the high-latitude meteor burst communication channel
- AUTH: A/WEITZEN, JAY A.; B/SONDA, MICHAEL J.; C/SCOFFIDIO, ROB A.; D/QUINN, JOHN
PAA: A/(SIGNATRON, Inc., Lexington; Lowell, University, MA):
- D/(USAF, Rome Air Development Center, Hanscom AFB, MA) (ITCP/STP-8 Workshop on Meteor Burst Communication in the 1990's, Farnborough, England, June 1987) IEEE Transactions on Communications (ISSN 0090-6778), vol. COM-35, Oct. 1987, p. 1050-1058.
- ABS: High-latitude propagation phenomena, such as scatter from the aurora and sporadic-E propagation, can alter the communication characteristics of the meteor communication channel. This paper describes an experiment in which the fading and multipath profiles of the high-latitude meteor communication channel were characterized. The effects of high-latitude propagation phenomena on the capacity and reliability of meteor burst communication are discussed. 87/10/00 88A16374
- UTTL: Superradiance dynamics of three-dimensional media
- AUTH: A/ANDREEV, A. V.; B/TIKHOMIROV, O. IU.; C/SHAIYMKULOV, M. O.
PAA: A/(Moskovskii Gosudarstvennyi Universitet, Moscow, USSR) Akademiia Nauk SSSR, Doklady (ISSN 0002-3264), vol. 298, no. 1, 1987, p. 77-79. In Russian.
- ABS: The characteristics of superradiance of three-dimensional media with the Fresnel number less than 1 are analyzed, and the laws governing changes in the superradiance pulse parameters in this region are determined as a function of F. The analysis of superradiance dynamics is carried out for the case of Bragg diffraction in a thin crystalline film. The results of the study can be used in optimizing experimental systems in the F range investigated. 87/00/00 88A14747
- UTTL: Prediction of disturbances in HF radio channels at high latitudes
- AUTH: A/BLAGOVESHCHENSKII, D. V.; B/ZHEREBTSOV, G. A.
PAA: Radiotekhnika (ISSN 0033-8486), Aug. 1987, p. 63, 64. In Russian.
- ABS: The feasibility of using oblique sounding on high-latitude HF paths to predict global magnetic storms is demonstrated. The proposed approach makes it possible to predict the commencement of the main storm phase and the associated ionospheric disturbance several hours in advance. 87/08/00 88A14668
- UTTL: A scintillation theory of fading in long distance HF ionospheric communications
- AUTH: A/BOOKER, HENRY G.; B/TAD, JING-WEI; C/BEHR0021-T0051, AMIR B.
PAA: C/(California, University, La Jolla) Journal of Atmospheric and Terrestrial Physics (ISSN 0021-9169), vol. 49, Sept. 1987, p. 939-958. Research supported by the Los Alamos National Laboratory.
- ABS: In the present consideration of the fading of radio waves returned at oblique incidence from the ionospheric F-region in the HF band, in light of scintillation theory, emphasis is given to behavior near the maximum usable frequency for one-hop F-transmission over distances of up

- to 4000 km. Estimates are presented for long and short term fluctuations of phase, the fading correlation distance, the quasi-period of fading, the twinkling angular departure of the azimuth from the mean, and the correlation bandwidth. Theoretical estimates of the scintillation parameters are compared with experience in long distance HF ionospheric communications over the last 60 years. 87/08/00 88A12398
- UTTL: A scintillation theory of the fading of HF waves returned from the F-region - Receiver near transmitter
AUTH: A/BOOKER, HENRY G.; B/TAD, JING-WEI
PAA: B/(California, University, La Jolla) Journal of Atmospheric and Terrestrial Physics (ISSN 0021-9169), vol. 49, Sept. 1987, p. 915-938. Research supported by the Los Alamos National Laboratory.
- ABS: Scintillation theory is used to study the fading of HF radio waves returned from the ionospheric F-region to a receiver close to the transmitter. Estimates are made of (1) the fluctuations of phase both for long term and for short term, (2) the correlation distance, (3) the quasi-period of fading, (4) the angular divergence in the direction of arrival around the zenith, and (5) the correlation bandwidth. The calculations are made as a function of wave frequency for two ionospheric penetration frequencies representative of high day-time values and low pre-sunrise values. Results are compared with observations of fading made with ionosondes over the past 40 years. 87/08/00 88A12398
- UTTL: The possibility of using the regularization method in the problem of transionospheric sounding
AUTH: A/DANILKIN, N. P.; B/DENISENKO, P. F.; C/KOVALEV, V. A.; D/SOTSKII, V. V.
PAA: B/(Institut Prikladnoi Geofiziki, Moscow; Rostovskii Gosudarstvennyi Universitet, Rostov-on-Don, USSR) Geomagnetizm i Aeronomiya (ISSN 0013-7940), vol. 27, July-Aug. 1987, p. 550-552. In Russian.
- ABS: The regularization method is used to study the question of the accuracy with which vertical variations of ionospheric electron density can be determined from satellite radio-occultation measurements of the ionosphere. The investigation is carried out in the isotropic plane-stratified ionosphere approximation, and the results indicate the high efficiency of the regularization method when applied to the inverse problem of transionospheric sounding. 87/08/00 88A11355
- UTTL: Satellite positioning systems
AUTH: A/MEYDEL, W.
PAA: A/(DFVLR, Institut fuer Hochfrequenztechnik, Oberpfaffenhofen, Federal Republic of Germany) (Deutsche Gesellschaft fuer Ortung und Navigation, Navigationstagung ueber moderne Technologie in Ortung und Navigation, Duesseldorf, Federal Republic of Germany, May 6-8, 1987)
- Ortung und Navigation (ISSN 0474-7550), vol. 28, no. 2, 1987, p. 290-321. In German.
- ABS: The basic physical principles, technology, and capabilities of satellite positioning systems (SPFSs) are examined in a general overview. Topics discussed include the properties of EM waves as a basis for measurement; two-way (rader) SPFSs with active satellites (to locate passive targets); one-way SPFSs with active satellites (for self-location using a passive receiver); one-way SPFSs with passive satellites and active objects (for emergency search-and-rescue use); radar altimeters, range scatterometers, and SARs; Doppler methods; and range-difference and pseudorange time-of-flight methods. Consideration is given to problems of precision in time measurements and orbit measurement and prediction. Improved precision using differential methods, the predicted accuracy of Navstar GPS, propagation-related limitations, user demands, and political and economic factors influencing future SPFS development. 87/00/00 88A10683
- UTTL: An investigation of the forward scattering theorem
AUTH: A/KARAM, M. A.; B/FUNG, A. K.
PAA: B/(Texas, University, Arlington) CORP: Texas Univ. Remote Sensing Symposium, Ann Arbor, MI, May 18-21, 1987, Digest, Volume 2 (A87-53101 24-43). New York, Institute of Electrical and Electronics Engineers, Inc., 1987, p. 1007-1012.
- ABS: The calculation of an EM wave's extinction loss during propagation within an inhomogeneous medium, as in active and passive remote sensing modeling, can be undertaken either through the summation of the scattering and absorption losses or through the use of the forward scattering theorem. Attention is presently given to the similarities and differences of these two approaches as a function of dielectric properties of a spherical scatterer and the incident frequency. Scattering loss is obtainable by integrating the magnitude-squared of the scattered field over a spherical surface surrounding the scatterer; the scattered field and the field within the scatterer are computed according to Mie theory. 87/00/00 87A53220
- UTTL: Mid-latitude F-region irregularity characteristics obtained by spaced-receiver scintillation measurements
AUTH: A/KUMAGAI, H.; B/OGAWA, T.
PAA: B/(Ministry of Posts and Telecommunications, Radio Research Laboratories, Koganei, Japan) IN: International Beacon Satellite Symposium on Radio Beacon Contribution to the Study of Ionization and Dynamics of the Ionosphere and to Corrections to Geodesy and Technical Workshop, Dulu, Finland, June 9-14, 1986, Proceedings, Part 2 (A87-50101 22-46). Dulu, Finland, University of Dulu, 1986, p. 93-99.
- ABS: Using three closely spaced antennas, midlatitude nighttime scintillation at 136 MHz was observed. By means of correlation analysis, it is confirmed that the ionospheric

irregularities have well developed field-aligned structures, of which the mean minor radius and axial ratio are 182 m and 24, respectively. The axial ratio increases and the minor radius decreases with the increase in S4. The drift direction obtained is almost normal to that of irregularity elongation, and drift velocity is essentially less than 40 m/s. 86/00/00 87A50134

UTTL: Measurements of trans-ionospheric propagation

parameters in the polar cap ionosphere
AUTH: A/KLOBUCHAR, J. A.; B/ANDERSON, D. N.; C/BISHOP, G. J.;
D/DOHERTY, P. H.

PAA: C/USAF, Geophysics Laboratory, Hanscom AFB, MA);
D/Emmanuel College, Boston, MA) IN: International
Beacon Satellite Symposium on Radio Beacon Contribution to
the Study of Ionization and Dynamics of the Ionosphere and
to Corrections to Geodesy and Technical Workshop, Oulu,
Finland, June 9-14, 1986, Proceedings, Part 2 (A87-50101
22-46). Oulu, Finland, University of Oulu, 1986, p. 59-67.
Measurements of absolute TEC were made for the first time
from the polar cap station located at Thule, Greenland in
early 1984 using dual frequency group delay measurements
from high orbit satellites. Measurements of L-band
amplitude scintillation and dual frequency differential
carrier phase scintillation were also made. The
variability of the TEC was extremely large, with increases
above the background values of more than 100 percent
observed frequently. Quasi-periodic TEC enhancements with
periods as short as ten minutes were seen over several
time intervals of more than two hours. The absolute values
of TEC observed in the dark polar cap ionosphere at times
exceeded the diurnal maximum values from the midlatitude
ionosphere during this initial period of observations.
86/00/00 87A50132

ABS: UTTL: Scintillation and ionospheric irregularity studies
using GNSS satellites and Eiscat
AUTH: A/KERSLEY, L.; B/PRYSE, S. E.; C/WHEADON, N. S.
PAA: C/University College of Wales, Aberystwyth) IN:
International Beacon Satellite Symposium on Radio Beacon
Contribution to the Study of Ionization and Dynamics of
the Ionosphere and to Corrections to Geodesy and Technical
Workshop, Oulu, Finland, June 9-14, 1986, Proceedings,
Part 2 (A87-50101 22-46). Oulu, Finland, University of
Oulu, 1986, p. 51-57. SERC-supported research.
An experiment is described in which the Eiscat ionospheric
radar is scanned meridionally in a special program mode
designed to give f-layer electron densities and other
parameters with a horizontal resolution of a few
kilometers. This mode is run at times to coincide with
passes of GNSS satellites whose transmissions are being
monitored simultaneously by a computer-controlled
receiving system situated at Kiruna, Northern Sweden. Some
results are presented in which scintillation arising from
sub-kilometer scale irregularities can be identified with
features of larger scale observed by the Eiscat radar.

These include a strong equatorward gradient in electron density which may have been destabilized by an electric field, structures in electron density which appear to be associated with soft-particle precipitation and an isolated blob of enhanced electron concentration which appears to be related to a localized patch of scintillation. 86/00/00 87A50131

UTTL: URSI and Nachrichtentechnische Gesellschaft, General
Session, Kleinheubach, West Germany, Oct. 6-10, 1986.
Reports: Kleinheubacher Berichte (ISSN 0343-5725), vol.
30, 1987, 553 p. In German and English. For individual
items see A87-48609 to A87-48636.

FACTS affecting the atmospheric propagation of EM waves,
research on the ionosphere, and advances in reviews and
communications technology are examined in reviews and
reports. Topics discussed include refraction corrections
for radio astronomy and geodesy, speckle masking, radar
studies of atmospheric motion, EISCAT measurements in the
polar electrojet, active experiments in the polar
ionosphere, and dispersion relations for drift-Alfven and
drift-acoustic waves. Consideration is given to a
microcomputer prediction system for HF communications over
Europe, frequency determination of a hyperfine line of CH4
at 88 THz, multipath propagation in digital mobile
communication, a robust digital voice transmission
technique for land mobile radio, CMOS LSI for digital
signal processing in mobile radio equipment, the
representation of EM fields by dyadic Green functions,
scalarization of Maxwell's equations for anisotropic
media, and satellite antennas for land vehicles and
aircraft. 87/00/00 87A48608

UTTL: Wave depolarization during backscattering by
anisotropic irregularities of the ionosphere
AUTH: A/ZHIDOVLENKO, I. IU.; B/PRIKHOD'KO, L. I. Akademika
Nauk Turkmenko SSR, Izvestiya, Seriya
Fiziko-Tekhnicheskikh, Khimicheskikh i Geologicheskikh
Nauk (ISSN 0002-3507), no. 6, 1986, p. 16-19. In Russian.
Consideration is given to wave scattering by artificial
small-scale irregularities formed by the heating of the
f-layer by high-power short-wave radio waves vertically
incident on the ionosphere. Numerical results are
presented on the depolarization of the scattered field in
the case when the incident beam goes beyond the ionosphere
and a backscattered signal is observed on the ground. The
results obtained illustrate the effect of the anisotropy
of the correlation function of small-scale ionospheric
irregularities on the depolarization of backscattered
signals. 86/00/00 87A42950

UTTL: Effect of the meridional component of the neutral
wind on the macroscopic structure of the high-latitude
ionosphere
AUTH: A/GOLIKOV, I. A.; B/CHERNYSHEV, V. I.; C/ZABOLOTSKII, M.
S.

- PAA: C/(Toskii Gosudarstvennyi Universitet, Tomsk, USSR) Geomagnetizm i Aeronomiya (ISSN 0016-7940), vol. 27, Mar.-Apr. 1987, p. 318, 319. In Russian.
- ABS: It is shown that the magnitude and direction of the meridional component of the thermospheric wind have a significant effect on the macroscopic structure of the ionosphere at subauroral latitudes, particularly in the main ionospheric trough. The phase of this component during evening-morning periods has a substantial effect on the configuration, extent, magnitude, and location of the trough. It is concluded that the phase and magnitude of the meridional component should be taken accurately into account in models of the high-latitude ionosphere. 87/04/00 87A42028
- UTTL: An LMS adaptive array for multipath fading reduction A/DGAWA, YASUTAKA; B/OHMIYA, MANABU; C/IIOH, KIYOHiko C/(Hokkaido University, Sapporo, Japan) IEEE Transactions on Aerospace and Electronic Systems (ISSN 0018-9251), vol. AES-23, Jan. 1987, p. 17-23
- ABS: The application of a least-mean-square (LMS) adaptive array to the problem of multipath fading reduction is discussed. However, it is known that multipath components are in general correlated with one another. The effect of the correlation on the performance of the LMS adaptive array is examined. When the correlation coefficient does not equal or approximate 1, the LMS adaptive array suppresses the multipath signals significantly by nulling. On the other hand, when the correlation coefficient nearly equals 1, the LMS adaptive array prevents the output signal power from decreasing. Therefore, the LMS adaptive array may reduce the multipath fading effectively for any correlation coefficient value. A reference signal in the LMS adaptive array is also discussed. It is shown that synchronization in the reference signal generation must be extremely accurate. Moreover, a processor configuration is proposed which may generate the reference signal with the required accuracy. 87/01/00 87A39729
- UTTL: The USA builds its OTH-B radar barrier A/LOPEZ, RAMON Interavia (ISSN 0020-5168), vol. 42, April 1987, p. 324, 325.
- ABS: The USAF's Over-the-Horizon Backscatter (OTH-B) radar system, which is correctly under development, will, when operational in the 1990s, furnish long-range, all-altitude tactical early warning and surveillance of aircraft and cruise missiles approaching North America irrespective of their degree of stealth technologies' incorporation. OTH-B achieves its extensive range by bouncing very powerful high frequency signals off the ionosphere 50-250 miles above the earth's surface; returning echoes from targets follow the same path back to earth stations. 87/04/00 87A39477
- UTTL: The frequency management system of the Jindalee over-the-horizon backscatter HF radar
- AUTH: A/EARL, G. F.; B/WARD, B. D. B/Defence Science and Technology Organization, Electronics Research Laboratory, Adelaide, Australia) Radio Science (ISSN 0048-6604), vol. 22, Mar.-Apr. 1987, p. 275-291.
- ABS: Real-time frequency management is a vital element in the effective operation of an over-the-horizon backscatter (OTH-B) HF radar. In the case of the Australian project Jindalee OTH-B HF radar, a comprehensive frequency management system has been developed for this purpose. The frequency management system includes subsystems for ionospheric backscatter, vertical and oblique incidence sounding, HF spectral surveillance, and incorporates a low powered backscatter radar. The system is capable of providing real-time frequency management advice to the main radar, and of acquiring synoptic data for off-line analysis. In this paper the hardware architecture and signal processing schemes, together with sample data, are described for each of the subsystems. Consideration is also given to the manipulation of the environmental data in order to provide frequency management advice to the main radar. 87/04/00 87A37085
- UTTL: Array radars: An update. 1 A/BROOKNER, ELI A/(Raytheon Co., Equipment Div., Weyland, MA) Microwave Journal (ISSN 0026-2597), vol. 30, Feb. 1987, p. 117, 118, 120 (11 pp.).
- ABS: New radar developments are discussed with attention given to phase-phase steered arrays, one-dimensional electronic scanning, three-dimensional stacked beam systems, over-the-horizon radars, and bistatic radar systems. It is noted that considerable progress has been made in the development of monolithic microwave integrated circuits for radar from L band to X band. In addition, a new adaptive-adaptive array processing technique which reduces the processing complexity and transient time of adaptive array processing by orders of magnitude has been developed. 87/02/00 87A32108
- UTTL: Spontaneous decay of a tangential discontinuity A/HEYNE, M. F.; B/BIERNAT, H. K.; C/SEMENOV, V. S. B/(Oesterreichische Akademie der Wissenschaften, Institut fuer Weltraumforschung, Graz, Austria); C/(Leningradskii Gosudarstvennyi Universitet, Leningrad, USSR) (COSPAR, IAGA, and SCOSTEP, Plenary Meeting, 26th, Symposium on Solar Wind Interactions, 6th, Toulouse, France, June 30-July 11, 1986) Advances in Space Research (ISSN 0273-1177), vol. 6, no. 1, 1986, p. 115-117.
- ABS: Tangential discontinuities in a magnetized plasma are potential sources of large-scale events provided there is a reasonable shear in the magnetic field. Independent of the accurate trigger mechanism, the tangential discontinuity will spontaneously resolve into a combination of genuine slow shocks, centered slow expansion waves, and intermediate and contact

- discontinuities. In the present paper, the resolution of a tangential discontinuity problem is phrased as initial value problem, using the equations of ideal MHD to investigate nondispersive and nondissipative initial value problems and wave propagation problems. 86/00/00 87A23120
- UTTL: An analysis of the high-latitude thermospheric wind pattern calculated by a thermospheric general circulation model. II - Neutral parcel transport
- AUTH: A/KILLEEN, T. L.; B/ROBLE, R. G.
- PAA: A/(Michigan, University, Ann Arbor); B/(High Altitude Observatory, Boulder, CO) CORP: Michigan Univ., Ann Arbor.; Colorado Univ., Boulder; Journal of Geophysical Research (ISSN 0148-0227), vol. 91, Oct. 1, 1986, p. 11291-11307.
- ABS: A diagnostic package developed to analyze runs made by the National Center for Atmospheric Research thermosphere general circulation model is used to calculate neutral parcel trajectories in the high-latitude E and F regions. Parcel trajectories are presented for a number of different cases to illustrate the main characteristics of F region parcel transport in the winter high-latitude region. Several examples of E region parcel trajectories are similarly analyzed, concentrating on both the southern (summer) and northern (winter) regions. F region parcel trajectories are calculated backward in time from passage over a given geographical location to illustrate the 'genesis' of those parcels whose velocities can be monitored from a ground-based Fabry-Perot observatory. 86/10/01 87A20062
- UTTL: Comparison of superresolution algorithms for radio direction finding
- AUTH: A/JOHNSON, R. L.; B/MINER, G. E.
- PAA: B/(Southwest Research Institute, San Antonio, TX) IEEE Transactions on Aerospace and Electronic Systems (ISSN 0018-9251), vol. AES-22, July 1986, p. 432-442.
- ABS: The problem of high-frequency radio direction finding (HFDF) has perennially been compounded by the interference effects of multicomponent wavefields. The wavefields are generally produced by ionospheric multipath or coherent interference from other transmitted signals. Because HFDF systems must operate on short duration signals and are usually restricted to limited antenna array apertures, modern techniques of superresolution spectral analysis are applied to resolve the constancy of multicomponent wavefields. This paper presents a performance comparison of five superresolution spectral algorithms in solving the HFDF wave interference problem. 86/07/00 87A14963
- UTTL: FMCW channel sounder with digital processing for measuring the coherence of wideband HF radio links
- AUTH: A/SALOUS, S.
- PAA: A/(Yamouk University, Irbid, Jordan) IEEE Proceedings, Part F - Communications, Radar and Signal Processing (ISSN 0143-7070), vol. 133, pt. F, no. 5, Aug. 1986, p. 456-462. Research supported by the Royal Aircraft Establishment of England.
- UTTL: Multipath propagation, and in particular, the interference between the ordinary and the extraordinary waves, places a fundamental constraint on the performance of wideband HF skywave radio links. Furthermore, the dispersive nature of ionospheric propagation causes phase nonlinearity and hence distortion of narrow pulses. In this paper, an FMCW wideband sounder built for the purposes of characterizing the channel is described. Spectral analysis of the audio output of the sounder via the FFT algorithm is shown to permit measurement of the amplitude/frequency function, the polarization bandwidth, the fade rate, the fade depth and the distortion of a narrow pulse, all for a desired isolated ionospheric propagation mode. The sounder was used to collect data over an oblique path in the UK. The results of applying the FFT processing technique to the experimental data are presented. 86/08/00 87A10140
- UTTL: Full wave solutions for electromagnetic scattering and depolarization in irregular stratified media
- AUTH: A/BAHAR, E.
- PAA: A/(Nebraska, University, Lincoln) Radio Science (ISSN 0048-6604), vol. 21, July-Aug. 1986, p. 543-550.
- ABS: Using the complete expansions of the fields and imposing the exact boundary conditions at the interfaces of an irregular stratified medium, Maxwell's equations are transformed into a rigorous set of coupled first-order differential equations for the wave amplitudes. This full wave approach is applied to a large class of propagation problems. Since these solutions account for specular point as well as diffuse scattering in a unified self-consistent manner, it is not necessary to apply a hybrid physical optics-perturbation approach to problems of rough surface scattering. The full wave solutions satisfy realizability, duality and reciprocity relationships in electromagnetic theory. They are invariant to coordinate transformations. 86/08/00 86A48934
- UTTL: Ship detection with high-resolution HF skywave radar
- AUTH: A/BARNUM, J. R.
- PAA: A/(SRI International Remote Measurements Laboratory, Menlo Park, CA) (IEEE and URSI, Special Session on HF Radar Remote Sensing Techniques, University of British Columbia, Vancouver, Canada, June 18-20, 1985) IEEE Journal of Oceanic Engineering (ISSN 0364-9059), vol. OE-11, April 1986, p. 196-209. Navy-supported research.
- ABS: This paper presents an overview of ship detection by high-frequency (HF) skywave backscatter over-the-horizon radar (OTHR). Ships have been detected at ranges of 2000 km or more by OTHR that uses sufficient resolution in the radar spatial and Doppler frequency domains. The HF sea-echo Doppler spectrum limits the target signal-to-clutter ratio (SCR), as a function of the ocean wave-height distribution, wind direction, radio frequency,

and ship target radial velocity. Maximum sea-clutter spectrum purity, and hence larger SCR, is achieved with the use of stable single-mode ionospheric propagation. Real-time measurement and interpretation of ionospheric propagation features therefore must guide the choice of other operating frequency. Experimental data recorded at the DMR/SRI Wide Aperture Research Facility (WARF) bi-static OTH in central California demonstrate reliable ship detection in the Northeast Pacific Ocean. WARF transmits 1-MW average effective radiated power, using a linear frequency-modulated continuous-wave (FMCW) waveform, and receives with a 2.88-km broadband array of vertical monopole element pairs. Swept bandwidths as high as 200 kHz have been used. Sufficient spectral resolution is achieved with a coherent integration time (CIT) of 12.8 s. Longer CIT, and autoregressive (AR) spectral analysis techniques such as Marple's algorithm, have been used to improve Doppler resolution. 86/04/00 86A43732

UTTL: Ionospheric convection signatures observed by DE 2 during northward interplanetary magnetic field

AUTH:

PAA:

A/HILLIS, R. A.; B/HANSON, W. B.; C/REIFF, P. M.; D/MINNINGHAM, J. D.

UTTL: Ionospheric convection signatures observed by DE 2 during northward interplanetary magnetic field

AUTH:

PAA:

A/HILLIS, R. A.; B/HANSON, W. B.; C/REIFF, P. M.; D/MINNINGHAM, J. D.

UTTL: Ionospheric convection signatures observed by DE 2 during northward interplanetary magnetic field

AUTH: A/HILLIS, R. A.; B/HANSON, W. B.; C/REIFF, P. M.; D/MINNINGHAM, J. D.

RPT#: AD-A177503 AFOSR-TR-87-0273 86/05/01 86A41025

UTTL: Prediction and diagnostics of high-latitude short-wave radio channels

AUTH: A/BLAGOVESHCHENSKI, D. V. IN: Forecasting applied to the ionosphere and conditions of radio-wave propagation (ABG-19926 08-46). Moscow, Izdatel'stvo Nauka, 1986, p. 138-152. In Russian.

ABS: The paper examines questions relating to the short-term and long-term prediction of conditions on high-latitude ionospheric radio channels using a system of short-wave paths. It is found that a system of several short-wave paths can be used for the operational prediction of magnetospheric and ionospheric disturbances and for the diagnostics of large-scale structures in the high-latitude ionosphere. 85/00/00 86A18945

UTTL: Connections between short-period (Pc 1) pulsations and ionospheric parameters

AUTH: A/MARZ, F.

PAA:

A/(Magyar Tudományos Akademia, Geodéziai és Geofizikai Kutató Intézet, Sopron, Hungary) (COSPAR, SCOSTEP, IAGA, and URSI, Symposium, 9th, and Topical Meeting on Magnetospheric and Ionospheric Plasmas, Graz, Austria, June 25-July 7, 1984) Advances in Space Research (ISSN 0273-1177), vol. 5, no. 4, 1985, p. 233-236.

ABS: Long-term changes in Pc 1 pulsations and their dependence on latitude are analyzed using data recorded by five stations in Finland during the IMS. The daily Pc 1 occurrences at each station are plotted against the daytime fOF2 parameter. It is found that while the averaged daily durations of morning (Pc 1) pulsations generally decrease with increasing critical frequency (electron density) of the F2-layer, three somewhat different trends can be distinguished for the five stations. It is also found that the indirect connection between mid-latitude Pc 1 pulsations and increased ionospheric absorption of LF radio waves following certain geomagnetic storms (Marz and Vero, 1977) holds in the case of high-latitude Pc 1 data. 85/00/00 85A41959

UTTL: An assessment of the application of in situ ion-density data from DMSP to modeling of transionospheric scintillation

AUTH: A/SECAN, JAMES A. CORP: Northwest Research Associates, Inc., Bellevue, Wash.

ABS: Modern military communication, navigation, and surveillance systems depend on reliable, noise free transionospheric radio frequency channels. They can be severely impacted by small scale electron density irregularities in the ionosphere which cause both phase and amplitude scintillation. Basic tools used in planning and mitigation schemes are climatological in nature and thus may greatly over- and underestimate the effects of scintillation in a given scenario. This report describes the first year of an investigation into the feasibility of using in situ observations of the ionosphere from the USAG DMSP satellite to calculate estimates of irregularity parameters which could be used to update scintillation models in near real-time. Methods for calculating

estimates of the height-integrated irregularity strength parameter (CkL) from DMSP SSIES data are described, and the results of parametric studies of the effects of errors or uncertainties in both the observed quantities and the methods used to calculate the estimates of CkL are presented.

RPT#: AD-A188919 NRRA-CR-87-RO17 AFGL-TR-87-0269 SR-1 87/08/15
88N19840

UTTL: Wideband HF (High Frequency) modeling and simulation
A/HOFFMEYER, J. A.; B/NESEMERGS, M. CORP: National Telecommunications and Information Administration, Boulder, Colo. Sponsored by Joint Test Directorate (JOT/E), Fort Huachuca, Ariz.

ABS: An elementary review of ionospheric propagation is presented, which summarizes the recent work in spread spectrum technology targeted for the HF radio band. Thereafter follows a short section devoted to additive distortions, namely noise and interference, also in the HF band. Past narrowband HF models are assessed; their background, old validation tests, and, to be quite specific, the NTIA/ITS development of the Watterson simulator. That laboratory tool, judged best by many, works in real time and offers accurate representations of HF channel bandwidths up to 10 to 12 kHz. In the present study, an extension to wideband models is attempted. Unfortunately, it suffers from an apparently serious shortage of measured data for the time-varying channel transfer function. A possible wideband model is hypothesized, conjectures are made, and questions are raised. One is left faced with a requirement for an experimental program to ascertain the wideband (1 MHz or more) characteristics of multipath fading for digital radio transmissions in the 2 to 30 MHz band and over radio propagation paths of interest.

RPT#: P888-116116 NTIA-87-221 87/07/00 88N17874

UTTL: A new approach to modeling and interpreting

electromagnetic sounding data
A/LEE, K. H. CORP: California Univ., Berkeley. Lawrence Berkeley Lab.

ABS: A major impediment to the application and acceptance of controlled-source electromagnetics has been the difficulty of processing, displaying, and interpreting the data. Our goal has been to develop a method for imaging the subsurface conductivity distribution. We have sought a representation that would provide some direct visualization of the subsurface conductivity contrasts that give rise to the observed or calculated fields. We have discovered a new method for calculating the electromagnetic response of inhomogeneous conducting media that is not only computationally efficient but promises to provide the inverse solutions we have long sought. The method can be used to: (1) model EM problems (the forward solution); with a speed at least two orders of magnitude faster than conventional methods; and (2) provide

reflectivity images of subsurface conductivity contrasts similar to those obtained in reflection seismic methods.
RPT#: DE88-000460 LBL-23544 CNR-871164-1 87/05/00 88N12715

UTTL: Multi-technique study of ionospheric structures causing degradation in trans-ionospheric communications systems

AUTH: A/BASU, SUNANDA; B/DHERTY, PATRICIA; C/MACKENZIE, EILEEN; D/HAGAN, M. P. CORP: Emanuel Coll., Boston, Mass.

ABS: Multiple diagnostics have been used at different latitude regimes of the globe to probe large and small scale ionospheric structures which cause degradation in trans-ionospheric communication systems. It was determined that the equatorial anomaly crest had the most disturbed F-region irregularity environment giving rise to saturated GHz scintillation and phase scintillations as large as 16 radians at 244 MHz. At the magnetic equator a host of techniques during the Project Concor rocket campaign in Peru established that the largest GHz scintillations maximize in association with extended 3m backscatter plane structures and that speed-receiver scintillation measurements yield irregularity drift velocities in fairly good agreement with the 50 MHz radar interferometer drifts. By combining in-situ data of irregularities with scintillations, a new class of extended VHF scintillation producing irregularities was isolated known as bottomside sinusoidal.

RPT#: AD-A183542 AFGL-TR-87-0148 87/04/20 87N29733

UTTL: Analytic description of the electromagnetic wave field for effective refractive indices with an infinity
A/LUNDBERG, BENGT CORP: Uppsala Ionospheric Observatory (Sweden). Submitted for publication

ABS: Formulas describing the wave pattern in the linear regime of an electromagnetic wave impinging vertically upon a horizontally stratified ionosphere, where the effective refractive index squared has an infinity, a first order pole, are derived within a uniform approximation employed in wave propagation problems. The formulas are also valid at wave reflection and transition points of the problem. Monotonically increasing electron density with height in the relevant region of the ionosphere is treated. Applications of the formulas derived are the X mode wave when the wave frequency is higher than the electron gyrofrequency and the O mode wave when the wave frequency is lower than the electron gyrofrequency.

RPT#: UIO-SR-87-04 ISSN-0349-2699 ETN-87-90082 87/02/00
87N27095

UTTL: The multipath and fading profile of the high latitude meteor burst communication channel

A/WEITZEN, JAY A. CORP: Signatron, Inc., Lexington, Mass.

ABS: High latitude propagation phenomenon such as scatter from the aurora and sporadic-E propagation can alter the

communication characteristics of the high latitude meteor communication channel. This report describes the results of several experiments conducted for the purpose of characterizing the fading and multipath profile of the high latitude meteor communication channel. The effect of high latitude meteor propagation phenomena on the capacity and reliability of meteor burst communications is discussed.

RPT#: AD-A174718 A447-15 RADC-TR-86-166 86/10/00 87N19559

UTTL: Multi-mode multistatics for passive/active airborne surveillance

AUTH: A/GRONNIK, ROBERT F. CORP: Rome Air Development Center, Griffiss AFB, N.Y. In AGARD Multifunction Radar for Airborne Applications 1 p (SEE N87-18721 11-32)

ABS: The increasing performance demands for air surveillance assets, as well as the necessity for continued surveillance operations in the presence of enemy jamming anti-radiation missile (ARM) attacks, have increased interest in passive surveillance. In particular multi-mode passive/active multistatic sensing. The use of noncooperative radiation as illuminators of opportunity combined with passive surveillance electromagnetic support measurement (ESM) sensors opens new horizons to multistatic surveillance from a passive airborne platform. Research and field tests have been conducted on ESM augmented bistatics as well as noncooperative multistatics which support the development of airborne multi-mode passive surveillance technology. This work has been conducted under such programs as the Bistatic Enhanced Altimeter Detection (BEAD) and the noncooperative Multistatic Passive Coherent Location (PCL). Both BEAD and PCL technology directly support the receiver, signal processing and target location/tracking operations necessary for passive surveillance. The demonstrated technologies for EM interference rejection and multistatic multi-target tracking and location under PCL provide a promising performance benchmark for passive surveillance in the presence of a complex electromagnetic environment. Passive receiver intercept performance under BEAD has provided a receiver design baseline for both look-down and look-up surveillance applications. The technologies under development in BEAD and PCL are presented along with the field test results and the sensor concepts. In particular, spin-off data such as bistatic look-down clutter, noise-floor limitation of noncooperative multistatics and sensitivity limitations set by passive surveillance using signal intercept techniques and illuminators of opportunity are provided. 86/07/00 87N18726

UTTL: UHF/SHF SATCOM propagation and system design

AUTH: A/JOHNSON, ALLEN L. CORP: Air Force Wright Aeronautical Labs., Wright-Patterson AFB, Ohio. In AGARD and Special Course on Interaction of Propagation and Digital Transmission Techniques 18 p (SEE N87-18703 11-32)

ABS: One year after the launch of the Russian Sputnik, the Americans orbited the world's first active communications

satellite, SCORE. The communications planners hoped that the line-of-sight communications through satellites would overcome the various propagation problems plaguing long-distance High Frequency (HF) communications. The communications satellite did overcome many of the traditional HF problems but due to the law of conservation of difficulty, a new set of propagation problems emerged. This section deals with some of those problems. A satellite orbiting at approximately 19,200 nautical mile altitude rotates at the same rate as the Earth and, if in an equatorial plane, appears to remain fixed over one point on the Earth. The equatorial synchronous satellite is discussed. The Earth-to-satellite link experiences a variety of propagation effects such as free space loss, attenuation, polarization changes, refraction, and delay as a result of the physics of the link and the normal Earth's atmosphere. These are also discussed. 86/10/00 87N18710

UTTL: Transverse resonances of Earth-ionosphere wave guide in auroral region

AUTH: A/SMIRNOV, V. S.; B/DSTAPENKO, A. A. CORP: Joint Publications Research Service, Arlington, Va. In its USSR Report: Earth Sciences (UPRS-UES-86-007) 1 p (SEE N87-12946 04-42)

ABS: Contemporary studies of low frequency radiation have defined the precise structure of such signals in the auroral region. A study is reported of spectral and polarized features of transverse resonances and the relationship to ionospheric parameters. So-called Schumann resonances were studied with frequencies from a few to tens of Hz. Strong attenuation in that range virtually excludes wave interference and makes it difficult to generate global resonances in the kilohertz frequency range. Thus, modulations in those frequencies are local in nature. They make it possible to use a plane model of the earth-ionosphere wave guide and allow direct determination of the wave equation, which is discussed. Results show that at high latitude degeneration effects are manifested in periods of leakage of hard particles when the ionosphere is at low altitudes; soft particles are found when the ionosphere limits are at higher altitudes. A stepped mathematical model gave a rough approximation of actual ionization. Ordinary and extraordinary modes were found to correspond to waves of left and right polarization, respectively, with relatively low values for particle disintegration. Theoretical values correlated well with experimental data on low-frequency radiation wave. 86/09/10 87N12956

UTTL: Observations of vertical winds and the origin of thermospheric gravity waves launched by auroral substorms and westward travelling surges

AUTH: A/PEES, D. CORP: University Coll., London (England). In NASA, Goddard Space Flight Center Thermosphere Dynamics Workshop, Volume 2 p 297-322 (SEE N86-29301 20-42)

ABS:

Several sequences of observations of strong vertical winds in the upper atmosphere are discussed, in conjunction with models of the generation of such winds. In the auroral oval, the strongest upward winds are observed in or close to regions of intense auroral precipitation and strong ionospheric currents. The strongest winds, of the order of 100 to 200 m/sec are usually upward, and are both localized and of relatively short duration (10 to 20 min). In regions adjacent to those displaying strong upward winds, and following periods of upward winds, downward winds of rather lower magnitude (40 to about 80 m/sec) may be observed. Strong and rapid changes of horizontal winds are correlated with these rapid vertical wind variations. Considered from a large scale viewpoint, this class of strongly time dependent winds propagate globally, and may be considered to be gravity waves launched from an auroral source. During periods of very disturbed geomagnetic activity, there may be regions within and close to the auroral oval where systematic vertical winds of the order of 50 m/sec will occur for periods of several hours. Such persistent winds are part of a very strong large scale horizontal wind circulation set up in the polar regions during a major geomagnetic disturbance. This second class of strong horizontal and vertical winds corresponds more to a standing wave than to a gravity wave, and it is not as effective as the first class in generating large scale propagating gravity waves and correlated horizontal and vertical oscillations. A third class of significant (10 to 30 m/sec) vertical winds can be associated with systematic features of the average geomagnetic energy and momentum input to the polar thermosphere, and appear in statistical studies of the average vertical wind as a function of Universal Time at a given location. 86/06/00 86N29325

UTTL: Transfer function analysis of thermospheric perturbations

AUTH: A/MAYR H. G.; B/HARRIS, I.; C/VAROSI, F.; D/HERRERO, F. A.; E/SPENCER, N. W.

PAA: C/(Science Applications Research, Riverdale, Md.) CORP: National Aeronautics and Space Administration, Goddard Space Flight Center, Greenbelt, Md. In its Thermosphere Dynamics Workshop, Volume 2 p 221-231 (SEE N86-29301 20-42)

ABS: Applying perturbation theory, a spectral model in terms of vectors spherical harmonics (Legendre polynomials) is used to describe the short term thermospheric perturbations originating in the auroral regions. The source may be Joule heating, particle precipitation or ExB ion drift-momentum coupling. A multiconstituent atmosphere is considered, allowing for the collisional momentum exchange between species including Ar, O₂, N₂, O, He and H. The coupled equations of energy, mass and momentum conservation are solved simultaneously for the major species N₂ and O. Applying homogeneous boundary conditions, the integration is carried out from the Earth's surface up to 700 km. In the analysis, the spherical

harmonics are treated as eigenfunctions, assuming that the Earth's rotation (and prevailing circulation) do not significantly affect perturbations with periods which are typically much less than one day. Under these simplifying assumptions, a given a particular source distribution in the vertical, a two dimensional transfer function is constructed to describe the three dimensional response of the atmosphere. In the order of increasing horizontal wave numbers (order of polynomials), this transfer function reveals five components. To compile the transfer function, the numerical computations are very time consuming (about 100 hours on a VAX for one particular vertical source distribution). However, given the transfer function, the atmospheric response in space and time (using Fourier integral representation) can be constructed with a few seconds of a central processing unit. This model is applied in a case study of wind and temperature measurements on the Dynamics Explorer B, which show features characteristic of a ringlike excitation source in the auroral oval. The data can be interpreted as gravity waves which are focused (and amplified) in the polar region and then are reflected to propagate toward lower latitudes. 86/06/00 86N29319

UTTL: Statistics of auroral radio absorption in relation to prediction models

AUTH: A/HARGREAVES, J. K.; B/FEELEY, M. T.; C/BURNS, C. J. CORP: Lancaster Univ. (England). In AGARD Propagation Effects on Military System in the High Latitude Region 10 p (SEE N86-27531 18-32) Sponsored in part by Royal Aircraft Establishment, Farnborough, England, and by the Science and Engineering Research Council

ABS: The prediction of HF propagation conditions at high latitude requires a knowledge of the statistics of radio absorption in the auroral ionosphere, a highly variable phenomenon depending on local time, magnetic latitude, season and solar activity. Data from riometer stations may be compiled to provide statistics on the auroral radio absorption. Questions regarding the probability distribution and variations with latitude, solar and geomagnetic activity, and longitude are considered. Difficulties concerning the smallest absorption values are pointed out. 85/11/00 86N27557

UTTL: The variability and predictability of the main F-region trough determined using digital ionospheric sounder data

AUTH: A/RODGER, A. S.; B/DUDENY, J. R. CORP: British Antarctic Survey, Cambridge (England) In AGARD Propagation Effects on Military Systems in the High Latitude Region 11 p (SEE N86-27531 18-32)

ABS: The main F-region (or mid-latitude) electron density trough occurs near $\lambda_{\text{min}} = 60$ degrees and is associated with significant meridional gradients in electron concentration. Despite many satellite studies of the trough, the causes of the variability of its shape as a

- function of time, geomagnetic and solar activity is still poorly understood. This is illustrated by the large discrepancies between the various empirical formulae that have been developed to estimate the trough latitude for specified geomagnetic conditions. These problems arise partly because satellite data cannot be used to differentiate adequately between spatial and temporal variations. In 1981, a new and powerful research tool for trough studies has become available. The observations from this equipment have significantly improved our understanding of several features of trough morphology and in particular the causes of some of the variability. The four aspects of this variability that are discussed here are the orientation of the poleward edge of the trough with respect to Halley; the variation of the maximum plasma frequency of the poleward edge; the signature of the Harang discontinuity in the poleward edge and the latitudinal movement of the poleward edge as a function of time and geomagnetic activity. A framework is described for incorporating these aspects of trough morphology into a realistic model for predicting the location and maximum plasma density of the poleward edge as a function of time and the prevailing geomagnetic conditions. 85/11/00 86N27555
- PAA: C/(SRI International Corp., Menlo Park, Calif.) CORP: Rutherford High Energy Lab., Chilton (England). In AGARD Propagation Effects on Military Systems in the High Latitude Region 14 p (SEE N86-27531 18-32)
- ABS: Sky-wave radars provide a means of ocean surveillance with a ground-wave radar. However, the ionosphere introduces a number of important propagation limitations. Firstly, it is necessary to provide illumination of the areas of interest, which may place restrictions on radar siting and periods of operation. Then, backscattered signals must have sufficient amplitude to provide adequate discrimination above the naturally occurring and interference backgrounds. A radar measures time-of-flight and such information needs transforming to equivalent ground range in terms of the prevailing ionospheric path. Finally, ionospheric motions create Doppler shifts and spreads of the returned signals which prevent spectral resolution of Bragg scattered components. The high-latitude ionosphere is characterised by features which exhibit marked spatial and temporal variability. Specific problems are discussed and possible ways of alleviating some of these considered. 85/11/00 86N27549
- UTTL: Propagation effects on satellite-borne synthetic aperture radars
- AUTH: A/RINDO, C. L.; B/DWEN, J. CORP: SRI International Corp., Menlo Park, Calif. In AGARD Propagation Effects on Military Systems in the High Latitude Region 1 p (SEE N86-27531 18-32)
- ABS: A numerical Synthetic Aperture Radar (SAR) simulator is discussed. The simulator can generate and process image segments with full or partial corrections for range walk and quadratic phase-error correction. The simulations also include the effects of coherent target speckle, which is important in assessing SAR image quality. Results show that moderate auroral-zone scintillation will degrade an image to about the same level as any undisturbed image processed with only partial range-walk compensation. Thus, propagation effects are undoubtedly present in many of the SEASAT-A high-latitude images, but the degradation is comparable to other distortions introduced in the processing itself. Phase error compensation is effective, but amplitude scintillation is also important for larger disturbances. Ramifications of SAR imaging are discussed. 85/11/00 86N27539
- UTTL: Media effects on systems in the high latitude region
- AUTH: A/THRANE, E. V. CORP: Norwegian Defence Research Establishment, Kjeller. In AGARD Propagation Effects on Military Systems in the High Latitude Region 16 p (SEE N86-27531 18-32)
- ABS: The effects of the transmission medium on radio systems in the high latitude regions are reviewed. First, some general properties of propagation media are discussed.

UTTL: Observations of very high latitude ionospheric irregularities with the Good Bay HF radar

AUTH: A/GREENWALD, R. A.; B/BAKER, K. B. CORP: Johns Hopkins Univ., Laurel, Md. In AGARD Propagation Effects on Military Systems in the High Latitude Region 17 p (SEE N86-27531 18-32)

ABS: The Goose Bay HF radar is a sophisticated instrument capable of providing detailed information on very high latitude E and F region ionospheric electron density irregularities which act as a source of clutter on OTH radar systems. Through the use of two parallel phased array antennas, this instrument is able to image the location of these irregularities within a three-dimensional volume covering much of northeastern Canada and Greenland. It is also capable of following the temporal variability of these irregularities as well as determining unambiguously the Doppler shift and broadening of radar signals scattered by them. Initial results with a single phased array antenna which represent typical examples of the spatial intensity distribution of these irregularities at different local times are presented. Examples of Doppler spectra of the irregularities at different local times are given. Data of this type are of appreciable value in ascertaining the techniques that must be utilized to improve clutter mitigation on high latitude radar systems. 85/11/00 86N27553

UTTL: Ionospheric factors affecting the performance of HF sky-wave sea-state radars at high latitudes

AUTH: A/BRADLEY, P. A.; B/GIBSON, A. J.; C/SCHLUBOHM, J. C.; D/WESTOVER, D. E.

followed by brief descriptions of the effects on radio waves of the Earth's surface, the troposphere and the ionosphere in high latitudes. General principles are illustrated by examples from observations and model calculations. 85/11/00 86N27533

UTTL: Propagation Effects on Military Systems in the High Latitude Region
 AUTH: A/SOICHER, H.
 PAA: A/(Army Communications-Electronics Command, Fort Monmouth, N.J.)
 CORP: Advisory Group for Aerospace Research and Development, Neuilly-Sur-Seine (France).
 AGARD-CP-382 ISBN-92-835-0383-X AD-A166595 85/11/00 86N27531

UTTL: Technical evaluation report on the Electromagnetic Wave Propagation Panel Symposium on Propagation Effects on Military Systems in the High Latitude Region
 AUTH: A/HUNSUCKER, R. D. CORP: Advisory Group for Aerospace Research and Development, Neuilly-Sur-Seine (France).
 ABS: Propagation effects on military systems in the high latitude region were examined. Topics discussed include: experimental studies of ionospheric irregularities and regular structure, results of ionospheric modification (HF heating) experiments, theoretical studies of ionospheric irregularity formation, global survey of ground conductivity, disturbance modeling studies, high latitude effects on HF radio communication, transionospheric communications, satellite synthetic aperture radar (SAR), HF radio broadcasting, spatially adaptive propagation, HF digital, Skywave HF sea state radar, and meteor burst communication.
 AGARD-AR-218 ISBN-92-835-1514-7 AD-A166595 85/11/00 86N24903

UTTL: Adaptive antenna nulling performance in a dispersive propagation medium
 AUTH: A/ISARAKI, R. Y.; B/TSUI, E. T. CORP: Maxim Technologies, Inc., Santa Clara, Calif.
 ABS: The Signal-to-Interference plus Noise Ratio (SINR) performance of a Generic Multi-Beam Antenna (MBA) and a Thinned Phased Array Antenna (TPAA) is evaluated for multiple jammer scenarios including the effect of angle-of-arrival distortion of the jamming signals caused by a stratified propagation media. The analysis is based on computer modeling of the antenna configurations using the optimal Wiener solution for the adaptive weight calculations. Statistically distributed SINR values in fading are obtained by applying the equivalent effect of independent two-dimensional sample functions of spatially varying flat fading at the antenna aperture.
 AD-A162708 AD-E301864 MT-TR-85025 DWA-TR-85-75 85/02/15 86N21739

REPORT DOCUMENTATION PAGE											
1. Recipient's Reference	2. Originator's Reference	3. Further Reference	4. Security Classification of Document								
	AGARD-LS-162	ISBN 92-835-0478-X	UNCLASSIFIED								
5. Originator	Advisory Group for Aerospace Research and Development North Atlantic Treaty Organization 7 rue Ancelle, 92200 Neuilly sur Seine, France										
6. Title	MEDIA EFFECTS ON ELECTRONIC SYSTEMS IN THE HIGH LATITUDE REGION										
7. Presented at											
8. Author(s)/Editor(s)	Various		9. Date								
			September 1988								
10. Author's/Editor's Address	Various		11. Pages								
			228								
12. Distribution Statement	This document is distributed in accordance with AGARD policies and regulations, which are outlined on the Outside Back Covers of all AGARD publications.										
13. Keywords/Descriptors	<table border="0"> <tr> <td>Latitude</td> <td>Target acquisition</td> </tr> <tr> <td>Polar regions</td> <td>Telecommunication</td> </tr> <tr> <td>Electromagnetic wave transmission</td> <td>Lower atmosphere</td> </tr> <tr> <td>Radar</td> <td></td> </tr> </table>			Latitude	Target acquisition	Polar regions	Telecommunication	Electromagnetic wave transmission	Lower atmosphere	Radar	
Latitude	Target acquisition										
Polar regions	Telecommunication										
Electromagnetic wave transmission	Lower atmosphere										
Radar											
14. Abstract	<p>▶ With the NATO northern flank nations (in both the European and North American sectors) situated in the high-latitude region, with NATO air routes across the Atlantic traversing that region, and with surveillance and early-warning systems looking in the direction of the region, the propagation characteristics of the high-latitude region are of critical importance to the mission of the alliance in the areas of communications, navigation and surveillance.</p> <p>The advent of new systems operating at high latitudes in the field of detection, navigation and communications and the new experiments at high latitudes ranging from incoherent scatter studies to satellites for studying high latitude structure make it of considerable importance to relate the advances in high latitude studies to military systems.</p> <p>The Lecture Series directs its attention to propagation problems and solutions for many systems. The topics include satellite communications over polar and auroral latitudes, over-the-horizon radar, low frequency propagation under high latitude conditions, remote sensing of targets and high latitude regions by active and passive EM systems and HF communications at auroral and polar latitudes. Unique lower atmospheric effects and multipath problems of importance at high latitudes are discussed.</p> <p style="text-align: right;">(12/71) = 12/71 12/71</p>										

<p>AGARD Lecture Series No.162 Advisory Group for Aerospace Research and Development, NATO MEDIA EFFECTS ON ELECTRONIC SYSTEMS IN THE HIGH LATITUDE REGION Published September 1988 228 pages</p> <p>With the NATO northern flank nations (in both the European and North American sectors) situated in the high-latitude region, with NATO air routes across the Atlantic traversing that region, and with surveillance and early-warning systems looking in the direction of the region, the propagation characteristics of the high-latitude region are of critical importance to the mission of the alliance in the areas of communications, navigation and surveillance.</p> <p>P.T.O</p>	<p>AGARD-LS-162</p> <p>Latitude Polar regions Electromagnetic wave transmission Radar Target acquisition Telecommunication Lower atmosphere</p>	<p>AGARD Lecture Series No.162 Advisory Group for Aerospace Research and Development, NATO MEDIA EFFECTS ON ELECTRONIC SYSTEMS IN THE HIGH LATITUDE REGION Published September 1988 228 pages</p> <p>With the NATO northern flank nations (in both the European and North American sectors) situated in the high-latitude region, with NATO air routes across the Atlantic traversing that region, and with surveillance and early-warning systems looking in the direction of the region, the propagation characteristics of the high-latitude region are of critical importance to the mission of the alliance in the areas of communications, navigation and surveillance.</p> <p>P.T.O</p>	<p>AGARD-LS-162</p> <p>Latitude Polar regions Electromagnetic wave transmission Radar Target acquisition Telecommunication Lower atmosphere</p>
<p>AGARD Lecture Series No.162 Advisory Group for Aerospace Research and Development, NATO MEDIA EFFECTS ON ELECTRONIC SYSTEMS IN THE HIGH LATITUDE REGION Published September 1988 228 pages</p> <p>With the NATO northern flank nations (in both the European and North American sectors) situated in the high-latitude region, with NATO air routes across the Atlantic traversing that region, and with surveillance and early-warning systems looking in the direction of the region, the propagation characteristics of the high-latitude region are of critical importance to the mission of the alliance in the areas of communications, navigation and surveillance.</p> <p>P.T.O</p>	<p>AGARD-LS-162</p> <p>Latitude Polar regions Electromagnetic wave transmission Radar Target acquisition Telecommunication Lower atmosphere</p>	<p>AGARD Lecture Series No.162 Advisory Group for Aerospace Research and Development, NATO MEDIA EFFECTS ON ELECTRONIC SYSTEMS IN THE HIGH LATITUDE REGION Published September 1988 228 pages</p> <p>With the NATO northern flank nations (in both the European and North American sectors) situated in the high-latitude region, with NATO air routes across the Atlantic traversing that region, and with surveillance and early-warning systems looking in the direction of the region, the propagation characteristics of the high-latitude region are of critical importance to the mission of the alliance in the areas of communications, navigation and surveillance.</p> <p>P.T.O</p>	<p>AGARD-LS-162</p> <p>Latitude Polar regions Electromagnetic wave transmission Radar Target acquisition Telecommunication Lower atmosphere</p>

<p>The advent of new systems operating at high latitudes in the field of detection, navigation and communications and the new experiments at high latitudes ranging from incoherent scatter studies to satellites for studying high latitude structure make it of considerable importance to relate the advances in high latitude studies to military systems.</p> <p>The Lecture Series directs its attentions to propagation problems and solutions for many systems. The topics include satellite communications over polar and auroral latitudes, over-the-horizon radar, low frequency propagation under high latitude conditions, remote sensing of targets and high latitude regions by active and passive EM systems and HF communications at auroral and polar latitudes. Unique lower atmospheric effects and multipath problems of importance at high latitudes are discussed.</p> <p>This material in this publication was assembled to support a Lecture Series under the sponsorship of the Electromagnetic Wave Propagation Panel of AGARD and the Consultant and Exchange Programme of AGARD presented on 29-30 September 1988 in Ottawa, Canada, on 24-25 October 1988 in Geilo, Norway and on 27-28 October 1988 in London, United Kingdom.</p> <p>ISBN 92-835-0478-X</p>	<p>The advent of new systems operating at high latitudes in the field of detection, navigation and communications and the new experiments at high latitudes ranging from incoherent scatter studies to satellites for studying high latitude structure make it of considerable importance to relate the advances in high latitude studies to military systems.</p> <p>The Lecture Series directs its attentions to propagation problems and solutions for many systems. The topics include satellite communications over polar and auroral latitudes, over-the-horizon radar, low frequency propagation under high latitude conditions, remote sensing of targets and high latitude regions by active and passive EM systems and HF communications at auroral and polar latitudes. Unique lower atmospheric effects and multipath problems of importance at high latitudes are discussed.</p> <p>This material in this publication was assembled to support a Lecture Series under the sponsorship of the Electromagnetic Wave Propagation Panel of AGARD and the Consultant and Exchange Programme of AGARD presented on 29-30 September 1988 in Ottawa, Canada, on 24-25 October 1988 in Geilo, Norway and on 27-28 October 1988 in London, United Kingdom.</p> <p>ISBN 92-835-0478-X</p>
<p>The advent of new systems operating at high latitudes in the field of detection, navigation and communications and the new experiments at high latitudes ranging from incoherent scatter studies to satellites for studying high latitude structure make it of considerable importance to relate the advances in high latitude studies to military systems.</p> <p>The Lecture Series directs its attentions to propagation problems and solutions for many systems. The topics include satellite communications over polar and auroral latitudes, over-the-horizon radar, low frequency propagation under high latitude conditions, remote sensing of targets and high latitude regions by active and passive EM systems and HF communications at auroral and polar latitudes. Unique lower atmospheric effects and multipath problems of importance at high latitudes are discussed.</p> <p>This material in this publication was assembled to support a Lecture Series under the sponsorship of the Electromagnetic Wave Propagation Panel of AGARD and the Consultant and Exchange Programme of AGARD presented on 29-30 September 1988 in Ottawa, Canada, on 24-25 October 1988 in Geilo, Norway and on 27-28 October 1988 in London, United Kingdom.</p> <p>ISBN 92-835-0478-X</p>	<p>The advent of new systems operating at high latitudes in the field of detection, navigation and communications and the new experiments at high latitudes ranging from incoherent scatter studies to satellites for studying high latitude structure make it of considerable importance to relate the advances in high latitude studies to military systems.</p> <p>The Lecture Series directs its attentions to propagation problems and solutions for many systems. The topics include satellite communications over polar and auroral latitudes, over-the-horizon radar, low frequency propagation under high latitude conditions, remote sensing of targets and high latitude regions by active and passive EM systems and HF communications at auroral and polar latitudes. Unique lower atmospheric effects and multipath problems of importance at high latitudes are discussed.</p> <p>This material in this publication was assembled to support a Lecture Series under the sponsorship of the Electromagnetic Wave Propagation Panel of AGARD and the Consultant and Exchange Programme of AGARD presented on 29-30 September 1988 in Ottawa, Canada, on 24-25 October 1988 in Geilo, Norway and on 27-28 October 1988 in London, United Kingdom.</p> <p>ISBN 92-835-0478-X</p>